Advances in Fatigue Crack Closure Measurement and Analysis

Second Volume

R. C. McClung
J. C. Newman
EDITORS

ASTM STP 1343

STP 1343

Advances in Fatigue Crack Closure Measurement and Analysis: Second Volume

R. C. McClung and J. C. Newman, Jr., Editors

ASTM Stock #: STP1343

ASTM
100 Barr Harbor Drive
West Conshohocken, PA 19428-2959

Library of Congress Cataloging-in-Publication Data

Symposium on Advances in Fatigue Crack Closure Measurement and Analysis (2nd: 1997: San Diego, Calif.).
Advances in fatigue crack closure measurement and analysis/R.C. McClung and J.C. Newman, Jr., editors.
(STP; 1343)
"ASTM stock #: STP1343."
ISBN 0-8031-2611-5
1. Materials–Fatigue Congresses. 2. Fracture mechanics Congresses. 3. Plasticity Congresses I. McClung, R. C. (R. Craig), 1959– . II. Newman, J. C. III. Title. IV. Series: ASTM special publication; 1343
TA418.38.S88 1997
620.1'126–dc21

Peer Review Policy

Each paper published in this volume was evaluated by two peer reviewers and at least one editor. The authors addressed all of the reviewers' comments to the satisfaction of both the technical editor(s) and the ASTM Committee on Publications.

The quality of the papers in this publication reflects not only the obvious efforts of the authors and the technical editor(s), but also the work of the peer reviewers. In keeping with long-standing publication practices, ASTM maintains the anonymity of the peer reviewers. The ASTM Committee on Publications acknowledges with appreciation their dedication and contribution of time and effort on behalf of ASTM.

Printed in Toronto, Ont., Canada
August 1999

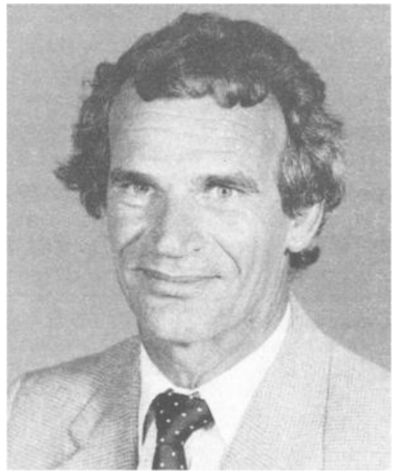

Dedication
of
ASTM STP 1343
to
Dr. Wolf Elber

Wolf Elber was born on 2 July, 1941, in Quellendorf, Germany. He earned both Bachelor of Science and Doctorate degrees in Civil Engineering from the University of New South Wales, Australia. While working on his doctorate, he discovered the phenomenon of plasticity-induced fatigue crack closure, which has revolutionized fatigue crack growth analyses. The publication of this pioneering work has become the most cited paper in the discipline.

Elber accepted a research position in 1969 at the Deutsche Forschungs-und Versuchsanstalt für Luft-und Raumfahrt, the German equivalent of NASA; and in 1970, accepted a National Research Council Postdoctoral Fellowship to continue his work on crack closure at the NASA Langley Research Center. He became a permanent NASA employee in 1972 and has served in several positions including the head of the Fatigue and Fracture Branch. Elber has served as the Director of the U.S. Army Research Laboratory Vehicle Technology Center (formally the Vehicle Structures Directorate) since October of 1992. He previously served as Director of the Aerostructures Directorate for the Army Aviation Command. His awards include the NASA Exceptional Scientific Achievement Award as well as numerous Special Achievement Awards.

The symposium marked the 30th anniversary of his discovery of fatigue crack closure. Wolf was presented with an ASTM Award of Appreciation at the symposium, "In recognition of his pioneering work on fatigue crack closure, for many significant contributions that the concept has made to fatigue crack growth research and applications, and the development of ASTM test method to measure crack closure."

FOREWORD

The Second Symposium on Advances in Fatigue Crack Closure Measurement and Analysis was held 12–13 November 1997 in San Diego, CA. The symposium was sponsored by ASTM Committee E8 on Fatigue and Fracture and was held in conjunction with the 10–12 November standards development meetings of that committee.

The symposium was chaired by R. Craig McClung, with Southwest Research Institute, San Antonio, TX and James C. Newman, Jr., at the NASA Langley Research Center in Hampton, VA. These men also served as editors of this resulting publication.

CONTENTS

OVERVIEW

The discovery of the phenomenon of plasticity-induced fatigue crack closure by Elber was truly a landmark event in the study of fatigue crack growth (FCG) and the development of practical engineering methods for fatigue life management. Subsequent research identified other contributing mechanisms for crack closure, including crack surface roughness and oxide debris. Fatigue crack closure is now understood to be an intrinsic feature of crack growth behavior that must be considered to understand or treat many FCG problems, although closure may not be an issue in all problems and does not always provide a complete explanation of crack growth behavior.

The first ASTM International Symposium on Fatigue Crack Closure was held in Charleston, South Carolina in May 1986, nearly twenty years after the Elber discovery. The large symposium audience and the thirty-nine papers in the resulting Special Technical Publication (*Mechanics of Fatigue Crack Closure, ASTM STP 982*) served effectively to document both the perspectives of that day and the high level of research interest in the topic.

As the thirtieth anniversary of the Elber discovery approached, the strong, continuing international interest in crack closure prompted the organization of another ASTM symposium. The Second Symposium on Advances in Fatigue Crack Closure Measurement and Analysis, sponsored by ASTM Committee E8 on Fatigue and Fracture, was held in San Diego, California on 12–13 November 1997. An international audience numbering over sixty-five persons heard thirty papers contributed by authors from twelve different countries, with more than half of the papers originating from outside the United States. This STP volume contains peer-reviewed manuscripts for twenty-seven of those presentations, plus one peer-reviewed paper that could not be presented at the symposium.

Closure researchers represented on the symposium program and in this volume employed a number of tools to conduct their investigations, including a variety of both experimental and analytical/numerical techniques. However, this STP volume is not segregated by research tool or technique, as is often the case. Instead, the STP is organized according to the particular class of closure problems or questions being addressed. Experiment and analysis are both shown to provide valuable, often complementary, perspectives on common issues. The experimentalist reader will be well-served by a careful study of the analysis papers, and the analyst reader should likewise pay close attention to the evidence published by the experimentalists.

Fundamental Studies

The first two papers address fundamental questions about the very existence of plasticity-induced crack closure and the adequacy of closure concepts to explain a wide range of growth behaviors. Since the first symposium on crack closure (*ASTM STP 982*), the question of plasticity-induced crack closure under pure "plane strain" conditions has been actively discussed, analyzed, and disputed. Continuum mechanics models and analyses under plane strain conditions exhibit closure but some recent dislocation models do not show closure. Riemelmoser and Pippan develop a discrete dislocation model that shows crack face contact in plane strain due to these dislocations.

Elber's effective stress intensity factor range was a simple modification of Paris's stress intensity factor range by replacing the minimum stress intensity factor with the crack opening stress intensity factor. But a number of attempts have been made to relate crack tip damage to a more fundamental parameter, such as the cyclic hysteresis energy. Ranganathan analyzed crack growth rate data on an aluminum alloy using the traditional crack closure concept and an energy-based method. Most of the crack growth effects attributed to closure could be explained using the energy concept.

Experimental Characterization of Closure

Among the most active current topics in closure studies are the optimum experimental method to measure crack opening levels and the correct way to incorporate this closure information in the effective value of the stress intensity factor range. Several researchers have observed previously that conventional remote measurement techniques indicate very high levels of closure near threshold, and the resulting conventionally calculated values of the effective stress intensity factor range appear to be inconsistent with near-threshold growth rate behavior. As a result, some have suggested that alternative experimental methods should be employed, or that some portion of the stress range below the crack opening level should be included in the effective stress range. Several authors in this volume have addressed this question by experimentally measuring closure and growth rates or by analyzing the mechanics of the fatigue crack and simulating experimental techniques.

Pippan, Riemelmoser, and Bichler employ simple models and experiments to evaluate the measurability of closure from asperity and wedge-like contact and the influence of closure on crack-tip shielding. Bray and Donald investigate the use of the new adjusted compliance ratio (ACR) technique to define an effective stress intensity factor range that is larger than the conventional value based on K_{open}, adding an additional K_{max} term to correlate FCG rate data. Donald and Phillips use the ACR method to analyze data from a previous ASTM round-robin on closure measurement methods and compare the results with the conventional closure analysis approaches. Graham, Tregoning, and Zhang also compare the ACR and current ASTM methods of characterizing closure from their tests on Ti-6Al-4V. McClung and Davidson use finite element closure analysis and high-resolution experiments to study crack-tip deformation above and below the crack-tip opening stress and to quantify the relationship between remote closure measurements and near-tip deformation, evaluating both the ACR and ASTM methods. Newman employs his modified Dugdale closure model to perform a similar study of crack-tip deformation and experimental methods, evaluating the contributions of stresses below the opening level to crack-tip damage and simulating various experimental measurement techniques. Sutton et al. describe a new high-resolution closure measurement system using computer vision and a far-field microscope to interrogate the near-tip region. In a companion paper, Riddell et al. use the new system to investigate closure in the near-threshold regime, in conjunction with three-dimensional finite element simulations that suggest an appropriate application of the experimental measurements to correlate FCG rates. Finally, Schindler introduces a new experimental technique to determine crack closure from residual stresses measured by the cut compliance technique.

Load History Effects

Perhaps the most useful application of the crack closure concept has been to develop life prediction methods accounting for retardation and acceleration effects under variable-amplitude and spectrum loading. These methods are in current use by aerospace and nuclear industries around the world. But as the research community conducts tests and analyses beyond the usual crack growth rate regimes, such as at very high stress ratios or under extreme environments, or by observing the crack-tip deformations with advanced techniques or methods, the current concepts are found to be lacking and numerous questions arise.

Bichler and Pippan make some direct observations of the residual plastic deformations caused by a single tensile overload in the mid-thickness of a specimen using scanning electron micrography and stereophotogrammetric reconstruction of the fracture surfaces. Lang attributes the changes in measured crack growth rates after single and multiple overload sequences to the compressive residual stresses in front of the crack tip. Stephens et al. study fatigue crack growth and closure at three different temperatures in a high-strength titanium alloy (Ti-62222) proposed for use in a future supersonic transport. Tests are conducted under constant-amplitude load-reduction procedures near threshold conditions and under single-spike overloads. McMaster and Smith study the effects of simple load excursions on fatigue crack growth and closure measurements in 2024-T351 aluminum alloy at two thicknesses, using both remote and local displacement gages. Jono, Sugeta, and Uematsu conduct an investigation on crack growth and closure on side-grooved specimens of a Ti-6Al-4V titanium alloy under constant-amplitude and repeated two-step loading.

Hsu, Chan, and Yu study crack growth and closure under simulated aircraft spectrum loading with a significant number of compression cycles. They use a local strain gage method to measure crack opening loads and apply an analytical crack closure model to predict the behavior under the spectrum loading. Varvani-Farahani and Topper conduct tests on SAE 1045 steel under load histories containing periodic compressive loads. They develop a model of plastic deformation of fracture surface asperities and compare the measured and calculated fatigue lives of solid cylindrical and tubular specimens. Romeiro, Domingos, and de Freitas extend crack growth and closure studies to very low stress ratios ($0.7 \geq R \geq -3$) on a carbon steel.

Since the discovery of crack closure, the finite element method has been widely used to study crack growth and closure. Park and Song use a two-dimensional finite element method to investigate various types of variable-amplitude loading.

Surface Roughness Effects

In the literature, the development of fatigue crack growth thresholds has been attributed to an increase in crack surface roughness due to the development of Stage I or Stage-I-like (alternating shear, zigzag) crack growth, as the threshold is approached. But how roughness interacts with plasticity-induced closure to affect crack growth rates is a fundamental question for life prediction methods, and researchers are actively pursuing this issue. Modeling of roughness-induced crack closure, in combination with plasticity-induced closure, has been very limited. Several authors in this volume have addressed this issue by developing models that include both effects.

Chen and Lawrence combine the strip-yield model of Newman (plasticity-induced crack closure) with the zigzag (Stage I) fatigue crack growth (roughness-induced crack closure) to develop a model to predict the total fatigue life of notched components using a fracture mechanics approach. Sehitoglu and Garcia develop a model that is characterized by the distribution of asperity heights, asperity densities, and asperity radii. Comparisons are made with plasticity-induced closure results to assess when one mechanism dominates the other. As Schijve pointed out in the first symposium on crack closure (*ASTM STP 982*), crack front incompatibility (flat or slant crack growth) can influence crack growth rates. Zuidema, van Soest, and Janssen study the effect of surface roughness induced by shear lips and conventional plasticity-induced closure on crack growth in aluminum alloys.

Closure Effects on Crack Behavior

Fatigue crack closure, as an intrinsic feature of growing fatigue cracks, can have an influence on many different aspects of crack growth. Daniewicz investigates the influence of closure variations around the perimeter of a surface crack on the evolution of the flaw shape itself, based on a modified strip-yield model employing the slice synthesis method. Dankert, Greuling, and Seeger demonstrate the role of crack closure in the growth behavior of short cracks growing from notch roots, developing a unified model that accounts not only for crack closure but also for notch root deformation and employs elastic-plastic fracture mechanics. Pawlik and Saff present a numerical method for predicting closure and its effects on thermomechanical fatigue crack growth, including the influence of constraint, temperature, and variable-amplitude loads. Toribio and Kharin suggest from their finite element studies that closure-induced residual stresses in the crack wake can have a significant influence on stress-assisted hydrogen diffusion towards rupture sites in the crack tip zone, and hence that crack closure has an indirect influence on hydrogen-assisted cracking. de Koning, ten Hoeve, and Henriksen use a strip-yield closure analysis to define the strain rate at the crack tip, expanding an existing FCG model to address the effects of environment and frequency on the crack growth rate.

Fundamental Studies

Franz O. Riemelmoser[1] *and Reinhard Pippan*[1]

On the ΔK_{eff} Concept: An Investigation by Means of a Discrete Dislocation Model

REFERENCE: Reimelmoser, F. O. and Pippan, R., **"On the ΔK_{eff} Concept: An Investigation by Means of a Discrete Dislocation Model,"** *Advances in Fatigue Crack Closure Measurement and Analysis: Second Volume, ASTM STP 1343,* R. C. McClung and J. C. Newman, Jr., Eds., American Society for Testing and Materials, West Conshohocken, PA, 1999, pp.1–13.

ABSTRACT: Some results of discrete dislocation mechanics concerning fatigue crack growth are discussed in two parts. The first part deals with the plasticity-induced crack closure under plane strain conditions. The equations describing the deformation of crack flanks induced by edge dislocations are derived. These equations predict crack face contact for an edge dislocation in the wake of a sharp crack. The principle of superposition then immediately shows that the crack flanks even may contact at blunted cracks. This is visualized first by a suitable choice of the dislocation arrangement and afterwards also by the results of simulations of the dislocation motion at a growing fatigue crack.

In the second part these simulations are investigated more closely. During the initial period of a constant-amplitude test the crack growth increment per loading cycle and the closure stress intensity are monitored. By applying Elber's ΔK_{eff} concept a conceptual crack growth rate is calculated and is compared with the real crack growth increment per loading cycle.

KEYWORDS: fatigue, plasticity-induced crack closure, dislocation mechanics, ΔK_{eff}-concept

Since the discovery of plasticity-induced crack closure by Elber [*1*] in the early 1970s much effort has been made to understand this phenomenon. Budiansky and Hutchinson [*2*] and Führing and Seeger [*3*] extended the Dugdale model to account for plasticity-induced crack closure in plane stress; Fleck and Newman [*4*], McClung et al. [*5*] and Gall et al. [*6*] showed by recourse to the finite element method that plasticity-induced crack closure occurs also under plane strain conditions.

These models and calculations are based on conventional continuum plasticity mechanics analyses. Therefore they are appropriate in the Paris regime but in the near-threshold regime the cyclic plastic crack tip opening displacement, ΔCTOD, is only on the order of a few Burgers' vectors. Here the dislocation nature of plasticity has to be taken into account in the elastic-plastic analysis [*7*].

While in the near-threshold regime oxide- and asperity-induced crack closure often dominates the crack growth resistance (for an overview see Ref *8*), the plasticity-induced crack closure in this regime is very important from the theoretical point of view. For a long time it has even been questioned whether it takes place at all, i.e.; whether the dislocation mechanics can predict plasticity-induced crack closure [*9*]. This is now clarified and its occurrence was demonstrated in Ref *10.* In this study the difficulties of evaluating the contact stresses was circumvented by raising K_{min} whenever the crack flanks came into contact.

An explanation based on plausibility arguments for the plasticity-induced crack closure under plane strain conditions, i.e., for the origin of the extra material necessary to produce crack closure, is given in Ref *11.* There we have shown that the plastic wedge in plane strain is, in contrast to the plane stress case, confined to a small region near the crack tip.

[1] Erich-Schmid-Institut for Material Science of the Austrian Academy of Sciences and the Institute of Metal Physics of the University Leoben, Jahnstr. 12, A-8700 Leoben, Austria.

Meanwhile we have developed a procedure which enables the evaluation of contact stresses and their influence on the dislocation motion. The procedure is explained in short in the Appendix. Readers who are interested in more details are referred to Ref *12*. This procedure was used to study a growing fatigue crack in a constant-amplitude test. We were interested in the change of the closure level and of the crack growth rate in the initial period until the steady state is achieved. In the present paper it is discussed whether the increase in closure can fully account for the decrease in the crack growth rate. This is done in the third section. But before, in the second section, we explain the principle of the plasticity-induced crack closure and we derive the equations describing the crack flank contour.

Dislocation and Plasticity-Induced Crack Closure

In the following we distinguish between dislocation and plasticity-induced crack closure. The term "dislocation-induced crack closure" is used when the position of the dislocation is arbitrary and can be freely chosen. The term "plasticity-induced crack closure" is used exclusively for dislocation arrangements that result from the simulations of growing fatigue cracks.

The basic equations for both kinds of crack closure, derived in the following section, are, of course, the same.

The Boundary Value Problem: Edge Dislocation Near Crack Tip

Let us assume a semi-infinite crack along the negative x-axis and an edge dislocation at position $z_0 = x_0 + iy_0$ with Burgers' vector $b = b_x + ib_y$ near the tip as shown in the schematic Fig. 1. There the coordinate system is given also.

The stresses σ and displacements u at an arbitrary point $z = x + iy$ in the complex plane are described by two potentials $\phi(z)$ and $w(z)$ according to Kolosov as follows:

$$
\begin{aligned}
\sigma_{xx} + \sigma_{yy} &= 2(\phi'(z) + \overline{\phi'(z)}) \\
\sigma_{yy} - i\sigma_{xy} &= \phi'(z) + \overline{w'(z)} + (z - \bar{z})\phi''(z) \\
u = u_x + iu_y &= \frac{1}{2\mu}(\kappa\phi(z) - (z - z)\overline{\phi'(z)} - \overline{w(z)})
\end{aligned}
\tag{1}
$$

In these equations a prime denotes a derivation with respect to z and a bar labels the complex conjugate function. The constant μ is the shear modulus and $\kappa = 3 - 4\nu$ for plane strain conditions, where ν is the Poisson's ratio. The complex potentials of an edge dislocation in an infinite and uncut plane are [*13*]:

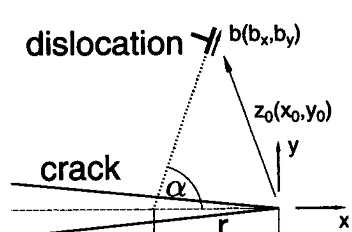

FIG. 1—*Dislocation-crack coordinate system.*

$$\phi_0'(z) = \frac{2A}{z - z_0}$$
$$w_0'(z) = \frac{2\bar{A}}{z - z_0} - \frac{2(z_0 - \bar{z}_0)}{(z - z_0)^2} A \tag{2}$$

The constant $A = \dfrac{\mu b}{2\pi i(\kappa + 1)}$ characterizes the material and the strength of the dislocation.

If now a crack is introduced, the tractions $p(t)$ at the crack surface must vanish. This is achieved by adding image fields $\phi_1'(z)$ and $w_1'(z)$ that have the same but negative value at the crack as the dislocation in the uncracked body. The image terms can be calculated, as shown by Muskhelishvili [*14*], with Eq 3:

$$\phi_1'(z) = \frac{1}{2\pi i\sqrt{z}} \int_{-\infty}^{0} \frac{\sqrt{t}}{t - z} p(t)\, dt$$
$$w_1'(z) = \overline{\phi'(\bar{z})} \tag{3}$$

The function $\sqrt{z}$ must be chosen with the branch cut along the negative x-axis. This function is purely imaginary for negative x-values when y tends either from above or from below to zero. After integrating Eq 3 by Cauchy's theorem, the total complex potential which is the sum of the "uncut" potential and the image term reads:

$$\phi'(z) = \phi_0'(z) + \phi_1'(z) = \frac{A}{z - z_0}\left[\sqrt{\frac{z_0}{z}} + 1\right] + \frac{A}{z - \bar{z}_0}\left[\sqrt{\frac{z_0}{z}} - 1\right]$$
$$+ \frac{\bar{A}(z_0 - \bar{z}_0)}{2(z - \bar{z}_0)^2}\left[\sqrt{\frac{\bar{z}_0}{z}} + \sqrt{\frac{z}{z_0}} - 2\right]$$
$$w'(z) = w_0'(z) + w_1'(z) = \frac{A}{z - z_0}\left[\sqrt{\frac{z_0}{z}} + 1\right] + \frac{A}{z - \bar{z}_0}\left[\sqrt{\frac{z_0}{z}} - 1\right]$$
$$- \frac{A(z_0 - z_0)}{2(z - \bar{z}_0)^2}\left[\sqrt{\frac{z_0}{z}} + \sqrt{\frac{z}{z_0}} + 2\right] \tag{4}$$

The same equations were derived in Ref *13*. A simple integration with respect to z finally leads to the potentials $\phi(z)$ and $w(z)$ which describe the displacements. Choosing the integration constant to keep the crack tip in the origin of the coordinate system we finally obtain:

$$\phi = \phi_0 + \phi_1 = 2A \log\left[\frac{z_0 - z}{z_0}\right] + \bar{A}\,\frac{z_0 - \bar{z}_0}{\bar{z}_0} \cdot \frac{\sqrt{z}}{\sqrt{z} + \sqrt{\bar{z}_0}}$$
$$- 2A \log\left[\frac{(\sqrt{z} + \sqrt{z_0})(\sqrt{z} + \sqrt{\bar{z}_0})}{\sqrt{z_0 \cdot \bar{z}_0}}\right]$$
$$w = w_0 + w_1 = 2\bar{A} \log\left[\frac{z_0 - z}{z_0}\right] + 2A\,\frac{z \cdot (z_0 - \bar{z}_0)}{z_0 \cdot (z - z_0)}$$
$$- A\,\frac{(z_0 - \bar{z}_0)}{z_0} \cdot \frac{\sqrt{z}}{\sqrt{z} + \sqrt{z_0}} - 2\bar{A} \log\left[\frac{(\sqrt{z} + \sqrt{\bar{z}_0})(\sqrt{z} + \sqrt{z_0})}{\sqrt{z_0 \cdot \bar{z}_0}}\right] \tag{5}$$

As branch cut of the logarithm the negative x-axis has to be used.

Dislocation-Induced Crack Closure: Sharp Crack

In order to visualize the deformation of the crack flanks induced by edge dislocations, given by Eqs 2 and 5, we introduce the variables α and r (see Fig. 1). The former is the angle between the positive x-axis and the slip plane of the dislocation and the latter variable, r, denotes the distance from the intersection point of the slip plane with the negative x-axis and the crack tip. Moreover, we have to take into account that the sum of Burgers' vectors must be zero. Let us that assume the dislocations are generated at the crack tip. In this case each dislocation leaves a ledge at the tip that can be considered as the negative counterpart of the generated dislocation. Needless to say, when the crack propagates by leaving behind the generated dislocation in the wake the ledge also "moves back," forming a step in the crack flanks. Dislocations whose slip plane intersect the crack tip are called "blunting dislocations," whereas dislocations whose slip plane intersects the negative x_1-axis are labeled "wake dislocations."

The calculated crack contours for six different locations of dislocations, which are given in the various diagrams, are shown in the Fig. 2.

In these figures the upper crack flank is drawn fully and the lower crack flank is dotted. In Fig. 2*a* the crack contour due to a blunting dislocation is depicted. The opening of the crack tip is, as aforementioned, produced by the ledge that forms during the generation of the dislocation. In this figure it is seen that the crack faces are bent back again elastically by the blunting dislocation but the crack is, in this special case, open everywhere; i.e., the full line is above the dotted line, along the entire negative x-axis. But if we consider a wake dislocation (Figs. 2*b* to 2*f*) the picture turns. Here the crack is also open at the left side of the step produced by the wake dislocation but it is closed between the step and the crack tip. Consider that the crack flanks in these figures even overlap. This is, of course, physically impossible. In reality, the crack flanks do contact but they do not penetrate. In the contact interval contact stresses develop that then influence the dislocation arrangement and thereby the fatigue crack growth rate.

For the moment we just want to show that dislocation-induced crack closure indeed occurs. Therefore we ignore the contact stresses and we allow the overlapping. In our simulations of the growing fatigue crack, however, the influence on the contact stresses are, of course, fully taken into account. This is achieved by a numerical procedure which is shortly described in the Appendix.

Dislocation-Induced Crack Closure: Blunted Crack

Figure 2 shows that sharp cracks close induced by the wake dislocations. We now proceed to demonstrate that the crack can even close when the crack tip is blunted. Therefore we take the blunted crack configuration of Fig. 2*a* and simply add the wake dislocation of Fig. 2*d*. This is justified by the principle of superposition of the theory of linear elasticity and gives as a result the partially closed and blunted crack of Fig. 3*c*. It seems to be important to emphasize that this result is obtained only by solving the equations of linear elasticity correctly. No other "trick" has been used as, e.g., was stated incorrectly in Ref *15* where the authors wrongly assert that we include a core relaxation of the dislocations. The discrepancy between our result and the one described in Refs *15* and *16* is simply reasoned by a mistake in the mathematics in the analysis of the wake dislocation problem by these authors. A more detailed discussion can be found in Ref *24*.

Plasticity-Induced Crack Closure in Case of a Growing Fatigue Crack

We have studied the dislocation arrangement and the crack closure during a constant-amplitude test. The procedure of the simulations is described in Ref *12*. The crack was cyclically loaded from $K_{\min} = 0.4k_e$ to $K_{\max} = 4.0k_e$, where k_e is the Rice-Thomson Ref *17* stress intensity factor to generate a dislocation at a crack tip. The material parameters entering the simulation are the shear modulus $\mu = 80\ 000$ MPa, the Poisson's ratio $\nu = 0.3$, the lattice friction stress $\tau_0 = \mu/1000$, the Rice-Thomson stress intensity $k_e = 0.5$ MPa, and the angle between the positive x-axis and the slip plane

$\alpha = 70.5$ deg. The change of the crack contour during crack propagation is depicted in Fig. 4. Each situation shows the crack at K_{min} but for different total crack extensions.

Figure 4*a* shows the crack after the first unloading. The crack is completely open. But when the crack propagates, more and more dislocations remain in the wake which induce the crack closure. After 50 cycles (Fig. 4*b*) the crack closes already a small distance from the crack tip. During further

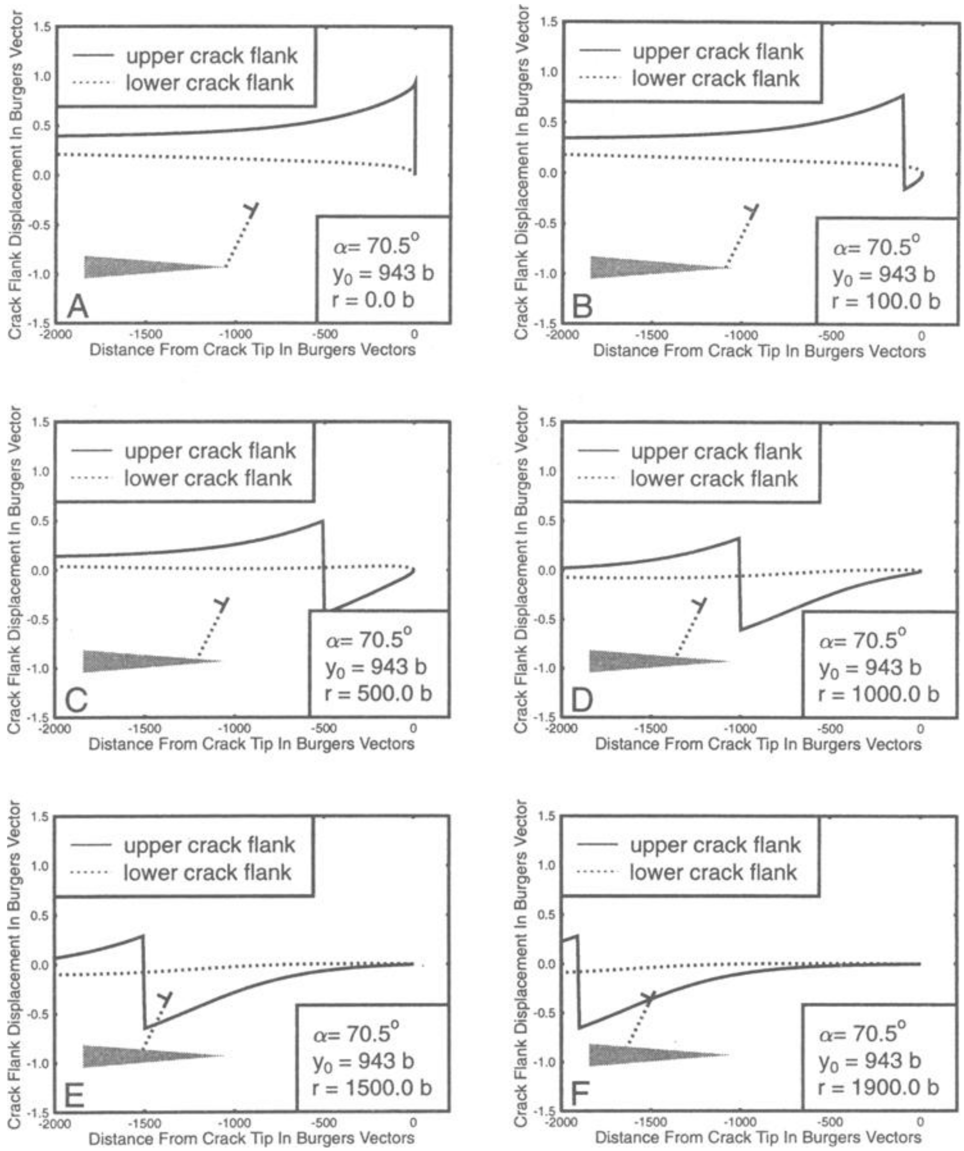

FIG. 2—*Crack contour due to edge dislocations. The upper crack flank is drawn fully, the lower one is dotted.* (A) *The blunting dislocation leads to an open crack.* (B) *to* (F) *Wake dislocations produce a penetrating crack at the right side of the intersection point between slip plane and crack flanks.*

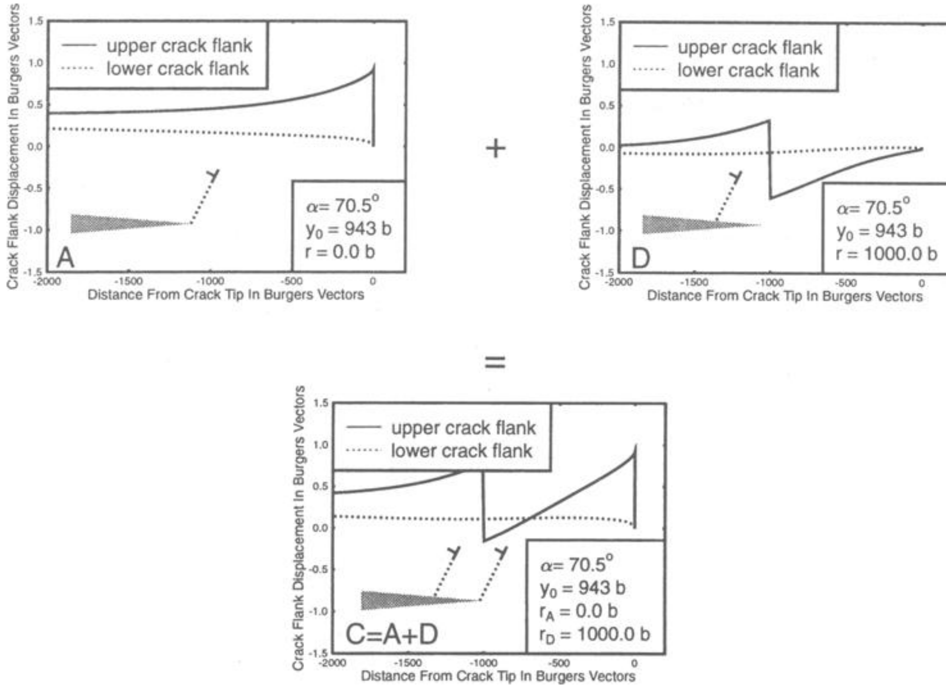

FIG. 3—*Superposition of Fig. 2A and Fig. 2D produces a blunted and partially closed crack.*

crack propagation the length through which the crack closes increases until after 750 cycles (Fig. 4*d*) the steady state is nearly achieved. The closure distance of about 5000 *b* seems to be small, but it can be readily understood by the small stress intensity range $\Delta K = 3.5\ k_e$. As we shall see later it has, nevertheless, a considerable influence on the crack propagation rate.

Readers who are not familiar with the explanation of the dislocation arrangement during crack propagation in Ref *18* may be astonished at the large steps in the crack faces. Briefly explained, they develop since the dislocations predominately arrange in slipbands and each slipband leaves a large step in the crack flanks. The distance between two slipbands, however, cannot get arbitrarily small because of their large elastic interaction force. In our simulations it turned out that the smallest distance between two slipbands near cracks and consequently between two slip steps is about 2000 *b*, i.e., about 0.5 μm.

A Consideration of the ΔK_{eff} Concept

In the early 1970s Elber discovered crack closure in tension [*1*]. As a result he introduced the ΔK_{eff} concept, which embraces two postulates:

1. The crack grows (in the loading sequence) as soon as it zips open.
2. The crack propagation rate is a unique function of the effective stress intensity range.

The first of these postulates is, from a mechanics point of view, beyond all doubts. When the crack opens, an elastic stress singularity develops at the tip which cannot be suffered by the material. The crack tip plastifies, the crack blunts and propagates.

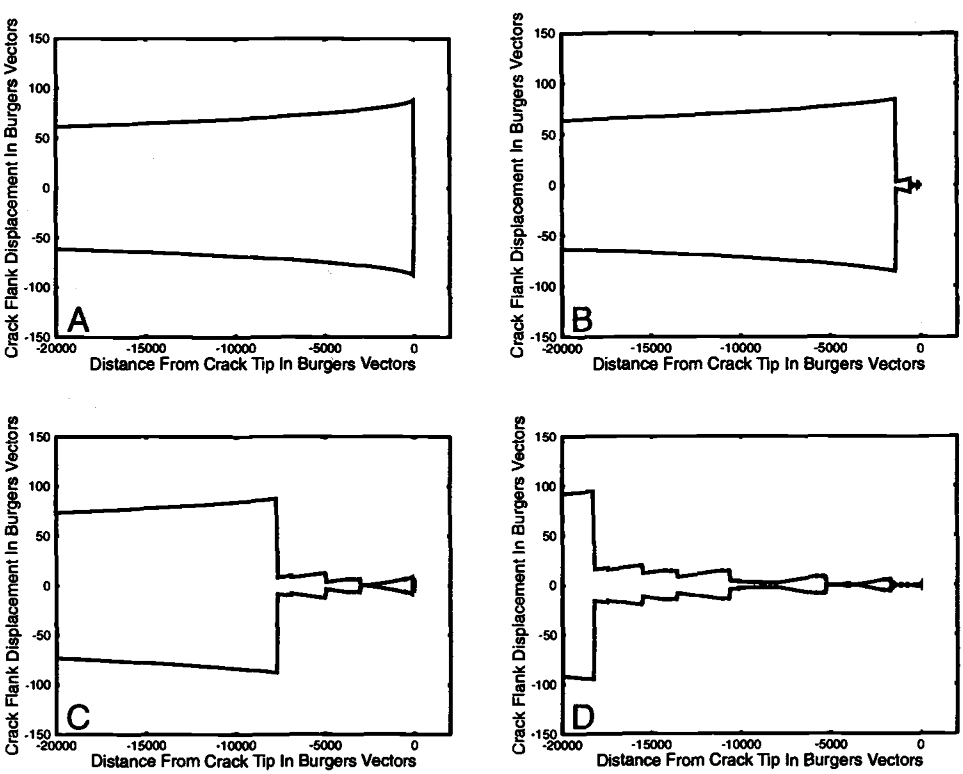

FIG. 4—*Crack contour during crack propagation depicted at* $K_{min} = 0.1 \cdot K_{max} = 0.4\ k_e$. (A) *After the first unloading;* (B) *50 cycle;* (C) *350 cycle;* (D) *750 cycle. The distance through which the crack closes increases during the crack propagation.*

Elber's second postulate, however, is much more complicated. In order to understand its implication we briefly compare a stationary crack and a growing fatigue crack in the steady state. The difference between both cracks is that there is a plastified strip in the wake of the growing crack in which long-range residual stresses act but in the case of the stationary crack the wake is purely elastic. This difference causes two measurable effects. First, at the growing crack, crack closure can be detected and, second, the cyclic plastic deformations are smaller than at the stationary crack. Now, the core of the second postulate is that the difference in the cyclic plastic deformation can be calculated by the crack closure, i.e., by the decrease in the effective stress intensity range. This can only be the case when the stresses near the tip induced by the plastic wake are expressible in terms of a stress intensity factor K within a region which is as large as, or even larger, than the cyclic plastic zone.

A direct proof would be to separate the stresses of the plastic wake and of the active plastic zone. This is, however, not possible so that the second postulate has to be proofed indirectly. The method which we have used is explained in the following section.

How to Proof the Second Postulate?

In the following an indirect proof of Elber's second postulate in a constant-amplitude test is introduced. The method itself would be more flexible; it can also be used, e.g., in overload experiments.

1. The virgin crack is loaded twice. During the second cycle ΔCTOD is monitored as a function of the stress intensity range ΔK. It is reasonable, and confirmed by our simulations, that crack closure

in the second loading cycle is negligible. Therefore the plot ΔCTOD-ΔK can be used as a ΔCTOD vs. ΔK_{eff} diagram.

2. The relation between ΔCTOD and the crack growth increment per loading cycle is evaluated. This is straightforward in our simulations but rather hard work in experiments.

3. The cyclic loading of the crack is continued until a steady state is achieved. During this initial period the change of the closure stress intensity K_{cl} and the crack growth rate are simultaneously measured.

4. The effective stress intensity range $\Delta K_{eff} = K_{max} - K_{cl}$ is calculated as a function of the total crack extension.

5. An effective ΔCTOD is computed using the result of point 4 and the diagram of point 3.

6. The effective ΔCTOD and the relation of point 2 is used to calculate the change of the conceptual crack growth increment $\Delta a_{concept}$ during the initial period of the constant amplitude test.

7. The conceptual and the real crack growth increment per loading cycle are compared.

If the ΔK_{eff} concept is true, the change of the crack growth increment in the initial period until the steady state is achieved is caused only by the change in the closure level. In this case the changes of the conceptual and of the really measured crack growth increment, Δa_{real}, are the same. Contrarily, if the residual stresses of the plastic wake cannot be fully described by a K-field, then a noticeable difference between the two crack growth increments should become visible.

The previously described methodology is not limited to dislocation mechanics. It can also be used for classical continuum mechanics analysis such as a finite element simulation and even for experimental data.

Results

The results of our simulations are discussed in the items of the methodology given above:

1. In Fig. 5 the calculated ΔCTOD-ΔK diagram is depicted. The factor ½ in the ordinate reflects the symmetric arrangement of dislocations.

2. Figure 6 shows that the symmetric dislocation arrangements in our simulations produce at the tip a V-notch. Therefore $\Delta a = \beta \cdot \Delta$CTOD, where $\beta = ½ \cot \alpha = 0.17$ for $\alpha = 70.5$ deg.

3. The change of Δa_{real} and of K_{cl} during the initial period until a steady state was (nearly) achieved is plotted in Fig. 7. In this initial period the crack growth rate decreases from about 30 b per cycle to about 20 b per cycle. At the same time K_{cl}/K_{max} raises from 0.1 to 0.22. Its initial value 0.1 is due to the chosen stress ratio $R = 0.1$ and means that no crack closure is detected. The steady-state

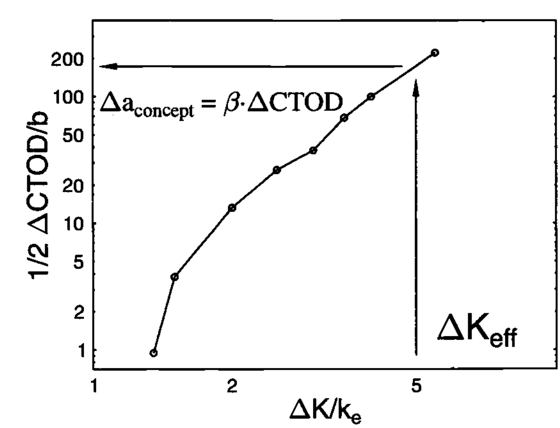

FIG. 5—*Calculated* Δ*CTOD* $- \Delta K_{eff}$ *diagram.*

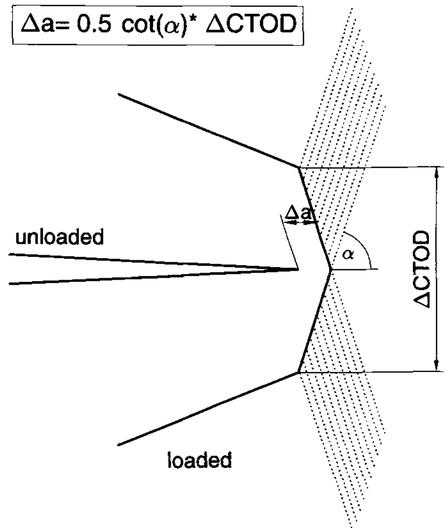

FIG. 6—*Relation between ΔCTOD and Δa in case of a V-notch.*

value $K_{cl}/K_{max} = 0.22$ is close to results obtained by finite element simulations in 2D [*6*], in 3D [*19*] and to the results of Newman's modified Dugdale model [*20*].

4. and 5. The data of Fig. 7 are used to compute the change in the effective stress intensity range. Then an effective ΔCTOD is calculated as shown in Fig. 5. The resulting diagrams are omitted in order to save space.

6. and 7. The effective ΔCTOD was then used to compute the conceptual crack growth increment per loading cycle, $\Delta a_{concept}$, by the aid of the relation of point 2. In Fig. 8 $\Delta a_{concept}$ and Δa_{real} are compared.

It is seen that the changes of the real and the conceptual crack growth increment per loading cycle agree qualitatively quite well, which indicates the importance of the crack closure. But on the other hand, it cannot be denied that a systematic deviation exists. In our opinion there are two possible rea-

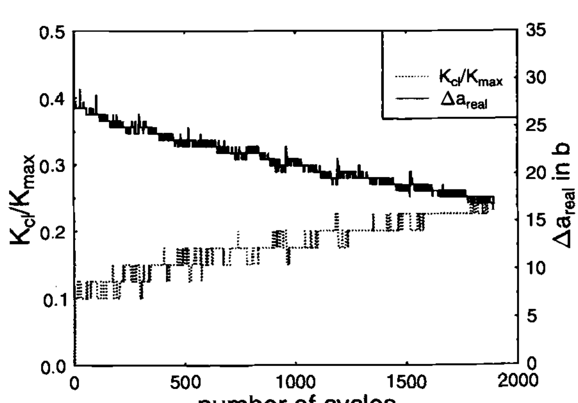

FIG. 7—*Change of closure stress intensity,* K_{cl}, *and of the measured crack growth increment per loading cycle,* Δa_{real}.

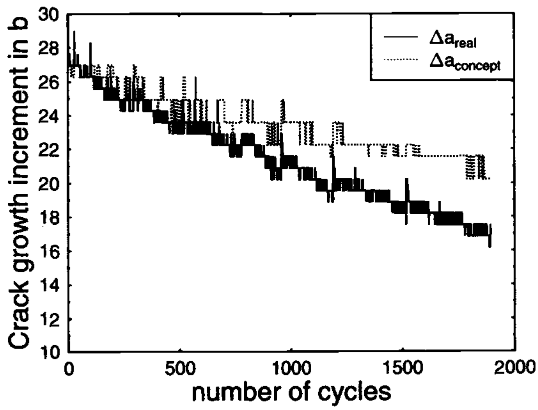

FIG. 8—*Comparison of real and conceptual crack growth increment per loading cycle.*

sons for the deviation. The first point gets obvious when we consider that in this investigation plasticity is described by means of discrete dislocations. While this is absolutely necessary when fatigue crack growth in the threshold regime should be understood [7], it also has its "drawbacks." One of these drawbacks is that in contrast to continuum plasticity theories, the discrete plasticity does not predict similitude. That is to say, the numbers of generated dislocations, i.e., ΔCTOD, is not just a function of ΔK_{eff} but depends also slightly on the stress ratio. Whether or not the same is true for real fatigue crack growth in the near-threshold regime is still an unanswered question. The loss of similitude, however, may produce an error in the estimation of $\Delta a_{\mathrm{concept}}$ since crack closure changes not only ΔK_{eff} but also the effective stress ratio.

A second reason for the deviation between $\Delta a_{\mathrm{concept}}$ and Δa_{real} could be that the crack closure alone possibly cannot fully account for the decrease in the crack growth rate. As mentioned previously, this is the case when the stresses in the cyclic plastic zone induced by the plastic wake are not describable by K-fields. This should not be forejudged but it certainly needs more consideration in future, at best by continuum plastic theories where the principle of similitude holds.

Conclusion

The mathematically correct solution of the linear elastic problem of a wake dislocation shows immediately that the crack faces contact due to these dislocations. Counterstatements in the literature are caused by a mistake in the mathematics by these authors.

In the second part the change of crack closure during a constant-amplitude test is calculated. Its steady-state value is similar to the predictions of continuum plasticity theories. The simulation is used to prove Elber's ΔK_{eff} concept. While the first postulate (the crack start propagating as soon as it zips open) is true for obvious reasons, the second postulate is more complicated. It states that the reduction of the crack growth rate in the initial period of the constant-amplitude test can be calculated by the increase in the closure stress intensity.

In our simulations it appeared that crack closure doubtless is important, but it cannot fully account for the decrease in the crack growth rate. This is explained either by the lack of similitude of the discrete plasticity approach or by a non-K stress field in the cyclic plastic zone induced by the plastic wake.

Acknowledgment

This work was financially supported by the FWF (Fonds zur Förderung der wissenschaftlichen Forschung), Project Nr. P 10116 TEC.

APPENDIX

In Ref *12* a procedure is described that enables the calculation of the contact stresses and their influence on the dislocation motion. Here a short summary is given where the method is explained on the basis of Fig. 9. This situation has been derived in one of our simulations at $K_{\min} = 0.4k_e$. Here only the upper half of the crack is shown. The lower one would lie symmetrically on the zero line. At the left side the crack is open, on the right side it is closed. In Fig. 9 the crack flanks overlap in the interval I_1. The contact stresses are evaluated iteratively by means of a collocation method. First the overlap interval is divided into m subdomains which we call elements.

Let us assume an element number j is loaded by a constant stress of magnitude "1." This stress displaces the midpoint, so-called collocation point, of the observed element and also the collocation points of all the other elements by an amount $\hat{g}_{ij}$. This function was derived by Tada et al. [*19*] and is given by

$$\hat{g}_{ij} = \frac{(\kappa + 1)}{\pi\mu}$$
$$\operatorname{Im}\left\{i\sqrt{x_i}(\sqrt{e_{j2}} - \sqrt{e_{j1}}) + (x_i - e_{j1}) \arctan\left[-i\sqrt{\frac{e_{j1}}{x_i}}\right] - (x_i - e_{j2}) \arctan\left[-i\sqrt{\frac{e_{j2}}{x_i}}\right]\right\} \tag{6}$$

Here Im denotes the imaginary part of a complex function. e_{j1} and e_{j2} are the coordinates of the left and the right boundary of a contact element, respectively.

The collocation point j is not only displaced by the stress in the element j but also by the stresses in the other $m - 1$ elements. Now a stress distribution $\hat{P}_j$ is sought such that the displacement of each collocation point is everywhere zero; i.e., the displacements at the collocation points produced by contact stresses must equal the displacement, $\hat{u}_i$, in the collocation points in the initial overlapping state. This reads

$$\hat{P}_j \hat{g}_{ij} = \hat{u}_i \qquad i, j = 1 \ldots n \tag{7}$$

Here Einstein's sum convention is applied to repeated indices. The linear algebraic equation system in Eq 7 is solved by the Gauss-Seidl procedure. This solution provides a first approximation. Phys-

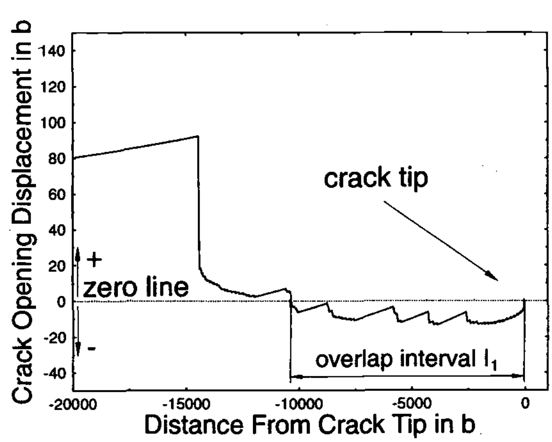

FIG. 9—*Crack flanks overlap before the contact stresses are applied.*

ically, contact stresses must be compressive. The above described method, however, provides, in the one or the other element, tension stresses. These elements must be canceled in the second iteration. The reduced equation system is solved once more, leading now to a better approximation of the contact problem. Again the tensile elements are canceled and so forth. The iteration is continued until the stress in each element is compressive. In our experience it needs about $n = 3$ iterations.

The results of this procedure are the real contact intervals, I_n, and the corresponding contact stress distribution. The iterative collocation method applied to Fig. *9* is depicted in Fig. *10*. Consider that due to the unregularities in the crack contour the crack flanks contact at some disconnected intervals behind the tip. This produces, in contrast to continuum mechanics analyses, a rather irregularly shaped contact stress distribution.

The next step is to evaluate the force on a dislocation caused by these contact stresses. Here we benefit from the fact that the contact stresses are already discretized, i.e., constant throughout the length of a single element. The force on the dislocation is given by the Eshelby integral [*20*], which has been transferred in the complex potential notation Eq 8 by Budiansky and Rice [*21*].

$$f = f_1 + if_2 = \frac{(\kappa + 1)i}{4\mu}\left[\oint_{|z-z_0|=r} \phi'^2(z)dz - 2 \cdot \oint_{|z-z_0|=r} \overline{\phi'(z)\psi'(z)dz}\right] \tag{8}$$

In Eq 8 we introduced the new complex potential $\psi(z) = w(z) - z\phi'(z)$.

The additional force on the dislocation caused by a single contact element is derived as:

$$f_{Pd} = \frac{i(\kappa + 1)}{\mu} \hat{P}_j .$$

$$\left\{2iA\, Im\left[2\frac{\sqrt{e_{1j}} - \sqrt{e_{2j}}}{\sqrt{z_0}} + \log\frac{\sqrt{z_0} - \sqrt{e_{1j}}}{\sqrt{z_0} + \sqrt{e_{1j}}} - \log\frac{\sqrt{z_0} - \sqrt{e_{2j}}}{\sqrt{z_0} + \sqrt{e_{2j}}}\right]\right. \tag{9}$$

$$\left. + \overline{A}\left(\frac{z_0}{\overline{z_0}} - 1\right)\left(\sqrt{\frac{e_{j1}}{z_0}}\frac{e_{j1}}{e_{j1} - \overline{z_0}} - \sqrt{\frac{e_{j2}}{z_0}}\frac{e_{j2}}{e_{j2} - \overline{z_0}}\right)\right\}$$

The total contact force on the dislocation due to the contact stresses is then simply the linear sum over all elements.

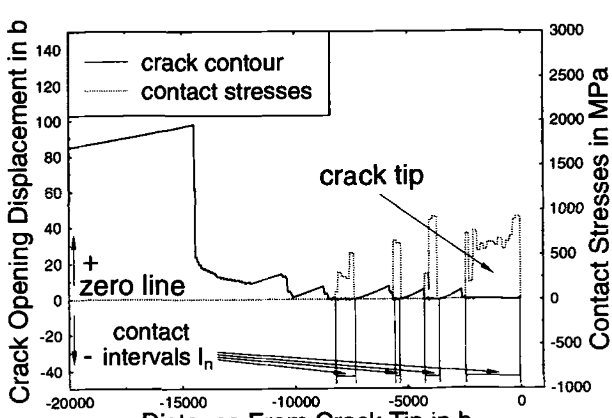

FIG. 10—*Crack contour and calculated contact stress distribution.*

References

[1] Elber, W. "Fatigue Crack Closure Under Cyclic Tension," *Engineering Fracture Mechanics*, Vol. 2, 1970, p. 37.

[2] Budiansky, B. and Hutchinson, W., "Analysis of Closure in Fatigue Crack Growth," *Journal of Applied Mechanics*, Vol. 45, 1978, pp. 267–276.

[3] Führing, H. and Seeger, T., "Dugdale Crack Closure Analysis of Fatigue Cracks Under Constant Amplitude Loading," *Engineering Fracture Mechanics*, Vol. 11, 1979, pp. 99–122.

[4] Fleck, N. A. and Newman, J. C., Jr., "Analysis of Crack Closure Under Plane Strain Conditions," *Mechanics of Fatigue Crack Closure, ASTM STP 982*, American Society for Testing and Materials, 1988, pp. 319–341.

[5] McClung, R. C., Thacker, B. H., and Roy, S., "Finite Element Visualization of Fatigue Crack Closure in Plane Stress and Plane Strain," *International Journal of Fracture*, Vol. 50, 1991, pp. 27–49.

[6] Gall, K., Sehitoglu, H., and Kadioglu, Y., "FEM Study of Fatigue Crack Closure Under Double Slip," *Acta Metallurgica*, Vol. 44, 1996, pp. 3955–3965.

[7] Riemelmoser, F. O., Pippan, R., and Stüwe, H. P., "An Argument for a Cycle-By-Cycle Crack Propagation in the Threshold Regime," submitted to *Acta Metallurgica*, 1997.

[8] Suresh, S., *Fatigue of Materials*, R. W. Cahn, E. A. Davis, and I. M. Ward, Eds., Cambridge University Press, Cambridge, MA, 1991.

[9] Riemelmoser, F. O. and Pippan, R., "Crack Closure: A Concept of Fatigue Crack Growth Under Examination," *Fatigue and Fracture of Materials Structures*, in press, 1997.

[10] Riemelmoser, F. O. and Pippan, R., "Plasticity Induced Crack Closure Under Plane Strain Condition in Terms of Dislocation Arrangement," *Proceedings, Fatigue '96*, Berlin, G. Lütjering and H. Nowack, Eds., 1996, pp. 363–368.

[11] Pippan, R. and Riemelmoser, F. O., "Visualization of Plasticity Induced Crack Closure Under Plane Strain Conditions," submitted to *Engineering Fracture Mechanics*, 1997.

[12] Riemelmoser, F. O., Pippan, R., and Kolednik, O., "Cyclic Crack Growth in Elastic Plastic Solids: A Description in Terms of Dislocation Theory," *Proceedings to IUTAM Symposium 1996*, Dublin, in press.

[13] Lin, L. H. and Thomson, R., "Cleavage, Dislocation Emission, and Shielding for Cracks Under General Loading," *Acta Metallurgica*, Vol. 34, 1986, p. 187.

[14] Muskhelishvili, N. I., *Some Basic Problems of the Theory of Elasticity*, Noordhof, Groningen, The Netherlands, 1963.

[15] Sadananda, K., Vasudevan, A. K., and Louat, N., "Dislocation Behavior Under Fatigue," *Recent Advances in Fracture*, R. K. Mahidhara, A. B. Geltmacher, P. Matic, and K. Sadananda, Eds., 1997, pp. 395–403.

[16] Vasudevan, A. K., Sadananda, K., and Louat, N., "Reconsideration of Fatigue Crack Closure," *Scripta Metallurgica et Materialía*, Vol. 27, 1992, p. 1673.

[17] Rice, J. R. and Thomson, R., "Ductile Versus Brittle Behavior of Crystals," *Philosophical Magazine, A*, Vol. 29A, 1974, p. 73.

[18] Riemelmoser, F. O. and Pippan, R., "Investigation of a Growing Crack by Means of a Discrete Dislocation Model," *Materials and Science Engineering*, Vol. A234–236, 1997, p. 135.

[19] Chermahini, R. G., Shivakumar, K. N., and Newman, J. C., Jr., "Three Dimensional Finite Element Simulation of Fatigue Crack Growth and Closure," *Mechanics of Fatigue Crack Closure, ASTM STP 982*, American Society for Testing and Materials, 1988, pp. 399–413.

[20] Newman, J. C., Jr., "A Crack Closure Model for Predicting Fatigue Crack Growth Under Aircraft Spectrum Loading," *Mechanics of Fatigue Crack Closure, ASTM STP 768*, American Society for Testing and Materials, 1981, pp. 53–84.

[21] Tada, H., Paris, P. C., and Irwin, G. R., *The Stress Analysis of Cracks Handbook*, Del Research Corporation, St. Louis, MO, 1985.

[22] Eshelby, J. O., "The Continuum Theory of Lattice Defects," *Solid State Physics*, Vol. 3, 1956, p. 79.

[23] Budiansky, B. and Rice, J. R., "Conservation Laws and Energy-Release Rates," *Journal of Applied Mechanics*, Vol. 40, 1973, p. 201.

[24] Riemelmoser, F. O. and Pippan, R., "Discussion of Error in the Wake Dislocation Problem," *Metallurgical and Materials Transactions A*, Vol. 24A, 1998, p. 2225.

N. Ranganathan[1]

Analysis of Fatigue Crack Growth in Terms of Crack Closure and Energy

REFERENCE: Ranganathan, N., "**Analysis of Fatigue Crack Growth in Terms of Crack Closure and Energy,**" *Advances in Fatigue Crack Closure Measurement and Analysis: Second Volume, ASTM STP 1343,* R. C. McClung and J. C. Newman, Jr., Eds., American Society for Testing and Materials, West Conshohocken, PA, 1999, pp. 14–38.

ABSTRACT: The fatigue crack growth behavior of the aluminum alloy 2024 is analyzed using the crack closure and an energy-based concept. The different test conditions studied include load ratio and environmental effects, crack growth retardation following a single overload, and crack propagation under block load tests. Crack opening loads using the compliance technique permit the effect of load ratio to be taken into account. After an overload, in the deceleration phase, the evolution of the crack opening load is not compatible with that of the crack growth rate. The measured crack opening levels under constant-amplitude loading conditions are comparable to those predicted under plane strain conditions for moderate ΔK levels. It is shown that most of the effects usually attributed to closure can be successfully explained using energy concepts. In particular, it is shown that there exists a linear relationship between the crack growth rate and the energy dissipated per cycle at high growth rates, which is valid for both the environments studied, and it corresponds to a crack growth mechanism characterized by striation formation during each cycle. For lower growth rates a power law relationship can be proposed between these two parameters. The above-mentioned linear relationship holds also for the block loading conditions based on total energy dissipated per block. Certain experimental facts bring out the effect of closure on the energy dissipated. It is further shown that the possible existence of a mixed (Mode I and Mode II) mode crack opening at the crack tip has to be taken into account to correctly evaluate the energy dissipated near the crack tip.

KEYWORDS: fatigue crack growth, crack closure, compliance method, potential drop method, overload effects, block load tests, energy dissipated, striation formation

Fatigue crack growth resistance of a material depends upon a number of factors, such as its composition, mechanical properties and heat treatment conditions, external loading and the ambient environment. The understanding of the mechanisms governing fatigue crack growth has made significant advances since the Paris Law proposed about 40 years ago [*1*]. The initial research to model material behavior was based on the determination of the strain amplitudes and damage accumulation in the plastically deformed zone in front of the crack tip [*2*]. One of the notable attempts is due to Weertman; he proposed that a crack advances when the energy accumulated at the crack tip attains a critical value, leading to the following crack growth law [*3*]:

$$da/dN = A\ \Delta K^4/(\mu \sigma_c^2 U) \tag{1}$$

where

da/dN = crack growth rate per cycle,
ΔK = stress intensity factor amplitude,
μ = shear modulus of the material,

[1]Professor, Université de Tours, Laboratoire de Mécanique et Rhéologie, EIT, 7 Avenue Marcel Dassault, 37200 Tours, France, formerly, Laboratoire de Mécanique et de Physique des Matériaux, 86960 Futorascaoe Cedex, France.

σ_c = critical stress at fracture,
U = critical energy to create a unit surface, and
A = a constant.

Different techniques have been developed in the past to determine the parameter U, such as by sub-grain size measurements [4], micro strain gages in the plastic zone [5], micro-calorimetry [6] and by direct evaluation of hysteresis energy under the loading line of a compact tension specimen [7]. These studies have shown that the parameter U has to be distinguished from the theoretical energy to separate the atoms and it is associated with the energy dissipated in the plastic zone near the crack tip, for ductile materials.

In 1971 Elber [8] proposed that a crack loaded in Mode I can remain closed during a part of the loading cycle even if the far-field loading is in tension owing to the existence of residual compressive stresses in the wake of the plastic zone. It was hence proposed that the crack growth rate should be correlated to the effective stress intensity factor amplitude after correction for closure. Since then, the attention of the scientific community has been largely focused on the understanding and application of this idea to a large field of fatigue crack growth such as effect of load ratio, load interaction effects, and variable-amplitude loading [9]. It has been shown that causes of crack closure are multiple such as crack surface roughness, oxide thickness relative to the crack tip opening displacement (near threshold), and existence of a mixed Mode I and Mode II opening at the crack tip [9]. To the author's knowledge no theoretical model has yet been proposed to take into account all the known effects of crack closure. Another school of thought attempts to minimize the effect of crack closure, suggesting that fatigue crack growth resistance depends upon ΔK and K_{max} and not on the effective stress intensity factor amplitude [10].

This paper presents a comparison of the crack closure and energy-based concepts based on experimental studies essentially on aluminum alloy 2024. The different aspects considered here are the effect of R ratio, environment, overload effect and fatigue crack propagation under block loading.

Brief Experimental Details

The tests presented here cover 20 years of study by the author and his collaborators and were mostly conducted on the 2024 Al alloy in the underaged condition, T351. Nominal composition and mechanical properties are given in Tables 1*a* and 1*b*.

TABLE 1*a*—*Nominal Composition of the Studied Alloy.*

Element	Si	Fe	Cu	Mn	Mg	Cr	Zn	Ti	Al
Mean %	0.1	0.22	4.45	0.66	1.5	0.01	0.04	0.02	Rest
Min %	...	...	3.8	0.3	1.2	...	...	...	...
Max %	0.5	0.5	4.9	0.9	1.8	0.1	0.25	0.2	...

TABLE 1*b*—*Nominal Mechanical Properties.*

Monotonic yield stress (MPa)	302
Elongation (%)	10.1
Strength coefficient, K (MPa)	343
Hardening coefficient (n)	0.06
Ultimate tensile strength (MPa)	474
Cyclic yield strength (MPa)	500
Cyclic strength coefficient, K' (MPa)	811.4
Cyclic hardening exponent, n'	0.078

Most of the tests were conducted using compact tension specimens 75 mm wide and of different thicknesses, 10 mm and 12 mm. Tests described here cover constant-amplitude (CA) and near-threshold tests at load ratios of 0.1 and 0.5 in air and in vacuum and constant-amplitude tests at R ratios of 0.01, 0.1, 0.33, 0.54 and 0.7 in air, single overload tests in air and in vacuum ($<10^{-3}$ Pa) and block load tests in air consisting four load levels. The tests were conducted at a nominal frequency of 20 Hz in air and 35 Hz in vacuum. Crack length was measured by optical techniques on the polished side of the specimen using a traveling microscope with a precision of 0.01 mm or by using the DC potential-drop technique.

Crack closure was measured using the differential compliance technique [*11*] and in some tests (in vacuum) using the potential-drop method. These recordings were made at quasi-static conditions, at a frequency of 0.2 Hz. Examples of the nominal and amplified load displacement diagrams are given in Fig. 1 and the different parameters measured are indicated. The crack opening level is determined from the differential crack opening δ' versus the load diagrams based on the following analysis

$$\delta' = \delta - \alpha \cdot P \tag{2}$$

where δ is the crack mouth opening displacement measured under the loading line, α is the maximum specimen compliance (measured under the loading line) during a cycle, and P is the load.

Thus during a loading cycle the derivative of the differential compliance diagram changes and in particular it becomes zero when the crack is fully open, which permits a clear identification of the crack opening load (diagram b in Fig. 1). This diagram is much easier to analyze than the nominal load versus displacement diagram (a in Fig. 1). The load versus potential-drop diagram is discussed later in the text.

Hysteresis energy, Q, was measured by numerically integrating the area under the load versus amplified displacement diagrams measured under the loading line of the specimen [*7*]. Specific energy, U, is defined as hysteresis energy dissipated per unit surface created

$$U = Q/(2b \cdot da/dN) \tag{3}$$

where b is the specimen thickness.

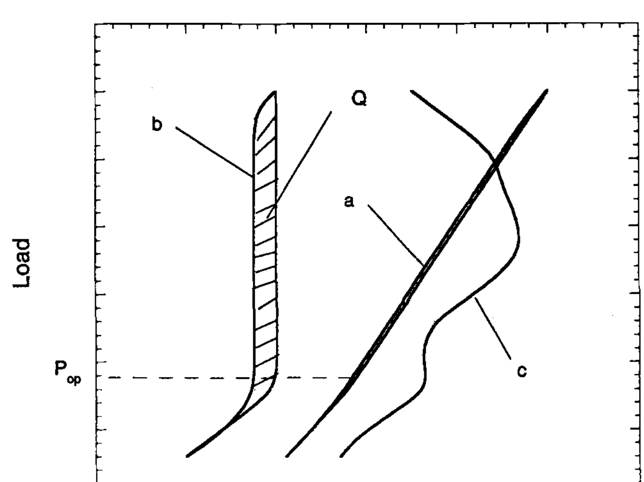

FIG. 1—*Examples of crack opening diagrams:* (a) *load versus displacement diagram,* (b) *load versus differential diagram,* (c) *load versus potential diagrams.*

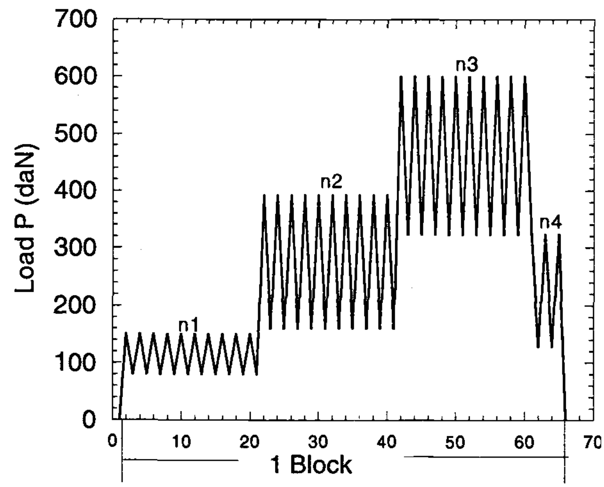

FIG. 2—*Configuration of the block loading studied.*

The configuration of the blocks and the number of cycles at the various load levels are given in Fig. 2 and Table 2, respectively. The block type studied consists of four load levels and essentially the number of cycles in the highest load level is varied from one block to another, except for block A.

Except for the threshold tests, the tests were carried out by computer control and the load amplitude was maintained to a precision of 5 *da/dN*. For certain critical experiments details are given in the relevant paragraphs.

Experimental Results

Crack Closure Analysis

Constant-Amplitude Test Conditions—Figures 3*a* and 3*b* show the relationship between the crack growth rate and the nominal ΔK level and the effective ΔK levels, respectively. It should be noted that the results presented here represent average values from three tests carried out under identical test conditions. It can be seen here that corrections for crack closure permit the reduction of scatter in the data. In general, for aluminum alloys a slope of about 4 is observed for crack growth rates greater than about 2×10^{-9} m/cycle and a lower slope for lower growth rates [*12*], in terms of effective ΔK.

Figures 4*a* and 4*b* correspond to crack growth behavior in vacuum. In this environment, when comparing load versus displacement and potential diagrams, Figs. 1*b* and 1*c*, the definition of crack open-

TABLE 2—*Load Levels and Number of Cycles at Different Steps in the Block Load Tests.*

Type of Block	Step 1 P_{min} = 80 daN P_{max} = 150 daN $n1$ (cycles)	Step 2 P_{min} = 160 daN P_{max} = 393 daN $n2$ (cycles)	Step 3 P_{min} = 323 daN P_{max} = 600 daN $n3$ (cycles)	Step 4 P_{min} = 138 daN P_{max} = 323 daN $n4$ (cycles)
A	1	1	1	1
B	10	10	10	2
C	10	10	50	2
D	10	10	100	2

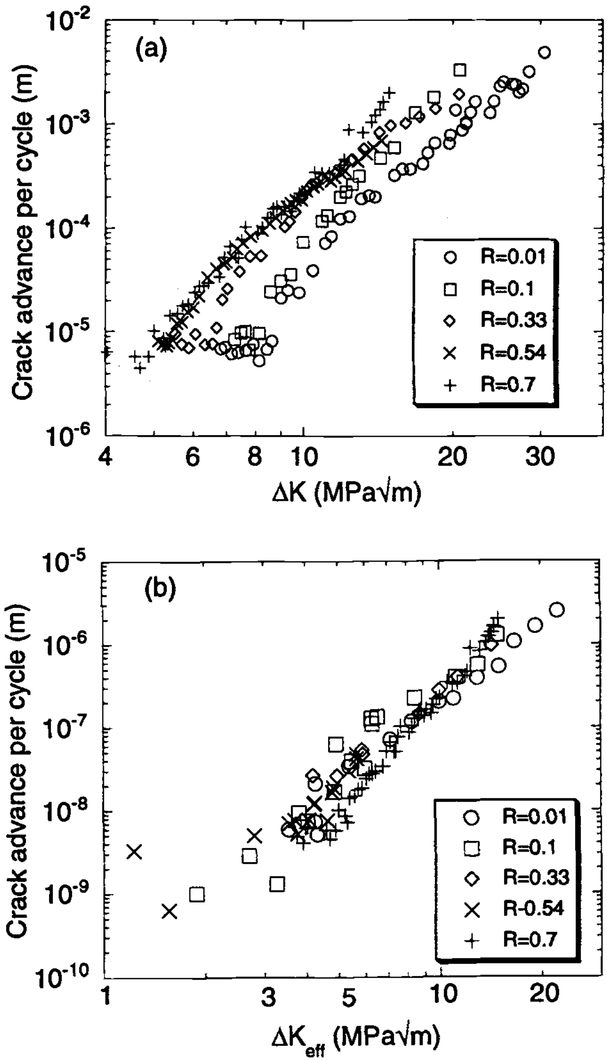

FIG. 3—(a) *Crack growth rate versus nominal* ΔK, *CA conditions in air,* (b) *crack growth rate evolution in terms of* ΔK_{eff}.

ing level is not very clear. As seen in the differential compliance diagram, a clear change in slope does mark the crack opening load which corresponds to a kink in the potential diagram. The potential increases further to reach a maximum. Considering that as the crack opens, the potential drop increases, the load corresponding to the peak in potential drop should represent the crack opening load. Moreover, a decrease in potential is seen near the maximum load which can correspond to the existence of contact between the two crack surfaces. It is difficult, at a first sight, to admit the existence of closure near the peak load. In order to maintain consistency with the results in air, corrections for closure are made using the same criterion as in Fig. 1*b* and the results are given in Fig. 4*b*. It can be seen that closure corrections do take into account the effect of R ratio, at least at moderate ΔK levels.

In order to further understand the significance of compliance changes, experiments were carried out using micro-strain gages stuck near the crack tip [13]. A set of ten strain gages of 500 to 640 μm size was stuck at about 37.5 mm from the loading axis (i.e., at about half the width of the specimen). The distance between each gage in a direction perpendicular to the nominal cracking plane is 0.87 mm. The tests were done at a constant ΔK of 16 MPa $m^{1/2}$ and with a load ratio of 0.1. Figure 5 shows the far-field compliance diagram along with strain changes at different locations ahead of the crack

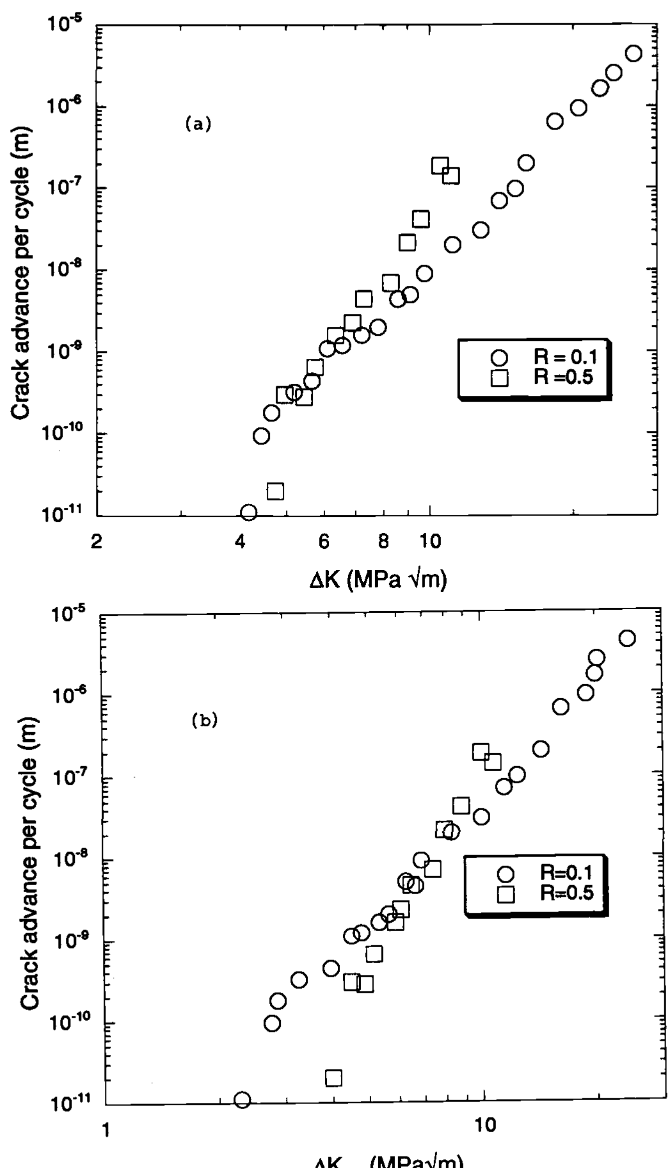

FIG. 4—(a) *Crack growth rate versus nominal* ΔK *in vacuum,* (b) *crack growth rate versus* ΔK_{eff}.

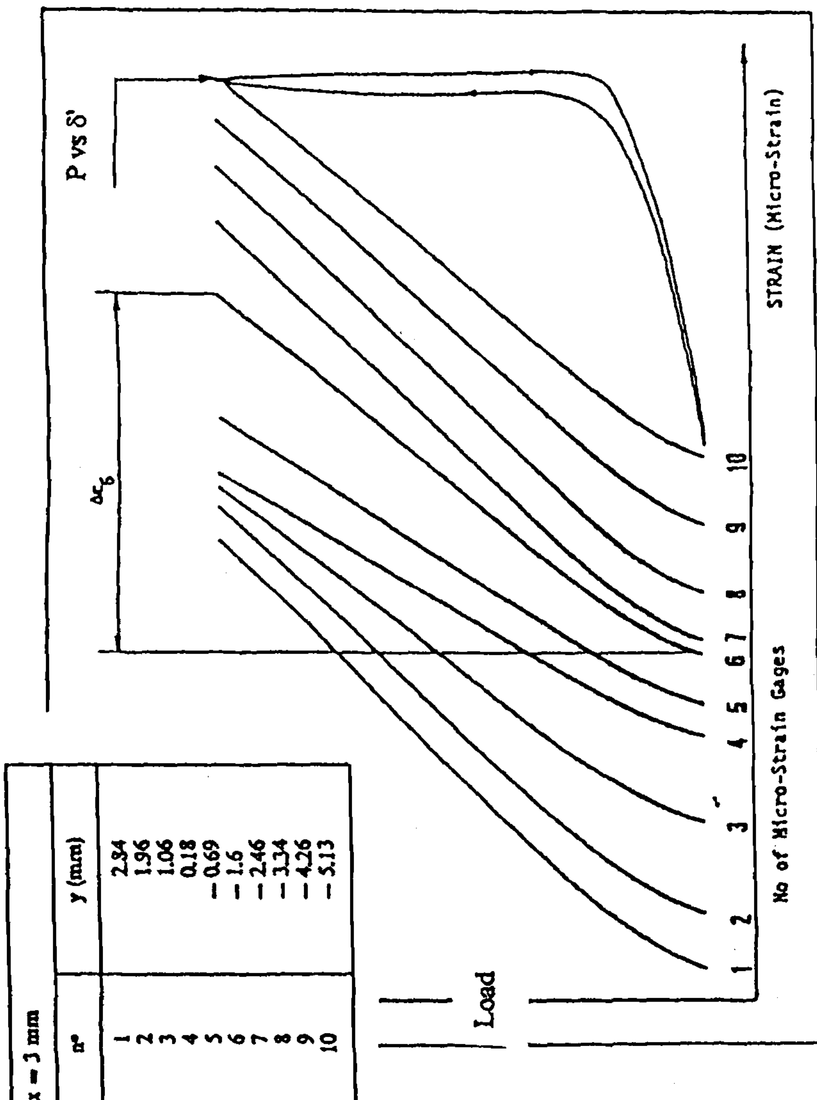

FIG. 5—*Far-field compliance changes compared with near crack tip strain changes.*

tip. Note that the strain amplitude depends upon the gage location. The crack was at about 3 mm from the gage location plane and the strain field analyzed is in the elastic range.

Note also that the strain amplitude depends upon the gage location as can be expected from fracture mechanics theory. For example, the strain amplitude measured by gage 6 ($\Delta\varepsilon_6$ in the figure) is twice as that measured by gage 5. Also, comparing these diagrams, observe that changes in slope in the load-versus-strain diagrams are at different loads depending upon the gage location; for example, this change in slope for gage 6 is observed at a load much higher than that for gage 9. Note that gage 6 is closer to the cracking plane than gage 9. There is no unambiguous relationship between the far-field closure level (measured by the load versus differential displacement diagram) and the near-field strain amplitude changes. Also, strain changes near the crack tip occur at loads lower than the nominal crack opening level (if no far-field stress is transmitted to the crack tip, one would expect the strain to be constant below the crack opening load), whose effects are not taken into account with the definition of crack opening level used in this study.

These experiments show some of the drawbacks of the conventional definition of closure. Despite these shortcomings, correction for crack closure does permit us to take into account the R ratio effect, Figs. 3*b* and 4*b*. However, the crack growth relationships obtained (after correction for closure) do not take into account the environmental effect.

The evolution of the measured crack opening levels in air, expressed in terms of the Elber's efficiency factor, U_E, is given in Fig. 6. This term represents the ratio of the effective to the nominal stress intensity factor amplitude. For the test conditions studied here, no closure was detected at the R ratio of 0.7. In Elber's original paper, U_E is considered to be constant for a given load ratio. Later studies show that this parameter depends upon various mechanical factors such as K_{max}, the nominal stress level, and whether the global loading is in plane stress or plane strain [*14,15*]. In the present study, the value of the crack opening levels measured are quite comparable to the ones determined by Newman [*15*], assuming plane strain conditions for $K_{max} > 17$ MPa m$^{1/2}$. Newman's analysis represents closure due to plasticity effects and the present study indicates that these effects are predominant for $K_{max} > 17$ MPa m$^{1/2}$ for the studied material. The fact that at lower K_{max} values the measured closure levels are much higher than the estimated ones for plasticity-induced closure indicates that under such conditions closure should be due to other mechanisms, such as roughness or fracture profile mismatch [*16*]. If such is the case this change in closure mechanism

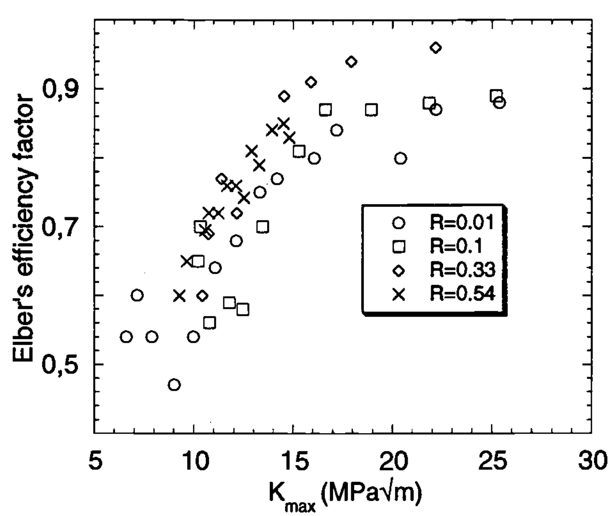

FIG. 6—*Elber's efficiency factor for CA tests in air.*

should take place at a particular monotonic plastic zone size, governed by K_{max} and independent of the load ratio.

It was also noted that crack opening loads were systematically lower in vacuum than in air, for a given ΔK. Limited experimental results show that the microhardness in the plastic zone can be much higher in vacuum than in air, indicating that the strain distribution in the plastic zone can be affected by the environment [17]. This can explain partially the differences in closure levels in air and in vacuum.

Overload Tests—Next, the changes in crack closure following a single overload for a test are presented. Figure 7*a* shows the evolution of the crack growth rate with respect to the crack length. A 100% overload is applied at a crack length of 29.3 mm. The test was conducted in air at a baseline load ratio of 0.1 with a baseline ΔK of 16 MPa $m^{1/2}$. Under such conditions, just after the overload, crack acceleration is observed following which the crack growth is retarded. After the point of minimum growth rate, the crack reaccelerates to reach the preoverload growth behavior. The numbers in this diagram represent crack positions where closure measurements, given in Fig. 7*b*, were carried out. For instance, diagram 1 was measured before the overload, diagram 2 just after it, and so on. In the initial acceleration phase, the measured crack opening load decreases concomitant with crack acceleration (see diagrams 1 and 2 in Fig. 7*b*). In the deceleration phase, the crack opening load remains lower than the preoverload level while the crack growth is considerably retarded (by comparing diagrams 1 and 3, Fig. 7*b*). Thus in this phase the evolution of the crack opening load is not in agreement with that of the crack growth rate. In the crack reacceleration phase (after the point of minimum growth rate), sometimes, one can note two kinks in the crack opening diagram (see diagrams 4 and 4′). According to Paris and Hermann [18], the lower kink represents far-field crack opening at the overload application point and the upper kink P_1, near crack tip opening. These results brings out the difficulties in identifying the crack opening load after an overload.

The evolution of the two crack opening loads is shown in Fig. 7*c*. In this diagram the maximum and then minimum loads are also given for reference. The distances a^* and a_d correspond to the crack advance after the overload application, *S*, to reach the minimum growth rates and the preoverload growth rates, respectively. It can be seen here that the evolution of the upper crack opening level is in agreement to that of the crack growth rate, in the crack reacceleration phase; i.e., P_1 decreases as *da*/*dN* increases. However, the preoverload crack opening level is not attained even though the crack growth rate has reached steady-state behavior.

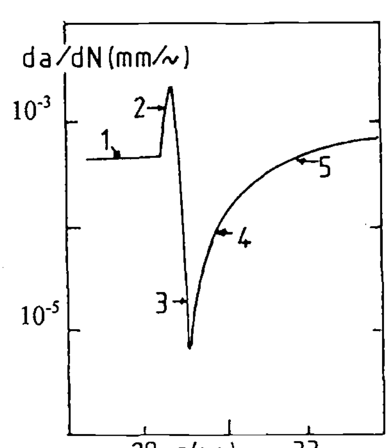

FIG. 7*a*—*Overload test: evolution of crack growth rate.*

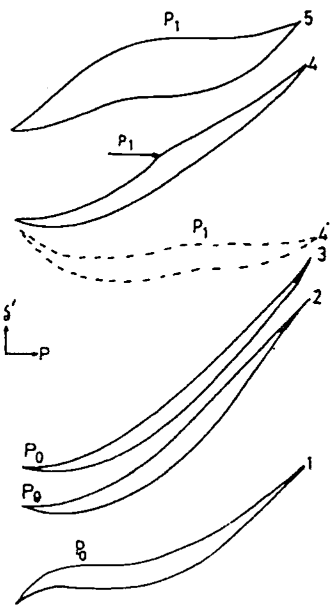

FIG. 7*b*—*Overload test: evolution of crack opening diagrams.*

The relationship between da/dN and ΔK_{eff} for overload tests in vacuum is now compared with that obtained from CA tests (Fig. 8). These tests cover a large baseline ΔK range from near-threshold conditions to 19 MPa $m^{1/2}$. The baseline load ratios were 0.1 and 0.5. About 80% of the measurement points representing overload-affected behavior fall within the scatter obtained for CA tests. The remaining 20% which are well outside the scatterband represent mostly crack growth in the decelera-

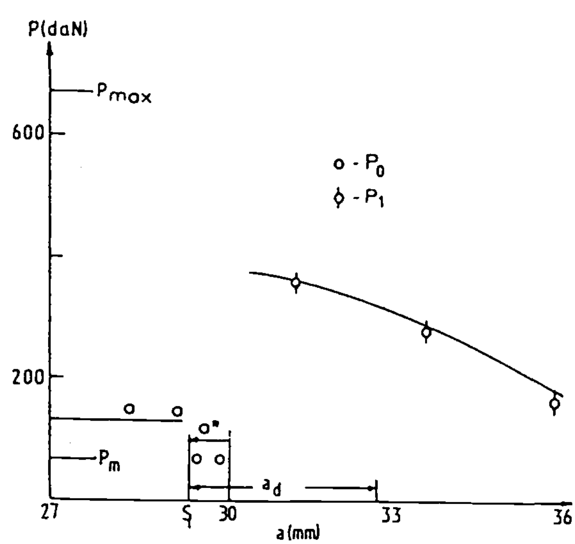

FIG. 7*c*—*Overload test: evolution of crack opening loads.*

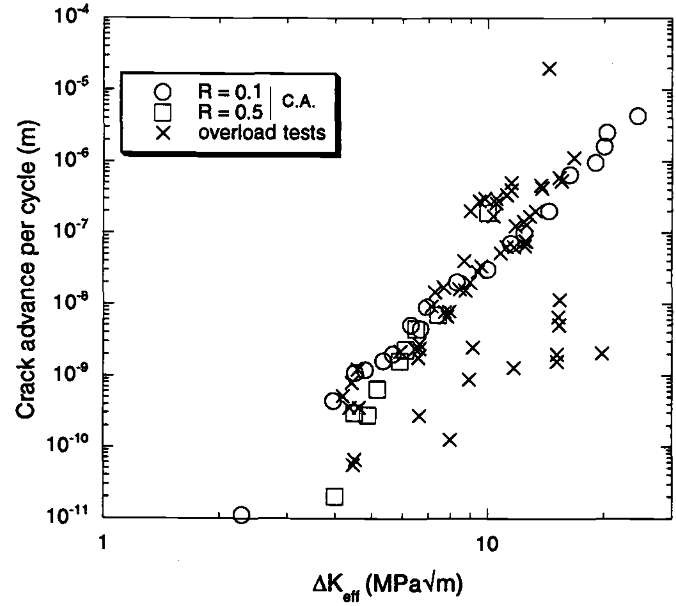

FIG. 8—*Relationship between* da/dN *and* ΔK_{eff} *for CA tests and post-overload behavior in vacuum.*

tion phase. It can be seen here that the overload-affected crack growth behavior cannot be unambiguously represented by the curve obtained from CA tests. Such results have been previously reported in Refs *19* and *20.*

Block Load Tests—The relationship between the average crack advance per block (from three companion tests) and the maximum stress intensity factor in the block (K_{maxB}) is given in Fig. 9. The

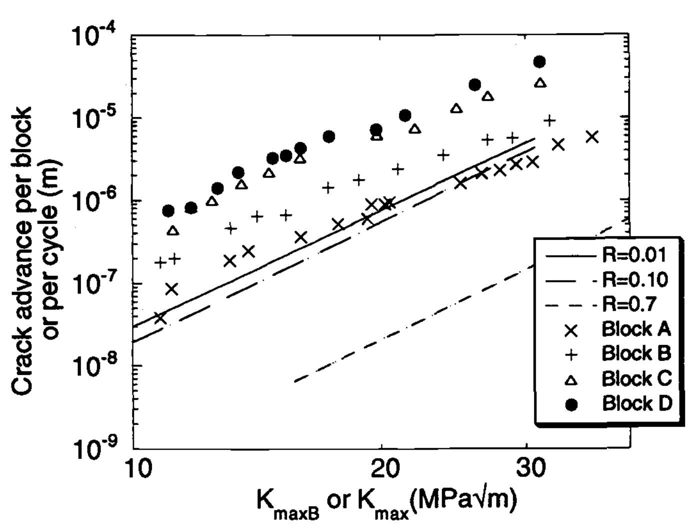

FIG. 9—*Crack advance per block versus maximum stress intensity factor in a block.*

constant-amplitude behaviors under selected R ratios are also given. It can be seen here that the crack advance per block for a given K_{maxB} for Block A (which contains one cycle at each load level) is almost comparable with that observed under CA conditions at $R = 0.01$. For the other blocks, the crack growth rates are 2 to 10 times higher than that observed for Block A. Blocks B, C and D contain the same number of cycles in levels 1, 2 and 4 (see Table 2) and only the number of cycles in level 3 increases from 10 to 100. Thus it can be seen that for these blocks, the crack growth rate increases as the number of cycles in level 3 increases.

An example of the load versus differential displacement diagram for Blocks A and B is given in Figs. 10*a* and 10*b*. The numbers in the diagram 10*a* refer to load reversal points. The block starts at point 1, then goes to point 2 and to point 3 and finally to point 9, describing all the load excursion in the block. A large change in slope in the load versus displacement diagram is observed and, similar to the definition of the crack opening load under CA conditions, the crack opening load can be iden-

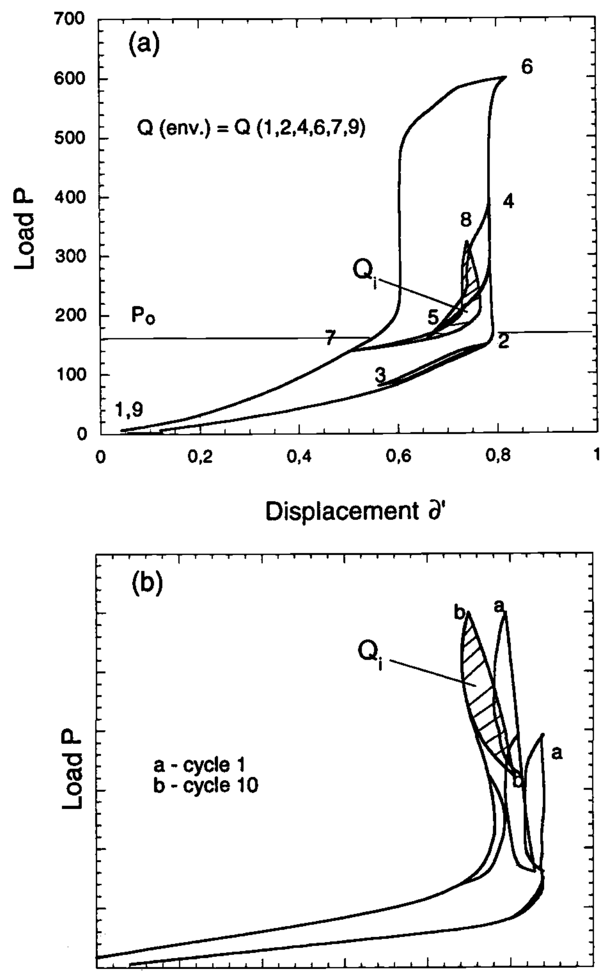

FIG. 10—*Crack opening diagrams for block load tests:* (a) *Block A,* (b) *Block B,* (c) *crack opening loads for block load tests compared with CA tests.*

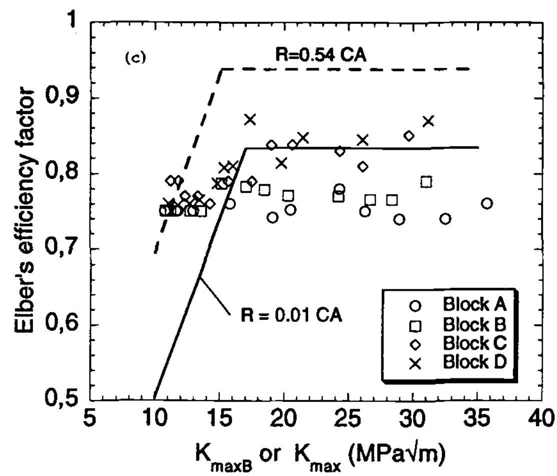

FIG. 10—*Continued*

tified (corresponding to the load P_o in Fig. 10*a*). Figure 10*b* corresponds to the crack opening diagram for Block B and again a global crack opening load P_o can be identified. These diagrams are further described in the following energy analysis subsection.

Figure 10*c* compares the evolution of the crack opening level for these tests to those obtained from CA tests. It can be seen that for Blocks A and B the global crack opening level is even lower than the ones observed for constant-amplitude conditions at $R = 0.01$, while for Blocks C and D the results obtained are comparable to the ones obtained for CA conditions at $R = 0.01$. It was suggested by Schijve [*21*] that for stationary and short spectra, the crack opening load should be governed by the peak-to-peak load ratio (which in our case is equal to $R = 0.01$). The present results show that such a result is obtained only for Blocks C and D.

Energy Based Analysis

Constant Amplitude Loading Conditions—The results presented above are now analyzed in terms of the energy-based method. Figure 11 shows the relationship between the crack growth rate and the energy dissipated per cycle for CA tests in air. It can be seen here that at growth rates above 8×10^{-5} cycle a unique linear relationship, independent of R ratio, is obtained with a scatter of the same order as that seen in Fig. 3*b*. From a least-squares fit this relationship is given by

$$da/dN = 2\ 10^{-4*} \cdot Q \tag{4}$$

At lower growth rates, despite the scatter, a power-law relationship can be proposed of the form

$$da/dN = 2.22\ 10^{-5} \cdot Q^{3.8} \tag{5}$$

When comparing tests in air and in vacuum, Fig. 12, it is found that the linear relationship given by Eq 4 is applicable for crack growth in vacuum too. The effect of environment is discernible at lower growth rates where this linear growth law (Eq 4) is not valid in terms of the energy dissipated per cycle.

Figure 13 shows the relationship between the specific energy and the nominal ΔK level for both the studied environments. The specific energy is not constant and the relationship between these two

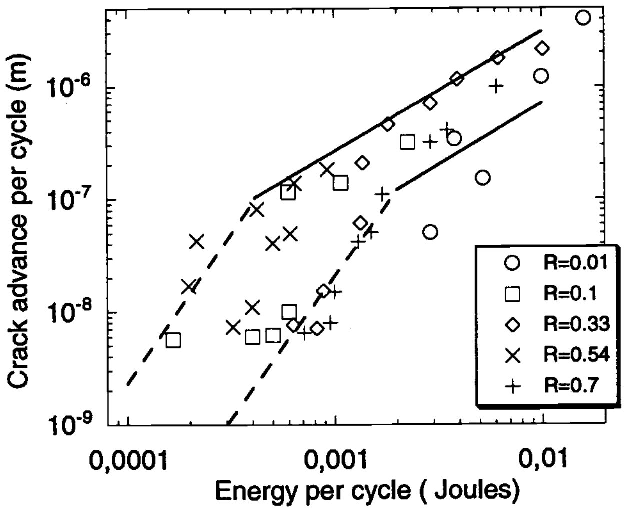

FIG. 11—*Evolution of the crack growth rate with respect to the energy dissipated per cycle in air.*

parameters depends upon the R ratio and the environment. It can be seen here that independently of the environment the specific energy reaches a minimum steady-state value, called U_{cr} at about 2.2×10^5 J/m^2. This value is quite comparable to that of 2.7×10^5 J/m^2 obtained by Ikeda et al. [5] by using micro-strain gages for the 2024 T4Al alloy. The value of ΔK at which this critical energy level is reached depends upon the test conditions, as can be seen in this figure. For lower ΔK values, the spe-

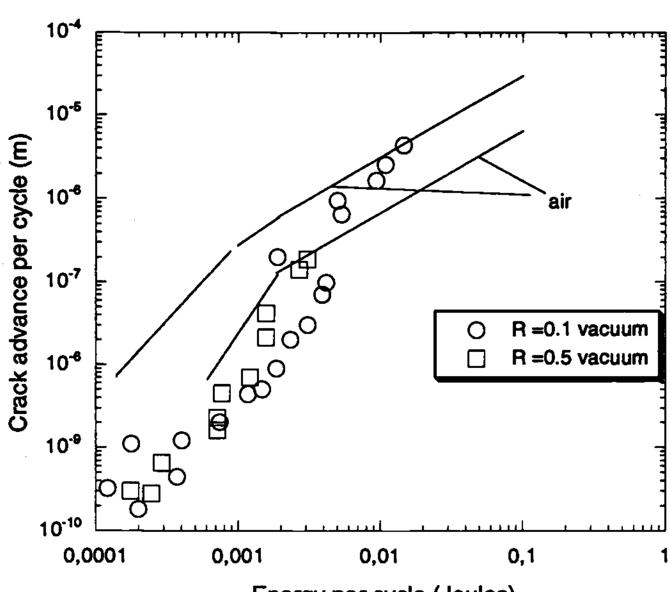

FIG. 12—*Comparison between tests in air and in vacuum in terms of energy dissipated.*

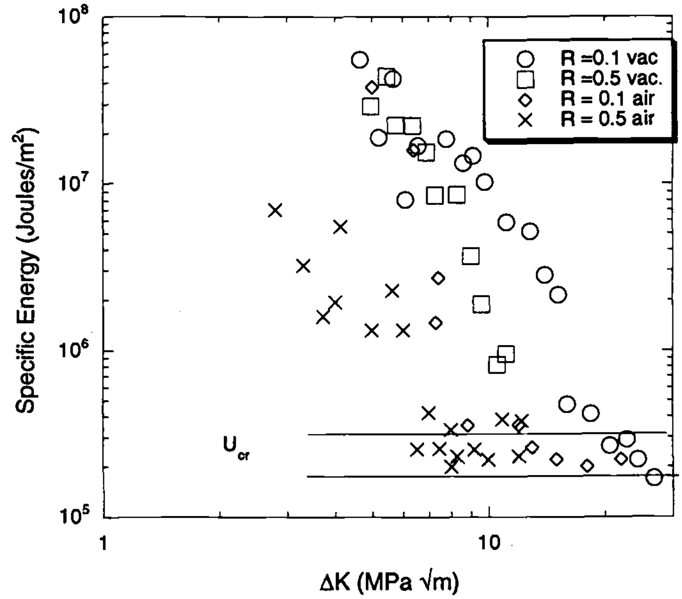

FIG. 13—*Relationship between the specific energy and* ΔK.

cific energy increases when threshold conditions are reached. It should be mentioned that such an evolution has been suggested by Davidson [*4*].

Overload Tests—The evolution of the energy parameters for the overload test given in Fig. 7 is now presented in Fig. 14. It can be seen here in phase A there is a slight increase in Q concomitant with an increase in growth rate followed by a decrease of Q in phase B which is characterized by crack retardation. The increase of Q in phase C is also compatible with the evolution of the crack growth rate. The specific energy accordingly increases in the retardation phase, reaching values comparable to that existing near threshold. Thus the evolution of the energy dissipated per cycle after an overload correlates unambiguously with that of the growth rate.

Block Load Tests—For the block load tests presented here in Figs. 9 and 10, the energy analysis was slightly modified. Referring to Figs. 10*a* and 10*b*, two different cases can be identified. For Block A essentially, it can been that apart from the individual cycles, one large cycle can be identified corresponding to the peak-to-peak load—to the load excursion 1-9-1 (see Fig. 10*a*)—and the hysteresis loops are closed during the entire block. Thus, for Block A and for other blocks at low $K_{\max B}$ values, the energy dissipated per block was equated to the sum of the energies dissipated during each cycle (Q_i) and to the envelop energy (Q_{env} corresponding to the area enclosed by points 1, 2, 4, 6, 7 and 9 in Fig. 10*a*), which represents the energy dissipated for the peak-to-peak load excursion. For other cases, the treatment is slightly different as in the example shown in Fig. 10*b*, which corresponds to Block B. This block contains ten cycles at steps 1, 2 and 3 and two cycles at step 4 (see Table 2). In this figure, cycles 1 and 10 for levels 2 and 3 are distinguished by letters *a* and *b*. For the test conditions presented here, there is a significant crack advance per block as can be seen by the fact that the first and tenth cycles corresponding to levels 2 and 3 do not coincide. Since the crack advance was significant during a block, the summation was carried out for individual cycles only [22]; i.e.,

$$Q_{tot} = \sum Q_i + Q_{env} \qquad (6a)$$

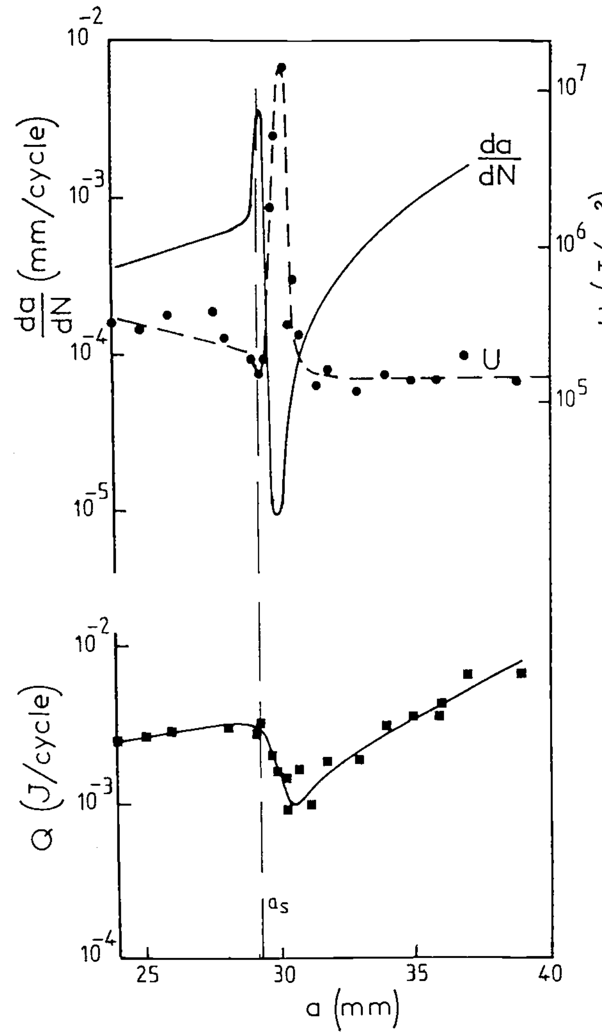

FIG. 14—*Evolution of energy parameters for the overload test in Fig. 7.*

for Block A for the all the test conditions and for other blocks at low K_{maxB} values

$$Q_{tot} = \sum Q_i \tag{6b}$$

for other test conditions.

The relationship between the crack advance per block and the total energy thus defined is then given in Fig. 15, comparatively to the linear relationship obtained for CA tests at high growth rates. It can be seen here that this linear relationship holds good for block load tests as well, correlating the crack advance per block to the total energy dissipated at high growth rates. At lower growth rates for block load tests no relationship can be proposed considering the limited number of data points.

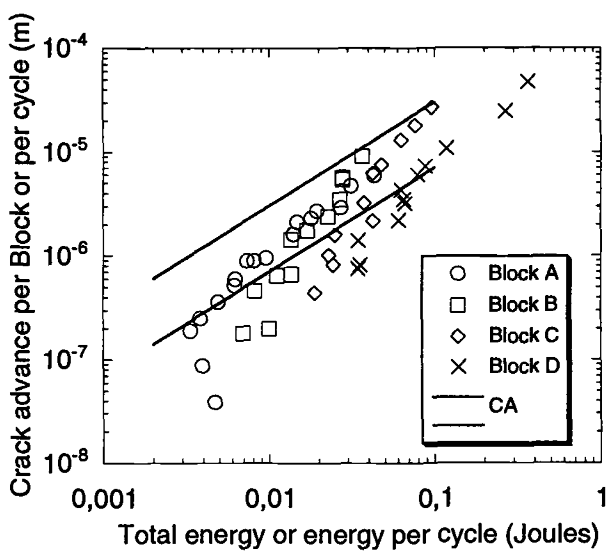

FIG. 15—*Crack growth rate versus energy dissipated, CA and block tests.*

Discussion

Modified Weertman's Law—The results presented above show that for constant amplitude test conditions both the crack closure concept and the energy based analysis developed here can be successfully applied. Applying the effective ΔK concept leads to crack growth laws depending upon the environment (see Figs. 3*b* and 4*b*).

Now looking at Weertman's Law (Eq 1), the specific energy is assumed to be constant. But the present study shows that the specific energy reaches a minimum constant level only after a critical ΔK level, depending upon the R ratio and the environment. Such an evolution of the specific energy has been analyzed in terms of a change in micromechanism of crack growth. The specific energy is constant when the crack advances during each cycle by a striation mechanism. At lower ΔK levels the crack advances by a step-by-step mechanism over Nf cycles, where $Nf > 1$ represents the number of cycles necessary for the crack to advance by a microscopic step [*23*].

Such a mechanism has been previously observed by Davidson based on in situ fatigue testing in a scanning electron microscope [*24*]. Striation formation is known to occur in this alloy for growth rates greater than or equal to 8×10^{-8} m/cycle [*23,25*], which corresponds to the growth rate above which a linear relationship is observed between the energy dissipated per cycle and the crack growth rate. The crack growth laws based on closure do not highlight this change in micromechanism of crack growth.

Now, considering that changes in U represent the damaging capacity of a cycle (the capacity to create a new surface during each cycle or not), Weertman's Law (Eq 1) can be modified by injecting variable values of U. One should expect a linear relationship between da/dN and $\Delta K^4/U$. The results obtained from various test conditions presented here (except block load tests) are shown in Fig. 16. It is seen here that a linear relationship between these two parameters is indeed obtained for both the environments, for constant-amplitude and post-overload test conditions with an acceptable scatter and covering about six decades of growth rates.

However, the constant A obtained from linear regression is equal to 0.069, which is lower than that proposed by the theoretical estimation of Weertman ($A = 0.259$). Other theoretical estimates propose a value closer to the present estimation [*26*].

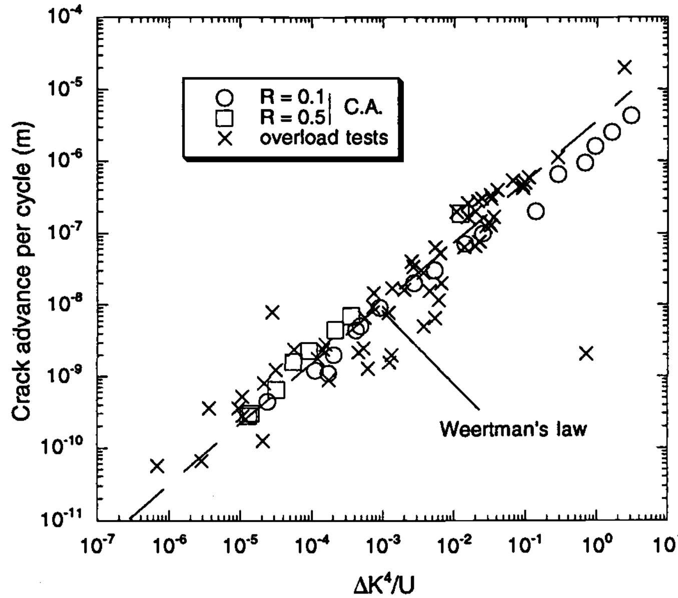

FIG. 16—*Verification of the modified Weertman's model.*

Relationship between Energy and ΔK—Let us now examine the relationships between the energy dissipated per cycle and the fracture mechanics parameter ΔK. Figure 17 shows the relationship between Q and ΔK for tests in vacuum. It can be seen here that Q is proportional to ΔK^4 and there is a large transition between data points near threshold and data at high ΔK values. For a given value of ΔK, Q is about the same for the two load ratios studied. However closure is observed at the lower R

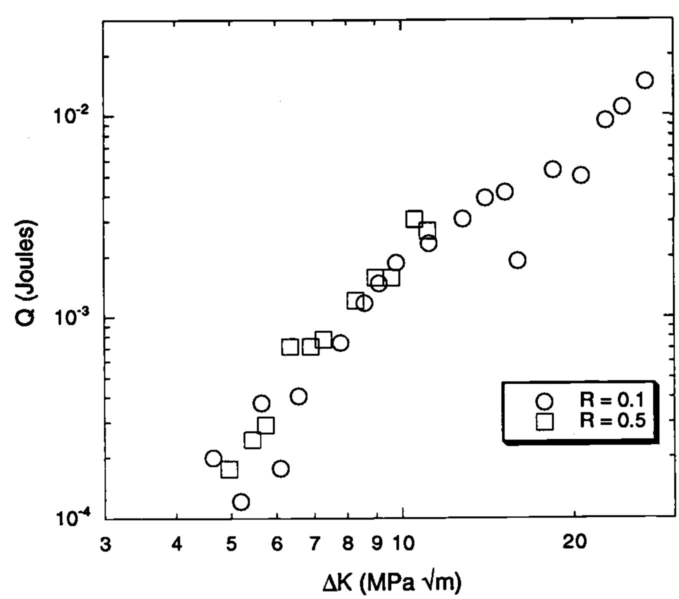

FIG. 17—*Relationship between energy dissipated and* ΔK *in vacuum.*

ratio. This indicates that the effect of closure on energy dissipated is negligible at moderate ΔK values. In this regard, the elegant experiments of Bowles using the infiltration technique are recalled [*27*]. His study showed clearly that regions of physical contact between the opposite crack faces are heterogeneously distributed along the crack front and as such the closure phenomenon is not uniform. Moreover, even at loads lower than the nominal closure level, parts of the crack were open. The load versus potential-drop diagram shows that electrical contact between the opposite crack faces changes gradually, supporting the hypothesis of a gradual crack opening and closure process. With this aspect in mind, and the fact that strain changes occur below the nominal closure level, it is not surprising that at moderate ΔK levels the energy dissipated is independent of R ratio.

To understand further the relationship between closure and energy, the evolution of Elber's efficiency factor, U_E, for tests at $R = 0.1$ is shown in Fig. 18 (U_E is the ratio between ΔK_{eff} and ΔK). The transitions shown in Fig. 17 are also seen in the evolution of the factor U_E. The transition in the ΔK range 11 to 15 MPa $m^{\frac{1}{2}}$ is marked by a clear diminution of the crack closure level. Hence, it appears that changes in crack closure levels are marked by concomitant changes in energy dissipated per cycle.

Comparison between Estimated and Measured Energies—To analyze this aspect in more detail, estimated energy per cycle by finite element studies from Ref *28* and by the analytical method based on Tracy's modelization [*29*] of the plastic zone shape in Mode I are compared with the measured values in Fig. 19. It can be seen here while the estimations confirm a fourth-power dependence of the energy dissipated per cycle on ΔK, the measured values are 10 to 100 times higher than the estimated ones. This difference can be attributed to two major factors. Firstly, the plastic zone size and the distribution of the strains within it do not necessarily follow the assumptions made in these two studies. Measurement of the plastic zone sizes using Nomarski interferometry shows that the plastic zone sizes are much greater than those given by Tracy's model [*30*], especially in the cracking plane.

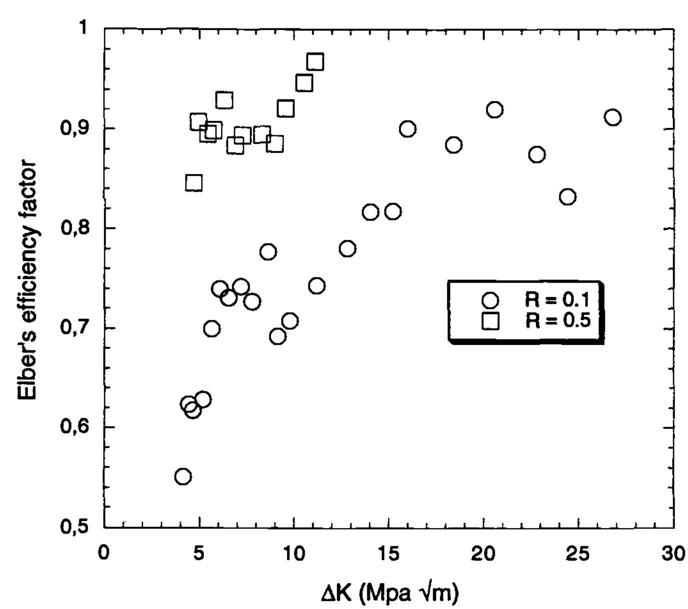

FIG. 18—*Elber's efficiency factor for tests in Fig. 17.*

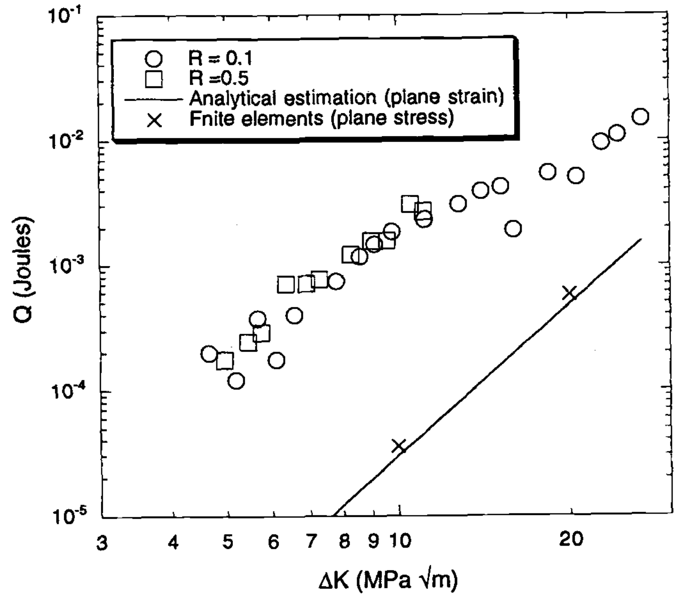

FIG. 19—*Comparison between theoretical and experimental estimations of energy dissipated.*

The second reason for these differences is the fact that these two estimations do not take into account the existence of Mode II displacements at low ΔK levels. Figures 20*a* and 20*b* compare the crack profiles observed at moderate and low ΔK levels in this alloy. The existence of a mixed crack mode displacement is evident at low ΔK levels. The cracking plane is not perpendicular to the loading axis and there is strong evidence of multiple crack branching, and under these conditions it is quite difficult to define the fracture mechanics parameters [*29*]. Now, considering a Mode II opening the plastic zone size and shape are quite different from those in Mode I and especially for the same K value the plastic zone can be three times as big as that in Mode I [*31*]. These factors have to be taken into account to make an acceptable prediction of the energy dissipated per cycle. The study in Ref *29* shows that the energy dissipated in the plastic zone is directly related to its area squared. The fact that the plastic zone area in Mode II can be three times as large as that of Mode I can alone lead to a tenfold increase in energy dissipated. However, it is quite difficult to predict the relative proportions of Mode I to Mode II opening occurring at the crack tip.

It should also be mentioned that according to Davidson, the region of constant specific energy is related to the development of a fully Mode I crack growth as against a mixed Mode I and Mode II crack growth near threshold [*32*]. The same author also suggests an increase in specific energy when threshold conditions are reached, an aspect which is confirmed in the present study. Moreover, the drop in potential occurring near the maximum load at low ΔK levels, Fig. 2*c*, can be attributed to a contact between the two crack surfaces due to Mode II sliding. It is quite difficult to talk of closure in Mode II as, per definition, the crack surfaces are always in contact.

In the case of overload tests, the results show here that the energy-based approach seems to give a better description of the crack growth rate as compared with the evolution of the crack opening loads. To get a clearer insight into this aspect, a test was carried out on the 2024 alloy in the annealed (O) condition. An 80% overload was applied and the crack was left to grow in the retarded phase. The evolutions of the crack growth rates and the crack opening diagrams are given in Fig. 21. As before, the numbers next to the crack opening diagrams permit identification of

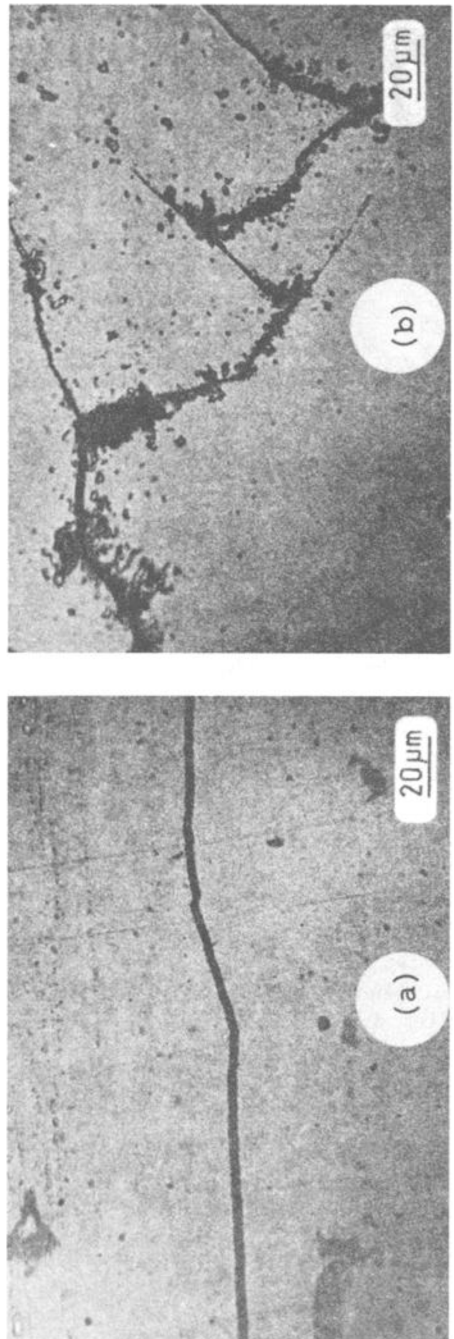

FIG. 20—*Crack profiles in vacuum: (a) crack profile at moderate* ΔK, *(b) crack profile near threshold.*

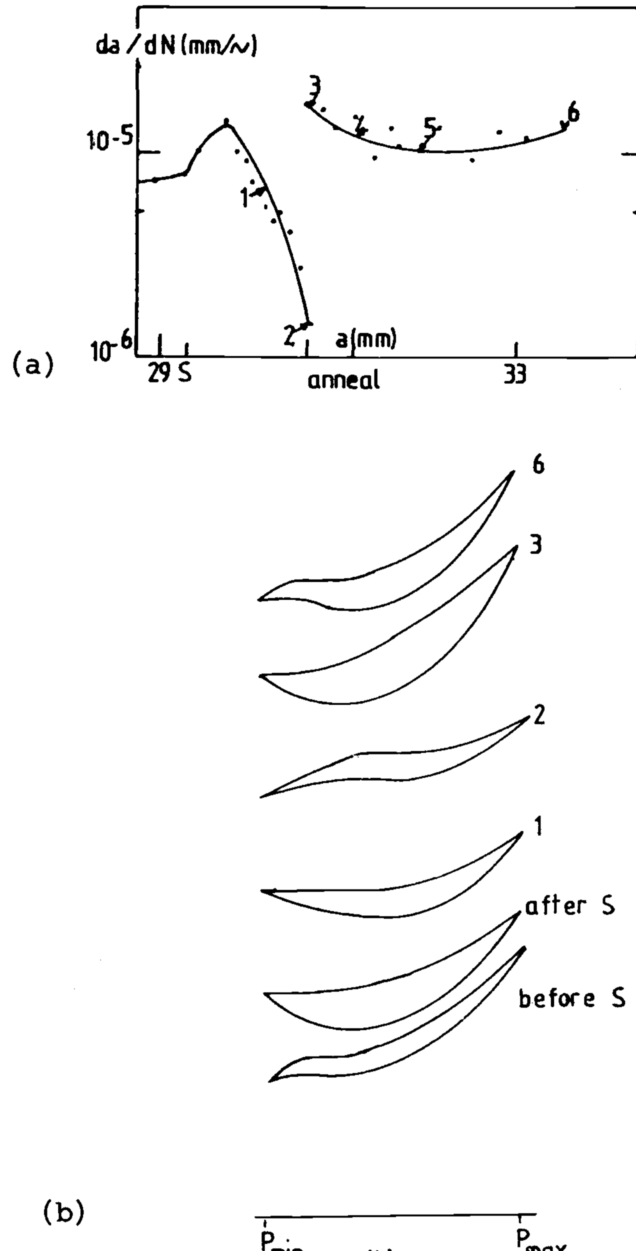

FIG. 21—*Evolution of crack opening diagrams for a test with an annealing treatment to remove residual stresses after an overload:* (a) *crack growth rate,* (b) *crack opening diagrams.*

when the measurement was made with respect to the overload. Comparing the measurements made just before and after the overload, it can be seen that the crack accelerates, energy increases and the crack opening level decreases. It can also be seen in the figure that as the crack retards (diagrams 1 and 2), significant closure is developed and the energy dissipated decreases. At this point, the test specimen was reannealed to remove the residual stresses in the overload plastic zone and the cycling was continued. Just after annealing (diagram 3), crack growth rate suddenly increases, as can be expected if the residual stresses due to the overload are annulled. At the same time, by comparing diagrams 2 and 3, it can be seen that there is no closure observed and at the same time the energy dissipated increases. For further crack growth, closure develops and concomitantly energy decreases. This test clearly shows the relationship between the energy parameters and the crack opening loads.

Limitations of Both Approaches—At this point it should be borne in mind that all the analyses presented above, both for the crack closure and the energy model, assume a uniform crack growth, all along the crack front. It is a well-documented fact that, especially after a strong overload, crack tunneling occurs in the middle of the specimen due to static crack advance following which the crack front remains blocked in the central plane strain regions of the crack front with crack growth limited close to the surface [*33*]. Under such heterogeneous crack growth conditions, it is more appropriate to talk of crack surface created than crack length (which implicitly assumes homogeneous crack advance all along the crack front). Bearing this in mind, the specific energies in phase B, in Fig. 15, are approximate as they are estimated by assuming uniform crack growth. It is at the same time difficult to assume the same definition of the fracture mechanics parameters (again estimated for a straight crack front) for such a nonuniform crack front. As a result, following an overload, the terms da/dN, ΔK and U have only limited meanings in the retardation phase.

Comments on Variable Amplitude Crack Growth—As far as block load tests are concerned, the energy-based analysis shows that at high growth rates the relationship between the crack advance and the total energy dissipated is the same as that obtained from CA tests. At lower growth rates, limited data indicate that this linear relationship does not hold good. The fracture surface analysis of these tests indicates that at high growth rates where the linear relationship is valid, the crack advances by a continuous process during each block, while at lower growth rates, individual blocks cannot be identified and the crack advances by a step-by-step mechanism [*34*]. The definition of the energy dissipated per block adds the envelop energy to the energies dissipated in each cycle for low growth rates and for Block A. This definition implicitly assumes a rainflow analysis as the peak-to-peak load is identified from this analysis [*35*]. The fact that at higher growth rates the crack advance per block is significant and that envelop energy loses its meaning suggests a limitation to the application of a rainflow kind of analysis to long spectra.

At higher growth rates the linear relationship between the crack advance per block and the total energy dissipated (i.e., at constant specific energy levels) suggests an efficient tool to estimate crack propagation behavior under variable-amplitude loading. However, the concepts developed in the present study have to be verified for different spectra with significant load interaction effects, which are negligible in the block loading tested here [*36*].

Conclusions

Fatigue crack behavior under a large range of experimental conditions covering R ratio effects, environmental effects, overload, and block load tests has been examined using crack closure concepts and an energy-based model. The following conclusions can be drawn from this study.

1. Most of the aspects of crack growth behavior essentially attributed to crack closure can be successfully explained via an energy-based analysis.

2. The energy analysis is based on a discontinuous crack growth at low growth rates as against a cycle-by-cycle growth mechanism at high growth rates. No such distinction is made for crack growth laws based on crack closure.

3. In the case of a single overload, conventional closure measurements fail to explain the evolution of the crack growth rates in the retardation phase, while the energy-based method seems to be more efficient in explaining the load interaction effect. However, limitations exist for both methods, especially in the retardation phase marked by a heterogeneous crack growth.

4. A modified Weertman's Law can be proposed to describe crack growth behavior independent of the environment and the test conditions.

5. In the case of block load tests the energy analysis shows that the growth law established at high growth rates for constant-amplitude tests holds well for crack advance during each block as well. The same analysis exposes the limitations of the rainflow method used for cycle counting under variable-amplitude conditions.

6. Examination of the relationship between the fracture mechanics and energy parameters indicates the strong possibility of mixed Mode I and Mode II displacements in the vicinity of the crack tip as threshold conditions are reached.

References

[1] Paris, P. C. and Erdogan, F., *Transactions of ASME, Journal of Basic Engineering,* Vol. 85, 1963, p. 263.
[2] Mc Clintock, F. A., *Fracture of Solids,* Wiley, New York, 1963, p. 65.
[3] Weertman, J., *International Journal of Fracture,* Vol. 9, 1973, p. 125.
[4] Davidson, D. L. and Lankford, J., *Proceedings,* Symposium on Environmental Sensitivity and Fracture of Engineering of Materials, TMS ASME, Warrendale, 1980, p. 59.
[5] Ikeda, S., Liaw, P. K., and Fine, M., *Engineering Fracture Mechanics,* Vol. 9, 1977, p. 123.
[6] Gross, T. S. and Weertman, J., *Metallurgical Transactions,* Vol. 13A, 1982, p. 2165.
[7] Ranganathan, N., Petit, J., and de Fouquet, J., *Strength of Metals and Alloys,* H. J. McQueen et al., Eds., Pergamon Press, U.K., Vol. 2, 1985, p. 1267.
[8] Elber, W., *The Significance of Fatigue Crack Closure, ASTM STP 486,* American Society for Testing and Materials, Philadelphia, 1976, p. 236.
[9] Liaw, P. K., *ASTM STP 982,* American Society for Testing and Materials, 1988, p. 62.
[10] Vasudevan A. K., Sadananda, K., and Louat, N., *Scripta Metturgica,* Vol. 28, 1993, p. 65.
[11] Kikukawa, M. and Kawahara, K., *Journal of Materials Science,* Vol. 26, 1977, p. 1964.
[12] Petit, J., *Fatigue Crack Threshold Concepts,* D. L. Davidson and S. Suresh, Eds, TMS AIME, New York, 1984.
[13] Ranganathan, N., Jendoubi, K., and Merah N., *Journal of Materials and Technology,* Vol. 116, 1994, p. 187.
[14] Schijve, J., *Engineering Fracture Mechanics,* Vol. 14, No. 3, 1981, p. 461.
[15] Newman, J. C., Jr., *ASTM STP 748,* American Society for Testing and Materials, 1981, p. 53.
[16] Ranganathan, N. and Petit, J., *ASTM STP 911,* American Society for Testing and Materials, 1983, p. 464.
[17] Bouchet, B., Thesis, University of Poitiers, France, 1976.
[18] Paris, P. C. and Hermann, L., *Fatigue Thresholds,* J. Backlund, et al., Eds., EMAS Publications, Wareley, U.K., 1981, p. 11.
[19] Brown, R. D. and Weertman, J., *Engineering Fracture Mechanics,* Vol. 10, 1978, p. 867.
[20] Ranganathan, N., Quintard, A., Petit, J., and de Fouquet, J., *ASTM STP 1043,* American Society for Testing and Materials, 1990, p. 374.
[21] Schijve, J., *ASTM STP 595,* American Society for Testing and Materials, 1976, p. 3.
[22] Benguediab, M., Ranganathan, N., Petit, J., Cazus, M. R., Lachaud, B., and Thomas, J. M., *Fatigue Crack Propagation under Variable Amplitude Loading,* J. Petit, et al., Eds., Elsevier Applied Science Publications, U.K., 1988, p. 309.
[23] Ranganathan, N., Bouchet, B., and Petit, J., *ASTM STP 948,* American Society for Testing and Materials, 1987, p. 424.
[24] Davidson, D. L., same as Ref 22, p. 3.
[25] Nix, K. J. and Flower, H. M., *Materials, Experimentation and Design in Fatigue,* F. Sherraft and J. B. Sturgeon, Eds., Westbury House Publications, Surrey, U.K., 1981, p. 116.
[26] Mura, T. and Villmann, *Journal of Applied Mechanics,* Vol. 9, 1986, p. 122.
[27] Bowles, C. Q., *ASTM STP 911,* American Society for Testing and Materials, 1983, p. 146.

[*28*] Anquez, L., Same as Ref 22, p. 194.
[*29*] Ranganathan, N., Thesis, University of Poitiers, France, 1985.
[*30*] Ranganathan, N., Lafarie-Frenot, M. C., and Petit, J., *International Journal of Fracture*, Vol. 19, 1982, p. R31.
[*31*] Shih, C. F., *ASTM STP 560*, American Society for Testing and Materials, 1974, p. 187.
[*32*] Davidson, D. L., *Fatigue and Fracture of Engineering Materials and Structures*, Vol. 3, 1981, p. 229.
[*33*] Ranganathan, N., Bouchet, B., and Petit, J., *Engineering Fracture Mechanics*, Vol. 11, 1979, p. 775.
[*34*] Endo. T., "Damage Evaluation for Metals under Random Loading," *Proceedings*, Symposium on the Mechanical Behavior of Metals, Society of Material Sciences, Japan, 1974, p. 372.
[*35*] Ranganathan, N., Benguediab, M., Henaff, G., and Adiwijayanto, F., *ASTM STP 1203*, American Society for Testing and Materials, 1993, p. 326.
[*36*] Ranganathan, N. and Desforges, J. R., *Fatigue and Fracture of Engineering Materials and Structures*, Vol. 19, 1996, p. 997.

Experimental Characterization of Closure

R. Pippan,[1] F. O. Riemelmoser,[1] and C. Bichler[1]

Measurability of Crack Closure

REFERENCE: Pippan, R., Riemelmoser, F. O., and Bichler, C., **"Measurability of Crack Closure,"** *Advances in Fatigue Crack Closure Measurement and Analysis: Second Volume, ASTM STP 1343,* R. C. McClung and J. C. Newman, Jr., Eds., American Society for Testing and Materials, West Conshohocken, PA, 1999, pp. 41–56.

ABSTRACT: Crack closure can be measured either with compliance techniques or by means of crack propagation methods.

Each of these methods has its own specific limitation. We have performed simulations to show that the results of the measurements with compliance technique near the tip depend strongly on the position of the displacement gages and that the compliance curves of the remote clip gages are often too insensitive to detect the near-crack-tip closure.

Apart from the sensitivity of the various methods for measuring near-tip closure there are also problems in determining the effective stress intensity ranges from the load-displacement curves. The different procedures proposed in the literature are discussed, too. It will be shown that the measured stress intensity where the crack physically opens is the parameter which determines the effective stress intensity range. Only in the case of a minute number of contacts with a width very small in relation to the distance to the crack tip does the stress intensity factor, where the contacts open, underestimate the real acting effective stress intensity range at the tip.

KEYWORDS: crack closure measurement, compliance technique, plasticity-induced crack closure, asperity-induced crack closure

In intrinsic ductile materials the fatigue crack growth rate is governed by the cyclic plastic deformation at the crack tip. If the crack is open during the complete cycle and small-scale yielding conditions prevail, then the stress intensity range, ΔK, and the yield strength of the material characterize the cyclic plastic deformation at the crack tip. Hence ΔK often is labeled as the fatigue crack driving force.

But fatigue crack surfaces are in contact during a certain part of the load amplitude. Such contacts transfer stresses between the crack flanks and they reduce the real driving stresses at the crack tip. In other words, these contact stresses shield the crack tip from the applied loading [*1–3*]. For the determination of the real acting driving force at the crack tip, one has to take into account the applied load amplitude and the contact stresses.

There are different types of fracture surface contacts, wedge-like contacts, asperities (point contacts), sliding contacts and bridges [*2,3*]. In metals under Mode I loading the wedge-like contacts and the asperities are the most important types. Hence we will restrict our considerations to these types of contacts, which makes the discussion much easier.

Usually the effective driving force ΔK_{eff} is not calculated from the applied load and the stresses acting on the fracture surfaces; instead it is determined by

$$\Delta K_{\mathrm{eff}} = K_{\max} - K_{\mathrm{cl}} = K_{\max} - K_{\mathrm{op}} \tag{1}$$

[1]Vice director and research assistants, respectively, Erich-Schmid-Institut für Festkörperphysik der Österreichischen Akademie de Wissenschaften, A-8700 Leoben, Jahnstr. 12, Austria.

where K_{max} is the maximum stress intensity factor and K_{cl} or K_{op} is the stress intensity factor where the crack tip closes or opens, respectively. It should be noted that K_{cl} ($= K_{op}$) is defined as the K-level above which the compliance behavior appears to be linear and below which it is nonlinear. It will be shown that the crack tip is not necessarily closed at $K < K_{cl}$ if there are asperities between the two crack flanks behind the crack tip.

This determination of ΔK_{eff} is based on the assumption that cyclic plastic deformation, and hence the crack propagation, starts only when the crack becomes open. We will denote this as the closure concept, which is widespread in engineering application and the fatigue literature. In spite of the success of the closure concept there are many discrepancies concerning the experimentally and theoretically determined quantitative contribution of closure, the techniques to measure the effect of closure and the significance of the different closure mechanisms. In this study we will try to answer two critical and fundamental questions:

1. Is the effective driving force given by $K_{max} - K_{cl}$?
2. Is K_{cl} or K_{op} really measurable?

For the sake of clearness we distinguish between the near crack tip and the remote crack closure. This classification is somewhat arbitrary. The reason for this separation is that in case of remote crack closure there is no problem to detect K_{cl} or K_{op} with the standard compliance technique. We can consider only the question: Is the measured ΔK_{eff} a real effective driving force?

The paper starts with a brief classification of the measurement techniques. Then we discuss the remote tip closure, at first the case of a single asperity and then the effect of multiple asperities. In Section 4 the near-tip closure will be considered, where we start with some fundamental differences of the plasticity-induced closure in plane strain and plane stress. We will discuss the significance of the near-tip contact, where we estimate the minimum length of a contact to cause a complete shielding of the crack tip, and the measurability of the near tip closure.

Methods to Measure Crack Closure

For the discussion we will divide the different techniques into two groups: compliance techniques and crack propagation techniques.

The compliance techniques measure the mechanical response of the contact stresses. Figure 1 shows schematically typical load displacement, respectively, load strain curves. There are many dif-

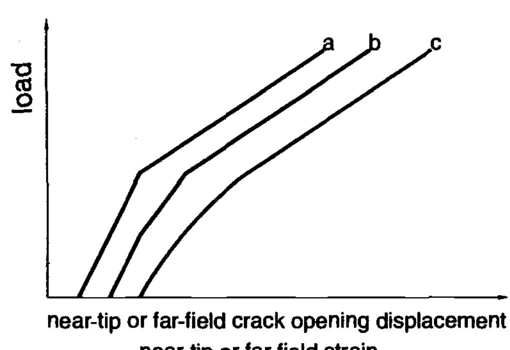

FIG. 1—*Schematic illustration of different compliance curves where the effect of cyclic plasticity is not taken into account.* (a) *Effect of single or multiple asperities which close at a certain load;* (b) *effect of two types of asperities which come into contact at two different loads;* (c) *continuous unzipping of the crack.*

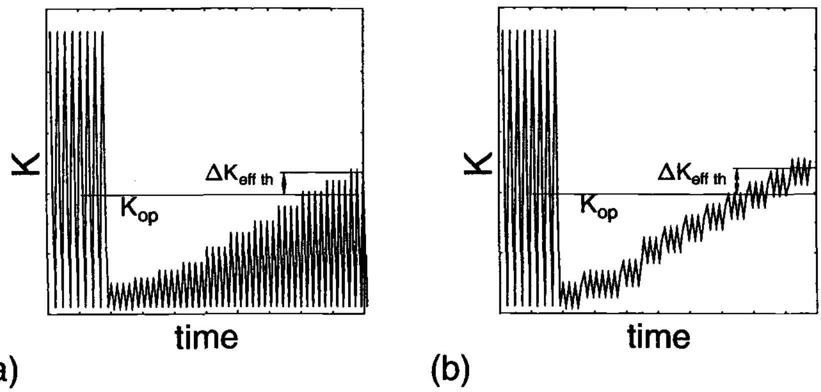

FIG. 2—*Schematic representation of the loading procedures to measure the opening load of a crack after Ref* 14.

ferent methods applied to measure the strain or the displacement: mechanical strain or displacement gages [*1,4*], interferometric [*5–7*]—in situ optical microscope—or in situ scanning electron microscope observation [*8*]. Each method has is own specific limitation. But there are no essential differences between near crack tip or remote from crack tip and between strain or displacement techniques.

The propagation techniques measure the influence of crack closure on the crack tip deformation or directly on the crack growth rate. This group can be divided into two subgroups:

- In the first subgroup one assumes that a unique relation exists between ΔK_{eff} and the crack growth rate. A comparison between the observed crack growth rate at the given ΔK and the da/dN - ΔK_{eff} relation gives directly the contribution of the effect of crack closure. Many different techniques were proposed to measure the necessary da/dN - ΔK_{eff} relation; see for example Refs *9–13*.
- The second subgroup is based on the assumption that a crack does not propagate when it is closed and it can only start to propagate if ΔK is larger than the effective threshold of stress intensity range, $\Delta K_{eff\ th}$, and if K_{max} is larger than K_{op} + $\Delta K_{eff\ th}$ [*14–18,21*]. Two possible loading procedures to determine K_{op} are depicted in Fig. 2. In both cases the crack growth experiments are interrupted at minimum load. In the first example a very small load amplitude is applied and increased in steps until the crack starts to propagate (Fig. 2*a*). The other possibility (Fig. 2*b*) is to apply a small load amplitude which corresponds to ΔK which is somewhat larger than $\Delta K_{eff\ th}$ and increase the mean load until the crack starts to propagate. From this K_{max} value and the given $\Delta K_{eff\ th}$ one can now determine K_{op}.

Other techniques as, e.g., potential drop and the acoustic emission method, which do not measure the mechanical response of crack closure (for example, such techniques indicate sliding contacts, which do not transfer a significant amount of stresses in Mode I loading [*19*], are not discussed in this paper.

Remote Crack Tip Contacts

The fatigue crack growth experiments of Herzberg et al. [*20*] on specimens with a single artificial contact with different contact height indicate that the measured opening stress intensity overestimates the effect of crack closure. Vasudevan and Sadananda [*22,23*] also pointed out that the compliance technique for measuring asperity-induced crack closure predicts too small effective stress intensity factors. This leads to some modified methods to determine the effective stress intensity range [*24,25*].

In order to make the discussion of this problem easier we will consider contacts which are loaded at larger distances from the crack tip because in this case there is no problem to detect the fracture surface contact with remote or near-tip compliance techniques and a simple linear elastic consideration is applicable.

Single Asperity

In our model, Fig. 3, it is assumed that a very small rigid vertical asperity is present at a short distance behind the crack tip (i.e., relatively short if compared with the crack length). The asperity will touch the upper and lower crack face when K is reduced to K_{cl}. Because of the short distance between the asperity and the crack tip, this K_{cl} will be recognized as the crack closure K-level in the usual compliance type measurement techniques to determine K_{cl}. However, the physical crack tip is still open, and after further unloading the crack flanks at both sides of the asperity will still show further displacements; see Fig. 3.

A through-thickness asperity is assumed. This allows a plane consideration. The width of the contact is $\frac{1}{1000}$ of the distance between the crack tip and the asperity. Since the length of the crack and the specimen size are large in relation to the distance between the crack tip and the asperity, the contour of the crack flanks at the first contact is given by the applied stress intensity and the height of the asperity. A detailed description of the calculations of the stresses on the asperity and the resulting contour is given in Ref *26*. Figure 3 shows the calculated contour of the crack flanks at K_{cl} where the first contact between the fracture surfaces (dotted line) and the asperity occurs, and the contour of the unloaded crack (full line).

One can clearly see that during unloading below K_{cl} the deformation between the crack tip and the contact does not stop. A significant relaxation occurs until the cracked body is completely unloaded. The real shielding caused by such a small single asperity for a completely unloaded crack is 0.22 K_{cl} and not the complete part of the amplitude where the crack is partially closed. Hence a determination of the effective driving force by $\Delta K_{eff} = K_{max} - K_{cl}$ significantly underestimates the real Δk_{tip} (ef-

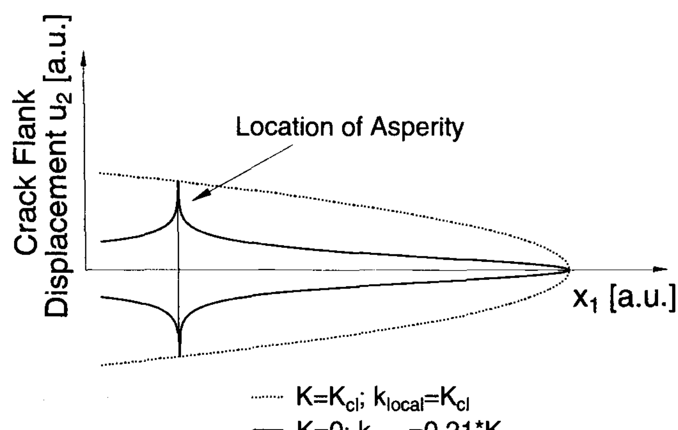

FIG. 3—*Calculated contour of the flanks of an elastic crack at* K_{cl} *(dotted line; at this* K *the first contact of the asperity with a crack flank occurs) and* $K = 0$ *(full line). The width of the rigid asperity is* $\frac{1}{1000}$ *of the distance between the crack tip and the asperity.* k_{local} *is the real acting local stress intensity factor at the crack tip. If no contact of the crack flanks occurs,* k_{local} *is equal to the applied or global stress intensity factor* K. *If a perfect fitting wedge is inserted in the mouth of a crack* $k_{local} = K_{cl}$ *(in the case of* $K < K_{cl}$*). In the case of a single asperity* k_{local} *can be significantly smaller than* K_{cl}*, which can be seen from the elastic relaxation from the contour of the crack.*

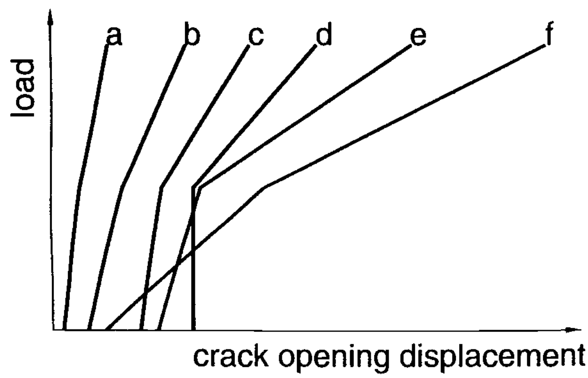

FIG. 4—*Schematic representation of the load versus crack opening displacement curve measured at different distances behind the crack tip of a crack with a single asperity. The gage is located very near the crack tip for curve (a), between the crack tip and the asperity for curves (b) and (c), at the position of asperity for curve (d) and behind the asperity curves (e) and (f).*

fective driving force at the crack tip). What can we now learn from the compliance in such a case? Figure 4 shows schematically the load vs. crack-tip opening displacement curves obtained at different positions behind the crack tip. At all positions a change in the compliance at K_{cl} can be observed. Curve "a" is determined very near the crack tip; here the crack opening displacement (COD) is proportional to the local driving force. In this case the technique proposed by Chen et al., which is based on the comparison of closure-free and closure-affected COD vs. load curves, gives the correct driving force. But this technique fails if we apply it to the COD vs. load curve at the position of the contact. We would conclude that $\Delta K_{eff} = K_{max} - K_{cl}$ because there is no change of the COD below K_{cl}. In other words, the COD vs. load curve at the considered small contact is equal to a COD vs. load curve of a wedge-like contact which fills perfectly the crack at K_{cl} and such a wedge would shield completely the crack tip. If we do not know where the contact is located and if we measure only one of the other COD vs. load curves, b, c, d, e or f, we can gather no information about

—the real driving force at the crack tip,
—where the contact is located, or
—the size of the contact.

What is now the result if we apply the crack propagation technique in the single asperity case?

- A comparison of the actual crack propagation rate with a da/dN vs. ΔK_{eff} curve will give us "per definition" the real driving force at the crack tip.
- The technique to determine K_{op} by measuring the first crack propagation in a rising ΔK or in a rising mean load (see Fig. 2) experiment does not give useful results. If in the rising mean load experiment (Fig. 2*b*) the chosen $\Delta K < 1.2\ \Delta K_{eff\,th}$, no crack extension below $K_{max} = K_{cl} + \Delta K_{eff\,th}$ should be observed. In this case one would determine K_{cl} or K_{op} but not the real driving force at the crack tip. If $\Delta K > 1.3\ \Delta K_{eff\,th}$ at each mean load the crack propagates, and therefore one would assume that no crack closure occurs.

From this point of view many crack closure measurements in the literature seem to be unreliable. But fortunately in reality crack closure is not caused by a very small single contact.

Multiple Asperities

In order to demonstrate that an increase of the number of asperities or an increase of the width of the contact reduces the elastic relaxation at the crack tip, we calculated the contour of the unloaded

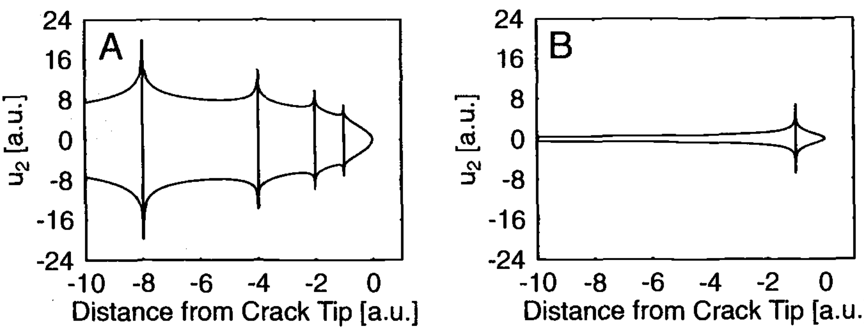

FIG. 5—*Comparison of the calculated contour of the flanks of an elastic crack at* K = 0 *with a single (A) and four (B) asperities, where the width of the asperities is* 1/1000 *of the distance between the crack tip and the first asperity.*

crack for two examples. The geometrical assumption made for the calculations of the contour in Figs. 5 and 7 looks very artificial, but the aim of these figures is only to demonstrate the significance of the effect of the number of asperities and the width of the asperity.

Figure 5 shows again a contour of a crack with one and four contacts when the applied load is zero. The four contacts are located at 1000, 2000, 4000 and 8000 times the width of the first contact, the contact width is equal to the distance between the contact and the crack tip divided by 1000, and the height is chosen in such a way that all asperities close at the same stress intensity factor. Furthermore, it is assumed that the distance between the asperities and the crack tip is small in relation to the crack length; this allows a more general consideration of this problem. A comparison of the contours shows that the elastic relaxation of the unloaded crack tip is significantly smaller in the case of four asperities. The local stress intensity at the crack tip at the applied stress intensity $K = 0$ in the case of one contact is 0.21 K_{cl} and in case of four contacts it is already 0.55 K_{cl}.

In Fig. 6 this increasing of crack tip shielding is depicted as a function of the number of equidistant very small contacts; the width is assumed as 1/1000 of the distance between the crack tip and the

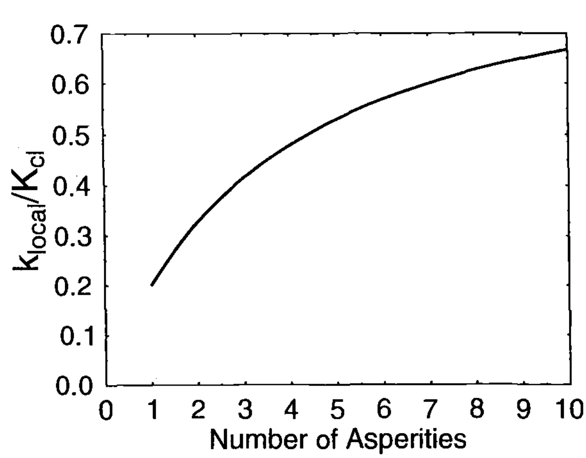

FIG. 6—*Influence of the number of contacts on the normalized shielding stress intensity* ($K_s/K_{cl} = k_{local}/K_{cl}$). *Equidistant asperities with a width of* 1/1000 *of the distance between the crack tip and contact are assumed.*

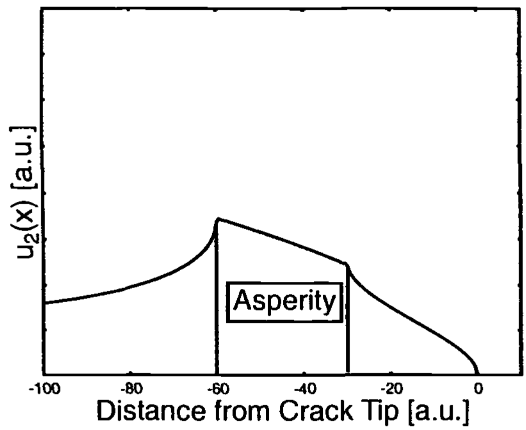

FIG. 7—*Calculated contour of the flanks at zero load of an elastic crack. The width of the asperity is assumed equal to the distance between the crack tip and its first contact point.*

contact. One can see that ten very small contacts cause a shielding of the unloaded crack tip, which is about 70% of K_{cl}. A very similar behavior can be observed when we increase the width of the contacts. Figure 7 shows the contour of the unloaded crack, where the width of the contact is equal to the distance between the crack tip and the beginning of the contact. The height is equal to crack tip opening displacement at K_{cl}. A comparison with the contour of the very small contact in Fig. 4 shows clearly that the elastic relaxation of the crack tip in the closed phase of the load amplitude is significantly reduced by the larger contact.

This discussion shows that only in the case of few very small contacts is the real shielding contribution significantly smaller than the usually assumed value $K_{cl} - K_{min}$. Only in this case are the problems addressed in the preceding subsection (single asperity) important. But roughness-induced or corrosion debris-induced closure is usually caused by many contacts; hence the standard measurement of K_{cl} from the compliance or by means of the propagation technique is a useful approach to determine the effect of closure.

Near Tip Crack Closure

From the mechanical point of view the fracture surface contacts can be classified into two extreme types, very small contacts and the wedge-like contacts. In reality we have a mixture of both types. By small contacts are meant asperities whose widths are small in relation to their distances to the crack tip. They may be caused by a mismatch of rough fracture surfaces, corrosion debris or by plastic humps induced by a single overload. The general problems in measuring the effect of such contacts have been discussed in Section 3. However, the width of a wedge-like contact (corrosion layers or a plastic wake field) is large in view of the distance between the contact and the crack tip. In such cases the crack tip is of completely shielded below K_{cl}. Therefore we have no problem with the explanation of how one should measure the driving force. Difficulties in the experimental determination of crack closure arise only when the contact between the fracture surfaces is localized to a small region near the crack tip.

The wedge-like contacts are caused by corrosion layers, or by the plastic wake. The influence of the corrosion layer or the plastic wedge in the plane stress case is widely accepted, but there exist extreme discrepancies in the fatigue community concerning the plasticity-induced closure under plane strain conditions. A number of fatigue experts [*22,23,27–30*] believe that it cannot occur under constant-amplitude loading. These problems are caused

—by a lack of simple explanation [*31,32*], or

—by some errors in the analyses [*22*].

But it really takes place [*25,31–37*]. This can clearly be seen in Fig. 8, where the crack-tip opening displacement at mid-thickness of a thick specimen as a function of the stress intensity is depicted for a steady-state growing crack. The small-scale yielding and the plane strain conditions were fulfilled in these experiments [*39*]. At this large stress intensity range (70 MPa$\sqrt{m}$) the contribution of oxide and roughness-induced crack closure can be neglected. Hence, the closure of the crack below about 25% of the maximum stress intensity is induced by the plastic wake. The aim of this paper is not to clarify the misunderstanding concerning plasticity-induced closure under plane strain condition. This is done elsewhere [*26,32*]. But one essential difference between the plane strain and the plane stress plasticity-induced crack closure should be pointed out. At constant stress intensity range under steady-state conditions (which means that crack extension is significantly larger than the plastic zone size) in the plane stress case the effect of the plastic wake can be represented by a wedge of constant thickness all along the crack. In the plane strain case the plastic wedge is limited to the immediate vicinity behind the crack tip. This is illustrated in Fig. 9 where the crack tip opening displacement at K_{max} and at $K_{min} = 0$ is schematically depicted for both plane stress (Fig. 9*a*) and plane strain (Fig. 9*b*). It should be noted that the Dugdale model is not applicable to describe the deformation under plane strain conditions; nevertheless we use it here to visualize the differences of the two types of wedges. In the plane stress case the unloaded crack is closed all along the crack and in the plane strain case it is limited to a region somewhat smaller than the size of the plastic zone.

The question which arises is whether such small wedges reduce the driving force significantly. In order to show that it does indeed, we discuss in the following the problem of how large a wedge has to be in order to completely shield the crack tip.

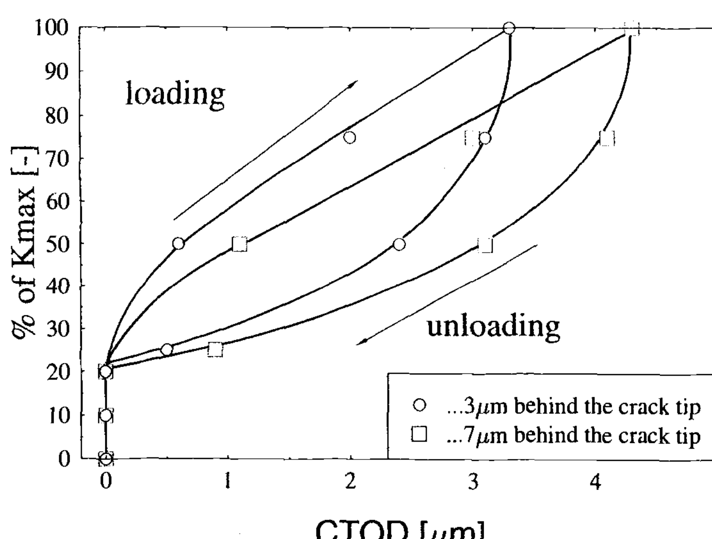

FIG. 8—*Crack-tip opening displacement measured in the midsection of a thick specimen of a steady-state propagating crack [39]. The experiments were performed in a cold-rolled austenitic steel at* ΔK = *70 MPa$\sqrt{m}$ and* R = *0.*

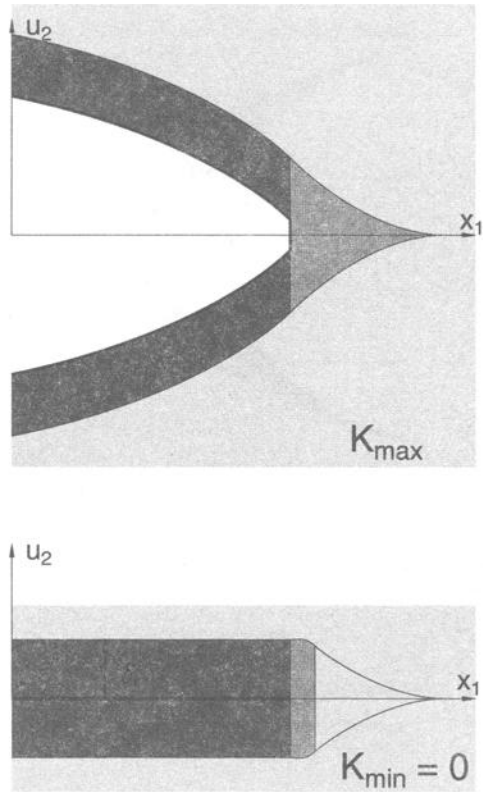

(a)

FIG. 9—*Schematic representation of the plastic wedge under plane stress* (a) *and plane strain conditions* (b). *For both cases the Dugdale model is used as a basis to describe the crack-tip deformation at* K_{max} *[38]. The effect of plasticity can be represented as a wedge of constant thickness (attached at the flanks of the crack) and a limited wedge with a maximum height at the tip in the plane stress and the plane strain case, respectively.*

What is the Minimum Size of a Wedge to Cause a Complete Shielding?

We imagine an open crack at maximum load and locate an artificial wedge immediately behind the tip which should completely prevent the deformation during unloading. What is the minimum length of such a wedge? In order to solve this question we shall use the Dugdale model and the McClintock-Rice superposition principle. Figure 10 shows schematically the crack flanks at maximum load and the unloaded crack. The corresponding stress distribution along x_1 is depicted in Fig. 10*b*.

In the Dugdale model the plastic zone is envisioned as a narrow strip which extends a distance ω ahead of the crack tip and is loaded by tractions equal to the yield stress σ_y over the length ω. The tractions along ω cause a negative stress intensity factor with an absolute value which is equal to the positive stress intensity factor caused by the far-field loading. The size of the monotonic plastic zone under small-scale yielding condition is then given by $\omega = (\pi/8)\ (K/\sigma_y)^2$. The cyclic plastic zone is given in the same way as the monotonic plastic zone with the exception that the loading parameter is replaced by the load range and the tractions in the strip, located in front of the actual physical crack,

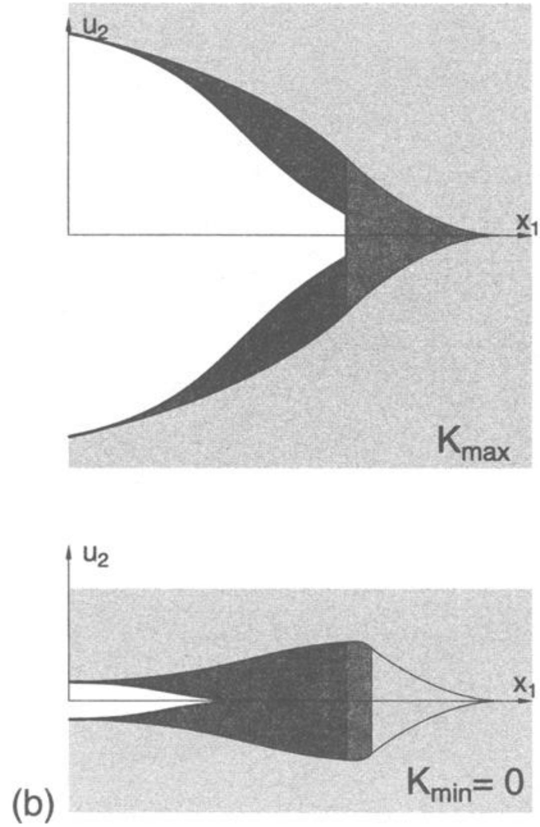

FIG. 9—*Continued*

are replaced by twice their value ($2 \cdot \sigma_y$) during the monotonic loading. The stress intensity caused by the tractions in the case of complete unloading and in the absence of crack closure is also equal to the stress intensity caused by the far-field loading at maximum load.

If we want to prevent the deformation during unloading we arrange a strip loaded by tractions (caused by the artificial wedge) behind the crack tip. The tractions of the unloaded crack along x_w should cause a stress intensity factor which is also equal to the absolute value of the stress intensity factor caused by the tractions along ω at the maximum load. In other words, the traction along x_w should cause the same stress intensity factor as the far-field loading at maximum load. The tractions are equal to the yield stress, because the possible maximum stress at the wedge is equal to the yield stress; otherwise the crack flanks would be deformed. The calculation of x_w is therefore identical to the derivation of ω. Hence the minimum length of the wedge to cause a complete shielding (i.e., to cause no cyclic plastic deformation) is equal to the size of the monotonic plastic zone

$$x_w = \omega \tag{2}$$

Therefore, the relative short plastic wedge in the plane strain case can induce a significant amount of shielding of the crack tip. But the experimental verification of this shielding may be difficult.

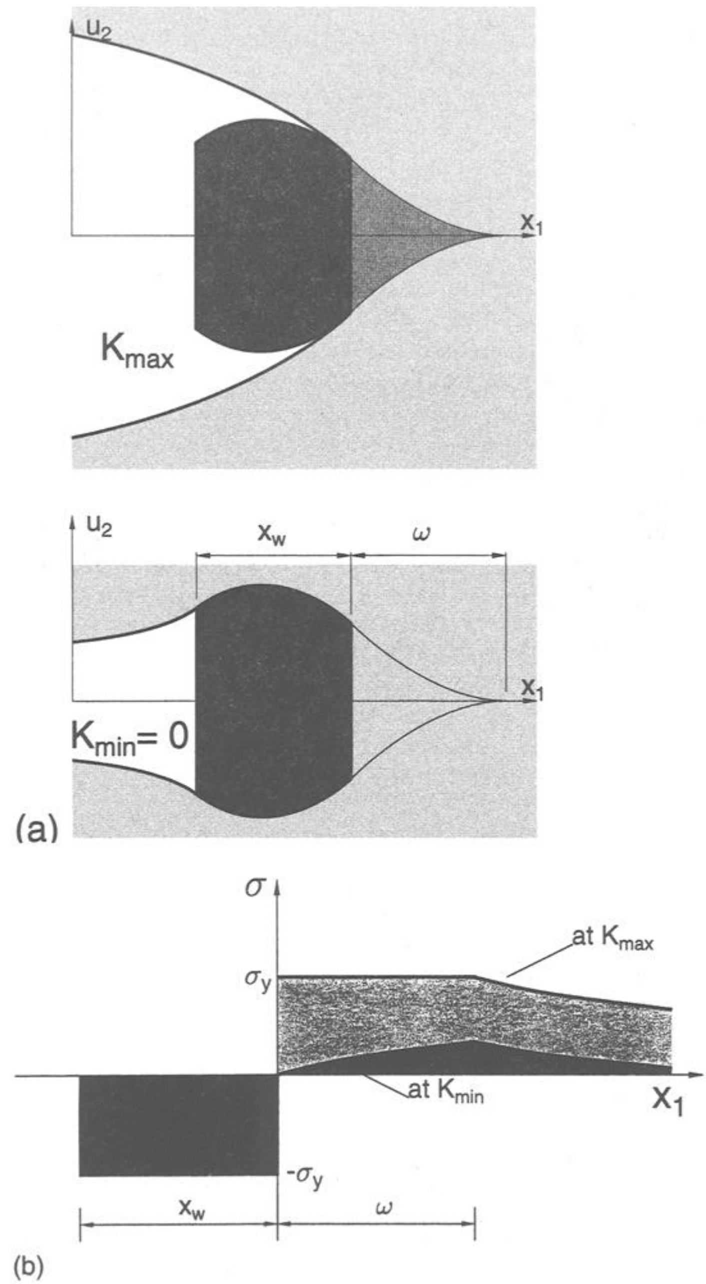

FIG. 10—*Schematic illustration of the effect of an artificial wedge which should completely prevent a deformation during unloading:* (a) *Crack-tip opening displacement at* $K_{max} = 0$, *and* (b) *stress distribution at* K_{max} *and* K_{min}.

For example, at $\Delta K = 3$ MPa$\sqrt{m}$ (stress ratio $R = 0$) and a yield stress of 300 MPa, which is typical for a high strength aluminum alloy or a medium-strength steel, Eq 1 gives for ω and therefore the minimum length of a wedge to cause a complete shielding $x_w = \omega = 30$ μm. This is the result for the plane stress case. Under plane strain conditions the size of ω especially along x_1 is significantly reduced, to about one-third of ω in plane stress or somewhat smaller. Hence a wedge with a width of 10 μm may cause a complete shielding in the considered case.

Measurability of the Opening of the Crack Tip

The opening of a crack with a wedge-like contact is a continuous process; i.e., it is a continuous unzipping of the crack flanks. Hence the change of the compliance is also a continuous process, as depicted in Fig. 1 (curve C). The relative change of the slope depends on the location of the strain gage. It is larger near the tip and small for remote gages. Due to the limits to detect a change in the slope the measurability of the crack opening stress intensity is limited. The minimum length of a wedge-like contact at the tip of a crack which can be detected by a certain technique is comparable to its accuracy to measure a change in the crack length. The detection limit to measure a change in the crack length with a far-field compliance technique is in general larger than 20 μm (typically about 50 μm). The application of a near-tip technique can reduce this limit by about the factor of 5 or even up to 10.

We have seen that a contact over a length of a few μm can cause a significant amount of shielding. The K value determined from the first detected deflection of the slope of the compliance curve is therefore only a lower limit for K_{cl} or K_{op}. In other words, the real opening or closure of the crack tip occurs at K values somewhat larger than the measured K_{cl}. Hence we can conclude that the measured values under-estimate the effect of closure in the case of wedge-like contacts.

Since cracks can propagate only if their tip is open, the crack propagation technique gives correct opening stress intensities independent of the size of the wedge-like contact. Nevertheless this technique also has its limitations:

- It is applicable without problems only for large load amplitudes and steady-state conditions where K_{cl} does not significantly change with crack extension.
- Under variable-amplitude loading the closure load can change with increasing crack length. In the case of a decreasing closure load there is no problem; the cracks start and continue to grow if at the beginning the propagation conditions are fulfilled. In the case of increasing closure load the necessary K_{max} for crack propagation increases with increasing crack length. Therefore, the determination of K_{op} is limited by the detectability of the first extension and the change of K_{op} as a function of the crack length.
- In the near-threshold region the uncertainty in the knowledge of $\Delta K_{eff\ th}$ and the closure transient effects which might occur at the small load amplitudes in combination with the limitation of the measurability of the first extension of the crack can significantly reduce the accuracy of this technique.

In order to demonstrate the discussed points the results of different techniques are compared in Figs. 8, 11 and 12. In all experiments the steady-state crack propagation in an austenitic steel [*39*] at $\Delta K = 70$ MPa$\sqrt{m}$ at $R = 0.05$ is investigated. As already noted, Fig. 8 shows the real deformation immediately behind the crack tip at mid-thickness of a thick specimen (B = 25 mm) where the plane strain conditions prevail. From this it is evident that the crack tip closes at about 25% of K_{max}.

The fractographs of Fig. 11 present the results of the crack propagation technique. The crack growth experiment with constant-load amplitude at $\Delta K = 70$ MPa$\sqrt{m}$ was interrupted and a load of 100 000 cycles at a small load amplitude was applied with a K_{max} somewhat smaller than the expected $K_{op} + \Delta K_{eff\ th}$ value. Then the specimen was loaded with ten additional loads cycles at $\Delta K = 70$ MPa$\sqrt{m}$ and the test was interrupted again to apply 100 000 cycles with a somewhat larger "small" load amplitude. This load sequence was continued until the K_{max} of the small load amplitudes was

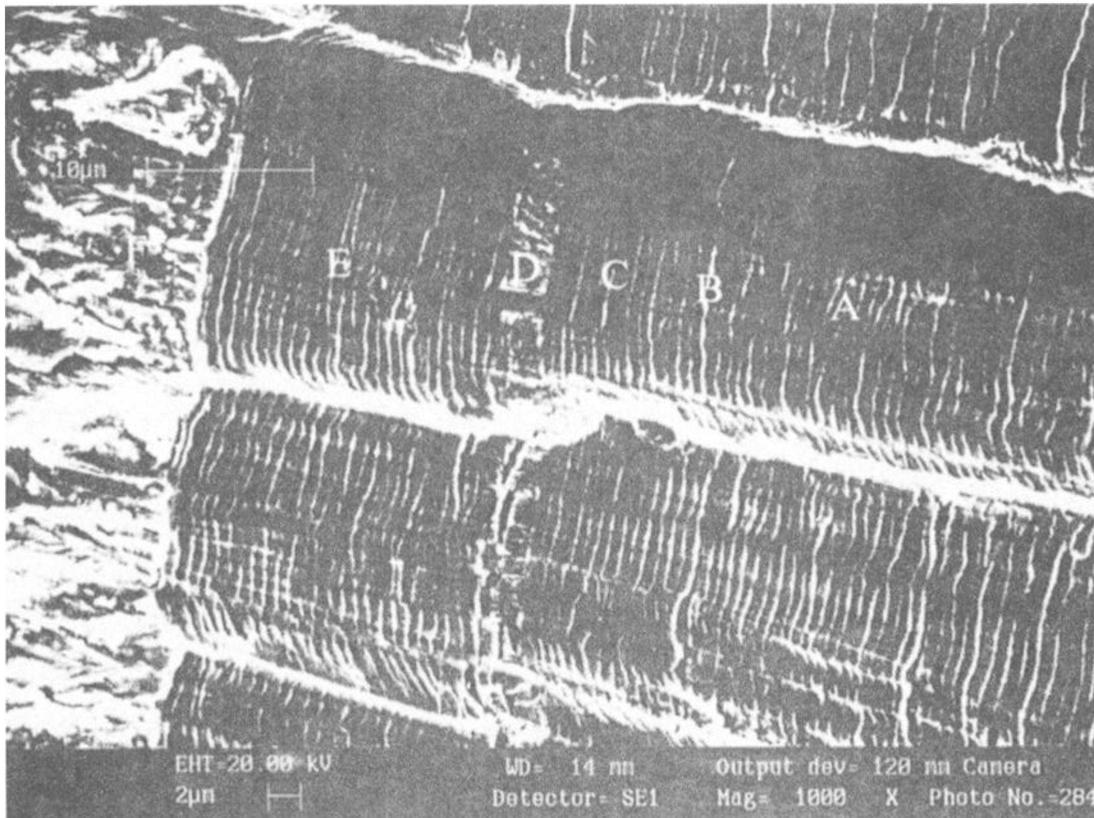

FIG. 11—*SEM-fractograph of crack opening load determination with the crack propagation technique (for details see text). The test was performed in a similar way as shown in Fig. 2a. The only difference was that between every increase of a small load amplitude about ten marker cycles at* $\Delta K = 70\ MPa\sqrt{m}$ *were applied (regions A, C and E). D marks the fracture surface where the first propagation occurred and B the region where no propagation at the small load amplitude was detected.*

somewhat larger than the expected $K_{op} + \Delta K_{eff\,th}$ value. From such a fractograph (Fig. 11) we can clearly see at which K_{max} the crack starts to propagate. The determined K_{op} value was between 21% and 25% of K_{max}.

Figure 12 shows the load versus far-field displacement curve at $\Delta K = 70$ MPa$\sqrt{\text{m}}$ and $R = 0$. In Fig. 12*a* the curve of a 25-mm-thick specimen and in Fig. 12*b* the curve of a 9-mm-thick specimen are depicted. One can clearly see that crack closure is easier to detect in the more plane stress domi-

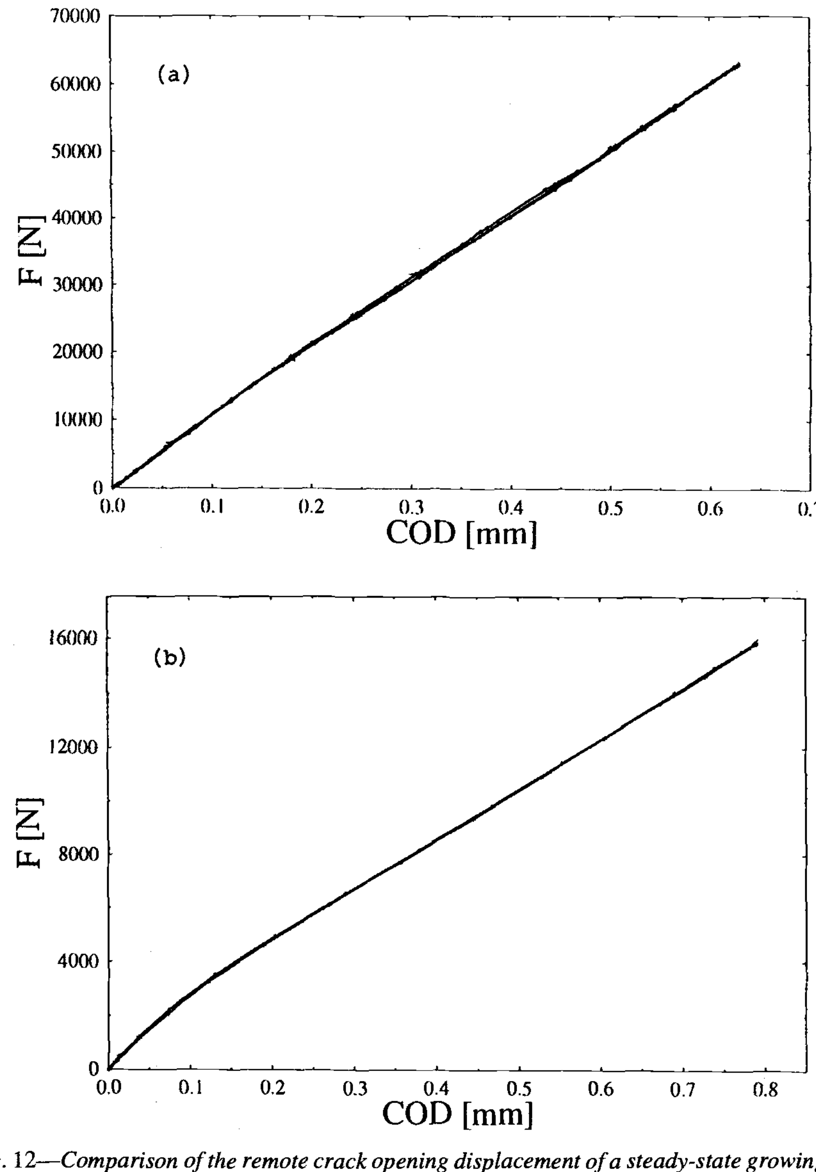

FIG. 12—*Comparison of the remote crack opening displacement of a steady-state growing fatigue crack at* $\Delta K = 70$ *MPa*$\sqrt{m}$, $R = 0.0$ *in a cold-rolled austenitic steel of* (a) *25 mm, and* (b) *9 mm specimen thickness, where in the 25-mm-thick specimen the plastic deformation is dominated by the plane strain condition and in the 9-mm-thick specimen the plane stress conditions become more important.*

nated thin specimen. One would assume that a crack-tip shielding of 20 $MPa\sqrt{m}$ is very easy to measure. But in both specimens the first deflection from the straight line is difficult to determine.

Besides the discussed basic problems there are many other problems associated with the measurability of closure which are not considered in the present paper. For example:

- The difference between the mid-thickness and surface behavior.
- The influence of the shape of the crack front.
- A careful consideration of the limitation of the validity of a unique relation between *da/dN* and ΔK_{eff}.

Summary

1. Only in the case of a few very small asperity-type contacts between the two crack flanks is the real crack-tip shielding induced by closure significantly smaller than $K_{cl} - K_{min}$.

2. For more than ten very small contacts or for few asperities with larger width the difference between $K_{op} - K_{min}$ and the real shielding of the crack tip becomes small. Hence, the usually measured K_{cl} or K_{op} value is applicable to determine ΔK_{eff} (= $K_{max} - K_{cl}$).

3. The minimum size of a wedge-like contact of the plastic wake field to cause a complete shielding of the crack tip is equal to the size of the plastic zone. This indicates that a relatively small wedge-like contact, as in the case of the plasticity-induced closure under plane strain, can cause a significant crack-tip shielding.

4. The difficulties of measuring the significant contribution of the near-tip closure might be the main reason for the discrepancies about the quantitative contribution of the effect of crack closure.

Acknowledgment

This work was supported by the Fonds zur Förderung der wissenschaftlichen Forschung, Project Nr.: P11622-TEC.

References

[1] Elber, W., "Fatigue Crack Closure Under Cyclic Tension," *Engineering Fracture Mechanics*, Vol. 2, 1970, pp. 37–45.

[2] Ritchie, R. O., "Mechanisms of Fatigue Crack Propagation in Metals, Ceramics and Composites: The Role of Crack Tip Shielding," *Materials Science and Engineering*, Vol. 103, 1988, pp. 15–28.

[3] Suresh, S., *Fatigue of Materials*, Cambridge University Press, U.K., 1991.

[4] Allison, J. E., "The Measurement of Crack Closure During Fatigue Crack Growth," *Fracture Mechanics: Eighteenth Symposium, ASTM STP 945*, D. T. Read and R. P. Reed, Eds., American Society for Testing and Materials, 1988, pp. 913–933.

[5] Sharpe, W. N., Jr. and Grandt, A. F., Jr., "A Preliminary Study of Fatigue Crack Retardation Using Laser Interferometry to Measure Crack Surface Displacements," *Mechanics of Crack Growth, ASTM STP 590*, American Society for Testing and Materials, 1976, pp. 302–320.

[6] Pitoniak, F. J., Grandt, A. F., Montulli, L. T., and Packman, P. F., "Fatigue Crack Retardation and Closure in Polymethylmethacrylate," *Engineering Fracture Mechanics*, Vol. 6, 1974, pp. 663–670.

[7] Dawicke, D. S., Grandt, A. F., Jr., and Newman, J. C., Jr., "Three-Dimensional Crack Closure Behaviour," *Engineering Fracture Mechanics*, Vol 36, pp. 111–121.

[8] Davidson, D. L., "Fatigue Crack Closure," *Engineering Fracture Mechanics*, Vol. 38, 1991, pp. 393–402.

[9] Pelloux, R. M., Faral, M., and McGee, W. M., "Fractographic Measurements of Crack-Tip Closure," *Fracture Mechanics: Proceedings of the Twelfth National Symposium, ASTM STP 700*, American Society for Testing and Materials, 1980, pp. 35–48.

[10] Schijve, J., "Fatigue Crack Closure: Observation and Technical Significance," *Mechanics of Fatigue Crack Closure, ASTM STP 982*, J. C. Newman, Jr. and W. Elber, Eds., American Society for Testing and Materials, 1988, pp. 5–34.

[11] Pippan, R., Plöchl, L., Klanner, F., and Stüwe, H. P., "The Use of Fatigue Specimens Precracked in Compression for Measuring Threshold Values and Crack Growth," *Journal of Testing and Evaluation*, Vol. 22, 1994, pp. 98–103.

[12] Hertzberg, R. W., "On the Calculation of Closure Free Fatigue Crack Propagation Data in Monolitic Metal Alloys," *Materials Science and Engineering*, Vol. A190, 1995, pp. 25–32.

[13] Sunder, R. and Dash, P. K., *International Journal of Fatigue,* 1982, pp. 97–105.
[14] Döker, H. and Bachmann, V., "Determination of Crack Opening Load by Use of Threshold Behaviour," *Mechanics of Fatigue Crack Closure, ASTM STP 982,* J. C. Newman, Jr. and W. Elber, Eds., American Society for Testing and Materials, 1988, pp. 247–259.
[15] Marci, G., Hartmann, K., and Bachmann, V., "Experimentelle Bestimmung des ΔK_{eff} für Ermüdungsrißfortschritt," *Materialwiss. und Werkstofftechnik,* Vol. 21, 1990, pp. 174–184.
[16] Lang, M., "Quantitative Untersuchung von Reihenfolgeeinflüssen auf Ermüdungsrißfortschritt," Ph.D. thesis, Universität Karlsruhe, Germany, 1996.
[17] Zhang, S. J., Döker, H., Nowack, H., Schulte, K., and Trautmann, K.-H., "Exact Determination at ΔK_{eff} and Crack Propagation Prediction for Selected Loading Sequences," *Advances in Fatigue Lifetime Predictive Techniques, ASTM STP 1211,* M. R. Mitchell and R. W. Landgraf, Eds., American Society for Testing and Materials, 1993, pp. 54–71.
[18] Pippan, R., Bichler, Ch., Sommitsch, Ch., and Kolednik, O., "Direct Observation of the Crack Tip Deformation and the Crack Closure," *Proceedings,* Fatigue '96, Elsevier Science Ltd., 1996, pp. 411–416.
[19] Pippan, R., Haas, G., and Stüwe, H. P., "Comparison of Two Methods to Measure Crack Closure in Ultra-High Vacuum," *Engineering Fracture Mechanics,* Vol. 34, 1989, pp. 1078–1084.
[20] Hertzberg, R. W., Newton, C. H., and Jaccard, R., "Crack Closure: Correlation and Confusion," *Mechanics of Fatigue Crack Closure, ASTM STP 982,* J. C. Newman, Jr. and W. Elber, Eds., American Society for Testing and Materials, 1988, pp. 139–148.
[21] De Koning, A. U., "A Study of Cyclic Crack Tip Plasticity and Crack Closure Under Variable Amplitude Loading," NLR TR 81141L, National Aerospace Laboratory, NLR, Amsterdam, 1981.
[22] Louat, N., Sadananda, K., Duesbery, M., and Vasudevan, A. K., *Metallurgical Transactions,* Vol. 24A, 1993, pp. 2225–2231.
[23] Vasudevan, A. K., Sadananda, K., and Louat, N., "A Review of Crack Closure, Fatigue Crack Threshold and Related Phenomena," *Materials Science and Engineering,* Vol. A188, 1994, pp. 1–22.
[24] Chen, D. L., Weiss, B., and Stickler, R., "A New Evaluation Procedure for Crack Closure," *International Journal of Fatigue,* Vol. 13, 1991, pp. 327–331.
[25] Wu, X. J., "An Energy Approach to Crack Closure," *International Journal of Fracture,* Vol. 73, 1995, pp. 263–273.
[26] Riemelmoser, F. O. and Pippan, R., "Crack Closure: A Concept of Fatigue Crack Growth Under Examination," *Fatigue and Fracture of Engineering Materials and Structures,* 1997, in press.
[27] Lindley, T. C. and Richards, C. E., *Materials Science and Engineering,* Vol. 14, 1974, pp. 281–293.
[28] Ewalds, H. L. and Furnée, R. T., "Crack Closure Measurement Along the Fatigue Crack Front of Center Cracked Specimens," *International Journal of Fracture,* Vol. 14, 1978, pp. R53–R55.
[29] Minakawa, K., Levan, G., and McEvily, A. J., "The Influence of Load Ratio on Fatigue Crack Growth in 7090-T6 and in 9021-T4 P/M Aluminum Alloys," *Metallurgical Transactions,* Vol. 17a, 1984, pp. 1787–1795.
[30] Fleck, N. A. and Newman, J. C., Jr., "Analysis of Crack Closure Under Plane Strain Conditions," *Mechanics of Fatigue Crack Closure, ASTM STP 982,* J. C. Newman, Jr. and W. Elber, Eds., American Society for Testing and Materials, 1988, pp. 319–341.
[31] McClung, R. C., Thacker, B. H., and Roy, S., "Finite Element Visualisation of Fatigue Crack Closure in Plane Stress and Plane Strain," *International Journal of Fracture,* Vol. 50, 1991, pp. 27–49.
[32] Pippan, R. and Riemelmoser, F. O., "Visualisation of the Plasticity-Induced Crack Closure Under Plane Strain Conditions," to be published.
[33] Sehitoglu, H. and Wei Sun, "Mechanisms of Crack Closure in Plane Strain and in Plane Stress," *Fatigue under Biaxial and Multiaxial Loading,* ESIS 10, K. Kussmaul, D. McDiarmid, and D. Socie, Eds., Mechanical Engineering Publications, London, 1991, pp. 1–21.
[34] Ghermahini, R. G., Shivakumar, K. N., Newman, J. C., Jr., and Blom, A. F., "Three-Dimensional Aspects of Plasticity-Induced Fatigue Crack Closure," *Engineering Fracture Mechanics,* Vol. 34, 1989, pp. 393–401.
[35] McClung, R. C., "The Influence of Applied Stress, Crack Length and Stress Intensity Factor on Crack Closure," *Metallurgical Transactions,* Vol. 22A, 1991, pp. 1559–1571.
[36] Dawicke, D. S., Newman, J. C., Jr., and Grandt, A. F., Jr., "Through the Thickness Fatigue Crack Closure Behavior in an Aluminum Alloy," *Proceedings,* Fatigue '90, MICEP, Birmingham, 1990, pp. 1283–1288.
[37] Llorca, J. and Sánchez Gálvéz, V., "Modelling Plasticity-Induced Fatigue Crack Closure," *Engineering Fracture Mechanics,* Vol. 37, 1990, pp. 185–196.
[38] Budiansky, B. and Hutchinson, J. W., "Analysis of Closure in Fatigue Crack Growth," *Journal of Applied Mechanics,* Vol. 45, 1978, pp. 267–277.
[39] Bichler, Ch. and Pippan, R., "Direct Observation of the Formation of Striations," *Proceedings,* Engineering Against Fatigue, in press.

Gary H. Bray[1] *and J. Keith Donald*[2]

Separating the Influence of K_{max} from Closure-Related Stress Ratio Effects Using the Adjusted Compliance Ratio Technique

REFERENCE: Bray, G. H. and Donald, J. K., "**Separating the Influence of K_{max} from Closure-Related Stress Ratio Effects Using the Adjusted Compliance Ratio Technique,**" *Advances in Fatigue Crack Closure Measurements and Analysis: Second Volume, ASTM STP 1343,* R. C. McClung and J. C. Newman, Jr., Eds., American Society for Testing and Materials, West Conshohocken, PA, 1999, pp. 57–78.

ABSTRACT: In a common interpretation of crack closure, the crack is visualized as "peeling" open as stress is applied. This interpretation, while useful, has led to the assumption that the driving force for crack propagation, ΔK_{eff}, exists only when the crack tip is fully open (above K-opening). However, evidence of significant crack-tip cyclic strain below the K-opening will be presented. The exclusion of this additional driving force can yield misleading values of ΔK_{eff}. This is particularly so in the near-threshold regime where opening loads are typically high. The new analysis technique for estimating ΔK_{eff} is referred to as the adjusted compliance ratio (ACR) method and is based on an interpretation of crack closure as a stress redistribution (or load transfer) on a relatively compliant crack wake. The ACR method is evaluated using the results of fatigue crack growth tests on 6013-T651, 2324-T39 and 7055-T7751 aluminum alloys using the center crack tension M(T) specimen geometry and stress ratios ranging from -1.0 to above 0.96. The experimental results of this study indicate that the fatigue crack growth rate is not determined solely by ΔK_{eff} but also depends on K_{max}. It was observed that this K_{max} dependence takes the form of a power law with the magnitude of the exponent being a measure of K_{max} sensitivity. As a result, ΔK_{eff} curves from all test conditions could be collapsed to a unique intrinsic FCGR curve using a simple modification to the Paris Law. It is expected that continued research in this area will lead to improvements in fatigue life prediction methodology.

KEYWORDS: fatigue, fatigue threshold, crack propagation, effective stress intensity, crack closure, stress ratio

Properly characterizing both the "extrinsic" and "intrinsic" nature of the long crack fatigue crack growth rate (FCGR) curve is desirable for fatigue-life prediction methodology, especially in the near-threshold regime. An intrinsic or "closure free" relationship should provide a basis for a better understanding of the small crack phenomena and the transition from small crack to long crack behavior. This intrinsic relationship is represented by the FCGR curve as a function of the effective stress intensity factor range, ΔK_{eff}. In this paper, ΔK_{eff} refers to the actual driving force for crack propagation and is not tied to a particular method for its estimation. It will be shown that properly correlating stress ratio effects in long cracks requires first, an accurate closure methodology to estimate ΔK_{eff}, and second, an evaluation of the K_{max} contribution. To this end, an experimental program was conducted on 6013-T651, 2324-T39 and 7055-T7511 aluminum alloys to provide a unique intrinsic FCGR curve.

Previous attempts to understand stress ratio effects in FCGR data have often emphasized one important contribution, such as crack closure, without considering other factors such as K_{max} depen-

[1]Staff engineer, Alcoa Technical Center, 100 Technical Drive, Alcoa Center, PA 15069.
[2]Director, Fracture Technology Associates, 2001 Stonesthrow Road, Bethlehem, PA 18015.

dence. In the past, correlating stress ratio effects using closure has been hampered by nonrepeatable measurements of closure and by contradictory results. Experimental evidence indicates that "closure" or interference of crack faces does not entirely isolate the crack tip but does cause an alteration and diminution of damaging strains [1]. Therefore, an understanding of the partial shielding mechanism of closure is essential.

A new analysis technique for estimating ΔK_{eff} is referred to as the "adjusted compliance ratio" technique (ACR) and is based on an interpretation of crack closure as a stress redistribution (or load transfer) on a relatively compliant crack wake. This concept accounts for the contribution of cyclic crack-tip strain below the opening load to fatigue crack growth. In fact, this concept accounts for contributions to crack closure both near the crack tip (i.e., near-field) and remote from it (i.e., far-field), thus allowing the near crack-tip "process zone" to be analyzed for only nonclosure mechanisms of behavior. This has resulted in the observation that the fatigue crack growth rate is not determined solely by ΔK_{eff} but also depends on K_{max}. It has been observed that this K_{max} dependence takes the form of a power-law with the magnitude of the exponent being a measure of K_{max} sensitivity. This relationship suggests that incorporation of a K_{max} effect into a crack growth law might be relatively straightforward.

Background

The understanding of fatigue crack growth behavior was revolutionized when Paris [2] recognized the relationship between fatigue crack growth rates and the linear elastic fracture mechanics parameter K leading to the formulation of what is now known as the Paris Law:

$$da/dN = C(\Delta K)^m \tag{1}$$

where ΔK is the applied stress intensity factor range corresponding to the applied cyclic load range $P_{max} - P_{min}$. It is widely believed that the fundamental cause of fatigue crack growth is the accumulation of microstructural damage resulting from cyclic plastic strain ahead of the crack tip. The use of applied ΔK in correlating fatigue crack growth rates is only possible because the linear fracture mechanics parameter K approximates the crack tip stress fields under small-scale yielding conditions. The plastic strain is then related to stress through a material's constitutive relationships. An increase in applied ΔK results in an increase in the cyclic plastic strain range; hence, greater microstructural damage and an increase in crack growth rates.

The next revolutionary leap forward in the understanding of fatigue crack growth was precipitated by the discovery of crack closure by Elber in 1970 [3,4]. Elber demonstrated experimentally that a fatigue crack can be closed for a part of the load cycle, even when the loading cycle is fully in tension. Previously, it was thought that a fatigue crack could only close under compressive loading [5]. The effect of crack closure is to reduce the cyclic plastic strain range at the crack tip. Elber concluded that the crack tip conditions responsible for crack propagation cannot be solely described by the applied stress intensity factor range ΔK, but rather by an effective stress intensity factor range ΔK_{eff} that accounts for crack closure. This was reflected in the following modification to the Paris Law:

$$da/dN = C(\Delta K_{eff})^m \tag{2}$$

The crack closure concept represented in the modified Paris Law has led to an improved understanding of several fatigue crack growth phenomena, including stress ratio effects, small crack effects, and crack retardation under variable-amplitude loading. As a result, the concept has been widely accepted and applied by the technical community.

The great difficulty with crack closure has not been conceptual but rather in the experimental determination of ΔK_{eff}. Elber postulated that ΔK_{eff} corresponds to that portion of load cycle where the crack tip is fully open. This seems reasonable since a closed crack is no longer expected to have the crack tip singularity and concomitant stress intensification experienced by an open crack. Thus, experimental methods have focused on determining the applied stress intensity factor (K_{op}) at which the crack tip fully opens. The effective stress intensity factor range is then estimated to be:

$$\Delta K_{eff} = K_{max} - K_{op} \tag{3}$$

Many experimental methods have been devised for measuring K_{op} including potential drop, ultrasound, acoustic emission, compliance and optical interferometry, to name a few. Multiple analysis techniques have also been applied in some cases to interpret data from a given experimental method. Several observations have been noted in applying these different experimental methods and analysis techniques: (1) K_{op} is often sensitive to measurement location and its distance from the crack tip [*6*]; (2) K_{op} depends significantly on the measurement method and the analysis technique applied to the data [*7,8*]; (3) K_{op} exhibits significant scatter even for a given measurement method and analysis technique [*9*]; and (4) local or "near-tip" measurements typically give higher K_{op} than global or bulk measurements [*10*].

The ASTM Opening Load Method

To address the issues of scatter and to provide a common method which would allow reliable comparisons of crack closure from different sources, ASTM in 1995 introduced a standardized method which is embodied in Appendix X2 of the ASTM Standard Test Method for Measurement of Fatigue Crack Growth Rates (E 647). Like most other approaches, the standardized method is based on the Elber postulate that $K_{max} - K_{op}$ defines that portion of the applied ΔK contributing to fatigue crack propagation. The method recommends the use of either a crack-mouth opening displacement (CMOD) gage or back-face strain (BFS) gage for a C(T) specimen, or in the case of an M(T) specimen, a COD gage on the longitudinal centerline of the specimen. The load versus displacement (or strain) is collected during a load cycle (Fig. 1). A straight line is fitted to the upper linear portion of the curve. This corresponds to the compliance of the specimen when the crack is fully open. The lower portion of the curve is nonlinear because the compliance gradually changes as the crack faces open and close upon loading and unloading. The point at which the crack first attains the constant value of the upper part of the curve is assumed to correspond to K_{op}. However, the exact determination of this point is quite difficult due to the gradual change of compliance and system noise. For this reason, an offset method is used where the opening load is defined to correspond to a compliance that is some percentage less than the compliance of the fully open crack. The offset value typically used is 2%. This method will hereafter be referred to as the ASTM opening load method.

The Elber postulate, while attractive in its simplicity, has not always been supported by the experimental evidence. For example, Hertzberg et al. [*11*] observed a lack of correlation between effective stress intensities using remote opening load measurements and observed crack growth rates. Similarly, Donald [*1*] obtained unrealistically low values of ΔK_{eff} and poor correlation of crack growth rates in the near-threshold region. Allison and You [7] found that the percentage offset necessary to correlate fatigue crack growth rates was material- and stress intensity range-dependent. At threshold, ΔK_{eff} was underpredicted, even with a 15% offset which yielded a K_{op} well below that corresponding to the initial point of deviation in the load versus displacement curve.

While it is tempting to attribute the lack of correlation between crack growth rates and ΔK_{eff} observed in these cases to the experimental difficulty in obtaining a precise measurement of K_{op}, other possibilities should also be considered. One possibility is that $K_{max} - K_{op}$ may not provide an accurate estimate of ΔK_{eff} under all conditions. Recently, Chen et al. [*12*] using simple test procedures involving stress ratio changes at threshold provided evidence that the lower portion of the loading cy-

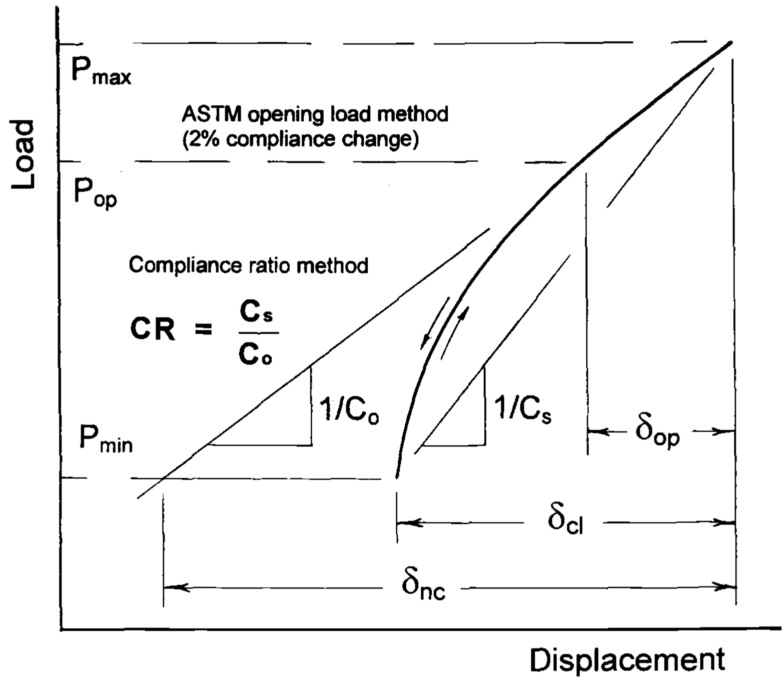

FIG. 1—*Schematic showing analysis of load versus displacement in accordance with opening load method and ACR method.*

cle below K_{op} can also contribute to crack propagation. This implies that additional crack-tip plastic strain is occurring below K_{op}.

The implicit assumption in all opening load methods, including the standardized ASTM method, is that the cyclic plastic strain range at the crack tip is related to $K_{max} - K_{op}$ and that no significant plastic strain occurs below K_{op}. This assumption seems reasonable when considering only the loading portion of the load cycle. Typically, tensile yielding at the crack tip does not occur until the compressive contact stresses in the crack wake are overcome at K_{op} and the stress singularity is "turned on" resulting in tensile stresses ahead of the crack tip. However, the situation is different on the unloading portion of the load cycle. The compressive stresses responsible for reverse yielding are not "turned off" when the crack closes so additional compressive yielding below K_{op} is still possible [*13,14*]. The magnitude of this additional plastic strain depends on the effectiveness of the crack closure mechanism at shielding the crack tip. This depends on the "stiffness" of the closure mechanism which is related to the modulus of the contacting material and the area of contact. When the closure mechanism is "stiff" or noncompliant, the contact forces build rapidly and magnitude of the additional plastic strain below K_{op} is expected to be small. When the closure mechanism is "soft" or compliant the additional plastic strain below K_{op} may be significant. For example, roughness-induced closure can be viewed as a "softer" closure mechanism than plasticity-induced closure because contact first occurs over a small area at the largest asperities. Continued Mode II displacements at the crack tip are also possible as the asperities slide on each other. Thus, the magnitude of additional plastic strain below K_{op} is expected to be greater for roughness-induced closure than plasticity-induced closure.

The extent to which the additional plastic strain below K_{op} contributes to fatigue crack propagation depends on the level of K_{op} relative to K_{max}. When K_{op} is large, as it often is near threshold, the additional plastic strain below the opening load may represent a significant portion of the total plastic strain range and contribute significantly to crack propagation. When K_{op} is small, as is often the case in the Paris region, the contribution will be substantially less.

Adjusted Compliance Ratio Concept

Recently, Donald [*1*] introduced a new technique for estimating ΔK_{eff} called the adjusted compliance ratio (ACR) method, designed to account for the contribution of that part of the load cycle below K_{op} to crack propagation. The experimental setup, instrumentation, and data collection are the same for this method as for the ASTM opening load method. The only difference between the two methods is in the analysis of the load versus displacement curve (Fig. 1). In the ACR method, the opening load marks a transition point below which the applied load is no longer directly proportional to the local crack-tip strain field magnitude. The estimate of ΔK_{eff} is related to the ratio of the actual displacement range ($\Delta \delta_{cl}$) to the displacement range that would have occurred in the absence of the closure ($\Delta \delta_{nc}$). This ratio is equivalent to the secant compliance between the minimum and maximum load-COD points (C_s) and the compliance of the specimen above the opening load (C_o). Evidence has shown this assumption to be extremely sensitive to crack length and measurement location and useful only if it were practical to continuously and correctly monitor the near crack-tip elastic strain [*1*]. Since measurement of local crack-tip strain for the compliance ratio technique is not practical, an alternative method has been devised to accomplish the same end using remote compliance measurements. The alternative method is referred to as the adjusted compliance ratio (ACR) technique and is determined by subtracting the compliance prior to the initiation of a crack (C_i) from both the secant compliance (C_s) and the compliance above the opening load (C_o) as follows:

$$\mathrm{ACR} = \frac{C_s - C_i}{C_o - C_i} \tag{4}$$

where

ACR = adjusted compliance ratio,
$C_s = \delta_s/P$ (inverse slope of secant drawn between minimum load-displacement and maximum load-displacement),
$C_o = \delta_o/P$ (inverse slope of load-displacement above opening load), and
$C_i = \delta_i/P_i$ (inverse slope of load-displacement prior to initiation of a crack).

This results in a compliance that is due solely to the presence of the crack. The adjustment parameter, C_i, compensates for much of the measurement location and crack length sensitivity. The resulting ratio can then be used to calculate ΔK_{eff} directly. It is this ratio that accounts for the bulk shielding mechanism in the wake of the crack and its effect on the elastic cyclic strain field immediately in front of the crack. The effective stress intensity factor is then obtained by multiplying the applied stress intensity by ACR as follows:

$$\Delta K_{eff} = \mathrm{ACR} \cdot \Delta K_{app} \tag{5}$$

Since the ACR method measures elastic compliance from a remote measurement location, it cannot be expected to capture the essence of the plastic crack-tip strain. This is not a serious limitation since the method does capture a first order estimate of the reduction in elastic cyclic strain. The reduction in elastic strain near the crack tip will, of course, have a direct impact on cyclic plastic crack-tip strain. However, limitations and sources of error due to second-order effects remain to be resolved. It should be noted that the ACR provides a proportionality between dC_s/da and dC_o/da. Therefore, it is not unreasonable to assume that the ACR at least approximates $\Delta K_{eff}/\Delta K_{app}$ since the slope of the compliance curve as a function of crack length is paramount to the derivation of stress intensity solutions. Since no direct determination of K_{op} is necessary, the experimental and analytical difficulties associated with this task and the resulting scatter are eliminated.

Values of ΔK_{eff} from both the ASTM opening load method and ACR method should be considered estimates since a gage remote from the crack tip captures the elastic response of a cracked specimen while fatigue crack growth rates are a consequence of plastic strain at the crack tip. The extent to which these estimates differ from each other depends on the shape of the load versus displacement curve (Fig. 2). When K_{op} is small relative to K_{max} or the closure mechanism is "stiff" or noncompliant, ΔK_{eff} obtained from the two methods should be identical or nearly so. When K_{op} is large relative to K_{max} or the closure mechanism is "softer" or more compliant, the difference in ΔK_{eff} obtained from the two methods could be quite large. This being the case, it was expected that the ACR method would always give the larger ΔK_{eff} but that the greatest difference between the two methods would be evident in the near-threshold region. The objective of this study was to evaluate which method provides the better estimate of the "true" ΔK_{eff} over the widest range of experimental conditions.

Experimental Procedures and Results

FCGR testing was conducted on aluminum alloys 6013-T651, 2324-T39 and 7055-T7751 to evaluate the ACR and ASTM opening load methods for estimating ΔK_{eff}. These alloys represent a range of strength and fatigue crack growth behavior. The tensile properties of the materials tested are given in Table 1. This work was performed in two phases. In Phase 1, each method was evaluated to determine sensitivity to experimental factors. More specifically sensitivity to measurement location and crack length were evaluated. The results were compared to "closure-free" crack growth rate data to evaluate which method better represents the "true" ΔK_{eff}. The testing in Phase 1 focused on the near-threshold region since this is the region where the greatest difference in the two methods is expected. In Phase 2, the two methods were evaluated over a wide range of stress ratios and ΔK to evaluate their robustness. A summary of Phase 1 and 2 test conditions is given in Table 2. All experiments were conducted on a servo-controlled, hydraulically-actuated, closed-loop mechanical test machine inter-

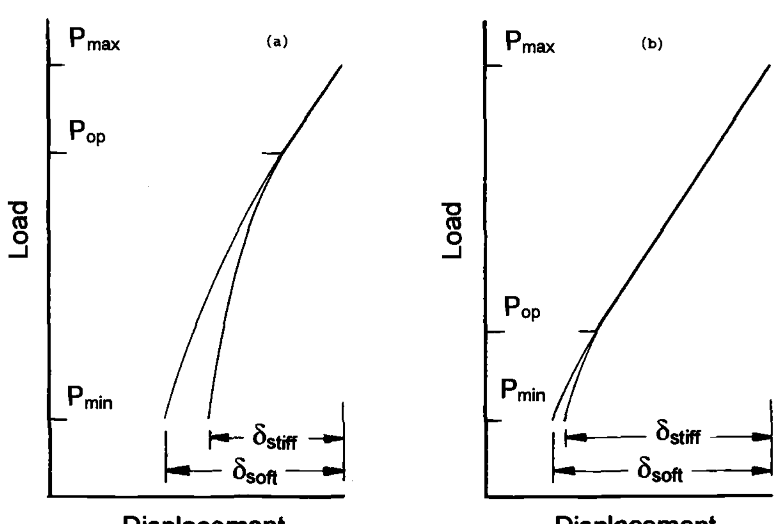

FIG. 2—*Schematics showing comparison of effective portion of the load versus displacement curve for ASTM opening load and ACR methods for:* (a) *high closure level, and* (b) *low closure level.*

TABLE 1—*Tensile Properties at Room Temperature.*

Alloy	Yield Strength MPa	Ultimate Tensile Strength MPa	Elongation, %
6013-T651	347	379	15.7
2324-T39	453	496	14.0
7055-T7751	610	635	9.4

TABLE 2—*Summary of Test Conditions.*

Specimen type:	$C(T)$, $B = 9.52$ mm, $W = 76.2$ mm, $a_0 = 25.4$ mm (L-T orientation) $M(T)$, $B = 6.35$ mm, W = 101.6 mm, $2a_0 = 10.2$ mm (L-T orientation)		
Test frequency:	2 to 20 Hz	(Phase 1)	(Phase 2)
Environment:	Lab air, 24°C,	R.H. = 38 to 48%	R.H. > 90%
da/dN:	5×10^{-8}	to 2×10^{-5}	to 5×10^{-2} mm/cycle

Test ID	Specimen Type	Stress Ratio	K-gradient (1/mm)	K_{max} (MPa $\sqrt{m}$)
		(PHASE 1)		
6013-1A, -2B	C(T)	0.1	0.00[1] −0.10[5]	6.6[3]
6013-1B-, 2C-	C(T)	var.	−0.59, −0.79[4]	5.3 − 38.5
2324-1A, -2B	C(T)	0.1	0.00[1] −0.10[5]	6.6[3]
2324-1B-, 2C-	C(T)	var.	−0.59, −0.79[4]	5.3 − 55.0
7055-1A-2B	C(T)	0.1	0.00[1] −0.10[5]	6.6[3]
7055-1B-, 2C-	C(T)	var.	−0.59 −0.79[4]	3.4 − 27.5
2324-8A, 9B	M(T)	0.1	0.00[1] −0.10[5]	6.6[3]
2324-8B-, 9C-	M(T)	var.	−0.59 −0.79[4]	5.3 − 55.0
		(PHASE 2)		
6013-1	M(T)	−1.0	−0.08, +0.12[2]	7.7, 6.6[3]
6013-2	M(T)	0.1	−0.08, +0.12[2]	7.7, 6.6[3]
6013-3	M(T)	0.3	−0.08, +0.12[2]	8.8, 7.7[3]
6013-4	M(T)	0.5	−0.08, +0.12[2]	9.9, 8.8[3]
6013-5	M(T)	0.7	−0.08, +0.12[2]	11.0, 8.8[3]
6013-6A, -6E	M(T)	var.	−0.59[4]	7.7, 11.0, 16.5, 24.2, 33.0
2324-1	M(T)	−1.0	−0.08, +0.12[2]	6.6, 4.9[3]
2324-2	M(T)	0.1	−0.08, +0.12[2]	6.6, 6.0[3]
2324-3	M(T)	0.3	−0.08, +0.12[2]	7.7, 6.6[3]
2324-4	M(T)	0.5	−0.08, +0.12[2]	8.8, 6.6[3]
2324-5	M(T)	0.7	−0.08, +0.12[2]	11.0, 8.8[3]
2324-6A, -6E	M(T)	var.	−0.59[4]	6.6, 9.9, 14.8, 22.0, 33.0
7055-1	M(T)	−1.0	−0.08, +0.12[2]	5.0, 3.8[3]
7055-2	M(T)	0.1	−0.08, +0.12[2]	5.0, 3.8[3]
7055-3	M(T)	0.3	−0.08, +0.12[2]	6.0, 5.0[3]
7055-4	M(T)	0.5	−0.08, +0.12[2]	7.1, 6.0[3]
7055-5	M(T)	0.7	−0.08, +0.12[2]	8.8, 6.6[3]
7055-6A, -6E	M(T)	var.	−0.59[4]	5.0, 7.4, 11.0, 16.5, 24.7

[1] K-control is constant K_{max}, constant ΔK, constant R.
[2] K-control is decreasing K_{max}, ΔK, constant R followed by increasing K_{max}, ΔK, constant R.
[3] Initial value of K_{max} for constant R test.
[4] K-control is constant K_{max}, decreasing ΔK, variable R.
[5] K-control is decreasing K_{max}, decreasing ΔK, constant R.

faced to a computer for control and data acquisition. A full report of Phase 1 test conditions and results is given in Ref *15*. Highlights of Phase 1 follow.

Phase 1 Highlights—Evaluation of Method Sensitivity to Experimental Factors

1. *ACR method was insensitive to measurement location whereas ASTM method was not*—This is illustrated by Fig. 3 which shows the results for alloy 6013 of a decreasing ΔK, $R = 0.1$ test on a C(T) specimen in the near-threshold region. Both ΔK_{app} and ΔK_{eff} curves are shown with ΔK_{eff} based on the ACR method (ACR1 and ACR2) and the ASTM opening load method (OP1 and OP2). The ΔK_{eff} curves ACR1 and OP1 correspond to a clip gage on the front face of the specimen, while the ΔK_{eff} curves ACR2 and OP2 correspond to a measurement location spanning the notch tip with a gage length of 15.2 mm. The ΔK_{eff} curves obtained from each location using the ASTM opening load method were separated from each other, while the two curves obtained by the ACR method coincided. The independence of the ACR method with respect to measurement location is significant considering there is an order of magnitude of difference in C_i, the initial compliance of the uncracked specimen, between the two locations. C_i is used in Eq 4 to obtain the adjusted compliance ratio. Since the ACR method considers compliances solely due to the presence of a crack, it is hypothesized that an arbitrary location may be selected for measurement without affecting the results. On the other hand, because the ASTM opening load method relies on a compliance offset to estimate K_{op}, it is not surprising that the measurement location closest to the crack tip (OP2) gives a higher K_{op}, hence a lower level of ΔK_{eff} at a given crack growth rate, than the more remote measurement location (OP1).

2. *The ACR method was less sensitive than the ASTM method to crack length*—This is illustrated by Fig. 4, which shows crack closure measurements from a constant ΔK tests on alloy 6013 at

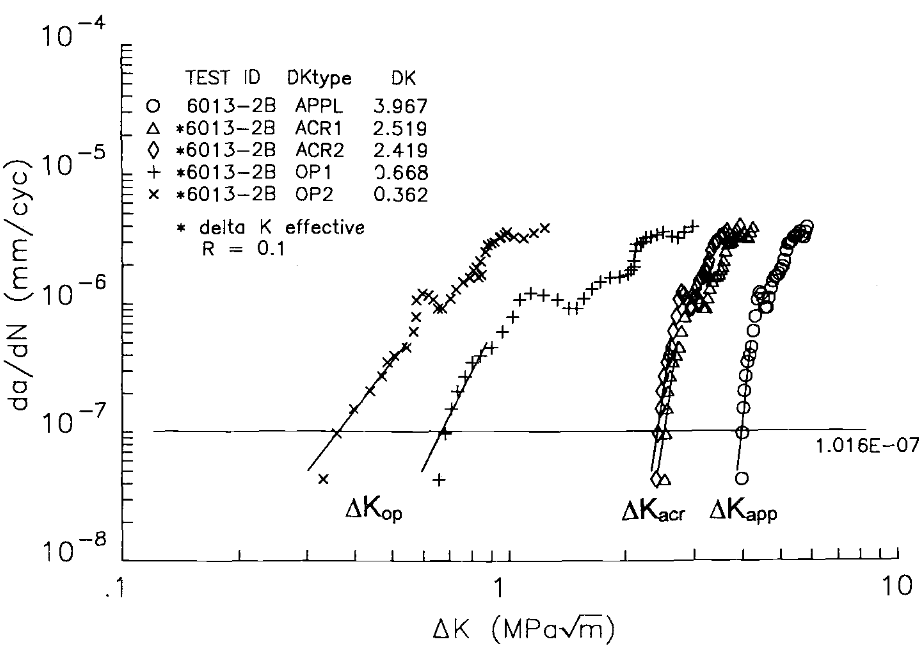

FIG. 3—*FCGR response of alloy 6013 plotted versus* ΔK_{app} *and* ΔK_{eff} *based on ASTM opening load and ACR closure measurement techniques at two gage locations (1 and 2).*

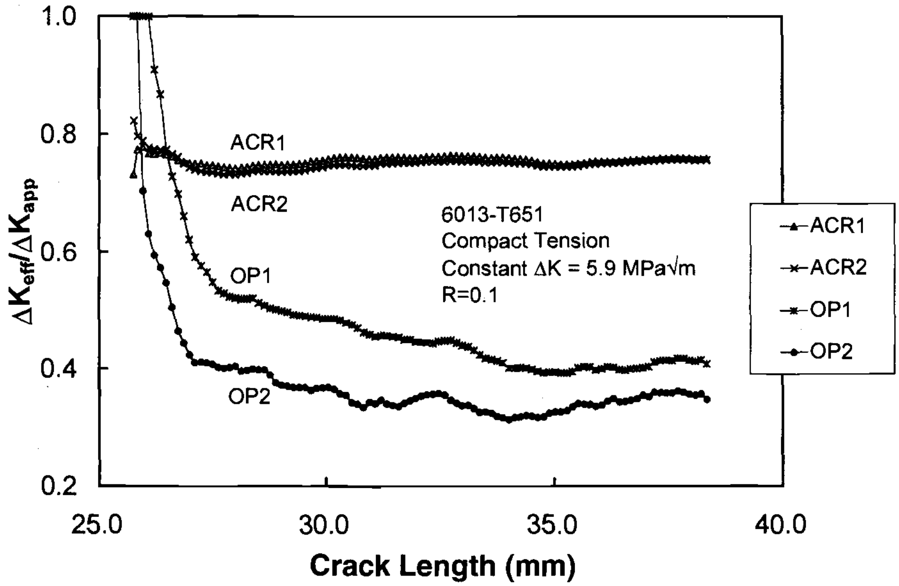

FIG. 4—*Comparison of crack closure measurements by the ASTM opening load (OP) and adjusted compliance ratio (ACR) methods versus crack length at two gage locations (1 and 2).*

$R = 0.1$. A constant ΔK of 5.9 MPa$\sqrt{m}$ was maintained for a total crack length extension of 12.7 mm. Crack closure measurements were monitored continuously. The crack growth rates in these tests were reasonably constant over the range of crack extension implying that "true" ΔK_{eff} experienced by the crack tip was also constant. The crack closure is plotted in terms of $\Delta K_{eff}/\Delta K_{app}$. The ratio of $\Delta K_{eff}/\Delta K_{app}$ is used in lieu of K_{op} since the ACR method provides this ratio directly and does not measure opening load level. A ratio of one indicates there is no crack closure and ΔK_{eff} and ΔK_{app} are equivalent. A low value of the ratio indicates high levels of crack closure and a ΔK_{eff} that is significantly reduced from the applied ΔK. The ratio of $\Delta K_{eff}/\Delta K_{app}$ varied over the crack length interval for both the ASTM opening load method and the ACR method. Since the crack growth rate was essentially constant over the range of crack extension indicating that the "true" ΔK_{eff} was constant, the ratio of $\Delta K_{eff}/\Delta K_{app}$ should have remained constant. The fact that it does not indicates the estimate of ΔK_{eff} obtained by either method has some degree of sensitivity to crack length. However, the sensitivity observed was much less for the ACR method than the ASTM opening load method. The ACR method also exhibited significantly less point to point variability or "scatter" than the ASTM method, as anticipated. The strong sensitivity of the ASTM opening load method to measurement location and the insensitivity of the ACR method was evident in these tests as well. The crack closure measurements from the ACR method were virtually the same from both locations (compare ACR1 and ACR2) over the entire interval whereas those from the ASTM method were significantly different (compare OP1 and OP2).

3. *The ACR method provided a better estimate of the "true" ΔK_{eff} than did the ASTM method in the near-threshold region*—This was determined by a series of decreasing ΔK, constant K_{max} tests (Fig. 5). At a crack growth rate of 1.02×10^{-7} mm/cycle the stress ratio in these tests was at all times greater than $R = 0.6$ and exceeded $R = 0.96$ at the largest value of K_{max}. Crack closure was not detected in any tests by either method, so the constant K_{max} curves are assumed to represent closure free data (i.e., $\Delta K_{eff} = \Delta K_{app}$). The shift of the curves with increasing K_{max} indicates that crack growth rate is not determined solely by ΔK_{eff} but also depends on K_{max} at least in the near-threshold region.

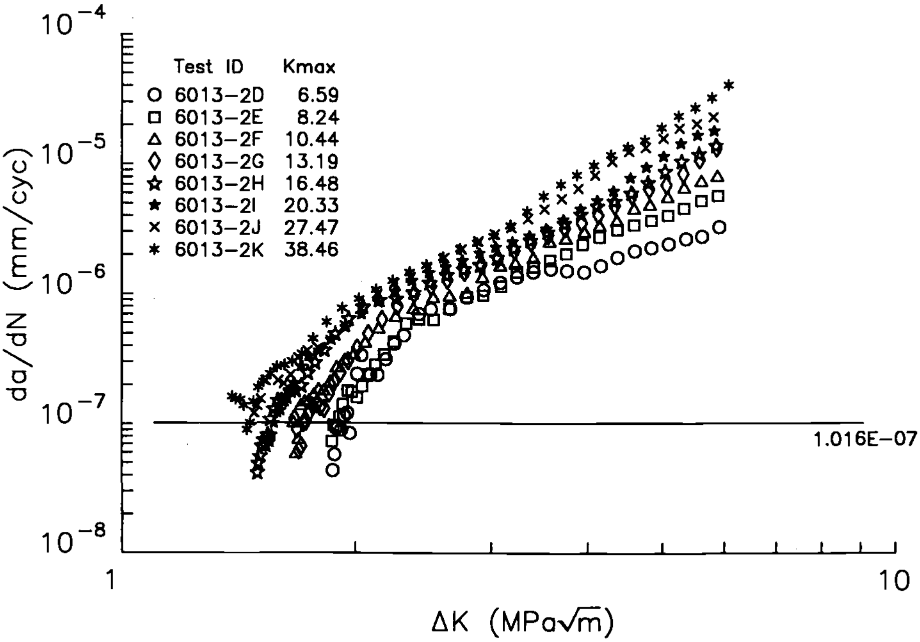

FIG. 5—*FCGR response of alloy 6013 for a series of constant* K_{max}, *decreasing* ΔK *tests showing* ΔK *and* K_{max} *determination at equivalent crack growth rates.*

ΔK_{eff} values were plotted against K_{max} on a log-log scale for a near-threshold crack growth rate of 1.02×10^{-7} mm/cycle (Fig. 6). The solid line is a power law fit to the data, which is linear on a log-log scale. The power law fit has been extrapolated to the value of K_{max} equal to that in the $R = 0.1$ tests (see Fig. 3). The extrapolated value of ΔK_{eff} can then be compared against the estimated ΔK_{eff} obtained from the $R = 0.1$ tests using the ASTM opening load method and ACR method to gage their accuracy. In all cases, the estimate of ΔK_{eff} obtained from the ACR method at $R = 0.1$ was in good agreement with that obtained by extrapolation of the constant K_{max} tests results, while the estimate of ΔK_{eff} obtained from the ASTM opening load method was significantly lower than the extrapolated value. These results indicate that the ACR method yields a significantly better estimate of the "true" ΔK_{eff} in the near-threshold region than does the ASTM opening load method.

This point is reinforced by a summary of the Phase 1 test results presented in Fig. 7. Both lower region 2 and near-threshold results are shown. This figure provides the ratio between ΔK_{eff} estimated from the two measurement locations and two measurement methods (ACR and OP) and ΔK_{eff} obtained from the extrapolated "closure-free" data. Assuming that ΔK_{eff} obtained from extrapolation of the "closure-free" data is very close to the "true" ΔK_{eff}, a ratio of one indicates that the estimated value of ΔK_{eff} from the $R = 0.1$ tests is equivalent to the "true" ΔK_{eff}. The ACR method yielded ΔK_{eff} values within 10% of the extrapolated values in 11 out 14 cases and was within 20% for the remaining three cases. In comparison, the ASTM opening load method yielded ΔK_{eff} values ranging from 16 to 74% of the extrapolated values.

Phase 2—Study of Stress Ratio Effects and K_{max} Effects

Phase 2 testing is presented in the bottom portion of Table 2. All Phase 2 testing was performed on M(T) specimens having a width of 101.6 mm and a thickness of 6.4 mm. Clip-on displacement gages

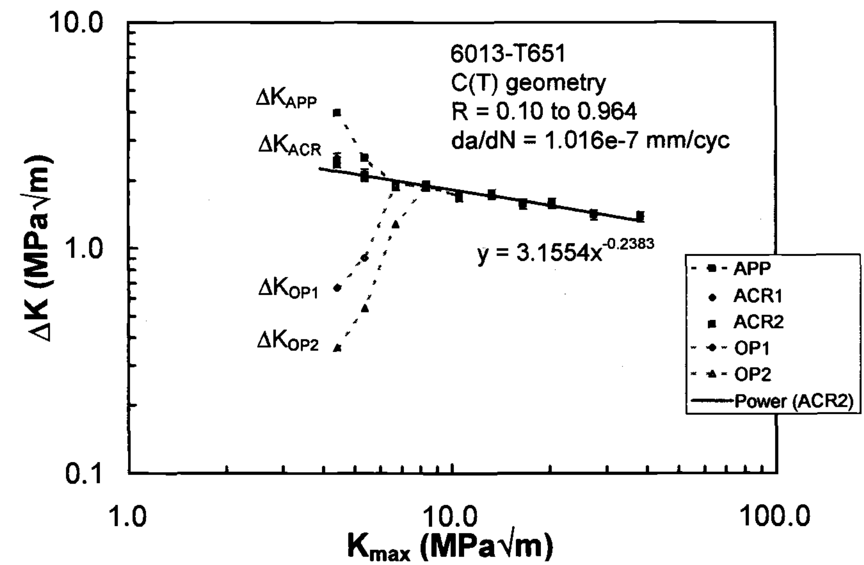

FIG. 6—ΔK *versus* K_{max} *at an equivalent crack growth rate on log-log scales.* ΔK_{eff} *from ACR method gives best agreement with "true"* ΔK_{eff} *obtained by extrapolation of high R "closure-free" data to* R = *0.1.*

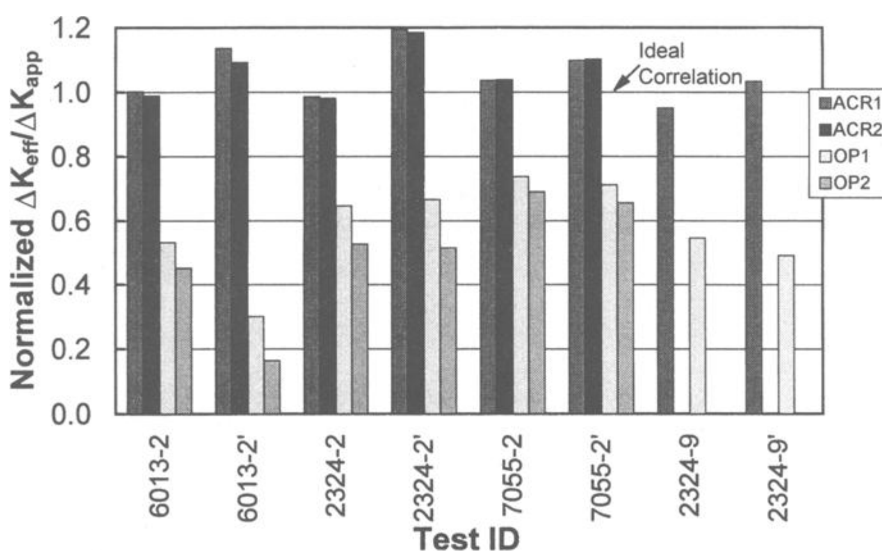

FIG. 7—*Summary of Phase 1 test results showing ratio of* ΔK_{eff} *estimated by ASTM and ACR methods normalized by "true"* ΔK_{eff} *obtained by extrapolation of high* R *"closure-free" data to* R = *0.1. Ratio of 1.0 indicates perfect agreement. Results include lower Paris region 2, and near-threshold (indicated by test ID with prime symbol).*

(gage length = 15.2 mm) were placed on both sides of the specimen at center-width and load versus displacement monitored continuously. The response of the two gages was averaged. Tests were performed under both decreasing ΔK (below 10^{-5} mm/cycle) and increasing ΔK, constant R conditions at stress ratios of $R = -1.0, 0.1, 0.3, 0.5$ and 0.7 and under decreasing ΔK, constant K_{max} conditions at a K_{max} ranging from 5.0 to 33.0 MPa$\sqrt{m}$ (see Table 2). The constant K_{max} tests covered stress ratios from -1.0 to greater than 0.96. This wide range of test conditions was selected to evaluate the robustness of the two closure measurement methods and to provide ample data to evaluate the K_{max} sensitivity of crack growth rates observed in Phase 1. All tests were performed in a humidity chamber having a relative humidity of greater than 90%. The load versus displacement traces were analyzed by both the ACR method and the ASTM opening load method to obtain ΔK_{eff}.

Comparison of ΔK_{eff} *Curves Obtained by ACR and ASTM Opening Load Methods*—The fatigue crack growth curves from the steady state, constant R tests are plotted in terms of ΔK_{app} in Fig. 8. (Full range ΔK has been plotted for $R < 0$). The FCGR curves for all three alloys exhibited behavior typical of monotonic alloys; i.e., increasing crack growth rates with increasing stress ratio. The ΔK_{eff} curves obtained using the ACR method are shown in Fig. 9. The spread in ΔK_{eff} curves is much less than the spread in ΔK_{app} curves indicating that crack closure is primarily responsible for the observed stress ratio effects in the ΔK_{app} curves. However, the ΔK_{eff} curves are not collapsed to a common curve, but instead shift to the left with increasing stress ratio. In other words, for a given ΔK_{eff}, the crack growth rate increases with increasing K_{max} (i.e., increasing R). Possible mechanisms for this K_{max} dependence are presented in the discussion section.

The ΔK_{eff} curves obtained using the ASTM opening load method are shown in Fig. 10. In region 2, the spread in ΔK_{eff} curves obtained by this method is also less than the spread in the ΔK_{app} curves again indicating that crack closure is mostly responsible for stress ratio effects. However, at near-threshold crack growth rates, the ΔK_{eff} curves obtained by the ASTM opening load method also do not collapse to a common curve, but instead shift to the right with increasing stress ratio. The authors can think of no plausible mechanism for a negative K_{max} dependence on crack growth rates and consider it an artifact of the ASTM opening load method.

Evaluation of Methods with "Closure Free" High Stress Ratio Data—The accuracy of the two methods was evaluated in Phase 2 by comparing the applied ΔK and ΔK_{eff} curves at low stress ratios with the applied ΔK curves at $R = 0.7$. No closure was measured by either method at $R = 0.7$ (except at near-threshold growth rates for the 6013 alloy) so the applied ΔK and ΔK_{eff} curves are presumed to be equivalent. The low stress ratio ΔK_{eff} curves obtained by the ACR method lie just to the right of the $R = 0.7$ curves (see Fig. 9) indicating the method is providing a good estimate of the "true" ΔK_{eff} over the entire range of ΔK. The slight separation in the curves is attributed to the K_{max} dependence on crack growth rates. K_{max} at $R = 0.7$ is three times that at $R = 0.1$ for a given applied ΔK. In comparison, the low stress ratio ΔK_{eff} curves obtained by the ASTM opening load method (see Fig. 10) lie close to the $R = 0.7$ curve in the Paris region, but are widely separated in the near-threshold region. In both regions the ASTM method is underpredicting ΔK_{eff}. The magnitude of the underprediction is small in the Paris region but very large in the near-threshold region as evidenced by the fact that the ΔK_{eff} curves lie absurdly to the left of the $R = 0.7$ curve. Thus, the two methods behave as anticipated, both providing similar estimates of ΔK_{eff} in the Paris region while ΔK_{eff} from the ACR method is significantly higher in the near-threshold region. However, it is the ACR method which provides the better estimates of the "true" ΔK_{eff} over the largest range of applied ΔK.

K_{max} *Sensitivity Concept Applied to Phase II Results*—As a result of the K_{max} sensitivity observed in Phase 1 testing, a methodology was developed to enable the K_{max} effect to be incorporated into a crack growth rate law. This methodology is fully described in Ref *16*. Crack growth rate is plotted

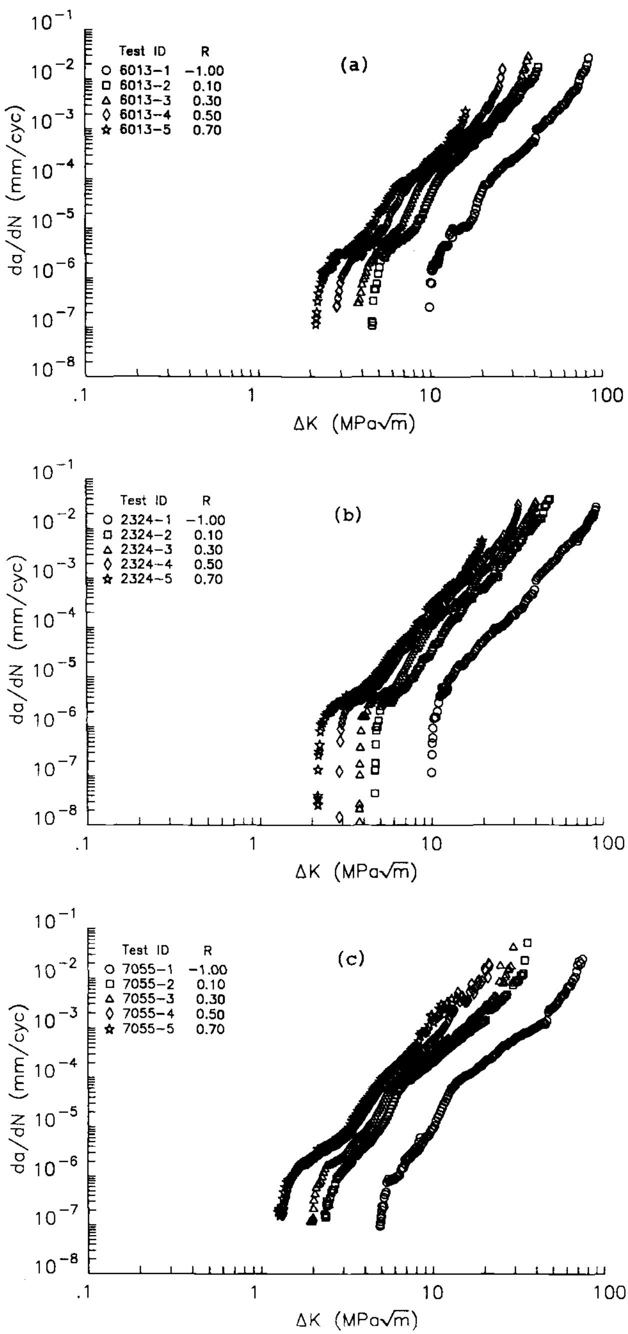

FIG. 8*a,b,c*—*FCGR response of alloys 6013, 2324 and 7055 at* R $= -1.0, 0.1, 0.3, 0.5$ *and* 0.7 *plotted versus* ΔK_{app}.

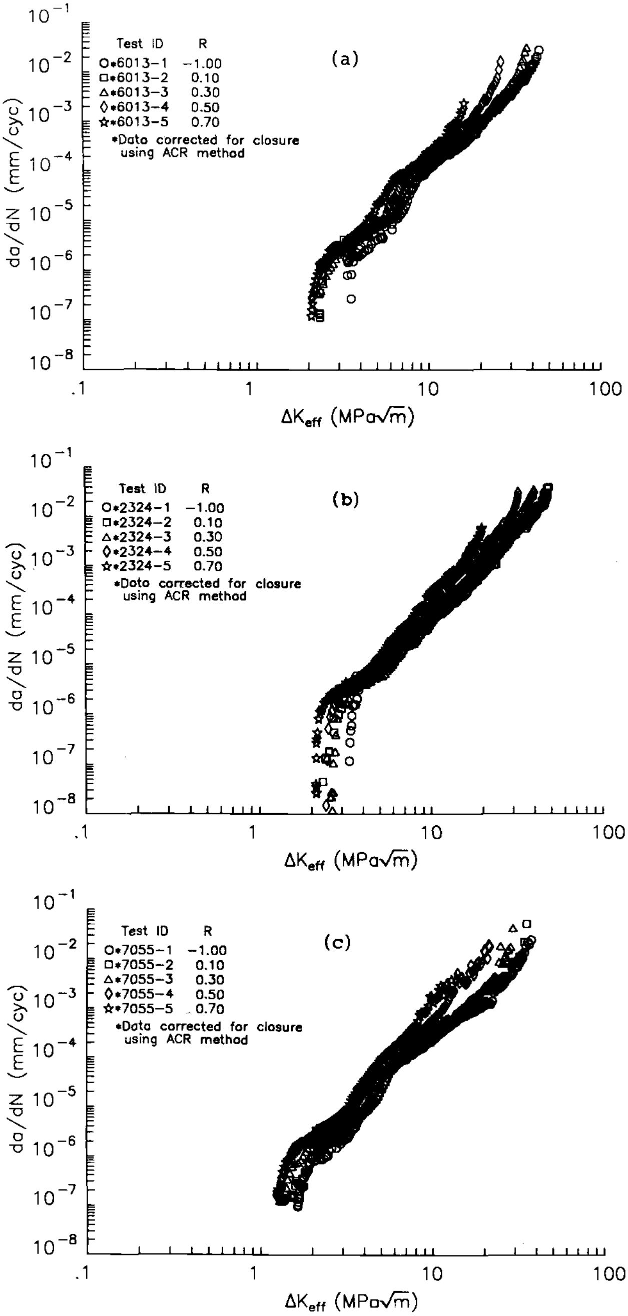

FIG. 9*a,b,c—FCGR response of alloys 6013, 2324 and 7055 at* R $= -1.0, 0.1, 0.3, 0.5$ *and 0.7 versus* ΔK_{eff} *obtained by the ACR method.*

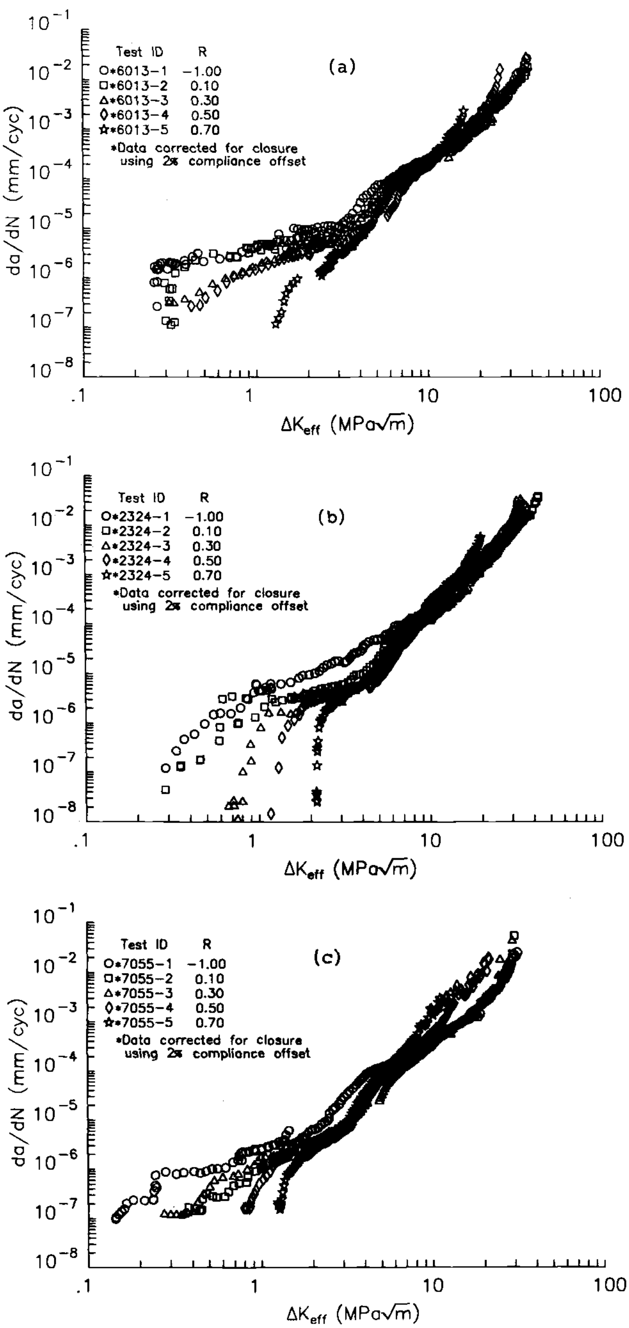

FIG. 10a,b,c—FCGR response of alloys 6013, 2324 and 7055 at R = *−1.0, 0.1, 0.3, 0.5 and 0.7 versus* ΔK_{eff} *obtained by the ASTM opening load method.*

versus a normalized K which combines the effects of ΔK_{eff} and K_{max}. The normalized K is given by the relationship:

$$K_{norm} = \Delta K_{eff}^{(1-n)} \cdot K_{max}^{n} \tag{6}$$

where n is the normalized K_{max} sensitivity exponent.

In the limiting condition, for $n = 0$, $K_{norm} = \Delta K_{eff}$, indicating that crack growth rates depend only on ΔK_{eff} and are independent of K_{max}. For $n = 1$, $K_{norm} = K_{max}$, indicating that crack growth rates depend only on K_{max} and are independent of ΔK_{eff}. An $n = 0.5$ would indicate that crack growth rates are equally dependent on K_{max} and ΔK_{eff}. A lesser value would indicate ΔK_{eff} dominance and higher values would indicate K_{max} dominance.

Some early empirical models of crack growth, for example Walker [*17*], correlated crack growth rates with equations similar to Eq 6. However, these models were applied to FCGR curves plotted on the basis of applied ΔK, and, therefore, incorporated stress ratio effects from crack closure and K_{max} effects. In contrast, Eq 6 is applied to FCGR curves plotted on the basis of ΔK_{eff}, and, therefore, is appropriate for describing small crack behavior and other situations where crack closure effects are absent or minimal. Some of the earlier equations may also provide reasonable correlation of crack growth rates for that purpose.

To illustrate the significance of incorporating both the ACR closure and the K_{max} sensitivity concept, Figs. 11*a*, 12*a* and 13*a* show all of the previous constant R data from Fig. 8 as well as a series of five constant K_{max} tests all plotted on the basis of ΔK_{app}. This provides an overall stress ratio range from $R = -1.0$ to $R > 0.96$. When crack growth rates were plotted against K_{norm} using $n = 0.25$ a unique intrinsic FCGR curve was obtained as shown in Figs. 11*b*, 12*b* and 13*b*. It is quite remarkable that a single parameter, the K_{max} sensitivity exponent (n), in combination with ΔK_{eff} estimated by the ACR method, can collapse all the data for such a wide range of ΔK and stress ratios. It is possible that the K_{max} term in Eq 6 is accounting for some of the effects of crack closure not being fully accounted for in the ACR estimate of ΔK_{eff}. However, the observation of a K_{max} dependence at high stress ratios in the constant K_{max} tests suggest this is not the case to any great extent.

Discussion

In Phases 1 and 2, fatigue crack growth rates in 6013, 2324, and 7055 depended not only on ΔK_{eff} but also on K_{max}. This dependence was observed in both the "closure-free" fatigue crack growth data obtained under constant K_{max} test conditions in Phases 1 and 2 and in the ΔK_{eff} curves obtained at different stress ratios in Phase 2. Its observance under high R, "closure free" conditions eliminates the possibility that this is simply an artifact of the ACR method. However, at low stress ratios it was only possible to separate the K_{max} dependence from crack closure effects with the ACR method. The ΔK_{eff} curves obtained by the ASTM opening load method exhibited a negative K_{max} sensitivity which cannot be rationalized. It is quite possible that a K_{max} dependence on crack growth rates in the near-threshold region and Paris region has not been systematically observed in prior studies using the ASTM and other opening load methods because of their nonrepeatability, measurement location sensitivity, and large error in the near-threshold region. The ACR technique is sufficiently repeatable and accurate that K_{max} sensitivity can be recognized as an inherent part of the fatigue process over the entire range of the fatigue crack growth curve.

This paper is not the first to recognize the importance of K_{max} in the near-threshold region. Döker and Peters [*18*], and more recently, Sadanada and Vasudevan [*19,20*], have stated the significance of using both ΔK and K_{max} in characterizing fatigue crack growth behavior in the near-threshold region. However, the current study provides a significant quantity of additional experimental evidence for a

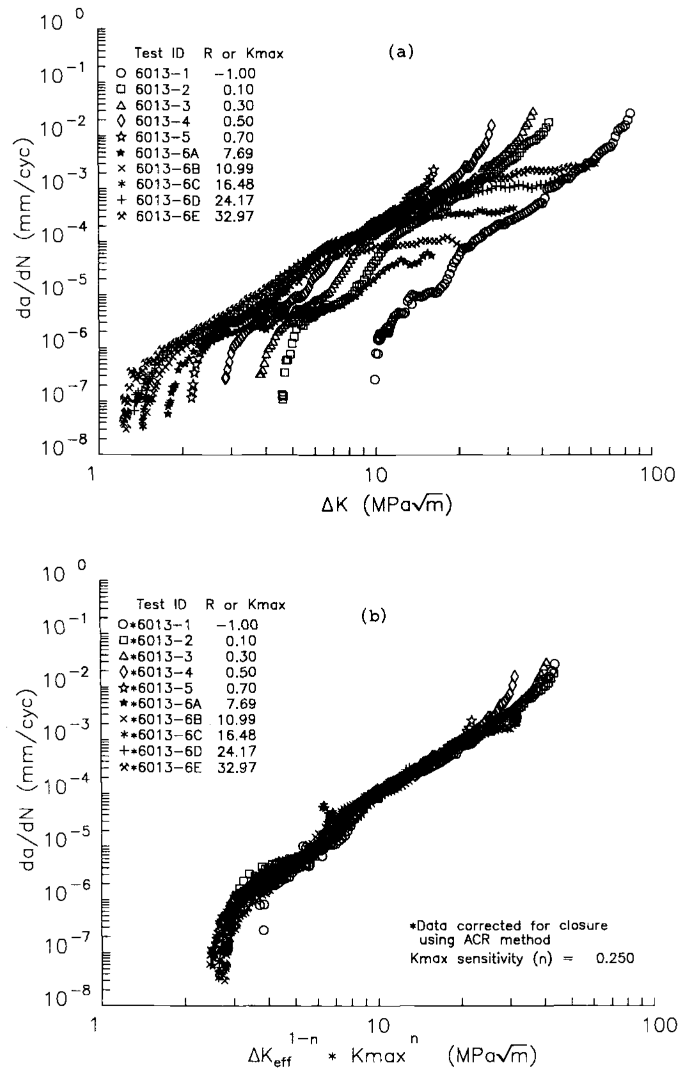

FIG. 11*a,b—FCGR response of alloy 6013 for* R $= -1$, *0.1, 0.3, 0.5 and 0.7 and constant* K_{max}*-values of 7.7, 11.0, 16.5, 24.2 and 33.0 MPa*$\sqrt{m}$ *when plotted against* ΔK_{app} *and* K_{norm}.

K_{max} dependence in the threshold region and indicates that this K_{max} dependence also extends into the Paris region for the investigated aluminum alloys. A possible cause for this K_{max} dependence was postulated in Ref *16* which related it to the ratio of the monotonic to the cyclic plastic zone size. An analogous interpretation is to relate this dependence to mean strain effects. An increase in K_{max} at a given ΔK_{eff} raises the mean strain at the crack tip while leaving the cyclic plastic strain range unaffected. Crack tip strain is approximately proportional to the plastic zone size or crack tip opening displacement (CTOD) which are proportional to the K^2. Thus, the maximum plastic strain and minimum plastic strain after accounting for crack closure are approximately proportional to $(K_{max})^2$ and (K_{max}

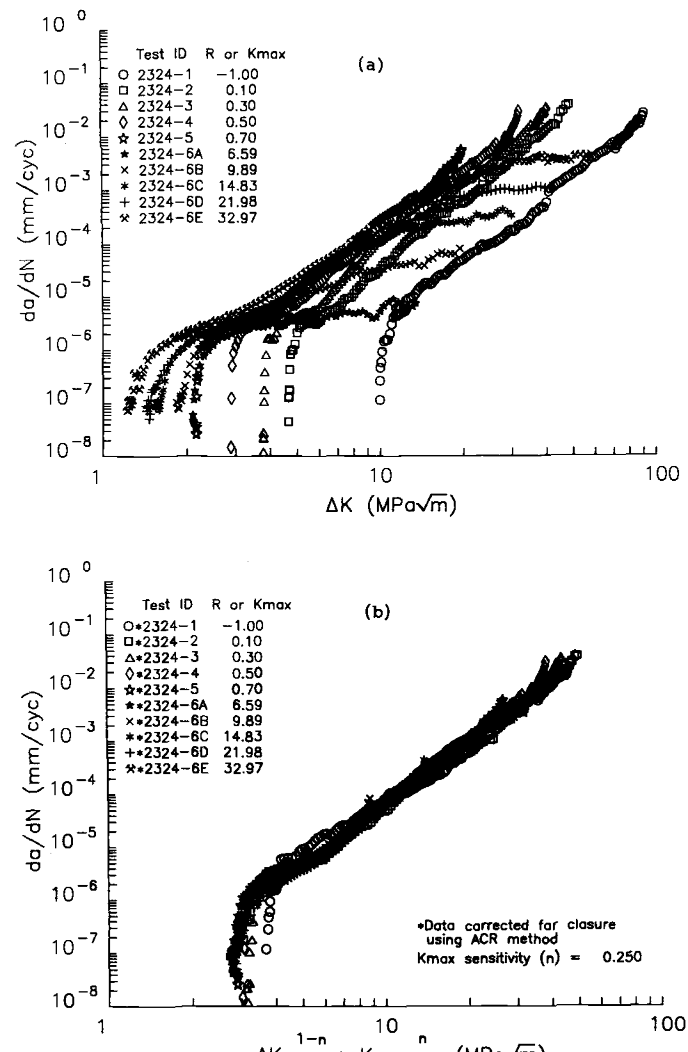

FIG. 12*a,b—FCGR response of alloy 2324 for* R $= -1$, *0.1, 0.3, 0.5 and 0.7 and constant* K_{max} *values of 6.6, 9.9, 14.8, 22.0 and 33.0 MPa*$\sqrt{m}$ *when plotted against* ΔK_{app} *and* K_{norm}.

$-\ \Delta K_{eff})^2$ and the mean strain of the cyclic plastic strain range is proportional to $(K_{max}^2 + (K_{max} - \Delta K_{eff})^2)/2)$. The cyclic plastic strain range is proportional to $(\Delta K_{eff})^2$. The mean strain increases significantly with increasing stress ratio. For example, at a ΔK_{eff} of 2 MPa$\sqrt{m}$ the mean strain at $R_{eff} = 0.5$ is approximately five times larger than that at $R_{eff} = 0$, while that at $R_{eff} = 0.7$ is 16 times larger and that at $R_{eff} = 0.9$ is 180 times larger. The ratio of mean strain to the cyclic plastic strain range also increases significantly with increasing stress ratio. At $R_{eff} = 0$ the mean strain is estimated to be half the cyclic plastic strain range while that at $R_{eff} = 0.5$ is 2.5 times larger, that at $R_{eff} = 0.7$ is eight times larger and that at $R = 0.9$ is 90 times larger. Since crack tip strains are quite large even at low stress ratios it is not difficult to accept that a dramatic increase in mean strain with increasing R or in-

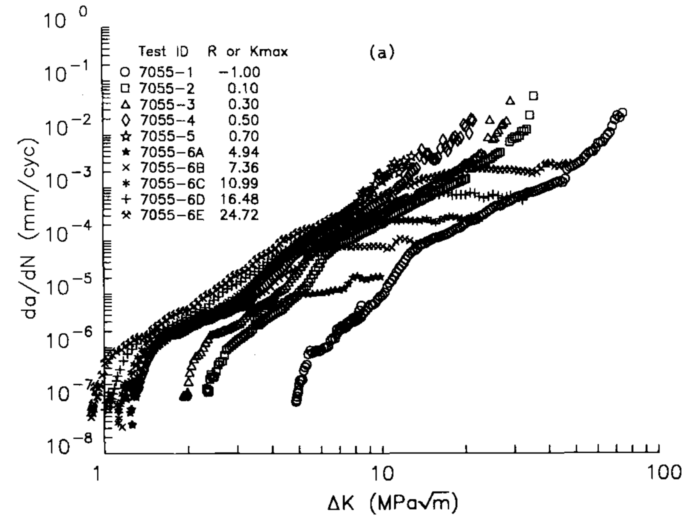

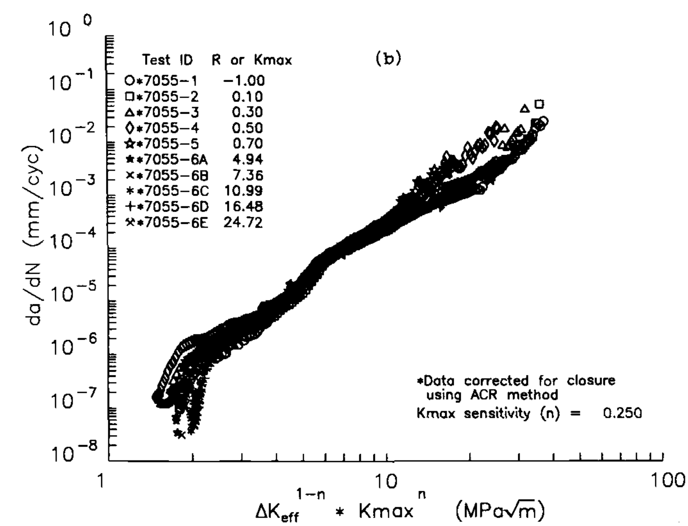

FIG. 13*a,b*—*FCGR response of alloy 7055 for* R $= -1$, *0.1, 0.3, 0.5 and 0.7 and constant* K_{max} *values of 5.0, 7.4, 11.0, 16.5 and 24.7 MPa*$\sqrt{m}$ *when plotted against* ΔK_{app} *and* K_{norm}.

creasing $K_{\max}$ contributes to damage ahead of the crack tip resulting in an increase in crack growth rates. The work of Davidson and Lankford [*21*] suggest that these ratios may be underestimates. Using crack-tip stereoimaging techniques in 7075 alloy they found crack tip plastic strain range proportional to $\Delta K^{2.7}$ instead of ΔK^2.

The other possible cause for the $K_{\max}$ dependence observed in this study is an environmental contribution to fatigue crack growth rates. Moist air is an aggressive environment for aluminum alloys with respect to fatigue crack growth. Fatigue crack growth rates for aluminum alloys in the near-threshold region are 10 to 100 times faster in lab air than in a vacuum [*22*]. Moist air is believed to reduce the cyclic ductility of the material, thus reducing its ability to sustain fatigue damage. As crack tip opening displacements increase with increasing K_{max}, the embrittling species have greater access to the crack tip. The role of environment in the current study can be examined by comparing the Phase 1 and Phase 2 results. Phase 1 testing was performed in laboratory air controlled at a humidity between 38 and 48%. The Phase 2 tests were conducted in humidity chamber having a humidity greater than 90%. The K_{max} sensitivity exponent (n) from Phase 1 ranged from 0.175 to 0.200 while those in Phase 2 were typically 0.250. This increase in K_{max} sensitivity with relative humidity is consistent with an environmental contribution to the observed K_{max} dependence.

The K_{max} sensitivity concept used to describe the observed K_{max} dependence in this study is unique in that a single value of the K_{max} sensitivity exponent (n) is able to describe the K_{max} dependence over a wide range of fatigue crack growth rates and tests conditions. The unique, intrinsic curve obtained for each alloy after accounting for crack closure and K_{max} effects suggests the following modification to the Paris Law for monotonic alloys:

$$da/dN = C[\Delta K_{eff}^{(1-n)} \cdot K_{max}^{n}]^{m} \tag{7}$$

When $n = 0$, indicating no K_{max} sensitivity, this crack growth law simplifies to the Paris Law as modified by Elber (see Eq 2) to account for crack closure effects. The near linear appearance of the intrinsic curves for 6013, 2324 and 7055 aluminum alloys (see Figs. 11*b*, 12*b* and 13*c*) on the log-log plot indicates that this modified law might be useful over a large range of crack growth rates from very near threshold to very near K_c in monotonic alloys. The modified law might also be prove to be useful in situations where K_{max} effects are widely acknowledged to influence crack growth rates such as corrosion fatigue, elevated temperature fatigue crack growth, and in more brittle materials such as ceramics and composites.

Summary and Conclusions

A two phase investigation was conducted using aluminum alloys 6013-T651, 2324-T39 and 7055-T7751 to compare the ASTM opening load and ACR methods for estimating ΔK_{eff} in constant amplitude fatigue crack growth. Phase 1 of this study, which evaluated the sensitivity of the two methods to experimental factors, is fully documented in Ref *15*. Phase 2, which examined the methods over a wide range of stress ratios and applied ΔK, is documented in this paper. Side by side comparisons of the ACR method and the ASTM opening load method in Phases 1 and 2 provide significant evidence that the ACR method gives the better estimate of the "true" ΔK_{eff} or driving force for fatigue crack propagation over the widest range of experimental conditions and loading parameters. Other advantages of the ACR method over the ASTM opening load method observed in this study include insensitivity to measurement location, less crack length sensitivity, the uniqueness of the measurement (no arbitrary percent offset required) and better measurement repeatability (less scatter). The latter two advantages derive from the fact that the full range of the load versus displacement curve is used instead of that portion corresponding to an arbitrary percentage deviation from linearity.

The fundamental difference between these two methods is that the ACR method is designed to account for the contribution of that portion of the load cycle below K_{op} to the driving force for fatigue crack propagation, while the ASTM opening load method is not. In the Paris region, the estimates of ΔK_{eff} from the ACR and ASTM opening load methods were still different but less so, in part due to smaller values of K_{op}. However, in the near-threshold region, ΔK_{eff} obtained by the ACR method provided a reasonable estimate of the "true" ΔK_{eff} while that obtained by the ASTM opening load method significantly underestimated the "true" ΔK_{eff}. This indicates that the contribution of that portion of the load cycle below K_{op} is significant in this region and must be accounted for to obtain an accurate ΔK_{eff}.

The results of this study are also consistent with earlier studies which show that fatigue crack growth rates depend not only on ΔK_{eff} but also have a K_{max} dependence [*17–19*]. Possible mechanisms for the K_{max} dependence include crack-tip mean strain and environmental effects. That the latter mechanism was at least partly responsible was supported by the observation of a greater K_{max} dependence with increasing humidity. Remarkably, this K_{max} sensitivity could be described by a single parameter, the K_{max} sensitivity exponent (n), over the broad range of ΔK, stress ratio and K_{max} evaluated. As a result, ΔK_{eff} curves from all test conditions could be collapsed to a unique intrinsic FCGR curve using a simple modification to the Paris Law (see Eq 7). This K_{max} dependence and crack closure effects could only be separated at low stress ratios using the ACR method. The results of this study indicate that both crack closure and K_{max} effects must be considered to properly characterize stress ratio effects in aluminum alloys.

References

[*1*] Donald, J. K., "Introducing the Compliance Ratio Concept for Determining Effective Stress Intensity," *International Journal of Fatigue,* Vol. 19, Supplement No. 1, 1997, pp. 191–195.

[*2*] Paris, P. C., Gomez, R. E., and Anderson, W. E., "A Rational Analytic Theory of Fatigue," *The Trend in Engineering,* Vol. 13, No. 1, University of Washington, 1961, pp. 9–14.

[*3*] Elber, W., "Fatigue Crack Closure Under Cyclic Tension," *Engineering Fracture Mechanics,* Vol. 2, 1970, pp. 37–45.

[*4*] Elber, W., "The Significance of Fatigue Crack Closure," *Damage Tolerance in Aircraft Structures, ASTM STP 486,* American Society for Testing and Materials, 1971, pp. 230–242.

[*5*] Rice, J. R., "Mechanics of Crack Tip Deformation and Extension by Fatigue," *Fatigue Crack Propagation, ASTM STP 415,* American Society for Testing and Materials, 1967, pp. 247–309.

[*6*] Macha, D. E., Corbly, D. M. and Jones, J. W., "On the Variation of Fatigue-crack-opening Load with Measurement Location," *Experimental Mechanics,* June 1979, pp. 207–213.

[*7*] Allison, J. E. and You, C. P., "Problems Associated with the Quantification of Fatigue Crack Closure," *Fatigue '90,* H. Kitigawa and T. Tanaka, Eds., Materials and Components Engineering Publications, Ltd., United Kingdom, 1990, pp. 1249–1255.

[*8*] Phillips, E. P., "Results of the Round Robin on Opening-Load Measurement," NASA Technical Memorandum 101601, 1989, Langley Research Center, Hampton, VA.

[*9*] Phillips, E. P., "Results of the Second Round Robin on Opening-Load Measurement," NASA Technical Memorandum 109032, 1993, Langley Research Center, Hampton, VA.

[*10*] Hudak, S. J., Jr. and Davidson, D. L., "The Dependence of Crack Closure on Fatigue Loading Variables," *Mechanics of Closure, ASTM STP 982,* J. C. Newman, Jr. and W. Elber, Eds., American Society for Testing and Materials, 1988, pp. 121–138.

[*11*] Hertzberg, R. W., Newton, C. H. and Jaccard, R., "Crack Closure: Correlation and Confusion," *Mechanics of Fatigue Crack Closure, ASTM STP 982,* American Society for Testing and Materials, 1988, pp. 139–148.

[*12*] Chen, D. L., Weiss, B. and Stickler, R., "Contribution of the Cyclic Loading Portion Below the Opening Load to Fatigue Crack Growth," *Materials Science and Engineering,* Vol. A208, 1996, pp. 181–187.

[*13*] McClung, R. C., "Crack Closure and Plastic Zone Sizes in Fatigue," *Fatigue and Fracture of Engineering Materials and Structures,* Vol. 14, 1991, pp. 455–468.

[*14*] Fuhring, H. and Seeger, T., "Dugdale Crack Closure Analysis of Fatigue Cracks Under Constant Amplitude Loading," *Engineering Fracture Mechanics,* Vol. 11, 1979, pp. 99–122.

[*15*] Donald, J. K., Bray, G. H. and Bush, R. W., "An Evaluation of the Adjusted Compliance Ratio Technique for Determining the Effective Stress Intensity Factor," *29th National Symposium on Fatigue and Fracture Mechanics, ASTM STP 1332,* T. L. Panontin and S. D. Sheppard, Eds., American Society for Testing and Materials, 1997.

[*16*] Donald, J. K., Bray, G. H. and Bush, R. W., "Introducing the K_{max} Sensitivity Concept for Correlating Fatigue Crack Growth Data," *High Cycle Fatigue of Structural Materials (Professor Paul C. Paris Symposium),* W. Soboyejo, and T. S. Srivatsan, Eds., The Minerals, Metals & Materials Society (TMS), 1997.

[*17*] Walker, K., "The Effect of Stress Ratio During Crack Propagation and Fatigue for 2024-T3 and 7075-T6 Aluminum," *Effects of Environment and Complex Load History on Fatigue Life, ASTM STP 462,* American Society for Testing and Materials, 1970, pp. 1–14.

[*18*] Döker, H. and Peters, M., "Fatigue Threshold Dependence on Material, Environment and Microstructure," *Fatigue 84,* Vol. 1, C. J. Beevers, Ed., Engineering Materials Advisory Services, U. K., 1884, pp. 275–285.

[*19*] Sadananda, K. and Vasudevan, A. K., "Analysis of Fatigue Crack Closure and Thresholds," *Fracture Mechanics: 25th Volume, ASTM STP 1220,* Erdogan and Hartranft, Eds., American Society for Testing and Materials, 1995, pp. 484–501.

[20] Sadananda, K. and Vasudevan, A. K., "Short Crack Growth Behavior," *Fatigue and Fracture Mechanics: 27th Volume, ASTM STP 1296,* R. Piascik, N. Dowling, and J. Newman, Eds., American Society for Testing and Materials, 1997, pp. 301–316.
[21] Davidson, D. L. and Lankford, J., "Fatigue Crack Tip Strains in 7075-T6 Aluminum Alloy by Stereoimaging and Their Use in Crack Growth Models," *Fatigue Mechanisms: Advances in Quantitative Measurement and Physical Damage, ASTM STP 811,* J. Lankford, D. L. Davidson, W. L. Morris, and R. P. Wei, Eds., American Society for Testing and Materials, 1983, pp. 371–399.
[22] Gangloff, R. P., Piascik, R. S., Dicus, D. L. and Newman, J. C., Jr., "Fatigue Crack Propagation in Aerospace Aluminum Alloys," *Paper ICAS-90-4.5.1, Proceedings of the 17th Congress of the International Council of the Aeronautical Sciences,* Stockholm, 1990, pp. 894–908.

J. Keith Donald[1] *and Edward P. Phillips*[2]

Analysis of the Second ASTM Round-Robin Program on Opening-Load Measurement Using the Adjusted Compliance Ratio Technique

REFERENCE: Donald, J. K. and Phillips, E. P., "**Analysis of the Second ASTM Round-Robin Program on Opening-Load Measurement Using the Adjusted Compliance Ratio Technique,**" *Advances in Fatigue Crack Closure Measurement and Analysis: Second Volume, ASTM STP 1343,* R. C. McClung and J. C. Newman, Jr., Eds., American Society for Testing and Materials, West Conshohocken, PA, 1999, pp. 79–93.

ABSTRACT: The results of the Second Round-Robin on Opening-Load Measurement established the basis for a recent addition to ASTM E 647—"Recommended Practice for Determination of Fatigue Crack Opening Load from Compliance." The technique involves characterizing the deviation in linearity of a load-displacement curve and reporting, as a minimum, the opening load corresponding to a 2% slope offset. The opening load and associated ΔK_{eff} values reported showed significant scatter although this scatter was reduced when the data were subjected to a rigorous accept/reject criterion. Refinements in the method of handling data with high "noise" have further reduced scatter compared with the original analysis. Since each participant provided digitized load-displacement curves, the data from 17 test samples (10 participants) were reanalyzed using the "adjusted compliance ratio" (ACR) technique to evaluate ΔK_{eff}. A comparison between the two methods shows that the ACR technique gives a higher mean value of ΔK_{eff} than does the ASTM procedure. The ACR technique also shows a stronger correlation with crack growth rate data than does the ASTM procedure, with a slope comparable to that of a typical fatigue crack growth rate test. However, the mean value of ΔK_{eff} based on the ASTM procedure shows better agreement with high stress ratio "closure free" data than does the ACR technique. This seemingly contradictory result can be partially explained in terms of second-order effects not normally considered significant.

KEYWORDS: fatigue, fatigue threshold, crack propagation, effective stress intensity, crack closure

The results of two experimental round-robin programs on opening-load measurement [*1,2*] provided the basis for an ASTM Recommended Practice for Determination of Fatigue Crack Opening Load from Compliance (ASTM E 647-95, Appendix X2). In the first Round Robin program, all of the participating laboratories determined the opening load by analyzing specimen compliance behavior, but several different methods were used. The results indicated that there were significant differences among laboratories using the same analysis method and also systematic differences produced by different analysis methods applied to the same raw load and displacement/strain data. It was clear that to achieve more consistent results among laboratories, some standardized procedures for determining opening load would be required.

The objectives of the second round-robin program were to generate specimen compliance data in several laboratories for the same test conditions and to use the data to evaluate: (1) procedures for establishing the acceptability of the raw load and displacement/strain data, and (2) nonsubjective meth-

[1] Director, Fracture Technology Associates, 2001 Stonesthrow Road, Bethlehem, PA 18015.
[2] Research engineer, NASA Langley Research Center, MS 188E, Hampton, VA 23681.

ods for analyzing the compliance data to determine the opening load. The results of this effort were to serve as the basis for proposing a recommended procedure for determining the opening load from specimen compliance data.

The intent of the test plan was to specify the test and measurement conditions sufficiently so that opening-load measurements would be made under nominally identical conditions. All test specimens were fabricated from a single plate of 9.5 mm thick 2024-T351 aluminum alloy according to Fig. 1. For the "basic program" all tests were conducted in ambient air at a stress ratio of 0.1 and a constant ΔK of 5.9 MPa $\sqrt{m}$. Crack opening loads were measured at crack lengths of 25.4, 27.9 and 38.1 mm. Participants provided digitized load-displacement data for each crack length using either crack mouth opening displacements (CMOD) or back face strain (BFS) measurements. They also provided load-displacement data for each specimen before a crack was initiated at the notch. Although originally fourteen laboratories provided test results, only the ten laboratories that provided digitized load versus displacement/strain data submitted on a magnetic diskette were included in the analysis. The purpose of this investigation is to re-analyze the previous data using a new methodology for determining ΔK_{eff} referred to as the "adjusted compliance ratio" (ACR) technique and to compare and comment on differences between opening load and ACR procedures.

ΔK_{eff} Determination Methodology

The opening load concept implies that the crack essentially "peels" open as load is applied. The opening load is defined as the minimum load at which the fatigue crack is open at the tip during the increasing-load part of a fatigue cycle. ΔK_{eff} is based on the cyclic load range above the opening load. In this case, the compliance of the closure mechanism is considered a second-order effect and is generally neglected. As such, a "true" measurement of the opening load would provide a lower bound on the determination of ΔK_{eff} simply because the strain contribution below the opening load is ignored.

The ACR concept [3,4] is based on an interpretation of crack closure as a stress redistribution (or load transfer) on a relatively compliant crack wake. Therefore, the opening load marks a transition

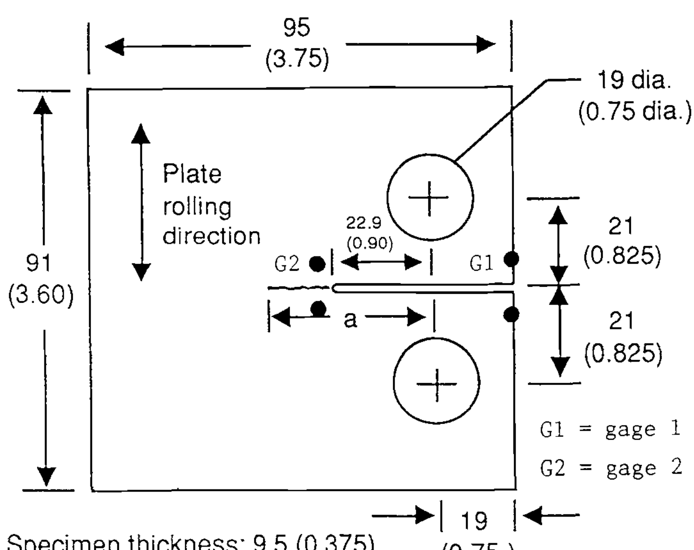

FIG. 1—*Diagram of compact tension specimen used in Round Robin (dimensions in millimeters (inches)).*

point, whereby the applied load is no longer directly proportional to the local crack-tip strain field magnitude. However, the calculation of ΔK_{eff} includes the full range of the applied load and therefore does not require an opening-load measurement. The ΔK_{eff} computed from this interpretation will be larger than that based on opening load since additional crack-tip strain is included below the opening load. The "peeling open" characteristic of the crack is considered a second-order effect and is not taken into account. In fact, the ACR method would provide an upper bound on ΔK_{eff} simply because of the ignored "peeling open" characteristic.

With each concept, the same raw load-displacement/strain data are analyzed. The difference in the two concepts lies strictly in the interpretation of the data. There are, however, traits common to both methods as follows: (1) The measurement location, either CMOD or BFS, is a global measurement of the elastic strain response. The magnitude of the plastic crack-tip strain is too small to measure remotely. (2) The deviation in linearity of the load-displacement response due to closure is a measurement of the bulk shielding response. There is no currently accepted method to distinguish shielding contributions near the crack tip from those relatively far from the crack tip. (3) The global or remote measurement represents an average through-the-thickness response. A local measurement near the crack-tip is not only more difficult, but may represent the conditions at the surface of the sample only and not the average through-the-thickness behavior. (4) An experimental procedure cannot discriminate among the various closure mechanisms such as plasticity, roughness, oxide and/or residual stress. Only the combined influence of the mechanisms can be measured.

Experimental Determination of ΔK_{eff} from Opening Load

As mentioned earlier, one way to estimate ΔK_{eff} is to experimentally determine the crack opening load and to assume that ΔK_{eff} can be computed based on the cyclic load range above the opening load. Any contribution to the crack driving force from loads less than the opening load is neglected. The opening load is usually defined as the minimum load at which the crack tip is fully open at the tip during the increasing load part of a fatigue cycle. The opening load is determined from load/displacement data as that load above which the specimen exhibits a constant compliance (that is, the load above which the load against displacement curve is linear). Although conceptually a simple task, in practice this task is very difficult due to the gradual change in compliance as it approaches the open-crack value and to the variability in the compliance data. It was clear from the first Round Robin program [*1*] that (1) a nonsubjective method of analyzing load/displacement data to determine opening load, and (2) an accept/reject criteria on raw data quality were needed to achieve consistent results among laboratories. The second Round Robin [2] evaluated two methods for evaluating the opening load: (1) the compliance offset method, and (2) the correlation coefficient method. Only the compliance offset method will be described here, since it was eventually selected for inclusion in the ASTM standard and is the method used for comparison with the ACR method.

The current ASTM method for determining crack opening load is as follows. Using the raw displacement against load data, a straight-line is fit to approximately the upper 25% of the cyclic load range. The slope of this line is the compliance value that is assumed to correspond to the fully open crack. Next, the variation of the slope (compliance) with load is discretized by fitting straight lines to small overlapping segments of the data as shown in Fig. 2. This variation of compliance with load is plotted as shown in Fig. 3, where now the differences (offsets) between the open-load compliance and the segment compliances are plotted as percentages of the upper 25% compliance. The opening load is then determined as the lowest load at which the compliance offset is equal to the selected offset criterion (2% in this case). It is clear from Fig. 3 that the opening load determined by this procedure is lower than the load at which the compliance attains a constant value (that is, lower than the load when the crack becomes fully open). A finite compliance offset (as opposed to a 0% offset) was selected as the criterion for defining the opening load based on two considerations: (1) use of a finite offset results in lower scatter in opening load, and (2) recognition that the opening at the crack tip does not

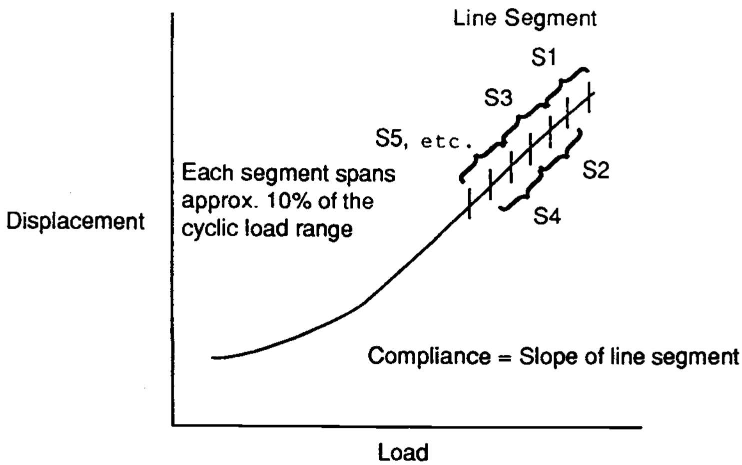

FIG. 2—*Evaluation of variation of compliance with load for use in determination of opening load.*

occur at the same load at various locations through the thickness and that some load lower than the fully-open load might produce better correlations of crack growth data. The selection of a 2% offset as the criterion was arbitrary and was based on judgment in trading off the effects on scatter and on proximity to the fully-open load. Another offset criterion might eventually prove to be more appropriate.

It should be noted here that the scatter in the opening loads observed in the second Round Robin report [2] is higher than reported in this paper for the same raw data because the method used to determine opening load in the current ASTM standard and in this paper is somewhat different from that used in the second Round Robin report. The two methods produce the same opening loads for data sets with low variability (like that shown in Fig. 3), but produce different

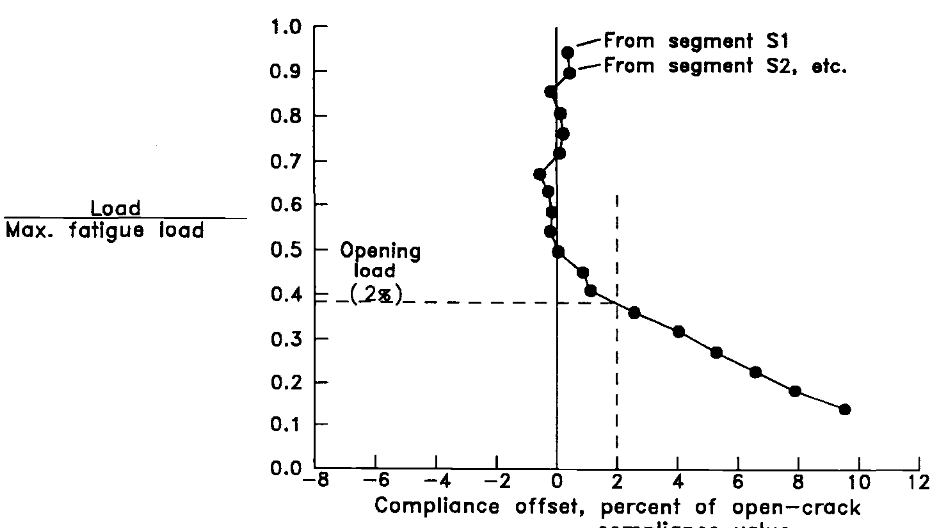

FIG. 3—*Determination of opening load using the current ASTM method (2% compliance offset).*

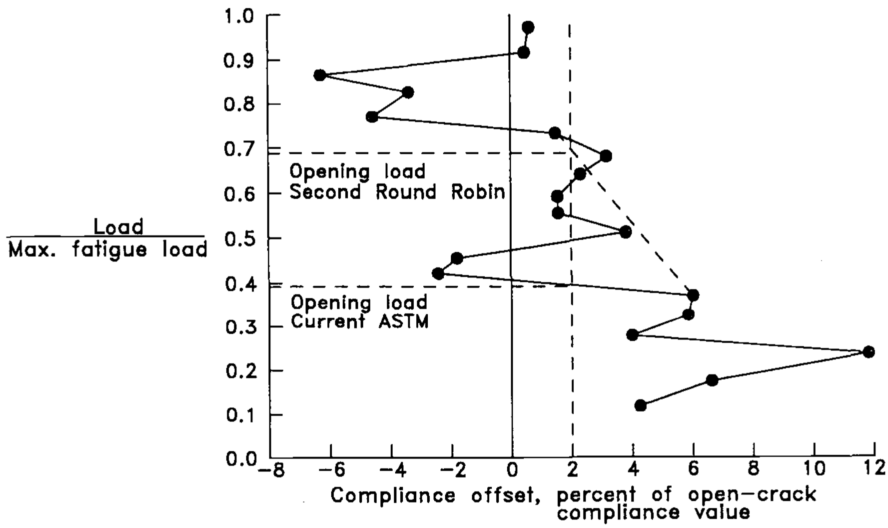

FIG. 4—*Determination of opening loads from high-variability raw data by the current ASTM and second Round Robin methods.*

opening loads for data sets having high variability in the raw data. The difference between the two methods is illustrated in Fig. 4 which shows the variation of compliance with load in the same format as in Fig. 3 (current standard). The difference lies in the way the opening load is picked from this plot. In the second Round Robin method, the opening load was defined from a line that connected the highest load point below which there were no crossings of the offset criterion level to the lowest load point above which there were no crossings of the offset criterion level. In the current ASTM method, the opening load is defined as the lowest load crossing of the offset criterion level. The second Round Robin method resulted in some very high opening load determinations for some high variability data sets, and as a consequence the overall scatter in opening loads was greater.

Regardless of which opening-load method (current ASTM or second Round Robin) is used, lower scatter in opening loads will be obtained when only high quality raw data are accepted for analysis. In the second Round Robin, linearity and variability (noise) accept/reject criteria were formulated based on load/displacement data collected from the uncracked specimen. The uncracked specimen should exhibit linear load/displacement behavior for the entire load cycle. When the data from the second Round Robin were screened using the data quality criteria, the scatter in opening loads was substantially reduced. The current ASTM recommended practice for determining opening load includes the data quality accept/reject criteria. The reanalysis of the second Round Robin data in this paper includes data that do not meet the data quality criteria.

Experimental Determination of ΔK_{eff} from the Adjusted Compliance Ratio

In the simplified case of a single element contributing to crack-tip shielding (Fig. 5*a*), the point of first contact or opening load at point 2 might not be as important in determining ΔK_{eff} as is the relative compliance of this element and the extent to which the crack tip is shielded from the driving force below the opening load (point 2 to point 3). At high opening loads, this contribution below K-opening cannot be ignored. In reality, a large number of elements makes the point of first contact difficult to distinguish on a standard load-displacement trace (Fig. 5*b*).

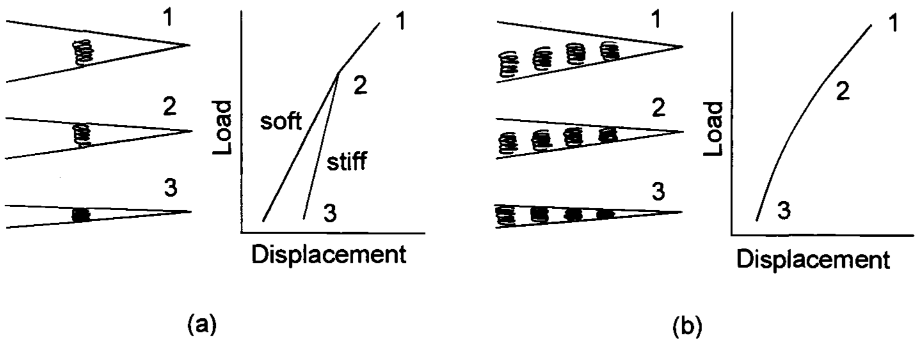

FIG. 5—*(a) Simplified case of single element contributing to crack-tip shielding. First contact is indicated by point 2. The relative compliance of this element influences crack-tip shielding. (b) In reality, a large number of elements makes the point of first contact difficult to distinguish.*

Previous work [*3*] has illustrated an alternative means of interpreting ΔK_{eff} based on near crack-tip strain measurements. It is assumed that the crack driving force, ΔK_{eff}, should be proportional to the near crack-tip elastic strain field magnitude. Therefore, ΔK_{eff} is based on the ratio of the measured strain magnitude (proportional to the secant compliance, C_s) to that which would have occurred in the absence of closure (proportional to the fully open compliance C_o). This ratio is then multiplied by ΔK_{app} to determine ΔK_{eff}. Evidence has shown this assumption to be extremely crack length- and measurement location-sensitive and only useful if it were practical to continuously and correctly monitor the near crack-tip elastic strain.

Since measurement of local crack-tip strain for the compliance ratio technique is more difficult than remote measurements, an alternative method has been devised to accomplish the same end using remote compliance measurements. The alternative method is referred to as the adjusted compliance ratio (ACR) technique and is determined as follows:

$$\mathrm{ACR} = \frac{C_s - C_i}{C_o - C_i} \tag{1}$$

where

ACR = adjusted compliance ratio,

C_s = compliance determined from secant drawn between minimum load-displacement and maximum load-displacement,

C_o = compliance determined from linear upper portion of load-displacement curve (assumed to represent fully open crack), and

C_i = compliance determined from linear upper 45% portion of load-displacement curve prior to initiation of a crack.

It is believed that this results in a compliance ratio that is due solely to the presence of the crack. The resulting ratio appears to be independent of measurement location and can be used to directly calculate ΔK_{eff}. It is this ratio that accounts for the bulk shielding mechanism in the wake of the crack and its effect on the cyclic strain field immediately in front of the crack. To compensate for a possible bias in the secant compliance (C_s) or open-crack compliance (C_o) due to signal conditioning noise or nonlinearity, the ACR may be normalized (ACR_n) as follows:

$$\mathrm{ACR}_n = \frac{C_{oi}}{C_{si}} \cdot \frac{C_s - C_i}{C_o - C_i} \tag{2}$$

where

ACR_n = normalized adjusted compliance ratio,
C_{oi} = compliance determined from secant drawn between minimum and maximum load-displacement prior to initiation of a crack, and
C_{si} = compliance determined from upper 45% portion of load-displacement curve prior to initiation of a crack.

This is an important step in the re-analysis of the second Round Robin data since the nonlinearity or noise characteristics of the original load-displacement data can now be normalized. The change in the C_s and C_o can then be compared with the initial C_{si} and C_{oi} characteristics. The effect is most pronounced for small increments of crack extension. For example, a 0.5% change in the C_{oi}/C_{si} ratio results in about a 4% change in ACR_n after 2.5 mm of crack extension but accounts for less than a 1% change in ACR_n after 15 mm of crack extension. Out of 20 data sets investigated, six had C_{oi}/C_{si} ratios that differed from 1.00 by greater than 0.5% although none differed by more than 1.0%. In this study, only ACR_n was used, so the direct impact of this additional analysis step on data scatter was not evaluated. As a final step, the effective stress intensity is determined directly by multiplying the applied stress intensity by ACR_n as follows:

$$\Delta K_{\mathrm{eff}} = \mathrm{ACR}_n \cdot \Delta K_{\mathrm{app}} \tag{3}$$

where ΔK_{eff} is the effective stress intensity and ΔK_{app} the applied stress intensity.

Perhaps the most startling revelation of the ACR technique is the apparent insensitivity to measurement location. To illustrate this, a test sample identical to the size and geometry used in the second Round Robin program was machined from a 6013-T651 aluminum alloy in the L-T orientation [*4*]. As before, the test was conducted in ambient air at a stress ratio of 0.1 and a constant ΔK of 5.9 MPa$\sqrt{\mathrm{m}}$. As required for the ACR technique, the initial C_i, C_{oi} and C_{si} were obtained prior to initiation of a crack. Continuous crack closure measurements were made using both the opening load technique and the ACR technique covering a crack length from 25.4 (notch length) to 38.1 mm. In addition to the standard CMOD measurements (gage location G1), a second pair of clip-in displacement transducers (one on each side of the sample for increased sensitivity and linearity) was attached directly in line with the notch tip with a gage length of 15.2 mm (gage location G2, Fig. 1).

Figure 6 illustrates the C_o and C_s compliance for each gage location after the original compliance C_i is subtracted. It was observed that the resulting ratio (Eq 1) for each gage location is proportional to the slope of the compliance curves as a function of crack length (dC/da). Since the slope of the compliance curve can be used to derive the stress intensity, it follows that the ratio of the compliance slopes may be directly proportional to the ratio of $\Delta K_{\mathrm{eff}}/\Delta K_{\mathrm{app}}$ regardless of the measurement location. For each gage location and closure measurement method, the ratio of $\Delta K_{\mathrm{eff}}/\Delta K_{\mathrm{app}}$ is plotted as a function of crack length in Fig. 7. The ratio of $\Delta K_{\mathrm{eff}}/\Delta K_{\mathrm{app}}$ is used in lieu of K_{op} since the ACR method provides this ratio directly and does not measure an opening level. This figure clearly shows measurement location insensitivity for the ACR technique (ACR1 and ACR2 correspond to gage locations G1 and G2.) whereas the ASTM opening load method shows sensitivity to measurement location (OP1 and OP2 correspond to gage locations G1 and G2). On the other hand, the ACR technique gives a higher mean value of ΔK_{eff} than does the ASTM procedure.

Experimental Procedure and Results

A total of 22 data sets from ten laboratories were reanalyzed to compare the opening load method to the ACR method. Each data set includes digitized load-displacement/strain data for one complete load cycle at four crack lengths (including the notch length prior to initiation of a crack). Nine samples used CMOD transducers, three samples used BFS gages and five samples used both CMOD and

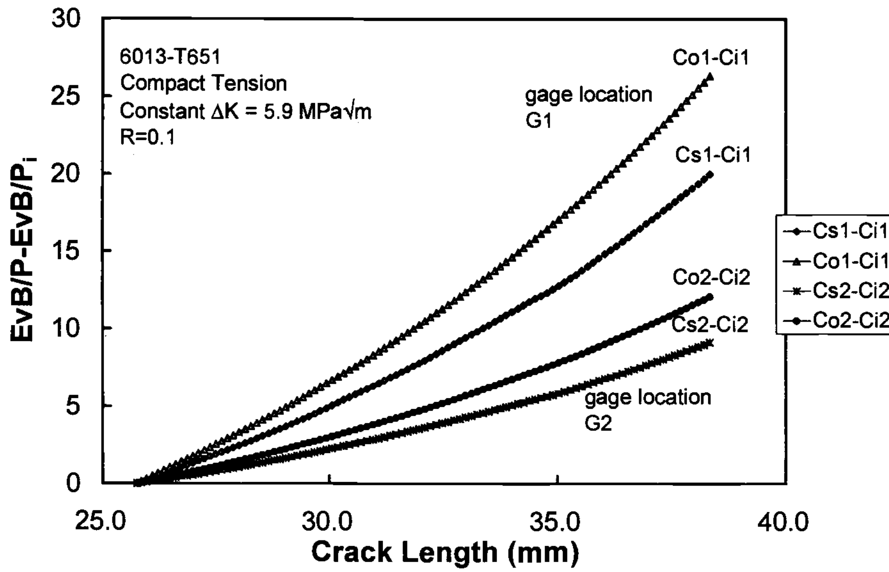

FIG. 6—*Relationship between fully open compliance (C_o) and the secant compliance (C_s) once the initial compliance (C_i) is subtracted. Plot shows two measurement locations as a function of crack length.*

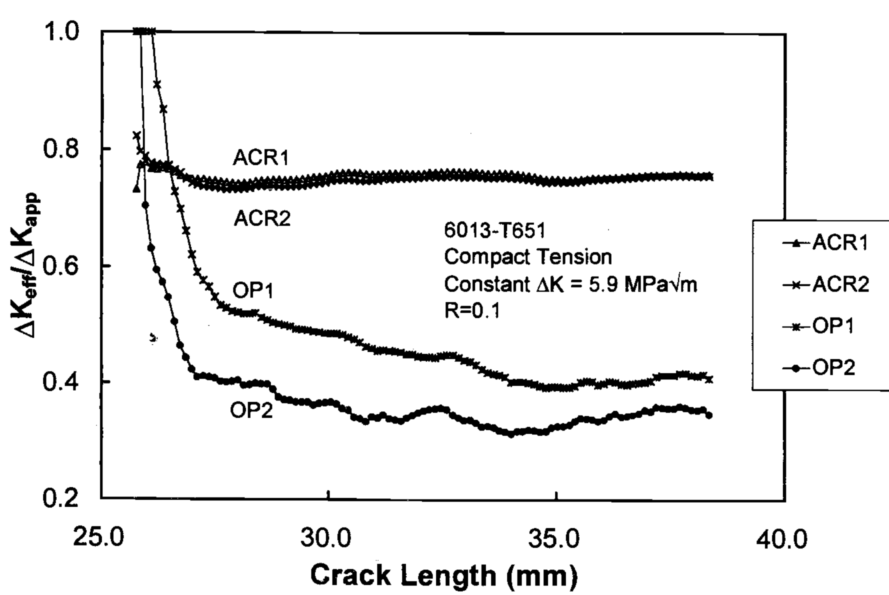

FIG. 7—*Two types of closure measurement techniques are displayed using two measurement locations as a function of crack length.*

BFS locations for a total of 17 test samples. Of the 22 data sets, one data set was eliminated since data for only one of three crack lengths was available. Another was eliminated since the linear portion of the load-displacement data (above 55% of maximum load) had a poor correlation coefficient of 0.995 instead of a typical value of 0.9997 to 0.9999. A third data set was eliminated from the crack growth rate correlation evaluation simply because the range of crack growth rate data reported at the three crack lengths of interest varied by 40% whereas all other results varied by 20% or less. Of the remaining 15 test samples, four had both CMOD and BFS locations allowing the relative measurement location sensitivity to be evaluated for each method.

Originally all the data sets were re-analyzed using the upper-most 25% of the cyclic load range to determine the compliance value that corresponds to the fully-open crack configuration. An initial evaluation of the results indicated that all of the opening loads corresponding to a 2% offset were less than 55% of maximum load. Therefore, the data sets were re-analyzed based on using the load displacement data above 55% of maximum load to determine the compliance value corresponding to the fully-open crack configuration. This adjustment had no observable effect on the mean values of ΔK_{eff} determined from either method but did reduce the data scatter slightly.

The opening load results from twenty tests are plotted in Fig. 8 for a compliance offset criteria of 2%. Both CMOD (suffix M) and BFS (suffix B) measurement locations are shown. The opening load results are represented as the ratio of $\Delta K_{eff}/\Delta K_{app}$ in order to facilitate comparing these results with the ACR method. No further qualification of the data was performed to accept or reject data sets with "high" noise or nonlinearity. The data scatter is less than originally reported in the second Round Robin because of a difference in how data sets with "high" noise are analyzed.

The ACR results using the same basic data are plotted in Fig. 9. This method does shift the mean value of the ratio $\Delta K_{eff}/\Delta K_{app}$. This is expected since the contribution to the crack driving force below the opening load is now taken into account. Although not statistically significant, the ACR method appears to shows a slight rise in the ratio of $\Delta K_{eff}/\Delta K_{app}$ as a function of increased crack length. It is assumed that $\Delta K_{eff}/\Delta K_{app}$ should remain constant for both methods since the fatigue

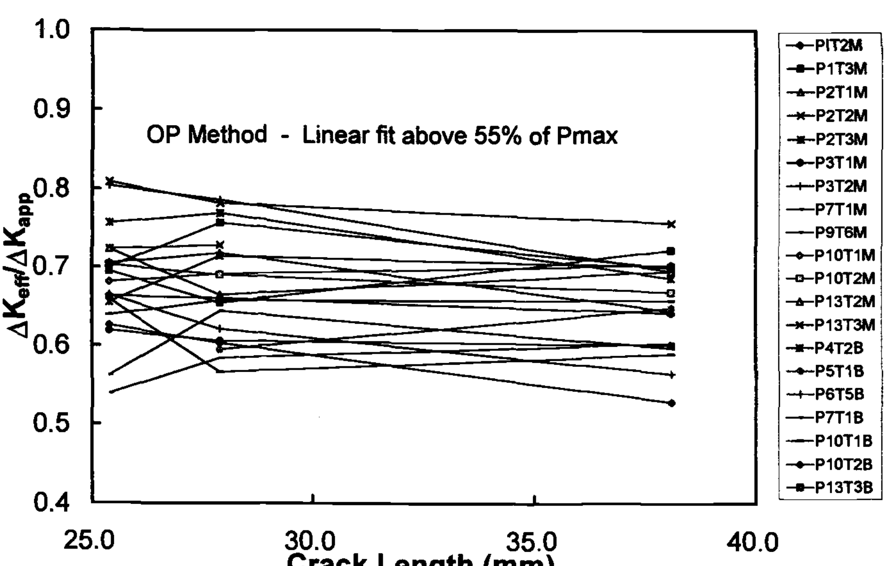

FIG. 8—*Ratio of* $\Delta K_{eff}/\Delta K_{app}$ *determined by the opening load corresponding to a 2% compliance offset as a function of crack length.*

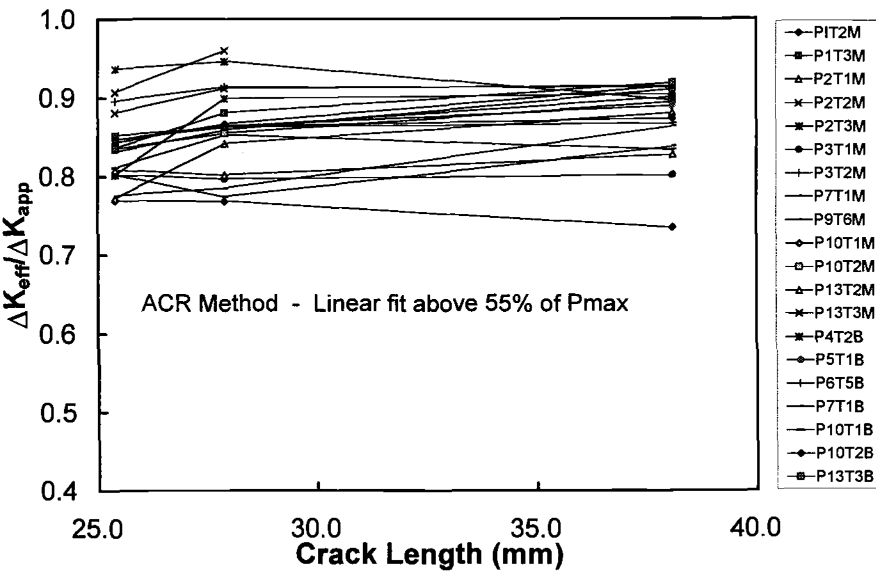

FIG. 9—*Ratio of* $\Delta K_{eff}/\Delta K_{app}$ *determined by the ACR method as a function of crack length.*

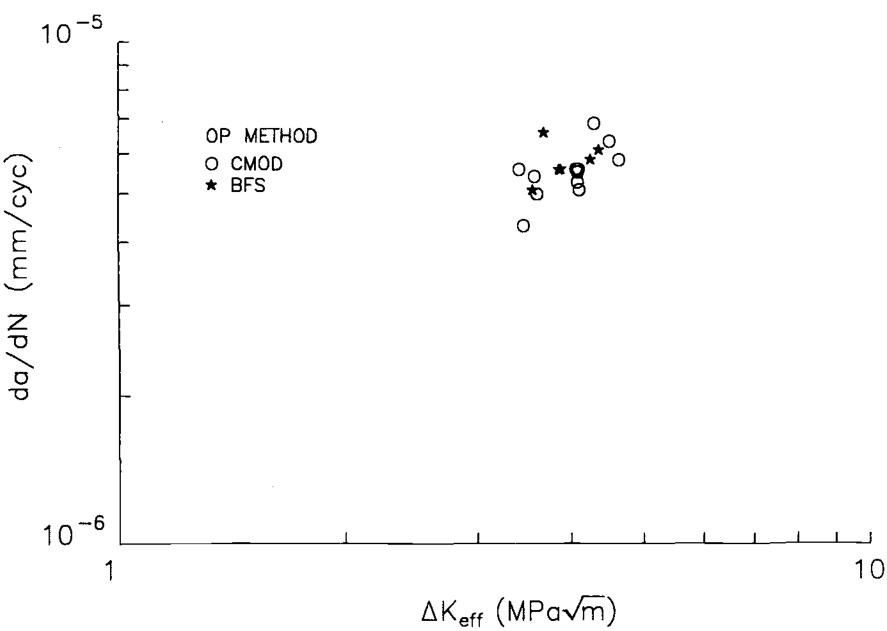

FIG. 10—*Crack growth rate response as a function* ΔK_{eff} *determined by the opening load corresponding to a 2% compliance offset showing no systematic crack growth correlation.*

crack growth rate remains essentially constant. It is likely that the ACR technique as proposed is not entirely independent of crack length. It is also likely that the method only partially captures the near crack-tip interference due to closure.

Fatigue Crack Growth Rate Correlation

It is not obvious from the results shown in Figs. 8 and 9 that the ACR technique offers a reduction in data scatter. However, since each participant also provided crack growth rate data, the correlation with this data was also investigated. For each data set, the average ΔK_{eff} (2% compliance offset method) at three crack lengths and the corresponding average crack growth rate were plotted in Fig. 10. As can be seen, there is no systematic correlation. If only the data that met the data quality criteria of the second Round Robin are included, an improved crack growth rate correlation is indicated in Fig. 11. However, since the ACR analysis technique includes an additional step to compensate for variability due to "high" noise or nonlinearity (ACR_n), a data quality criteria was not used for the ACR method. Therefore, when the original data sets are reanalyzed using the ACR technique, the plotted values (Fig. 12) show a strong correlation with a slope comparable to that which would be obtained in a fatigue crack growth rate test at similar growth rates but at a higher "closure free" stress ratio. This implies that the scatter observed with the ACR technique is due less to measurement error than to material variability.

To investigate this observation further, a series of constant K_{max}-decreasing ΔK tests were conducted on a spare sample from the same heat of 2024-T351 aluminum alloy. As K_{max} was varied from 11.5 to 36.7 MPa $\sqrt{m}$, the stress ratio ranged from 0.65 to 0.91 over the same crack growth rate range as the second Round Robin data. A comparison of the second Round Robin data with the high stress

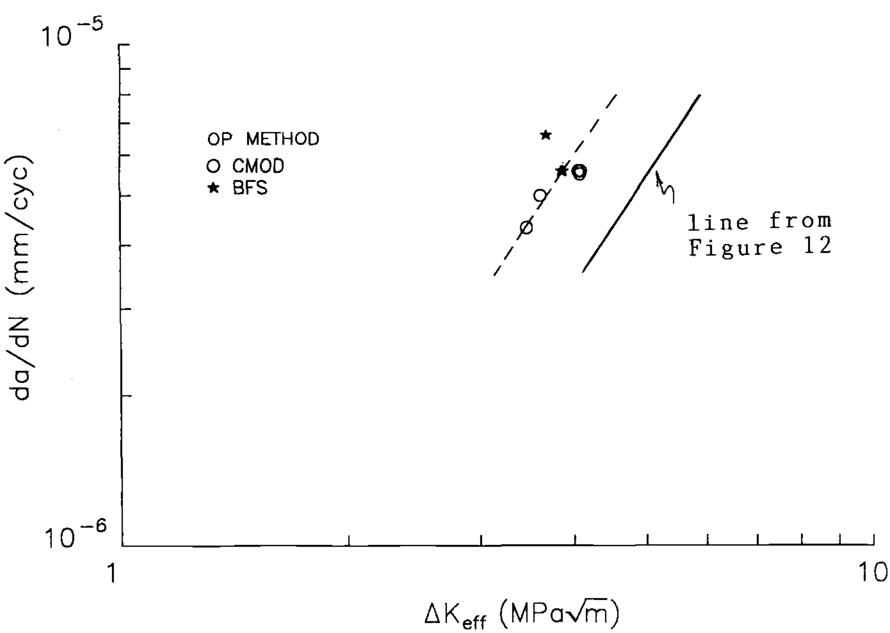

FIG. 11—*Crack growth rate response as a function ΔK_{eff} determined by the opening load corresponding to a 2% compliance offset. Only data that met the data quality criteria of the second Round Robin are included. The straight line through the data is the slope of the ACR data shifted to the left for comparison.*

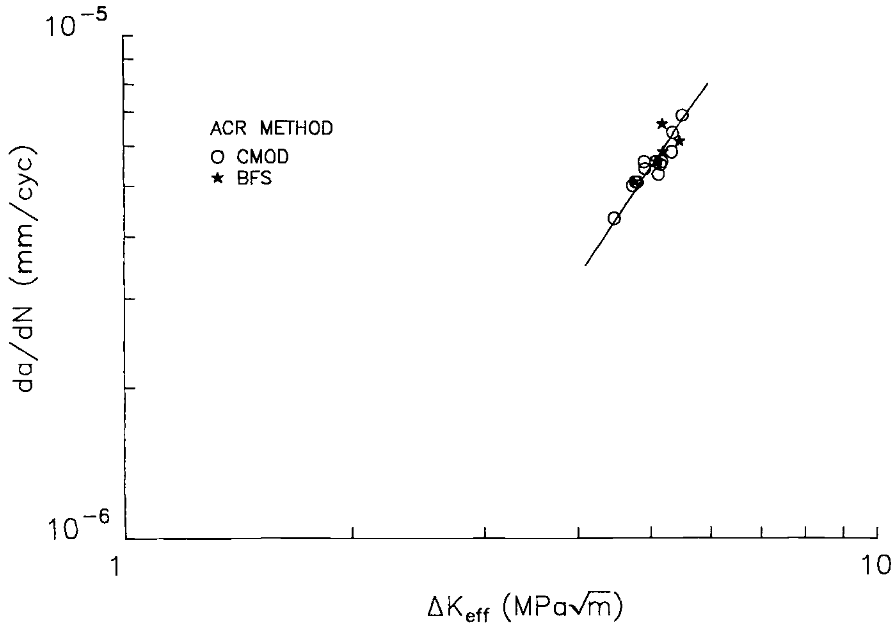

FIG. 12—*Crack growth rate response as a function ΔK_{eff} determined by the ACR technique showing strong crack growth correlation.*

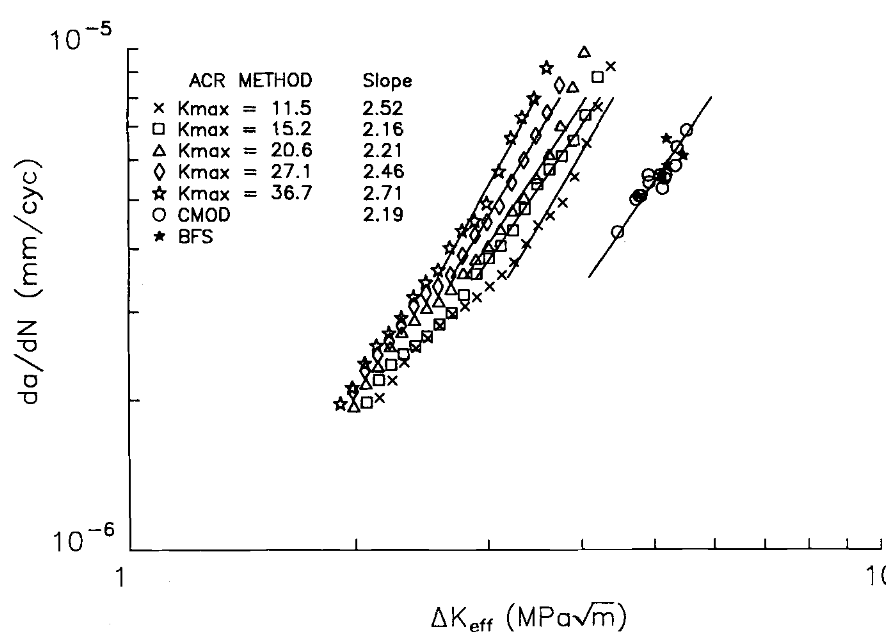

FIG. 13—*Comparison of ΔK_{eff} values determined by the ACR technique with closure free constant K_{max} data showing K_{max} effect and Paris Law slope similarity.*

ratio "closure free" data shows a similar Paris Law slope for all test data as well as a K_{max} effect on the crack growth behavior (Fig. 13). This observed K_{max} effect is consistent with the observations reported in previous work [5]. On the other hand, the results shown in Fig. 14 indicate that the average response of the ΔK_{eff} determined by the 2% compliance offset criteria agrees well with the "closure-free" data at a constant K_{max} of 11.5 MPa $\sqrt{m}$. This observation is consistent with a similar finding in the second Round Robin report. Previous work [6] has shown that an acceptable correlation between ΔK_{eff} determined using a 2% compliance offset and region 2 "closure free" data (R = 0.7) is not uncommon. However, at near-threshold crack growth rates, no systematic correlation is likely to exist. ΔK_{eff} determined from a 2% offset compliance has been shown to be sometimes higher than but often substantially lower than values determined from "closure free" crack growth rate data. Since ignoring the strain contribution below the opening load will shift the ΔK_{eff} to the left, and the effect of K_{max} may account for a shift to the right, it is reasonable to assume that the variability and contradictions observed, may be partially the result of two competing and often neglected second order effects. It appears that an opening-load method is most appropriate if the source of interference is predominately near the crack-tip whereas the ACR method may be most appropriate if the interference forces are distributed over the entire wake of the crack. It is likely that each method has limitations that warrant further investigation.

Measurement Location Sensitivity

Since an earlier evaluation of the ACR technique showed measurement location insensitivity (Fig. 7), a similar comparison was performed on the four samples in the second round-robin program that had both CMOD and BFS measurement locations. In this case, the ACR method gives an average relative difference in the determination of ΔK_{eff} between CMOD and BSF measurement locations of ~1% whereas the ASTM method gives ~4% (Fig. 15). Given the small number of comparisons and

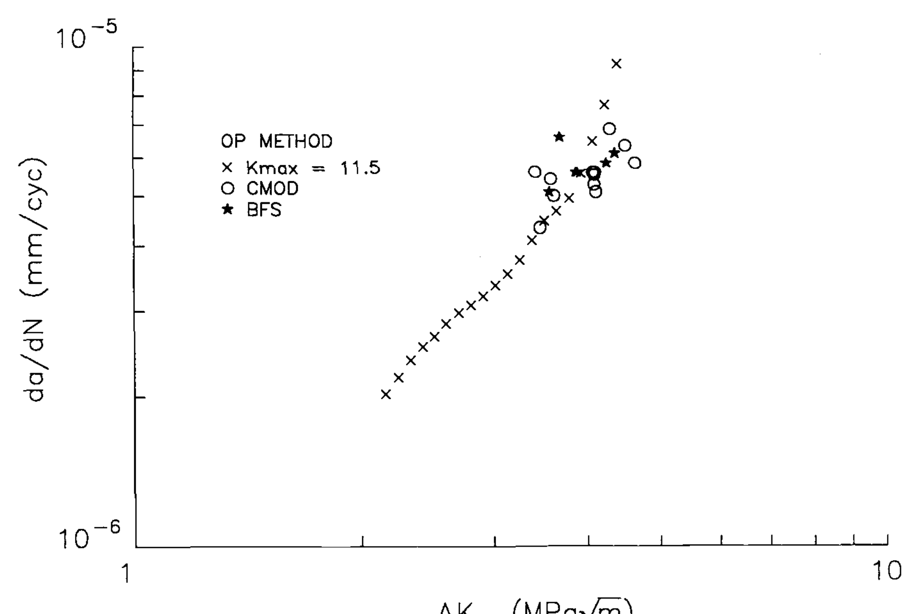

FIG. 14—*Comparison of* ΔK_{eff} *values determined by the opening load corresponding to a 2% compliance offset with closure free constant* K_{max} *data at a* K_{max} = *11.5 MPa*$\sqrt{m}$.

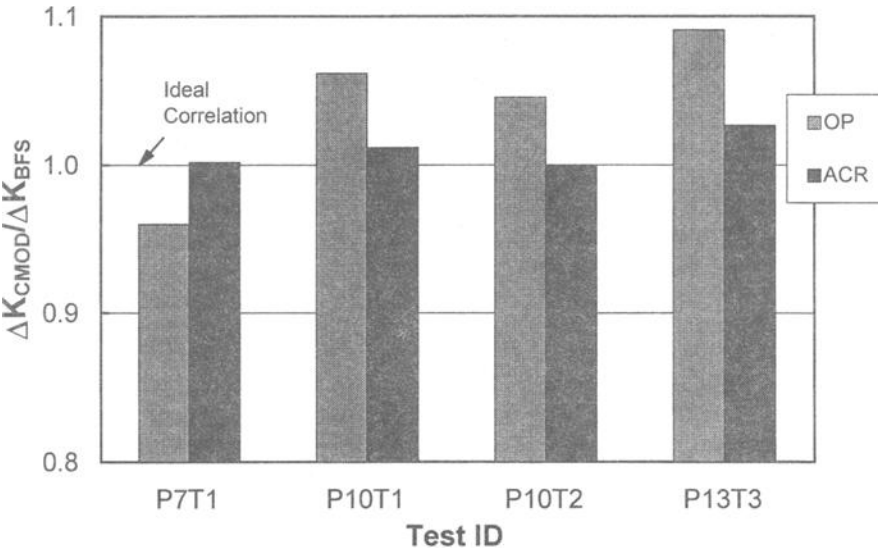

FIG. 15—*Comparison between measurement locations showing relative difference in* ΔK_{eff} *values determined by the two methods.*

small percentages relative to typical scatter, the difference may not be statistically significant. However, the trend is consistent with expectations.

Summary and Conclusions

The opening-load concept represents a lower bound on ΔK_{eff} since strain contributions below the opening load are ignored. In contrast, the ACR concept represents a upper bound since no attempt has been made to adjust for second-order effects due to crack extension and the distribution of bulk shielding mechanism.

The experimental determination of ΔK_{eff} using the opening-load concept is sensitive to measurement location, the arbitrary nature of the percent offset, and the variability associated with selecting a specific percent offset due to noise and nonlinearity. In contrast, the experimental determination of ΔK_{eff} using the ACR method is insensitive to measurement location, and is unique (no arbitrary percent offset required) and repeatable since full range load and displacement are measured instead of the deviation in linearity between load and displacement/strain.

Attempts to correlate stress ratio effects on the basis of crack closure alone have been hampered by nonrepeatable measurements of closure, measurement location sensitivity and other neglected second-order effects. The ACR approach is sufficiently repeatable to suggest that $K_{\max}$ sensitivity is part of the fatigue process and not just unique to $K_{\max}$ values approaching K_c.

The ACR method provides another method to extract crack closure information from BFS or CMOD measurements. Although the method is largely empirical in nature and relies on a normalization procedure to correct for apparent nonlinearities in the data, it does appear to (1) reduce the scatter apparent in closure load determination and (2) reduce apparent conservatism at near-threshold crack growth rates by providing a higher ΔK_{eff} when compared with the ASTM 2% method. The empirical nature of both methods implies that future development of either should focus on determining the most physically relevant, as opposed to empirically derived and developed, measurement procedure. In view of the unique characteristics of the ACR technique, further investigation is warranted to properly model the concept and to identify limitations and sources of error.

References

[1] Phillips, E. P., "Results of the Round Robin on Opening-Load Measurement," NASA Technical Memorandum 101601, Langley Research Center, Hampton, VA, 1989.

[2] Phillips, E. P., "Results of the Second Round Robin on Opening-Load Measurement," NASA Technical Memorandum 109032, Langley Research Center, Hampton, VA, 1993.

[3] Donald, J. K., "Introducing the Compliance Ratio Concept for Determining Effective Stress Intensity," presented at the First International Conference on Fatigue Damage in Structural Materials, Hyannis, MA, Sept. 1996 (to be published in *International Journal of Fatigue*).

[4] Donald, J. K., Bray, G. H., and Bush, R. W., "An Evaluation of the Adjusted Compliance Ratio Technique for Determining the Effective Stress Intensity Factor," *29th National Symposium on Fatigue and Fracture Mechanics, ASTM STP 1332,* T. L. Panontin and S. D. Sheppard, Eds., American Society for Testing and Materials, 1997.

[5] Donald, J. K., Bray, G. H., and Bush, R. W., "Introducing the K_{max} Sensitivity Concept for Correlating Fatigue Crack Growth Data," *High Cycle Fatigue of Structural Materials (Professor Paul C. Paris Symposium),* W. Soboyejo and T. S. Srivatsan, Eds., The Minerals, Metals & Materials Society (TMS), 1997.

[6] Donald, J. K., "A Procedure for Standardizing Crack Closure Levels," *Mechanics of Fatigue Crack Closure, ASTM STP 982,* J. C. Newman, Jr. and W. Elber, Eds., American Society for Testing and Materials, 1988, pp. 222–229.

Stephen M. Graham,[1] Robert Tregoning,[2] and X. Jie Zhang[2]

Evaluation of the Adjusted Compliance Ratio Technique for Measuring Crack Closure in Ti-6A1-4V

REFERENCE: Graham, S. M., Tregoning, R., and Zhang, X. J., **"Evaluation of the Adjusted Compliance Ratio Technique for Measuring Crack Closure in Ti-6A1-4V,"** *Advances in Fatigue Crack Closure Measurement and Analysis: Second Volume, ASTM STP 1343,* R. C. McClung and J. C. Newman, Jr., Eds., American Society for Testing and Materials, West Conshohocken, PA, 1999, pp. 94–105.

ABSTRACT: Standard fatigue crack growth rate tests within the upper threshold and Paris Law regions were conducted on specimens from three large, standard-grade Ti-6Al-4V forgings in order to evaluate the adjusted compliance ratio (ACR) method for closure correction. Constant R-ratio tests were conducted to generate data containing crack-tip closure, and constant K_{max} tests were performed to produce high R ratio, and hence closure-free, data in the threshold and upper threshold regimes. Direct comparisons are made of the closure corrected data generated using the current ASTM slope offset method and the ACR method. While it is clear that the ACR technique is easier to implement and will always lead to less closure correction than the slope offset technique, it is not clear which is more accurate. It appears that the slope offset method may be overcorrecting for closure effects and the ACR method may be undercorrecting.

KEYWORDS: fatigue crack growth, closure, Ti-6Al-4V, adjusted compliance ratio (ACR)

It is well known that crack-tip closure is present in most metallic materials at low R-values, and that the full ΔK_{app} range does not contribute to crack growth [*1*]. According to the traditional theory of crack closure, there is a point during unloading of a crack when the faces close and the crack tip is shielded from any further stresses or strains that contribute to crack growth [*1*]. If the load at the point of crack closing (P_{cl}) can be determined, then the effective stress intensity factor range that contributes to crack growth is defined as $\Delta K_{eff} = K\,|_{P\max} - K\,|_{Pcl}$. The ΔK_{eff} parameter has historically been used to correct for crack closure effects [*2*]. The closing of the crack faces causes a change in the compliance of the specimen and thereby provides a means to determine P_{cl}. The slope offset method in the ASTM Test Method for Measurement of Fatigue Crack Growth Rates (E 647-95a) uses a percent change in compliance to define P_{cl}. In practice, changes in compliance are gradual, which leads to some uncertainty in determining a distinct closure load. More important, it has been argued that the ΔK_{eff} concept is fundamentally flawed because it ignores any contribution to cyclic crack growth for loads below P_{cl} [*3,4*]. The adjusted compliance ratio (ACR) technique has been developed [*5,6*] in an attempt to correct for these deficiencies.

Overview of Adjusted Compliance Ratio Concept

The adjusted compliance ratio method is based on the premise that there is no distinct closure load below which the crack tip is shielded from further damage. Strain measurements made by Donald

[1] Senior scientist, VECTOR Research, 3206 Tower Oaks Boulevard, Rockville, MD 20852.
[2] Senior engineer and materials scientist, respectively, Fatigue and Fracture Branch, NSWC Carderock Division, 9500 MacArthur Boulevard, West Bethesda, MD 20817.

ahead of a crack tip [5] led to the observation that the crack tip strain decreases continually down to (P_{min}), and that the strain is not proportional to the load once the crack faces begin to touch. Donald proposed a definition of closure based on the ratio between the actual crack tip strain range and the hypothetical strain range that would exist in the absence of crack closure (Fig. 1). Because it is not practical to measure crack tip strain, the ACR technique makes use of displacement measurements remote from the crack tip to infer crack tip strain. In general, the relationship between remote displacement and crack-tip strain is a function of measurement location. The adjusted compliance ratio attempts to remove the dependence on measurement location by expressing the ratio as the change in secant compliance, relative to the notched (or uncracked) specimen, over the change in compliance above opening load

$$\mathrm{ACR} = \frac{C_s - C_i}{C_o - C_i} \tag{1}$$

where

C_s = secant compliance for current crack length (defined in Fig. 1),
C_o = compliance for current crack length above opening load, and
C_i = initial compliance of notched, uncracked specimen prior to testing.

This ratio is further normalized by the ratio of initial compliance above opening load (C_{oi}) to initial secant compliance (C_{si}) in an effort to account for any irregularities or nonlinearities due to misalignment [6]. The active stress intensity factor range that governs the crack growth rate is then defined as:

$$\Delta K_{\mathrm{ACR}} = \frac{C_{oi}}{C_{si}} \frac{C_s - C_i}{C_o - C_i} \Delta K_{\mathrm{app}} = \mathrm{ACR_n}\, \Delta K_{\mathrm{app}} \tag{2}$$

The postulation is that this stress intensity range correctly accounts for crack-tip closure and more accurately describes the effective stress intensity factor range seen by the crack tip than does the traditional ΔK_{eff} as determined by the slope offset method.

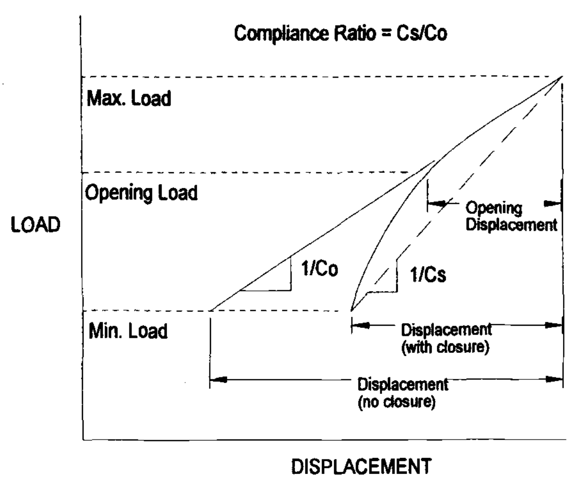

FIG. 1—*Schematic illustration of load-displacement trace showing definition of compliance ratio.*

In this investigation, several Ti 6-4 specimens were tested from the same forging in an effort to compare the established slope offset method for determining ΔK_{eff} with the proposed ACR method. Constant low R-ratio testing was conducted to generate data containing crack-tip closure. This data was then closure corrected using both the ACR and the slope offset methods. Constant K_{max} testing was also performed to produce high R ratio, and hence closure free, data in the threshold and upper threshold regimes. The constant K_{max} testing was intended to serve as a baseline for comparison with the closure corrected results.

Material and FCGR Test Specimens

The Ti 6-4 forging material studied in this work was manufactured to meet ASTM B381-87, grade F-5 specifications. The beta transus temperature was reported by the manufacturer to be between 990 and 1010°C. The forging was alpha-beta forged near 750°C and finished to an approximately hemispherical shape with a 760 mm base diameter and 25.4 mm thickness. Final annealing was conducted at 700°C for two hours, followed by air cooling down to room temperature. The resulting general microstructure consists of roughly equivalent partitions of primary equiaxed α grains in a matrix of transformed β containing acicular α, i.e., $(\alpha + \beta)$. The primary α and $(\alpha + \beta)$ size is approximately 25 μm.

Six chemistry samples were removed from various disparate locations around the forging and tested as per ASTM E-120 to determine both the primary alloying elements and important trace elements. The composition was fairly consistent among the tested locations and the average values of these measurements (Table 1) are typical of standard grade Ti 6-4. All specification values in this table are maximum allowable values unless a range is given. Tensile properties were measured in both the circumferential (C) and radial (R) directions as per ASTM E-8 using 12.8-mm diameter round bar tensile specimens. Specimens were centered about the mid-thickness plane and three tests were conducted in each orientation. The average results are presented in Table 2 along with the specification minimum requirements. These tensile properties are also typical for standard grade Ti 6-4.

Experimental Procedure

Fatigue crack growth rate tests were conducted on three C(T) specimens with B = 9.53 mm (0.375 in.) and W = 38.1 mm (1.50 in.). The specimens were oriented in the C-R direction. Tests were conducted in room temperature laboratory air at frequencies of 10 to 20 Hz. Closure measurements were made using both the slope offset method and the ACR method. For the slope offset method, the closure loads were determined based on a 2% change in compliance. Computer control was used to vary the applied ΔK to achieve a specific ΔK-gradient according to the equation:

$$\Delta K_{app} = \Delta K_o e^{C(a-a_o)} \tag{3}$$

where

ΔK_o = applied ΔK at start of test segment,
a = crack length,
a_o = crack length at start of segment, and
C = applied gradient.

TABLE 1—*Ti 6–4 Chemical Composition.*

	Al (%)	V (%)	O (%)	Fe (%)	C (%)	H (ppm)	N (%)
Measurement average	6.38	4.18	0.18	0.22	0.016	40	0.006
ASTM B381-87, Grade F-5	5.50–6.75	3.50–4.50	0.20	0.40	0.10	125	0.05

TABLE 2—*Ti 6-4 Mechanical Properties.*

	Spec. Orient.	0.2% σ_{ys} (MPa)	σ_{ult} (MPa)	Reduction in Area (%)	Elong. in 50 mm (%)
Measurement average	C	938	1014	40	16
	R	917	979	45	16
ASTM B381-87, Grade F-5	—	827	896	25	10

Each of the specimens was tested under unique conditions. Multiple test segments were applied to each specimen, although within a given segment, either K_{max} or R remained constant. The specific parameters utilized for each specimen are outlined in Table 3, where the specimen identification is listed at the head of each section. At the beginning of each new test segment, the crack was typically grown about 0.76 mm (0.030 in.) using the test parameters for the next segment and a gradient of zero. This was done to establish a steady crack tip condition before starting the next segment.

Results

Difficulties were encountered with implementation of the slope offset technique near the crack growth threshold in several of the tests. The difficulties resulted primarily from perturbations in the

TABLE 3—*Specimen Testing Conditions.*

Test Segment	Description	Gradient 1/mm (1/in.)	Initial ΔK MPa$\sqrt{m}$ (ksi$\sqrt{in.}$)	Final ΔK MPa$\sqrt{m}$ (ksi$\sqrt{in.}$)	Final Stress Ratio
	M1R61				
a	constant K_{max} = 16.5 MPa$\sqrt{m}$ (15 ksi$\sqrt{in.}$)	−0.079 (−2)	14.8 (13.5)	14.0 (12.7)	0.16
b	constant K_{max} = 16.5 MPa$\sqrt{m}$ (15 ksi$\sqrt{in.}$)	−0.118 (−3)	14.8 (13.5)	3.82 (3.48)	0.77
c	constant K_{max} = 16.5 MPa$\sqrt{m}$ (15 ksi$\sqrt{in.}$)	−0.394 (−10)	3.7 (3.4)	2.41 (2.19)	0.85
d	constant R = 0.1	−0.118 (−3)	14.8 (13.5)	5.67 (5.16)	0.1
	M1R63				
a	constant K_{max} = 7.7 MPa$\sqrt{m}$ (7 ksi$\sqrt{in.}$)	−0.394 (−10)	6.92 (6.30)	3.09 (2.81)	0.60
b	constant K_{max} = 9.9 MPa$\sqrt{m}$ (9 ksi$\sqrt{in.}$)	−0.394 (−10)	8.90 (8.10)	2.77 (2.52)	0.72
c	constant K_{max} = 12.1 MPa$\sqrt{m}$ (11 ksi$\sqrt{in.}$)	−0.394 (−10)	10.9 (9.90)	2.69 (2.45)	0.78
d	constant K_{max} = 14.3 MPa$\sqrt{m}$ (13 ksi$\sqrt{in.}$)	−0.394 (−10)	12.9 (11.7)	2.54 (2.31)	0.82
e	constant K_{max} = 22.0 MPa$\sqrt{m}$ (20 ksi$\sqrt{in.}$)	−0.394 (−10)	19.8 (18.0)	2.59 (2.36)	0.88
	M1R64				
a	constant R = 0.1	0.118 (+3)	11.0 (10.0)	38.1 (34.7)	0.1
b	constant R = 0.1	−0.157 (−4)	35.6 (32.4)	6.07 (5.52)	0.1

measured load/displacement response, which became a greater percentage of the measured signal near threshold. These perturbations stemmed from vibration, system hysteresis, electrical noise, and other sources. The slope offset algorithm for measuring the closure load requires a smooth load/displacement trace with a gradual change in compliance. These perturbations significantly affected the ability of the slope offset method to differentiate closure levels, and thereby caused the measured closure levels to become highly erratic. This problem was encountered near threshold in all of the tests where decreasing ΔK_{app} gradients were used to measure threshold. When this did occur, ΔK_{eff} values for the slope offset method are not reported in these results.

Constant K_{max} *Tests*

These tests were conducted using specimens MIR61 and MIR63. A constant K_{max} was maintained throughout the specified test segment (Table 3) and ΔK_{app} was decreased using the gradient shown in the table until the growth rate dropped below approximately 1E-07 mm/cycle (4E-09 in./cycle).

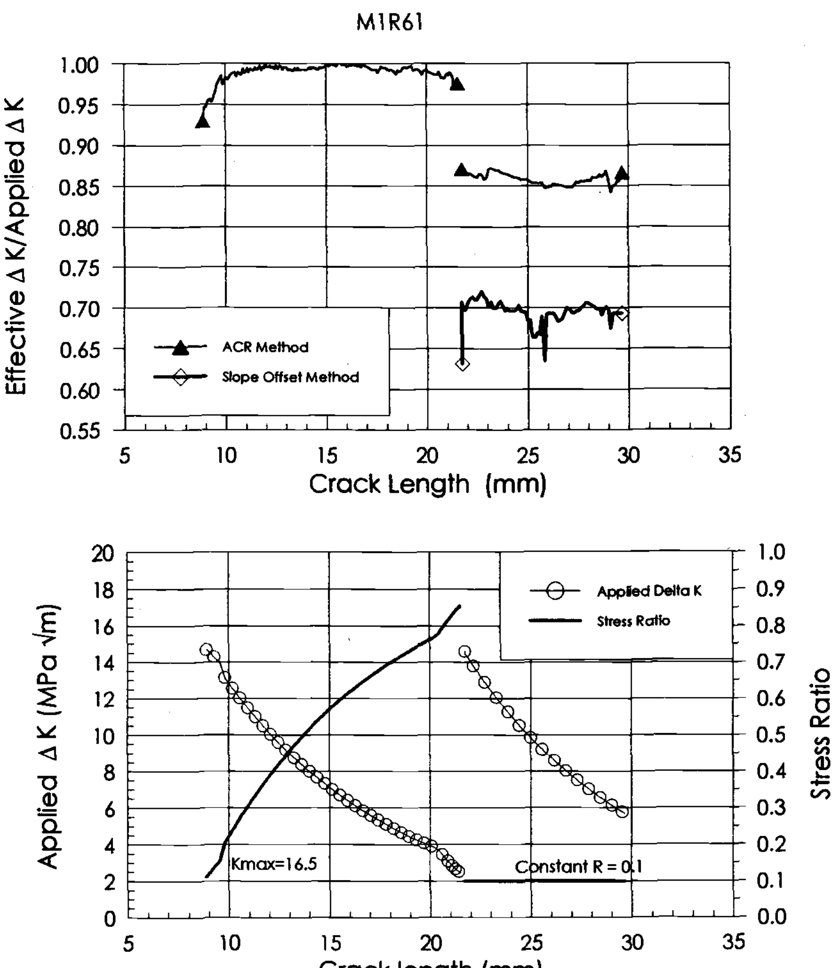

FIG. 2—*Effective* ΔK *and applied* ΔK *for M1R61.*

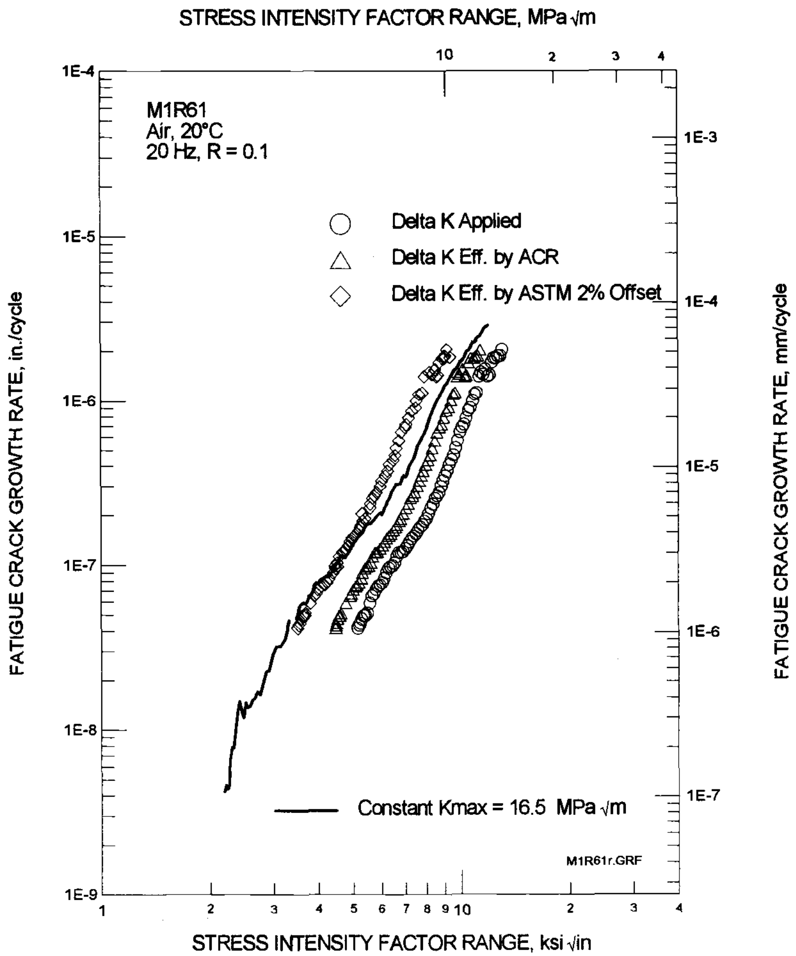

FIG. 3—*Comparison of constant* K_{max} *and constant* R *tests of M1R61.*

Several different K_{max} levels were used to investigate the effect of K_{max} on the threshold ΔK_{app} and closure. The level of K_{max} determines the maximum plastic zone (or process zone) during the cycle. Constant K_{max} testing maintains a constant process zone size throughout the test segment in order to minimize the effects of the prior cyclic history on the current crack closure behavior.

The crack growth history for M1R61 is shown in Fig. 2. There is little closure in the first test segment since the test started from a relatively short crack, without a long plastic wake, and R was steadily increasing with a constant K_{max}. After threshold was reached, the next testing segment was conducted using a constant R-ratio of 0.1, and ΔK_{app} was decreased from 14.8 to 5.7 MPa$\sqrt{m}$ using a moderately steep gradient in order to generate closure. This test segment is characterized by a decreasing K_{max}, a corresponding decreasing plastic zone size, and a long plastic wake. Indeed, the sudden drop in P_{min} causes significant closure immediately, as indicated by the sudden decrease in the ratio $\Delta K_{eff}/\Delta K_{app}$. In all of the tests, ΔK_{eff} is lower than ΔK_{ACR}. The growth rate curves for the constant K_{max} and constant R test segments on specimen MIR61 are shown in Fig. 3. As mentioned previously, there were difficulties encountered in measuring closure during the constant K_{max} segment using the slope offset method, so only the ACR closure corrections are shown for that segment.

The next test specimen, MIR63, was used to measure threshold ΔK at five constant K_{max} levels. The crack growth history for this test is shown in Fig. 4, and the growth rate curves are shown in Fig. 5. In each test segment the stress ratio begins at $R = 0.1$ and increases as ΔK_{app} is decreased at a constant K_{max}. Each test segment has a higher K_{max} than the previous segment, so the crack tip plastic zone increases with each subsequent segment. This minimizes the effect of prior history on crack growth and closure behavior. As ΔP continues to decrease with increasing crack length, the slope offset measurements became erratic and eventually closure measurements could no longer be made using this method. Both methods initially measure high closure levels at $R = 0.1$, and the measured closure decreases as R increases. It is interesting to note that for both methods the ratio $\Delta K_{eff}/\Delta K_{app}$ reaches a maximum and begins to decrease as R continually increases near threshold; however, the trend is more pronounced with the ACR method. This trend was observed at every K_{max} level in this test, and contradicts the expectation that closure should steadily decrease as R increases in a constant K_{max} test.

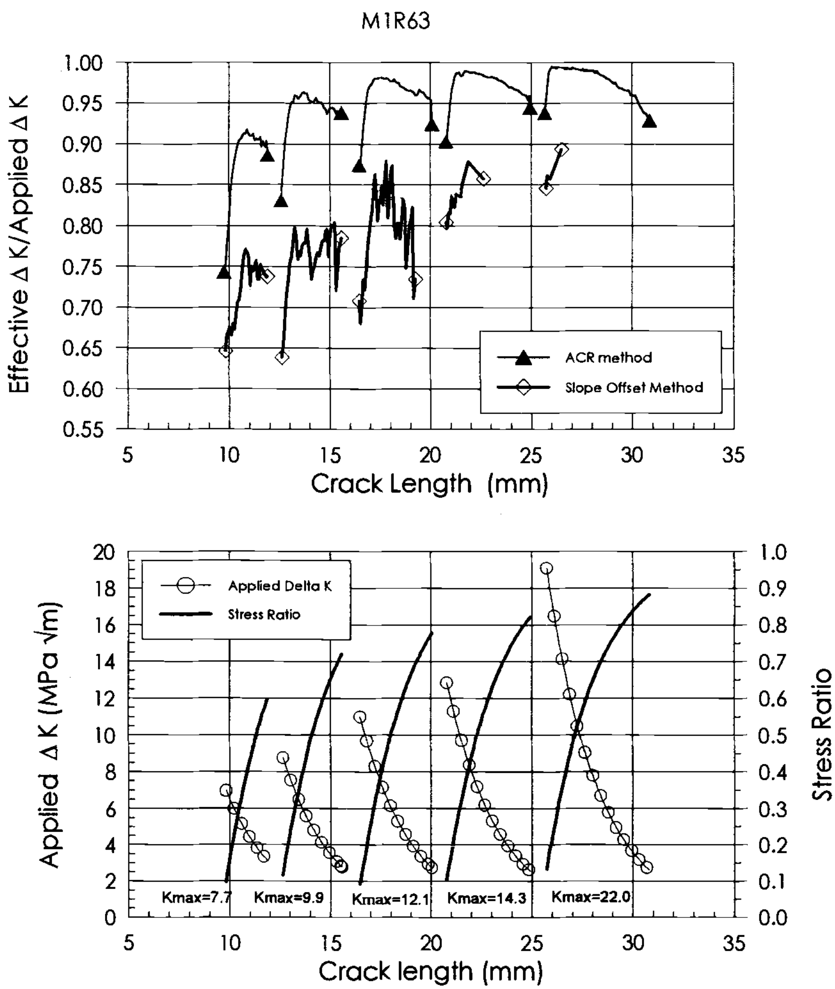

FIG. 4—*Effective* ΔK *and applied* ΔK *for M1R63.*

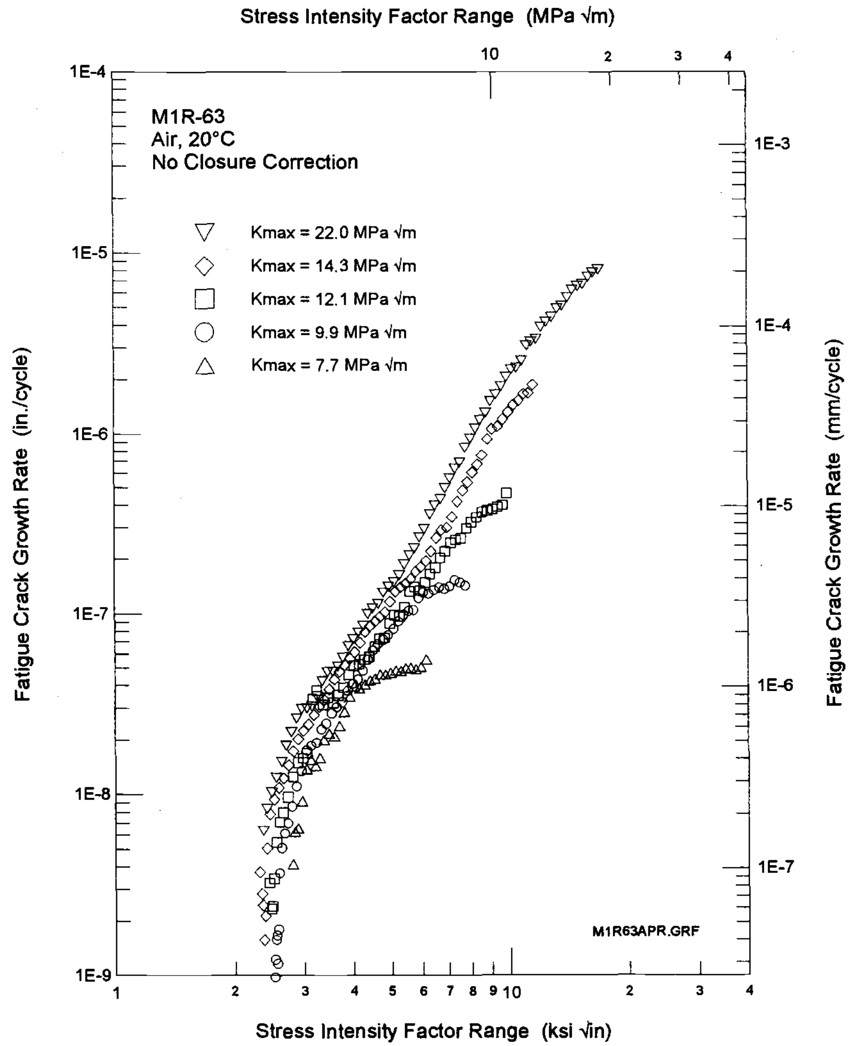

FIG. 5—*Growth rate curves for constant* K_{max} *tests of M1R63.*

Constant R *Tests*

Specimen MIR64 was tested at a constant $R = 0.1$ with both increasing and decreasing ΔK gradients. The crack growth history for M1R64 is shown in Fig. 6, and the growth rate curves are shown in Fig. 7. The amount of closure decreases throughout the first segment of this test as ΔK_{app} increases. This is to be expected since the current process zone is always larger than the zone from prior loading. Consistent with previous observations, ΔK_{eff} is considerably less than ΔK_{ACR}. The ACR method predicts that closure effects have vanished by $\Delta K_{app} = 38$ MPa$\sqrt{m}$, while the slope offset method still shows a 15% reduction in ΔK_{app} due to closure. When the ΔK_{app} gradient is changed from $+0.157$ to -0.118 mm^{-1} ($+4$ to -3 in.$^{-1}$), the slope offset ΔK_{eff} drops suddenly while ΔK_{ACR} experiences a gradual decrease with ΔK_{app}. The closure corrected crack growth results (Fig. 7) illustrate

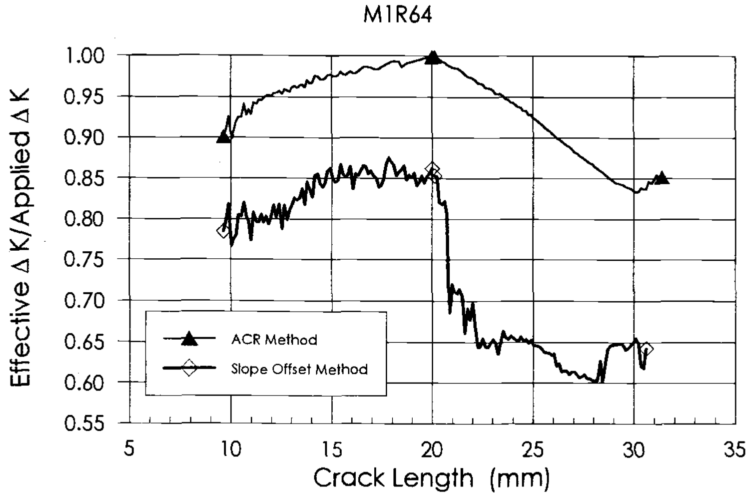

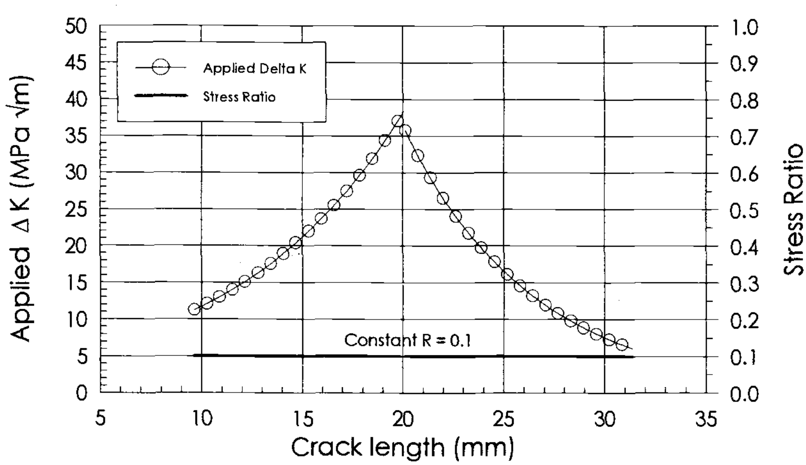

FIG. 6—*Effective* ΔK *and applied* ΔK *for M1R64.*

that the slope offset ΔK_{eff} relationship is substantially altered by the simple change from K-increasing to K-decreasing loading, while the ΔK_{ACR} results are unaffected.

Discussion

It is interesting to note that for specimen M1R61 the closure-corrected ΔK_{eff} results for the constant R segment agree more closely with the constant K_{max} test results than the ΔK_{ACR} results do below a ΔK_{app} of about 6.6 MPa$\sqrt{m}$ (or da/dN = 6E-06 mm/cycle, Fig. 3). The ΔK_{ACR} data is to the right of the constant K_{max} results, especially at lower ΔK_{app} levels. Notice also that the decreasing K-gradient ΔK_{ACR} data of M1R64 (Fig. 7) is in good agreement with the constant K_{max} data for M1R61 at the higher growth rates (>1E-05 mm/cycle), while the ΔK_{eff} curve appears to line up better at growth rates below 2E-06 mm/cycle. There are two possible explanations for this; either the ACR method is underestimating closure effects near threshold, or there may be a K_{max} effect causing a decrease in threshold with increasing R, thereby shifting the constant K_{max} curve to the left. In order to investigate this further, ΔK_{app}, ΔK_{eff}, ΔK_{ACR} were determined at a growth rate of 1E-6 mm/cycle for each of the constant K_{max} and constant R tests. The resulting ΔKs at that growth rate are plotted versus K_{max} in Fig. 8. It was not possible to accurately measure ΔK_{eff} by the slope offset method for most of the tests where K_{max} was greater than 10 MPa$\sqrt{m}$ because the data were too erratic.

If there were no closure in the constant K_{max} tests, the closure-corrected ΔK for the $R = 0.1$ tests should agree with the trend in the applied ΔK in the constant K_{max} tests. Based on this assertion, it appears that the ACR closure correction most closely follows the trend of the "closure-free" data and that the slope offset method may be overcorrecting for closure. However, both the slope offset and the ACR methods indicate that closure was present at K_{max} levels less than 14 MPa$\sqrt{m}$. When this is taken into account, it appears that the applied ΔK for the constant K_{max} tests may be overestimating the effect of K_{max} on ΔK near threshold. In fact, comparison of the ΔK_{eff} results for M1R64 at $R = 0.1$ with the constant K_{max} results for M1R63 at $K_{max} \geq 15$ MPa$\sqrt{m}$ indicates that there may be no K_{max} effect. If this is the case, then the ACR method is undercorrecting for closure. Even if there

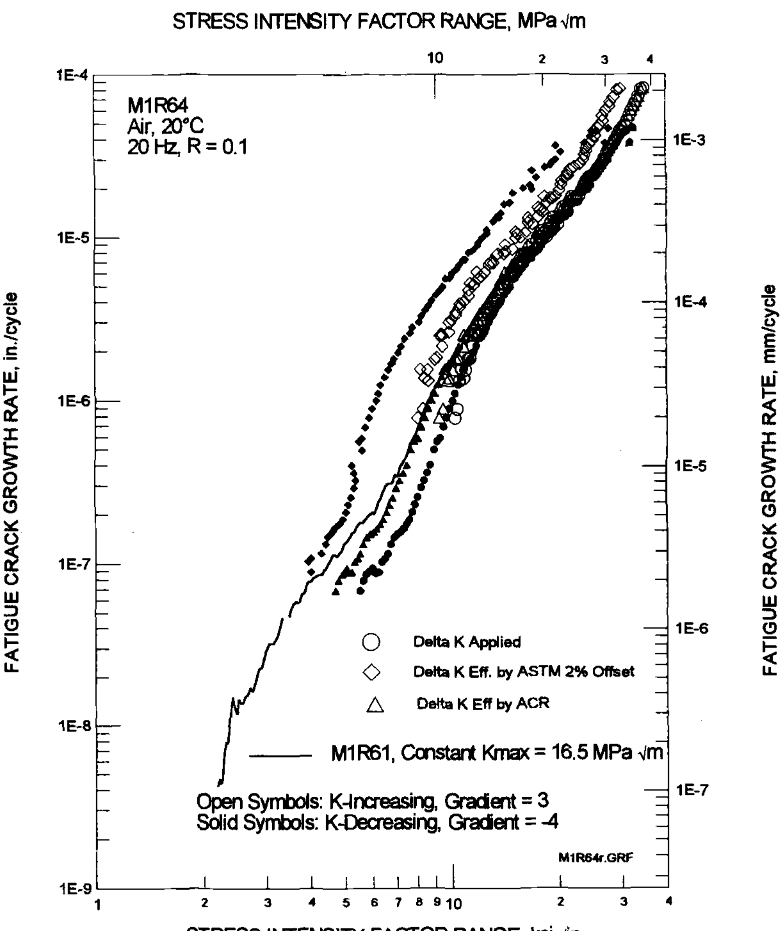

FIG. 7—*Growth rate curves for constant* R *tests of M1R64.*

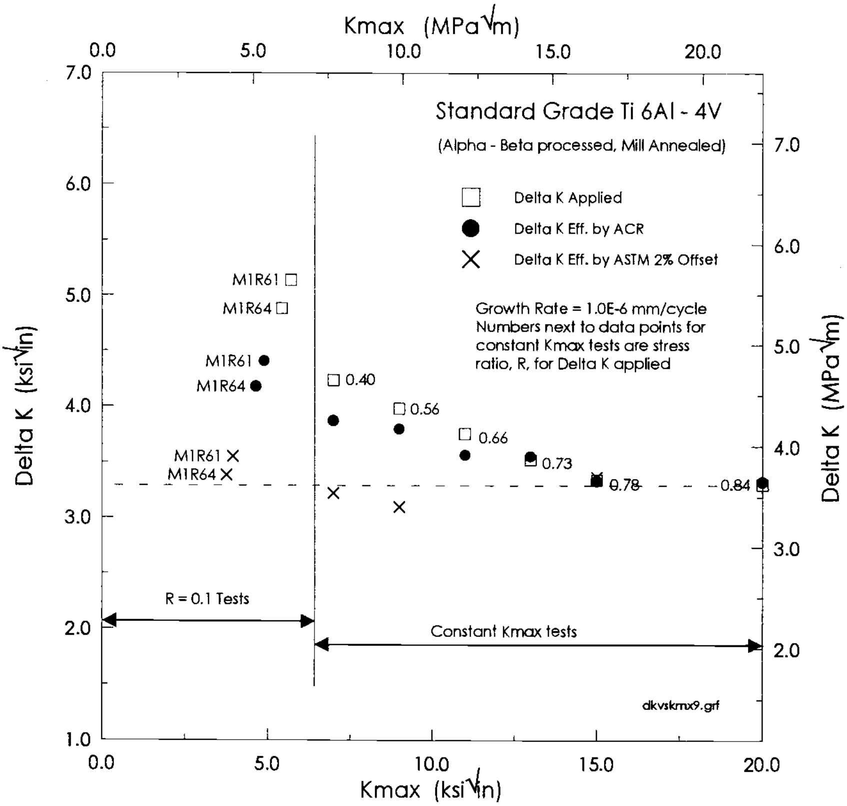

FIG. 8—ΔK *versus* K_{max} *at growth rate of 1E-06 mm/cycle.*

is no K_{max} effect, under some circumstances the slope offset method still appears to be overcorrecting for closure, such as the constant K_{max} segments for M1R63 where K_{max} = 7.7 and 9.9 MPa$\sqrt{}$m. Other evidence that the slope offset method may be overcorrecting can be seen in Fig. 6, where a change in gradient from increasing to decreasing caused a sudden drop in ΔK_{eff} even though K_{max} and R had not changed much at all.

Conclusions

The ACR method for determining crack closure has a distinct advantage over the slope offset method in terms of practical implementation, especially at near-threshold growth rates. It is easier to measure the displacement range, as in the ACR method, than it is to measure changes in slope. Because of this, the ACR technique does not exhibit the sudden changes in the measured closure levels under gradual changes in the applied loading history that the slope offset method does (i.e., near the transition point from a K-increasing to K-decreasing test).

While it is clear that the ACR method will always lead to less closure correction than the slope offset method, it is difficult to determine which technique more accurately corrects for closure near threshold. Simple comparison of constant R and constant K_{max} test results favors the slope offset method. However, if there is a K_{max} effect on threshold in this alloy, then this simple comparison is misleading. Attempts to determine if there is a K_{max} effect in this alloy met with limited success. In retrospect, it is questionable whether constant K_{max} testing can be used to uncover the true "closure-free" behavior for low K_{max} levels because the stress ratio is low near threshold for these tests, and closure effects are still present. If there is a true K_{max} effect on threshold for this alloy, then the ACR closure corrections appear to be more accurate. Overall, the observations from these tests indicate that the slope offset method may be overcorrecting for closure and the ACR method may be undercorrecting.

The slope offset technique does not consider the influence of loading below P_{c1} on cracking, which is likely inaccurate, but the ACR technique ignores the specific path dependence of the load/displacement response and does not provide a clear link to the crack-tip stress intensity factor. The ability of these, and other techniques, to accurately correct for closure affects can be ascertained only through more fundamental testing which uncouples, as much as possible, the mechanics of the crack-tip field, the crack growth history, and the experimental technique.

References

[1] Elber, W., "The Significance of Fatigue Crack Closure," *Damage Tolerance in Aircraft Structures, ASTM STP 486,* American Society for Testing and Materials, Philadelphia, 1971, pp. 230–242.

[2] Schijve, J., "Fatigue Crack Closure: Observations and Technical Significance," *Mechanics of Fatigue Crack Closure, ASTM STP 982,* J. C. Newman, Jr. and W. Elber, Eds., American Society for Testing and Materials, Philadelphia, 1988, pp. 5–34.

[3] Chen, D. L., Weiss, B., and Stickler, R., "Contribution of the Cyclic Loading Portion Below the Opening Load to Fatigue Crack Growth," *Materials Science and Engineering,* Vol. A208, 1996, pp. 181–187.

[4] Wallhead, I. R., Edwards, L., and Poole, P., "A Study of Crack Closure Using the Optical Method of Caustics and Consequences for the Use of ΔK_{eff} as a Fatigue Crack Driving Force," *Engineering Fracture Mechanics,* Vol. 60, No. 3, 1998, pp. 291–302.

[5] Donald, J. K., "Introducing the Compliance Ratio Concept for Determining Effective Stress Intensity," *International Journal of Fatigue,* Vol. 19, Supplement No. 1, 1997, pp. 191–195.

[6] Donald, J. K., Bray, G. H., and Bush, R. W., "An Evaluation of the Adjusted Compliance Ratio Technique for Determining the Effective Stress Intensity Factor," *29th National Symposium on Fatigue and Fracture Mechanics, ASTM STP 1332,* T. L. Panontin and S. D. Sheppard, Eds., American Society for Testing and Materials, West Conshohocken, PA, 1998.

R. Craig McClung[1] *and David L. Davidson*[1]

Near-Tip and Remote Characterization of Plasticity-Induced Fatigue Crack Closure

REFERENCE: McClung, R. C. and Davidson, D. L., "**Near-Tip and Remote Characterization of Plasticity-Induced Fatigue Crack Closure,**" *Advances in Fatigue Crack Closure Measurement and Analysis: Second Volume, ASTM STP 1343,* R. C. McClung and J. C. Newman, Jr., Eds., American Society for Testing and Materials, West Conshohocken, PA, 1999, pp. 106–127.

ABSTRACT: An elastic-plastic finite element model and high resolution experimental measurements of growing fatigue cracks are employed in partnership to investigate the relationship between crack closure, near-tip deformation behavior, and remote load-displacement measurements. The model focuses on plasticity-induced closure effects for fatigue cracks in the Paris regime, while the experiments study fatigue cracks in the Paris and near-threshold regimes in a variety of materials. The suitability of the ASTM compliance offset method and the recently-proposed adjusted compliance ratio (ACR) method to characterize near-tip closure effects is evaluated. The experiments and analyses both show that crack-tip strains below the crack-opening stress, S_{op}, are a relatively small fraction of the total crack-tip strain range for cracks in the Paris regime, and therefore may be insignificant for crack-tip deformation and damage and crack growth. The experiments further indicate that crack-tip strains below S_{op} are a relatively larger fraction of the total crack-tip strain at lower ΔK values, nearer the threshold, where S_{op} values are higher. The current ASTM compliance offset procedure for determining the crack opening load is shown to provide accurate information about true crack-tip opening loads in theory. However, due to the limited sensitivity of the method in practice, and the corresponding need to employ a non-zero compliance offset, the method gives underestimates of opening and closing loads that may be considerably in error relative to the true crack-tip values. The current ACR technique does not appear to do a good job of characterizing the near-tip deformation response for cracks in the Paris regime, because remote displacement measurements do not appear to be adequately sensitive to near-tip strains.

KEYWORDS: fatigue crack growth, fatigue crack closure, crack opening load, elastic-plastic finite element modeling, experimental measurement, scanning electron microscope, stereoimaging, ASTM compliance offset method, adjusted compliance ratio, crack-tip strain, remote displacements

The discovery by Elber [*1*] that a propagating fatigue crack may be partially or completely closed at some positive load has inspired nearly 30 years of study and application of the fatigue crack closure concept. From an engineering perspective, perhaps the most significant hypothesis forwarded by Elber [2] was that the effect of crack closure on fatigue crack growth rates could be characterized simply (a) by identifying the applied stress at which the crack was first fully open all the way to the tip, S_{op}, (b) by calculating an effective stress range, $\Delta S_{eff} = S_{max} - S_{op}$, during which the crack tip is fully open, (c) by replacing ΔS with ΔS_{eff} in the calculation of the crack driving force ΔK, and (d) by replacing ΔK in a Paris-type equation to calculate crack growth rates with the resulting ΔK_{eff}. This simple characterization approach has been followed by literally hundreds of researchers and engineers in the years since.

The Elber hypothesis about the significance of S_{op} implies that the correct determination of the true crack opening stress is one of the most critical questions to be addressed in fatigue crack growth. In reply, many different experimental and analytical methods have been employed to measure or calcu-

[1] Manager and Institute scientist, respectively, Southwest Research Institute, San Antonio, TX 78228-0510.

late S_{op}. Many researchers have found that the crack tip "peels open" during the crack opening process, so that the crack opens last immediately at the tip itself (and closes first at the tip during unloading). Therefore, high resolution experimental or analytical methods that are able to measure or calculate the displacements or stresses in the immediate vicinity of the crack tip seem to be the most accurate means of characterizing S_{op}.

However, the fundamental Elber hypothesis about S_{op} itself remains open to critical questioning. In particular, the implication of his hypothesis that the stress range below S_{op} has no effect at all on crack growth behavior has been questioned, most recently by authors such as Chen [*3,4*] and Donald [*5,6*]. They have argued that deformation occurring below S_{op} can also influence crack growth, especially near threshold when S_{op} is often observed to be a larger fraction of S_{max}. Some of these authors have been motivated by observations that the Elber approach is sometimes unable to correlate crack growth rates in the near threshold region with closure-free data obtained at high stress ratios, because the measured S_{op} is too high near threshold. In turn, these authors have proposed new characterizations of the effects of crack closure on the effective crack driving force, ΔK_{eff}, such that ΔK_{eff} is a larger value than would be calculated based on S_{op} and the Elber hypothesis.

Whether the Elber hypothesis is correct or incorrect, experimental investigators are left with a common problem in characterizing the crack closure process. While the important events in the process likely occur very close to the crack tip (near-tip crack opening, or crack-tip deformation), direct experimental measurements of these near-tip events are difficult, if not impossible, to achieve. What is much easier to measure is the remote response of the crack, such as changes in the compliance of the cracked body that are related to crack opening and closing. The critical challenge is to interpret these remote measurements in a manner that accurately reflects the near-tip behavior most significant for the crack driving force.

The search for a reliable remote measurement of the crack opening stress, S_{op}, has received a great deal of attention ever since the original Elber discovery. An extensive standardization activity within ASTM recently culminated in a recommended practice for determination of fatigue crack opening load from experimentally measured compliance, now published as Appendix X2 to Standard Test Method for Measurement of Fatigue Crack Growth Rates (ASTM E 647-95). This practice outlines a data analysis methodology that can be applied to crack mouth displacement or back face strain measurements from C(T) specimens or centerline displacement measurements from M(T) specimens. However, earlier research employing high resolution measurements of crack opening behavior at the crack tip itself suggested that the remote closure measurement techniques in use at that time could give significantly lower values of S_{op} than were indicated by the near-tip measurements [*7*].

More recently, Donald [*5*] has suggested a new experimental method for characterizing the effects of closure on the effective crack driving force ΔK_{eff}. His "adjusted compliance ratio" (ACR) is based on remote measurements of compliance but takes into account the deformation of the cracked body below the S_{op} level. The inherent assumption in this proposal is that the remote displacement measurements accurately reflect the actual strains near the crack tip that are important for crack growth behavior.

The research described in this paper was designed to investigate some of the critical issues and challenges outlined above. The tools employed in the research were high resolution numerical analyses and high resolution experimental measurements of growing fatigue cracks, with a special emphasis on the crack opening process. Both the analytical and experimental methods permit direct characterization of crack opening and deformation behavior at the crack tip itself. The particular numerical method employed also permitted simultaneous calculation of remote displacement behavior, thereby simulating experimental techniques based on remote compliance determinations. These tools were used to address two general questions: (1) "What is the relationship between the local crack opening stress, S_{op}, and the crack-tip deformation behavior?", and (2) "What is the relationship between near-tip opening/deformation behavior and remote measurements/analyses of closure based on compliance changes?"

Approach

Numerical Method

The high resolution numerical method employed in this study was a finite element (FE) model of a growing fatigue crack that has been described in detail in previous publications [*8,9*]. The meshes were composed of four-noded linear strain elements. At each occurrence of minimum load in the cycle, the boundary conditions at the crack-tip node were changed to allow the crack to grow by one element length through a group of very small, uniformly sized elements along the crack line. Remote stresses were applied in many small steps (typical step size was two percent of the maximum applied stress). Stresses and displacements along the crack line behind the crack tip were closely monitored on each load step, and boundary conditions on the crack surfaces were appropriately changed as the crack opened or closed.

All analyses discussed in this paper were plane stress. The constitutive model followed linear kinematic hardening with $H/E = 0.01$, where E is the elastic modulus and H is the slope of the plastic line. The flow stress, σ_0, is the intersection of the elastic and plastic lines. The material simulated in this research was an aluminum alloy with $E = 70\,000$ MPa and $\sigma_0 = 430$ MPa. However, it should be noted that previous results [*10*] indicated essentially no effect of σ_0/E on crack opening behavior at common values of H/E and S_{max}/σ_0.

The investigations described in this paper were conducted with a common mesh but different boundary conditions to simulate two different specimen geometries, a middle-crack tension specimen, M(T), and a single edge cracked tension specimen, SE(T). The M(T) and SE(T) geometries exhibited similar behavior, and so for convenience only the M(T) results are shown in this paper. The crack was grown from an initial length of $a/W = 0$ with a final target length (the length at which the crack behavior was characterized in detail) of $a/W = 0.3$. Because loads are applied directly to the remote boundary of the specimen as traction stresses, no length scale must be assigned to the specimen. The total width W of the specimen (by symmetry, the half-width of the M(T) specimen) was characterized as 1000 mesh units, so the target crack length was 300 mesh units. The element length in the fine mesh region (and hence the crack growth step size) was 2 mesh units.

In nearly all previous investigations using this particular FE model, the crack was advanced by one element length on every cycle. This was a convenient choice to minimize total computer execution time, and was shown to have only a small influence on the crack opening behavior. In this investigation, it was particularly important to develop stable closed stress-strain and load-displacement loops. Therefore, the crack was advanced after each two cycles of loading, and numerical data were taken from the second cycle, during which the crack length did not change. In general, crack opening levels were slightly lower on the second cycle than on the first cycle, but crack closing levels were relatively unchanged.

Experimental Method

Large fatigue cracks were initiated from notches in single edge notched and compact tension specimens, usually about 3 mm thick, and grown in a laboratory servo-hydraulic loading frame under load control. After growth of the cracks to a length beyond the influence of the notch, loads were adjusted to obtain the crack growth rates and ΔK values of interest. For detailed observation and closure related measurements, the specimen was then transferred to a loading stage that fit within the scanning electron microscope where the same loads as used in the laboratory machine could be applied. A detailed description of the techniques used for closure measurements may be found in Ref *11*. The technique used is briefly described below.

Typically, several measurements were made as load was increased. It is known from many observations that fatigue cracks "peel open," i.e., they open sequentially from the notch end of the crack as load is applied. To measure this phenomenon, the crack was observed at various magnifications as load was being slowly applied. Fatigue cracks are usually tightly closed at minimum load, and sometimes it is difficult to determine the crack path and the location of the tip.

Photographs were taken at minimum load, and, as appropriate, as load was increased. The location of the end of the open crack could be determined by looking for crack opening at high magnification and by stereoimaging photographs made at load against the same magnification at minimum load. In this way, the distance from the actual crack tip to the point of opening of the crack vs. load was determined. Photographs of the crack tip region were made at various loads, starting with minimum load, and at loads below opening, at the load when the crack had fully opened to the tip (defined as the opening load), and at maximum load. The DISMAP system [*12*] was used to measure displacements vs. the same region at minimum load, and strains were computed as gradients of displacements via the stereoimaging technique. Three elements of the symmetric strain tensor are computed: strain parallel and perpendicular to the loading direction and shear strain. Principal strains and the maximum shear strain are then computed from these three strains. Strains determined by this method may be considered as delta strain because they are referenced to the minimum load rather than a state of no strain. Note that the derived strains are total strain, incorporating both elastic and plastic strain components. Plastic strains are not easily separated from elastic values, and this has not been attempted. From these measurements, strains occurring at and near the crack tip were determined vs. applied load. Measurements of closure were generally made at stress intensity values ranging from the lower end of the Paris (linear) region of the growth rate vs. cyclic stress intensity curve to the near threshold region of that curve.

In this paper, results are reported from tests with five different materials. 7091-T7E69 is a powder metallurgy aluminum alloy manufactured by Alcoa during the 1980's. 7075-T6 is an aluminum alloy, also manufactured by Alcoa, and the lot of material used originated in the 1970's. IN-9052 is a mechanically alloyed Al-4Mg-1C-0.9O material made by INCO during the 1970's. These aluminum alloys are face centered cubic (fcc) materials. Representing body centered cubic materials (bcc) are both pure niobium and an experimental single phase niobium alloy having the composition Nb-35Ti-6Al-5Cr-8V-1W-0.3Hf-0.5Mo. Both of the bcc alloys are mildly strain rate sensitive, whereas the fcc alloys are typically insensitive to strain rate. Thus, the experimental closure measurements represent a broad range of materials.

Numerical Method vs. Experimental Method

It should be emphasized that both the numerical and the experimental method employed in this investigation are mature methods that have been used successfully for many years. The FE method has been validated through extensive comparisons with other numerical and analytical methods and with the results of experimental studies. Of particular note, a previous study [*13*] directly compared these specific numerical and experimental methods in considerable detail. That study found that the FE model exhibited good agreement with the experimental measurements of near-tip strains, crack opening displacements, and crack closure. The numerical model captured the correct qualitative behavior in nearly every case, and was quantitatively accurate in a majority of the comparisons when proper nondimensionalizations were employed. The few cases where the model and measurements disagreed highlighted important limitations of the numerical model that will be cited as appropriate in the present study.

Given this previously documented agreement, note that the purpose of the present investigation is *not* to compare the numerical model and the experimental measurements. The numerical and experimental methods are particularly well suited to look at different aspects of the critical questions identified in the Introduction. Each method was used in this study to obtain the data for which it was most suited, in the manner that was most efficient for that particular method. The numerical and experimental results are therefore complementary, and they work together in partnership to provide a broader view of the issues in question.

The FE model addresses only crack closure induced by plastic deformation, including the related effects of the plastic wake behind the crack tip and the residual stresses both ahead of and behind the crack tip. The modeled crack is mathematically flat and deformation is mathematically symmetrical above and below the crack, so no roughness or mixed mode effects are permitted, and no oxides are included in the model. The experimental method is not limited in this manner; it simply observes what happens in the vicinity of the crack tip on the specimen surface. However, it should be noted that many years of observations by the second author using these experimental techniques have indicated that plastic deformation is apparently the primary source of near-tip closure at the specimen surface, where the measurements are made. While fracture surfaces are found to be rough, the mismatching of opposing rough surfaces has not been observed to be a significant contributor to crack closure in the vicinity of the crack tip at the specimen surface. It is possible that roughness could play a more significant role in the specimen interior, where constraint is higher and plasticity is more limited.

Results

Local Behavior

The FE analysis clearly shows how plasticity-induced closure arises as a natural consequence of crack-tip plasticity. Figure 1 shows the cumulative axial (y) plastic strains at zero load for a plane stress crack that has grown under $R = 0$ loading from left-to-right into the current field of view [*9,14*]. The plastic strains out in front of the crack tip were induced by the most recent load cycle, as the crack tip singularity elevated the stresses ahead of the crack well into the plastic regime. Since these plastic strains are not reversed upon unloading to zero remote load, they remain as permanently stretched material while the crack tip moves ahead, leaving behind the plastic wake clearly shown in the contour plot. The material required to feed this plastic stretch comes from plastic contraction in the out-of-plane (z) direction; the plastic strains in the z-direction are nearly mirror images of the plastic strains in the y-direction. A similar mechanism has been found to operate in plane strain [*9*]; however,

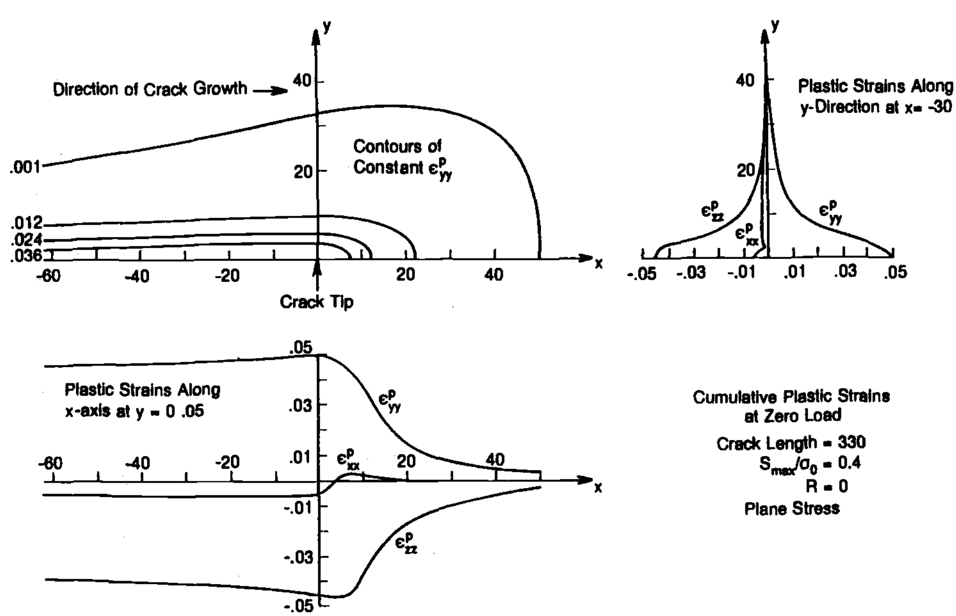

FIG. 1—*Calculated cumulative plastic strains at zero load near a plane stress fatigue crack [14].*

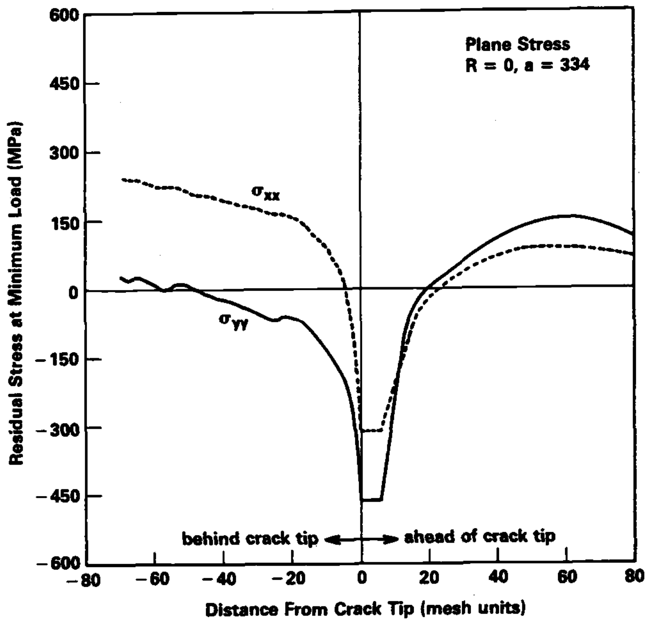

FIG. 2—*Calculated residual stresses along the crack line at minimum load for a plane stress fatigue crack [9].*

in plane strain, the plastic stretch in the axial direction causing closure is fed by plastic contraction in the in-plane transverse (x) direction. Since this deformation is considerably more constrained, the overall magnitude of the plastic stretch, and hence of the closure effect itself, is considerably smaller.

The material remote from the crack tip, which remains elastic, constrains the plastic wake upon unloading, and induces compressive axial stresses that serve to clamp the crack closed even at some nonzero remote loads. The residual stresses at zero load corresponding to the crack of Fig. 1 are shown in Fig. 2. Note, in particular, the compressive axial (y) stresses that extend for an appreciable distance behind the crack tip, gradually increasing in intensity near the crack tip.

As the crack is loaded remotely, these residual stresses are gradually overcome closer and closer to the crack tip, causing the crack to gradually "peel open." This peeling-open process is directly illustrated in Fig. 3, which includes results from both the FE method and the experimental method [*13*]. A proper comparison of the two methods here requires an appropriate normalization, since it is not convenient to exercise the FE method and the experimental method under precisely the same conditions. The relationship between applied load and length of closed crack describes the load at which the crack opens to a specific distance behind the true crack tip. As the load increases, the crack opens closer and closer to the true crack tip until it is fully open. Note in Fig. 3 that the FE and experimental results agree closely at the larger ΔK value. However, the FE results cannot simulate the significantly higher crack opening loads observed at the lower ΔK value, closer to threshold. This disagreement apparently arises because of fundamental changes in the near-tip deformation mechanisms close to threshold (evidenced by significant mode II contributions) that cannot be emulated by the continuum mechanics formulation of the FE model [*13*].

The relationship between remote stress and crack tip strain is illustrated by the FE results in Fig. 4 for two different maximum applied stress values ($S_{max}/\sigma_0 = 0.2$ and 0.3) and two different stress ratios ($R = 0$ and -1). The crack opening stress and crack closing stress as identified from the stresses and displacements at the nodes along the crack line behind the crack tip are indicated on the figures.

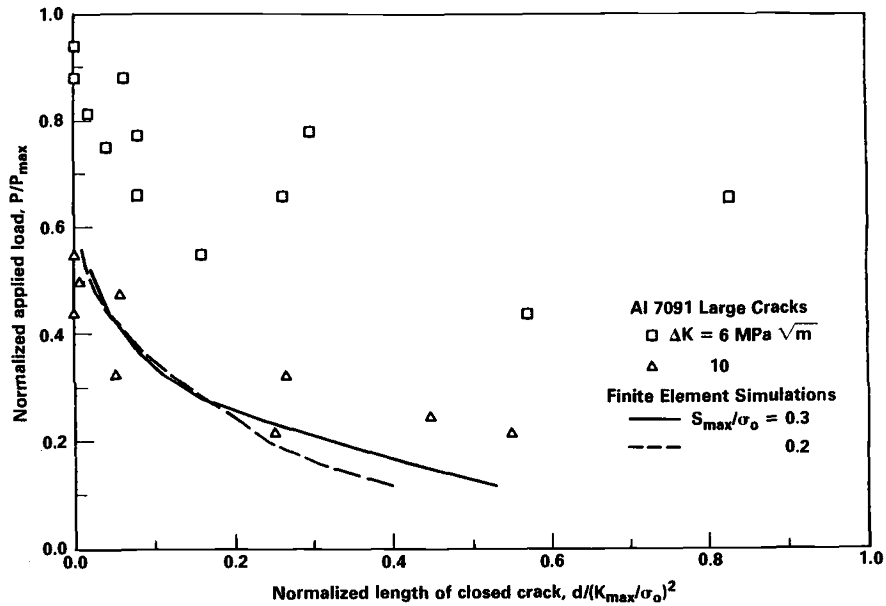

FIG. 3—*Comparison of measured experimental data and finite element calculations of crack opening process behind the crack tip [13].*

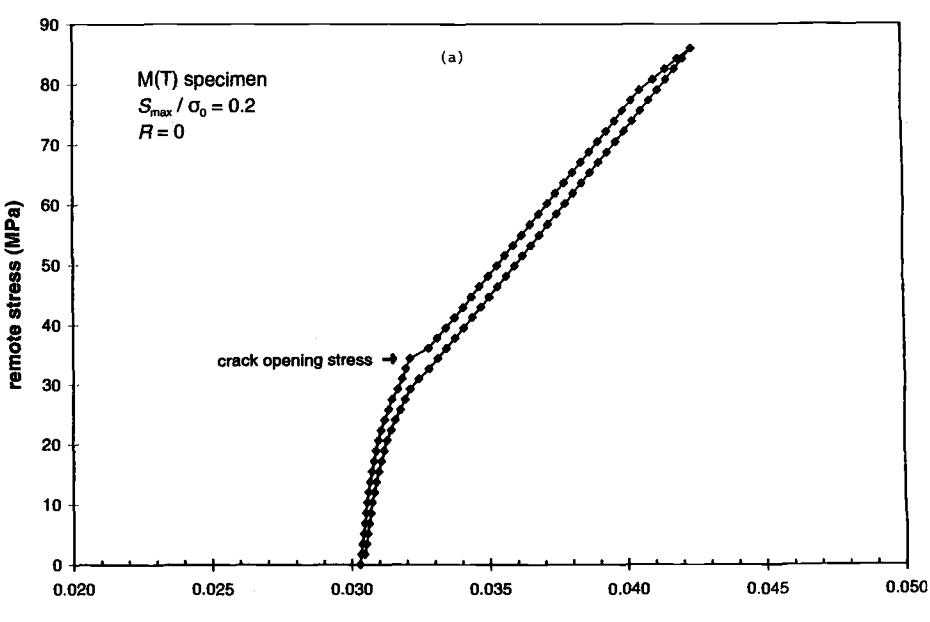

FIG. 4—*Calculated crack-tip strains versus remote applied stress for growing fatigue cracks, (a) $S_{max}/\sigma_O = 0.2$, R = 0, (b) $S_{max}/\sigma_O = 0.3$, R = 0, and (c) $S_{max}/\sigma_O = 0.3$, R = −1.*

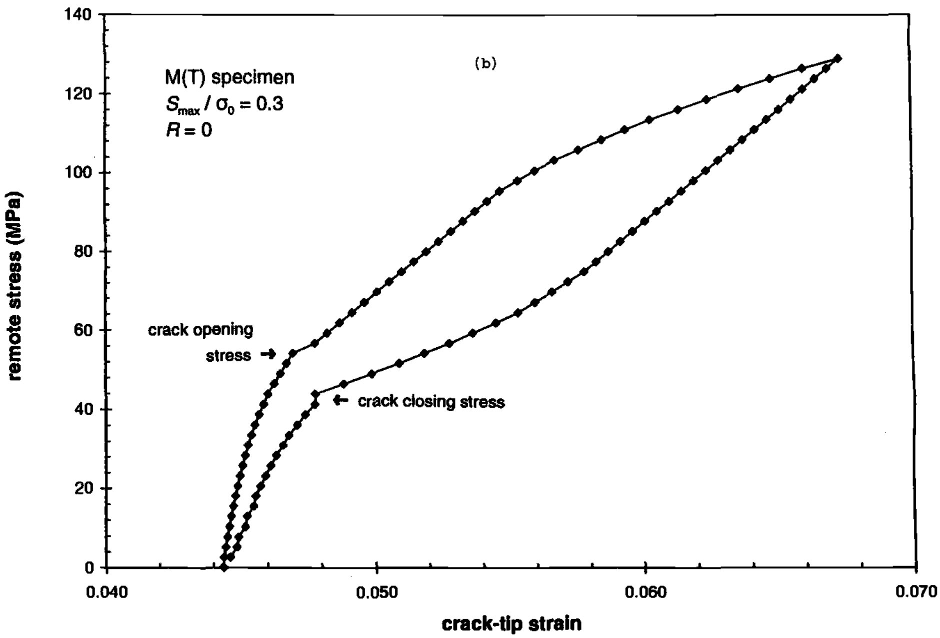

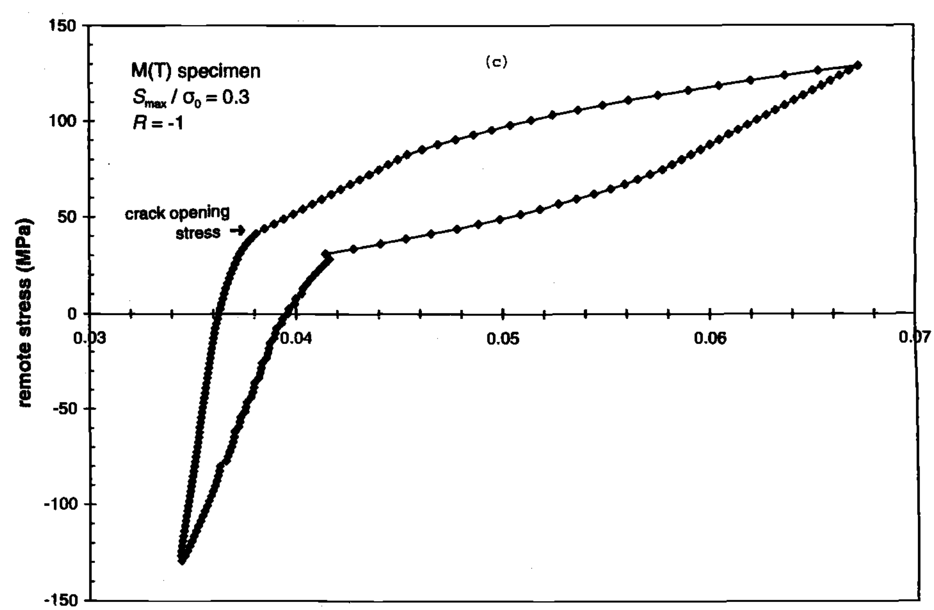

FIG. 4—*Continued*

In every case, the last node to open and the first node to close was the node immediately behind the crack tip. The "crack tip strain" shown in these and following graphs is the total axial strain component ε_{yy} at the integration point closest to the current crack tip node in the element immediately ahead of the crack tip node (a standard 2 $\times$ 2 integration scheme was employed in these linear strain elements).

These results indicate that relatively little crack-tip strain occurs while the crack tip is closed. Once the crack tip itself opens, which restores the "singularity" at the crack tip, the crack-tip strain increases rapidly to maximum load. The strain then decreases rapidly with remote unloading until the crack tip closes and shuts off the local singularity. Even under fully reversed ($R = -1$) remote stressing, where the crack tip is closed for about two-thirds of the total remote stress range, the crack-tip strain range while the crack is closed is a relatively small fraction of the total range. In all three simulations shown here, the $\Delta\varepsilon$ occurring while the crack tip is closed is only about 10 to 15% of the total crack tip strain range.

The deformation behavior at the crack tip is further elucidated by Fig. 5 for the $R = 0$, $S_{max}/\sigma_0 = 0.3$ simulation. Here the crack-tip stress σ_{yy} (actually, the stress at the same integration point cited earlier) is plotted against the crack-tip strain ε_{yy}. When the first node behind the crack tip first opens (the definition of crack opening in this simulation), the local stress just ahead of the crack tip is still compressive. The local stresses and strains then increase rapidly once the crack tip is open. However, this simulation indicates that the near-tip strains are still elastic even for some portion of the load ramp after the crack has opened.

This delay in the onset of crack tip plastic deformation after crack opening can probably also be attributed, at least in part, to the absence of a true numerical singularity in the finite element formulation. The fine mesh of linear strain quadrilateral elements does provide for a steep stress and strain gradient around the crack tip, but no special element formulations or nodal placements are employed to force a mathematical singularity at the crack tip itself. Such a formulation is not practical or per-

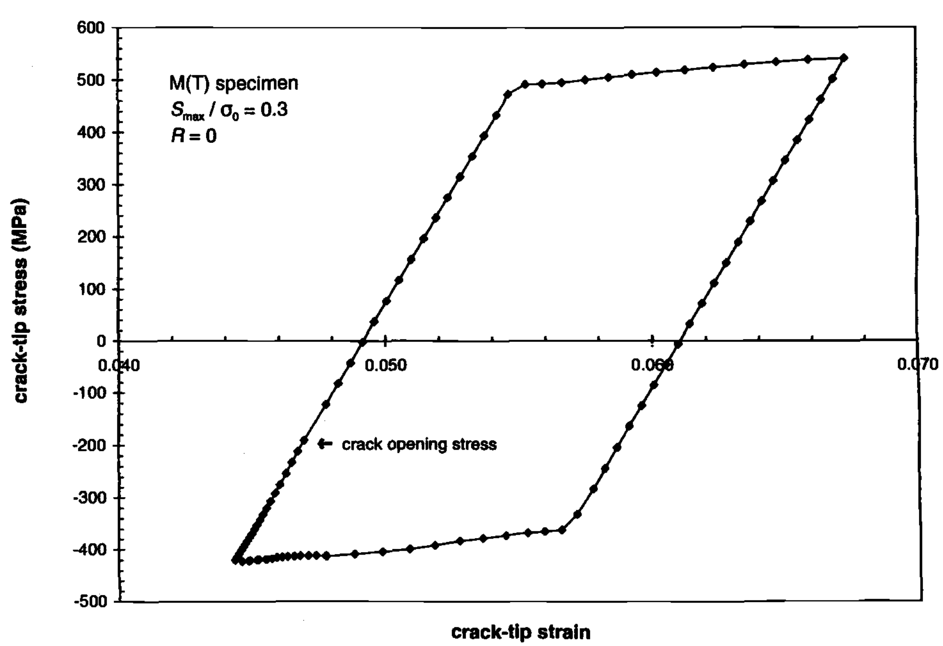

FIG. 5—*Calculated crack-tip stress versus crack-tip strain for* $S_{max}/\sigma_0 = 0.3$, R $= 0$.

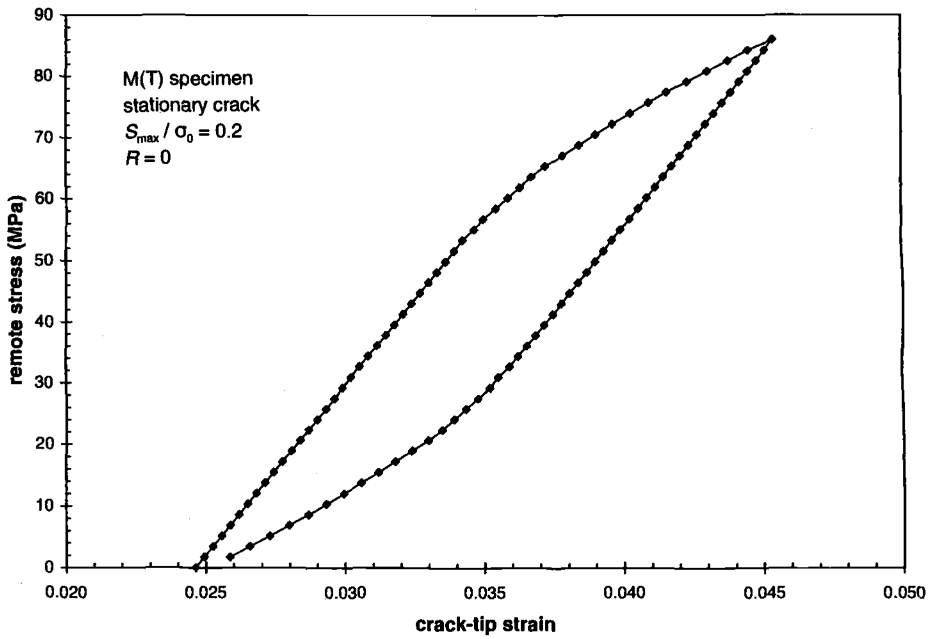

FIG. 6—*Calculated crack-tip strains versus remote applied stress for a stationary fatigue crack with* $S_{max}/\sigma_0 = 0.2$, $R = 0$.

haps even desirable, since the proper order of the singularity for a growing elastic-plastic fatigue crack has not been established. Nevertheless, the key result from Fig. 5 is that cyclic plastic deformation did not occur in the immediate vicinity of the crack tip while the crack tip was closed.

The effect of fatigue crack closure on crack tip deformation can also be discerned by comparing the behavior of the growing fatigue crack with the behavior of an idealized stationary crack. The stationary crack was analyzed with the same finite element mesh and program and was subjected to the same cyclic remote stresses, but the initial crack length was chosen to be the same as the final crack length of the fatigue crack (a = 300 mesh units). Because the stationary crack has no prior history and has not grown in length, it has not developed a plastic wake and does not experience closure.

Figure 6 shows the remote stress vs. crack-tip strain history for the stationary crack with S_{max}/σ_0= 0.2, R = 0. By comparison with Fig. 4*a*, it is clear that fatigue crack closure has significantly reduced the total strain range at the crack tip. The total strain range for the growing fatigue crack (with closure) is about one-half of the total strain range for the corresponding stationary crack (with no closure).

Experimental data for crack tip strain as a function of remote load are given in Figs. 7–10 for a variety of different materials. In several of the figures, strains are expressed in more than one form based on the available experimental data from the specimen surface: strain in the loading direction ($\Delta\varepsilon_{yy}$ in the coordinate system of the FE model), in-plane maximum shear strain, and in-plane effective strain. The strain components are roughly proportional in most of the measurements, indicating that any one of the strain representations provides an accurate description of trends. Note that the crack opening load, and sometimes the crack closing load, are also indicated on the figures. These opening and closing loads were obtained experimentally at the crack tip itself from stereoimaging of SEM photomicrographs.

The remote load vs. local strain data for IN-9052 in Fig. 7 [*15*], corresponding to a ΔK of 10 MPa$\sqrt{m}$, look a great deal like the FE results: the crack opens at a relatively low applied load, and the crack-tip strain occurring while the crack tip is closed is a very small fraction of the total crack-

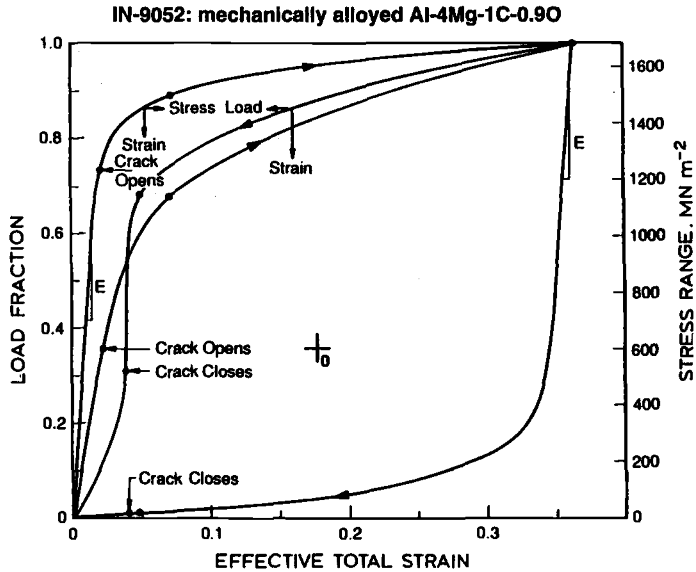

FIG. 7—*Measured crack-tip strains versus remote applied load and estimated crack-tip stress for a growing fatigue crack in IN-9052 [15].*

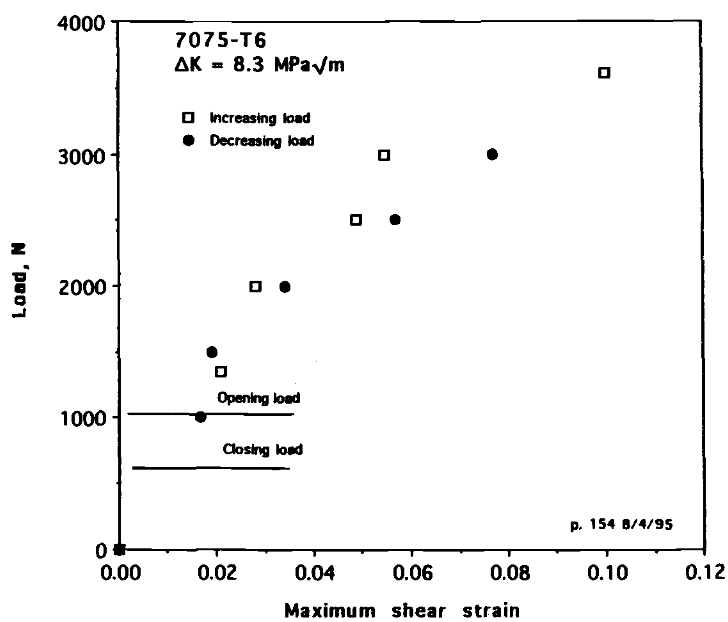

FIG. 8—*Measured crack-tip strains versus remote applied load for a growing fatigue crack in Al 7075-T6.*

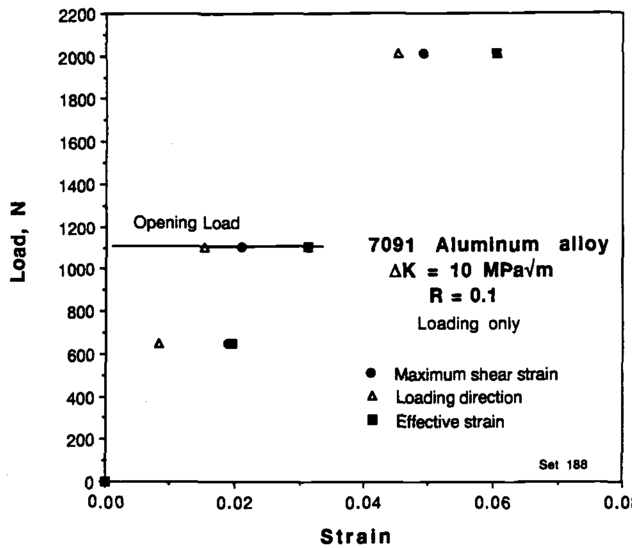

A

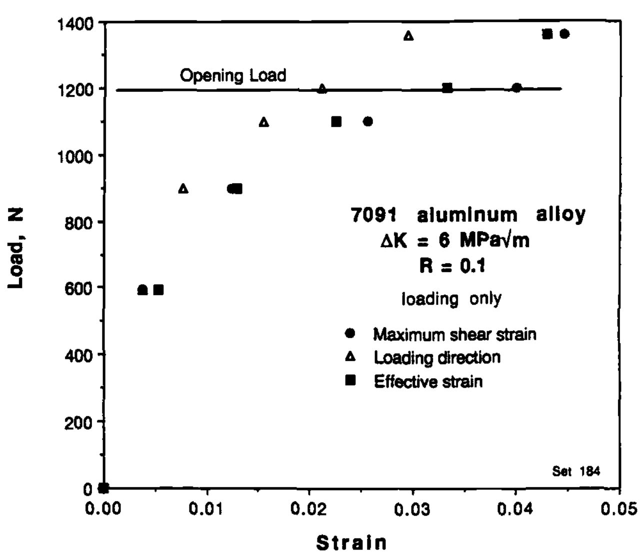

B

FIG. 9—*Measured crack-tip strains versus remote applied load for growing fatigue cracks in Al 7091, (top)* $\Delta K = 10\ MPa\sqrt{m}$*, (bottom)* $\Delta K = 6\ MPa\sqrt{m}$.

tip strain range. The crack-tip stress vs. crack-tip strain loop in the same figure, which was constructed based on some idealized assumptions (since crack-tip stress cannot be directly measured), also indicates that strain at the crack tip prior to crack opening is primarily elastic. The remote load vs. local strain data for 7075-T6 in Fig. 8 also bear a general resemblance to the numerical results in terms of both opening load and pre-opening crack-tip strain as fractions of maximum load and total strain range, respectively.

In contrast, the data for Al 7091 at $\Delta K = 6\ \mathrm{MPa}\sqrt{\mathrm{m}}$ (Fig. 9), and for the niobium alloys (Fig. 10), show higher crack opening loads (as a fraction of maximum load). Furthermore, the crack-tip strain

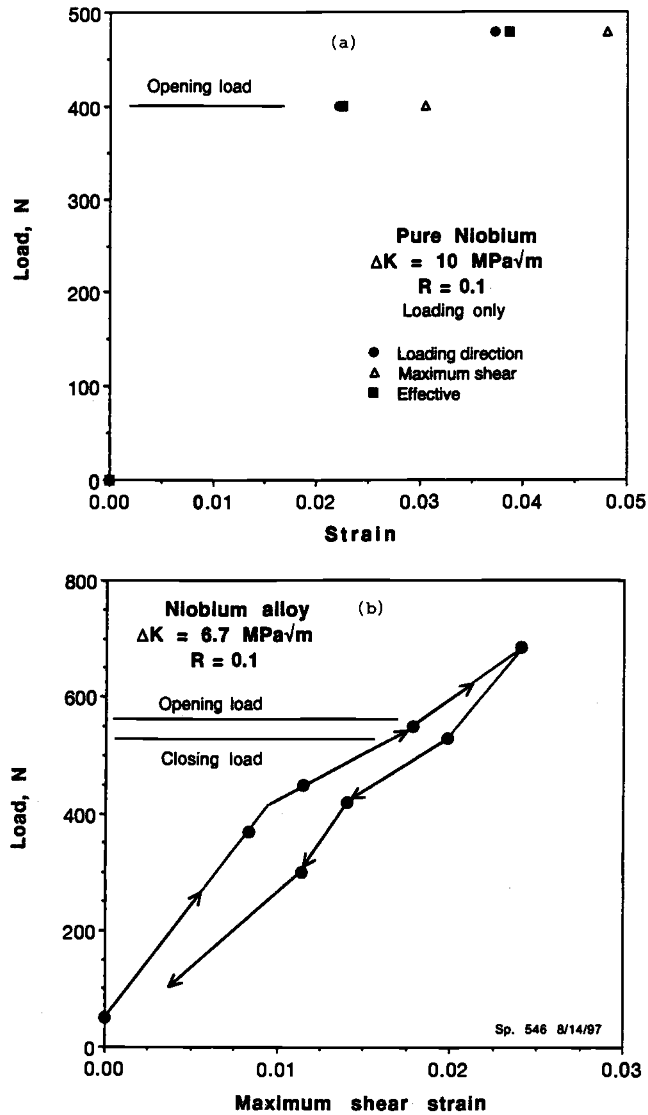

FIG. 10—*Measured crack-tip strains versus remote applied load for growing fatigue cracks in niobium materials.*

occurring prior to crack-tip opening is a larger fraction of the total crack-tip strain range—sometimes well over 50%.

It is difficult to draw definitive conclusions from these few data sets, especially due to the typical scatter observed in high resolution experiments of this type (scatter which reflects the true variability in local deformation response in real materials with real microstructures). However, a few general trends seem to hold true. It appears that the crack-tip strain occurring prior to crack opening is a relatively small fraction of the total crack-tip strain range when the crack opening level is relatively low.

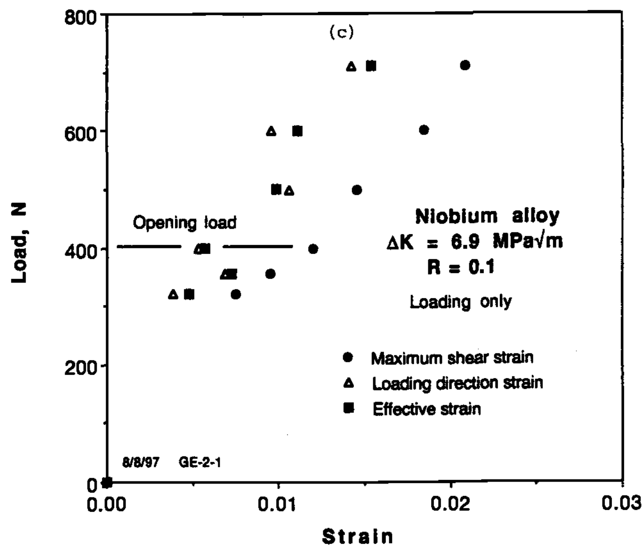

FIG. 10—*Continued*

When the crack opening level is relatively high, the crack-tip strains below the opening load are a larger fraction of total crack-tip strains.

In the aluminum alloys, high crack opening loads are generally associated with smaller values of the applied ΔK, closer to threshold (for example, the apparent threshold for pure mode I fatigue crack growth in Al 7091 is 5.4 MPa$\sqrt{\text{m}}$, in comparison to $\Delta K = 6$ MPa$\sqrt{\text{m}}$ in Fig. 9). Lower crack opening loads are generally associated with slightly larger ΔK values, more into the Paris regime. This is the regime of fatigue crack behavior that is simulated by the FE model; remember Fig. 3, where the FE model agreed closely with the experimental measurements of crack opening at larger ΔK values, but not near threshold, where this particular FE model apparently cannot simulate the near-threshold deformation mechanisms.

Furthermore, it is interesting that the values of the crack tip strains at crack opening are relatively similar in all of the experimental data shown here. What varies much more widely (both with different ΔK and with different material) is the maximum crack-tip strain. When the maximum crack-tip strain is larger, the pre-opening strain is therefore a smaller fraction of the total or maximum strain. When the maximum crack-tip strain is smaller (e.g., near threshold), the pre-opening strain may be a larger fraction of the total strain.

Remote Behavior

The FE method can also easily provide information about displacements remote from the crack tip. In particular, the FE model can be used to simulate the displacements that would be measured by conventional laboratory instrumentation, such as a crack mouth clip gage.

Figure 11 shows the simulated remote stress vs. remote displacement information for the same $S_{max}/\sigma_0 = 0.3$ simulations presented earlier, for both $R = 0$ and -1. The remote displacements in these graphs correspond to the displacement of a point (node) on the centerline of the M(T) specimen, located 103.1 mesh units above the crack line. A displacement gage centered about the crack at this location, then, would have a total gage length of 206.2 mesh units (in comparison, remember that the target crack half-length was 300 mesh units, with a total specimen half-width of 1000 mesh units).

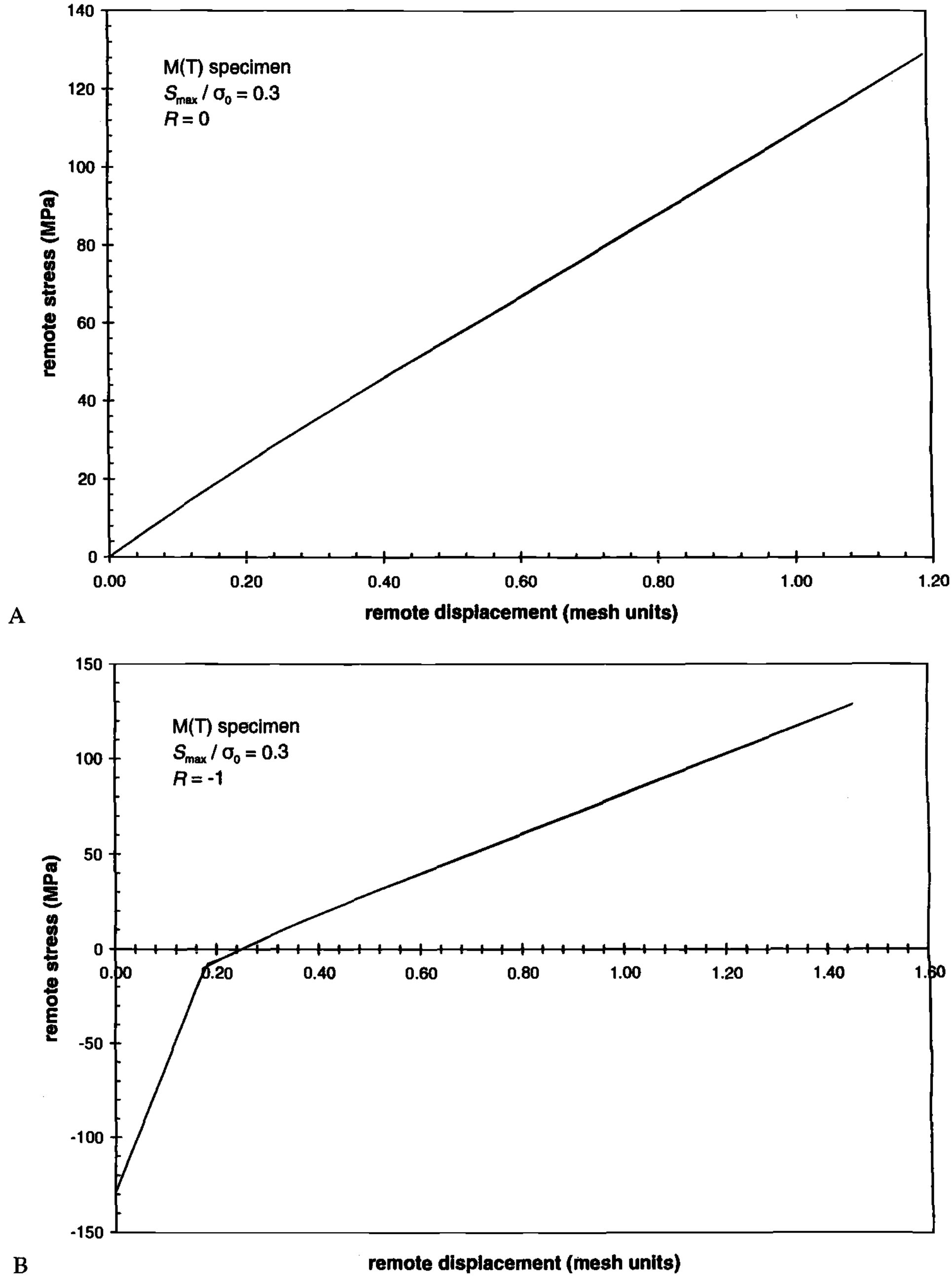

FIG. 11—*Calculated remote stress versus remote displacement for a growing fatigue crack, (top)* $S_{max}/\sigma_0 = 0.3$, *R* = 0, *(bottom)* $S_{max}/\sigma_0 = 0.3$, *R* = −1.

The $R = 0$ simulation shows very little change in compliance during the load cycle. Even at minimum (zero) load, the simulated crack is not fully closed along its entire length. The compliance change is more dramatic for the $R = -1$ crack, in which case the crack fully closes at a small negative applied stress.

ASTM Compliance Offset Method—The remote stress vs. remote displacement data obtained from this simulation were analyzed according to the ASTM recommended practice for the determination of fatigue crack opening load from compliance, Appendix X2 in Test Method E 647. This recommended practice requires first using a least-squares method to determine the average slope of the load vs. displacement line over approximately the upper 25% of the cyclic load range. This corresponds to the fully-open crack configuration. Then, starting just below maximum load, least-squares straight lines are fit to overlapping segments of the curve that each span about 10% of the cyclic load range. In this simulation, data were available at load increments of 2%, and each segment had 5 data points. For clarity, the segments were chosen here to overlap more closely than the ASTM recommendation of 5%: the sliding "window" for the least-squares regression moved by only one data point per segment, so that an average slope was determined at the individual load point in the middle of each five-point window. Compliance offset was then calculated for each segment according to the formula

$$(\text{Compliance offset}) = \frac{[(\text{open-crack compliance}) - (\text{compliance})](100)}{(\text{open-crack compliance})} \tag{1}$$

The resulting graphs of compliance offset vs. applied stress are shown in Fig. 12 for the same three simulations documented previously. The compliance offset method appears to be remarkably sensitive in indicating the remote applied stress at which the crack tip itself first opens. However, this is true only because the finite element output is "clean" enough to detect very small changes of significance in the compliance offset. In fact, this high sensitivity and clean signal actually cause some minor difficulties, because the FE output strongly detects the small but systematic change in open-crack compliance at the upper end of the loading cycle due to crack-tip plasticity. This explains the systematic change in compliance offset at the upper end of the load increasing data for $S_{max}/\sigma_0 = 0.3$, and makes the least-squares determination of the open-crack compliance a somewhat arbitrary function of the specific segment size chosen.

The more important, issue, however, is that the actual experimental load vs. displacement signal will be somewhat noisier than the idealized FE "signal." Recognizing this likelihood, the ASTM practice recommends that the opening load be determined at some specified nonzero compliance offset, such as 1, 2, or 4%. It is clear from Fig. 12 that an "opening stress" defined in this manner will always be lower than the actual crack-tip opening stress. For example, the 2% offset opening stress for the $S_{max}/\sigma_0 = 0.2$, $R = 0$ simulation would be about 18 MPa, in comparison to the actual crack-tip opening stress of about 34 MPa. Of course, the specific "error" introduced in this way will be a function of the sensitivity of the specific specimen geometry and instrumentation employed in a given experiment. The general conclusion that can be drawn from this brief study of the ASTM compliance offset method is that for "perfect" sensitivity and a zero offset, the method indicates the correct crack-tip opening stress. For real sensitivities and nonzero offsets, the method will give a lower value than the actual crack-tip opening stress. It may be possible to obtain a better estimate of the actual crack-tip opening stress by extrapolating the nonzero compliance offset data below S_{op} back up to the zero percent offset line. Unfortunately, these adjustments would make the measured S_{op} even higher, which would exacerbate the problem (noted in the Introduction) of correlating near-threshold data with closure-free data on the basis of the Elber effective stress range.

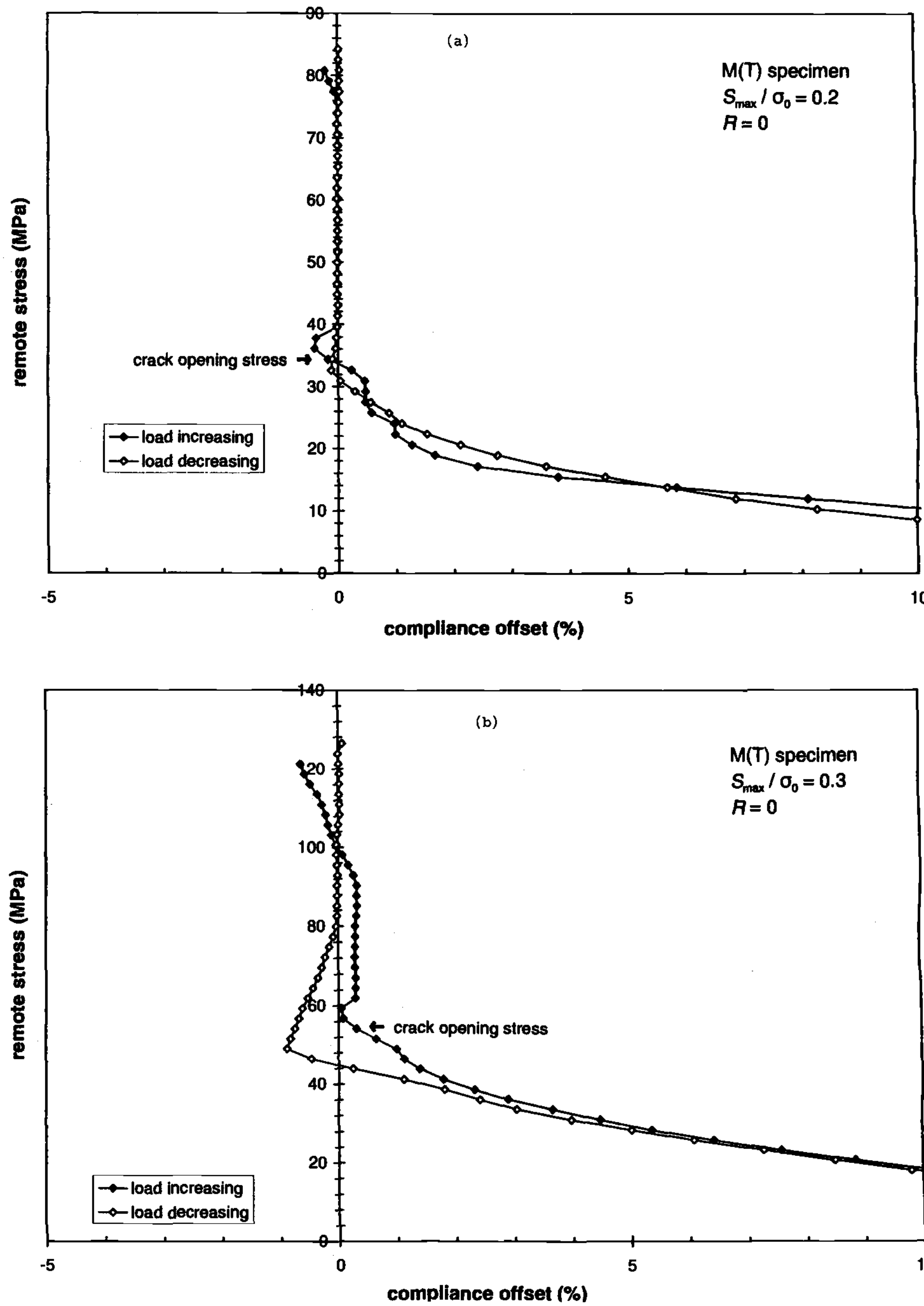

FIG. 12—*Calculated compliance offset versus remote applied stress for a growing fatigue crack, (a)* $S_{max}/\sigma_0 = 0.2$, $R = 0$, *(b)* $S_{max}/\sigma_0 = 0.3$, $R = 0$, *and (c)* $S_{max}/\sigma_0 = 0.3$, $R = -1$.

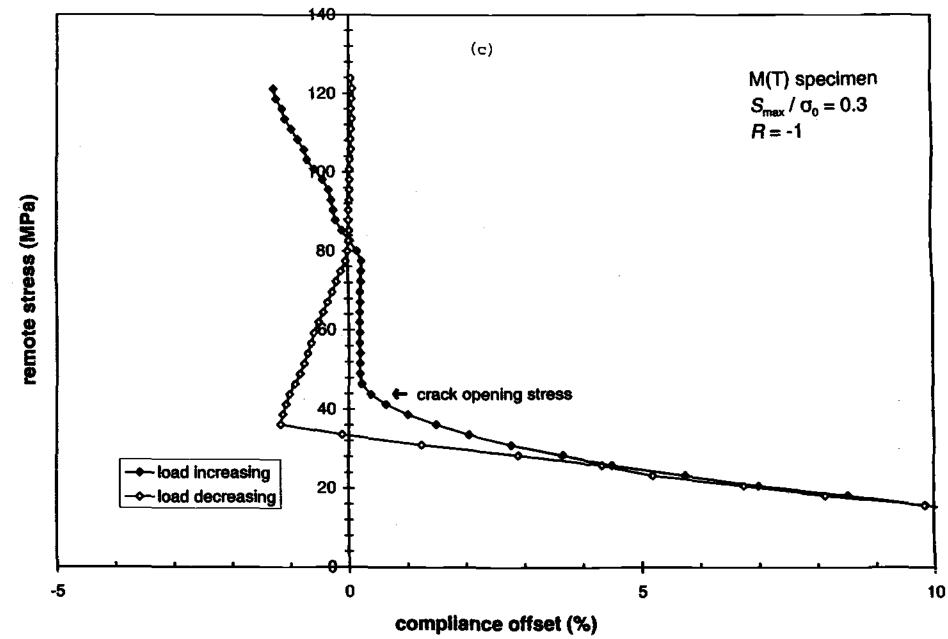

FIG. 12—*Continued*

Adjusted Compliance Ratio Method—The remote stress vs. remote displacement data were also analyzed to determine the adjusted compliance ratio (ACR) [*5,6*]. The ACR was calculated according to

$$\mathrm{ACR} = \frac{C_s - C_i}{C_o - C_i} \tag{2}$$

where

C_o = inverse slope of stress vs. displacement above opening load;
C_s = inverse slope of secant drawn between minimum and maximum stress-displacement values; and
C_i = inverse slope of stress vs. displacement prior to initiation of a crack.

In this study, C_i was interpreted literally as the compliance of the uncracked body, the M(T) specimen with zero crack length and no prior notch.

For the two $R = 0$ simulations documented in this paper, the ACR was calculated to be about 0.96. This value very close to 1 is consistent with the general appearance of the $R = 0$ stress-displacement curve in Fig. 11, which deviates only slightly from total linearity. The ACR for the $R = -1$ simulation was calculated to be 0.51.

Discussion

The investigations described in this paper have obviously been limited in scope and preliminary in nature. While the authors have investigated more numerical configurations and experimental conditions than specifically presented in the paper, many other conditions have not been addressed. In particular, the numerical method considered only continuous, plasticity-induced closure for two plane stress specimen geometries under constant amplitude loading over a limited range of crack lengths. The numerical method was not capable of emulating true near-threshold behavior. The experiments considered only specialized specimens designed for the SEM loading stage, at positive stress ratios, and did not include traditional crack mouth opening displacement measurements. Some of these scope limitations can be easily overcome through further investigations, while others are inherent in the research tools currently employed. Nevertheless, some general trends have emerged from these investigations, and seem worthy of elaboration or reiteration to provide a basis for further research. Some of these trends also invite additional speculation.

A fatigue crack that naturally develops a plastic wake will generally exhibit a continuous, "peeling open" crack opening process for constant (or, perhaps, for mildly varying) load amplitudes. Under these conditions, the true crack tip will experience only limited amounts of strain while it is still closed, and the theoretical singularity is turned "off." Therefore, the amount of crack tip damage which might promote crack growth appears to be limited for a closed crack. This is especially true in a comparative sense relative to the large amounts of crack-tip strain experienced by a crack in the typical Paris regime.

However, near threshold, the total crack-tip strain range is itself a relatively small value. Under near-threshold conditions, when crack opening stresses are relatively high, the small amounts of crack-tip strain experienced prior to crack opening could nonetheless be relatively significant in comparison to the total strain. Or perhaps the pre-opening strains are not so significant. If the pre-opening strains are all elastic, and the strains that promote crack-tip damage and therefore crack growth must be plastic, then the pre-opening strains might still be relatively inconsequential.

Experimentally, it has been shown that constraint is high for fatigue cracks growing near ΔK_{th} [*16*]. High constraint is maintained because of the low levels of strain at the crack tip near ΔK_{th}. At higher ΔK, this constraint is relaxed due to increased crack tip plastic strain. The high levels of constraint near the crack tip is an indication that a large proportion of the total strain range is elastic. Thus, it is expected that most of the strain in Fig. 9 (bottom) for Al 7091 at $\Delta K = 6$ MPa$\sqrt{\text{m}}$ and Fig. 10 (*b, c*) for the niobium alloy at $\Delta K = 6.7$ and 6.9 MPa$\sqrt{\text{m}}$ is elastic, which agrees with the opening loads being high fractions of the maximum load. Yield stress is elevated by high constraint, and the strain to yield is proportionally larger than in a tension test.

Clearly, further data are needed to address this issue. However, previous observations [*17*] that correlations of fatigue crack growth rates near threshold based on crack opening loads and the original Elber hypothesis about ΔK_{eff} tended to overcorrect growth rates are consistent with the possibility that some crack-tip strains below S_{op} could be important for near-threshold growth.

Given this prospect, the ACR method is one proposed means of characterizing the contributions of pre-opening crack tip strains. What do the numerical simulations in the current investigations say about the ACR? Table 1 summarizes the calculated values of the ACR, the effective stress range ratio $U = (S_{max} - S_{op})/(S_{max} - S_{min})$ based on the Elber hypothesis, and some interesting strain ratios. The ratio $\Delta\varepsilon$(fatigue)/$\Delta\varepsilon$(stationary) is the ratio of the total crack-tip strain for the growing fatigue crack and the stationary crack (the ratio of Fig. 6 to Fig. 4). The ratio $\Delta\varepsilon$(open)/$\Delta\varepsilon$(fatigue) quantifies the ratio of the crack-tip strain range while the crack tip is open to the total crack-tip strain range, both for the growing fatigue crack.

TABLE 1—*Summary of Some Important Closure Ratios.*

S_{max}/σ_0	R	U	ACR	$\Delta\varepsilon_{fatigue}/\Delta\varepsilon_{stationary}$	$\Delta\varepsilon_{open}/\Delta\varepsilon_{fatigue}$
0.2	0	0.60	0.97	0.58	0.85
0.3	0	0.60	0.96	0.51	0.89
0.3	−1	0.34	0.51	0.44	0.89

The calculated ACR values for the two $R = 0$ simulations, based on the remote compliance measurements, suggest that almost the entire stress range is effective in propagating the crack; i.e., crack closure has relatively little impact on the crack driving force. By implication, the ACR suggests that the crack-tip strain below S_{op} is an important contributor to crack growth. In contrast, the Elber approach suggest that the effective stress range ratio is about 0.60; i.e., only a little more than half of the total stress range is effective in growing the crack. The comparison of the stationary and growing fatigue crack-tip strain ranges indicates that crack closure reduces the crack-tip strain to about 0.51 – 0.58 of the nonclosure value, and this ratio is certainly more consistent with the Elber U than with the ACR.

However, it is not necessarily the case that this strain ratio should correspond directly with the driving force ratio $\Delta K_{eff}/\Delta K$. It is not immediately obvious how a reduction in total crack tip strain, or a reduction in total crack tip plastic strain, should be quantitatively related to a change in the crack tip driving force ΔK or to a change in the crack growth rate. Furthermore, crack closure has a more complex effect on crack-tip deformation than simply reducing the crack-tip strain range. Crack closure also slightly reduces the maximum stress at the crack tip [18], due to the residual stress state around the growing fatigue crack.

The ACR as currently formulated also contains an ambiguity that could have an appreciable impact on its calculated value. The "uncracked compliance" C_i can be interpreted rigorously as the compliance of an uncracked, unnotched specimen, as was done in the present study, or as the compliance of an uncracked, notched specimen (e.g., a C(T) specimen with no precrack, or an M(T) specimen with a blunt starter notch but no precrack), as is currently practiced by the original authors of the ACR method. Of course, the uncracked compliance could itself change with the depth of such an uncracked notch. In the present investigations, an alternative simulation in which the initial "uncracked" compliance was determined from an initial crack size of $a_0 = 209$ mesh units gave an ACR value of 0.93 instead of 0.97 for the $S_{max}/\sigma_0 = 0.2$ case, so the effect was relatively small. However, it is not difficult to create sample problems in which changes in the initial notch size have a larger impact on the calculated ACR. Some standardization of the definition of the "uncracked" compliance in the ACR is needed to avoid these difficulties.

The experience of Donald and his colleagues with measuring the ACR for $R = 0.1$ tests in the Paris regime have found typical values in the general range of 0.7 to 0.85, in contrast to the much higher values of 0.93 to 0.97 obtained in these numerical simulations. Why this difference? One possibility is that in the simulations, the residual plastic wake was not fully developed along the entire length of the crack. Although the crack was grown from zero length, the fine mesh region was limited to the longer crack lengths, and the coarser mesh at the shorter crack lengths could not adequately capture crack-tip plasticity. This modeling limitation was not significant for accurate simulation of the near-tip behavior at the longer crack lengths. However, this limitation could have had an impact on the calculated ACR values, because the diminished plastic wake would increase the specimen compliance when the crack was mostly, but not entirely, closed. But this "limitation" in the analysis actually may point out a more fundamental limitation in the ACR approach: changes in the specimen compliance due to changes in closure behavior far away from the crack tip (which do not affect crack-tip behavior) nevertheless can change the ACR value. For example, premature crack face contact (well below S_{op} but still above $S = 0$) far behind the crack tip due to fracture surface roughness could change the specimen compliance and hence the ACR without having any appreciable impact on near-tip behavior. In fact, roughness-induced closure is particularly likely to occur farther away from the crack tip due to mismatching of the opposing fracture surfaces, and this may even be another source of the difference between the measured and calculated ACR values.

It should again be emphasized that the numerical simulations in this research were limited to plasticity-induced closure behavior. It is possible that the ACR is more suitable for characterizing near-tip behavior under the influence of other forms of closure, such as roughness-induced. When roughness-induced closure is a significant mechanism, the closure of the crack may be a more discontinuous process that does not necessarily occur at the crack tip itself. In this case, first contact of opposing crack surfaces may not "turn off" the crack-tip singularity so abruptly. However, it should be noted that the introduction of fracture surface roughness effects does not eliminate plasticity-induced closure effects, and so plastic wake effects on the crack tip may still be important. The many high resolution experimental investigations of crack closure by one of the current authors, cited earlier, have not observed significant roughness-induced closure behavior at the specimen surface in the vicinity of the crack tip, even near threshold. Even near threshold, plasticity appears to be the primary near-tip closure mechanism at the specimen surface, with premature contact due to mismating fracture surfaces only significant farther behind the crack tip.

Even if the ACR turns out to be a more suitable characterization of closure effects for roughness, its ultimate value as a correlating parameter for fatigue crack growth rates will depend on whether or not it can give consistently accurate answers under the influence of different closure mechanisms. Therefore, difficulties in characterizing crack-tip deformation in the presence of plasticity-induced closure may still be a stumbling block.

While the use of remote measurements to characterize near-tip behavior is obviously a difficult challenge, the need for practical methods to measure closure behavior is nevertheless a significant one due to the expense of making highly local measurements. Further research is needed to evaluate the suitability and sensitivity of both the ASTM and ACR methods to characterize near-tip closure behavior. Future work could systematically investigate the effects of measurement location, crack length, specimen geometry, and specimen stress state (plane stress vs. plane strain) on near-tip and remotely inferred crack opening loads. Modifications to the FE formulation could enable some study of roughness effects. More direct comparisons of model and measurement could provide additional insight on exactly what is being measured and what it means for the growth of the fatigue crack.

Ultimately, of course, the true value of a closure characterization is found in its ability to help do a better job of describing FCG rate behavior. However, evaluation of the ASTM or ACR methods on the basis of FCG rate data correlation is beyond the scope of the current paper. Instead, the focus of this paper, as noted in the Introduction, has been to assess the suitability of various remote measurement and analysis schemes to describe accurately the closure and deformation behavior at the crack tip itself. In principle, a scheme that accurately characterizes the relevant damage mechanisms at the crack tip should be most successful in characterizing crack growth rates.

Conclusions

1. High resolution experiments and analyses indicate that crack-tip strains below S_{op} are a relatively small fraction of the total crack-tip strain range for cracks in the Paris regime, and therefore may be insignificant for crack-tip deformation and damage and crack growth.

2. High resolution experiments indicate that crack-tip strains below S_{op} could potentially be more important at lower ΔK values, nearer the threshold, where S_{op} values are higher. Here the crack-tip strains below S_{op} are a relatively larger fraction of the total crack-tip strain range. However, it is not clear to what extent these crack-tip strains below S_{op} contribute to crack-tip damage and growth.

3. In theory, the current ASTM compliance offset procedure for determining the crack opening load can provide accurate information about true crack-tip opening loads. However, due to the limited sensitivity of the method in practice, and the corresponding need to employ a non-zero compliance offset, the method gives underestimates of opening and closing loads that may be considerably in error relative to the true crack-tip values.

4. The current ACR technique does not appear to do a good job of characterizing the near-tip deformation response for cracks in the Paris regime, where plasticity-induced closure is the dominant closure mechanism. Remote displacement measurements do not appear to be adequately sensitive to near-tip strains.

Acknowledgments

Helpful discussions with Keith Donald and Jim Newman are gratefully acknowledged.

References

[1] Elber, W., "Fatigue Crack Closure Under Cyclic Tension," *Engineering Fracture Mechanics*, Vol. 2, 1970, pp. 37–45.

[2] Elber, W., "The Significance of Fatigue Crack Closure," *Damage Tolerance in Aircraft Structures, ASTM STP 486*, American Society for Testing and Materials, 1971, pp. 230–242.

[3] Chen, D.-L., Weiss, B., and Stickler, R., "A New Evaluation Procedure for Crack Closure," *International Journal of Fatigue*, Vol. 13, 1991, pp. 327–331.

[4] Chen, D. L., Weiss, B., and Stickler, R., "Contribution of the Cyclic Loading Portion Below the Opening Load to Fatigue Crack Growth," *Materials Science and Engineering*, Vol. A208, 1996, pp. 181–187.

[5] Donald, J. K., "Introducing the Compliance Ratio Concept for Determining Effective Stress Intensity," presented at the First International Conference on Fatigue Damage in Structural Materials, Hyannis, MA, September 1996 (to be published in *International Journal of Fatigue*).

[6] Donald, J. K., Bray, G. H., and Bush, R. W., "An Evaluation of the Adjusted Compliance Ratio Technique for Determining the Effective Stress Intensity Factor," *29th National Symposium on Fatigue and Fracture Mechanics, ASTM STP 1332*, T. L. Panontin and S. D. Sheppard, Eds., American Society for Testing and Materials, 1999, pp. 674–695.

[7] Hudak, S. J., Jr. and Davidson, D. L., "The Dependence of Crack Closure on Fatigue Loading Variables," *Mechanics of Fatigue Crack Closure, ASTM STP 982*, J. C. Newman, Jr. and W. Elber, Eds., American Society for Testing and Materials, Philadelphia, 1988, pp. 121–138.

[8] McClung, R. C. and Sehitoglu, H., "On the Finite Element Analysis of Fatigue Crack Closure—1. Basic Modeling Issues," *Engineering Fracture Mechanics*, Vol. 33, 1989, pp. 237–252.

[9] McClung, R. C., Thacker, B. H., and Roy, S., "Visualization of Fatigue Crack Closure in Plane Stress and Plane Strain," *International Journal of Fracture*, Vol. 50, 1991, pp. 27–49.

[10] McClung, R. C. and Sehitoglu, H., "On the Finite Element Analysis of Fatigue Crack Closure—2. Numerical Results," *Engineering Fracture Mechanics*, Vol. 33, 1989, pp. 253–272.

[11] Davidson, D. L., "Plasticity Induced Fatigue Crack Closure," *Mechanics of Fatigue Crack Closure, ASTM STP 982*, J. C. Newman, Jr. and W. Elber, Eds., American Society for Testing and Materials, Philadelphia, 1988, pp. 44–61.

[12] Franke, E. A., Wenzel, D. J., and Davidson, D. L., "Measurement of Micro*dis*placements by *Ma*chine Vision *P*hotogrammetry (DISMAP)," *Review of Scientific Instruments*, Vol. 62, 1991, pp. 1270–1279.

[13] McClung, R. C. and Davidson, D. L., "High Resolution Numerical and Experimental Studies of Fatigue Cracks," *Engineering Fracture Mechanics*, Vol. 39, 1991, pp. 113–130.

[14] McClung, R. C., "Finite Element Perspectives on the Mechanics of Fatigue Crack Closure," *Proceedings*, FATIGUE '96, Sixth International Fatigue Congress, Berlin, 1996, Vol. 1, pp. 345–356.

[15] Davidson, D. L. and Lankford, J., "Fatigue Crack Growth in Metals and Alloys: Mechanisms and Micromechanics," *International Materials Reviews*, Vol. 37, 1992, pp. 45–76.

[16] Davidson, D. L. and McClung, R. C., "Local Constraint Near Fatigue Cracks in Alloys and Particulate Composites," *International Journal of Fracture*, Vol. 84, 1997, pp. 81–98.

[17] Bray, G. H. and Donald, J. K., "Separating the Influence of K_{max} from Closure-Related Stress Ratio Effects Using the Adjusted Compliance Ratio Technique," this publication.

[18] McClung, R. C., "Crack Closure and Plastic Zone Sizes in Fatigue," *Fatigue and Fracture of Engineering Materials and Structures*, Vol. 14, 1991, pp. 455–468.

J. C. Newman, Jr.[1]

An Evaluation of Plasticity-Induced Crack Closure Concept and Measurement Methods

REFERENCE: Newman, J. C., Jr., "**An Evaluation of Plasticity-Induced Crack Closure Concept and Measurement Methods,**" *Advances in Fatigue Crack Closure Measurement and Analysis: Second Volume, ASTM STP 1343*, R. C. McClung and J. C. Newman, Jr., Eds., American Society for Testing and Materials, West Conshohocken, PA, 1999, pp. 128–144.

ABSTRACT: An assessment of the plasticity-induced crack closure concept is made, in light of some of the questions that have been raised on the validity of the concept, and the assumptions that have been made concerning crack-tip damage below the crack-opening stress. The impact of using other crack-tip parameters, such as the cyclic crack-tip displacement or cyclic crack-tip hysteresis energy, to model crack-growth rate behavior was studied. Crack-growth simulations using the modified Dugdale crack closure model showed a close relation between traditional ΔK_{eff} and the cyclic crack-tip displacement ($\Delta\delta_{eff}$) for an aluminum alloy and a steel over a wide range in stress ratios. Evaluations of the cyclic hysteresis energy demonstrated that the cyclic plastic damage below the crack-opening stress was negligible in the Paris crack-growth regime. Some of the standard and newly proposed remote measurement methods to determine crack-opening stresses and the "effective" crack-tip driving parameter were evaluated from crack-growth simulations made on middle-crack tension specimens. Here, analyses were conducted under both constant-amplitude and single-spike-overload conditions. A potential source of the K_{max} effect on crack-growth rates was studied at high stress ratios and at high stress levels for an aluminum alloy. Results showed that the ratio of K_{max} to K_c had a strong effect on crack-growth rates at high stress ratios and at low stress ratios for very high stress levels. The crack-closure concept and the traditional crack-growth rate equations were able to correlate and predict crack-growth rates under these extreme conditions.

KEYWORDS: fatigue crack growth, fracture mechanics, cracks, stress-intensity factor, crack closure, plasticity, constraint

In 1968, Elber observed that fatigue-crack surfaces contact each other even during tension-tension cyclic loading and he subsequently developed the crack closure concept [*1*]. This observation and the explanation of crack-closure behavior revolutionized the damage-tolerance analyses and began to rationally explain many crack-growth characteristics, such as crack-growth retardation and acceleration. Since the discovery of plasticity-induced fatigue-crack closure, several other closure mechanisms have been identified, such as roughness- [*2*] and oxide-induced [*3*] closure, which appear to be more relevant in the near-threshold regime. Recently, some researchers have questioned the validity of the crack-closure concept [*4,5*] and whether crack-tip damage occurs below the crack-opening stress [*6,7*]. Other measurement methods, from remote load-displacement records, are being proposed [*6,7*] to define an "effective" crack-tip damage parameter, other than the traditional effective stress-intensity factor range, ΔK_{eff}. In addition, K_{max}-constant testing at extreme values (greater than 0.75 K_c) have produced very high crack-growth rates at extremely small values of ΔK [*8*]. Testing at high stress ratios, in the absence of crack closure, is producing different crack-growth rates at the same applied ΔK (or ΔK_{eff}) value [*9*].

[1] Senior scientist, NASA Langley Research Center, Hampton, VA 23681.

The objective of this paper is to make an assessment of the crack-closure concept, in light of some of these questions and assumptions. The paper will study the impact of using other crack-tip parameters, such as the cyclic crack-tip displacement $\Delta\delta_{eff}$ [*10,11*], or the cyclic crack-tip hysteresis energy W^p_{eff} [*12*], to model crack-growth rate behavior and to assess the differences induced by using the ΔK_{eff} parameter. The $\Delta\delta_{eff}$ and W^p_{eff} parameters are directly relatable to the effective cyclic J-integral [*13*]. Crack-growth simulations, using the modified Dugdale [*14*] crack-closure model [*15,16*], will be conducted over a wide range in stress ratios (R) to assess the impact of using cyclic crack-tip displacement as a crack-tip parameter. Some of the standard and newly proposed remote measurement methods to determine traditional crack-opening stresses or "effective" crack-driving parameters will be evaluated from the plasticity-induced crack-closure model analyses on middle-crack tension specimens. Analyses will be conducted under both constant-amplitude and single-spike-overload conditions. A potential source of the K_{max} effects on crack-growth rate data will be studied at high stress ratios and at high stress levels on test data from an aluminum alloy.

Plasticity-Induced Crack Closure Model

The plasticity-induced crack-closure model, shown in Fig. 1, was developed for a through crack in a finite-width plate subjected to remote applied stress. The model was based on the Dugdale strip-yield model [*14*] but modified to leave plastically deformed material in the wake of the crack. The details of the model are given elsewhere and will not be presented here (see Newman [*15,16*]). One of the most important features of the model is the ability to model three-dimensional constraint effects. A constraint factor, α, is used to elevate the flow stress (σ_o) at the crack tip to account for the influence of stress state ($\alpha\sigma_o$) on plastic-zone sizes and crack-surface displacements. (The flow stress σ_o is taken as the average between the yield stress σ_{ys} and ultimate tensile strength σ_u of the mate-

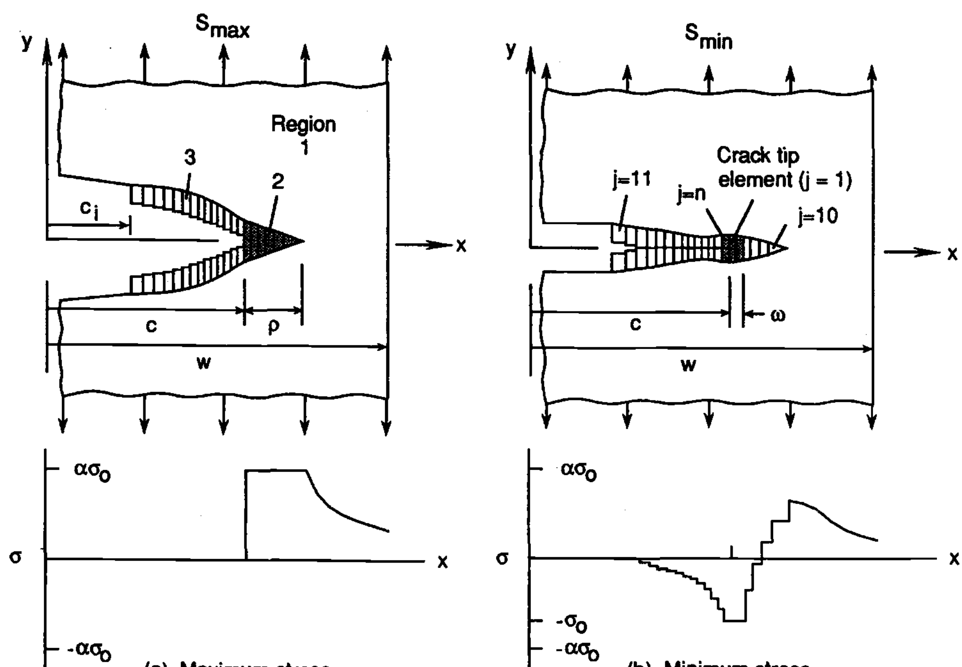

FIG. 1—*Schematic of strip-yield model at maximum and minimum applied loading.*

rial.) For plane-stress conditions, α is equal to unity (original Dugdale model); and for simulated plane-strain conditions, α is equal to 3. Although the strip-yield model does not model the correct yield-zone shape for plane-strain conditions, the model with a high constraint factor is able to produce crack-surface displacements and crack-opening stresses quite similar to those calculated from three-dimensional, elastic-plastic, finite-element analyses of crack growth and closure for finite-thickness plates [*17*].

The calculations performed herein were made with FASTRAN Version 3.0. The modifications made to FASTRAN-II (Version 2.0 described in Ref *16*) were made to improve the crack-opening stress calculations under variable-amplitude loading, to improve the element "lumping" procedure to maintain the residual plastic deformation history, and to improve computational efficiency. From the model, the crack-mouth opening displacements (CMOD) are calculated at the centerline of the model ($x = 0$). The cyclic crack-tip displacements and the cyclic hysteresis energy were calculated from the crack-tip element ($j = 1$) in Fig. 1*b*. The crack-opening stress, S_o, is calculated from the contact stresses shown in Fig. 1*b*, see Refs *15* or *16*, by equating the applied stress-intensity factor at S_o to the stress-intensity factor caused by the contact stresses. CMOD results under cyclic loading were used to determine the crack-opening stresses using the reduced-displacement or the compliance-offset methods, and an alternative effective stress-intensity factor range from the adjusted-compliance-ratio method [*7*].

Effective Stress-Intensity Factor Range Against Crack-Growth Rate Relations

The linear-elastic effective stress-intensity factor range developed by Elber [*1*] is

$$\Delta K_{\text{eff}} = (S_{\max} - S_o) F \sqrt{\pi c} \tag{1}$$

where $S_{\max}$ is the maximum stress, S_o is the crack-opening stress and F is the boundary-correction factor. The crack-growth rate equation proposed by Elber states that the crack-growth rate is a power function of the effective stress-intensity factor range (like the Paris equation), as shown by the dotted line in Fig. 2. However, fatigue crack-growth rate data plotted against the ΔK or ΔK_{eff}, commonly show a "sigmoidal" shape, as illustrated by the solid curve shown in Fig. 2. To account for this shape,

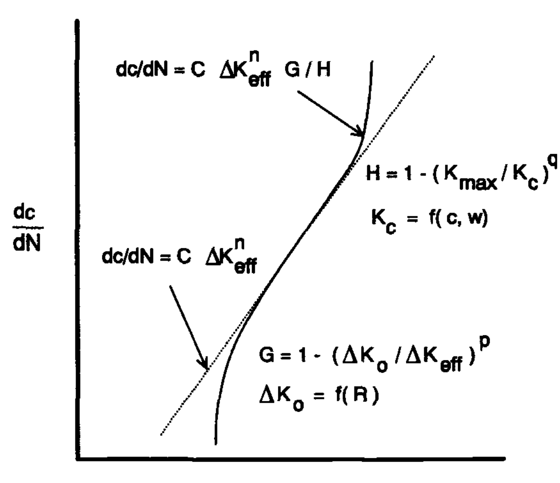

FIG. 2—*Schematic of effective stress-intensity factor against crack-growth rate relations showing influence of threshold and fracture toughness.*

the power relation was modified by Newman [*15*] to

$$dc/dN = C\,(\Delta K_{\text{eff}})^n\, G/H \tag{2}$$

where $G = 1 - (\Delta K_o/\Delta K_{\text{eff}})^p$ and $H = 1 - (K_{max}/C_5)^q$. The function G accounts for threshold variations with stress ratio (ΔK_o is a function of stress ratio) and the function H accounts for the rapid crack-growth rates approaching fracture. The parameter C_5 is the cyclic fracture toughness. As cracked specimens are cycled to failure, the fracture toughness is generally higher than the toughness for cracks grown at a low load and then pulled to failure. This is caused by the shielding effect of the plastic wake [*18*]. The cyclic fracture toughness (C_5), like the elastic fracture toughness (K_{Ie}), is a function of crack length, specimen width, and specimen type. Nonlinear fracture mechanics methods, in general, are required to model the fracture process. Later, a two-parameter fracture criterion will be used to model the fracture process. A discussion of the threshold behavior is beyond the scope of the present paper. Thus, G is set to unity. Only the function H will be considered in the present analyses to account for nonclosure-induced K_{max} effects.

Cyclic Hysteresis Energy and Cyclic CTOD Evaluations

In order to assess the cyclic crack-tip damage for stresses below the traditional crack-opening stress, the cyclic plastic crack-tip displacements from the crack-tip element ($j = 1$) in Fig. 1*b* were calculated for middle-crack tension M(T) specimens subjected to various constant-amplitude loading conditions. The simulations were made on both 2024-T3 aluminum alloy and 4340 steel specimens. Some typical results on the aluminum alloy are shown in Fig. 3. Here a constraint factor $\alpha = 2$ (near plane-strain conditions) was applicable at low crack-growth rates. This figure shows the applied stress plotted against the plastic crack-tip displacement for loading and unloading (no crack growth was allowed in the model during this load cycle). These results are quite similar to the remarkable experimental measurements made by Bichler and Pippan [*19*] on near-crack-tip cyclic deformations. The solid symbol on the loading curve shows the crack-opening stress (S_o) and the arrow indicates the closure stress (S_c) during unloading. The traditional effective stress range, ΔS_{eff}, was calculated

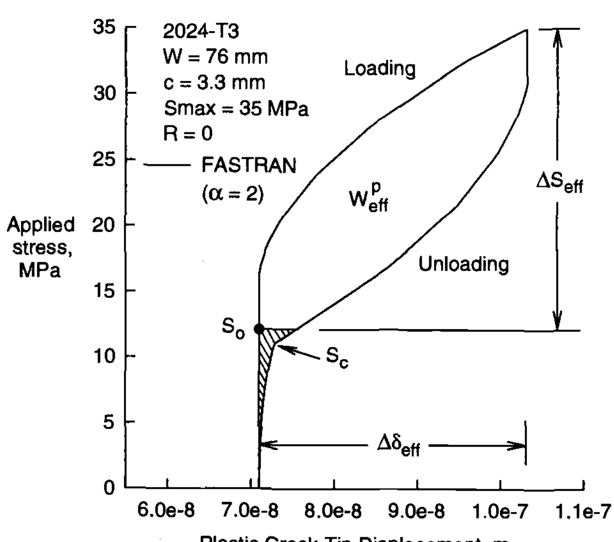

FIG. 3—*Calculated cyclic plastic crack-tip deformations under constant-amplitude loading.*

from the difference between S_{max} and S_o. The effective cyclic crack-tip displacement ($\Delta\delta_{eff}$) is given by the difference between the maximum and minimum plastic displacements. The total cyclic crack-tip hysteresis energy W^p_{eff} was given by the area between the loading and unloading curves. The cross-hatched region is the cyclic plastic deformations that occur at applied stresses below the crack-opening stress. Thus, there is cyclic plasticity below the crack-opening stress. However, the cross-hatched area is a small percentage of the total (here it is only about 3.5% of the total area). For large-scale yielding conditions, the cross-hatched area becomes a larger percentage of the total, but here nonlinear fracture-mechanics parameters, such as ΔJ_{eff}, are needed to correlate crack-growth-rate data. However, for the Paris crack-growth regime, the effects of cyclic plasticity below the crack-opening stress on crack-growth rates are small and can be neglected. For the calculations made on the aluminum alloy and steel, the influence of cyclic plasticity below the opening load on crack-growth rates was estimated to be less than about 5%, assuming that crack-growth rates are nearly linearly related to the cyclic hysteresis energy.

The concept of using cyclic crack-tip displacements to characterize crack-growth rate behavior has been applied for many years (see Weertman [*10*] and Tomkins [*11*]). It is thought that the cyclic crack-tip displacement is a more fundamental parameter to characterize crack-tip damage. To evaluate the differences induced by using the traditional ΔK_{eff} concept, crack-growth simulations were made on aluminum alloy and steel specimens assuming that the material behaves under a simple power-law relation in terms of ΔK_{eff}. The crack-growth constants for the two materials are given in Fig. 4. The n-power on the aluminum alloy was 4 and on the steel was 2. The respective constraint factors ($\alpha = 2$ for aluminum alloy and $\alpha = 2.5$ for steel) are the values needed to correlate stress-ratio data on these materials using ΔK_{eff}. Simulations were made over a wide range in stress ratio ($R = -1$ to 0.8). Figure 4 shows the elastic modulus (E) times the effective cyclic crack-tip displacement ($\Delta\delta_{eff}$) plotted against the predicted crack-growth rate from ΔK_{eff}. The results are remarkably linear over several orders of magnitude in rates with the slope on the aluminum alloy being 2 and the steel being unity. These results are reasonable because the crack-tip displacement is related to the square of the stress-intensity factor for small-scale yielding. But these results do show a

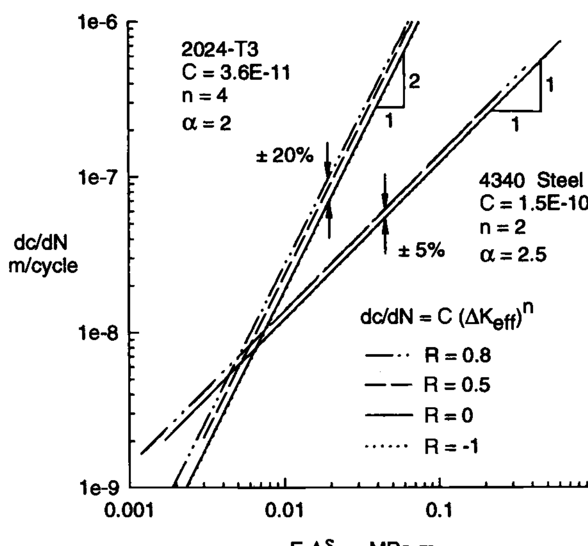

FIG. 4—*Calculated elastic modulus times effective cyclic crack-tip displacement against crack-growth rate for an aluminum alloy and steel over a wide range of stress ratios.*

slight spread in the results for various R ratios. The aluminum alloy would correlate within $\pm 20\%$ on rates whereas the steel would correlate within $\pm 5\%$ on rates. Part of this discrepancy may be due to neglecting the elastic contribution to the cyclic crack-tip displacement, in that the high R ratio simulations would have had a slightly higher elastic displacement than the low R ratio results. (Rigid plastic elements are used in the strip-yield model.) But, these results show that the traditional ΔK_{eff} and the effective cyclic crack-tip displacements are essentially equivalent concepts in the Paris crack-growth regime.

Remote CMOD Evaluations of Crack-Tip Opening Stresses and Effective Stress-Intensity Factor Ranges

The ability to measure the true crack-opening load has been a very difficult task. Nonlinearities in displacement or strain measurement systems and electronic noise have contributed to this problem. In addition, the crack-closure process is three-dimensional in nature with more closure occurring at and near the free surface than in the interior [*20*]. On the other hand, the two-dimensional strip-yield or finite-element models have a unique crack-opening load. Thus, the 2D models may be used to study the various methods of determining the crack-opening loads and crack-tip parameters. But the 3D analyses are ultimately needed to assess the best method to experimentally determine the most appropriate opening load to use in defining an effective crack-front parameter to characterize fatigue-crack growth (see Riddell et al. [*21*]).

In the following, the strip-yield model will be used to evaluate current and newly developed methods to determine either crack-opening loads or the effective stress-intensity factor ranges. Remote crack-mouth-opening displacements will be used to determine the crack-tip opening loads from reduced CMOD [22] and compliance-offset [ASTM Test Method for Measurement of Fatigue Crack Growth Rates (E 647-95a)] methods, and an alternative ΔK_{eff} from the adjusted-compliance-ratio method [*7*] under constant-amplitude loading. Comparison between measured and computed crack-opening loads will be made under a single-spike overload condition.

Constant-Amplitude Loading

Reduced CMOD Method—Crack-growth analyses were performed on a 2024-T3 aluminum alloy M(T) specimen under nearly plane-stress conditions ($\alpha = 1.2$) for constant-amplitude loading ($R = 0$). The CMOD traces from loading and unloading for three different crack lengths are shown in Fig. 5. The solid symbols are the calculated crack-opening stresses S_o determined from the contact stresses at minimum load. The S_o values were essentially independent of crack length. These results illustrate why it is very difficult to determine the opening load from the very linear applied stress against CMOD records. Because there are global elastic deformations below the opening load for measurement method away from the crack tip, it is apparent why some researchers [*6*] have assumed that there is additional crack-tip deformations below the opening load.

As Elber [22] had pointed out many years ago, the reduced displacement technique is require to extract the crack-opening load from the nearly linear CMOD record. The applied stress against reduced CMOD are shown in Fig. 6 for the largest crack length considered. The true opening load is obtained from the loading record when the loading curve becomes vertical. Again, the solid symbol is the opening load computed from the contact stresses at the minimum load. Here the computed opening load is slightly lower than the true opening load.

The crack-opening load determined from the reduced CMOD method from the 2D crack-growth simulations is independent of measurement location. Crack-opening loads determined from various local and remote measurement locations produced the same crack-opening loads. Thus numerically, the crack-opening load can be determined from any measurement location in a cracked body. However, from a testing standpoint, the amplification of the reduced CMOD record may be such that experimental noise may prevent reliable determination of the true opening load.

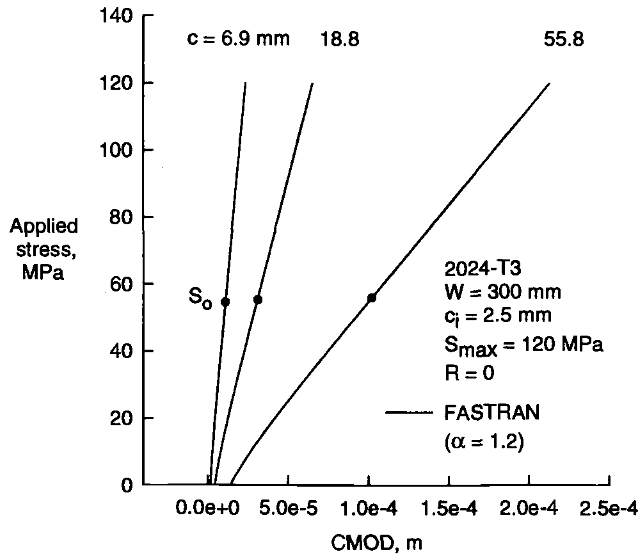

FIG. 5—*Calculated crack-mouth opening displacement under constant-amplitude loading for several crack lengths.*

CMOD Compliance Offset Method—Figure 7 shows the CMOD compliance offset record for the largest crack length considered in the previous example. The 1% and 2% offset values, commonly used in practice, produce crack-opening values that are considerably lower than the true opening stress. It is apparent from these calculations why the offset method is not able to correlate fatigue-crack-growth-rate data [7]. In addition, crack-opening loads from the 1% or 2% offset method have also been shown to be dependent upon the measurement location [7].

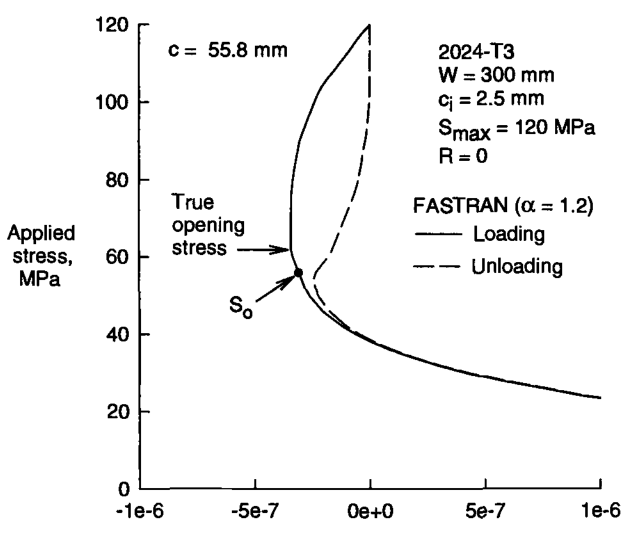

FIG. 6—*Calculated reduced crack-mouth opening displacement under constant-amplitude loading.*

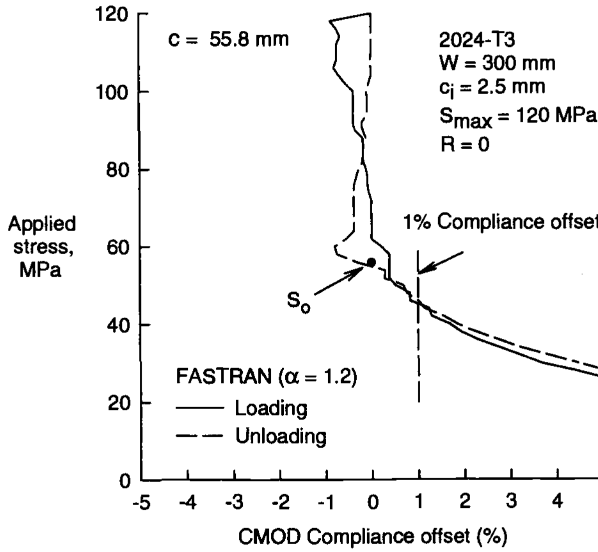

FIG. 7—*Calculated CMOD compliance offset under constant-amplitude loading.*

Adjusted Compliance Ratio Method—Recently, a new method to determine an effective stress-intensity factor range has been introduced to help overcome some of the difficulties with the compliance offset method. This method is called the Adjusted Compliance Ratio (ACR) method [*23*]. The ACR $= U_{ACR} = (C_s - C_i)/(C_o - C_i)$ where C_s is the secant compliance (from minimum to maximum load), C_o is the compliance above the opening load, and C_i is the compliance prior to initiation of a crack. C_i is assumed to be the compliance of the initial sawcut or notch in the specimen. The effective stress-intensity factor range is defined as $\Delta K_{eff} = U_{ACR}\,\Delta K$. To compare ΔK_{eff} from ACR and the traditional crack-opening concept, a crack-growth simulation was performed on an M(T) specimen made of 2024-T3 aluminum alloy under nearly plane-stress conditions at $S_{max} = 120$ MPa at $R = 0$. The specimen had an initial crack length (or sawcut) of 6.4 mm and a total width (W) of 76 mm. Figure 8 shows the U values plotted against crack length from ACR (U_{ACR}, dashed curve) and from crack-opening theory (solid curve) where $U_{op} = (K_{max} - K_o)/(K_{max} - K_{min})$. At crack length *A,* the U values are nearly equal and the rate is 1.1E-6 m/cycle based on Eq 2. This is the reference point, since the U values and rates are equal. At crack length *B,* based on crack-opening theory, the rate reaches a minimum of 4.5E-7 m/cycle, and at crack length *C* the rate is 8E-7 m/cycle (rate is still less than that at point A). These changes in rate are consistent with experimental measurements made on 2024 aluminum alloy for a crack initiating at a sawcut or notch; see Broek [*24*]. However, the ACR method predicts that the rates at point B and C are greater than that at point A, since ΔK_{ACR} and K_{max} values are greater at point B and C than at point A. Thus, the ACR method currently cannot explain the crack-growth transients for a crack initiating at a sawcut or notch. Whether the ACR method gives a more fundamental effective stress-intensity factor range than the traditional crack-closure concept must await further evaluations.

Single-Spike Overload

Wu and Schijve [*25*] have measured crack-opening stresses under single-spike overloads and underloads using the reduced CMOD method. The crack-closure model was used to simulate crack growth under these conditions [*26*]. The predicted crack-growth delays due to overloads and under-

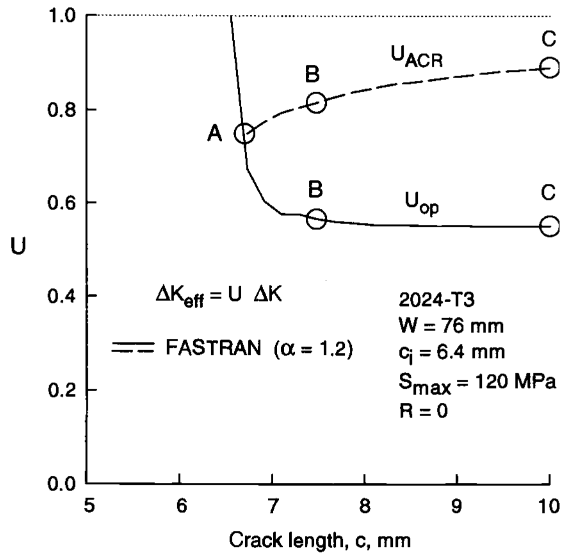

FIG. 8—*Calculated effective stress-intensity factors under constant-amplitude loading using traditional and adjusted compliance ratio methods.*

loads were in good agreement with the experimental measurements. Figure 9 shows the remote CMOD record for the spike overload simulation at some point after the application of the overload. The test was conducted at a constant-amplitude loading with S_{max} = 100 MPa at R = 0 and a factor of two overload was applied when the crack reached 6 mm. The solid curve shows the calculated loading and unloading curves. The dashed line is the slope of the loading curve above the calculated

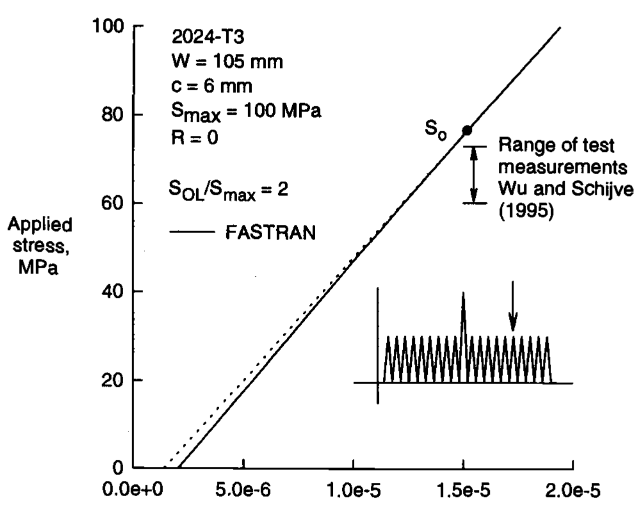

FIG. 9—*Calculated CMOD after a single-spike overload and comparison of measured and calculated crack-opening stresses.*

crack-opening load (solid symbol). The range of measured crack-opening stresses is as indicated by the arrows. This range was lower than the calculated value but significantly above the value measured under constant-amplitude loading (about 40 MPa).

A comparison of calculated reduced CMOD for the constant-amplitude (dashed curve) and single-spike overload (solid curve) is shown in Fig. 10. The solid symbol and arrow show the crack-opening stress for constant-amplitude and spike overload, respectively. These results demonstrate why it may be easier to measure the opening loads under spike overloads because a large compliance change occurs when the crack surface separates following the spike overload.

Effects of K_{max} on Crack Growth in Aluminum Alloys

In the past few years, the study of K_{max} effects on crack-growth rates has intensified [*4,7–9*]. However, the study of these effects is not new; see Paris and Erdogan [*27*]. From the early 1960's, many researchers had seen these effects and they referred to them as K_{max} or stress-level effects. Numerous equations have been proposed to account for these effects on crack-growth rates, even in the presence of crack closure. But why are researchers seeing more K_{max} effects? First, specimen sizes that are being used in the laboratory are becoming smaller, tests are being conducted at very high R ratios (greater than 0.7), and K_{max} values are approaching the elastic fracture toughness of the cracked specimen and material.

Herein, the K_{max} effect will be studied on two sets of data on 2024 aluminum alloy. The first dataset is a recent study [*9*] on small, extended compact, EC(T), specimens (W = 76 mm) tested at low ΔK values but over a very wide range in stress ratios. The second dataset [*28*] was conducted on large M(T) specimens (W = 305 mm) at low and high R ratios but at extremely high stress levels (0.6 to 0.75 σ_{ys}).

The effective stress-intensity factor range against crack-growth rate data for the 2024-T3 aluminum alloy used in these two studies [*9,28*] is shown in Fig. 11. These data were obtained from Hudson [*29*] and Phillips [*30*] over a wide range in stress ratio (symbols). An assessment of these data indicated that there were no K_{max} effects in these data because of the low R ratios tested and that K_{max}

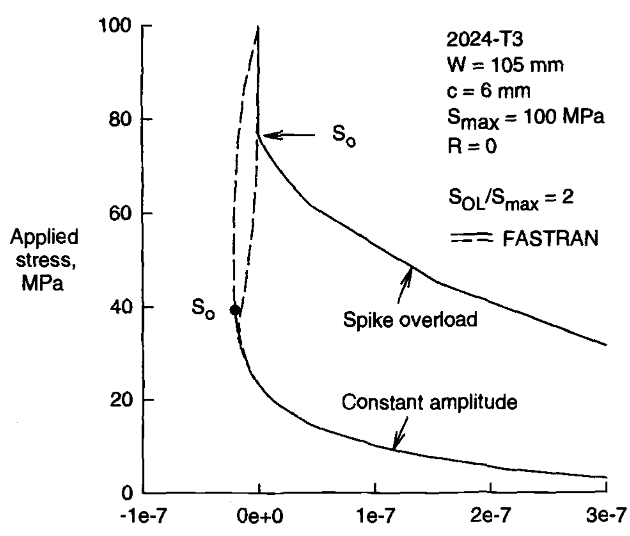

FIG. 10—*Comparison of reduced CMOD for constant-amplitude and single-spike overload conditions.*

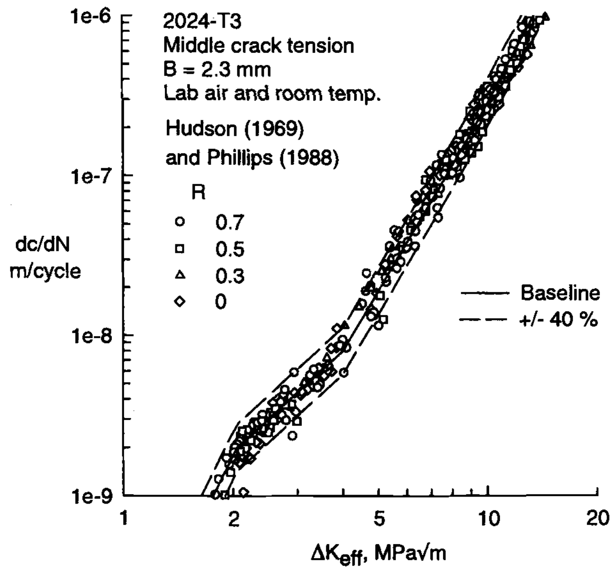

FIG. 11—*Effective stress-intensity factor range against crack-growth rate for a thin-sheet aluminum alloy for a wide range in stress ratios.*

was less than 0.3 of the elastic fracture toughness for these tests. The solid curve is the baseline curve used in the subsequent analyses and the dashed curves show the scatter ($\pm 40\%$) that is typical of these type of data correlation. The data have been shown over only three orders of magnitude in rates, because this covers the rate range measured by Riddell and Piascik [9] in their constant-ΔK tests. In the crack-growth analyses, Eq 2 was used to model crack growth. Because transitions or slope changes occur in the data (such as the rate data below 1E-8 m/cycle), the coefficient C and power n are a function of rate range. Because large-crack thresholds are not relevant to the subsequent calculations and the subject is beyond the scope of the present paper, $G = 1$ in Eq 2. The function $H = 1 - (K_{max}/C_5)^q$ accounts for the rapid crack-growth rates observed as K_{max} approaches the elastic fracture toughness. The parameter C_5 is the cyclic elastic fracture toughness, like K_c. But before the crack-growth analyses are made, a methodology to predict the elastic fracture toughness, as a function of crack length and width, needs to be considered.

The elastic fracture toughness (K_{Ie}) for compact C(T) specimens made of the 2024-T3 material is shown in Fig. 12. K_{Ie} is calculated from the initial crack length (before stable tearing) and the maximum failure load. (This is consistent with the way K_{max} is calculated in current fatigue-crack-growth analyses.) The solid symbols are test data on C(T) specimens for various specimen widths (w). The solid curve is the Two-Parameter Fracture Criterion (TPFC) [*31*] with a value of K_F and m chosen to fit these data. The TPFC equation is

$$K_F = K_{Ie}/[1 - m\,(S_n/S_u)] \text{ for } S_n < \sigma_{ys} \quad (3)$$

where K_F and m are the two fracture parameters, S_n is the nominal stress, and S_u is the nominal stress at the plastic-hinge condition using the ultimate tensile strength (σ_u). The upper dotted curve is the values of K_{Ie} at the plastic-hinge condition using the yield stress (nominal stress S_n calculated at the crack tip is 1.61 σ_{ys} under these conditions). The dashed curve is the condition when the nominal stress is equal to the yield stress. The open symbol shows the estimated elastic fracture toughness for

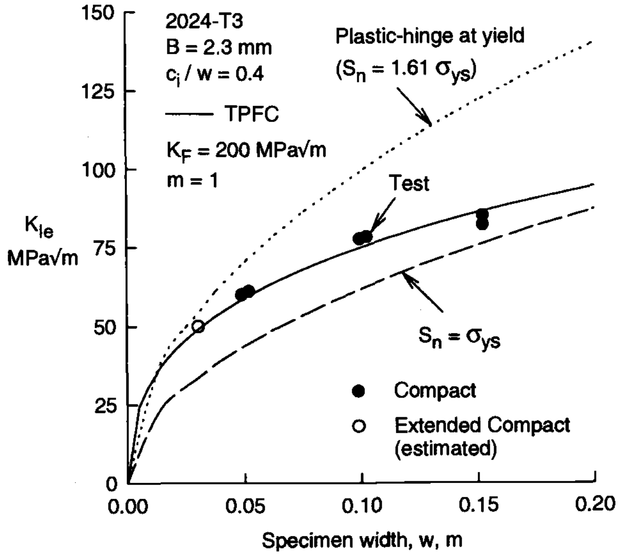

FIG. 12—*Elastic fracture toughness as a function of specimen width for compact specimens.*

a small extended compact specimen (w = 38.1 mm at c_i/w = 0.4). This value, $K_{Ie} = K_c = C_5 = 50$ MPa$\sqrt{m}$, will be used in the crack-growth analyses. For a given specimen width (w = 38.1 mm), the elastic fracture toughness is a function of crack length, as shown in Fig. 13, for the extended compact specimen. The K solution for the extended compact specimen was obtained from Piascik and Newman [*32*]. Here the values of K_F and m from the compact specimens were used in the TPFC analysis to predict crack length effects for the extended compact specimen. The arrow along the c/w axis

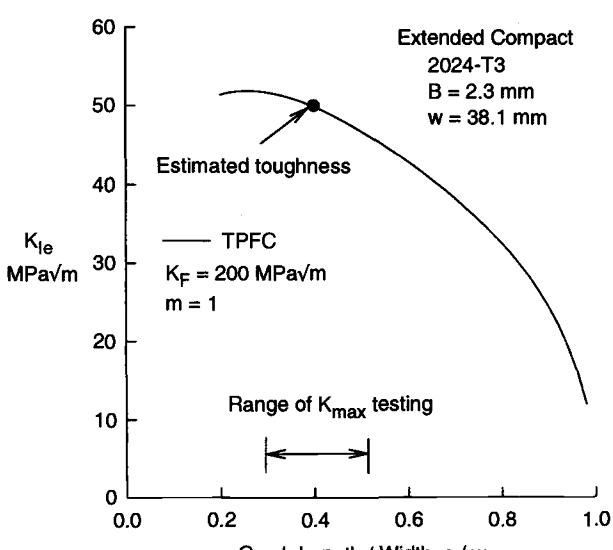

FIG. 13—*Calculated elastic fracture toughness for extended compact tension specimens.*

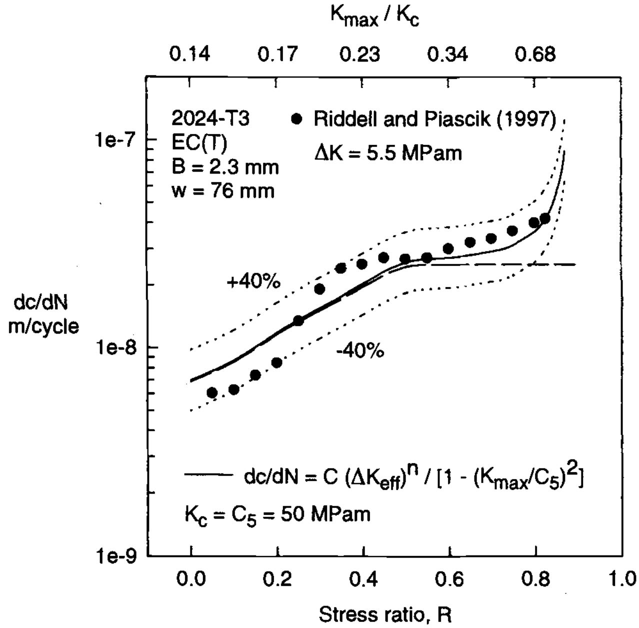

FIG. 14—*Comparison of measured and calculated crack-growth rates at constant* ΔK *value.*

shows the range of testing in Ref *9*, and the solid symbol is the estimated elastic fracture toughness used in the crack-growth analyses. These results show that K_{max} effects may intensify for larger crack lengths because the elastic fracture toughness drops sharply.

Riddell and Piascik [*9*] tested small extended compact specimens under constant-ΔK values for a very wide range in stress ratios. Some typical results at 5.5 MPa$\sqrt{m}$ are shown in Fig. 14 as the solid symbols. The upper axis shows the ratio of K_{max}/K_c for these test data. The solid curve is the predicted results from Eq 2 where the power on the K_{max}/C_5 ratio was $q = 2$. The power of $q = 2$ had been previously selected for aluminum alloys [*15*]. The dotted lines show the ±40% scatterband about the solid curve. All of the test data fall within the scatterband. For comparison, the dashed curve shows the calculated results using only ΔK_{eff} without the K_{max} term.

Figure 15 shows how different values of the power q affect the predicted crack-growth rates. When $q = \infty$, the K_{max} term is eliminated, but when $q = 1$, rates are affected at all stress ratios. Because of the scatter in the test data, a q value of 1.5 to 2 seems to fit the data reasonably well. Constant-ΔK test results at lower and higher ΔK values are shown in Fig. 16 with the predicted results from Eq 2 with and without the K_{max} term. Comparisons between test data and predicted results (solid curves) are reasonable.

Dubensky [*28*] tested M(T) specimens ($W = 305$ mm) over a wide range in stress ratios ($R = 0$ to 0.7) and at extremely high values of applied stress (0.6 σ_{ys} to σ_{ys}). For clarity, only some of his data (symbols) are shown in Fig. 17 as ΔK plotted against measured rate. The open symbols are high R ratio data (nonclosure conditions from the analysis) and the solid symbols are low R ratio data. The dotted curve is the ΔK_{eff} baseline curve, an extension of the baseline curve from Fig. 11, developed from data by Hudson [*29*] and Phillips [*30*]. Below a rate of 1E-7 m/cycle, plane-strain conditions prevail ($\alpha = 2$) and for rates greater than 2.5E-6 m/cycle, plane-stress conditions prevail ($\alpha = 1$). (See Ref *33* for further information about constraint variations for this material.) The solid and dashed curves are the predicted ΔK against rate results from FASTRAN for the specimens tested at low and high R

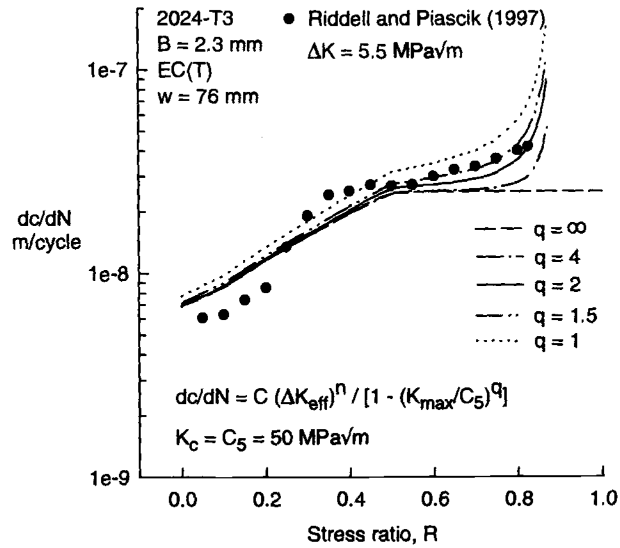

FIG. 15—*Influence of the power on* K_{max}/K_c *ratio on crack-growth rates.*

ratios. These results show that K_{max} or stress-level effects are present even at low stress ratios, if the tests are conducted at high applied stress levels, because the test data and predicted curve are not parallel to the baseline curve (dotted curve). Note that these tests were cycled to failure and that the cyclic fracture toughness K_F (chosen to fit the asymptotes) is considerably higher than the static value (K_F = 267 MPa$\sqrt{m}$) reported in Ref *31*.

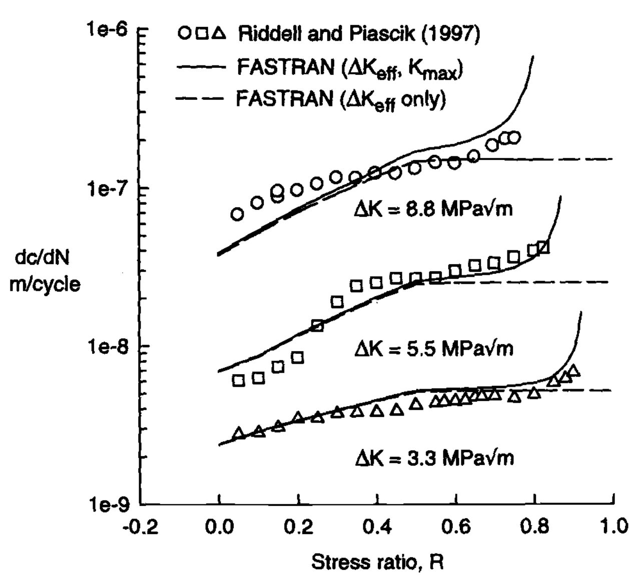

FIG. 16—*Comparison of measured and calculated rates for various* ΔK *values.*

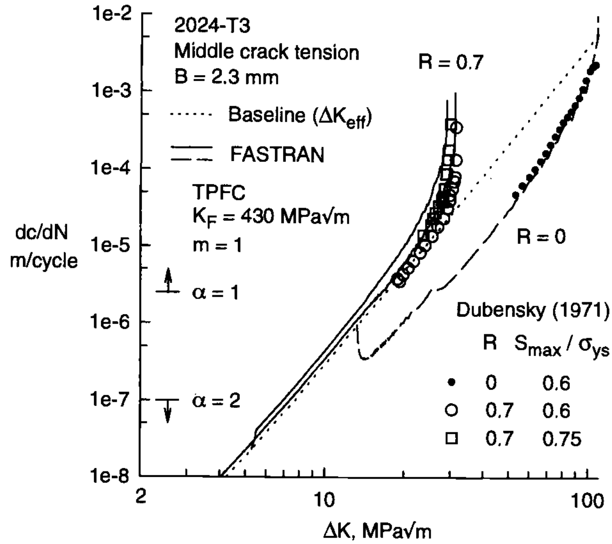

FIG. 17—*Measured and calculated crack-growth rates for high stress levels at low and high stress ratios on an aluminum alloy.*

In efforts to determine the appropriate crack-driving parameters, Vasudevan and Sadananda [*4,5*] and Donald et al. [*7,23*] plotted ΔK against K_{max} at constant crack-growth rates, as shown in Fig. 18. These data (symbols) were obtained from Donald [*23*] on 2024-T351 aluminum alloy compact specimens tested at a very high humidity. The tests were conducted under the ΔK-reduction procedure (ASTM E 647), which may induce other forms of closure, such as roughness or oxide-debris, in ad-

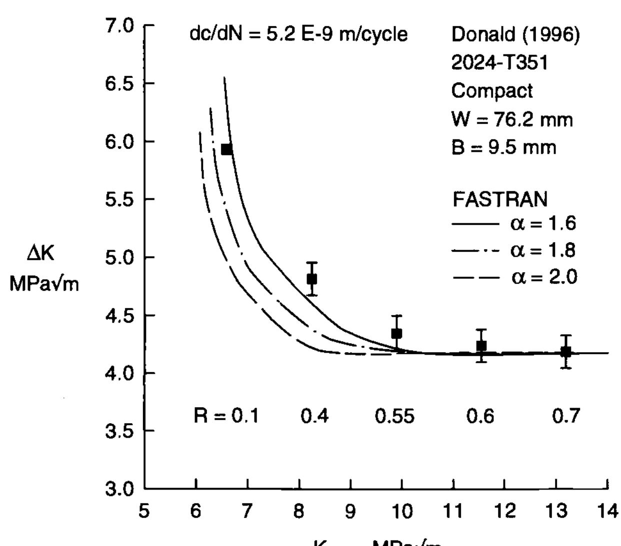

FIG. 18—*Measured and calculated crack-growth rates on an aluminum alloy under high humidity near threshold conditions.*

dition to plasticity from load-history effects. This crack-growth rate (5.2E-9 m/cycle) is slightly above the threshold region for this alloy. The effective stress-intensity factor range against rate baseline curve for this material and humidity was obtained from the $R = 0.7$ results ($\Delta K = \Delta K_{eff}$). The curves are calculated from the plasticity-induced crack-closure model for various values of constraint. Plane-strain conditions, such as $\alpha = 2$, are expected to prevail at the low crack-growth rate but lower values of α are required to fit the test data. These results illustrate a deficiency with the current plasticity model in that other forms of closure such as fretting-oxide-debris- and roughness-induced closure are not accounted for in the model. At present, a higher value of α is required to account for these additional sources of closure. Further study is needed in the threshold regime to develop a model which includes the three major forms of closure.

Conclusions

(1) For small-scale yielding conditions, the ΔK_{eff} crack-growth rate relation is directly related to the effective cyclic crack-tip-opening displacement ($\Delta\delta_{eff}$) over a wide range of stress ratios (-1 to 0.8) for aluminum alloy and steel.

(2) Based on the cyclic crack-tip hysteresis energy and the plasticity-induced crack-closure model, the crack-tip damage for applied stresses less than the "crack-opening" stress is negligible (less than 5% affect on crack-growth rates) for the Paris crack-growth regime.

(3) The compliance offset method (for 1% to 2% offset) measures significantly lower crack-opening stresses than physically occur in the crack-closure model.

(4) The effective stress-intensity factor range calculated from the crack-closure model for the adjusted compliance ratio method produces crack-growth rate trends opposite from those calculated from the traditional method for a crack initiating from a sawcut or notch.

(5) Effects of K_{max} on crack-growth rates can become significant when the specimen size becomes small (elastic fracture toughness becomes small), as stress ratios approach unity, and as the K_{max}/K_c ratio becomes greater than about 0.5.

References

[1] Elber, W., "The Significance of Fatigue Crack Closure," *Damage Tolerance in Aircraft Structures, ASTM STP 486*, American Society for Testing and Materials, 1971, pp. 230–242.

[2] Walker, N. and Beevers, C. J., "A Fatigue Crack Closure Mechanism in Titanium," *Fatigue and Fracture of Engineering Materials and Structures*, Vol. 1, No. 1, 1979, pp. 135–148.

[3] Paris, P. C., Bucci, R. J., Wessel, E. T., Clark, W. G., and Mager, T. R., "Extensive Study of Low Fatigue Crack Growth Rates in A533 and A508 Steels," *ASTM STP 513*, American Society for Testing and Materials, 1972, pp. 141–176.

[4] Vasudevan, A. K. and Sadananda, K., "Classification of Fatigue Crack Growth Behavior," *Metallurgical and Materials Transactions A*, Vol. 26A, May 1995, pp. 1221–1234.

[5] Sadananda, K. and Vasudevan, A. K., "Analysis of Fatigue Crack Closure and Thresholds," *Fracture Mechanics: 25th Volume, ASTM STP 1220*, F. Erdogan, Ed., American Society for Testing and Materials, 1995, pp. 484–501.

[6] Chen, D. L., Weiss, B., and Stickler, R., "A New Evaluation Procedure for Crack Closure," *International Journal of Fatigue*, Vol. 13, No. 4, 1991, pp. 327–331.

[7] Donald, J. K., Bray, G. H., and Bush, R. W., "An Evaluation of the Adjusted Compliance Ratio Technique for Determining the Effective Stress Intensity Factor," *Fracture Mechanics: 29th Volume, ASTM STP 1331*, T. L. Panontin and S. D. Sheppard, Eds., American Society for Testing and Materials, 1997.

[8] Marci, G., "Failure Mode Below 390K with IMI 834," *Fatigue '96 Proceedings of the Sixth International Fatigue Congress*, Berlin, G. Lütjering and H. Nowack, Eds., Vol. I, pp. 493–498.

[9] Riddell, W. and Piascik, R. S., "Stress Ratio Effects on Crack Opening Loads and Crack Growth Rates in Aluminum Alloy 2024," *Fracture Mechanics: 29th Volume, ASTM STP 1331*, T. L. Panontin and S. D. Sheppard, Eds., American Society for Testing and Materials, 1997.

[10] Weertman, J., "Rate of Growth of Fatigue Cracks Calculated from the Theory of Infinitesimal Dislocations Distributed on a Crack Plane," *International Journal of Fracture*, Vol. 2, 1966, pp. 460–467.

[11] Tomkins, B., "Fatigue Crack Propagation—An Analysis," *Philosophical Magazine*, Vol. 18, 1968, pp. 1041–1066.

[12] Ogura, K., Miyoshi, Y., and Nishikawa, I., "Fatigue Crack Growth and Closure of Small Cracks at the Notch Root," *Current Research on Fatigue Cracks,* T. Tanaka, M. Jono, and K. Komai, Eds., Society of Materials Science, Japan, 1985, pp. 57–78.
[13] Dowling, N. E. and Begley, J. A., "Fatigue Crack Growth During Gross Plasticity and the J-Integral," *Mechanics of Crack Growth, ASTM STP 590,* American Society for Testing and Materials, 1976, pp. 82–103.
[14] Dugdale, D. S., "Yielding of Steel Sheets Containing Slits," *Journal of the Mechanics and Physics of Solids,* Vol. 8, 1960, pp. 100–104.
[15] Newman, J. C., Jr., "A Crack-Closure Model for Predicting Fatigue Crack Growth under Aircraft Spectrum Loading," *Methods and Models for Predicting Fatigue Crack Growth under Random Loading, ASTM STP 748,* J. B. Chang and C. M. Hudson, Eds., American Society for Testing and Materials, 1981, pp. 53–84.
[16] Newman, J. C., Jr., "FASTRAN-II—A Fatigue Crack Growth Structural Analysis Program," NASA TM 104159, Feb. 1992.
[17] Blom, A. R., Wang, G. S., and Chermahini, R. G., "Comparison of Crack Closure Results Obtained by 3D Elastic-Plastic FEM and Modified Dugdale Model," *Localized Damage: Computer-Aided Assessment and Control,* M. H. Aliabadi et al., Eds., Computational Mechanics Publications, Springer-Verlag, Berlin, 1990, pp. 57–68.
[18] Newman, J. C., Jr., "Finite-Element Analysis of Crack Growth under Monotonic and Cyclic Loading," *Cyclic Stress-Strain and Plastic Deformation Aspects of Fatigue Crack Growth, ASTM STP 637,* American Society for Testing and Materials, 1977, pp. 56–80.
[19] Bichler, C. and Pippan, R., this volume, pp. 191–206.
[20] Chermahini, R. G., Shivakumar, K. N., and Newman, J. C., Jr., "Three-Dimensional Finite-Element Simulation of Fatigue Crack Growth and Closure," *Mechanics of Fatigue Crack Closure, ASTM STP 982,* J. C. Newman, Jr. and W. Elber, Eds., American Society for Testing and Materials, 1988, pp. 398–413.
[21] Riddell, W. T., Piascik, R. S., Sutton, M. A., Zhao, W., McNeill, S. R., and Helm, J. D., this volume, pp. 157–174.
[22] Elber, W., "Crack-Closure and Crack-Growth Measurements in Surface-Flawed Titanium Alloy Ti-6A1-4V," NASA TN D-8010, National Aeronautics and Space Administration, Washington, DC, Sept. 1975.
[23] Donald, J. K., "Introducing the Compliance Ratio Concept for Determining Effective Stess Intensity," First International Conference on Fatigue Damage in Structural Materials," Hyannis, MA, Sept. 22–27, 1996.
[24] Broek, D., "The Propagation of Fatigue Cracks Emanating from Holes," National Aerospace Laboratory, NLR Technical Report 72134U, 1972.
[25] Wu, Yisheng and Schijve, J., "Fatigue Crack Closure Measurements on 2024-T3 Sheet Specimens," *Fatigue and Fracture of Engineering Materials and Structures,* Vol. 18, 1995, pp. 917–921.
[26] Newman, J. C., Jr., "Crack Growth under Variable Amplitude and Spectrum Loading in 2024-T3 Aluminum Alloys," *Proceedings of the Symposium on High Cycle Fatigue of Structural Materials,* TMS-ASM Fall Meeting, Indianapolis, IN. The Metallurgical Society-American Society for Metals, Sept. 16–18, 1997.
[27] Paris, P. C. and Erdogan, F., "Critical Analysis of Crack Propagation Laws," *Transactions of ASME, Journal of Basic Engineering,* Vol. 85, 1963, pp. 528–534.
[28] Dubensky, R. G., "Fatigue Crack Propagation in 2024-T3 and 7075-T6 Aluminum Alloys at High Stress," NASA CR-1732, National Aeronautics and Space Administration, Washington, DC, 1971.
[29] Hudson, C. M., "Effect of Stress Ratio on Fatigue-Crack Growth in 7075-T6 and 2024-T3 Aluminum Alloy Specimens," NASA TN D-5390, National Aeronautics and Space Administration, Washington, DC, 1969.
[30] Phillips, E. P., "The Influence of Crack Closure on Fatigue Crack Growth Thresholds in 2024-T3 Aluminum Alloy," *Mechanics of Fatigue Crack Closure, ASTM STP 982,* J. C. Newman, Jr. and W. Elber, Eds., American Society for Testing and Materials, 1988, pp. 505–515.
[31] Newman, J. C., Jr., "Fracture Analysis of Various Cracked Configurations in Sheet and Plate Materials," *Properties Related to Fracture Toughness, ASTM STP 605,* American Society for Testing and Materials, 1976, pp. 104–123.
[32] Piascik, R. S. and Newman, J. C., Jr., "An Extended Compact Tension Specimen for Fatigue Crack Growth and Fracture Testing," *International Journal of Fracture,* Vol. 76, 1996, pp. R43–R48.
[33] Newman, J. C., Jr., "Effects of Constraint on Crack Growth under Aircraft Spectrum Loading," *Fatigue of Aircraft Materials,* A. Beukers, T. deJong, J. Sinke, A. Vlot, and L. B. Vogelesang, Eds., Delft University Press, 1992, pp. 83–109.

Michael A. Sutton,[1] Wei Zhao,[1] Stephen R. McNeill,[1] Jeffrey D. Helm,[1] Robert S. Piascik,[2] and William T. Riddell[2]

Local Crack Closure Measurements: Development of a Measurement System Using Computer Vision and a Far-Field Microscope

REFERENCE: Sutton, M. A., Zhao, W., McNeill, S. R., Helm, J. D., Piascik, R. S., and Riddell, W. T., **"Local Crack Closure Measurements: Development of a Measurement System Using Computer Vision and a Far-Field Microscope,"** *Advances in Fatigue Crack Closure Measurement and Analysis: Second Volume, ASTM STP 1343,* R. C. McClung and J. C. Newman, Jr., Eds., American Society for Testing and Materials, West Conshohocken, PA, 1999, pp. 145–156.

ABSTRACT: An accurate and relatively simple methodology for estimating crack closure loads has been developed. Using this method, measurements may be taken at a user-specified position behind the crack tip during the entire fatigue crack growth process. The methodology has three distinct components: (*a*) an imaging system having adequate magnification with minimal distortion, (*b*) a simple, Windows-based procedure for image acquisition and image analysis, and (*c*) techniques for applying a random, high contrast pattern on the specimen's surface.

To meet the imaging requirements, a far-field microscope objective capable of high magnifications was employed to image small regions on the order of 0.5 mm by 0.5 mm. The regions were near the crack tip. To meet the requirements of a user-friendly system, a Windows-based data-acquisition interface was developed to run the system on a common PC. Using the interface, images are acquired automatically during a loading/unloading cycle and stored digitally. Image analysis is performed on the saved images to rapidly obtain the crack opening displacement as a function of load; these data are used to estimate the crack closure load. Finally, two methodologies for applying a random, high-contrast pattern with average sizes of 4 to 20 μm were developed. The first method uses 11 μm filter paper and a low-pressure compressed air supply to apply small particles of photocopier toner powder to the surface of the specimen. The second method uses contact lithography to achieve a random pattern with smaller feature sizes, on the order of 2 to 8 μm.

Baseline tests of the overall system have demonstrated that it is both easy to use and accurate. Specifically, (*a*) the PC interface has demonstrated that images can be acquired automatically while the loading frame is cycling at 0.01 Hz, and (*b*) the crack tip opening displacement data have been shown to have errors on the order of 0.05 pixels for the toner powder patterns, corresponding to 27 nm for the magnification used.

KEYWORDS: fatigue crack closure, crack opening displacement, random speckle pattern, computer vision, two-dimensional digital image correlation

Crack closure is a well-documented phenomenon that has been shown to have a strong effect on fatigue crack growth behavior. As first discussed by Elber [*1,2*], fatigue cracks in metallic materials

[1] Professor, adjunct professor, associate professor, and Ph.D. candidate, respectively, Department of Mechanical Engineering, University of South Carolina, Columbia, SC 29208.

[2] Senior research scientist and National Research Council resident research associate, respectively, Mechanics and Materials Branch, NASA Langley Research Center, Hampton, VA 23665.

can remain closed under substantial nominal tensile loading. Numerical analyses [3–6] have shown that the effect observed by Elber can be predicted by including the effects of the plastic wake that is present along the crack flanks as the crack grows. This effect, known as plasticity-induced closure, causes a deviation from the Paris Law [7], which can be modeled by using ΔK_{eff}, defined as $\Delta K_{eff} = K_{max} - K_{op}$, where K_{op} is the stress intensity factor at which the crack opens fully. In recent years, a wide variety of physical phenomena has been linked to the process of crack closure. Examples of these include roughness-induced closure [8], oxide-induced closure [9,10], viscous-fluid induced closure, and material phase transformation-induced closure [11].

To quantify the onset of closure, a variety of experimental methods has been developed to measure the crack opening displacement (COD) at various positions behind the crack tip [12]. As shown in Fig. 1, when the slope of the load-COD curve attains a lower constant value during the loading portion of the load cycle, the crack is assumed to be fully open and the crack-tip region experiences the effect of the applied load. Methods commonly used to measure COD include the replica technique, clip gages, scanning electron microscopy (SEM), interferometic strain/displacement gages (ISDG) and moiré. Each of these methods has advantages as well as disadvantages for this application. In particular, the replica technique provides a crack opening profile at a fixed load, but is not particularly useful for closure load measurements. Clip gages are relatively simple to use and provide quantitative measurements of COD at a remote position. However, the relationship of these measurements to the crack-tip response is less obvious. In this regard, it is noted that recent work by Davidson [13], using a specially designed load frame for fatigue testing in an SEM, has shown that the estimated crack closure load from COD measurements is a strong function of the location at which COD is measured, with $P_{closure} = P_{max} \{1 - m \log (d + 1)\}$, where d is measured in microns and m is an experimentally derived constant. Thus, the effects of measurement position on crack closure load estimation is important. The ISDG method employs laser light reflected from two microhardness indentations spanning the crack line to obtain an interference pattern which is used to quantify the local COD values. The method offers excellent resolution in COD (± 5 nm) when using the method in its high-resolution mode. In addition, ISDG can be used to measure displacements at elevated temperatures over a gage length less than 50 μm. The method does have some disadvantages. It may be somewhat difficult to use in typical laboratory settings. It requires well-polished specimen surfaces and lacks the ability to obtain COD at the same distance behind the crack tip during crack growth without additional indentation pairs. Moiré interferometry has been used to measure the crack-tip opening displacement (CTOD, measured in close vicinity to the crack tip, in contrast to the COD)

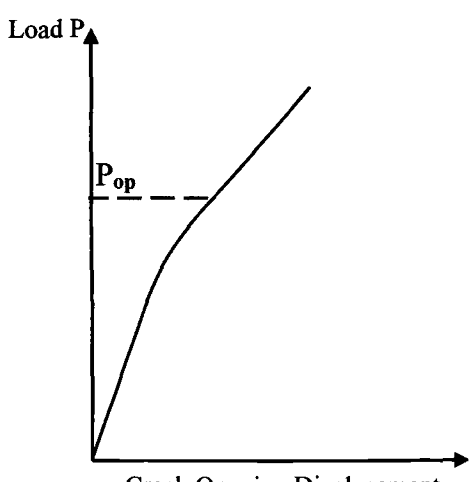

FIG. 1—*Schematic of crack closure effect.*

[14], as well as crack-tip strain fields [15–17], in recent years. The moiré method is also quite accurate and can be used to quantify CTOD along the crack line. Accuracy of $\pm p/10$ has been obtained by several investigators, where p is the pitch of the moiré grid. For a 2000 lines/mm grid, this corresponds to an accuracy of ± 50 nm. The major disadvantages with the method are its vibration sensitivity, as well as requirements for a well-polished surface, laser illumination and application of a high-resolution grating to the specimen surface.

Additional methods which have been used for quantifying the closure load include back-face and side-face strain gages [18]. Similar to the COD measurement processes, the change in gage response during the loading-unloading cycle is related to the crack opening process. These methods suffer the same drawback as ISDG since the position of the crack tip relative to the gage changes with crack growth, thereby altering the response characteristics of the gage with crack growth.

To provide a means for estimating crack closure load at a fixed distance behind the *current* crack tip location during the fatigue process, a vision-based methodology is proposed that (*a*) employs a far-field microscope to image a 0.5 mm by 0.5 mm region just behind the current crack tip location, (*b*) utilizes accepted digital image analysis methods [19,20] to determine CTOD as a function of loading, and (*c*) has a Windows-based vision interface for acquisition, storage and analysis of images to obtain the closure load measured at user-defined positions behind the crack tip. In the following sections, details of the system and estimates of the errors in the method are presented. It is noted that the proposed method can only measure displacements on the specimen surface. However, it was shown in Ref *21* that the measurements at a proper distance behind the crack tip can reflect the overall closure effect through the specimen thickness, which correlates fatigue crack growth data well.

System Development

The components of the measurement system used in this work are shown in Fig. 2. It can be seen that the system consists of a far-field microscope, a three-dimensional (3D) translation stage, a

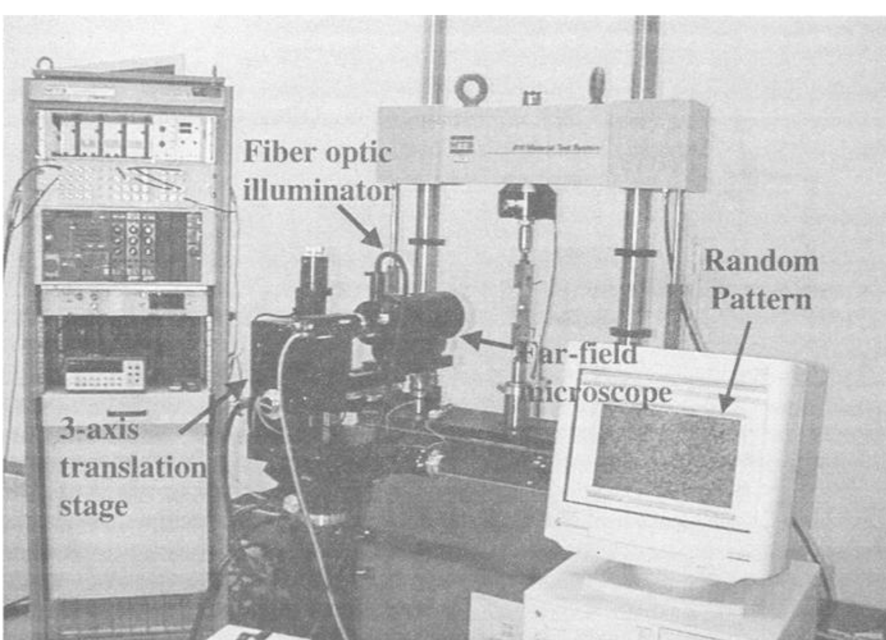

FIG. 2—*Setup of DIDS.*

charge-coupled device (CCD) camera, a fiber optic illuminator, and a Pentium PC equipped with image and data acquisition boards.

A schematic of the overall system is shown in Fig. 3. The software developed for image acquisition interfaces directly with both the image capture board and the board for sampling the load, via manufacturer-supplied dynamic-link libraries (DLLs). The 3-D translation stage is controlled by issuing commands through the serial communication port to the stepper motor controller. A detailed discussion of the software interface and its development is provided in the following section.

Image Acquisition and Analysis Interface

In general, the conversion of image data into load versus CTOD data for estimates of crack closure load has been a time-consuming process. However, since the image acquisition and analysis process (using digital image correlation algorithms) are fully computer-based, the process can be made relatively simple, efficient and rapid by development of a PC-based, image interface program. A flow chart for the program is shown in Fig. 4.

As shown in Fig. 5, the user interface (UI) was designed with ease of use by the operator as the primary objective. Thus all operations, from acquiring of images to determination of CTOD, are performed within a single, PC-Windows based, user-controlled program. The UI is written in Microsoft Visual Basic. The process of acquiring data and obtaining CTOD values within the UI is as follows.

First the user acquires image and load information for the test. About 100 images are taken during a load cycle for measuring crack closure. Images may be taken in one of two modes. The user may choose to take the sequence of images manually by pressing the acquisition command button for each image taken, or the user may take a series of images at a fixed time interval. By cycling the load frame at a slow rate (0.01 Hz) and using the timed image capture, the data necessary for the CTOD measurements may be taken in a matter of minutes. The computer also sends commands to the data acquisition board to measure the load each time an image is taken. The images are stored in a TIFF (Tagged Image File Format) with the load data stored with the image as a custom tag value. All images are stored sequentially using a generic naming procedure (filename_000.tif, filename_001.tif,

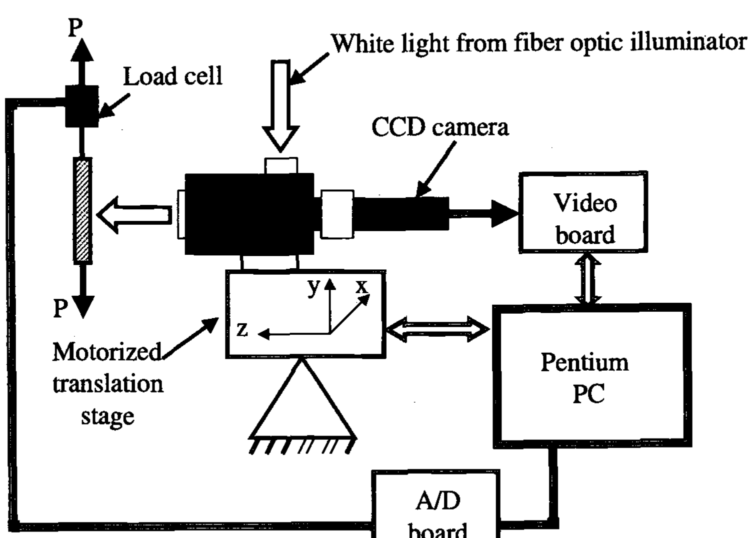

FIG. 3—*Schematic of major components of DIDS.*

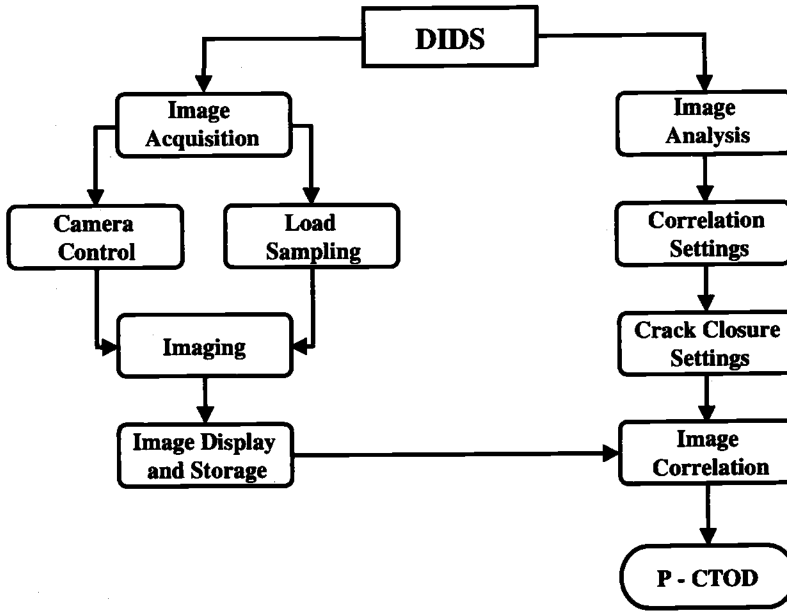

FIG. 4—*Flow chart of the DIDS.*

etc.) reducing the input required from the user. The current system supports three different types of cameras: Pulnix digital cameras, Videk Megaplus cameras and standard analog cameras.

Secondly, the images acquired by the video board are passed to the UI via the manufacturer-supplied DLL's for (*a*) display on the computer monitor and (*b*) storage on disk by the UI to minimize input from the user. The images are stored using the TIFF format, with the time and load information stored with the image in one of the tags.

Once all of the images are acquired, the displacements at user-defined locations behind the current crack tip are determined to quantify CTOD. As shown in Fig. 6, for each position behind the crack tip, the user must locate a pair of points (subsets of pixels in the image), one above and one below the crack line. The two points in a pair should be approximately on a vertical line to the crack, so that the V-component of the displacements represents the crack opening displacement. Up to six pairs of points can be analyzed at one time. Using a point-and-click procedure, an initial guess for the displacement of each point is obtained by selecting corresponding points in the images of the reference and loaded state. This is done only once for each pair of points. To determine the distance from the pair of points to the crack, the user also needs to locate the crack tip by point-and-click. Using the initial guess, the UI calls a Two-Dimensional (2D) Digital Image Correlation algorithm [*19,20*] to determine the displacements of each pair of points by sequentially correlating each of the images acquired during the loading and unloading cycle to the reference image. The 2D Digital Image Correlation algorithm [*19,20*] determines U and V displacements of a subset by establishing a best match of the subset in a loaded state to a subset in the reference state. The best match is obtained by minimizing an error function expressed in terms of gray levels representing the subsets. Automatic determination of initial guesses for subsequent images is achieved by using displacements determined for the previous images and the load increment information. Once the analyses are completed, a file is stored for each pair of the points, which contains (*a*) loads, (*b*) CTOD for the pair of points, (*c*) distance from crack tip to the pair of points, and (*d*) initial coordinates of

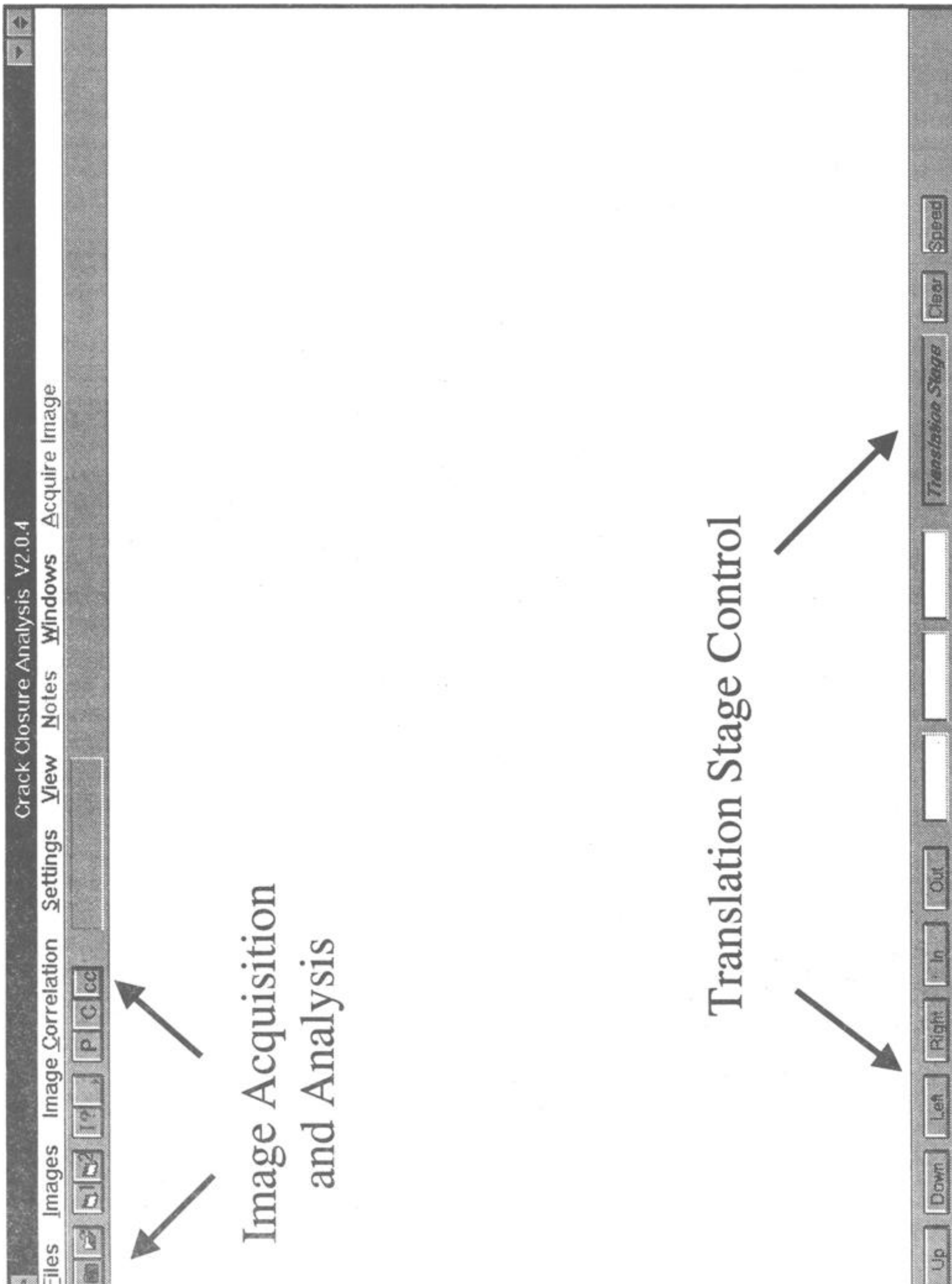

FIG. 5—*User interface from opening screen of DIDS.*

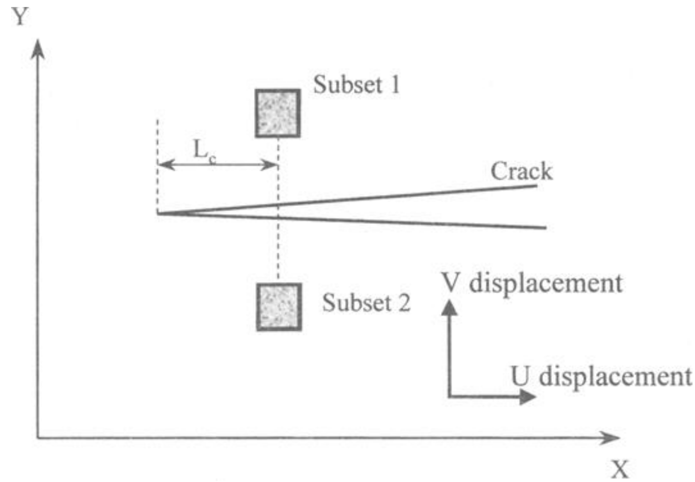

FIG. 6—*Pair of points behind crack tip for measuring crack closure.*

the pair of points and other related information. The load versus CTOD data are then used to determine the crack opening load.

Speckle Patterns

Random speckle patterns are required on the scale of subset sizes used. This is to ensure a unique one-to-one correspondence. That is, a subset in a loaded state can match one and only one subset in the reference state, or vice versa.

Two techniques have been developed for applying speckle patterns to the specimen surface. The first method uses 11 μm filter paper and a low-pressure compressed air supply to apply small particles of toner powder onto the surface of the specimen. The specimen with deposited toner particles is then heated to about 100°C for a few minutes by using a Tungsten electric bulb. This heating process is used to partially melt the toner particles so that they adhere to the specimen surface. This method can produce a random, high-contrast pattern with an average particle size of about 20 μm. The pattern generated this way is suitable for tests in a lab air environment, and was used to obtain measurements in this work and in Ref *21*. Figure 7 shows an example of a typical Xerox™ toner pattern used in a crack closure measurement.

The second method was developed for testing in environmental chambers, where the specimen may be tested in vacuum or in a corrosive environment. This method involved E-beam and contact lithography. E-beam lithography was used to fabricate a mask with the desired random pattern. The mask is manufactured only once and can be used repeatedly. Contact lithography was used to transfer the random pattern onto the specimen surface. The pattern was formed by evaporating a thin layer (700 angstrom) of tantalum onto a polished surface. Since this method can easily produce random features with precisely controlled sizes, on the order of 1 μm, it can be used for measurements with even higher magnifications than those achievable by the toner particle technique. Figure 8 shows an example of a pattern produced by using a mask with 8 μm by 8 μm features.

Baseline Experiment and System Accuracy

To evaluate the accuracy of the system, a simple tension test was performed using a dogbone specimen made of 2024-T3 aluminum alloy. Strain was measured using both strain gages and the digital

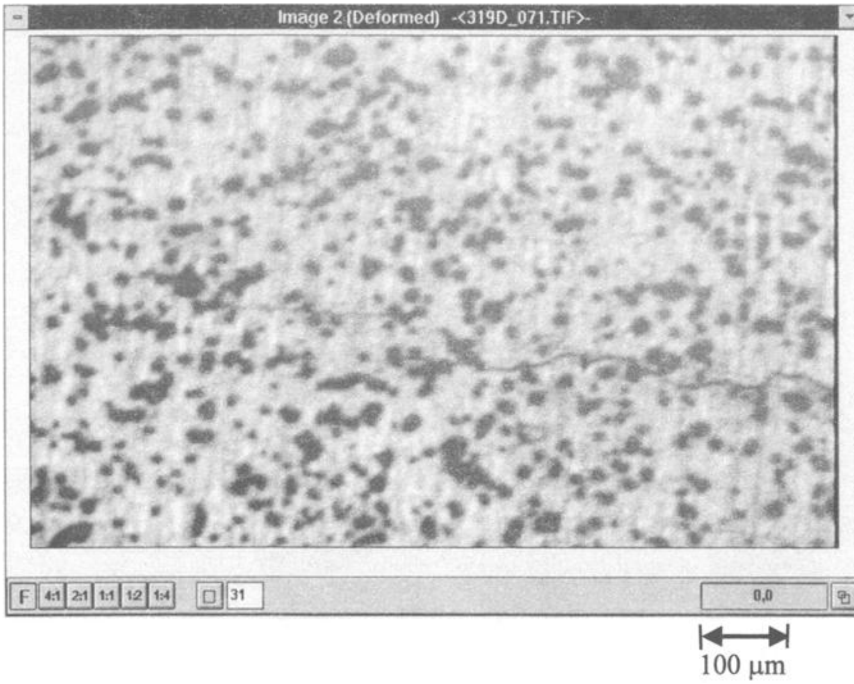

FIG. 7—*Example of patterns generated using toner powers.*

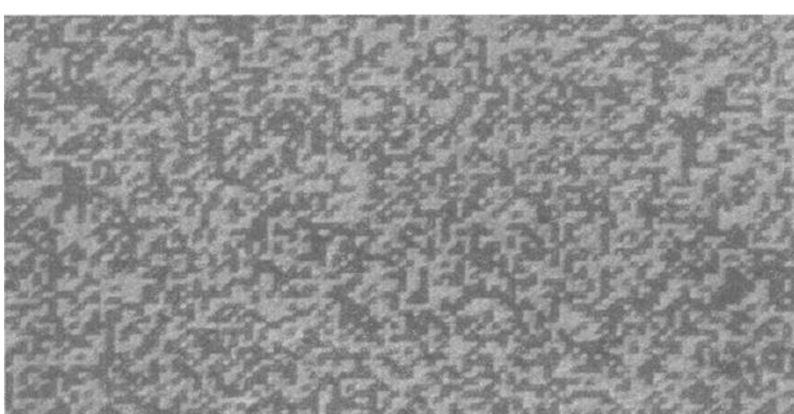

FIG. 8—*Example of lithography pattern generated using tantalum.*

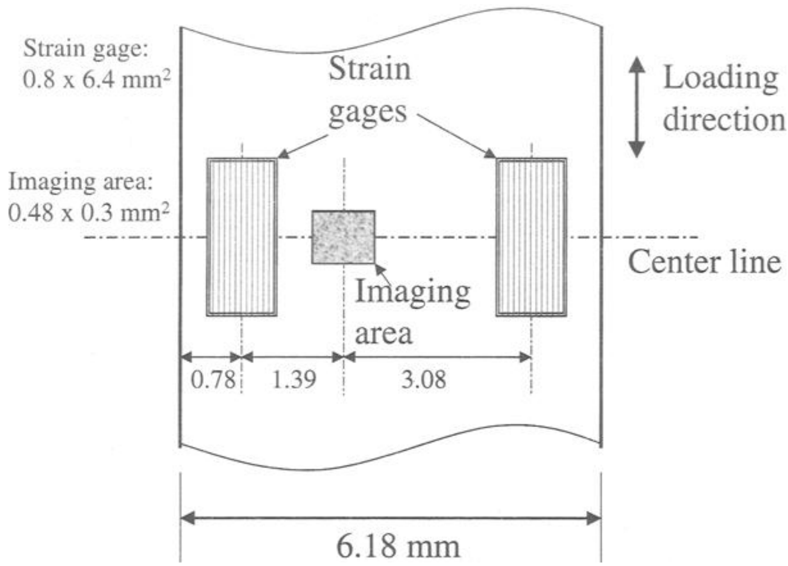

FIG. 9—*Schematic of measurement locations on a flat tensile specimen.*

image displacement system (DIDS) at a series of load increments. A schematic of the instrumentation is shown in Fig. 9, where the relative positions of two strain gages and the imaging area are shown. The imaging area was about 0.5 mm by 0.3 mm (0.00062 mm/pixel in the y-direction, calibrated by imaging a known grid under the same measurement conditions). Within this area, three pairs of subsets were selected for measuring relative displacements. Each subset had a size of 91 by 91 pixels (0.057 mm by 0.057 mm). The two subsets in a pair were about 250 pixels apart vertically (about 0.16 mm). The relative displacements were measured at every 44.5 N increment from 44.5 to 1779.3 N. Strain was calculated by dividing the measured relative displacements for each pair of points by the gage length (the vertical distance between the centers of the two subsets in a pair). The standard deviation with respect to the best-fit straight line of strain versus load was determined. The standard deviation in strain, σ_e, is $\sigma_e \sim 2 \times 10^{-4}$, which corresponds to a standard deviation in displacement of ~0.05 pixels (~30 nm). Figure 10 compares strains obtained from the strain gages and from the DIDS. Since the experiment did not provide a uniform strain field, one set of the strain gage results shown in Fig. 10 was obtained as a weighted average of the strains from the two strain gages. The strains were weighed with respect to the distances of the strain gages to the imaging area. Error bars of one standard deviation are also shown in Fig. 10, indicating reasonable agreement between both strain gage and image correlation measurement. It is pointed out that yielding will not affect the accuracy of the DIDS as long as the small strain kinematics applies.

An Example of Load Versus CTOD Result

Crack closure is a local phenomenon occurring near the crack tip. Therefore, a local measurement technique, such as the DIDS, is expected to provide more accurate results than measurements obtained remote from the crack tip. Figure 11 shows an example of load versus CTOD for an extended compact tension specimen, machined from aluminum alloy 8009. The specimen was 38.1 mm wide and 2.3 mm thick. The test was performed under constant $\Delta K = 6.6$ MPa $m^{1/2}$ with a constant load ratio of $R = 0.1$. When the crack length to width ratio was $a/w = 0.539$ the closure measurement was

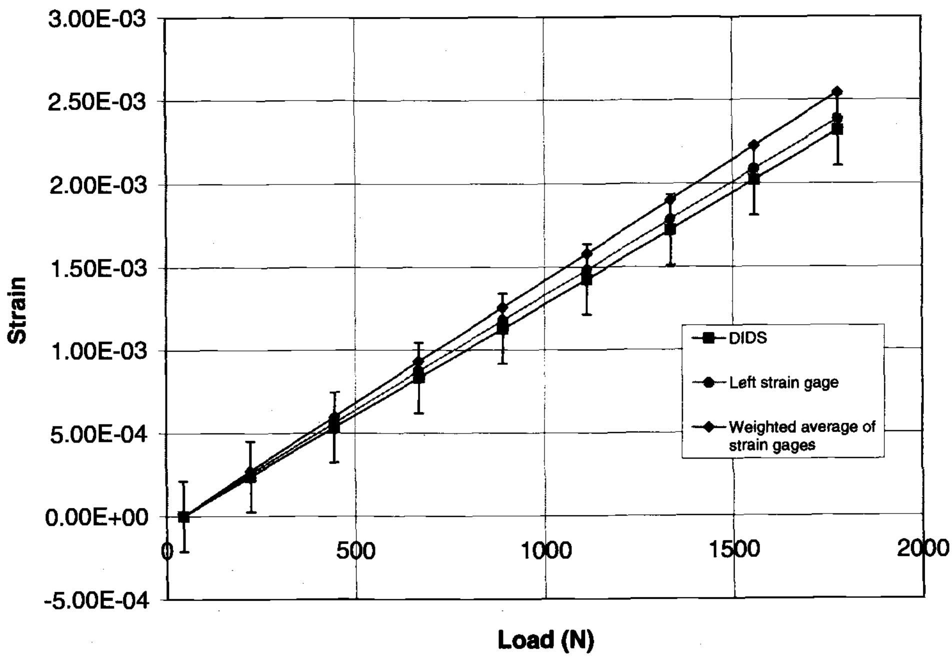

FIG. 10—*Comparison of strains from strain gages and from DIDS.*

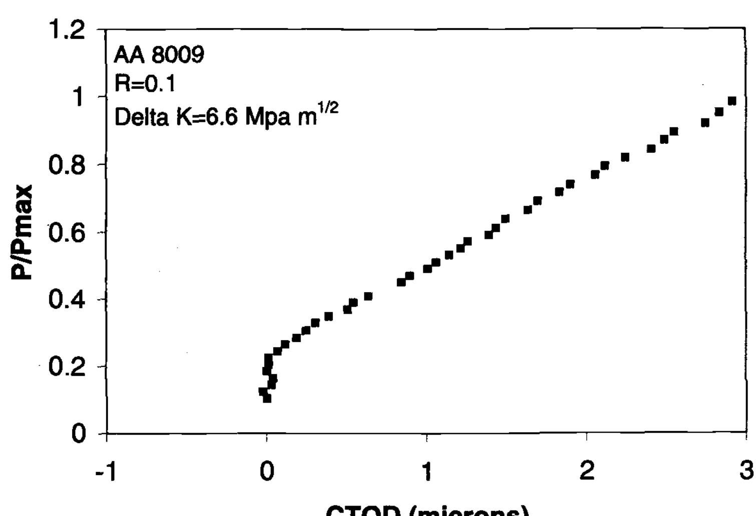

FIG. 11—*Example of load versus CTOD from DIDS.*

taken. The CTOD was measured at 0.208 mm behind the crack tip. As expected, a sharp change in load versus CTOD is observed, making it easier to identify the crack closure load. Detailed crack closure measurements and analysis using the DIDS are described in Ref *21*.

Conclusions

Based on the above development and evaluation, the following conclusions can be drawn.

1. The DIDS provides a convenient means of measuring crack closure at user-specified locations near the crack tip. Automation of the data acquisition and reduction process makes it possible to perform this traditionally tedious experiment in an efficient and accurate manner.
2. The capability of performing measurements close to a moving crack tip is advantageous in capturing the local response near the crack tip, especially since crack closure is a highly localized event. This capability provides better resolution in identifying the crack opening load, thus improving accuracy.
3. The ability to make measurements at various user-specified locations provides a convenient means to study the effect of measurement position on crack opening load.

Acknowledgments

The authors would like to express their sincere thanks to the Cornell Nanofabrication Facility staff for their help in E-beam and contact lithography, especially to Dr. Lynn Ruthburn, Mr. Garry Bordonaro, Mr. Dennis Costello and Mr. David Spencer. Help during the system development from Dr. Steve W. Smith, and during testing from Mr. J. A. Newman, NASA Langley Research Center, is deeply appreciated. Helpful discussions with Dr. James C. Newman, Jr., NASA Langley Research Center, and Dr. Anthony Reynolds, Mechanical Engineering Department, University of South Carolina, are also gratefully acknowledged. This research was performed while one author (WTR) was a National Research Council NASA Langley Research Center Associate.

References

[*1*] Elber, W., "Fatigue Crack Closure Under Cyclic Tension," *Engineering Fracture Mechanics*, Vol. 2, 1970, pp. 37–45.

[*2*] Elber, W., "The Significance of Fatigue Crack Closure," *ASTM STP 486*, American Society for Testing and Materials, Philadelphia, 1971, pp. 230–242.

[*3*] Newman, J. C., Jr., "A Finite Element Analysis of Fatigue Crack Closure," *ASTM STP 590*, American Society for Testing and Materials, Philadelphia, 1976, pp. 281–301.

[*4*] Budiansky, B. and Hutchinson, J. W., "Analysis of Closure in Fatigue Crack Growth," *Journal of Applied Mechanics*, Vol. 45, 1978, pp. 267–276.

[*5*] Newman, J. C., Jr., "A Crack-Closure Model for Predicting Fatigue Crack Growth Under Aircraft Spectrum Loading," *ASTM STP 748*, American Society for Testing and Materials, Philadelphia, 1981, pp. 53–84.

[*6*] Newman, J. C., Jr., "Prediction of Fatigue Crack Growth Under Variable Amplitude and Spectrum Loading Using a Closure Model," *ASTM STP 761*, American Society for Testing and Materials, Philadelphia, 1982, pp. 255–277.

[*7*] Paris, P. C. and Erdogan, F., "A Critical Analysis of Crack Propagation Laws," *Journal of Basic Engineering*, Vol. 85, 1960, pp. 528–534.

[*8*] Gray, G. T., Williams, J. C., and Thompson, A. W., "Roughness-Induced Crack Closure: An Explanation for Microstructurally Sensitive Fatigue Crack Growth," *Metallurgical Transactions*, Vol. 14A, 1983, pp. 421–433.

[*9*] Davidson, D. L. and Suresh, S., Eds., *Fatigue Crack Growth Threshold Concepts*, TMS-AIME, 1984.

[*10*] Gangloff, R. P., "Corrosion Fatigue Crack Propagation in Metals," *Proceedings of Environment-Induced Cracking of Metals*, 1989, pp. 55–109.

[*11*] Suresh, S., *Fatigue of Materials*, Cambridge Press, 1991.

[*12*] Sharpe, W. N., Jr., "Crack Tip Opening Displacement Measurement Techniques," *Experimental Techniques in Fracture*, 1993, pp. 219–252.

[13] Davidson, D. L., "Fatigue Crack Closure," *Engineering Fracture Mechanics*, Vol. 38, No. 6, 1991, pp. 393–402.
[14] Post, D., Han, B., and Ifju, P., *"High Sensitivity Moire; Ch 12.3.3"*, Springer-Verlag, New York, 1994.
[15] Dadkhah, A., Kobayashi, A. S., and Morris, W. L., "Crack Tip Displacement Fields and J-R Curves for Four Aluminum Alloys," *ASTM STP 1131*, American Society for Testing and Materials, Philadelphia, 1992, pp. 135–153.
[16] Dadkhah, M. and Kobayashi, A. S., "J-Integral and HRR Field Associated with Large Crack Extension," *Engineering Fracture Mechanics*, Vol. 34, 1989, pp. 253–262.
[17] Drinnon, R. H. and Kobayashi, A. S., "J-Integral and HRR Field Associated with Large Crack Extension," *Engineering Fracture Mechanics*, Vol. 41, 1992, pp. 685–694.
[18] Reynolds, A. P., "Constant Amplitude and Post-Overload Fatigue Crack Growth Behavior in PM Aluminum Alloy AA 8009," *Fatigue and Fracture of Engineering Materials and Structures*, Vol. 15, No. 6, 1992, pp. 551–562.
[19] Sutton, M. A. and McNeill, S. R., "The Effects of Subpixel Image Restoration Using Computer Vision and Digital Image Correlation," *Optical Engineering*, Vol. 27, No. 3, 1988, pp. 173–185.
[20] Bruck, H. A., Sutton, M. A., McNeill, S. R., and Turner, J. L., "Determination of Deformations Using Digital Correlation with the Newton-Raphson Method for Partial Differential Corrections," Vol. 20, No. 3, 1989, pp. 261–267.
[21] Riddell, W., Piascik, R. S., Sutton, M. A., Zhao, W., McNeill, S. R., and Helm, J. D., this volume, pp. 157–174.

W. T. Riddell,[1] R. S. Piascik,[2] M. A. Sutton,[3] W. Zhao,[3] S. R. McNeill,[3] and J. D. Helm[3]

Determining Fatigue Crack Opening Loads from Near-Crack-Tip Displacement Measurements

REFERENCE: Riddell, W. T., Piascik, R. S., Sutton, M. A., Zhao, W., McNeill, S. R., and Helm, J. D., **"Determining Fatigue Crack Opening Loads from Near-Crack-Tip Displacement Measurements,"** *Advances in Fatigue Crack Closure Measurement and Analysis: Second Volume, ASTM STP 1343,* R. C. McClung and J. C. Newman, Jr., Eds., American Society for Testing and Materials, West Conshohocken, PA, 1999, pp. 157–174.

ABSTRACT: The aim of this research was to develop a near-crack-tip measurement method that quantifies crack closure levels in the near-threshold fatigue crack growth regime—a regime where crack closure is not well characterized by remote compliance methods. Further understanding of crack closure mechanics was gained by performing novel crack growth experiments in conjunction with numerical simulations of three-dimensional crack-front propagation. Steady-state (i.e., constant growth rate) fatigue crack growth rates were characterized by performing constant cyclic stress intensity range (ΔK) experiments over a wide range of stress ratios (R). Near-crack-tip (less than 0.3 mm behind) load-versus-displacement measurements were conducted on the specimen surface using a novel noncontact experimental technique (Digital Imaging Displacement System—DIDS).

The experiments and simulations revealed that the three-dimensional aspects of fatigue crack closure must be considered to determine correct opening load levels from near-crack-tip load-versus-displacement data. It was shown that near-crack-front opening levels are nearly constant along the interior portion (greater than 90%) of the crack front, but increase near the free surface. The interior opening load was found to collapse closure-affected data to intrinsic rates, and thus shown to relate to the true crack-front driving force parameter. Surface opening load DIDS measurements made at an optimal distance behind the crack tip were used to correlate da/dN with ΔK_{eff}. Opening load determinations made less than the optimal distance behind the crack tip were shown to be too high to correlate fatigue crack growth rates.

KEYWORDS: fatigue crack growth, crack closure, stress ratio, mean stress, closure measurement, aluminum alloy 8009, aluminum alloy 2024, three-dimensional, finite element method

It has been well documented that stress ratio (R) can affect Paris regime [*1–3*] and near-threshold regime [*4–6*] fatigue crack growth rate behavior of various alloys. The stress ratio effect has been attributed to the premature contact of fatigue crack surfaces, defined as crack closure [*7,8*]. The crack closure concept typically presumes that little fatigue damage occurs when the crack faces are in contact, so that fatigue crack growth rates (da/dN) correlate with the effective crack-tip stress intensity factor range ($\Delta K_{eff} = K_{max} - K_{open}$).

Despite the considerable research that has been conducted on crack-wake closure effects [*9*], the effect of stress ratio and crack closure on fatigue crack propagation is still debated. Some research

[1] Structures and Dynamics Division DTS-76, U.S. DOT/Volpe National Transportation Systems Center, Kendall Square, Cambridge, MA 02142-1093. Formerly: National Research Council Postdoctoral Associate, Resident at Mechanics of Materials Branch, NASA Langley Research Center.

[2] Mechanics of Materials Branch MS-188E, NASA Langley Research Center, Hampton, VA 23681-0001.

[3] Mechanical Engineering Department, University of South Carolina, Columbia, SC 29208.

suggests that fatigue crack growth rates are dependent on stress ratio, regardless of crack closure effects [*10,11*]. Other research debates the current closure standard practices, and suggest that significant fatigue damage occurs both above and below the crack opening load [*12*].

The reduced strain technique, suggested by Elber [*13*], can be used to discern the change from nonlinear to linear load-versus-strain or load-versus-displacement behavior. This change in stiffness reflects a discrete closure event, namely, the change from partially closed to fully opened crack configurations. Other methods are used to interpret far-field load-versus-displacement or load-versus-strain data [*14*]. Most of these methods use either a fixed deviation from the load-displacement slope of an uncracked specimen [*15*], or the intersection of two slopes [*16*] to define an opening load. These techniques result in opening load determinations that are somewhat less than Elber's fully open load. These procedures define a single opening load that is a gross interpretation of the opening process. The definitions are often acceptable when applied to the far-field measurements commonly used for Paris-regime closure measurements.

The characterization of near-threshold closure behavior is especially complex. It is likely that various crack closure mechanisms such as plasticity, roughness, corrosion product and oxide layers are dependent on many variables (such as material type, loading conditions and environment) and combine in varying proportions to alter fatigue crack growth rates [*17–20*]. In addition, direct, accurate closure measurements are difficult to make, and correct interpretation of these measurements are widely debated, making the quantification of near-threshold effects extremely complex [*21*]. Near-crack-tip measurements can discern the closure process with much greater sensitivity than far-field techniques allow, making near-crack-tip techniques ideal for near-threshold closure measurements. However, near-crack-tip measurements will discern near-surface crack-opening behavior that is not reflective of the true crack-front driving force. In contrast, far-field techniques are typically not sensitive enough to measure this near-surface behavior. Therefore, near-crack-tip measurements require more careful interpretation to identify the discrete opening events that relate to crack-front driving force than far-field measurements require.

This paper will discuss the relationship between near-crack-tip displacement behavior and the fatigue crack closure process, with the aim of identifying the effective cyclic crack-tip driving force for constant amplitude loading. Near-crack-tip measurement techniques were used to maximize the sensitivity to near-crack-tip opening events. The aim of this study is to quantify fatigue crack opening loads from experimentally observed near-crack-tip load-versus-displacement behavior under highly controlled laboratory conditions.

Background

To interpret near-crack-tip displacement measurements, a review of crack opening behavior is required. Figure 1 describes the opening behavior of a crack grown under tension-tension ($R > 0$) loading in terms of "local opening" and "fully opened" crack configurations. On the left-hand side of Fig. 1 are schematic diagrams showing the crack opening configuration at four increasing loads, (a) through (d). The points just above and below the crack face identify three displacement measurement locations behind the crack-tip. At each location, the relative displacement between the point on either side of the crack face is considered. The plot in Fig. 1 represents the relative-displacement-versus-load response measured between each of the three pairs of points. For illustrative purposes, the schematic represents an idealized elastic-plastic load-versus-relative-displacement response. The table in Fig. 1 notes the "fully opened" (f.o.) and "local opening" (l.o.) points defined by the crack-tip schematic and the corresponding relative-displacement-versus-load curve. This terminology will be used throughout this paper.

At minimum load, point (a) in Fig. 1, much of the crack faces are in contact. However, location 3 is far enough behind the crack-tip so that the faces are open at minimum load, resulting in positive relative displacements at the minimum load. As the load increases to point (b) in Fig. 1, more of the

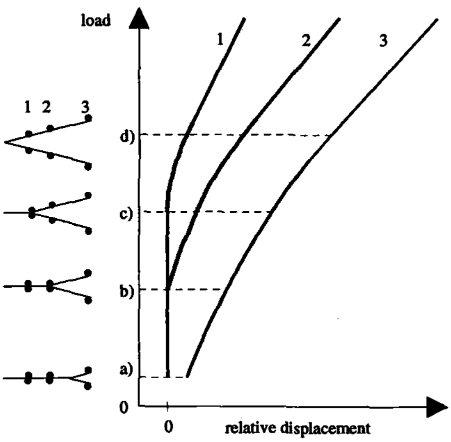

LOAD	LOCATION 1	2	3
d)	f.o.	f.o.	f.o.
c)	l.o.	open	open
b)	closed	l.o.	open
a)	closed	closed	open

FIG. 1—*Schematic showing the near-crack-tip configuration and the corresponding load-versus-relative-displacement behavior as the remote load* (R > 0) *is increased. The load-versus-relative-displacement traces reveal the fully opened (f.o.), local opening (l.o.) and locally closed (closed) configurations.*

crack faces separate, and the slope of the relative-displacement-versus-load plot measured from location #3 decreases continuously. Relative displacements for locations #1 and #2 exhibit no change in displacement for a load increase from points (a) to (b). For a further increase in load to point (c), a continuous increase in relative displacement is measured at locations #2 and #3 and no displacement change is monitored at location #1. Loading the crack to point (d) results in a fully opened crack and an increase in relative displacement is monitored at all locations behind the crack tip, locations #1, #2 and #3. Increasing the load beyond the fully opened load (defined at point(d)) results in a linear increase to each load-versus-relative-displacement curve shown in Fig. 1 [*7,8*].

Local opening loads, characterized by a distinct change in load-displacement slope, are defined in the context of a specific measurement location. As seen in Fig. 1, change in local opening load with respect to location describes the "peeling" of the crack faces as the load is increased [*22*], and the fully open load is the load at which there is no crack face contact. Unlike the local opening load, the fully open load results in only a subtle change in the relative-displacement-versus-load slope. Therefore, the "reduced strain" or "reduced displacement" technique [*13*] is employed for discerning the fully open load. The fully open load is the maximum of all local opening loads and, in theory, can be discerned from measurements taken anywhere on the specimen.

Procedure

To study near-crack-tip behavior in a model material, specialized fatigue crack growth testing was combined with near-crack-tip relative displacement measurements and finite element analyses of three-dimensional elastic-plastic crack-fronts.

Material

A series of fatigue crack growth experiments was performed to investigate fatigue crack closure in a powder metallurgy (PM) aluminum alloy (AA) 8009 in laboratory air. This alloy was chosen as a model material because it contains an ultra-fine grain structure [*23*] that results in a microstructurally smooth fatigue crack surface. The flat fatigue fracture surface greatly reduces (possibly eliminates) the complexities introduced by crack wake effects produced by roughness-induced fatigue crack clo-

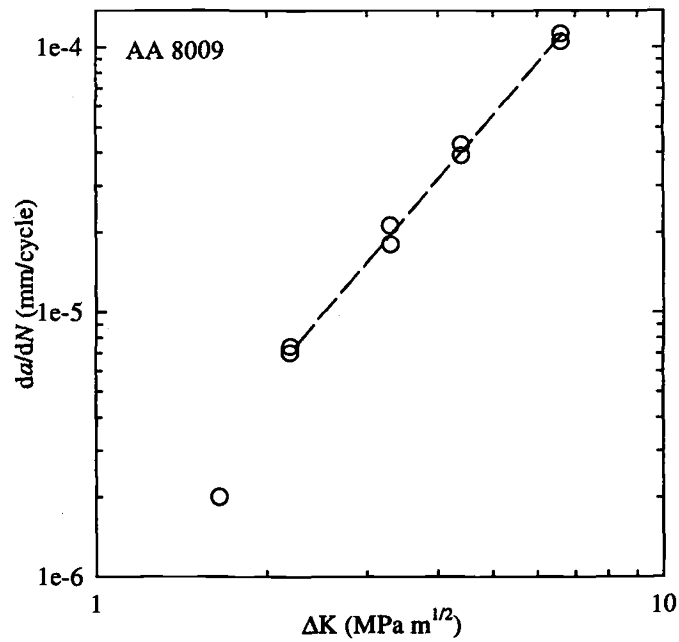

FIG. 2—*Intrinsic (stress ratio independent) fatigue crack growth rates for AA 8009. Paris-regime behavior is represented by the dashed line.*

sure [*24*]. The nominal composition is Al-8.5Fe-1.3V-1.7Si (% by weight). The material is non-heat-treatable, and is planar flow casted, followed by ribbon comminution, vacuum hot pressing and extrusion followed by rolling. The resulting microstructure is very fine, consisting of grains about 0.5 μm with dispersoids of Al_2 (Fe,V)$_3$ Si with an average diameter of 40 to 80 nm. The material properties for AA 8009 are: σ_y = 428 MPa, σ_{ult} = 482 MPa and E = 82 GPa.

Fatigue crack growth rates for AA 8009 at 11 Hz [*25*] are shown in Fig. 2. These data are for the range of R (typically 0.4 to 0.8) where crack growth rates are independent or nearly independent of stress ratio. Here, crack closure and K_{max} effects have minimal influence on fatigue crack growth rates, resulting in the observed R-independence for these data. For the purposes of this paper, intrinsic rates are defined to be those which are free from closure and other stress ratio effects.[4] In this sense, the data shown in Fig. 2 are intrinsic crack growth rates. These intrinsic rates fall onto a straight line (dashed line in Fig. 2) in log-log space for ΔK between 2.2 and 6.6 MPa m$^{1/2}$. The fatigue crack growth rate for ΔK = 1.65 MPa m$^{1/2}$ is below this straight line, representing the onset of threshold behavior. Crack growth rates in the linear (Paris) range can be interpolated by

$$\frac{da}{dN} = 1.0 \times 10^{-6} (\Delta K)^{2.49} \qquad (1)$$

[4] The purpose of the research presented in this paper is to investigate the relationship between the fatigue crack opening process and cyclic fatigue damage, not to separate environmental from mechanical components of crack front driving forces. The definition of "intrinsic" used herein reflects this objective. A more general definition of intrinsic crack growth rates would preclude environmental driving forces, and refer to crack growth rates resulting from tests in ultra-high vacuum. However, this distinction is not necessary for the purposes of this paper, so long as the environment remains constant throughout testing.

where the units for da/dN are mm/cycle and for ΔK are MPa $m^{1/2}$. As crack closure is not operative for the data shown in Fig. 2, these data also establish the da/dN-ΔK_{eff} relationship for conditions where K_{max} effects are not significant. The intrinsic da/dN-ΔK_{eff} relationship shown in Fig. 2 is considered the baseline to be compared to ΔK_{eff} values obtained from experimentally measured and numerically predicted opening loads obtained for the same environment.

Steady-State Fatigue Crack Growth Testing

Load history can affect crack-wake effects such as closure [4]. To limit crack-wake history effects and ensure steady-state fatigue crack growth, all crack growth tests were conducted at constant ΔK and stress ratio. All tests were conducted using the pin-loaded extended compact tension specimen [26] shown in Fig. 3. A computer-controlled servohydraulic test system was used to perform the automated K-controlled tests at 11 Hz. For each ΔK level, a series of constant ΔK, constant R tests were conducted for stress ratio (R) that ranged from 0.1 to near 1.0. Front-face or back-face compliance methods were used to monitor crack lengths [27]. Typical constant ΔK crack-length-versus-load-cycles (α-versus-N) data are shown in Fig. 4 for AA 8009 at a constant ΔK = 6.6 MPa $m^{1/2}$, constant R = 0.3. The first two datapoints (open circles) exhibit some nonlinearity in the α-versus-N relationship when compared to the remaining 13 datapoints (closed circles). A linear regression analysis

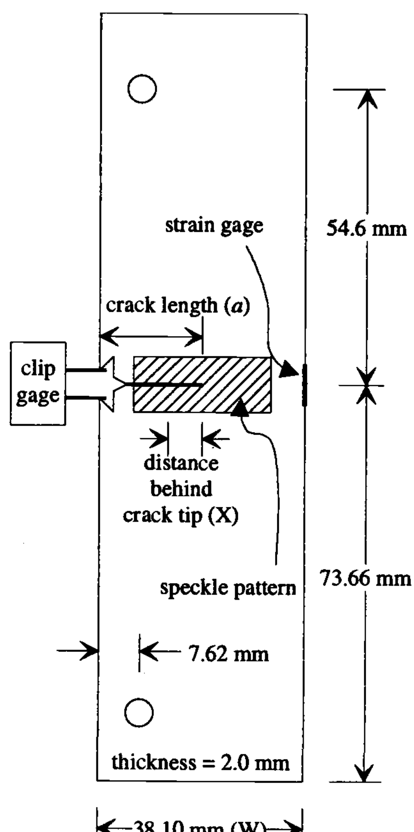

FIG. 3—*Schematic showing the extended compact tension specimen.*

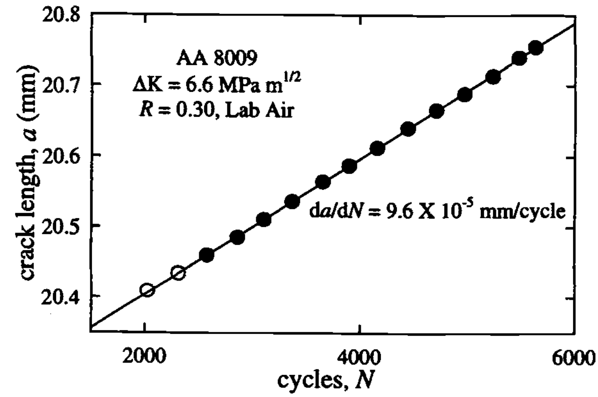

FIG. 4—*Plot of crack length* (a) *versus load cycles* (N) *showing typical constant* ΔK, *constant* R *test data for AA 8009.*

(solid line in Fig. 4) of the data shows that a steady-state crack growth rate (*da/dN*) of 9.6×10^{-5} mm/cycle was achieved for the last 13 datapoints, or 0.3 mm of crack growth. Steady-state crack growth behavior was verified for each constant ΔK test.

Figure 5 is a plot of steady-state fatigue crack growth rate versus stress ratio for 16 constant-ΔK (6.6 MPa $m^{1/2}$), constant-R tests conducted at stress ratios ranging from 0.1 to 0.7. At each level of stress ratio, a steady state crack growth rate was obtained, similar to the $R = 0.3$ example shown in Fig. 4. Fatigue crack growth rates obtained in this manner are extremely sensitive to changes in growth rates associated with subtle changes in crack driving force. Fatigue crack growth rates are plotted on a linear, rather than log, scale, which highlights the sensitivity of these data. The plot of steady-state crack growth rate versus stress ratio shown in Fig. 5 reveals three distinct regions of crack growth [*28,29*]. For $\Delta K = 6.6$ MPa $m^{1/2}$, fatigue crack growth rates (Region I) at low R (< 0.40) are closure affected. Accelerated fatigue crack growth rates for $R = 0.68$ to 0.70 (Region III) may be a result of extrinsic K_{max} effects [*28,29*]. Region II fatigue crack growth rates, at intermediate R (0.4

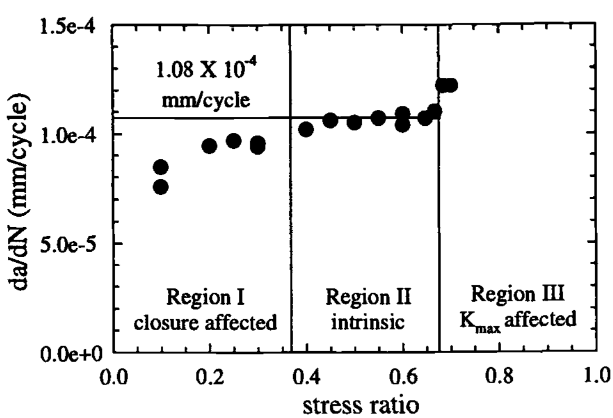

FIG. 5—*Plot of steady state fatigue crack growth rate against stress ratio for AA 8009 revealing three regions of crack growth at a* $\Delta K = 6.6$ *MPa* $m^{1/2}$*: Region I—closure effected* da/dN, *Region II—intrinsic or* R*-independent* da/dN, *and Region III—*K_{max} *influenced* da/dN.

to 0.65), are nearly independent of stress ratio, and represent the intrinsic (as defined in this paper) fatigue crack growth behavior for $\Delta K = 6.6$ MPa m$^{1/2}$, under lab air conditions. The intrinsic fatigue crack growth rate curve shown in Fig. 2 was developed from Region II data generated from a series of constant ΔK constant R data for five different values of ΔK.

Rate-Calculated Opening Loads

The method for establishing the correct opening load is based on comparing closure affected (Region I) steady-state fatigue crack growth rates to the intrinsic (Region II) da/dN-ΔK relationship. Region II is free from closure effects, so the true cyclic driving force, ΔK_{eff}, is equal to the applied, ΔK. Region I fatigue crack growth is influenced by crack closure, which is an extrinsic effect that causes the true driving force to be less than the applied ($\Delta K_{eff} = K_{max} - K_{open}$). The relationship between opening load and crack-tip driving force (ΔK_{eff}), and the relationship between ΔK_{eff} and fatigue crack growth rate, can be used to establish a "rate-calculated opening load" (RCOL). Opening levels at each stress ratio were determined by comparing the observed closure-affected fatigue crack growth rates (Region I in Fig. 5) with the intrinsic, closure-free fatigue crack growth rate relationship shown in Fig. 2. For AA 8009, the intrinsic Paris-regime da/dN is described by Eq 1. From the inverse function of Eq 1, the true driving force, ΔK_{eff}, is given by

$$\log(\Delta K_{eff}) = \frac{\log\left(\frac{da}{dN}\right) + 5.9976}{2.49} \tag{2}$$

where the units for da/dN are mm/cycle and the units for ΔK_{eff} are MPa m$^{1/2}$. The opening load ratio (P_{open}/P_{max}) can be calculated from ΔK_{eff} and K_{max} by

$$\frac{P_{open}}{P_{max}} = \frac{K_{max} - \Delta K_{eff}}{K_{max}} \tag{3}$$

This opening load will collapse observed Region I da/dN-ΔK_{eff} data to intrinsic (Region II) da/dN-ΔK data. For example, for $\Delta K = 6.6$ MPa m$^{1/2}$, $R = 0.1$, the fatigue crack growth rate is 7.56×10^{-5} mm/cycle. Equation 2 predicts a ΔK_{eff} of 5.665 MPa m$^{1/2}$ for this rate, and Eq 3 gives an opening load (P_{open}/P_{max}) = 0.23. For Region II (intrinsic) crack growth behavior, $\Delta K_{eff} = \Delta K$, and the RCOL is defined to be the stress ratio. These rate-calculated opening loads are considered the baseline opening loads. For the remainder of this paper, ZIP3D-predicted and DIDS-measured near-crack-tip opening loads are compared to the baseline RCOL data.

Near-Crack-Tip Displacement Measurements

Load-versus-displacement measurements were performed at several locations behind the crack-tip (less than 0.3 mm) after steady-state fatigue crack growth rates were confirmed for each constant-ΔK, constant-R test. A near-crack-tip measurement was chosen because it is more sensitive to closure events than far-field techniques such as back-face strain or front-face clip gages are. This is particularly true for near-threshold fatigue load levels, where traditional far-field techniques sometimes result in anomalous da/dN-ΔK_{eff} data. However, near-crack-tip techniques measure surface behavior, which might not be characteristic of behavior along most of the interior crack front. Constraint can have a profound effect on plasticity-induced closure levels, creating a crack closure gradient from the interior to the free surface [*30–35*]. For Paris and near-threshold regime fatigue crack growth, plane strain or nearly plane strain conditions prevail over much of the crack front, even for relatively thin (2 mm) sheet materials. However, plane stress or nearly plane stress conditions exist very near the side surface of the specimen. Unless properly interpreted, near-surface and near-crack-tip displacement measurements for crack opening determination can be biased by variable subsurface constraint, resulting in measured crack-tip opening loads that are too high to correlate fatigue crack growth rates with ΔK_{eff} [28,29]. Therefore, it is essential to understand the three-dimensional aspects (discussed in the Results and Discussion section) of near-crack-tip load-versus-displacement surface measurements so that the true crack-tip driving force (ΔK_{eff}) can be determined.

In situ near-crack-tip load-versus-displacement measurements were obtained using a visual imaging technique named Digital Image Displacement System (DIDS) [36]. A micron-sized speckle pattern was applied to the side surface of the fatigue specimen, as shown in Fig. 3. As the applied load is increased, DIDS obtains a series of high-magnification digital images of the specimen surface within 0.3 mm of the crack tip from a long-focal-length microscope. DIDS obtains near-crack-tip displacements from the series of images using an image correlation algorithm [37] that follows the movement of preselected speckles, located near the crack-tip, during the load cycle. This technique produces relative displacement measurements with a standard deviation of 0.03 μ [36]. A schematic example of three near-crack-tip load-versus-relative-displacement traces measured using DIDS is shown in Fig. 1.

Numerical Simulations

Numerical simulations of three-dimensional, elastic-plastic fatigue crack growth were performed using the finite element code, ZIP3D [38]. Three-dimensional analyses were utilized so that no assumptions regarding the stress state (i.e., constraint) along the crack front were needed. Rather, conditions could vary from plane stress at the free surface to plane strain at the midplane, as the mechanics dictate. These analyses were similar to those performed by Chermahini et al. [32,33] except for details of the configuration analyzed, values of loads applied, and mesh refinement. The purpose of these analyses was to determine the relationship between surface displacements, which can be experimentally observed, and through-the-thickness crack opening loads, which are likely to have a significant effect on fatigue crack growth rates. It should be noted that the simulations were not used to predict exact crack closure levels. Rather, simulations were used to characterize the general relationship between surface and through-the-thickness fatigue crack closure. From this relationship, a methodology was developed to determine through-the-thickness closure levels from surface behavior for the model alloy, AA 8009 in the Paris regime. Ultimately, the methodology is used to determine fatigue crack opening loads in the Paris and near-threshold regime of an engineering alloy, AA 2024.

The finite element mesh, shown in Fig. 6, used for these analyses consisted of six layers of elements through the half-thickness of the simulated specimen. One quarter of an extended compact tension specimen was modeled, taking advantage of two planes of symmetry. Through the thickness of the specimen, the boundaries of these layers were at Z = 0.0000, 0.5842, 0.9652, 1.0922, 1.1430, 1.1684, and 1.1811 mm from the centerline of the specimen. The thickness of the layers were graded to allow for a finer mesh near the free surface, where steep gradients in constraint conditions exist. The elements near the final crack-tip are 0.0037 mm wide in the direction of crack growth. Nodes on the Z = 0 plane of the specimen were constrained from translating in the Z-direction, nodes on the uncracked portion ($X > a$) of the Y = 0 plane were constrained from translating in the Y-direction, and nodes on the cracked portion of the Y = 0 plane were constrained against negative Y-displacements. Also, the node at X = 38.1 mm, Y = Z = 0 was restrained in the X-direction. These boundary conditions reflect the two planes of symmetry that are appropriate for this problem, a single degree of freedom fixed to prevent rigid body displacements, and the conditions that the crack faces do not "pass through" each other.

Simulations were performed for a ΔK = 6.6 MPa $m^{1/2}$ and stress ratios ranging from 0.1 to 0.6. To simulate the cyclic plasticity behavior of AA 8009, the model used an elastic-perfectly-plastic material with E = 82 000 MPa, and σ_0 = 470 MPa [39]. Cyclic loads were applied at the desired load lev-

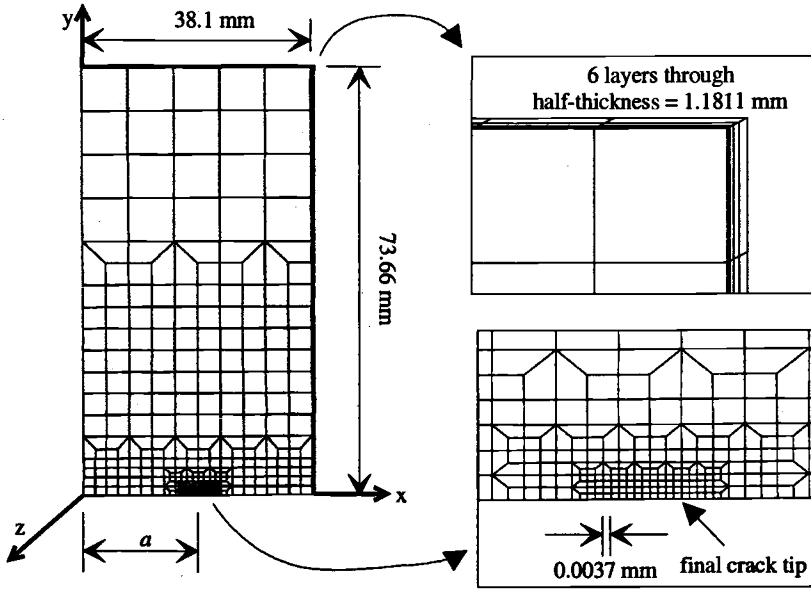

FIG. 6—*Finite element mesh used for ZIP3D analyses.*

els, and fatigue crack growth was simulated by releasing all seven nodes along the current crack front at the peak load of each cycle. Nineteen load cycles were applied, simulating a total 0.134 mm of crack growth. Two distinct types of data were obtained from these simulations: load-versus-displacement traces, and nodal opening loads. Predicted load-versus-displacement behavior was obtained for several specific node locations. These nodes were chosen to simulate back-face strain gage (1 node) response, front face clip gage (1 node) response, and near crack-tip, behind-the-crack displacements on the side surface of the specimen (5 nodes). The linear portion of the load-displacement relation at the virtual clip gage and load-strain relation at the virtual strain gage agree with the relations given in [26] for $a/W = 0.5$. This agreement validates the global behavior of the three-dimensional model. Predicted nodal opening loads were recorded each time a node on the simulated crack surface ($X < a$) lifted from the $Y = 0$ plane. The predicted near-crack-tip behavior is compared to experimental observations in the next section.

Results and Discussion

Near-Crack-Tip Behavior

Numerically predicted and experimentally observed near-crack-tip load-versus-relative-displacement behavior for AA 8009 at three different locations behind the crack-tip on the side surface of the test specimen are shown in Fig. 7*a*. Relative displacement is defined as the displacement between two points on opposite sides of the crack faces. All relative displacements discussed herein are in the Y-direction. Symmetry causes the relative displacements in the X-direction to be zero. As anticipated, experimental measurements of the relative displacements in the X-direction were small compared to those in the Y-direction. Relative displacement measurements obtained after 0.5 mm of steady-state crack growth at a constant $\Delta K = 6.6$ MPa m$^{1/2}$, constant $R = 0.1$ are shown in Fig. 7. The predicted load-versus relative displacement traces were obtained following 19 load cycles and 0.134 mm of simulated fatigue crack growth. The local opening load for each load-displacement trace shown in

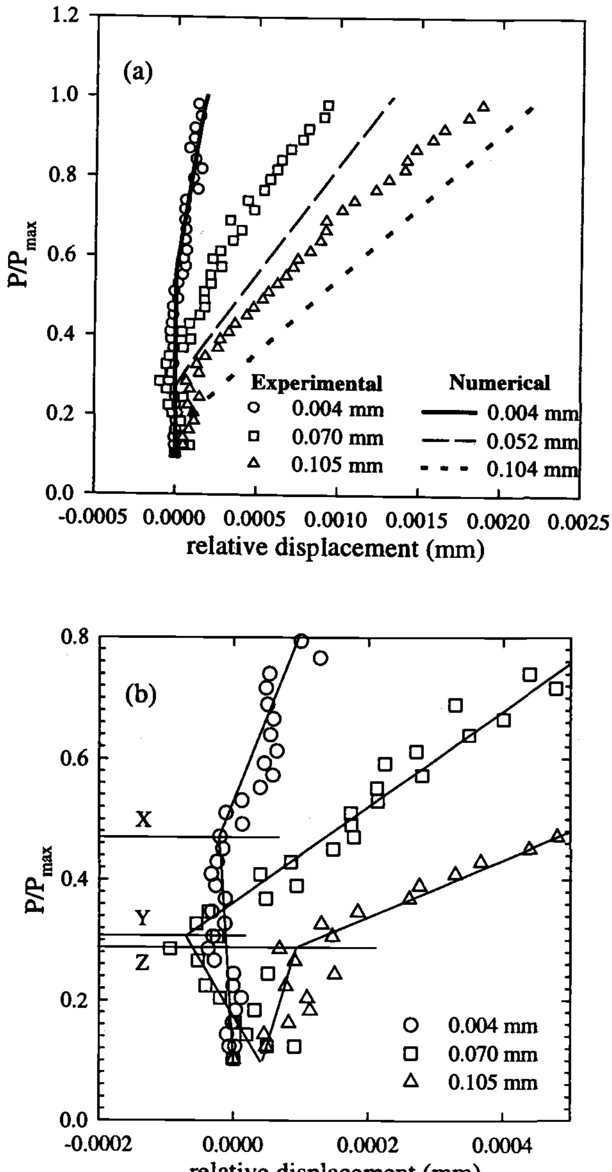

FIG. 7—(a) *Plot comparing experimental and predicted near-crack-tip relative-displacement-versus-load behavior for AA 8009,* $\Delta K = 6.6$ *MPa* $m^{1/2}$, $R = 0.1$. (b) *An expanded view showing the experimentally determined opening load at X, Y, Z for 0.004 mm, 0.070 mm and 0.105 mm behind the crack tip, respectively.*

Fig. 7*a* was obtained by noting the deviation from the vertical or near-vertical slope. Experimentally determined data are shown in Fig. 7*b* on an expanded scale for displacements less than 0.0005 mm. Even though these data exhibit considerable scatter, three distinct inflection points (local opening loads) are easily noted at loads X, Y, and Z in Fig. 7*b*. The numerically predicted and experimentally observed traces in Fig. 7*a* show similar trends; both experimental and predicted results show that the local opening loads decrease as the measurements are made further from the crack-tip. Both the experimentally observed and predicted load-displacement results are in good agreement near the crack-tip (0.004 mm). Although the numerically predicted opening loads 0.052 mm and 0.104 mm behind the crack tip (dashed and dotted lines, respectively) are lower than the corresponding experimentally observed opening loads, the predicted load-versus-relative-displacement slopes agree with the corresponding experimentally observed slopes for values of P/P_{max} greater than the opening loads.

Figure 8 shows that the surface opening load decreases with increasing distance behind the crack tip. Similar trends were observed by Hudak and Davidson [*40*]. Local opening loads were experimentally determined from near-crack-tip load-versus-relative-displacement DIDS measurements (open square and circle symbols) and numerically predicted using ZIP3D finite element analyses (solid line). RCOL levels are represented by the dashed lines. Two values of RCOL are shown for $R = 0.1$ and $R = 0.3$, reflecting two separate tests for each R. The $R = 0.1$ experimental data shown in Fig. 8*a* are the results of two sets of DIDS measurements (open squares and circles) from the same crack tip, indicating good reproducibility of the DIDS-based local crack opening data. Both the experimentally observed and predicted values for $R = 0.1$, 0.3, and 0.6 reveal that the local opening load

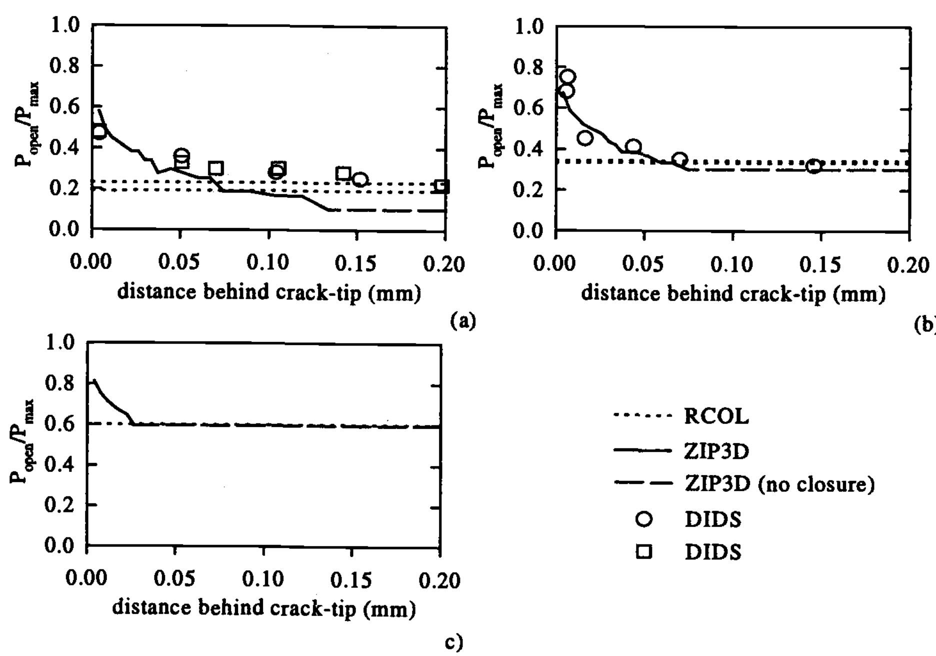

FIG. 8—*Plotted are values of P_{open}/P_{max} numerically predicted and experimentally observed at different distances behind the crack tip for* $\Delta K = 6.6$ *MPa* $m^{1/2}$ *and* (a) R = *0.1,* (b) R = *0.3, and* (c) R = *0.6. Two different symbols used for* R = *0.1 denote the results of local opening loads measured for two different tests. Two sets of dotted lines for* R = *0.1 and 0.3 represent RCOL calculated from rates observed for two tests at each stress ratio. No closure was observed with DIDS for* R = *0.6. Therefore, no DIDS symbols are shown on this plot.*

decreases with increased distance behind the crack tip. Numerically predicted local opening loads agree well with the experimental values of P_{open}/P_{max} for R = 0.1 and 0.3. The results at high stress ratio (R = 0.6) shown in Fig. 8*c*, suggests that local closure rapidly diminishes with increased distance behind the crack-tip; here, predictions show that local closure only exists within 0.02 mm behind the crack-tip, whereas experimental measurements indicated no local closure. It is important to note that for all cases (R = 0.1, 0.3 and 0.6), both the experimentally observed and numerically predicted opening loads rapidly approach the RCOL value at a distance of approximately 0.06 mm behind the crack-tip. To correlate these surface observations to crack-tip driving force, ZIP3D based predictions of though-the-thickness opening behavior were studied.

Figure 9 compares the ZIP3D-predicted (solid line) crack-tip opening load occurring along the crack front (through-the-thickness) to the RCOL (horizontal dashed line) for R = 0.1, 0.3 and 0.6. Predicted opening loads occurring along the interior portion of the crack front agree with the RCOL. Near the free surface, the predicted opening loads exhibit a significant increase in crack closure compared to interior levels. For fatigue crack growth at R = 0.1, shown in Fig. 9*a*, predicted P_{open}/P_{max} = 0.26 is slightly greater than experimental RCOL (P_{open}/P_{max} = 0.24 and 0.19). At R = 0.3, shown in Fig. 9*b*, both predicted and two experimental RCOL determinations revealed an interior P_{open}/P_{max} = 0.35. Both RCOL and ZIP3D predict no interior crack closure at R = 0.6, so the interior P_{open}/P_{max} was defined as the stress ratio (R = 0.6). The results shown in Fig. 9 reveal that crack opening levels predicted by ZIP3D along the interior 90% of the crack front correlate well with experimentally based RCOL. From Fig. 9, it is strongly suggested that

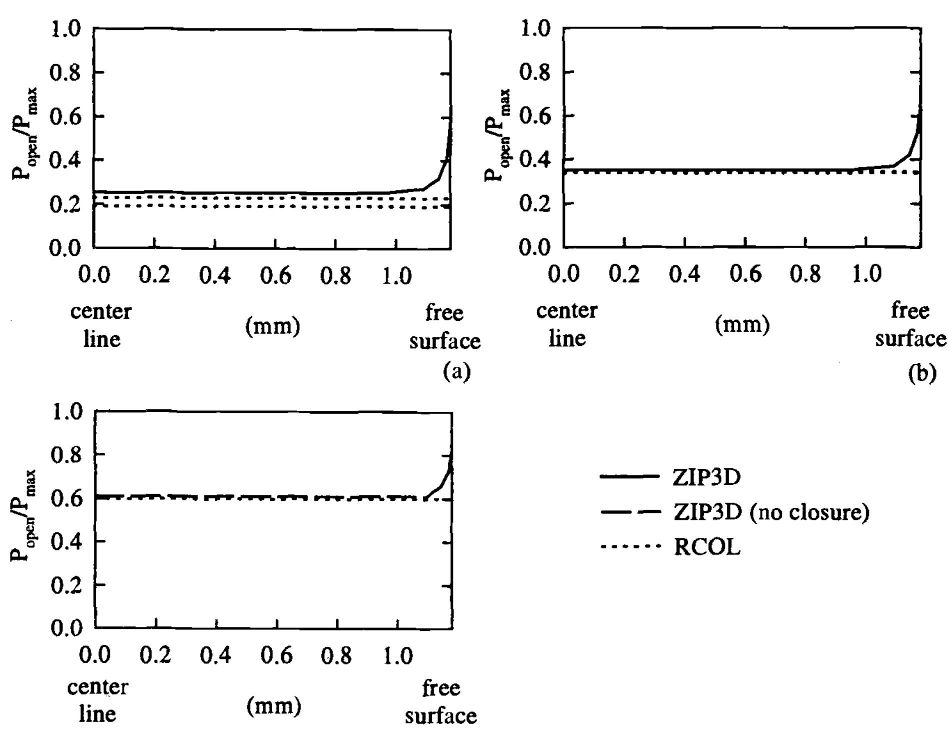

FIG. 9—*Plotted are RCOL and numerically predicted through-the-thickness* P_{open}/P_{max} *values for AA 8009, at* $\Delta K = 6.6$ *MPa* $m^{1/2}$ *and* (a) R = *0.1,* (b) R = *0.3, and* (c) R = *0.6.*

- Crack-front driving force is directly related to interior crack-front opening; Region I and II *da/dN,* shown in Fig. 5, are primarily influenced by interior crack-front opening.
- Increased crack-front opening loads near the free surface exhibit little influence on overall crack front driving force.
- The increase in crack-front opening loads near the free surface influences near crack-tip load displacement surface (DIDS) measurements. Therefore, it is important to perform near crack-tip measurements at an optimum distance behind the crack tip, where local P_{open}/P_{max} is similar to RCOL (refer to Fig. 8).

Further consideration of Figs. 8 and 9 suggests that a ΔK_{eff} calculated from local opening loads measured at an optimum near-crack-tip location on the side surface can be used to correlate closure-affected fatigue crack growth rates with the intrinsic fatigue crack growth behavior. The optimum location for $\Delta K = 6.6$ MPa m^{½} is numerically predicted to be 0.06 mm and experimentally observed to be 0.10 mm to 0.15 mm behind the crack-tip (refer to Fig. 8). Here, the experimentally observed local opening load is relatively independent of measurement location. Cyclic driving force is directly related to the local opening load measured at the optimum location—where surface opening loads correlate directly with both RCOL and opening loads along the interior of the crack front (shown in Fig. 9).

Comparison of Numerically Predicted and Experimentally Observed Opening Loads to RCOL

The near-crack-tip behavior described above reveals that the fatigue crack surfaces gradually separate (peel) with increasing load. However, the three-dimensional nature of the opening behavior makes the process much more complex than shown in the simple schematic of Fig. 1. A consequence of this complexity is that there is not a unique opening load that can describe the crack opening process along the entire crack front. However, current global methods [*14–16*] successfully use the concept of a single opening load to estimate ΔK_{eff} for Paris regime crack growth rates. In the near-threshold regime, where global methods lack the required resolution for acceptable opening load determination, sensitive measurements of near-crack-tip displacement behavior provide a viable alternative to quantify crack closure effects. The increased resolution of near-crack-tip techniques allows precise observations of crack opening behavior. However, the three-dimensional effects shown in Figs. 8 and 9 must be accounted for when using near-crack-tip surface measurements. In other words, the sensitivity of near-crack-tip measurements necessitate a careful interpretation of the process of crack opening. To determine true crack-tip driving force from surface measurements, one must be able to monitor the crack surface "peeling" process by characterizing near-crack-tip surface opening load shown in Fig. 8 and correlating the surface measurements with the opening load along the interior of the crack front shown in Fig. 9.

Figure 10 is a plot of P_{open}/P_{max} versus stress ratio at a $\Delta K = 6.6$ MPa m^{½}, comparing the results of experimentally and numerically based opening loads. Four types of opening loads are shown in this figure: (1) RCOL (open circle), (2) local opening load at the optimum distance behind the crack-tip as measured using DIDS (open triangles) and predicted by ZIP3D (solid line), (3) fully open load as measured using DIDS (open squares) and predicted by ZIP3D (long dashed line), and (4) ZIP3D predicted opening load at the interior of the crack front (short dashed line). The RCOL is presumed to be the value of P_{open}/P_{max} that best reflects the true effective cyclic driving force and is calculated from experimentally observed intrinsic fatigue crack growth rates (Region II rates, similar to those shown in Fig. 5) using Eqs 2 and 3. When no closure is predicted or observed, the opening load is defined as the minimum load (stress ratio). The experimental and ZIP3D predicted values of fully open P_{open}/P_{max} (open squares and long dashed line) do not agree with RCOL. Predicted values of P_{open}/P_{max} at the interior of the crack front (short dashed line) and on the surface at the optimum distance (0.06 mm) near the crack-tip (solid line) compare well with RCOL. The DIDS local opening

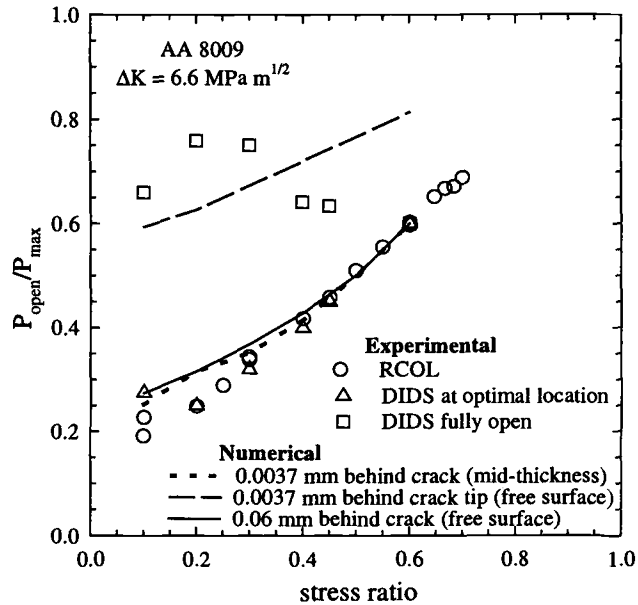

FIG. 10—*Plotted are RCOL, local opening and fully open loads for AA 8009,* $\Delta K = 6.6$ *MPa* $m^{1/2}$ *as a function of* R.

load measurements (open triangles) performed at an optimum distance behind the crack tip also correlate well with RCOL. These results show that local opening loads must be measured on the surface at an optimum distance behind the crack tip to agree with intrinsic based RCOL over the entire range of stress ratios.

Validation of Near-Crack-Tip Methodology for an Engineering Alloy

The purpose of this research was to develop a near-crack-tip measurement methodology for the near-threshold fatigue crack growth regime. However, finite element simulations of three-dimensional elastic plastic fatigue crack growth are not, at present, feasible for stress intensity factors significantly less than 6.6 MPa $m^{1/2}$, as the ratio of element size to cyclic plastic zone size becomes too large at small ΔK. Figure 11*a* shows the ZIP3D based local opening loads on the surface as a function of distance behind the crack-tip for $\Delta K = 6.6$ and 9.9 MPa $m^{1/2}$, $R = 0.1$. Since the mid-thickness closure levels were approximately the same for both levels of ΔK ($P_{open}/P_{max} = 0.25$ for $\Delta K = 6.6$, $P_{open}/P_{max} = 0.29$ for $\Delta K = 9.9$ MPa $m^{1/2}$), it is apparent that the optimum distance behind the crack-tip for the measurement of local crack opening loads changes with ΔK. Figure 11*b* shows the same data plotted in Fig. 11*a*, except that the distance behind the crack-tip is scaled by cyclic plastic zone size, ω_y, approximated by Rice [*41*] as

$$\omega_y = \frac{1}{4\pi}\left(\frac{\Delta K}{\sigma_o}\right)^2 \tag{4}$$

where σ_o is the cyclic yield stress of the material.

When the distance behind the crack-tip is scaled by the cyclic plastic zone size calculated by Eq 4, the predicted local opening loads for the two levels of ΔK match closely. Therefore, the

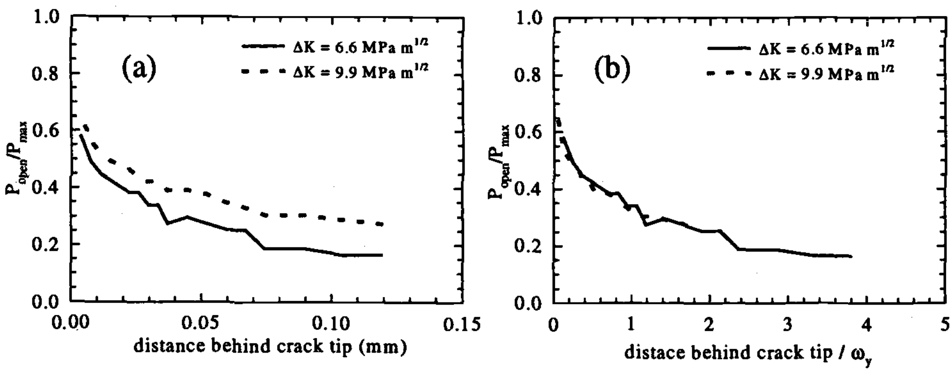

FIG. 11—*Plotted are numerically predicted near-crack-tip surface crack opening loads for AA 8009 at two different values of* ΔK *as functions of* (a) *distance behind crack-tip and* (b) *distance behind crack-tip scaled by cyclic plastic zone size.*

optimum distance behind the crack-tip for local open load surface measurements, X_c, is proposed to vary with ΔK as

$$X_c = b\left(\frac{\Delta K}{\sigma_o}\right)^2 \tag{5}$$

where b is a constant. Given that the experimentally observed optimum distance for AA 8009 at a $\Delta K = 6.6$ MPa m$^{1/2}$ is approximately 0.125 mm, $b = 0.6$. Equation 5 gives the optimum distance for $\Delta K = 3.3$ and 2.2 MPa m$^{1/2}$ as 0.03 and 0.014 mm, respectively. To validate the methods developed above using the model 8009 alloy, a similar analysis was performed using a well characterized engineering alloy (AA 2024-T3). Here, near crack-tip (DIDS) and far field (back-face strain gage and a front-face clip gage) load displacement measurements were performed to characterize the effects of crack closure on near threshold fatigue crack growth. Figure 12 is a plot of da/dN versus ΔK and ΔK_{eff} showing the results of fatigue crack growth tests conducted at constant ΔK (2.2 and 3.3 MPa m$^{1/2}$), constant R. Each data point in Fig. 12 represents steady-state fatigue crack growth that was obtained using methods identical to that described earlier in Fig. 4. The solid line in Fig. 12 shows the intrinsic (Region II) fatigue crack growth rate characteristics for AA 2024 [*28,29*]. The intrinsic data represent closure free, K_{max} independent (defined by R-independent Region II in Fig. 5) fatigue crack growth rates. The local opening load based data (solid symbols) that were obtained by DIDS measurements performed near the optimum location based on Eq 5 (0.05 to 0.01 mm behind the crack tip) correlate well with the intrinsic crack growth rate curve. The experimentally observed local opening loads do not vary much with distance behind the crack-tip in this range. Therefore, the exact measurement location is not critical for these data. Figure 12 reveals that the fully open load data (open symbols) exhibit a high level of scatter and do not correlate with the intrinsic curve.

The good agreement between ΔK_{eff} calculated from local opening loads and the intrinsic curve suggests that near crack-tip load displacement data, measured near the optimal location predicted by Eq 5, can adequately account for crack closure effects on fatigue crack growth rates in both Paris and near-threshold regimes. However, crack closure mechanisms such as roughness and oxide layers might influence near-threshold data. It is possible that the difference between the intrinsic ΔK curve (straight line) and local opening ΔK_{eff} curve (solid symbols) in the near-threshold regime reflects the effect of roughness and oxide on the critical location for local opening load measurement. Therefore, further research to study the effect of non-plasticity-induced crack closure on near-crack-tip displacement behavior is required.

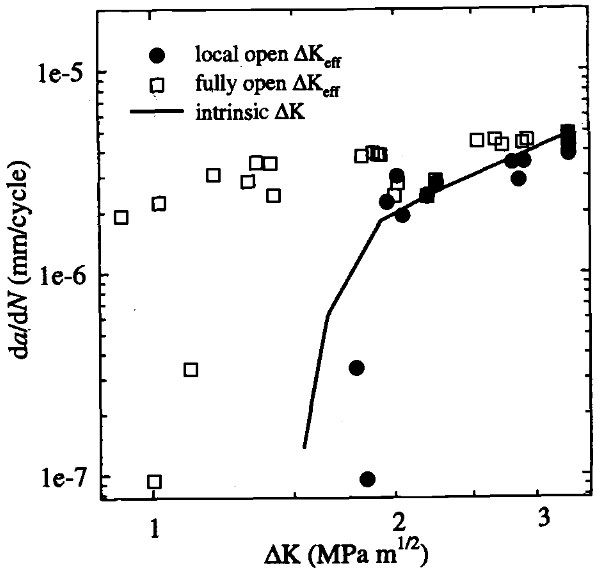

FIG. 12—*Near-threshold fatigue crack growth rates for AA 2024-T3 (L-T) versus Region II (intrinsic)* ΔK *and* ΔK_{eff} *calculated from fully open and local opening loads.*

Concluding Remarks

The study of fatigue crack growth using novel experimental and computational methods revealed the three-dimensional nature of crack closure. Near crack-tip displacement measurements, coupled with elastic-plastic finite element analysis of the growing fatigue crack front, showed that crack opening is a complex process. Both experimental and computational observations showed that the crack gradually peels as loading is increased; local opening loads vary with both distance behind the crack tip and with through-the-thickness location. It was found that no unique opening load can be used to completely describe the opening process. However, it was determined that a single near crack-tip opening load could be used to estimate the effective crack-tip driving force (ΔK_{eff}).

Near crack-tip load-displacement measurements are influenced by near surface crack closure phenomenon. These surface measurements are meaningful only if through-the-thickness crack-front opening behavior is considered. Finite element modeling of the crack-front has shown that the crack opening loads are constant along the interior 90% of the fatigue crack-front and rise rapidly as the free surface is approached. The interior opening load was found to correlate with the rate calculated opening load (RCOL) and thus shown to relate directly to the true crack-front driving force parameter. Near-crack-tip, surface measurements (obtained at less than optimum distance behind the crack-tip) result in erroneously high crack opening levels compared to RCOL due to increases in opening load resulting from surface effects.

The surface measurement of near crack-tip load displacement can be used to estimate fatigue crack-front closure effects accurately for constant-amplitude loading conditions. Finite element analyses of the crack-front region were used to determine the optimum location for surface opening load measurement: where surface local opening loads approximate interior crack front opening loads. Surface local opening loads were used to correlate closure-affected crack growth data with the intrinsic da/dN-ΔK results in both the Paris and near-threshold regimes of AA 2024. However, further research is suggested to consider the effects of non-plasticity-induced fatigue crack closure mechanisms on the critical measurement location in the near-threshold regime.

Acknowledgments

The authors gratefully acknowledge Dr. Stephen W. Smith and Ms. Chelsey Gallik for helping with experimental measurements, and Dr. James C. Newman, Jr. and Dr. David S. Dawicke for their technical guidance. The finite element mesh described in this paper was based on a mesh developed by Dr. R. G. Chermahini and modified using the preprocessor, CASCA. CASCA was developed by the Cornell Fracture Group under the direction of Dr. Anthony Ingraffea. This research was performed while one author (WTR) was a National Research Council NASA Langley Research Center Research Associate.

References

[*1*] Hudson, C. M., "Effect of Stress Ratio on Fatigue Crack Growth in 7075-T6 and 2024-T3 Aluminum Alloy Specimens," NASA TN D-5390, National Aeronautics and Space Administration, Washington, DC, 1969.

[*2*] Ibrahim, F. K., "The Effects of Stress Level, Compressive Peak Stress and Maximum Stress Level on Fatigue Behavior of 2024-T3 Aluminum Alloy," *Fatigue and Fracture of Engineering Materials and Structures*, Vol. 12, No. 1, 1989, pp. 1–8.

[*3*] Bilir, O. G. and Harun, M., "Effect of Stress Ratio on the Rate of Crack Growth in Fatigue Cracks in 1100 Al-Alloy," *Engineering Fracture Mechanics*, Vol. 37, No. 6, 1990, pp. 1203–1206.

[*4*] Phillips, E. P., "The Influence of Crack Closure on Fatigue Crack Growth Thresholds in 2024-T3 Aluminum Alloy," *Mechanics of Fatigue Crack Closure, ASTM STP 982*, J. C. Newman, Jr. and W. Elber, Eds., American Society for Testing and Materials, 1988, pp. 505–515.

[*5*] Couper, M. J. and Griffiths, J. R., "Effects of Crack Closure and Mean Stress on the Threshold Stress Intensity Factor for Fatigue of an Aluminum Casting Alloy," *Fatigue and Fracture of Engineering Materials and Structures*, Vol. 13, No. 6, 1990, pp. 615–624.

[*6*] Salivar, G. C., Heine, J. E., and Haake, F. K., "The Effect of Stress Ratio in the Near-Threshold Fatigue Crack Growth Behavior of Ti-8Al-1Mo-1V at Elevated Temperature," *Engineering Fracture Mechanics*, Vol. 32, No. 5, 1989, pp. 807–817.

[*7*] Elber, W., "Fatigue Crack Closure Under Cyclic Tension," *Engineering Fracture Mechanics*, Vol. 2, 1970, pp. 37–45.

[*8*] Elber, W., "The Significance of Fatigue Crack Closure," *Damage Tolerance in Aircraft Structures, ASTM STP 486*, American Society for Testing and Materials, 1971, pp. 230–242.

[*9*] Newman, J. C., Jr. and Elber, W., Eds., *Mechanics of Fatigue Crack Closure, ASTM STP 982*, American Society of Testing and Materials, 1988.

[*10*] Vasudevan, A. K., Sadananda, K., and Louat, N., "Two Critical Stress Intensities for Threshold Fatigue Crack Propagation," *Scripta Metallurgica et Materialia*, Vol. 28, 1993, pp. 65–70.

[*11*] Lal, D. N., "A Detailed Physical Analysis of the R-Effect on LEFM Fatigue Crack Growth—II. On the Combined Roles of Growth Mechanisms and Stress Ratio," *Engineering Fracture Mechanics*, Vol. 55, No. 2, 1996, pp. 289–312.

[*12*] Chen, D. L., Weiss, B., and Stickler, R., "The Effective Fatigue Threshold: Significance of the Loading Cycle Below the Crack Opening Load," *Fatigue*, Vol. 16, 1994, pp. 485–491.

[*13*] Elber, W., "Crack Closure and Crack Growth Measurements in Surface-Flawed Titanium Alloy Ti-6Al-4V," NASA TN D-8010, National Aeronautics and Space Administration, Washington, DC, 1975.

[*14*] Yisheng, W. and Schijve, J., "Fatigue Crack Closure Measurements on 2024-T3 Sheet Specimens," *Fatigue and Fracture of Engineering Materials and Structures*, Vol. 18, No. 9, 1995, pp. 917–921.

[*15*] *ASTM Standard E 647: Standard Test Method for Measurement of Fatigue Crack Growth Rates*, American Society for Testing and Materials, 1997.

[*16*] Chen, D.-L., Weiss, B., and Strickler, R., "A New Procedure for Crack Closure," *International Journal of Fatigue*, Vol. 13, No. 4, 1991, pp. 327–331.

[*17*] Park, D. H. and Fine, M. E., "Origin of Crack Closure in the Near-Threshold Fatigue Crack Propagation of Fe and Al-3% Mg," *Fatigue Crack Growth Threshold Concepts*, D. L. Davidson and S. Suresh, Eds., The Metallurgical Society of AIME, 1983, pp. 146–161.

[*18*] Gerberich, W. W., Yu, W., and Esaklul, K., "Fatigue Threshold Studies in Fe, Fe-Si, and HSLA Steel: Part 1. Effect of Strength and Surface Asperities on Closure," *Metallurgical Transactions A*, Vol. 15A, 1984, pp. 875–888.

[*19*] Romaniv, O. N., Tkach, A. N., and Lenets, Y. N., "Effect of Fatigue Crack Closure on Near Threshold Crack Resistance of Structural Steels," *Fatigue and Fracture of Engineering Materials and Structures*, Vol. 10, No. 3, 1987, pp. 203–212.

[20] Soboyejo, W. O. and Knott, J. F., "Effects of Stress Ratio on Fatigue Crack Propagation in Q1N (HY80) Pressure Vessel Steel," *International Journal of Fatigue,* Vol. 12, No. 5, 1990, pp. 403-407.

[21] Allison, J. E., Ku, R. C. and Pompetzki, M. A., "A Comparison of Measurement Methods and Numerical Procedures for the Experimental Characterization of Fatigue Crack Closure," *Mechanics of Fatigue Crack Closure, ASTM STP 982,* J. C. Newman, Jr. and W. Elber, Eds., American Society for Testing and Materials, 1988, pp. 171–185.

[22] Davidson, D. L., "Plasticity Induced Fatigue Crack Closure," *Mechanics of Fatigue Crack Closure, ASTM STP 982,* J. C. Newman, Jr. and W. Elber, Eds., American Society of Testing and Materials, 1988, pp. 44–61.

[23] Leng, Y., Porr, W. C., Jr., and Gangloff, R. P., "Tensile Deformation of 2618 and Al-Fe-Si-V Aluminum Alloys at Elevated Temperatures," *Scripta Metallurgica et Materialia,* Vol. 24, 1990, pp. 2163–2168.

[24] Reynolds, A. P., "Constant Amplitude and Post-Overload Behavior in PM Aluminum Alloy AA 8009," *Fatigue and Fracture of Engineering Materials and Structures,* Vol. 15, No. 6, 1992, pp. 551–562.

[25] Newman, J. A., Riddell, W. T., and Piascik, R. S., "Stress Ratio Effects on Crack Growth Rates in Aluminum Alloy 8009," in preparation for a NASA TM.

[26] Piascik, R. S., Newman, J. C., Jr., and Underwood, J. H., "The Extended Compact Tension Specimen," *Fatigue and Fracture of Engineering Materials and Structures,* Vol. 20, No. 4, 1997, pp. 559–563.

[27] *User's Reference Manual for Automated Fatigue Crack Growth (Compliance).* Fracture Technology Associates, Star Route, Pleasant Valley, PA, 1991.

[28] Riddell, W. T. and Piascik, R. S., "Stress Ratio Effects on Crack Opening Loads and Crack Growth Rates in Aluminum Alloy 2024," *Fatigue and Fracture Mechanics: 29th Volume, ASTM STP 1321,* T. L. Panotin and S. D. Sheppard, Eds., American Society for Testing and Materials, in press.

[29] Riddell, W. T. and Piascik, R. S., "Stress Ratio Effects on Crack Opening Loads and Crack Growth Rates in Aluminum Alloy 2024," NASA TM-1998-206928, National Aeronautics and Space Administration, Washington, DC, 1998.

[30] Marci, G. and Packman, P. F., "The Effects of Plastic Wake Zone on the Conditions for Fatigue Crack Propagation," *International Journal of Fracture,* Vol. 16, No. 2, 1980, pp. 133–153.

[31] Dawicke, D. S., Shivakumar, K. N., Newman, J. C., Jr., and Grandt, A. F., Jr., "An Inverse Method for the Calculation of Through-Thickness Fatigue Crack Closure Behavior," *Fracture Mechanics: Twenty Second Symposium (Vol. II), ASTM STP 1131,* S. N. Atluri, J. C. Newman, Jr., I. S. Raju, and J. S. Epstein, Eds., American Society for Testing and Materials, 1992, pp. 46–57.

[32] Chermahini, R. G., Shivakumar, K. N., and Newman, J. C., Jr., "Three Dimensional Finite Element Simulation of Fatigue Crack Growth and Closure," *Mechanics of Fatigue Crack Closure, ASTM STP 982,* J. C. Newman, Jr. and W. Elber, Eds., American Society of Testing and Materials, 1988, pp. 398–413.

[33] Chermahini, R. G., Shivakumar, K. N., Newman, J. C., Jr., and Blom, A. F., "Three Dimensional Aspects of Plasticity Induced Fatigue Crack Closure," *Engineering Fracture Mechanics,* Vol. 34, No. 2, 1989, pp. 393–401.

[34] Chermahini, R. G., Shivakumar, K. N., and Newman, J. C., Jr., "Fatigue Crack Growth and Closure Behavior of Semi-Circular Elliptical Surface Flaws," *International Journal of Fatigue,* Vol. 15, No. 4, 1993, pp. 259–263.

[35] Seshadri, B. R., Dattaguru, B., and Ramamurthy, T. S., "Three Dimensional Elastic-Plastic Finite Element Analysis of Crack Closure in CT Specimen," *Contemporary Research in Engineering Science,* R. C. Batra, Ed., Springer-Verlag, Berlin, 1995, pp. 491–515.

[36] Sutton, M. A., Zhao, W., McNeill, S. R., Helm, J. D., Piascik, R. S., and Riddell, W. T., "Local Crack Closure Measurements: Development of a Measurement System Using Computer Vision and a Far-Field Microscope," *Second Symposium on Crack Closure Measurement and Analysis, ASTM STP 1343,* R. C. McClung and J. C. Newman, Jr., Eds., American Society for Testing and Materials, 1999.

[37] Sutton, M. A., Chao, Y. J., and Lyons, J. S., "Computer Vision Methods for Surface Deformation Measurements in Fracture Mechanics," *Novel Experimental Techniques in Fracture Mechanics,* AMD-Vol. 176, American Society for Mechanical Engineers, 1993, pp. 203–217.

[38] Shivakumar, K. N. and Newman, J. C., Jr., "ZIP3D—An Elastic-Plastic Finite-Element Analysis Program for Cracked Bodies," NASA TM 102753, National Aeronautics and Space Administration, Washington, DC, 1990.

[39] Reynolds, A. P. and Lyons, J. S., "Isotropic and Kinematic Hardening in a Dispersion Strengthened Aluminum Alloy," *Metallurgical and Materials Transactions A,* Vol. 28A, 1997, pp. 1205–1211.

[40] Hudak, S. J., Jr. and Davidson, D. L., "The Dependence of Crack Closure on Fatigue Loading Variables," *Mechanics of Fatigue Crack Closure, ASTM STP 982,* J. C. Newman, Jr. and W. Elber, Eds., American Society for Testing and Materials, 1988, pp. 121–138.

[41] Rice, J. R., "Mechanics of Crack Tip Deformation and Extension by Fatigue," *Fatigue Crack Propagation, ASTM STP 415,* American Society of Testing and Materials, 1967, pp. 247–309.

Hans-Jakob Schindler[1]

Experimental Determination of Crack Closure by the Cut Compliance Technique

REFERENCE: Schindler, H.-J., "**Experimental Determination of Crack Closure by the Cut Compliance Technique,**" *Advances in Fatigue Crack Closure Measurement and Analysis: Second Volume, ASTM STP 1343,* R. C. McClung and J. C. Newman, Jr., Eds., American Society for Testing and Materials, West Conshohocken, PA, 1999, pp. 175–187.

ABSTRACT: The cut compliance method was developed to measure residual stress profiles. Its idea is to release them by introducing progressively a cut into the considered body. From the strain change due to progressive cutting it is possible to calculate the distribution of the released stresses. Since the method uses fracture mechanics principles the stress intensity factor due to residual stresses is delivered as well. Being a special type of residual stresses, the distribution of the contact stresses of fatigue crack closure and the corresponding closure stress intensity factors can be suitably determined by this method. Furthermore, it enables the residual stresses in front of the crack tip to be determined, which in crack retardation play a role as important as the closure effects. The basic theoretical relations for some frequently used fatigue specimens are analytically derived. They also can serve to evaluate the contact stresses from the commonly used unloading compliance technique, which is often used to identify crack closure effects. Some preliminary examples demonstrate the capability of the suggested method.

KEYWORDS: crack closure, closure stress intensity factor, experimental, influence functions, residual stress

The phenomena associated with crack closure result from contact stresses between the crack faces of a fatigue crack in the vicinity of its tip. Being in self-equilibrium, these stresses can be considered as a special type of residual stresses, so in principle methods to determine the latter can also be used to determine closure stresses. A suitable mechanical method to measure the distribution of residual stresses has been suggested and developed by Cheng and Finnie, the so-called crack compliance method [*1,2*] (see Ref *2* for further references). A similar procedure was independently used also by Fett [*3*] and by Kang et al. [*4*]. Its basic idea is to introduce progressively, step by step, a cut along the plane where the residual stresses are to be measured, and to record the change in strain at a suitable location, where the strain is affected by progressive cutting. Therefrom, the released stresses can be calculated. To establish the corresponding mathematical equations, some basic relations of linear elastic fracture mechanics can be utilized, which simplifies the analysis. Recently the cut compliance method (CC-method) was extended by the present author and co-workers such that it became—as will be shown herein—a particularly well-suited tool to determine fatigue crack closure effects: Firstly, the possibility to determine directly the stress intensity factors (SIF) due to the residual stresses was introduced [*5,6*]; secondly, an incremental forward inversion technique was introduced that is able to deal even with steep stress gradients without convergence problems [*7,8*]; and thirdly, closed-form solutions were derived for the required relation between the strain change at the rear edge of the plate and the stress intensity factor (SIF) due to the residual stress at the cut tip [*9*], particularly for cases of relatively deeply notched plates [*10*]. (Note—To avoid confusion with other compliance

[1] Senior research engineer, Swiss Federal Labs. for Materials Testing and Research (EMPA), Ch-8600 Duebendorf, Switzerland.

methods that are often used to measure closure effects [11–13], the term "cut compliance method" is used in the present paper instead of "crack compliance method" as in most of the given references.)

In principle the idea of introducing a cut into the closure zone of a fatigue crack to release and measure the closure stresses is not new; it already was used in Ref 14 to get information about closure effects. The objective of the present paper rather is to show how to adapt and to use the CC-method for this purpose, and to point out its experimental and theoretical advantages regarding simplicity, sensitivity and accuracy. Being based on exact analytical solutions and requiring only one strain gage measurement as input-data, it is experimentally rather simple as well as theoretically accurate. In the following the basic theory of the method will be recapitulated and the relevant influence functions for cracked specimens as used in fatigue testing are derived. Furthermore the relation of the CC-method to other unloading compliance techniques as often used in fatigue is worked out. The suitability and capability of the method are demonstrated by some experimental results.

Principle of the CC-Method

A cut has to be progressively introduced along the plane where the residual stresses are to be measured, which in the case of closure stresses means in the plane of the fatigue crack. Figure 1 exemplifies the case of a rectangular plate containing a fatigue crack of a length a_f, which was initiated at the tip of a notch of length a_n. The actual length of the cut is denoted by "a". In an overall view, the cut can be considered as a perfect crack (see discussion at the end of this paper), so the basic equations of linear elastic fracture mechanics still hold and can serve to establish the required mathematical relation between the residual stress (in the present paper this term also covers contact stresses in the closure area) and the strain ε_M at the measurement point M. It can be easily shown [5] that the SIF at the tip of the cut due to the residual stresses (we restrict ourselves to Mode I, which is predominating in the case of closure stresses) is given by

$$K_{\mathrm{Irs}}(a) = \frac{E'}{Z(a)} \frac{d\varepsilon_M}{da} \tag{1}$$

where E' denotes the generalized Young's modulus (i.e., $E' = E$ for plane stress and $E' = E/(1 - \nu^2)$ for plane strain) and $Z(a)$ the so-called influence function. The latter is a unique function that depends on the component geometry, on the cut plane and on the location of the strain gage, but not on the residual stress distribution. To evaluate Eq 1, $\varepsilon_M(a)$ has to be recorded during the cutting process as a function of the cut depth. In principle the measurement point M is arbitrary, but there are large

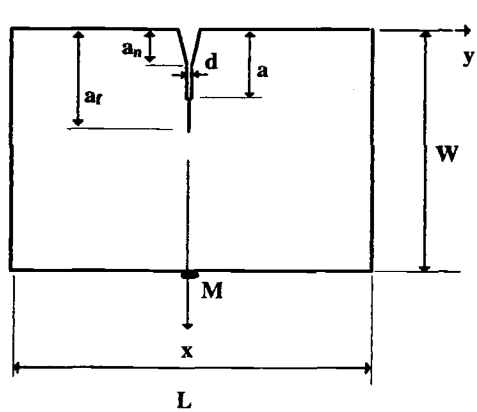

FIG. 1—*A cut of length* a *introduced in the plane of a fatigue crack of length* a_f.

differences regarding its sensitivity, which is characterized by the absolute value of $Z(a)$. Usually the most sensitive location is the one on the rear surface's intersection with the crack plane, as indicated in Fig. 1. Determination of $Z(a)$ is the crucial and—with regard to the theoretical and computational effort—the most demanding step of the CC-method [4,5,8]. However, $Z(a)$ needs to be determined only once for a certain geometry and measurement location. In the next section, solutions of $Z(a)$ for some specimen shapes that are commonly used in fatigue testing are presented.

The cut width d should be chosen as small as possible. However, as long as $a \gg d$ and $(W - a) \gg d$ the effect of the correspondingly blunt notch tip (compared with the theoretically required crack) is negligible. One can show that the energy released due to widening of a narrow crack to a notch of width d is of the same order of magnitude as due to a crack prolongation of the amount $\Delta a = d$. Thus, the finite cut width is just averaging the resulting stresses over a distance of about $\Delta x = d$, which is acceptable since in 2D they are averaged over the specimen thickness B anyway.

If $a < a_f$, $K_{Irs}(a)$ as delivered by Eq 1 represents the SIF due to the closure stresses. Its value at $a = a_f$ represents the well known quantity closure SIF K_{cl}:

$$K_{cl} = K_{Irs}\,(a = a_f) \tag{2}$$

For $a > a_f$, the effect of the residual stresses in front of the crack tip is included in $K_{Irs}(a)$ as well.

From the experimentally determined function $K_{Irs}(a)$ it is possible to calculate the initial distribution $\sigma_{rs}(x)$ of the residual normal stresses (which for $a < a_f$ is the distribution of the contact pressure) by inversion of the general relation

$$K_{Irs}\,(a) = \int_0^a h(x,a)\cdot\sigma_{rs}\,(x)\cdot dx \tag{3}$$

where $h(x,a)$ denotes the so-called weight function as introduced by Bueckner [15]. Formulas of $h(x,a)$ for the specimen geometries considered here can be found in Ref *16*. The inversion of Eq 3 can be achieved by the step-by-step procedure suggested in Ref *8* and summarized below.

Influence Functions

Being a unique function independent on the stress distribution, $Z(a)$ as required in (1) can be calculated by considering an arbitrary load case, the so-called reference load case, by

$$Z(a) = \frac{E'}{K_{Iref}\,(a)} \cdot \frac{d\varepsilon_{Mref}}{da}\,(a) \tag{4}$$

where $K_{Iref}(a)$ and $\varepsilon_{Mref}(a)$ denote the stress intensity factor and the strain at M, respectively, for the reference load case [5,6]. In general, numerical methods, e.g., the finite element method (FEM), have to be used to evaluate (4). In the following, closed-form solutions for $Z(a)$ are given for three crack geometries that are often used in fatigue testing (Fig. 2). Formulas (5), (6), and (7*b*), which are "exact" solutions, are derived in the Appendix. Equation 7*a* is an approximation obtained from FEM results and curve fitting.

Distribution of Closure Stresses

From $K_{Irs}(a)$ as obtained experimentally by using (1), it is possible to calculate the residual stress distribution $\sigma_{rs}(x)$ by inversion of Eq 3, which can be performed according to Ref *8* as follows. The residual stress distribution $\sigma_{rs}(x)$ is approximated by a series of small steps as shown schematically in Fig. 3, so the stress level at each step can be calculated by applying Eq 3 to a hypothetical, incre-

a) Disk-shaped CT-specimen 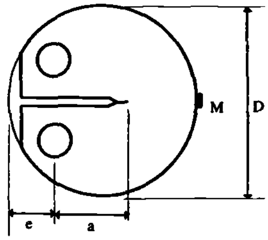	$$Z(a) = -\frac{7.952}{\pi \cdot D^2} \cdot \sqrt{\frac{a+e}{\left(1-\frac{a+e}{D}\right)^3}} \quad (5)$$
b) Standard CT-specimen 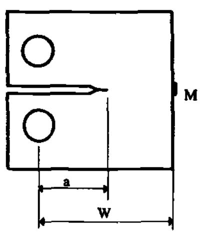	$$Z(a) = \frac{-2.532}{(W-a)^{3/2}} \quad (6)$$ (for a>0.5W)
c) Beam-shaped specimen (L>2W) 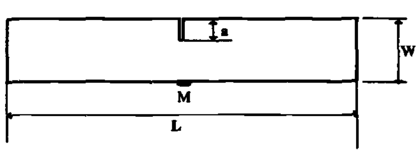	$$Z(a) = \frac{-2.532}{(W-a)^{3/2}} \sqrt{1-25 \cdot \left(a/W - 0.2\right)^2} \cdot \left[5.926 \cdot \left(0.2 - a/W\right)^2 - 0.288 \cdot (0.2 - a/W) + 1\right]$$ (for a/W≤0.2) (7a) $$Z(a) = \frac{-2.532}{(W-a)^{3/2}}$$ (for 0.2<a/W<1) (7b)

FIG. 2—*Three specimen types often used in fatigue testing, and corresponding influence functions* Z(a).

mentally prolonging crack. The stress level of the first increment, σ_0, which represents the average stress acting near the front surface in the range $0 < x < a_0$ (where $a_0 \ll W$ should be fulfilled) is obtained from the well-known relation between the stress and the SIF of a short edge crack, i.e.:

$$\sigma_0 = \frac{K_{\mathrm{Irs}}(a_0)}{1.12 \cdot \sqrt{\pi \cdot a_0}} \quad (8)$$

If the fatigue crack is—as usual—initiated by a starter notch of depth a_n, then a_0 and σ_0 shall be chosen $a_0 = a_n$, and $\sigma_0 = 0$, respectively, since there are no closure stresses on the initial notch. In order to calculate the average stress level σ_1 of the next step (i.e., the average stress in the range $a_0 < x < a_0 + \Delta a$), we extend the hypothetical crack by the increment Δa and apply Eq 3. Then a further crack increment is assumed, for which the corresponding stress level follows again from Eq 3, and so forth across the whole cross section. Denoting the length of the hypothetical crack after i prolonga-

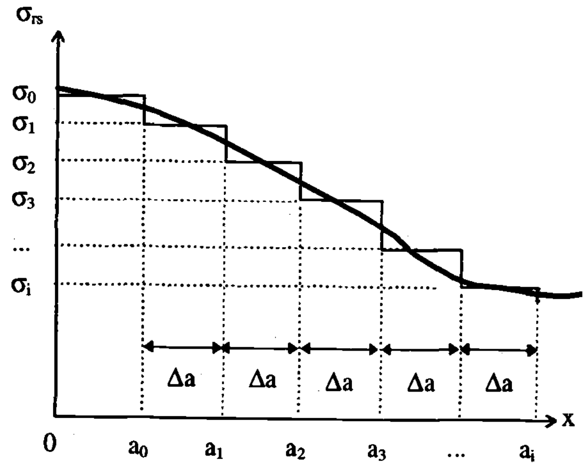

FIG. 3—*Step-wise determination of the residual stress distribution* σ_{rs}(x).

tion increments Δa by a_i (i.e., $a_i = a_0 + i\cdot\Delta a$), and the average stress in the corresponding interval $a_{i-1} < x < a_i$ by σ_i (see Fig. 3), Eq 3 is approximated by

$$K_{\mathrm{Irs}}\,(a_i) = \sigma_0\cdot\int_0^{a_0} h(x,a_i)\cdot dx + \sum_{j=1}^{i-1} \sigma_j\cdot\int_{a_{j-1}}^{a_j} h(x,a_i)\cdot dx + \sigma_i\cdot\int_{a_{i-1}}^{a_i} h(x,a_i)\cdot dx \qquad (9)$$

which allows σ_i to be calculated for each step. The resulting step distribution converges to the exact solution $\sigma_{rs}(x)$ as $\Delta a \to 0$. Some difficulties (mathematical instabilities) may arise in the region near the rear surface (i.e., for $W - a \ll W$), because weight functions, which usually are approximations, might be not accurate enough in this range [7]. For this reason it is recommended to replace for cut depths of about $a_i > 0.8\ W$ Eq 9 by

$$K_{\mathrm{Irs}}\,(a_i) = \sum_{j=0}^{i} \left\{ \frac{3.97\sigma_j\cdot\Delta a\cdot[0.264W + 0.736a_i - (a_0 + j\cdot\Delta a)]}{(W - a_i)^{3/2}} + \frac{1.46\sigma_j\Delta a}{(W - a_i)^{1/2}} \right\} + 2\sigma_i\sqrt{\frac{2}{\pi}\,q\cdot(W - a_i)} \qquad (10)$$

as explained in Ref *8*. The nondimensional factor q, which is about 0.03, can be determined from the condition that transition from Eq 9 to Eq 10 at the chosen transition cut depth $a = a_i$ shall deliver a continuous function $\sigma_{rs}(x)$ at $x = a_i$. Using Eq 10 guarantees that the condition of self-equilibrium of the calculated residual stresses will be fulfilled.

Closure Stresses from the Unloading Compliance

It is well known that the slope of the force-vs.-displacement or force vs. strain curve of a specimen that contains a crack is changing when an increasing or decreasing external force is applied. This effect is due to the geometrical nonlinearity resulting from the load dependence of the contact area in the closure zone, which acts like a changing crack length. If the load F is increasing, the effective crack length seems to grow from $a = a_{cl}$ at $F = 0$ to $a = a_f$ at $F = F_{op}$, where F_{op} is the so-called opening load and a_f the actual length of the fatigue crack. Regarding the compliance in the sense of the CC-method, a continuous loading has the same effect as a continuous cutting. Thus, instead of cutting, an increasing external load can be applied, provided the required strain-vs.-force curve is accurate enough to exhibit the changes in the slope of the curve, which are small. To avoid interference with plastic effects which also contribute to nonlinearities, unloading instead of loading is preferable. As shown below, the analysis of the CC-method can be easily extended to make it applicable to cracks that are extended or contracted by external forces.

The strain that results at M due to the load F and the increasing effective crack length, a, which in the considered case means the length of the contact-free zone of the crack faces, follows readily from (1) to be

$$\varepsilon_M(a, F) = \varepsilon_M(a_{cl}) + \frac{1}{E'} \cdot \int_{a_{cl}}^{a} K_I(F, a) \cdot Z(a) \cdot da \tag{11}$$

The compliance with respect to the strain at M is obtained therefrom to be

$$C_\varepsilon(a) = \frac{d\varepsilon_M(a, F)}{dF} = C_\varepsilon(F = 0) + \frac{1}{E'} \cdot \int_{a_{cl}}^{a} k_I(a) \cdot Z(a) \cdot da \tag{12}$$

where $k_I(a) = K_I(a)/F$. By (12), the actual effective crack length, a, corresponding to the actual load, F, can be obtained from the actual slope of the curve $\varepsilon_M(F)$ (Fig. 4). Once knowing the effective crack length, the corresponding SIF, which is equal to the SIF due to the contact stresses, thus equivalent to $K_{Irs}(a)$ as given in (1) for $a_{cl} < a < a_f$, follows from

$$K_I(a, F) = F \cdot k_I(a) = K_{Irs}(a) \tag{13}$$

From $K_{Irs}(a)$ as given by (13) the distribution of the closure stresses can be obtained as described in the previous section. The total closure SIF is $K_{cl} = K_{Irs}(a_f)$.

As an example we consider the case of a relatively deeply notched beam or rectangular plate (Fig. 5, $a > 0.25W$) subjected to 4-point bending as external forces to open the crack. The SIF for this case can be approximated by [20]

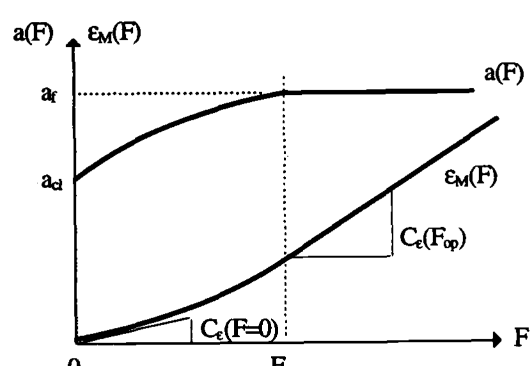

FIG. 4—*Behavior of the effective crack length* a *and the strain for increasing or decreasing external load* F *(schematic).*

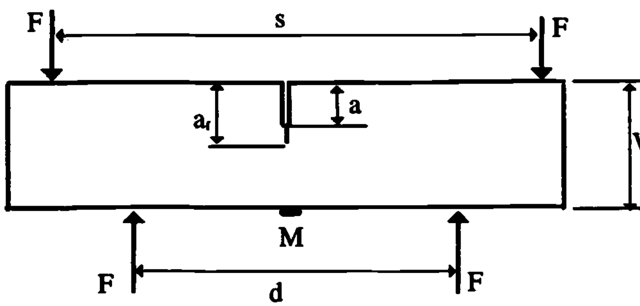

FIG. 5—*Edge crack in a beam opened by 4-point bending.*

$$K_{\mathrm{Irs}}(a) = \frac{3.97 \cdot F \cdot (s-d)}{2B \cdot (W-a)^{1.5}} \quad \text{thus:} \quad k_{\mathrm{I}} = \frac{1.98 \cdot (s-d)}{B \cdot (W-a)^{1.5}} \tag{14}$$

$Z(a)$ for this case is given by (7*b*). Therewith, (12) leads to

$$\Delta C_\varepsilon(F, F_{\mathrm{op}}) = \frac{5.026}{E' \cdot B \cdot W^2} \cdot \left[\left(1 - \frac{a_f}{W}\right)^{-2} - \left(1 - \frac{a}{W}\right)^{-2}\right] \tag{15}$$

where $\Delta C_\varepsilon(F, F_{\mathrm{op}}) = C_\varepsilon(F_{\mathrm{op}}) - C_\varepsilon(F)$ denotes the difference of the slope of the force vs. strain curve between the opening load F_{op} and the actual load F. This equation can easily be solved for the actual crack length a

$$\frac{a}{W}(F) = 1 - \sqrt{\left[\left(1 - \frac{a_f}{W}\right)^{-2} - \frac{\Delta C_\varepsilon(F, F_{\mathrm{op}}) \cdot E' \cdot B \cdot W^2}{5.026}\right]^{-1}} \tag{16}$$

By this equation, the actual length of the contact area can be determined from the experimentally determined change in the slope of the compliance curve and the optically measured a_f. Together with (14) it is possible to get $K_{\mathrm{Irs}}(a)$, i.e., the same information as given by (1), but limited to the closure zone $a_{\mathrm{cl}} < a < a_f$.

Examples

Two CT-specimens of $W = 50$ mm made of a mild austenitic stainless steel ($R_p = 200$ MPa) were fatigued in accordance with the standard ASTM E 813. The initial notch depth was $a = a_n = 27$ mm, the fatigue crack length $a = a_f \approx 30$ mm. The cut was produced by electrical discharge machining (EDM). The SIF resulting from (1) and (6) for specimen S1 is shown in Fig. 6. The stresses calculated from the SIF-distribution by (8) and (9) are shown in Fig. 7. The second specimen, *E*1, was additionally subjected to an overload up to the plastic range. The measured SIF and stresses are also shown in Figs. 6 and 7. Comparing the results of these two experiments shows that the contact pressure that is present in specimen S1 in the range 27.5 mm $< a <$ 30 mm has vanished in the specimen E1 due to the overload. On the other hand, the overload significantly increased the residual stresses in the ligament. This corresponds qualitatively to the expected behavior. There are two further theoretically expected features of these curves: First, the SIF due to residual stresses (Fig. 6) should tend to zero as the cut depth a approaches the rear surface, and second, the residual stresses (Fig. 7) should be in self-equilibrium. Just by visual inspection of the corresponding curves these requirements seem to be fulfilled, which is another indication that the method works properly and the results are reliable.

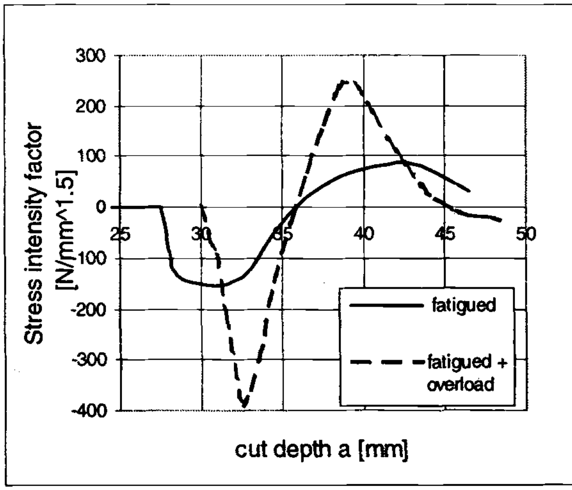

FIG. 6—*SIF as a function of cut depth a for two CT-specimens: specimen S1 (fatigued) and specimen E1 (with additional single overload).*

To further explore the capability of the CC-method it was applied to a short surface crack. For this purpose, a beam-shaped specimen of $W = 13.5$ mm with a starter notch of a depth $a_n = 1.5$ mm was loaded in cyclic bending until a crack of about 0.5 mm length was formed at the notch. Then a surface layer as thick as the depth of the notch was removed, so a flat beam-shaped specimen of $W = 12$ mm containing an edge crack of about 0.5 mm depth remained. The resulting SIF-distribution obtained from (1) and (7*a*) is shown in Fig. 8. Figure 9 shows the corresponding contact pressure and residual stress distribution. Obviously such special problems can also be handled by the CC-method.

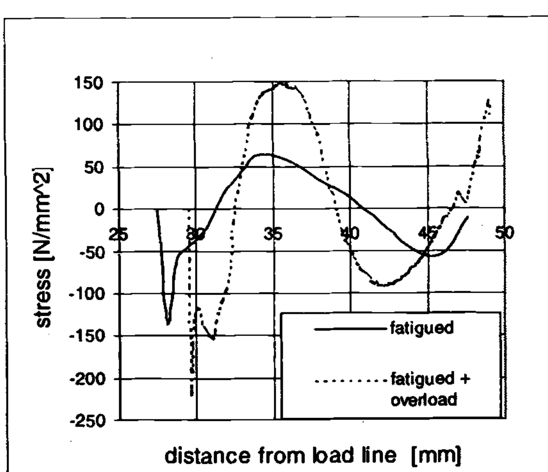

FIG. 7—*Closure and residual stresses as a function of the distance from the load line (see Fig. 2) corresponding to SIF as given in Fig. 6.*

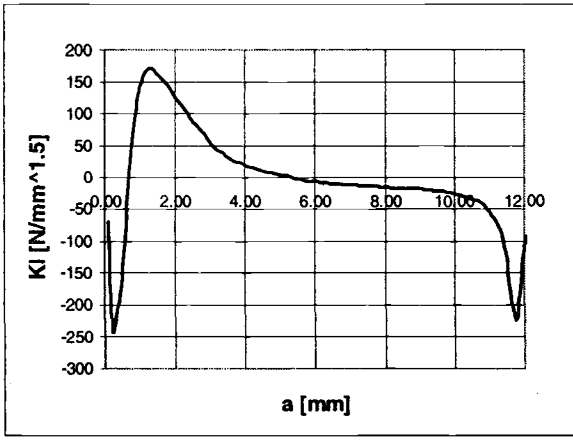

FIG. 8—*Stress intensity factor due to closure and residual stresses in the case of a beam containing a short surface crack.*

Discussion and Conclusions

It is shown that the cut compliance technique offers the possibility to determine experimentally crack closure effects, which includes the distribution of contact stresses in the closure zone of the crack surface, the corresponding stress intensity factor as well as the residual stresses in front of the crack tip. Experimentally, this method is remarkably simple. One just needs to introduce progressively a narrow cut along the crack plane and to measure the resulting strain change at the back surface of the specimen. The slope of the strain-vs.-cut depth curve is proportional to the SIF due to the closure stresses, with the so-called influence function representing the corresponding linear relation. Though exact, the latter is particularly simple for the cases of deeply notched specimens that are common in fatigue testing. Thus this method represents a very suitable means to identify crack closure effects and to investigate related crack retardation mechanisms.

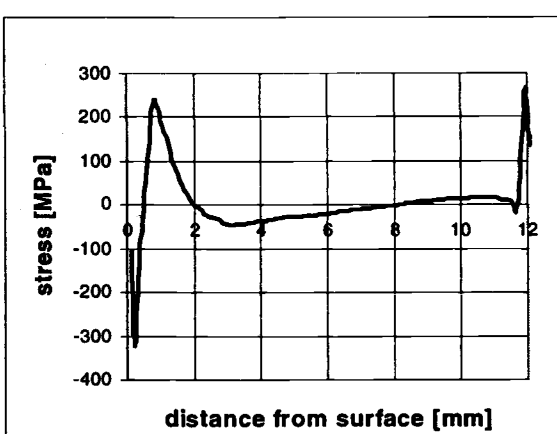

FIG. 9—*Closure stress and residual stress corresponding to Fig. 8.*

Crack retardation effects are often categorized as so-called extrinsic and intrinsic. Crack closure belongs to the former, whereas residual stresses in front of the crack tip to the latter. However, as shown by the exemplary experimental results (Figs. 6–9), the contact stresses in the wake of the crack and the residual stresses in front of the crack tip follow a continuous curve, as does the resulting SIF. Both curves exhibit no indication of the exact position of the crack tip. The closure SIF is defined as the value of the SIF-curve at the tip of the fatigue crack. In general, the latter is hard to define, since the crack front in general does not form a straight line. Thus, it is hardly possible to unambiguously distinguish between crack closure in the wake, on one hand, and residual stresses in front of the crack tip on the other. This implies that a strict distinction between these two categories, which from a theoretical point of view is helpful, but from a physical point of view is less relevant. It seems that they should rather be considered as interacting mechanisms, which have a similar effect on the further crack propagation. For instance, compare the results of the CT-specimens with and without overload (Figs. 6 and 7): the overload of specimen E1 obviously wiped out the fatigue closure stresses, but increased the residual stresses in front of the crack. It is well known that such an overload causes additional crack retardation. Actually, the residual stress ahead of the crack tip reflects, to a certain extent, the future closure stresses that the crack will feel as it grows through the zone of compressive residual stresses.

In this sense, being able to deliver the corresponding experimental data, the CC-method applied to fatigue cracks will probably open some new insight in crack retardation mechanisms.

APPENDIX

Determination of Influence Functions

Generally, the influence function as defined in (1) can be obtained by (3), i.e.

$$Z(a) = \frac{E'}{K_{\mathrm{Iref}}(a)} \cdot \frac{d\varepsilon_{\mathrm{Mref}}}{da}(a) \tag{17}$$

where $K_{\mathrm{Iref}}(a)$ and $\varepsilon_{\mathrm{Mref}}(a)$ denote the stress intensity factor and the strain at M, respectively, for the considered reference load case. In the following the solutions for a circular disk containing a radial edge crack (Fig. 10) and a deeply edge-cracked plate or beam (Fig. 11) are derived, which form the basis of the formulas presented in this paper.

Circular Disk

Consider a radially cracked circular disk (Fig. 10). A suitable reference load case is a uniformly pressure p acting on the crack surface. For this load case the exact solution for the SIF is given in Refs *17* and *18* to be

$$K_{\mathrm{Iref}} = 1.988 \cdot p \cdot \sqrt{\frac{a}{(1 - a/D)^3}} \tag{18}$$

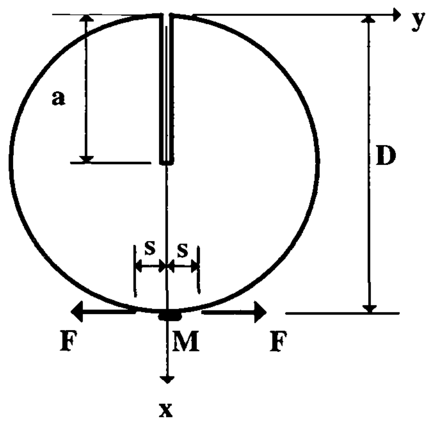

FIG. 10—*Circular disk containing an edge crack.*

According to Castigliano's principle [*19*], the reference strain $\varepsilon_{\mathrm{Mref}}(a)$ is obtained by

$$\varepsilon_{\mathrm{M}} = \frac{1}{2} \frac{\partial^2 U}{\partial F \partial s}\bigg|_{\substack{F=0 \\ s=0}} \tag{19}$$

where F denotes a pair of virtual forces acting at $y = \pm s$ from M, as shown in Fig. 10, and U the strain energy, which is

$$U = \frac{B}{E'} \int_0^a [K_{\mathrm{Irs}} + K_{\mathrm{IF}}]^2 \, da \tag{20}$$

K_{IF}, the stress intensity factor due to the virtual forces F, can be written as

$$K_{\mathrm{IF}}\,(s) = \int_0^a h(x,a) \cdot \sigma_{\mathrm{yF}}\,(x,s) \cdot dx \tag{21}$$

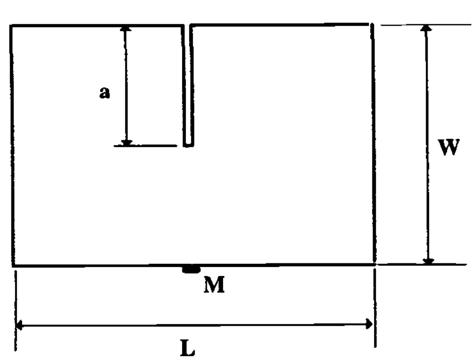

FIG. 11—*Deeply cracked rectangular plate.*

where $\sigma_{yF}(x,s)$ is the distribution of the normal stresses along the x-axis due to F in the absence of a crack. It is obtained from the general exact solution given in Ref *5* to be

$$\sigma_{yF}(x,s) = \frac{2F}{\pi \cdot B} \cdot \left\{ \frac{s^3}{[(D-x)^2 + s^2]^2} - \frac{2s}{D^2} \right\} \tag{22}$$

Using (17) and (19–22) one finds

$$Z(a) = -\frac{4}{\pi \cdot D^2} \int_0^a h(x,a)dx \tag{23}$$

The same integral appears when the SIF for the reference load case of a homogeneous pressure acting on the crack surface is calculated by the weight function technique (see (20)). From comparison with (18) one finds

$$\int_0^a h(x,a)dx = 1.988 \cdot \sqrt{\frac{a}{(1 - a/D)^3}} \tag{24}$$

Inserting (24) in (23) leads to

$$Z(a) = -\frac{7.952}{\pi \cdot D^{3/2}} \cdot \frac{a/D}{(1 - a/D)^3} \tag{25}$$

Based on exact solutions, (25) holds without restrictions for $0 < a < D$. Note that the crack length, a, is defined somewhat different from Fig. 2*a*.

Deeply Cracked Rectangular Plates

Consider an edge-cracked rectangular beam as shown in Fig. 2, loaded as a reference load by a uniform pressure acting on the crack surfaces. In the case of a relatively deep crack, which means for $a > 0.2W$ and $W - a < 0.6L$, the dominating geometrical quantity in the SIF as well as the strain at M is the ligament width $W - a$. Thus, a dimensional analysis leads to

$$Z(a) = -\frac{A}{(W-a)^{3/2}} \tag{26}$$

where A is a nondimensional constant, which is determined by the following limit analysis. K_{Iref}, ε_{Mref} as well as $Z(a)$ for the disk (Fig. 10) and the rectangular plate tend to coincide as $a \rightarrow D$ and $a \rightarrow W$, respectively. Therewith one readily finds

$$Z(a) = -\frac{7.952}{\pi \cdot (W-a)^{3/2}} \tag{27}$$

References

[1] Cheng, W. and Finnie, I., "Measurement of Residual Hoop Stresses in Cylinders Using the Compliance Method," ASME, *Journal of Engineering Materials and Technology*, Vol. 108, 1986, pp. 87–92.

[2] Cheng, W. and Finnie, I., "An Overview of the Crack Compliance Method for Residual Stress Measurement," *Proceedings*, 4th International Conference on Residual Stress, Baltimore, published by the Society of Experimental Mechanics, 1994, pp. 449–458.

[3] Fett, T., "Bestimmung von Eigenspannungen mittels bruchmechanischer Beziehungen," *Materialprüfung*, Vol. 29, No. 4, 1987, (in German), pp. 92–94.

[4] Kang, K. J., Song, J. H., and Earmme, Y. Y., "A Method for the Measurement of Residual Stress Using a Fracture Mechanics Approach," *Journal of Strain Analysis*, Vol. 24, 1989, pp. 23–30.

[5] Schindler, H. J., *Proceedings*, 27th Vortragsveranstaltung des DVM AK Bruchvorgänge, Deutscher Verband für Materialforschung und -prüfung e.V., Cologne, 1995 (in German), pp. 421–430.

[6] Schindler, H. J., Cheng, W., and Finnie, I., "Experimental Determination of Stress Intensity Factors due to Residual Stresses," *Experimental Mechanics*, Vol. 37, No. 3, 1997, pp. 272–279.

[7] Schindler, H. J., "Weight Functions for Deep Cracks and High Stress Gradients," *Advances in Fracture Resistance and Structural Integrity*, V. V. Panasyuk et al., Eds., Pergamon Press, Oxford, 1994, pp. 193–205.

[8] Schindler, H. J. "Determination of Residual Stress Distributions from Measured Stress Intensity Factors," *International Journal of Fracture*, Vol. 74, 1995, pp. R23–R30.

[9] Schindler, H. J. and Bertschinger, P., "Some Steps Towards Automation of the Crack Compliance Method to Measure Residual Stress Distributions," *Proceedings*, 5th International Conference on Residual Stresses, Linköping, Sweden, 1997.

[10] Schindler, H. J. and Finnie, I., "Determination of Residual Stresses and the Resulting Stress Intensity Factors in the Ligament of Pre-cracked Components," *Advances in Fracture Research*, B. L. Karihaaloo et al. Eds., *Proceedings*, 9th International Conference on Fracture), Sydney, Pergamon, Amsterdam, Vol. 1, 1997, pp. 523–530.

[11] James, M. N., "Some Unresolved Issues with Fatigue Crack Closure-Measurement, Mechanism and Interpretation Problems," *Advances in Fracture Research*, B. L. Karihaaloo et al. Eds., (*Proceedings*, 9th International Conference on Fracture), Sydney, Pergamon, Amsterdam, Vol. 5, 1997, pp. 2403–2413.

[12] Allison, J. E., et al., "A Comparison of Measurement Methods and Numerical Procedures for the Experimental Characterization of Fatigue Crack Closure," *Mechanics of Fatigue Crack Closure, ASTM STP 982*, J. C. Newman and W. Elber, Eds., American Society for Testing and Materials, 1988, pp. 171–185.

[13] Saxena, A. and Hudak, S. J., "Review and Extension of Compliance Information for Common Crack Growth Specimens," *International Journal of Fracture*, Vol. 14, No. 5, 1978, pp. 453–467.

[14] Ritchie, R. O. and Yu, W., "Short Crack Effects in Fatigue: A Consequence of Crack Tip Shielding," *The Metallurgical Society of AIME*, 1986, pp. 167–189.

[15] Bückner, H., "A Novel Principle for Computation of Stress Intensity Factors," *Zeitschrift für Angewandte Mathematik und Mechanik (ZAMM)*, Vol. 50, 1970, p. 529.

[16] Wu, X.-R. and Carlsson, A. J., *Weight Functions and Stress Intensity Factor Solutions*, Pergamon Press, Oxford, U.K., 1991.

[17] Gregory, R. D., "A Circular Disc Containing a Radial Edge Crack Opened by a Constant Internal Pressure," *Mathematical Proceedings of the Cambridge Philosophical Society*, Vol. 81, 1977, pp. 497–521.

[18] Gregory, R. D., "The Spinning Circular Disc with a Radial Edge Crack; an Exact Solution," *International Journal of Fracture*, Vol. 41, 1989, pp. 39–50.

[19] Timoshenko, S. P. and Goodier, N. P., *Theory of Elasticity*, 3rd Ed., McGraw-Hill, New York, 1970.

[20] Tada H., Paris, C. P., and Irwin, G. R., *The Stress Analysis of Cracks Handbook*, Del Research Corporation, Hellertown, PA, 1973.

Load History Effects

Christian Bichler[1] *and Reinhard Pippan*[1]

Direct Observation of the Residual Plastic Deformation Caused by a Single Tensile Overload

REFERENCE: Bichler, C. and Pippan, R., **"Direct Observation of the Residual Plastic Deformation Caused by a Single Tensile Overload,"** *Advances in Fatigue Crack Closure Measurement and Analysis: Second Volume, ASTM STP 1343,* R. C. McClung and J. C. Newman, Jr., Eds., American Society for Testing and Materials, West Conshohocken, PA, 1999, pp. 191–206.

ABSTRACT: The fatigue crack growth behavior following single tensile overloads at high stress intensity ranges in a cold-rolled austenitic steel has been studied experimentally. After tensile overloads, fatigue cracks initially accelerate, followed by significant retardation, before the growth rates return to their baseline level. The initial acceleration was attributed to an immediate reduction in near-tip closure. Scanning electron micrography and stereophotogrammetric reconstruction of the fracture surface were applied to study the residual plastic deformation caused by a single tensile overload in the mid-thickness of the specimen. The measured residual opening displacement of the crack as a function of the overload is presented and compared with simple estimations. Also, free specimen surface observations of the residual plastic deformation and crack growth rate were performed. In the midsection of the specimens the striation spacing-length, i.e., the microscopic growth rates, were measured before and after the applied overload. It will be shown that the measured plasticity-induced wedges from the single overload and the observed propagation behavior support the significance of the concept of crack closure.

KEYWORDS: residual plastic deformation, single tensile overload, stereophotogrammetric reconstruction, striation spacing, austenitic steel

The effect of overloads on fatigue crack growth rates has received a considerable amount of attention during the past number of years because a better fatigue life prediction under service conditions is necessary. The most documented load interaction effect is that of crack growth retardation of Mode I cracks following a single tensile overload. Different mechanisms have been presented by Schijve [*1*], Elber [2], Von Euw, Hertzberg and Roberts [*3*], Christensen [*4*], Hudson and Hardrath [*5*], Suresh [*6*], Jones [*7*], Knott and Pickard [*8*] and Forsyth [9].

These works are based on the following concepts:

- Residual stresses, where the strain produced by the tensile overload results in an increase of residual compressive stresses ahead of the crack [*1*].
- Crack closure, which results from fracture surface contact at nonzero load and reduces the effective stress intensity range [2,*3*].
- Plastic blunting [*4,5*] of the crack tip; the blunted crack tip behaves like a notch with a smaller stress concentration than the originally sharp crack tip.
- Crack deflection; a branching of the crack at the overload causes a reduction in the local stress intensity range at the crack tip [*6*].

[1] Research engineer and interimistic director, respectively, of the Erich-Schmid-Instutut für Festkörperphysik der Österreichischen Akademie der Wissenschaften, A8700 Leoben, Jahnstr. 12, Austria.

- Strain hardening [7,8] of the material in the overload plastic zone.
- Crack front profile [9]; large overload may change the crack front shape and reduces locally ΔK for subsequent growth.

In the 1980's the closure effect was an often considered mechanism to explain the retardation effect. In the past few years some doubts on the significance of the crack closure concept [10,11] were presented. In order to prove the assumptions of the different mechanisms and their consequence, the residual deformation on the fracture surfaces and the changes in the crack propagation rate after single overloads were investigated. A special technique was developed to measure the residual plastic deformation in the midsection of a specimen. It is based on a fractographic technique in combination with a stereophotogrammetric reconstruction of the fracture surface [12–16] which was developed at the author's institute. This allowed them to measure the real three-dimensional shape of the fracture surfaces.

Material and Test Conditions

The investigated material was a cold-rolled (reduction in thickness from 42 mm to 27 mm) austenitic Cr-Ni steel A220, with a yield strength of 890 MPa, an ultimate tensile strength of 1010 MPa and a fracture toughness K_{Ic} of 203 MPa$\sqrt{m}$. The grain size of the material varied between 1 mm and 2 mm. The chemical composition is given in Table 1. Optical micrographs of the microstructure before (Fig. 1*a*) and after (Fig. 1*b*) cold rolling are shown in Fig. 1. Figure 1*b* shows the slipbands in each grain which were produced during cold rolling of the material.

Fatigue crack growth tests were performed using compact tension specimens (width W = 96 mm, thickness B = 9 mm) in the long transverse orientation in laboratory air. The stress intensity factor chosen for these experiments was ΔK= 70 MPa$\sqrt{m}$ at a stress ratio ($R = K_{min}/K_{max}$) of 0.05. The single tensile overload had a maximum stress intensity factor which was 1.1, 1.2, 1.4, 1.6 and 2.0 times K_{max} of the constant stress intensity range. Crack length was measured using an optical microscope (accuracy 0.025 mm) and a d.c. electrical potential-drop method system which was used to maintain constant ΔK conditions as the crack advanced. The frequency varied between 1 Hz and 0.004 Hz. For the constant stress intensity range the authors used a frequency of 1 Hz, except for the measurement of the potential, the compliance (using a clip gage on the end of the notch) and the crack advance on the surface. Single overloads and the special measurements were applied at 0.004 Hz. For the 1.1, 1.2, 1.4 and 1.6 overload the small-scale yielding conditions are fulfilled. They have chosen this material and these loading conditions because they exhibit very nice and large striations with a striation spacing of about 1 μm (under steady-state conditions) which allows them a clear determination of the cycle-by-cycle crack propagation behavior after the overload in the middle of the specimen.

Determination of the Residual Plastic Deformation in the Midsection of a Specimen

The definition of the parameters (Fig. 2*b*) and the loading procedure (Fig. 2*a*) to measure the residual plastic deformation after a single overload is schematically illustrated in Fig. 2. The specimen was fatigued with a constant stress intensity range until it reached the steady-state condition. The test was interrupted to initiate an overload and than the experiment was continued with a constant stress in-

TABLE 1—*Chemical Composition (Cr-Ni-Mo Low Carbon).*

Element	C	Cr	Ni	Mo	Si	Mn	P	S	W
Weight %	0.018	17.24	14.53	2.56	0.61	1.71	0.018	0.001	0.07
Element	Cu	Al	N	...	...	...	...	...	...
Weight %	0.11	0.03	0.068	...	...	...	...	...	...

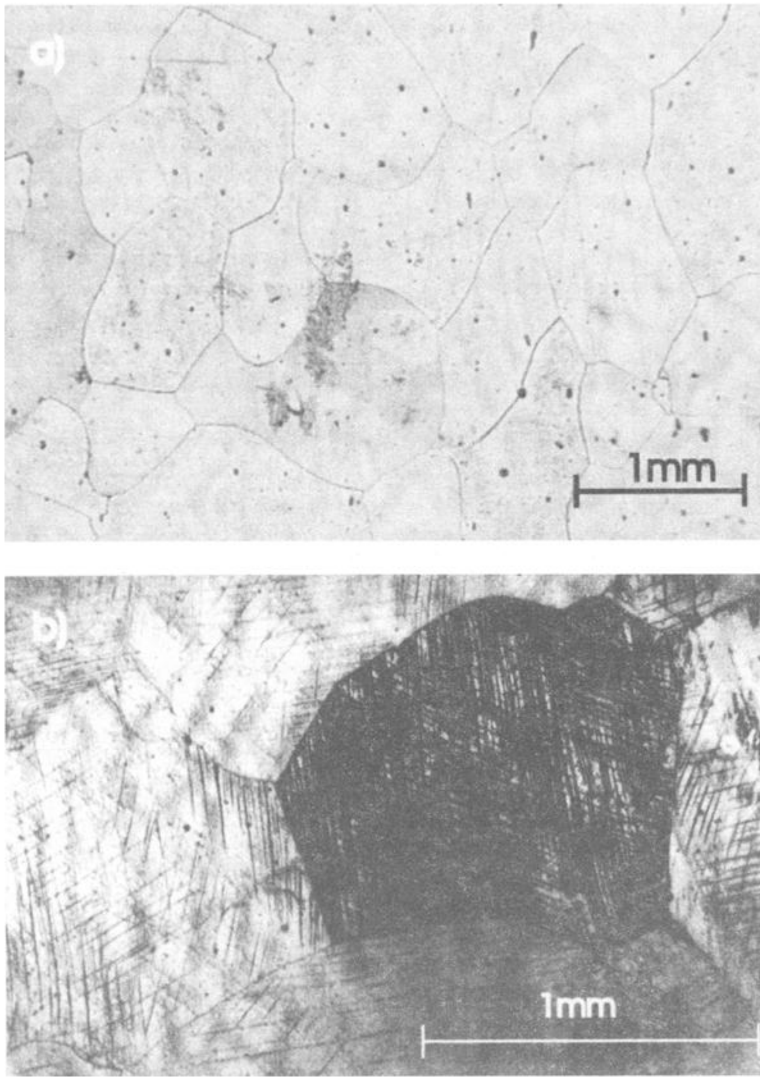

FIG. 1—*Optical micrograph of the microstructure:* (a) *Before cold rolling,* (b) *after cold rolling.*

tensity range. On one specimen approximately five overloads (10, 20, 40, 60, and 100%) were applied until the specimen failed. The residual deformation on both fracture surfaces due to the overload were then reconstructed. This was done by analyzing stereoscopic scanning electron microscope (SEM) images of the broken surface with an automatic image processing system. The technique is now explained for the determination of the deformation due to a 20% overload. Fig. 3*a* shows the SEM fractograph of the region where the constant ΔK test was interrupted and an overload was introduced. Figure 3*b* shows exactly the corresponding fracture surface of the second half of the specimen. Region A (points 3 to 4) marks the fracture surface which was produced at $\Delta K = 70$ MPa$\sqrt{m}$ ($R = 0.05$). Region B (points 2 to 3) shows the "blunting" produced at the overload and region C

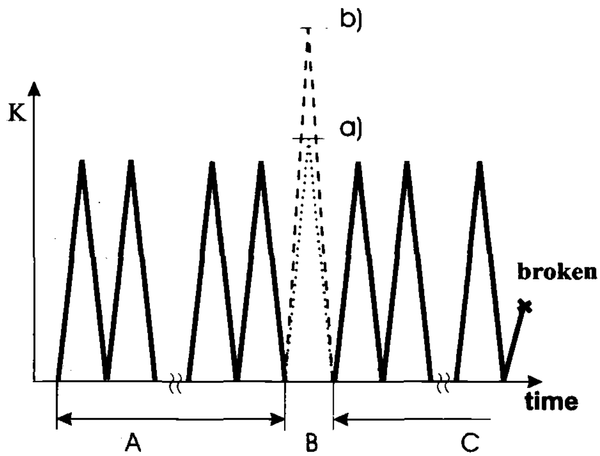

FIG. 2a—*Experimental procedure to determine the residual crack tip deformation (blunting) after a single tensile overload in the middle of the specimen:* (a) *for a 10% overload,* (b) *for a 60% overload.* (A) *fatigue with a constant* ΔK, (B) *single tensile overload,* (C) *fatigue with a constant load amplitude till the specimen failed.*

(points 1 to 2) marks the crack extension after the overload. These pictures indicate clearly the differences of the striation spacing before and after the overload which can be directly associated with a decrease of the crack closure level ($da/dN \sim$ CTOD $\sim \Delta K^2_{eff}$). The fracture surface of that particular region of the broken specimen was then analyzed by the stereophotogrammetric technique, where the stereo pairs were obtained by tilting the specimen by an angle of 10 deg in the SEM. To determine the residual crack tip opening displacement (CTOD) four images are needed: two stereo images from both specimen halves.

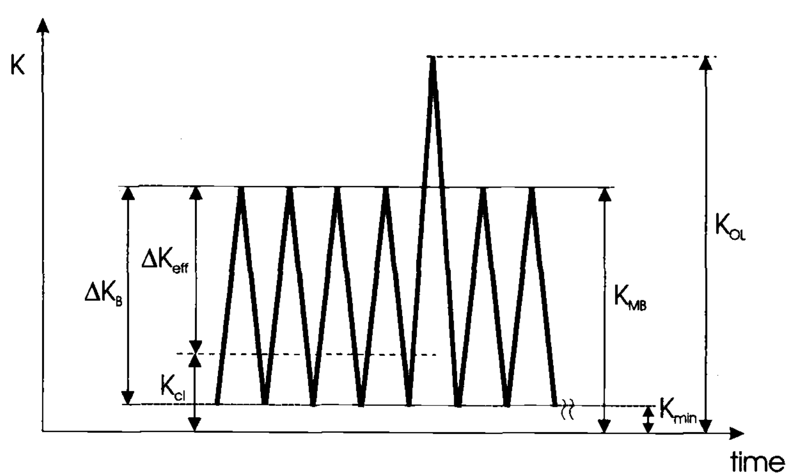

FIG. 2b—*Definition of parameters:* K_{min} = *minimum K,* $MPa\sqrt{m}$, K_{MB} = *maximum baseline* K, $MPa\sqrt{m}$, K_{cl} = *closure* K, $MPa\sqrt{m}$, ΔK_{eff} = *effective* ΔK_B, $MPa\sqrt{m}$, K_{OL} = *maximum overload* K, *overload magnitude* = $(K_{OL} - K_{MB})/K_{MB}$* *100%,* ΔK_B = *baseline range of* K, $MPa\sqrt{m}$ R = R-ratio (K_{min}/K_{MB}).

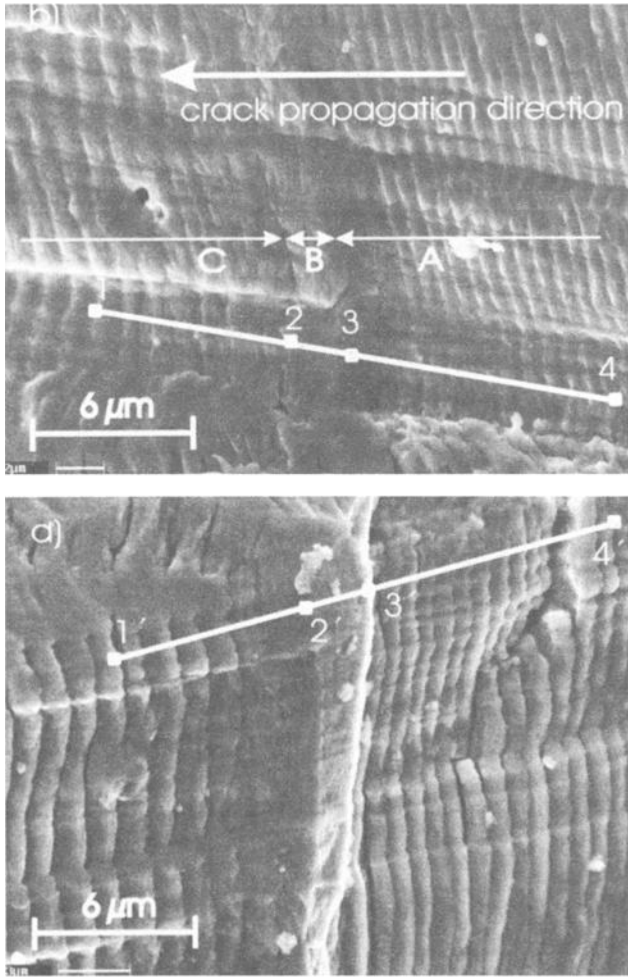

FIG. 3—*SEM fractograph at a 20% overload. The numbers mark the sample points of the height profile in Fig. 5:* (a) *shows specimen half S1,* (b) *corresponding specimen half S2,* (A) *fatigued with a constant load amplitude,* (B) *fracture surface produced during the single tensile overload,* (C) *fatigue with a constant load amplitude till the specimen failed, (1–4) sample points for the height profile, (1–4) corresponding sample points on the other specimen half.*

An automatic image processing system allowed the generation of a 3-dimensional model of the fracture surface. In Fig. 4 the 3D models from both fracture surfaces after a 40% overload are presented. By fitting them together one obtains the residual plastic deformation produced during the overload. The striations (region A), the blunting (region B) which occurs at the overload, and the fracture surface which was produced after the overload (region C) where they fit the models together are also indicated in Fig. 4. From such 3D models they can extract height profiles of exact corresponding lines on the fracture surfaces which allows one to determine the residual crack opening displacement of the crack tip after an overload. It is very important to take corresponding profiles; otherwise one gets a wrong residual crack opening displacement. The profile which is marked in Fig. 3 is presented in Fig. 5*b*. The points (1–4) in the profile are the same as marked in Fig. 3. Point 2 always marks the end of the overload.

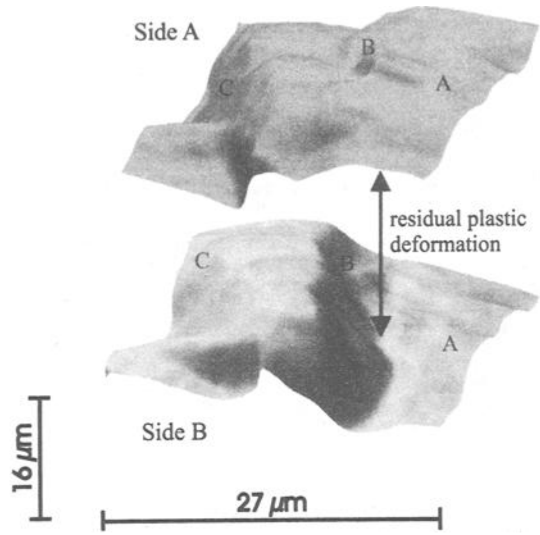

FIG. 4—*Three-dimensional surface model from both fracture surfaces at a 40% overload.*

The same measurements were performed at the 10, 40, 60 and 100% overload. From these 3D models we can calculate surface profiles at different overloads. This allows us to determine the residual plastic deformation of the crack in the midsection of the specimen as a function of the overload.

Results

Residual Plastic Deformation After a Single Tensile Overload

As first described by Schijve [*1*], the application of a single tensile overload results primarily in a delayed retardation in crack growth rates, which is shown schematically in Fig. 6.

The plot indicates several stages:

(a) steady-state crack growth at baseline level (A)
(b) crack growth during overload cycle (B)
(c) accelerated crack growth (C-D)
(d) retarded crack growth (D-E)
(e) returning to steady-state conditions (E-F)

The reason for the acceleration of the crack growth is shown in the height profiles (Figs. 5*a*–5*e*) at different overloads. Figure 5*a* shows a height profile at a 10% overload. The crack after the overload is fully open in the middle of the specimen but the residual CTOD is very small; it is only 2.2 μm, measured 7 μm behind the crack front of the overload. During further overloads (20%, 40%, . . .) the plastic deformation caused by the single overload increases more and more. This is illustrated in Figs. 5*b*–5*e*. Consider that in the Figs. 5*a*–5*d* the scales in the *y*-direction are equal but at the 100% overload profile (Fig. 5*e*) the authors have chosen a smaller one (three times smaller). From these profiles we can measure the residual CTOD 7 μm, 10 μm and 20 μm behind the overload cycle. The CTOD values as a function of the overload are given in Table 2.

The residual CTOD (measured 10 μm behind the overload) increases from 2.5 μm at a 10% overload to 24.7 μm at a 100% overload.

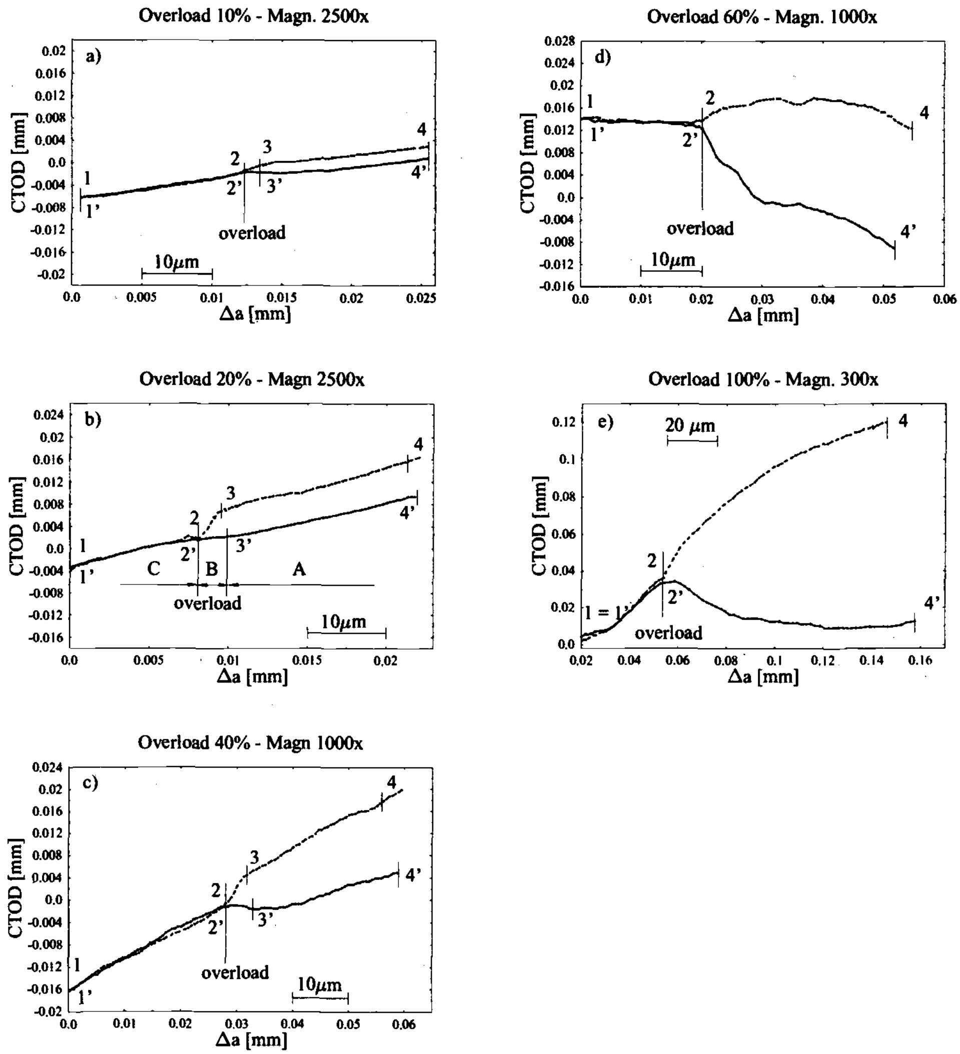

FIG. 5—*Residual plastic deformation after different single tensile overloads:* (a) *at a 10% overload,* (b) *at a 20% overload,* (c) *at a 40% overload,* (d) *at a 60% overload,* (e) *at a 100% overload.*

The effect of the tensile overload was to plastically blunt the sharp fatigue crack; hence at zero load, the crack was visibly open behind the crack tip. Acceleration is therefore caused by the removal or reduction of crack closure in the vicinity of the crack tip by the overload. This is supported by observations of larger crack opening displacements along the crack following the overload [*17*], and by the striation-spacing results which indicate clearly a reduction in near field closure [*21*] after the overload. The immediate post-overload crack growth may be associated to the short crack behavior.

From these observations we can see that only a 10% overload is great enough to open the crack at zero load in the midsection of the specimen and to destroy the near-field crack closure.[2]

[2] Additional measurements showed that the crack is fully closed in the midsection of the specimens with 25 mm thickness ("real plane strain conditions") after 10% overload.

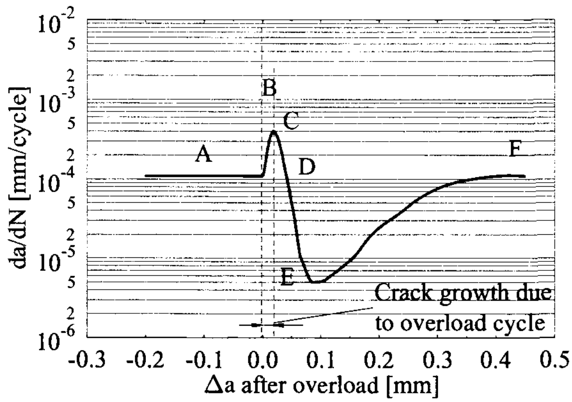

FIG. 6—*Typical crack growth rate curve showing delayed retardation following a tensile overload:* A = *steady-state crack growth rate,* B = *crack extension during overload cycle,* C-D = *accelerated crack growth,* D-E = *retarded crack growth,* E-F = *gradual return to steady state.*

Fractography—Striation Spacing Measurements and Near-Tip Crack Closure

The principle of the fractographic technique is based on the one-to-one correlation between crack-tip opening displacement and crack advance per cycle da/dN for the investigated ΔK range. Fractography was performed by scanning electron microscopy (SEM). Measurements of striation spacing were taken from the mid-thickness of the specimen. Figure 7*a* or Fig. 3 are typical SEM fractographs showing the initial acceleration or increase in striation spacing after a 20% overload. This acceleration of the crack growth occurs only during a few cycles, typically 15 to 30 cycles. After the short region of acceleration we observe a retardation in the crack growth rate which is indicated by a decreasing of the striation spacing to values smaller than the steady-state crack growth (1.1 μm/cycle). This can be seen in the Figs. 7*b* and 7*c* where the fracture surfaces 100 μm and 200 μm behind the overload are presented. The next two SEM images (Figs. 7*d*, 7*e*) show the striations 2000 μm and 3800 μm after the overload. An increase in the striation spacing (Fig. 7*d*) and the return to steady-state conditions can be clearly observed.

Surface Observation of the Residual Plastic Deformation

The surface observations of the overload were made directly in the SEM. Figures 8*a* and 8*b* show the scanning electron micrographs of the crack tip at a 20% overload and after unloading to zero load.

TABLE 2—*Measured Residual CTOD (Mean Values) at Different Distances Behind Crack Front of Overload.*

	CTOD Measured (xμm) Behind Overload, μm		
% of Overload	(7 μm)	(10 μm)	(20 μm)
10%	2.2	2.5	3.3
20%	4.5	4.7	...
40%	6.6	7.8	9.9
60%	13.4	16.6	19.4
100%	...	24.7	48.5

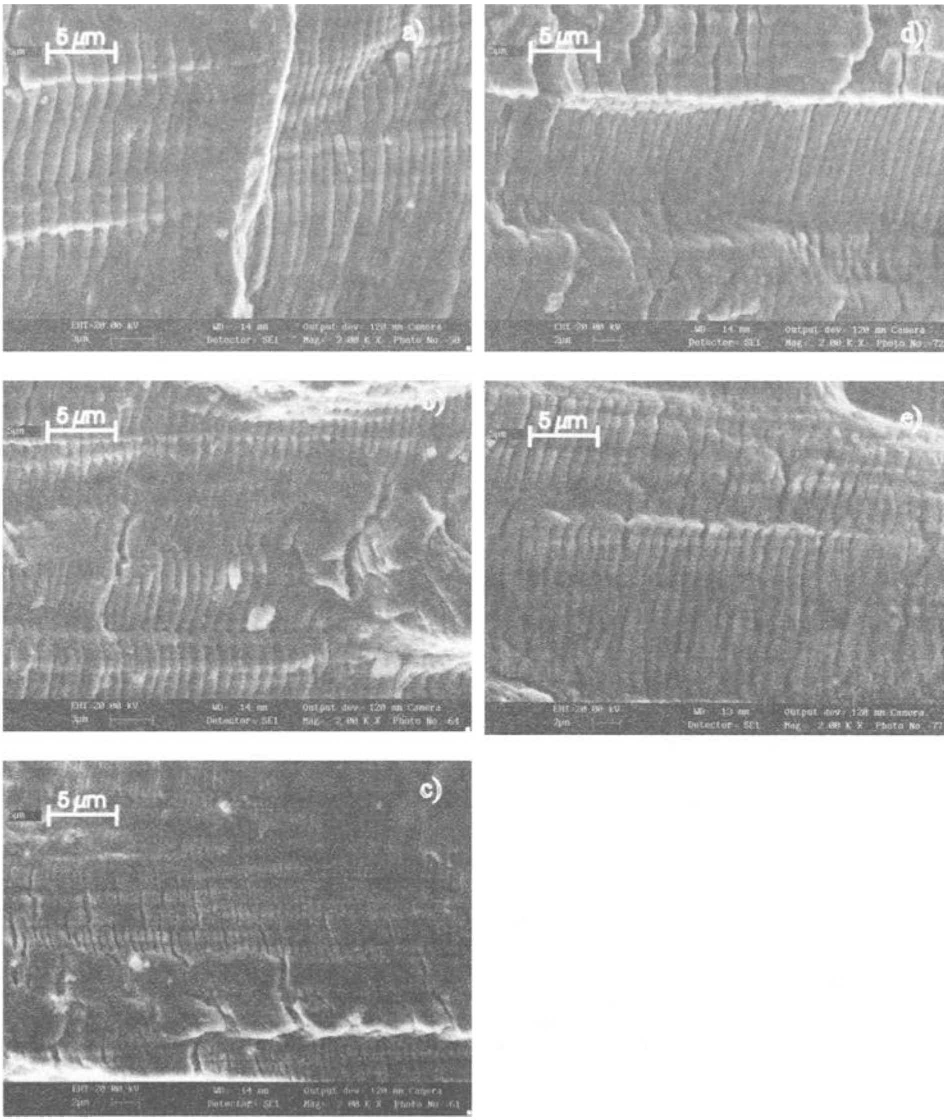

FIG. 7—*Striation spacing measurements after a 20% overload:* (a) *at the overload,* (b) *100 μm after the overload,* (c) *200 μm after the overload,* (d) *2000 μm after the overload,* (e) *3800 μm after the overload.*

The crack after the unloading is nearly fully closed. The residual plastic deformation measured 10 μm behind the overload is 0.5 μm (mean value), where it is 4.7 μm in the middle of the specimen. In the Figs. 8*c*–8*e* we see SEM images after a 40, 60 and 100% overload. Note that the magnifications of Figs. 8*a*–8*d* are equal but in Fig. 8*e* (100% overload) it is 2.5 times smaller. The residual CTOD values from the specimen surface as a function of the overload and distances behind the crack tip at the overload are presented in Table 3. If we compare these values (plane stress) with Table 2 (plane strain conditions) we see that the values are always higher than the observed data from the surface.

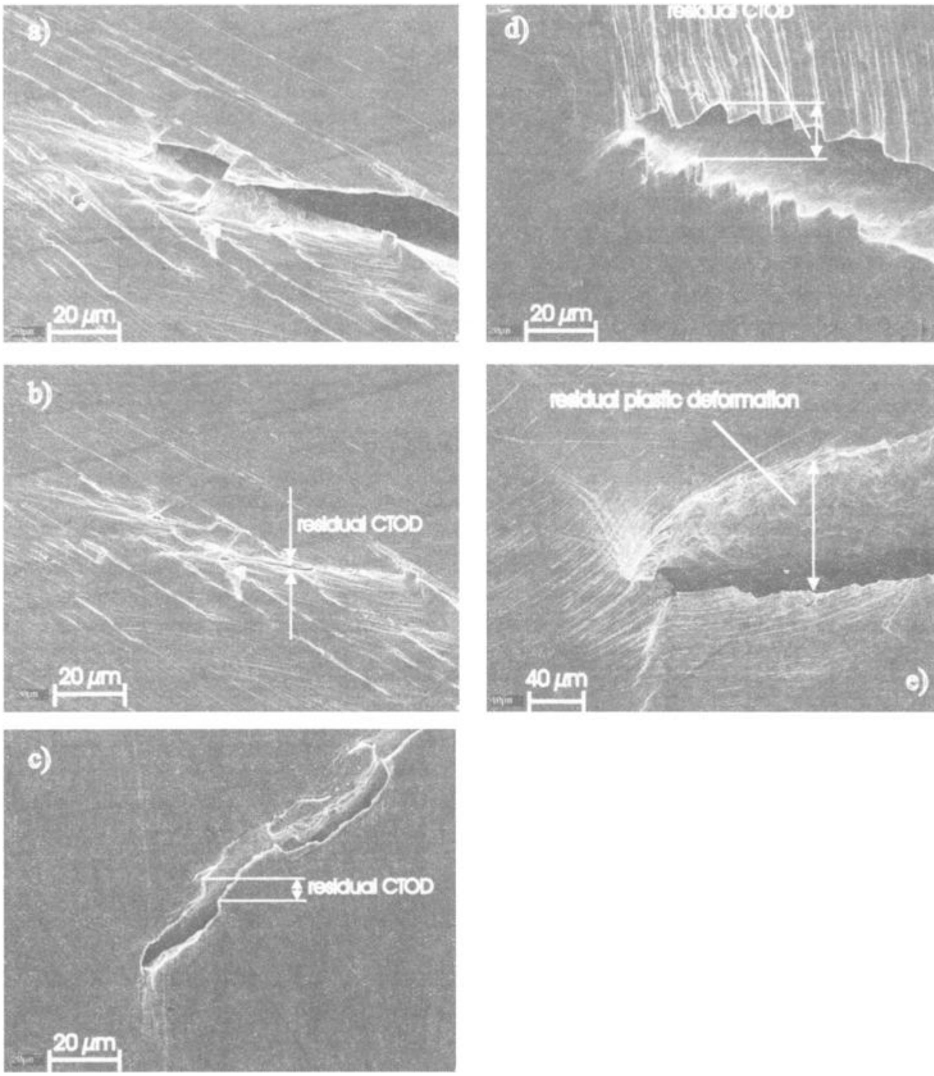

FIG. 8—*Scanning electron micrographs of the crack tip:* (a) *at a 20% overload,* (b) *after unloading to zero load,* (c) *residual plastic deformation after a 40% overload,* (d) *residual plastic deformation after a 60% overload,* (e) *residual plastic deformation after a 100% overload.*

The great differences between the residual CTOD values of the midsection and surface at small overloads may be caused by the higher crack closure level at the surface in the steady-state case.

Crack Growth Rates, Potential Measurements

The crack length after an overload was measured using a d.c. potential system, an optical microscope for the free specimen surface, and the striation spacing for the midsection of the specimen ("near" plane strain conditions), where the crack length increments were always measured perpen-

TABLE 3—*Measured Residual CTOD (Mean Values) on Free Specimen Surface at Different Distances Behind Crack Front of Overload.*

	CTOD Measured (xμm) Behind Overload, μm		
% of Overload	(10 μm)	(20 μm)	(40 μm)
10%	0	0	0
20%	0.5	1.1	...
40%	5.6–7.2	6.0–7.6	8.4
60%	11.2	16.0	19.2
100%	...	33.8	53.6

dicular to the crack front. The crack growth rates are plotted versus the crack extension after the overload. The behavior for the presented alloy is shown in the Figs. 9*a* and 9*b* for a 60% and a 100% overload at a baseline ΔK level of 70 MPa$\sqrt{\text{m}}$ ($R = 0.05$). In the figures the data from potential-drop signal, striation spacings, and optical measurements (surface) are shown; also the distances corresponding to the plane strain and plane stress sizes of the overload plastic zone are indicated. The distances are defined as follows:

$$r_{\text{pl,STRESS}} = \frac{1}{\pi} \times \frac{K_{\text{OL}}^2}{\sigma_y^2} \qquad \ldots \text{for plane stress} \tag{1}$$

and

$$r_{\text{pl,STRAIN}} = \frac{1}{3 \times \pi} \times \frac{K_{\text{OL}}^2}{\sigma_y^2} \qquad \ldots \text{for plane strain} \tag{2}$$

where

σ_y = yield strength, MPa
r_{pl} = plastic zone size, m

The main features of Fig. 9 are as follows:

- All crack length measurement methods indicate acceleration of crack growth rate for a few cycles after the peak overload followed by a strong retardation.
- The maximum crack retardation occurs at about 3/10 of the plane stress plastic zone size.
- The crack retardation at the free specimen surface is larger than in the center of the specimen, which agrees with Robin and Pelloux [*18*].
- The scatter in striation spacing is sometimes great. The reason is that the local crack growth direction is not always perpendicular to the load direction; therefore we observe a smaller striation spacing in the projection as in reality.
- The potential measurement is an average of the surface and the midsection results.
- The zone which affects the crack growth behavior is always larger than the calculated r_{pl}. The crack length increment to get the steady-state conditions is approximately equal to $4{*}r_{\text{pl,STRAIN}}$ and to $1.5{*}r_{\text{pl,STRESS}}$, in the midsection and the surface, respectively.

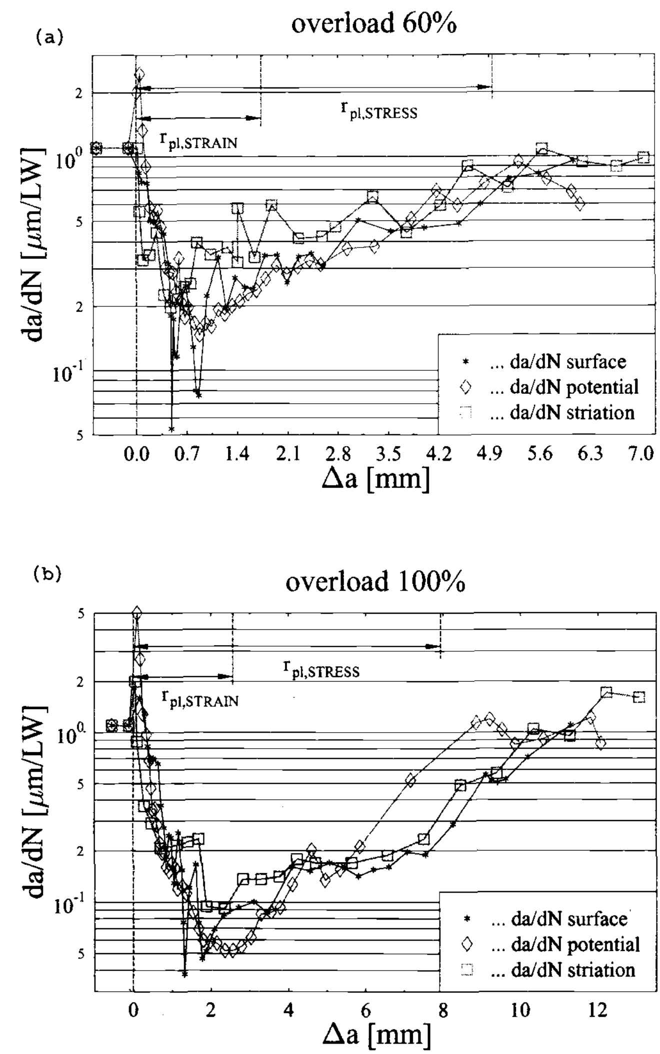

FIG. 9—*Crack growth rate at a 60%* (a) *and a 100% overload,* (b) *at a baseline* ΔK *level of 70* $MPa\sqrt{m}$ (R = *0.05).*

Discussion

If the overload is larger than 10% (of K_{max}) the presented study shows that a growing fatigue crack leaves behind a step on the fracture surfaces. This step is the result of residual crack tip opening displacement after the overload. In order to compare the measured residual CTOD values (in the mid-section) with calculated ones, we apply the simple approaches of Pelloux and Faral [*19*]. The definition of the loading levels is depicted in Fig. 10. The change of the CTOD value during the steady-state loading from $K_0 = K_{min}$ to $K_1 = K_{max}$ is equal to the CTOD during loading from K_4 to K_5:

$$(\mathrm{CTOD})_{0-1} = (\mathrm{CTOD})_{4-5} = \frac{\beta \times \Delta K^2_{\mathrm{eff},0-1}}{E \times 2\sigma_y} \tag{3}$$

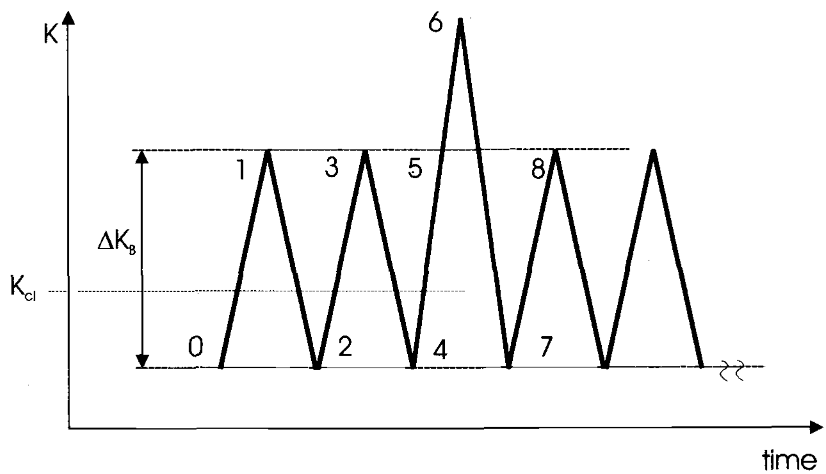

FIG. 10—*Sketch showing the values of stress intensity used to calculate crack-tip opening displacements.*

where

$\beta = 0.63$ . . . for the midsection [20]
$\sigma_y = 892$ MPa,
E = elastic module, 210 GPa, and
$\Delta K_{eff} = K_{max} - K_{cl}$, MPa.

The crack-tip opening displacement at the maximum load during the overload is assumed as the sum of the CTOD value at maximum load in the constant ΔK test, $(CTOD)_{4-5}$, and the change of CTOD during loading from K_5 to K_6, $(CTOD)_{5-6}$:

$$(\mathrm{CTOD})_{4-6} = (\mathrm{CTOD})_{4-5} + (\mathrm{CTOD})_{5-6} = \beta \times \frac{\Delta K^2_{\mathrm{eff},4-5}}{E \times 2\sigma_y} + \left(\beta * \frac{K_6^2 - K_5^2}{E \times \sigma_y}\right) \tag{4}$$

In this equation it is assumed that the change of $(CTOD)_{5-6}$ is describable by the deformation of an equivalent loaded stationary crack (nonpropagating crack without crack closure). The CTOD at the maximum load after the overload $(CTOD)_{7-8}$ is given by

$$(\mathrm{CTOD})_{7-8} = \beta \times \frac{\Delta K^2_{\mathrm{eff},7-8}}{E \times 2\sigma_y} \tag{5}$$

where before the overload $K_{cl} = 0.25 * K_{max}$, and after the overload $K_{cl} = 0 * K_{max}$(assumption).

Therefore the crack-tip opening displacement at the maximum load in the first cycle after the overload $(CTOD)_{7-8}$ is larger than $(CTOD)_{0-1} = (CTOD)_{4-5}$ (8.26 μm > 4.65 μm).

The relation between $(da/dN)_{0-1}$ and $(da/dN)_{7-8}$ measured from the striation spacing is proportional to $(CTOD)_{0-1}$ and $(CTOD)_{7-8}$, which supports the ΔK_{eff} concept.

We apply two estimations to calculate the residual plastic crack tip opening displacement after an overload:

(a) Residual CTOD (A) = ½*$(\text{CTOD})_{5-6}$ (6)

(b) Residual CTOD (B) = $(\text{CTOD})_{4-6} - (\text{CTOD})_{6-7} = (\text{CTOD})_{4-6} - \beta \times \dfrac{\Delta K^2_{\text{eff},6-7}}{E \times 2\sigma_y}$ (7)

Equation 6 assumes that the crack-tip opening caused by the cyclic part of the overload $(\text{CTOD})_{4-5}$ disappears during unloading and the monotonic part is reduced in the same way as a stationary crack. For $R = 0$ the change of the CTOD and the residual CTOD is equal ½ of the monotonic part of the crack-tip opening displacement.

In the second calculation (B) of the residual CTOD (Eq 7) the change of CTOD during the unloading from K_6 to K_7 is describable as a cyclic part of a stationary crack. For this determination, we assume that the initial closure disappears after the overload ($\Delta K_{\text{eff},6\text{–}7} = \Delta K_{6\text{–}7}$). In Table 4 the calculated and measured residual CTOD-values are presented. If we compare the calculated and measured residual CTOD we can see that the simple calculated value A gives a very good estimation of the measured CTOD in the midsection of the specimen.

At first this residual opening causes a reduction of the near-tip crack closure and hence an initial acceleration of the crack growth rate. The absence of near-tip closure leads to an initial crack growth rate twice of magnitude in the steady-state case. This can clearly be seen by the increase of the striation spacing after a 10% or 20% overload (Fig. 3). In Ref *21* it is noted that with larger overload cycles, the removal of closure behind the pre-overload crack tip may be offset by closure generated by the ductile crack growth increment formed by the overload cycle, in which case the acceleration may be reduced or absent. The authors observed this acceleration at all overloads. Note that the striations after the 60% and 100% overload are not so clearly visible, because the closure at minimum load causes extensive fretting damage on the fracture surface in a region about 300 μm after the overload.

After a small increase of the crack length (few cycles after the overload) the residual deformation acts as an additional plastic wedge (plasticity induced crack closure) [*17,22,23*] and causes a significant reduction of the crack propagation rate. This reduction of the crack growth rate can be seen in Figs. 7*b* and 7*c* for a 20% overload.

In the presented study a large decrease in the striation spacing was detected for the higher overloads. The crack growth rate is reduced from 1.1 μm/cycle to a value of 0.21 μm/cycle for a 60% overload and to 0.1 μm/cycle for a 100% overload. The distance over which the crack growth rate was affected by the overload in the midsection of the specimen was far larger then the calculated over-

TABLE 4—*Comparison of Measured and Calculated Residual Crack-Tip Opening Displacement After a Tensile Overload.*

	CTOD (xμm) Behind Overload, μm		
% of Overload	Measured Residual CTOD (7 μm)	Calculated Residual CTOD (A)	Calculated Residual CTOD (B)
10%	2.2	1.74	−1.87 (≡0)
20%	4.5	3.64	0
40%	6.6	7.93	4.32
60%	13.4	12.89	9.28
100%	...	24.8	21.2

load plastic zone in the plane strain condition (see Fig. 9). On the free specimen surface (plane stress) the behavior between the calculated overload plastic zone ($r_{\text{pl, STRESS}}$) and the affected crack growth length is better.

Conclusion

Based on experimental studies of fatigue crack growth behavior following a single tensile overload in an austenitic steel, the following conclusions can be drawn:

1. Stereoscopic scanning electron microscopy is a suitable method for the 3-dimensional reconstruction of microscopic objects. With the described system for automatic image analysis, we can reconstruct the fatigued fracture surface and use it to study the residual deformation caused by the single overload in the midsection of the specimen.
2. The measured residual plastic deformation correlates very well with the estimated values.
3. Based on midsection observations of the residual CTOD, a 10% overload is high enough to open the crack in the vicinity of the tip in the unloaded specimen.
4. The immediate acceleration in the growth rate following a tensile overload is associated with a crack-tip blunting which initiated a decrease in near-field closure.
5. After 20 to 50 cycles in the midsection of the specimen the crack growth rate decreases below the steady-state growth rate.
6. The maximum retardation of the crack growth rate was observed in the midsection at about $\frac{1}{10}$ to $\frac{2}{10}$ of the plane stress plastic zone size, and on the surface at about $\frac{2}{10}$ of the plane stress plastic zone size.

References

[1] Schijve, J., "Fatigue Crack Propagation in Light Alloy Sheet Material and Structures," NRL Report MP 195, National Aeronautical Research Institute, Amsterdam, Holland, 1960.
[2] Elber, W., "Significance of Fatigue Crack Closure," *Damage Tolerance in Aircraft Structures, ASTM STP 486,* American Society for Testing and Materials, 1971, pp. 230–242.
[3] Von Euw, E. F. J., Hertzberg, R. W., and Roberts, R., "Stress Analyses and Growth of Cracks," *ASTM STP 513,* American Society for Testing and Materials, 1973, pp. 230–259.
[4] Christensen, R. H., *Metal Fatigue,* McGraw-Hill, New York, 1959.
[5] Hudson, C. M. and Hardrath, H. F., "Effects of Changing Stress Amplitude on the Rate of Fatigue Crack Propagation of Two Aluminum Alloys," NASA Technical Note D-960, National Aeronautics and Space Administration, Washington, DC, 1961.
[6] Suresh, S., "Micromechanisms of Fatigue Crack Growth Retardation Following Overloads," *Engineering Fracture Mechanics,* Vol. 18, 1983, pp. 577–593.
[7] Jones, R. E., "Fatigue Crack Growth Retardation after Single Cycle Peak Overload in Ti-6A1-4V Titanium Alloy," *Engineering Fracture Mechanics,* Vol. 5, 1973, pp. 585–604.
[8] Knott, J. F. and Pickard, A. C., "Effects of Overloads on Fatigue Crack Propagation: Aluminum Alloys," *Engineering Fracture Mechanics, Metal Science,* Vol. 11, 1977, pp. 399–304.
[9] Forsyth, P. J. E., *Fatigue 84,* C. J. Beevers, Ed., Vol. 2, EMAS Ltd., Warley, U.K., 1984, p. 637.
[10] Vasudevan, A. K., Sadanada, K., and Louat, N., "A Review of Crack Closure," *Fatigue Crack Threshold and Related Phenomena, Material Science and Engineering,* 1994, pp. 1–22.
[11] Lang, M., "Quantitative Untersuchung von Reihenfolgeeinflüssen auf Ermüdungsriβ-fortschritt," Ph.D. thesis, Institut of Materials Research DLR, Köln, Cologne, Germany, 1996.
[12] Kolednik, O., "A Contribution to Stereophotogrammetry with the Scanning Electron Microscope," *Practica Metallurgica,* Vol. 18, 1991, pp. 562–573.
[13] Kolednik, O. and Kutlesa, P., "On the Influence of Specimen Geometry on the Critical Crack Tip Opening Displacement," *Engineering Fracture Mechanics,* Vol. 33, 1989, pp. 215–223.
[14] Kolednik, O. and Stüwe, H. P., "The Stereophotogrammetric Determination of the Critical Crack Tip Opening Displacement," *Engineering Fracture Mechanics,* Vol. 21, 1985, pp. 145–155.
[15] Stampfl, J., Scherer, S., Berchtaler, M., Gruber, M., and Kolednik, O., "Determination of Fracture Toughness by Automatic Image Processing," *International Journal of Fracture,* Vol. 78, 1995, pp. 35–44.

[16] Krasowsky, A. J. and Stepanenko, V. A., "A Quantitative Stereoscopic Fractographic Study of the Mechanism of Fatigue Crack Propagation in Nickel," *International Journal of Fracture,* Vol. 15, 1979, pp. 203–215.
[17] Ward-Close, C. M., Blom, A. F., and Ritchie, R. O., "Mechanisms Associated with Transient Fatigue Crack Growth under Variable-Amplitude Loading: An Experimental and Numerical Study," *Engineering Fracture Mechanics,* Vol. 32, No. 4, 1989, pp. 613–638.
[18] Robin, C. and Pelloux, R. M., "Fatigue Crack Growth Retardation in an Aluminum Alloy," *Material Science and Engineering,* Vol. 44, 1980, pp. 115–120.
[19] Pelloux, R. M. and Faral, M., "Assessment of Crack Tip Closure in an Aluminum Alloy by Electronfractography," *Fatigue of Engineering Materials and Structure,* Vol. 1, 1979, pp. 21–35.
[20] Bichler, C. H., "Comparison of the Cyclic Crack Tip Opening Displacement and the Crack Closure between the Middle and the Surface of a Specimen," Diploma thesis, Erich-Schmid-Institute for Solid State Physics of the Austrian Academy of Sciences, University of Leoben, Austria, 1995.
[21] Ward-Close, C. M. and Ritchie, R. O., "On the Role of Crack Closure Mechanisms in Influencing Fatigue Crack Growth Following Single Tensile Overloads in a Titanium Alloy: Near Threshold Versus Higher ΔK Behavior," *Mechanics of Fatigue Crack Closure, ASTM STP 982,* American Society for Testing and Materials, 1988, pp. 93–111.
[22] Shin, C. S. and Hsu, S. H., "On the Mechanisms and Behavior of Overload Retardation in AISI 304 Stainless Steel," *International Journal of Fracture,* Vol. 15, No. 3, 1993, pp. 181–192.
[23] Venkateswara Rao, K. T. and Ritchie, R. O., "Mechanisms for the Retardation of Fatigue Cracks Following Single Tensile Overloads: Behavior in Aluminum-Lithium Alloys," *Acta Metallurgica,* Vol. 36, No. 10, 1988, pp. 2849–2862.

Markus Lang[1]

Description of Load Interaction Effects by the ΔK_{eff} Concept

REFERENCE: Lang, M., "**Description of Load Interaction Effects by the ΔK_{eff} Concept,**" *Advances in Fatigue Crack Closure Measurement and Analysis: Second Volume, ASTM STP 1343,* R. C. McClung and J. C. Newman, Jr., Eds., American Society for Testing and Materials, West Conshohocken, PA, 1999, pp. 207–223.

ABSTRACT: An experimental study of load interaction effects in Al 7475-T7351 is presented. The crack propagation stress intensity factor, K_{PR}, was determined after different overload sequences, also involving subsequent compression loading. The results of these experiments demonstrate that the single overload can be described by a single function, which describes the *unloading process* after the overload. One main conclusion is that load interaction effects are governed by residual compressive stresses in front of the crack tip, while crack closure plays a minor role.

KEYWORDS: fatigue crack propagation, load interaction, overload effect, residual stresses, crack closure, compression loading

Nomenclature

a	Crack length
COD_{op}	Crack opening displacement at which crack opens
COD_w	Crack opening displacement at minimum load of a cycle
da/dN	Crack propagation increment per load cycle
F_{op}	Crack opening load
F_{PR}	Crack propagation load
K_C	Critical stress intensity factor (fracture toughness)
K_{min}, K_{max}	Minimum and maximum stress intensity factor
$K_{max,BL}$	Maximum stress intensity factor of a base load sequence (before overload)
$K_{max,OL}$	Maximum stress intensity factor of an overload
K_{PR}	Crack propagation stress intensity factor
$K_{PR,C}$	Crack propagation stress intensity factor after an unloading cycle, following constant amplitude loading
$K_{PR,OL}$	Crack propagation stress intensity factor after an overload sequence
${}^{P}K_{PR}$	Crack propagation stress intensity factor prior to an overload sequence
K_{op}	Crack opening stress intensity factor
K_{ul}	Unloading stress intensity factor
K_w	Stress intensity factor experienced by crack tip at minimum of applied load
N	Number of load cycles
N_{OC}	Number of overload/compression-load cycles
RCS	Residual compressive stress
R	Loading ratio $= K_{min}/K_{max}$

[1] Research engineer, Materials and Manufacturing Directorate, Air Force Research Laboratory, Wright-Patterson Air Force Base, OH 45433-7817.

R_{BL} Loading ratio of base loading
R_{tip} Loading ratio experienced by crack tip ($= K_w/K_{max}$)
R_{ul} Unloading ratio in the tension range ($= K_{ul}/K_{max,OL}$)
UR Unloading ratio; covers tension (R_{tip}) and the compression range (σ_P/σ_y)
ΔK Applied stress intensity factor range ($K_{max} - K_{min}$)
ΔK_B Cyclic amplitude during the CPLM
δ Step in mean load during the CPLM procedure
ΔK_{eff} Effective part of ΔK
ΔK_{tip} Stress intensity factor range experienced by crack tip
ΔK_T Intrinsic threshold value
σ_P Compressive far field stress
σ_y, σ_u Yield strength, ultimate tensile strength
σ_P/σ_y Compression ratio

The fatigue crack propagation (FCP) phenomenon complicates the design of engineering structures. The problem can be solved by safe life design, but this is not possible whenever increasing weight causes higher costs and a loss in performance, as it is in the aircraft or automotive industry. The consequent application of the damage tolerance design philosophy would be a solution of the problem, which is the current effort of various research programs in many countries [*1*]. The precondition for damage tolerant design is the capability of predicting fatigue crack growth life due to arbitrary loading conditions. An initial flaw has to be assumed because flaws can never be completely avoided in practice, despite highly developed detection capability. Therefore, the fatigue crack growth period is the critical issue. Although a lot of work has been done, FCP is still not completely understood. The main problems are load interaction phenomena which occur during variable-amplitude loading. The current paper focuses on that particular problem.

Conceptual Background

In 1961 Schijve found that tensile overloads retard subsequent crack growth and that a compression overload can reduce this retardation effect or can even lead to an acceleration in crack growth [*2*]. The physical reason for this effect was basically attributed to the processes associated with the plastic zone ahead of the crack tip. The plastic deformations ahead of the crack cause residual compressive stresses (RCS) which lead to crack growth retardation. In 1970, Elber found the crack closure phenomenon [*3*]. Since that time, many researchers tried to explain variable amplitude loading by applying the crack closure theory. Although the majority of researchers accepted the theory, considerable doubts on the capability of the crack closure concept to sufficiently explain FCP and load interaction effects have been reported since 1970. Experimental results were presented where crack closure was quantitatively determined, but the closure level did not fit the observed crack growth data [*4–10*]. Consequently, it was stated that crack closure does not properly account for load interaction effects. This opinion was also held in Refs *11–16* and in Refs *17–20,* where the contribution of closure to FCP was considered small. Although many things have been learned since crack closure was found more than 25 years ago, a conclusive picture of the influence of crack closure on FCP is still missing. The current conference is an example of many efforts to improve the understanding.

Crack closure is a well proven phenomenon, but it is also obvious that RCS in front of the crack tip are present. The RCS phenomenon, though, was never considered as *directly* reducing the applied ΔK to an effective amplitude, ΔK_{eff}. This is partly a result of the chronology of the discoveries and postulates in the science of FCP. In Ref *3* the ΔK_{eff} concept was postulated as a *consequence* of the crack closure finding. In fact we are dealing here with two different things, namely crack closure which is a physical effect, and the ΔK_{eff} concept which is a postulate. Concerning the overload problem, RCS [2] (or also crack tip blunting [21] or strain hardening, however, more unlikely) could also be considered as potential reducer of ΔK to ΔK_{eff}.

From our current knowledge, the ΔK_{eff} concept could also be postulated due to the results reported in Ref 2 based on a RCS argumentation, when crack closure was ten years away from being discovered. We could say that the constant amplitude sequence (2) after the overload shown in Fig. 1 is "less effective" than the constant amplitude sequence (1) before the overload (the unretarded case). Applying the postulate of the ΔK_{eff} concept (where the same ΔK_{eff} causes the same crack growth increment "*da*") to the overload data in Fig. 1, the ordinate in the *da*/*dN* versus *N* graph on the right side in Fig. 1 can be replaced by the respective ΔK_{eff} values, and a ΔK_{eff} curve would be obtained for constant amplitude loading ("unretarded") and the overload case ("retarded"). The physical explanation according to Ref 2 would be RCS in front of the crack tip, which would have directed the scientific attention at that time in a totally different direction. This example demonstrates that the ΔK_{eff} concept is not bound to the special phenomenon crack closure. The ΔK_{eff} concept just says that the applied amplitude is reduced to an effective amplitude. Unfortunately, crack closure and the ΔK_{eff} concept were "born" as twins and since then were not easy to distinguish.

Since load interaction effects apparently cannot be explained by crack closure [4–16], it is considered that RCS may play an important role during FCP. There is experimental evidence, to support this contention. In Refs 14,15 the processes around the crack tip were monitored via optical interferometry. During the loading process, the crack tip was found to be still under compression while the crack behind the tip region was already open. The same was found in a direct stress analysis of the crack tip region via X-ray [22–24].

Using knowledge reported in Refs 14,15 a crack propagation model is presented which separates the processes behind and in front of the crack tip. The results of the present investigation will be evaluated based on this model which shall be briefly described.

Model

Crack closure is treated as wedging action behind the crack tip as described in Ref 15. This wedging action reduces the amplitude that is actually experienced by the crack tip. In Fig. 2*a*, a compliance curve of a specimen with a crack with crack closure is shown. The part of the curve where no closure occurs is linear. When closure occurs, the compliance curve deviates from linearity. During the straight part of the curve, a linear relation exists between the applied load, *F*, and the stress in-

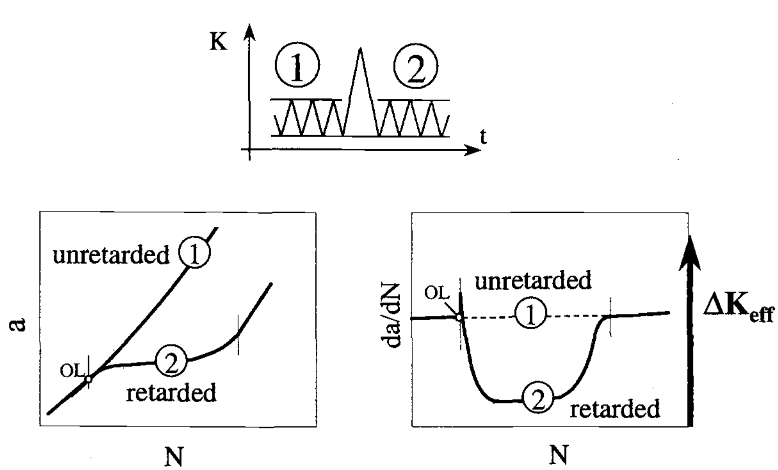

FIG. 1—*Application of the ΔKeff concept to the single overload problem.*

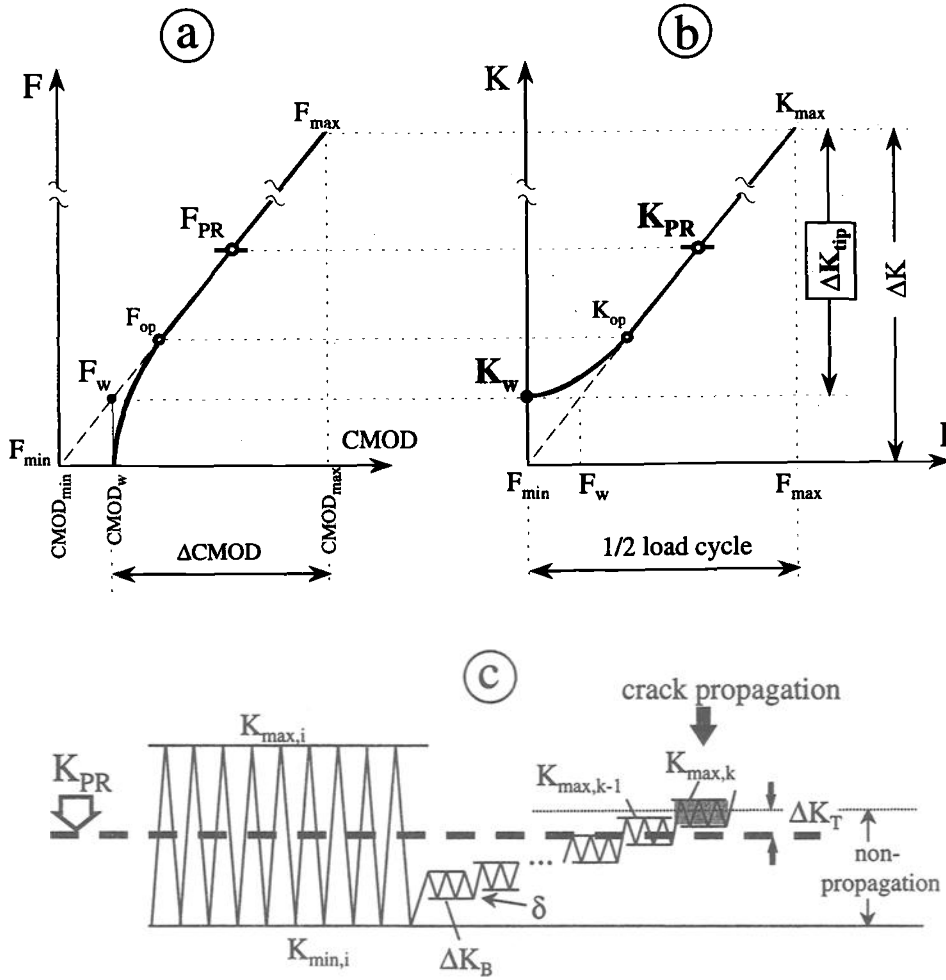

FIG. 2—(a) *and* (b) *the influence and the treatment of crack closure.* (c) *the crack propagation load measurement method.*

tensity factor, K, experienced by the crack tip (Fig. 2*b*). If crack closure occurs, this linear relationship is no longer valid and is replaced by a nonlinear function according to the curvature of the compliance curve, i.e., the amount of shielding due to closure. A rigid wedge would cause a vertical cut off in the compliance curve, but the closing process in a real crack is gradual as indicated by the compliance curve. The stress intensity factor experienced at the crack tip, though, is uniquely related to CMOD for a given load-displacement response. Therefore, the stress intensity factor, K_w, experienced at the crack tip at minimum applied load, can be calculated either from $CMOD_w$ or from F_w, which is the applied load that would be necessary to open a closure free specimen to $CMOD_w$ (linear dashed line in Fig. 2*a*). The applied amplitude experienced by the crack tip is given by

$$\Delta K_{tip} = K_{max} - K_w \tag{1}$$

The crack tip experiences the increased R_{tip} value, that is,

$$R_{tip} = \frac{K_w}{K_{max}} \tag{2}$$

At this point an important issue should be clarified. The closer the clip gage (or strain gage, etc.) is to the crack tip, the higher is the point where the curve deviates from the linear portion, and the more the clip gage monitors the consequences of the processes in front of the crack tip. In [*3*] the clip gage was mounted near the crack tip and thus, the consequences of the processes in front of the crack tip were monitored. On the other hand, the RCS effect in front of the crack tip cannot be called "closure." These problems underline the importance to separate the processes behind and in front of the crack tip. Therefore, crack closure (in this concept the parameter, K_w) is defined here to be determined on the compliance curve that is monitored by a *remotely* attached clip gage. This is important, since only a remotely attached clip gage can monitor wedging action due to the entire area of the crack surface. In practice, K_w can easily be determined by drawing a vertical line through the lowest point of the compliance curve (F_{min}) and a second line that is the extension of the linear part of the curve. The point of intersection determines F_w and therewith K_w.

The obtained ΔK_{tip} is the amplitude experienced by the crack tip, but it is not the effective amplitude. The RCS have to be overcome by further loading the specimen. The point where the material just ahead of the crack tip is free of compressive stresses equal to the von Mises yield stress is denoted as crack propagation stress intensity factor, K_{PR}. Shortly above that point, at ($K_{PR} + \Delta K_T$), plastic deformation will occur [*25*]. K_{PR} cannot be determined with a compliance curve as shown in Fig. 2*a,* since the point lies in the linear part of the curve. The method to determine K_{PR} will be explained in the next section. For constant-amplitude loading,

$$K_{PR} = f(R_{tip}) \cdot K_{max} \tag{3}$$

In [*19,20*] K_{PR} is given for other loading cases than constant-amplitude loading. The effective stress intensity factor range,

$$\Delta K_{eff} = (K_{max} - K_{PR}) - \Delta K_T \tag{4}$$

where ΔK_T is the intrinsic threshold value [*14*] (often called $\Delta K_{th,eff}$). The corresponding crack propagation increment per cycle is

$$\frac{da}{dN} = C \cdot (\Delta K_{eff})^{m} \tag{5}$$

K_{PR} is strictly to be distinguished from K_{op}. K_{op} is commonly determined via a compliance curve and was defined as the first deviation from linearity in the compliance curve [*3*]. However, as stated above, this point depends strongly on the measurement method and the position relative to the crack tip. This makes K_{op} a poorly defined term in contrast to K_{PR} that is defined by a "natural" event, namely crack propagation.

K_{PR} *Measurement Method (CPLM)*

The crack propagation stress intensity factor, K_{PR}, can be measured using the crack propagation load measurement method (CPLM), which is sketched in Fig. 2*c.* This method was introduced in Refs *14,26.* In Ref *14* the method was used to determine the point where the transition from compressive to tensile strain at the crack tip occurs, while in [*26*] an explanation in terms of a "threshold" was given. Practical improvements of the method which enhanced the experimental procedure were made in Refs *27,28*. Since the method had no appropriate name, it is called the CPLM method [*25*]. Figure 2*c* shows the determination of K_{PR} after constant amplitude loading, but the procedure is the same for any other sequence. The specimen is cycled with a small amplitude, ΔK_B, far below the expected K_{PR}. ΔK_B must be larger than ΔK_T (also called $\Delta K_{th,eff}$). If the crack does not propagate, the mean load of the small cyclic amplitude is increased by a small amount, δ. "Propagation" means that the crack growth rate is higher than 1×10^{-7} mm/cycle, which is the threshold crack growth rate. The mean load of the small blocks is repeatedly increased, until the crack starts to propagate (gray block in Fig. 2*c*). Then, K_{PR} can easily be calculated by

$$K_{PR} = \frac{(K_{max,k} + K_{max,k-1})}{2} - \Delta K_T \tag{6}$$

The crack length is to be monitored by potential drop signal.

The crack propagation stress intensity factor, K_{PR}, was determined for constant amplitude loading in Refs *20,27* for Al 7475-T7351 using the CPLM method. In Ref *19* K_{PR} was measured directly after the application of single and multiple overloads (only the "classical" overload case shown in Fig. 1) on the same material. In Ref *20* the influence of compression loads either as single compression overloads or constant-amplitude loading with $R < 0$ was studied on Al 7475-T7351.

This paper presents experiments where K_{PR} was determined after single overload sequences involving subsequent compressive overloads. The results will be discussed and the conclusions outlined.

Experimental Procedure

Two different test programs involving single overloads were conducted. The testing parameters for overload sequences with different subsequent unloading levels, K_{ul}, are given in Table 1. The constant-amplitude sequence prior to the overload is called "base loading." The R value of base loading, the magnitude of the overloads, and the subsequent unloading level, K_{ul}, were varied significantly. Directly after those sequences, K_{PR} was measured using the CPLM method as shown in the schematic in Table 1.

In a second test series, the influence of a tensile overload/compression-load sequence was studied which will be denoted as OL/CL sequence. The loading parameters for these tests are given in Table 2. R_{BL}, $K_{max,OL}$ and the magnitude of the subsequent compression overload were varied. The compressive overloads are given as far field stress, σ_P. The R value is not used in compression, because K_{min} in $R = K_{min}/K_{max}$ is not defined in the compression range, and σ_{max} in $R = \sigma_{min}/\sigma_{max}$ is not appropriate in the tension range, since it does not represent the stress intensity at the crack tip, which is a function of the crack length ($K = f(\sigma, a, Y)$).

Material, Specimens, Equipment

The aluminum alloy Al 7475-T7351 was used for this investigation (σ_y = 462 MPa, σ_u = 532 MPa, K_C = 50 MPa$\sqrt{m}$). C(T) specimens (W = 50 mm, B = 10 mm, *LT* direction) and M(T) specimens ($2W$ = 160 mm, B = 8 mm, length = 450 mm, *LT* direction) were cut out of a 10 mm thick plate. The C(T) specimens were used for the tests, given in Table 1, the M(T) specimens for those involving compression loads (Table 2). The M(T) specimens were precracked first by tension-compression loading and then by tension-tension loading to a crack length of $2a$ = 20–24 mm. A 400 kN servohydraulic test machine was used for those tests (buckling protection was used for the compression tests). The tests with C(T) specimens were conducted on a 10 kN machine. The frequency during base loading was 10 Hz. Before the application of the overload sequences to be investigated, the frequency was gradually reduced to 0.05 Hz. To avoid load sequence effects, the base loading se-

TABLE 1—K_{PR} *measurements after different overload sequences with different subsequent unloading levels.* K_{ul}*, in the tension range*

R_{BL}	$K_{max,BL}$ [MPa√m]	$K_{max,OL}$ [MPa√m]	OLR $K_{max,OL}/K_{max,BL}$	K_{ul} [MPa√m]
0.1	10	19 23 28	1.9 2.3 2.8	1; 4; 5 1; 4.5 1; 5
0.33	12	22.8 27.6	1.9 2.3	0.5; 2; 4; 8 1; 4; 10
0.47	15	24 31.5	1.6 2.1	1; 2.5; 7; 11 1; 7; 13
0.68	19	24.7 32.3	1.3 1.7	2.5; 13; 16 1; 13; 21
0.8	20	27 32	1.35 1.6	16 1.5; 16; 24

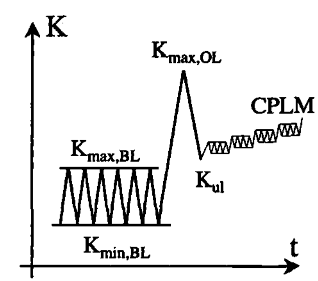

TABLE 2—K_{PR} *measurements after single overload/compression-load cycles.*

R_{BL}	$K_{max,BL}$ [MPa√m]	$K_{max,OL}$ [MPa√m]	OLR $K_{max,OL}/K_{max,BL}$	σ_P [MPa]
0.1	10	19	1.9	0, -92.5, -185, -231 -277, -314
		23	2.3	0, -92.5, -185 -231, -277
		28	2.8	-25, -80, -130, -185 -231, -277
		32	3.2	6.5, -92.5, -185, -277
0.33	12	27.6	2.3	-92.5, -231
0.47	15	31.5	2.1	-92.5, -231
0.68	19	32.3	1.7	-92.5, -231
0.8	20	32	1.6	-92.5, -231

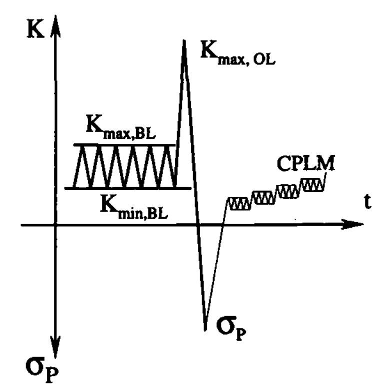

quence before an overload event in any of the tests in Tables 1 and 2 was conducted for 1 to 2 mm with steady state crack growth rate, which was continuously monitored.

The cyclic amplitude, ΔK_B, for the CPLM procedure was 1.6 MPa$\sqrt{m}$, which is ΔK_T + 0.6 MPa$\sqrt{m}$. The step in mean load, δ, was 0.2 MPa$\sqrt{m}$, which is also the minimum accuracy of the K_{PR} measurements. One loading block during the CPLM procedure consisted of 200 000 cycles. The frequency during the CPLM procedure was 50 Hz with C(T) specimens and 25 Hz with M(T) specimens. The DC potential difference method was used to detect crack propagation, which is important for the CPLM procedure. Additionally, the crack length was monitored using an optical microscope. The specimen temperature was monitored to correct the potential drop signal for variations in temperature.

During the tests with C(T) specimens (Table 1) a clip gage was mounted at the mouth of each C(T) specimen, and the compliance curve (F - CMOD) was monitored during base loading and the overload cycles to determine the amount of wedging action (K_w) during unloading in the tension range (Eqs 1 and 2, Fig. 2*a-b*).

Results

K_{PR} *for Tensile Overloads with Different* K_{ul}

The K_{PR} data after tensile overloads with different subsequent unloading levels are shown in Fig. 3*a*. The data which correspond to one R_{BL} and $K_{max,OL}$ but different K_{ul} (see Table 1) are connected by a line using one type of symbol for the data points. K_{PR} is plotted versus R_{ul}, which is the unloading R value in tension; $R_{ul} = K_{ul}/K_{max,OL}$. In the tests where R_{ul} was low, i.e., unloading below $K_{ul} \approx$ 2.5 MPa$\sqrt{m}$, the clip gage indicated crack closure. For those tests the $R_{tip,ul}$ value was determined as described in the section "Model" and introduced into Fig. 3*a*, which therefore represents only closure free data. The correction was marginal since there was not much closure. K_w was mostly 0.2 to 0.5 MPa$\sqrt{m}$ above K_{ul}, which causes only minor changes in the $R_{tip,ul}$ value. Figure 3*a* shows that K_{PR} after the overload decreases with decreasing R_{ul} values. Additionally, K_{PR} is higher with higher R_{BL} and $K_{max,OL}$ values. Dividing the data by their respective $K_{max,OL}$ values, yields Fig. 3*b*. The data are found to collapse onto a single line which rises with increasing R_{ul}. The K_{PR} value after an overload depends, therefore, only on $K_{max,OL}$ and R_{ul} and *not* on the R_{BL} value (or ΔK_{BL}) before the application of the overload.

K_{PR} *After a Single OL/CL Cycle*

The results of K_{PR} measurements after single OL/CL cycles are shown in Fig. 4*a*. K_{PR} was plotted versus far-field stress σ_P (upper scale in Fig. 4*a*), and σ_P/σ_y (lower scale) to show the dimensions of the compressive overload in terms of the elastic limit of the material. The term σ_P/σ_y is denoted as "compression ratio." It is assumed that the tensile yield strength is similar to that in compression (if not, the error for the normalization in Fig. 4*a* would be small). It can be seen that K_{PR} decreases with increasing compression stress. Moreover, K_{PR} increases with increasing $K_{max,OL}$. A normalization by $K_{max,OL}$, as done in Fig. 3*b*, leads to Fig. 4*b*. At very high compression ratios the data scatter to some extent; but in general, similar to the results from the tension range, the data fall fairly well onto a single curve. That means that the same overload level and subsequent compression load yield identical K_{PR}, independent of the R_{BL} value of the prior constant amplitude loading sequence. The "history" before the application of the OL/CL sequence is wiped out by a single OL/CL sequence.

Discussion

The results of the K_{PR} measurements after single overloads with different subsequent unloading levels in tension and those after single OL/CL cycles were given in Figs. 3*b* and 4*b*.

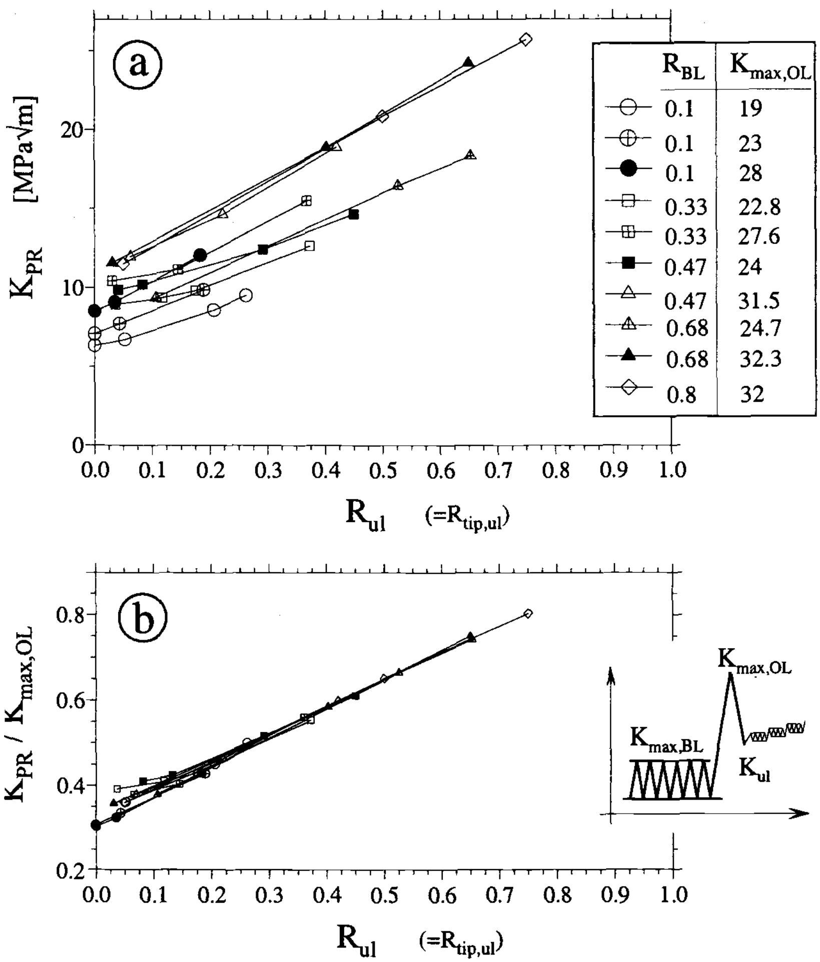

FIG. 3—*(a)* K_{PR} *and* (b) $K_{PR}/K_{max,OL}$ *after an overload with different subsequent unloading levels,* K_{ul} *(Al 7475-T7351).*

Combining those results leads to Fig. 5. The data from tests with the same R_{BL} and $K_{max,OL}$ value are connected by a respective line. It can be seen that the data from the tension range and compression range fall onto a single line. The different scales for the tension and compression range, R_{ul} and σ_P/σ_y, are generalized as the unloading ratio, *UR* (Fig. 5). The fact that the data from C(T) and M(T) specimens match one curve is not surprising. K_{PR} is based on a "natural" and clear criterion, namely crack propagation, i.e., plastic deformation at the crack tip during the loading process. Experience has shown that crack growth data based on *K* are nearly the same for different specimen geometries. It is therefore only logical that the critical parameter that is proposed to describe FCP is also consistent for different geometries (this is different for K_{op} which is even a function of the measurement location). The data in Fig. 5 were fit by a simple equation, that is,

$$K_{PR,OL} = (0.322 + 0.57 \cdot UR + 0.267 \cdot UR^2 - 0.16 \cdot UR^3) \cdot K_{max,OL} \, [-0.7 < UR < 1] \quad (7)$$

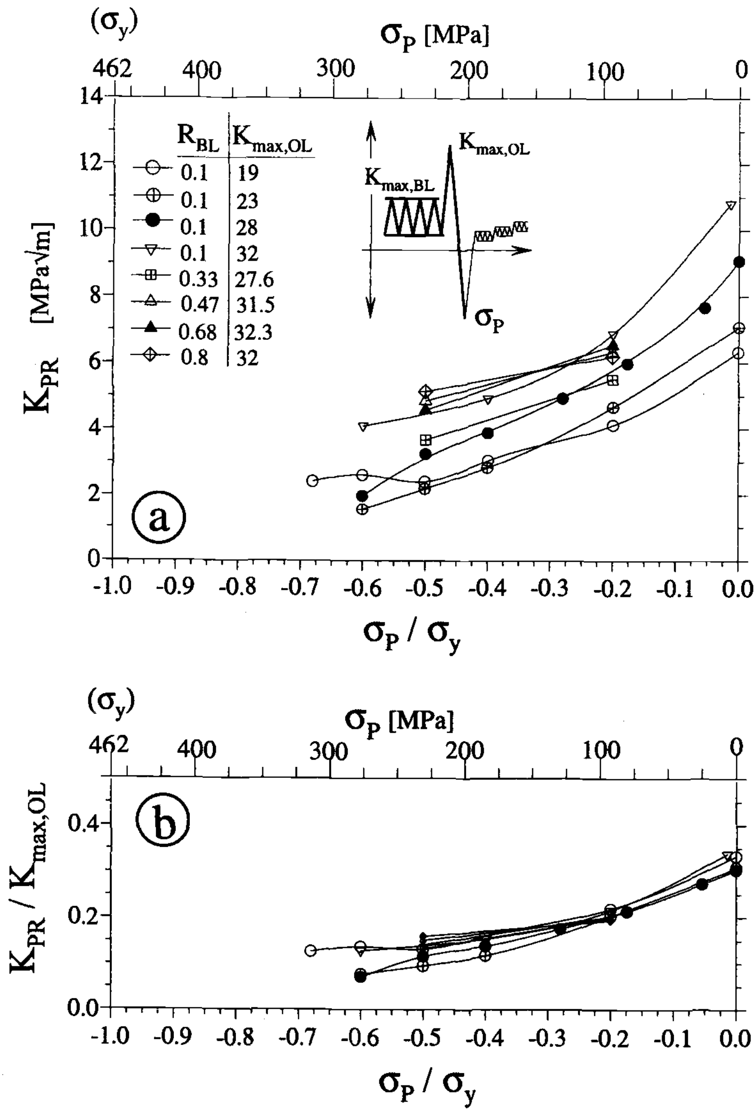

FIG. 4—(a) K_{PR} *after single OL/CL sequences,* (b) $K_{PR}/K_{max,OL}$ *versus* σ_P/σ_y, *(Al 7475-T7351).*

where

$$UR = R_{ul} = \frac{K_{ul}}{K_{max,OL}}, \qquad \text{in the tensile range.} \tag{8}$$

or

$$UR = \frac{\sigma_P}{\sigma_y}, \qquad \text{in the compression range} \tag{9}$$

$K_{PR,OL}$ denotes the crack propagation stress intensity factor after an overload sequence. The fit is

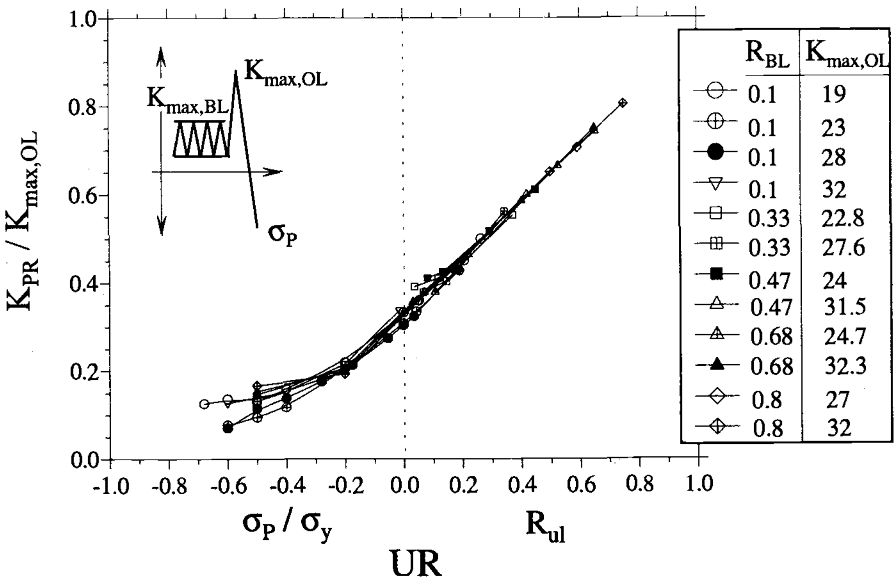

FIG. 5—*The influence of a single tensile overload and the subsequent unloading level on* K_{PR} *(Al 7475-T7351).*

given between $-0.7 < UR < 1$. The lower bound is the lower end of the investigated region. If closure occurs, the unloading ratio in the tension range has to be corrected, and Eq 8 changes to

$$UR = R_{tip,ul} = \frac{K_w}{K_{max,OL}} \quad \text{(if closure occurs)} \tag{10}$$

The different units in the tension and compression range create no difficulties in using Eq 7 (attention should be paid to use the negative sign for compressive stresses in σ_P/σ_y). Equation 7 can be generalized, that is

$$K_{PR,OL} = h(UR) \cdot K_{max,OL} \tag{11}$$

The function h has a polynomial form (Eq 7) where the constants are material dependent. Considering Fig. 5, the real meaning of the test results becomes obvious. Since the data match a single line and $K_{PR,OL}$ is independent of the R_{BL} value, a general description of the single overload phenomenon is obtained. Equation 7 represents the *unloading procedure* after a single overload, which means that it exhibits a "dynamic" character. This statement needs further explanation.

Let us consider an overload of any magnitude as is shown in the right part of Fig. 6. If the specimen is subsequently unloaded to $K_{ul} = 0.8 \cdot K_{max,OL}$, i.e., $UR = 0.8$, the respective $K_{PR,OL}$ value is defined by point A on the curve in Fig. 6, given by Eq 7. The respective unloading level during the unloading cycle (the current K/K_{max} in tension and σ/σ_y in compression) is indicated in Fig. 6 by a dashed line, denoted as "unloading." Further unloading to $UR = 0.4$, 0.0 or -0.4, leads to a lower $K_{PR,OL}$, according to Eq 7 (see points B, C and D). This demonstrates that Eq 7 describes a *process;* namely, it follows the unloading process from $K_{max,OL}$ ($UR = 1$) to the respective unloading ratio. This process takes place during *every* unloading cycle following a single overload. This is an important point for the concept of fatigue crack propagation. Only the unloading part of a cycle determines the critical parameter, K_{PR}, needed for the ΔK_{eff} concept. Equation 7 is quantitatively valid for Al

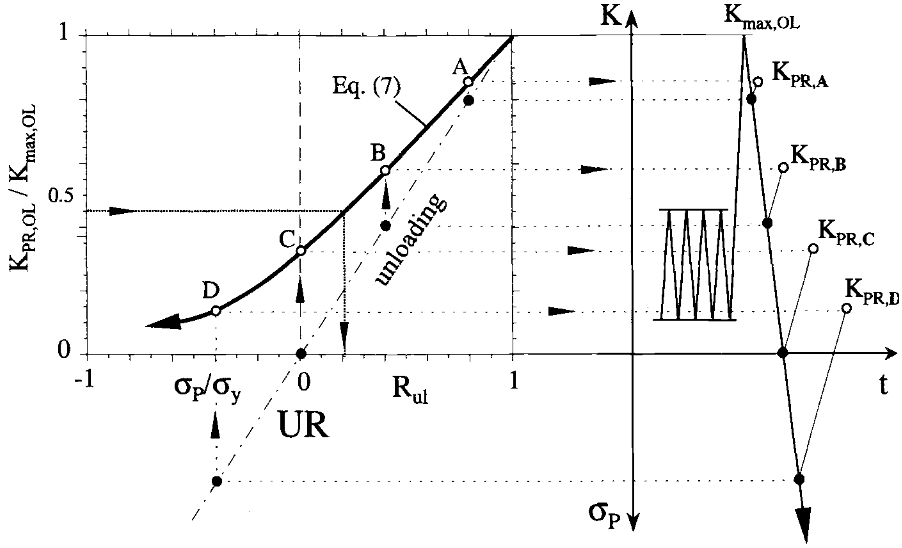

FIG. 6—*The "dynamic" character of Eq 7.*

7475-T7351, but the generalized relation given in Eq 11 is considered to exist for every homogenous metallic material. A newer study supports that postulate, where Eq 11 was found to exist for the titanium alloy Ti-6Al-2Sn-4Zr-2Mo [*29*].

The fact that all data in Fig. 5 collapse onto a single curve makes clear that the R_{BL} value has no influence on $K_{PR,OL}$. This is demonstrated in sequences I–VI in Fig. 7. The six different loading sequences consist of three different constant amplitude loading sequences prior to the tensile overload (same $K_{max,OL}$ in all six cases) and two different unloading ratios. In sequences I–III, the unloading after the overload reaches to the same subsequent unloading level, K_{ul}, while there are different stationary K_{PR} values prior to the overload (denoted as Nos. 1–3) due to different constant amplitude

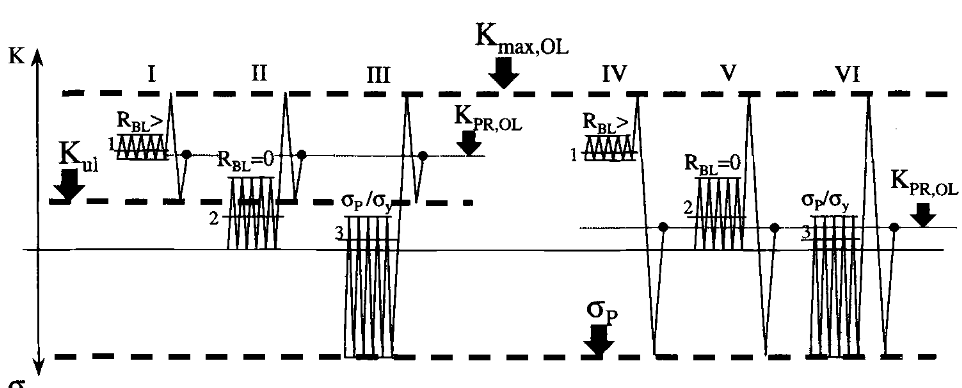

FIG. 7—*Sequences I–III and IV–VI lead to the same respective* $K_{PR,OL}$.

loading sequences. The stationary K_{PR} values are given by

$$K_{PR,C} = (0.453 + 0.34 \cdot UR + 0.134 \cdot UR^2 + 0.07 \cdot UR^3) \cdot K_{max} \quad [-0.7 < UR < 1] \tag{12}$$

which is in generalized form

$$K_{PR,C} = g\,(UR) \cdot K_{max} \tag{13}$$

where UR is also the unloading ratio and g is a polynomial function where the constants depend on the material. Equations 12 and 13 were developed in Ref *20* and they are valid both for constant amplitude loading and the unloading process following constant amplitude loading, and are to be applied in the same conceptual way as Eqs 7 and 11.

Despite the large difference in K_{PR} values prior to the overload in sequences I–III (Fig. 7), the same $K_{PR,OL}$ value is obtained according to Eq 7. In sequences IV–VI the same constant amplitude loading sequences were applied as in I–III. The unloading ratio is now below zero, i.e., a compression load was applied after the tensile overload. According to Eq 7, a lower $K_{PR,OL}$ value than after sequences I–III is established, but $K_{PR,OL}$ is the same after sequences IV–VI, since $K_{max,OL}$ and UR are identical. In [*20*] the independence of $K_{PR,OL}$ of the prior R_{BL} value was also found for the case of unloading after constant amplitude loading, as long as $K_{max,BL}$ is identical.

The phenomenological explanation of the results in Figs. 6 and 7 and the "dynamic" character of Eq 11 is seen in the RCS effect in front of the crack tip. No other than a stress related effect could provide such immediate, exact changes in K_{PR} and would provide such reproducibility. Moreover, the results literally show that load interaction effects cannot be explained by the crack closure but by local residual compressive stresses. This conclusion is supported by the following arguments:

1. Closure does not support the observed load interaction at high R values like $R = 0.8$, since it is limited to low R values [*5,10,30*].

2. The argument that an acceleration effect after a compression load is caused by deformation of the crack surfaces, leading to a decrease in crack closure, would not allow the results shown by sequences IV–V in Fig. 7. Due to the different R_{BL} values and ΔK, the amount of cyclic plasticity is different. Consequently, the roughness of the fracture surface has to be different (see fractographs in Ref *20*), and, therefore, the same compressive load should cause different K_{PR} values, which is obviously not the case. Another argument against closure to be responsible for the observed behavior (Eq 7) is that due to the closure concept, a fixed crack closure level would be assumed during base loading in sequence III (Fig. 7). The subsequent overload and unloading cycle to K_{ul} does not change the closure level, since the crack is open. Therefore, according to the closure concept, reloading the specimen above K_{ul} would result in instant crack propagation. However, according to the results presented, K_{PR} rises to the indicated level, and no crack propagation can occur if the specimen is cycled between K_{ul} and K_{PR}.

3. Since crack closure is a "stiff" contact phenomenon in comparison to a "dynamic" change in the stress field ahead of the crack tip, an immediate rise in K_{PR} after a single overload, e.g., due to sequences II, III and VI in Fig. 7, cannot be explained by crack closure. The crack tip is blunted after the application of an overload and therefore K_{op} drops down [*3*]. The single overload sequence is therefore the case where K_{op} and K_{PR} exhibit their greatest relative difference. The K_{op} value, e.g., after a high overload with $K_{max,OL} = 30$ MPa$\sqrt{m}$ and $UR = 0$ ($K_{ul} = 0$ MPa$\sqrt{m}$), following constant amplitude loading with $K_{max} = 10$ MPa$\sqrt{m}$ and $R_{BL} = 0$, is very low (≈ 0.5 MPa$\sqrt{m}$ or even zero [*31*]). The crack, though, does not propagate ($\Delta K_{eff} = 0$) until the stress intensity factor is increased to $K = K_{PR,OL} + \Delta K_T = 10.7$ MPa$\sqrt{m}$ (see Eqs 4 and 7, $\Delta K_T = 1$ MPa$\sqrt{m}$), while the crack is open up to the crack tip region. The specimen can be cycled between $K = 0$ and $K = 10.7$ MPa$\sqrt{m}$,

and no crack propagation $> 1 \times 10^{-7}$ mm/cycle will occur (threshold condition, e.g., not more than 10 μm in 100 000 cycles).

4. Only the unloading part of a cycle, determined by $K_{max,OL}$ and UR, decides the level of K_{PR}. The amount of blunting which occurs during the loading part of the cycle has no influence on K_{PR}. Due to the overload in sequence I (Fig. 7), blunting at the crack tip is much smaller than due to the overloads in sequences II or III, but $K_{PR,OL}$ is the same for all three sequences.

Figure 6 shows that after the unloading procedure, following an overload, the specimen always has to be loaded again to a certain level to propagate the crack. The "unloading" line lies below Eqs 7 and 11. Therefore,

$$K_{PR} \overset{!}{\geq} K_{min} \tag{14}$$

The difference between the "unloading" line and Eq 7 (see Fig. 6) is proportional to the magnitude of RCS in front of the crack tip that has to be overcome to propagate the crack. K_{PR} determines the stress intensity factor at which a material element in front of the crack tip leaves the von Mises yield surface (at $K_{PR} + \Delta K_T$ first plastic deformation occurs at the crack tip, i.e., the crack propagates). Therefore, it is important to know all data points in Fig. 5 refer to the same stress state in front of the crack tip. K_{PR} decreases during unloading, as can be seen in Fig. 6. However, the difference between the unloading level (full circles) and $K_{PR,OL}$ (see empty circles) increases, i.e., a greater load difference is needed to overcome the RCS in front of the crack tip. The residual compressive stresses are the result of the interaction of the elastically deformed specimen and the local plasticity in front of the crack tip. According to the magnitude of the overload, a monotonic plastic zone is formed. This region is small compared to the size of the specimen (small scale yielding). During unloading, the specimen acts like a spring that clamps the plastic zone that is now "too large" compared to the situation before the overload, because the plastically deformed material can not disappear (not to the sides and not much back into the crack). We can assume the material in front of the crack tip as being in a big forging machine or extrusion machine with no outlet. The result is reversed yielding, which causes on one hand the cyclic plastic zone ($-\sigma_y$), and on the other hand, for equilibrium, the introduction of RCS around this cyclic plastic zone. Those RCS have to be overcome during loading part of the next cycle to propagate the crack. Equations 7 and 11 characterize this "forging process," described above. As a conclusion, it can be stated that as long as cyclic plasticity is involved, crack propagation will occur and a K_{PR} must exist which is above K_{min} of a cycle (Eq 14). This is not only restricted to the experiments which were discussed in this paper, but applies generally during FCP. Therefore,

$$\Delta K \overset{!}{\neq} \Delta K_{eff} \tag{15}$$

which is contrary to the often-held opinion related to the closure concept that above a certain R value or K_{op}, the applied amplitude is equal to the effective amplitude. This is important for the determination of da/dN-ΔK_{eff} curves using da/dN-ΔK data.

If no cyclic plasticity occurs during a cycle, the loads of this cycle are either below the current K_{PR} due to prior loading, so that the RCS level cannot be overcome to propagate the crack, or the cyclic amplitude is smaller than or equal to the intrinsic material threshold value, ΔK_T. For the threshold condition,

$$K_{PR} = K_{min} \quad \text{(for threshold condition)} \tag{16}$$

An overload sequence with a respective subsequent UR can lead to either retardation or acceleration. By acceleration or retardation, we mean lowering or raising K_{PR} compared to K_{PR} before the overload. Equation 11 predicts $K_{PR,OL}$ independent of the prior R_{BL} value (if $K_{max,BL} < K_{max,OL}$; it has to be figured out how much the difference between $K_{max,OL}$ and $K_{max,BL}$ must be to call $K_{max,OL}$ an "overload" and not to use Eq 13). The question whether the overload cycle accelerates or retards the crack depends on the K_{PR} level before the overload. Sequence I in Fig. 7 leads to crack growth acceleration, while in sequence III pronounced retardation occurs. When the unloading sequence after the overload just wipes out the favorable retardation effect, $K_{PR,OL}$ is equal to K_{PR} prior to the overload, denoted as ${}^{P}K_{PR}$.

$$\text{if}\left(\frac{{}^{P}K_{PR}}{K_{max,OL}}\right) = \left(\frac{K_{PR,OL}}{K_{max,OL}}\right) = UR_B \Rightarrow \text{no load interaction} \tag{17}$$

The boundary at which no load interaction occurs, UR_B, is given by combining Eq 11 with Eq 17 so that

$$UR_B = j\left(\frac{{}^{P}K_{PR}}{K_{max,OL}}\right), \qquad \text{where } j = f(h) \tag{18}$$

An overload sequence that satisfies Eq 18 would not even be recognized, since $K_{PR,OL}$ would be the same as before the overload. (Maybe, some three-dimensional effects related to the shape of the crack front would cause some disturbance.) Since the transformation of the cubic Eq 7 is not very simple, the graphical determination is proposed for practical use. As can be seen in Fig. 6, the graph in is entered with the respective ${}^{P}K_{PR}/K_{max,OL}$ ratio (here = 0.45, dashed line) and the respective UR_B is obtained (UR_B = 0.2).

Equation 7 seems to flatten at very high compression ratios. The compression stress will eventually be so high that major plastic deformations occur and the described concept is no longer applicable (besides stability problems). Anyway, it seems nearly impossible to wipe out the overload effect by a subsequent compressive load for ${}^{P}K_{PR}/K_{max,OL} < 0.1$ due to the extreme high compressive loads, required.

It should be noted that in Refs *26,32* a similar function as Eq 7 was reported. The critical parameter, which can be compared to K_{PR}, was determined for the "classical" overload experiment ($K_{ul} = K_{min,BL}$) using a conceptually similar method to the CPLM method. This parameter was reported to be a linear function of the R value of base loading. However, the function was not understood as describing a (dynamic) process, and a threshold related explanation was given.

Concluding the paper, the author wants to state that the results clearly show that load interaction effects, and FCP in general, are governed by residual compressive stresses in front of the crack tip, which form characteristically according to a respective loading sequence. The consequences of these results and the respective conceptual framework for lifetime prediction methodologies will be published in a later paper.

Summary

Load interaction effects during fatigue crack propagation were studied experimentally using the aluminum alloy Al 7475-T7351. The crack propagation stress intensity factor, K_{PR}, was determined after different single overload sequences using the CPLM (crack propagation load measurement) method. The magnitude of the overload, the R value, and the post overload unloading level, including different compressive stress levels, were varied. The results of the single overload experiments were described by a single function, namely

$$K_{PR,OL} = h\,(UR)\cdot K_{max,OL}$$

where UR is the unloading ratio after the maximum of the overload and $K_{PR,OL}$ is the K_{PR} value after

an overload. It was found that K_{PR} after an overload is independent of the R value of the prior constant-amplitude sequence. The above equation is considered the "master curve" for the single overload sequence, i.e., the *general description of the single overload phenomenon in homogeneous metallic materials.* In particular, it describes the *unloading process* after a single overload. The master curve was quantitatively determined for Al 7475-T7351, and such an intrinsic relation should exist for every homogeneous metallic material. Crack closure is treated as an *extrinsic* effect that reduces the R value experienced by the crack tip. The results show that load interaction effects are governed by residual compressive stresses in front of the crack tip, while crack closure plays a minor role. The residual compressive stress influence is classified as an *intrinsic* effort. $K_{PR,OL}$ changes continuously with the unloading ratio, which demonstrates that the critical parameter for the ΔK_{eff} concept, K_{PR}, is solely decided during the unloading part of a cycle. The difference between the current stess intensity factor during the unloading process and the respective $K_{PR,OL}$ value according to the master curve (the above function) is a measure for the residual compressive stresses in front of the crack tip.

Acknowledgments

The experiments were carried out during the stay of the author at DLR-German Aerospace Research Establishment, D-51147 Cologne, Germany. The author expresses his thanks to Mrs. Xinue Huang, Mr. Alfred Assenmacher and Mr. Uwe Fuchs for their help with the experimental work at DLR. The author also gratefully acknowledges support by the U.S. National Research Council at the Air Force Research Laboratory, Wright Patterson Air Force Base, OH 45433-7817.

References

[1] *Proceedings of the First Joint DoD/FAA/NASA Conference on Aging Aircraft,* 1997, Ogden, Utah.
[2] Schijve, J., "Fatigue Crack Propagation in Light Alloy Sheet Material and Structures," *Advances in Aeronautical Sciences,* Pergamon Press, Oxford, U.K., 1961.
[3] Elber, W., "The Significance of Fatigue Crack Closure," *Damage Tolerance in Aircraft Structures, ASTM STP 486,* American Society for Testing and Materials, 1971, pp. 230–242.
[4] Chanani, G. R., and Mays, B. J., "Observation of Crack-Closure Behavior After Single Overload Cycles in 7075-T6 Single-Edge-Notched Specimens," *Engineering Fracture Mechanics,* Vol. 9, 1977, pp. 65–73.
[5] Garett, G. G. and Knott, J. F., "On the Effect of Crack Closure on the Rate of Fatigue Crack Propagation," *International Journal of Fracture,* Vol. 13, 1977, pp. 101–104.
[6] Brown, R. D. and Weertmann, J., "Effects of Tensile Overloads on Crack Closure and Crack Propagation Rates in 7050 Aluminum," *Engineering Fracture Mechanics,* Vol. 10, 1978, pp. 867–878.
[7] Robin, C., Chehimi, C., Louah, M., and Pluvinage, G., "Influence of Overloads on the Subsequent Crack Growth of a Fatigue Crack in a E36 Steel," *Proceedings of the 4th European Conference of Fracture,* 1982, pp. 488–494.
[8] Veccio, R. S., Crompton, J. S., and Hertzberg, R. W., "Anomalous Aspects of Crack Closure," *International Journal of Fracture,* Vol. 31, 1986, pp. R29–R33.
[9] Hertzberg, R. W., Newton, C. H., and Jaccard, R., "Crack Closure: Correlation and Confusion," *Mechanics of Fatigue Crack Closure, ASTM STP 982,* American Society for Testing and Materials, 1988, pp. 139–148.
[10] Marci, G., Castro, D. E., and Bachmann, V., "Closure Measurements Via a Generalized Threshold Concept," *ASTM STP 1074,* American Society for Testing and Materials, 1990, pp. 563–580.
[11] Shih, T. T. and Wei, R. P., "A Study of Crack Closure in Fatigue," *Engineering Fracture Mechanics,* Vol. 6, 1974, pp. 19–32.
[12] Bernard, P. J., Lindley, T. C., and Richards, C. E., "Mechanisms of Overload Retardation During Fatigue Crack Propagation," *ASTM STP 595,* American Society for Testing and Materials, 1976, pp. 78–97.
[13] Lucas, P. and Klesnil, M., "Transient Effects in Fatigue Crack Propagation," *Engineering Fracture Mechanics,* Vol. 8, 1976, pp. 621–629.
[14] Marci, G., "Effect of the Active Plastic Zone on Fatigue Crack Growth Rates," *ASTM STP 677,* American Society for Testing and Materials, 1979, pp. 168–186.
[15] Marci, G. and Packman, P. F., "The Effects of the Plastic Wake Zone on the Conditions for Fatigue Crack Propagation," *International Journal of Fracture,* Vol. 16, No. 2, 1980, pp. 133–153.

[16] Damri, D. and Knott, J. F., "Fatigue Crack Growth Retardation After Single Peak and Block Overloads in a Structural Steel," *Proceedings of the 4th International Conference on Fatigue and Fatigue Thresholds,* 15–20 July 1990, pp. 1505–1510.

[17] Vasudevan, A. K., Sadananda, K., and Louat, N., "A Review of Crack Closure, Fatigue Crack Threshold and Related Phenomena," *Materials Science and Engineering,* Vol. A188, 1994, pp. 1–22.

[18] Vasudevan, A. K. and Sadananda, K., "Classification of Fatigue Crack Growth Behavior," *Metallurgical Transactions,* Vol. 26A, 1995, pp. 1221–1234.

[19] Lang, M. and Marci, G., "The Influence of Single and Multiple Overloads on Fatigue Crack Propagation," accepted for publication in *Fatigue and Fracture of Engineering Materials and Structures,* 1998.

[20] Lang, M. and Huang, X., "The Influence of Compressive Loads on Fatigue Crack Propagation," *Fatigue and Fracture of Engineering Materials and Structures,* Vol. 21, No. 1, 1998, pp. 65–83.

[21] Christensen, R. H., *Metal Fatigue,* McGraw-Hill, New York, 1959.

[22] Welsch, E., Scholtes, B., Eifler, D., and Macherauch, E., "Residual Stress Distribution Caused by Overloading in the Neighborhood of Crack Tips and Their Influence on the Propagation of Fatigue Cracks," *Residual Stresses,* E. Macherauch and V. Hauk, Eds., DGM, Oberursel, Germany, 1986.

[23] Welsch, E., "Der Einfluβ riβspitzennaher Eigenspannungen auf die Ausbreitung von Ermüdungsrissen," Ph.D. Thesis, University of Karlsruhe, Germany, 1985, (in German).

[24] Jägg, S. and Scholtes, B., "Crack Propagation and Crack Tip Residual Stresses After Different Loading Histories of Steel S690QL1," *Proceedings of the 5th International Conference on Residual Stresses,* Lingköping, Sweden, 1997.

[25] Lang, M. and Marci, G., "Reflecting on the Mechanical Driving Force of Fatigue Crack Propagation," *Fatigue and Fracture Mechanics: 29th Volume, ASTM STP 1332,* T. L. Panontin and S. D. Sheppard, Eds., American Society for Testing and Materials, 1998, pp. 474–495.

[26] Pellas, J., Baudin, G., and Roberts, M., "Fatigue Crack Growth Model Prediction with Two Coupled Differential Equations," *4th International Conference of Fracture,* Vol. 2, Waterloo, Canada, 1977, pp. 1353–1560.

[27] Marci, G., Hartmann, K., and Bachmann, V., "Experimentelle Bestimmung des ΔK_{eff} für Ermüdungsriβ‴ fortschritt," *Materialwissenschaften und Werkstofftechnik,* No. 21, 1990, pp. 174–84 (in German).

[28] Döker, H. and Bachmann, V., "Determination of Crack Opening Load by Use of Threshold Behavior," *Mechanics of Fatigue Crack Closure, ASTM STP 982,* J. C. Newman, Jr. and W. Elber, Eds., American Society for Testing and Materials, 1988, pp. 247–259.

[29] Lang, M. and Larsen, J. M., "Fatigue Crack Propagation and Load Interaction Effects in a Titanium Alloy," *Fatigue and Fracture Mechanics, 30th Volume, ASTM STP 1360,* American Society for Testing and Materials, 1998, accepted for publication.

[30] Sunder, R., Porter, J., and Ashbough, N. E., "The Effect of Stress Ratio on Fatigue Crack Growth in the Absence of Closure," *International Journal of Fatigue,* Vol. 19, Supp. No. 1, 1997, pp. S211–S221.

[31] Yisheng, W. and Schijve, J., "Fatigue Crack Closure Measurements on 2024-T3 Sheet Specimens," *Fatigue and Fracture of Engineering Materials and Structures,* Vol. 18, No. 9, 1995, pp. 917–921.

[32] Pellas, J., Baudin, G., and Robert, M., "Mesure et Calcul du Seuil de Fissuration après Surcharges," *Recherches Aerospatiale,* Vol. 3, 1977, pp. 191–204 (in French), English translation ESA-TT (1987).

Robert R. Stephens,[1] Ralph I. Stephens,[2] David E. Lemm,[2] Shannon G. Berge,[2] Haakon O. Liknes,[1] and Christopher J. Cousins[1]

Role of Crack Closure Mechanisms on Fatigue Crack Growth of Ti-62222 Under Constant-Amplitude and Transient Loading at −54, 25, and 175°C

REFERENCE: Stephens, R. R., Stephens, R. I., Lemm, D. E., Berge, S. G., Liknes, H. O., and Cousins, C. J., **"Role of Crack Closure Mechanisms on Fatigue Crack Growth of Ti-62222 Under Constant-Amplitude and Transient Loading at −54, 25, and 175°C,"** *Advances in Fatigue Crack Closure Measurement and Analysis: Second Volume, ASTM STP 1343,* R. C. McClung and J. C. Newman, Jr., Eds., American Society for Testing and Materials, West Conshohocken, PA, 1999, pp. 224–245.

ABSTRACT: Fatigue crack growth behavior of Ti-62222 in sheet form was investigated at three temperatures under various load histories with a specific emphasis on crack opening measurements and mechanisms. Constant-amplitude $R = 0.1$ near-threshold results showed that based upon applied ΔK, fatigue crack growth rates were lower at the two temperature extremes in comparison with those at room temperature. Based upon ΔK_{eff}, a moderate temperature effect was observed. The various shifts in the ΔK_{eff} curves were a result of different controlling crack closure mechanisms at each temperature. Single tensile overloads at $2.5 \times K_{max}$ produced a delay in fatigue crack growth and was most significant at −54°C. Remote crack opening measurements showed no appreciable change during the delay period due to the small region along the crack front that experienced crack closure. Near crack tip opening measured for various combinations of overloads, underloads, and constant ΔK at 25°C revealed a general trend for higher near tip opening following a tensile overload. However, a sufficient number of measurements were inconsistent and thus only minimal confidence could be placed with the method. Scanning electron microscopy was used to evaluate surface fatigue crack growth profiles and fatigue crack growth fracture surface morphology.

KEYWORDS: titanium alloy, threshold, crack closure, overload, underload, temperature, delay, fractography

Fatigue crack closure has been widely studied for nearly 30 years and under flight simulation loading is likely the most significant load interaction mechanism present. The primary differences observed between constant and variable-amplitude loading conditions have been found to be associated with load interaction and crack closure mechanisms. This has been studied extensively [*1–5*] and has been attributed to surface debris, oxide formation, microroughness, plasticity, and other mechanisms. Perhaps the most widely studied transient effect on fatigue crack growth (FCG) is the application of a single tensile overload or a combination of a tensile overload followed by a compressive underload. Various mechanisms have been proposed to account for the observed transient responses. These include crack tip blunting, residual stresses, plasticity-induced closure, roughness-induced closure, and crack deflection [*6–10*].

[1] Associate professor and graduate research assistants, respectively, University of Idaho, Moscow, ID 83844.
[2] Professor and graduate research assistants, respectively, University of Iowa, Iowa City, IA 52242.

This paper contains a description of a research program involving fatigue crack growth behavior of Ti-62222 titanium alloy under various loading and temperature conditions. Titanium alloys have many attractive characteristics, and due particularly to a high strength to weight ratio, high temperature capabilities, and good damage tolerance, they are candidate materials for high speed aerospace applications. This requires excellent durability and damage tolerance at temperatures from −54°C to 175°C. The objectives of this research using Ti-62222 sheet at −54°C, 25°C, and 175°C were: (1) to compare near-threshold constant-amplitude fatigue crack growth behavior, (2) to evaluate load interaction effects following various combinations of tensile overloads and compressive underloads over a broad range of ΔK levels, and (3) to evaluate the contribution of crack closure to the fatigue crack growth response by means of crack opening measurements and fractographic observations.

Experimental Details

Material

The material used in this investigation was Ti-62222 (Ti-6Al-2Sn-2Zr-2Mo-2Cr) that was solution treated at 732°C for 30 min and aged at 510°C for 10 h followed by air cooling. This heat treatment was designed to produce a high strength titanium alloy. This resulted in an equiaxed alpha phase dispersed evenly throughout an alpha-plus-beta matrix. The resulting microstructure had an estimated grain size less than 10 μm and is presented in Fig. 1. Specimens were tested in the L-T orientation where the tensile properties in the longitudinal direction are provided in Table 1. Tensile strengths changed approximately 15% as the temperature was decreased or increased to −54°C or 175°C, respectively, from the room temperature conditions. Percent elongation at −54°C showed about a 20% decrease in comparison to 25°C and 175°C.

Specimen Details

For constant-amplitude near-threshold tests, specimens were machined from sheet material, approximately 1.65 mm thick, into extended compact tension specimens, EC(T). EC(T) specimens

FIG. 1—*SEM micrograph of Ti-62222 microstructure.*

TABLE 1—*Mechanical Properties of Ti-62222.*

	Ultimate Strength (MPa)	Yield Strength (MPa)	% Elongation
−54°C	1459	1397	7.8
25°C	1341	1223	9.5
175°C	1237	1015	9.4

were also used for single tensile overload tests performed at the three different temperatures. Middle tension, M(T), specimens were used for the overload and overload/underload combination study where tests were performed at 25°C. EC(T) specimens were nominally 38 mm × 142 mm and M(T) specimens were nominally 50 mm × 180 mm. Several EC(T) specimens and all M(T) specimens were polished and etched to reveal microstructural features associated with crack growth behavior at the surface.

Test Procedures

All tests were performed using 100 kN, computer controlled, closed-loop, servohydraulic test systems under load control. Tests were performed using a sinusoidal wave form at frequencies between 10 to 35 Hz at a stress ratio of $K_{min}/K_{max} = 0.1$. Crack length measurements were made using the compliance method of back face strain [*11*] for constant-amplitude near-threshold tests and crack mouth opening displacement (CMOD) for single tensile overload and overload/underload tests. A traveling microscope was used to check compliance accuracy for all testing conditions. Crack opening measurements were made using: (1) a global back face strain gage for constant-amplitude tests at all three temperatures, (2) a global CMOD gage for single tensile overload tests at all three temperatures, and (3) a local strain gage positioned near the crack tip for the 25°C overload/underload tests at 25°C. Data were collected automatically at predetermined crack growth increments. For all transient tests performed, data were collected every 0.04 mm (40 μm) as this was the smallest crack length increment attainable that produced repeatable results. Effective stress intensity values, ΔK_{eff}, were obtained using the equation,

$$\Delta K_{eff} = K_{max} - K_{op} \tag{1}$$

where K_{op} was determined using the ASTM E 647 recommended 1 or 2% offset compliance method for determination of fatigue crack opening load.

For constant amplitude near threshold tests, continuous load shedding was used to exponentially reduced ΔK, where the value of the load shedding constant used was $C = -0.08$/mm. These tests were analyzed for crack closure using a compliance offset of 2%. For elevated temperature tests the specimens were heated to 175°C using resistive heaters positioned above and below the mid-plane of the specimen. Temperature variations within the critical portion of the specimen were within 1% of the test temperature. This test temperature is consistent with the estimated temperature at control surface locations for supersonic speeds approaching Mach 2.4, consistent with the design constraints placed on the high-speed civil transport vehicle (HSCT). To achieve a temperature of −54°C, liquid nitrogen was sprayed through a nozzle into an insulated chamber surrounding the specimen and grips. Temperature variations were determined to be within ±2°C of the desired test temperature. This test temperature simulates the operating temperature at subsonic flight speeds at climbing and near cruise altitudes.

Single tensile overload tests of 150% (2.5 × K_{max}) were performed in triplicate at the three test temperatures at various constant ΔK levels, 6.6, 8, 10, 12, 14, and 15.4 MPa$\sqrt{\text{m}}$. Tests were conducted at a baseline load ratio of $R = 0.1$. Crack length and remote crack opening measurements were monitored using a crack mouth opening displacement gage (CMOD) positioned on the front face of the EC(T) specimen. Single tensile overloads were applied at 0.01 Hz after which baseline loading at the desired constant ΔK level was maintained. Values recorded as a result of the overload included delay distance, a_d, and delay cycles, N_d. The delay distance was defined as the distance the crack extended after the overload until steady state conditions were reached. The delay cycles was defined as the number of cycles required to grow the crack the delay distance after the point of the overload. The 150% ($2.5 \times K_{max}$) overload used in this part of the study is comparable to the overload ratio observed in the transport aircraft flight spectra miniTWIST for the most severe flight ($2.6 \times K_{mf}$). K_{mf} is the mean flight stress intensity based on the mean flight stress, σ_{mf}. It is anticipated that the most severe flight in the HSCT flight spectra will be similar.

Overload/underload tests were conducted at a temperature of 25°C. M(T) specimens were precracked 2 mm from the machined notch tips using ASTM Standard E 647 load shedding procedures. Crack extension was determined using the compliance method involving a CMOD clip gage. All tests were performed with crack length, $2a$, between 14 and 41 mm with corresponding $2a/w$ ratios between 0.28 and 0.81. All overload/underload tests were run in triplicate and were preceded and followed with constant ΔK sinusoidal loading. Overload/underloads were applied at 0.01 Hz. Eight to ten overload/underloads were performed on each test specimen. Constant ΔK values of 4.4, 8.8, 13.2 and 17.6 MPa$\sqrt{m}$ were chosen so as to represent near threshold and Paris region steady-state fatigue crack growth. Overload ratios were 2 and 2.5 while underload ratios were -0.5 and -1.0. Constant ΔK steady-state crack growth preceding and following overload/underloads involved about 10 to 20 crack length measurements taken at $\Delta a = 0.04$ mm intervals or about 0.5 to 1.0 mm of steady-state crack extension.

Crack opening measurements were made on 11 of the 24 different overload/underload test conditions as shown by X's in Table 2. These 11 tests were chosen to be representative of the entire test matrix. Crack opening measurements were obtained using 0.8 mm gage length foil strain gages mounted about 1 mm ahead of one crack tip in the crack plane. The strain gages were aligned in the loading direction and a new gage was mounted for each overload/underload. Load versus strain data were obtained during pre- and post-overload/underload steady-state conditions, just prior to and after the overload/underload and during FCG delay. Typical load versus strain behavior following an overload/underload is shown in Fig. 2. A straight line has been superimposed from the upper slope to better elucidate the small nonlinear behavior. Crack opening loads were obtained by reducing the load versus strain data using the ASTM standard E 647 recommended compliance offset method. The reduction of Fig. 2 is given in Fig. 3. Both 1 and 2% offset values are shown in Fig. 3. Either value could be used as per ASTM E 647 and as seen in Fig. 3, the difference in P_{op} for these two offset values is less than 10%. The 1% value was selected for these tests.

A detailed fractographic analysis was performed involving both surface profile observations and fracture surface behavior. These were performed using scanning electron microscopy (SEM) with the intent to compare the free surface and fracture surface crack growth observations with experimental crack opening results.

TABLE 2—*Test Combinations for Which Closure Measurements were Taken (Indicated by an X).*

	OLR/ULR					
ΔK (MPa$\sqrt{m}$)	2	2/−0.5	2/−1	2.5	2.5/−0.5	2.5/−1
4.4	X		X			
8.8	X		X	X		X
13.2	X		X	X	X	
17.6						X

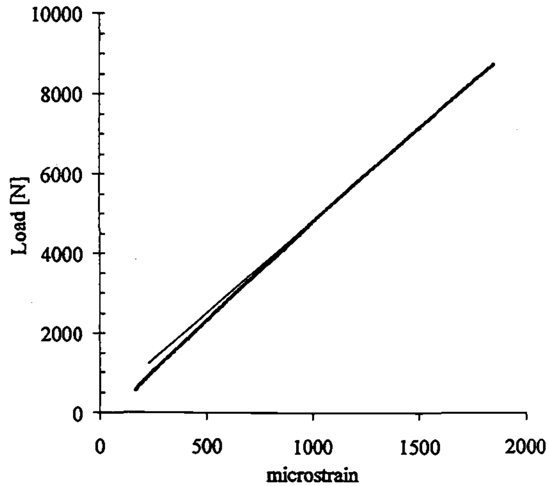

FIG. 2—*Typical load versus microstrain for* $\Delta K = 17.6\ MPa\sqrt{m}$ *with OLR = 2.5 and ULR = −1.*

Results and Discussion

Constant-Amplitude Near-Threshold Fatigue Crack Growth

Constant amplitude near threshold $R = 0.1$ fatigue crack growth curves for Ti-62222 are shown in Fig. 4. Figure 4a, which compares nominal ΔK behavior, indicates that at near threshold conditions −54°C and 175°C exhibit lower crack growth rates for a given ΔK than at 25°C. At slightly higher ΔK values, the crack growth rate at −54°C is lower than 25°C and 175°C while the crack growth rate for 25°C and 175°C converge. Figure 4b, shows the ΔK_{eff} behavior and indicates lower crack growth rate for −54°C in comparison to 25°C while the 175°C curve shows a significant shift to the left

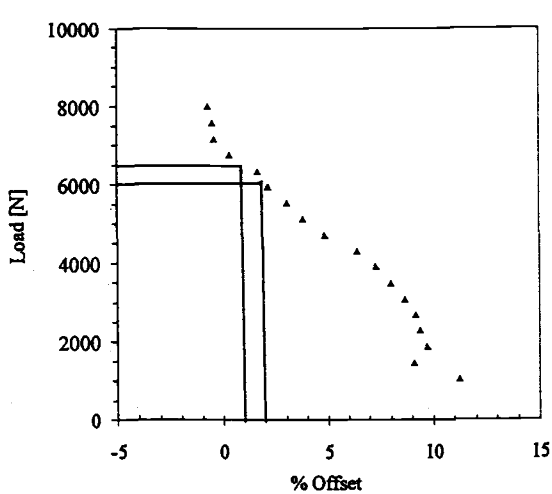

FIG. 3—*Compliance offset: 1 and 2 percent of open crack compliance value.*

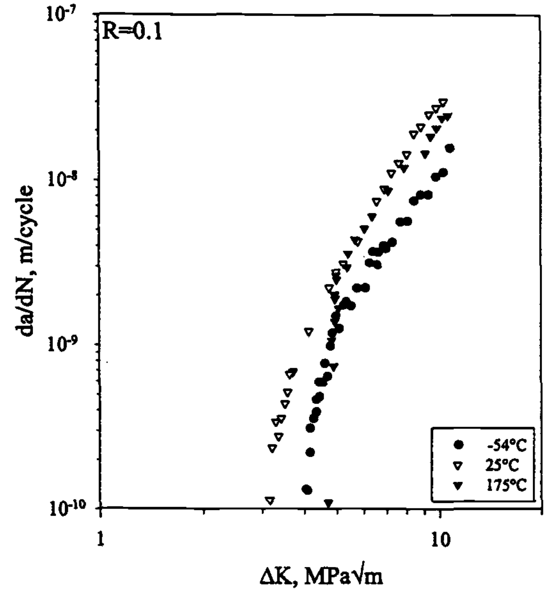

(a) da/dN versus ΔK for -54°C, 25°C, and 175°C

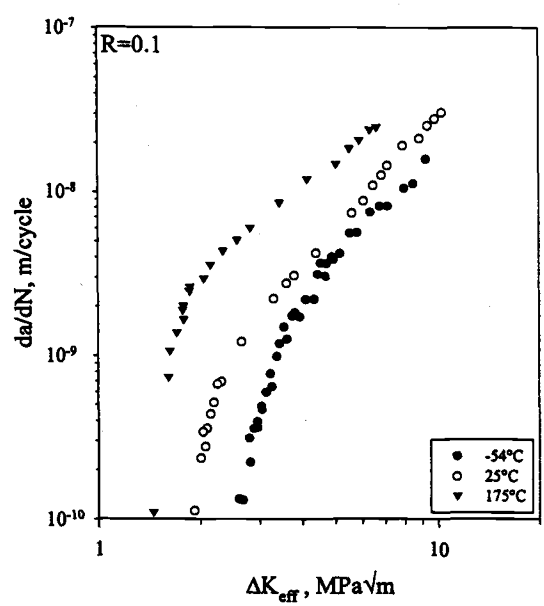

(b) da/dN versus ΔK_{eff} for -54°C, 25°C, and 175°C

FIG. 4—*Fatigue crack growth behavior for constant-amplitude loading;* (a) da/dN *versus* ΔK *for -54°C, 25°C, and 175°C,* (b) da/dN *versus* ΔK_{eff} *for −54°C, 25°C, and 175°C.*

TABLE 3—*Fatigue Crack Growth Rate Threshold Values, R = 0.1.*

	ΔK_{th} (MPa$\sqrt{m}$)	$\Delta K_{th,eff}$ (MPa$\sqrt{m}$)
−54°C	4.1	2.6
25°C	3.1	1.9
175°C	4.6	1.5

showing a temperature effect. ΔK_{th} and $\Delta K_{th,eff}$ results are summarized in Table 3. The large shift at 175°C is a result of the significantly higher crack opening loads observed in comparison to those observed at −54°C and 25°C as shown in Fig. 5. This figure compares the ratio of the crack opening stress intensity and maximum stress intensity (K_{op}/K_{max}) to the stress intensity range (ΔK). This shows that as ΔK decreased and approached threshold conditions, the opening load to maximum load ratio (K_{op}/K_{max}) increased at different rates for the three test temperatures resulting in the various shifts to the left of the ΔK_{eff} curves in Fig. 4b. The near threshold shifts in the fatigue crack growth rate curves for the various temperatures can be accounted for in terms of changes in surface oxidation, surface roughness, and small changes in yield strength. Figure 6 shows SEM micrographs of the fracture surface at near threshold conditions for the three temperatures. At elevated temperature, it was found that the surface roughness decreased in comparison to room temperature, as seen in Figs. 6a and b. A contributing factor to the increase in closure load at 175°C was the formation of an oxide layer. The oxide layer was found to be on the order of 70 nm as measured in the threshold region. The oxide layer was measured by sectioning, polishing, and coating the specimen with a thin layer of gold to minimize charging. SEM and X-ray diffraction were then used to determine the oxide layer thickness. With an oxide layer thickness of 70 nm on both crack surfaces, the combined thickness approaches the theoretical local crack tip opening displacement from the equation [*12*];

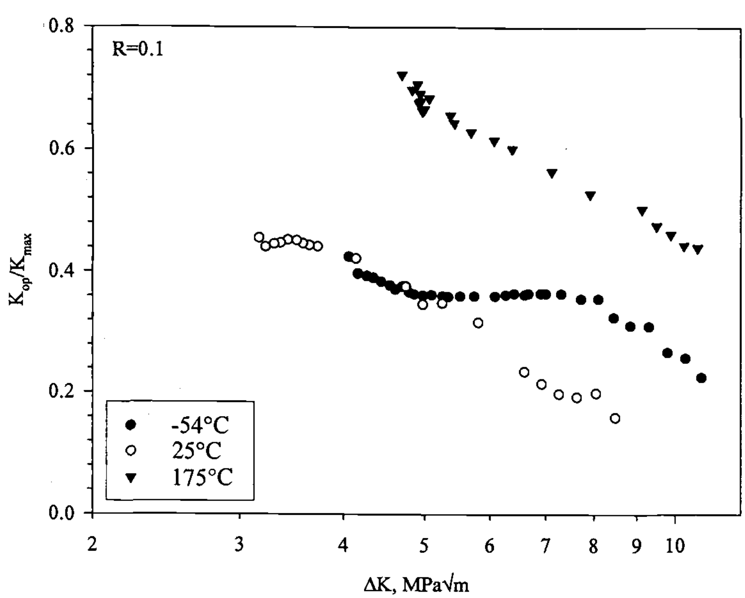

FIG. 5—*Comparison of* K_{op}/K_{max} *versus* ΔK *for constant-amplitude near-threshold loading.*

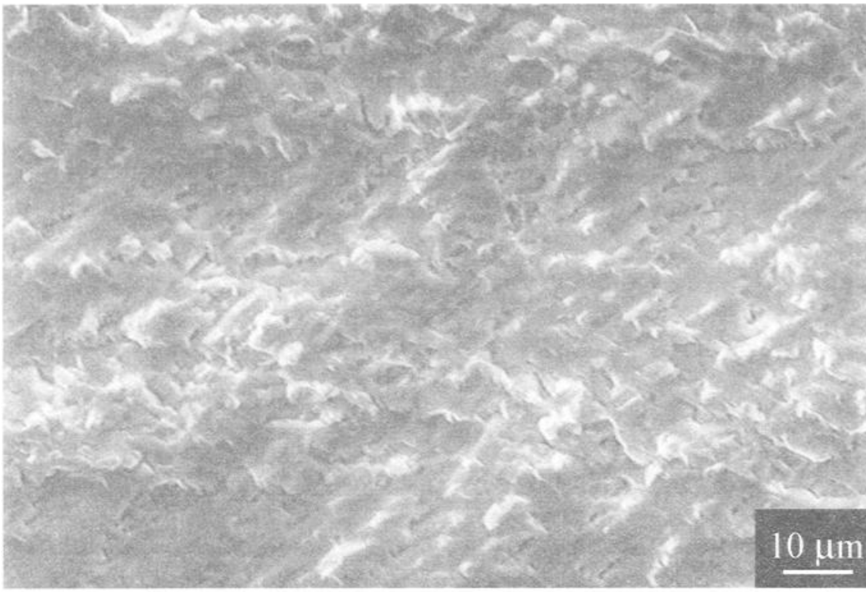

(a) 25°C

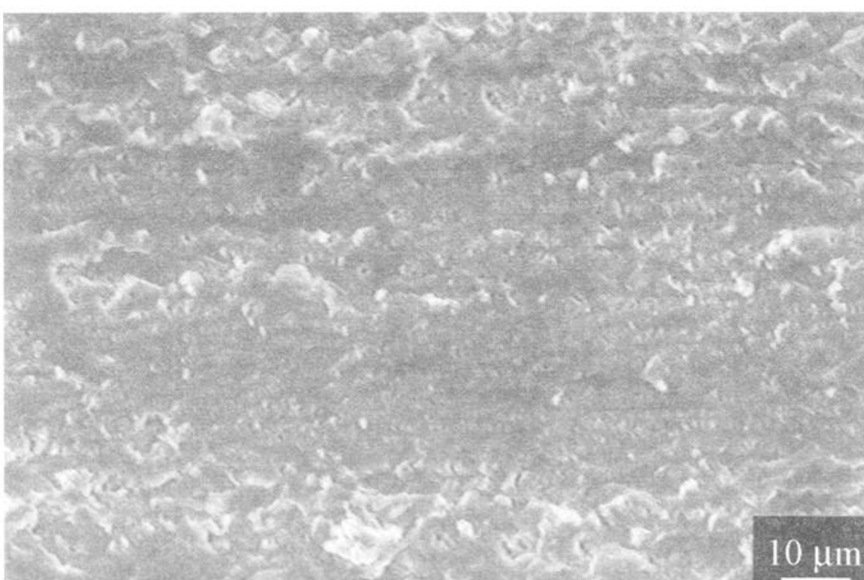

(b) 175°C

FIG. 6—*Near threshold fatigue crack growth fracture surfaces. Crack growth direction is from left to right.* (a) *25°C,* (b) *175°C,* (c) *−54°C.*

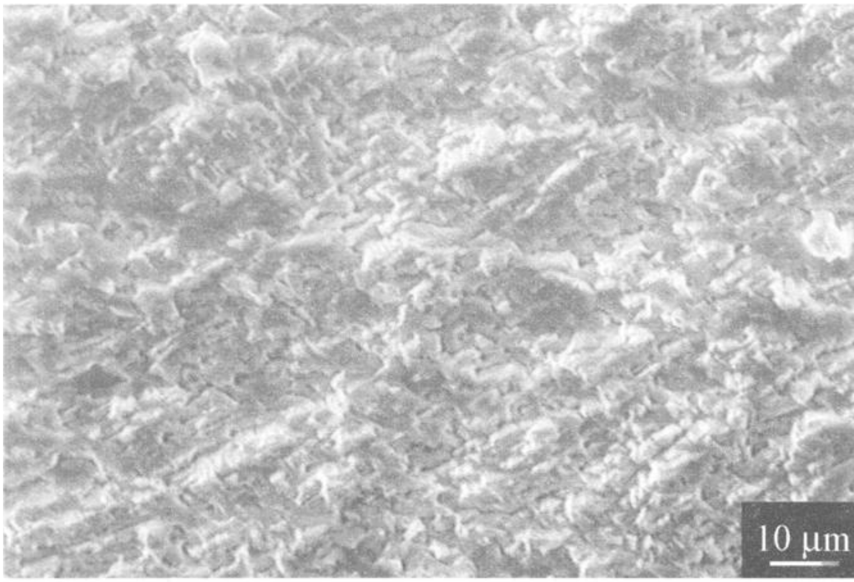

(c) -54°C

FIG. 6—*Continued*

$$\text{CTOD} = K^2/\sigma_{ys}E \quad (2)$$

Based on this equation at a ΔK of approximately 4 MPa$\sqrt{\text{m}}$, the CTOD is approximately 170 nm. Therefore while the surface roughness contribution to crack closure at 175°C was less than that observed at 25°C, surface oxidation on the other hand contributed largely to the increase in the opening loads experienced at 175°C as the sum of the oxide layer measured on both surfaces was on the order of the CTOD. This has been observed in other titanium alloys at elevated temperature ranging from 175°C to 800°C [*13–15*]. A discoloration of the fracture surface was also observed suggesting the presence of oxidation. A recent study [*16*] has shown that at 260°C, Ti-62222 is even more susceptible to surface oxidation as extensive fretting debris was also observed for near threshold loading. Crack opening loads were observed to be similar at 260°C to those observed at 175°C.

At −54°C, the surface roughness at near threshold conditions was found to increase in comparison to 25°C, as shown in Fig. 6c. The observed increase in fracture surface roughness coupled with any Mode II displacement will lead to crack face contact and hence elevated closure levels. Evidence of mechanical rubbing due to surface contact was also apparent on the fracture surface at near threshold conditions.

At 25°C, it was observed that the ratio K_{op}/K_{max} also increased as near threshold conditions were approached, however, the level of crack closure was less than that observed at the other two temperatures. Based on the observations made in this study at 175°C, oxide-induced crack closure was a dominant mechanism of crack closure, while at −54°C, an increase in surface roughness contributed to the elevation in opening load. While plasticity-induced crack closure is most prominent in plane stress conditions, even under threshold conditions the residual stress field will try to force the crack surfaces together prematurely. At near threshold conditions, where plane strain predominately exists, the residual stress field developed in the wake of the crack is limited but can still contribute to the closure observed. The effect of crack closure mechanisms such as roughness or oxide induced closure will be amplified due to plasticity-induced closure. While plasticity may contribute to the extent of crack closure observed, it does not appear to be the dominant closure mechanism for any one given temperature as the plastic zone size at a given ΔK is small and similar for the three test temperatures (at $\Delta K = 4$ MPa$\sqrt{\text{m}}$, r_y ranged between 1.6 and 3.0 μm).

Single Tensile Overloads

Results of load interaction tests for 150% overload ($2.5 \times K_{\text{max}}$) are shown in Figs. 7a and b. These figures compare the delay distance, a_d, and delay cycles, N_d, for a broad range of constant ΔK levels

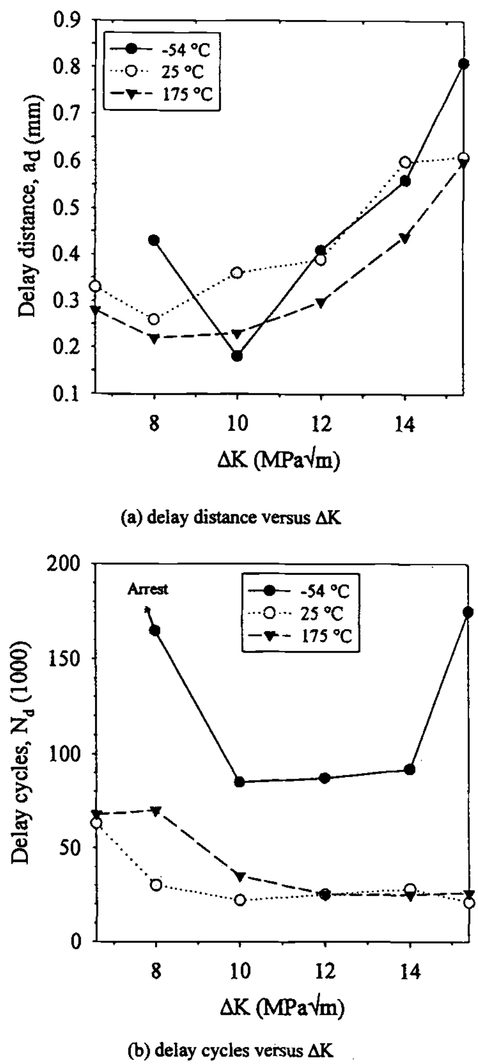

FIG. 7—*2.5 × K_{max} single tension overload comparison for −54°C, 25°C, and 175°C;* (a) *delay distance versus* ΔK, (b) *delay cycles versus* ΔK.

studied at three temperatures, $-54°C$, $25°C$, and $175°C$. The results represent the average of three tests. The crack growth behavior observed was documented in terms of crack growth rate (da/dN) versus delay distance and delay cycles. Results for $\Delta K = 15.4\ MPa\sqrt{m}$ are presented in Figs. 8a and b and represent the general behavior observed at all ΔK values studied with an OLR = 2.5 (tension only). Post overload behavior was characterized by an abrupt crack growth deceleration and then a gradual return to steady state. At $-54°C$ it was found that crack arrest occurred after the $2.5\times K_{max}$ overload at $\Delta K = 6.6\ MPa\sqrt{m}$, represented by the arrow in Fig. 7b. At the various levels of ΔK the overload induced an increment of crack growth, defined as the stretch zone. Compliance measure-

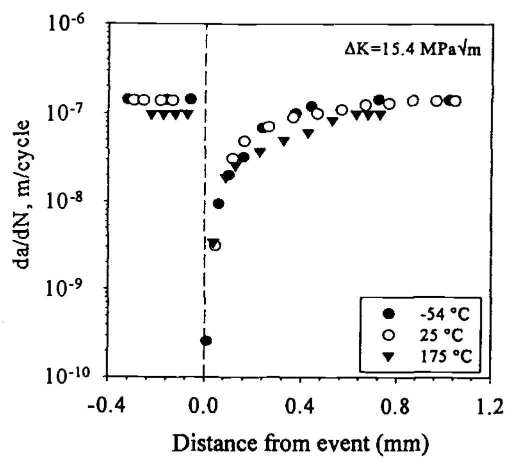

(a) da/dN versus distance from event

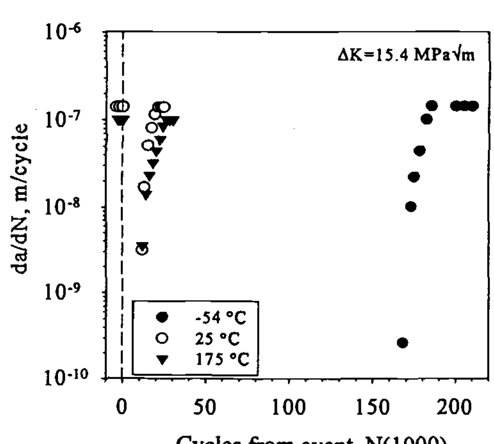

(b) da/dN versus cycles from event

FIG. 8—*FCG behavior for 2.5* $\times$ K_{max} *single tension overload for* $-54°C$*,* $25°C$*, and* $175°C$*;* (a) da/dN *versus distance from event,* (b) da/dN *versus cycles from event.*

ments suggested crack growth (stretch zone) to be less than 100 μm for all ΔK levels. Stretch zones were also measured on the fracture surface and supported compliance measurements. Stretch zones ranged from approximately 50 μm at low ΔK up to approximately 240 μm at high ΔK with no discernible difference observed between temperatures. The delay distance, a_d, generally followed a systematic trend where it increased as the constant ΔK level increased. It was determined there was not a significant difference between the three temperatures based on delay distance. Crack growth delay, N_d, was found to be much larger at $-54°C$ than at the other two temperatures, where at the high and low ΔK extremes, the number of cycles of delay were approaching an order of magnitude higher (at 6.6 MPa$\sqrt{m}$ $-54°C$, the crack arrested). At intermediate ΔK values, the differences were negligible between 25°C and 175°C. However, $-54°C$ still showed more delay cycles than the other two temperatures. The initial low values of crack growth rate, da/dN, following the overload, as shown in Fig. 8, were similar for 25°C and 175°C but was about an order of magnitude lower for $-54°C$. This lower value of da/dN following the overload contributed significantly to the overall delay cycles observed at $-54°C$.

The cyclic overload plastic zone, $2r_y'$, was calculated for each of the test conditions using Eqs 3 or 4 for plane strain or plane stress conditions, respectively [17];

$$\text{plane strain} \qquad 2r_y' = \frac{1}{3\pi}\left(\frac{\Delta K_{OL}}{2\sigma_{ys}}\right)^2 \tag{3}$$

$$\text{plane stress} \qquad 2r_y' = \frac{1}{\pi}\left(\frac{\Delta K_{OL}}{2\sigma_{ys}}\right)^2 \tag{4}$$

ΔK_{OL} is the overload stress intensity factor range and σ_{ys} is the 0.2% offset yield strength. Differentiation between plane strain and plane stress was based upon the ratio of thickness, 1.65 mm, to 2.5 $(K_{max}/\sigma_{ys})^2$. These calculations were performed to determine if there was a correlation between cyclic overload plastic zone and delay distance/cycles for the various temperature conditions. The extent of the delay cycles observed did not appear to be associated with the size of the cyclic overload plastic zone developed due to the overload. This is suggested because of the significantly larger delay cycles observed at $-54°C$ in comparison to the other two temperatures. Based on a $2.5 \times K_{max}$ overload, the overload plastic zone size at $-54°C$ was approximately 30% and 85% smaller in comparison to 25°C and 175°C, respectively, due to a larger yield strength. If the plastic zone size were the primary controlling delay parameter, one would expect the tests performed at 175°C to show the greatest delay. At higher ΔK values, the delay distance measured for the various temperatures exceeded the overload plastic zone size based on plane stress and at lower ΔK values the delay distances for conditions where crack arrest did not occur also exceeded the cyclic plastic zone sizes based on plane strain conditions. It should be noted that, based upon the a versus N data, the majority of the delay life was spent growing the crack approximately 40 μm (the resolution of the clip gage measuring crack extension) for all the tests performed while the total delay distance, a_d, varied up to 0.8 mm. For lower constant ΔK conditions (6.6 and 8 MPa$\sqrt{m}$) 40 μm far exceeded the size of the cyclic overload plastic zone size while at higher constant ΔK conditions, 40 μm is on the order of the cyclic overload plastic zone size. Therefore the size of the plastic zone associated with the overload did not solely control the crack growth delay observed.

Far field measurements of the fatigue crack opening load were made using CMOD compliance at all three temperatures for the various ΔK levels to determine the closure contribution to the delay experienced. This included measurements made before and after the overload. No observable change in the far field opening load was found following the single tensile overload nor during the return to steady state using either the 1 or 2% offset method. This was the case for all temperatures and ΔK conditions. Based on the delay cycles observed, one would expect an increase in opening load resulting in a decrease in ΔK_{eff}. However, it was determined that while measurement of far field crack

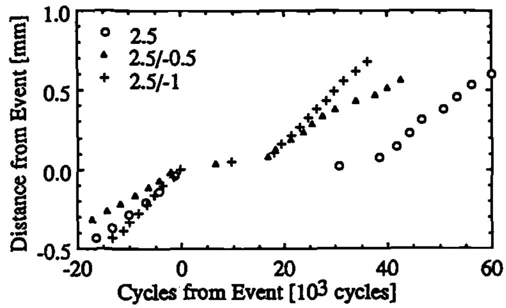

FIG. 9—*Crack length versus cycles for* $\Delta K = 8.8\ MPa\sqrt{m}$, *average of three tests.*

opening may represent global crack closure behavior, it was not sensitive enough to detect local changes in crack tip opening loads that could confirm changes in crack tip driving force due to the tensile overloads. Therefore the following study at 25°C contains near-tip opening measurements using strain gages mounted near the crack tip, where these results are compared to surface profile and fracture surface observations.

Tensile Overload/Compressive Underload

Each overload/underload test was evaluated based upon delay cycles, N_d, and delay crack extension, a_d, as previously defined. For the 24 different test conditions, N_d varied from zero to crack arrest and a_d varied from zero to 0.42 mm depending upon the constant ΔK level, the OLR, and the OLR/ULR. Triplicate a versus N behavior was averaged for each test condition and representative results for $\Delta K = 8.8$ MPa$\sqrt{\text{m}}$ with OLR equal to 2.5 and OLR/ULR equal to 2.5/−0.5 and 2.5/−1 are shown in Fig. 9. Here it is seen that N_d for the three test conditions varied from 16 700 to 43 000 cycles with a significant amount of the delay cycles occurring within the first 40 μm of crack extension. Both underloads decreased the amount of delay relative to the single tensile overload which was typical for most tests. The triplicate average a versus N curves were reduced to da/dN using a secant method for adjacent data points. This reduction for $\Delta K = 8.8$ MPa$\sqrt{\text{m}}$ from Fig. 9 is shown in Fig. 10 as a function of the crack distance from the application of the overload/underload. The minimum FCG rate following all overload/underloads ranged from no change up to almost two orders of magnitude below the steady-state FCG rate with the majority of the delay life for most tests spent growing the crack approximately 40 μm past the averaged stretch zone.

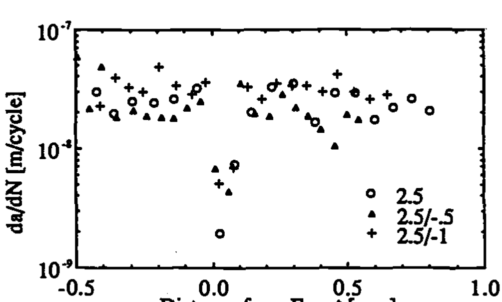

FIG. 10—*Crack growth rate versus crack length for* $\Delta K = 8.8\ MPa\sqrt{m}$, *average of three tests.*

Of the 11 crack tip strain gage closure measurement tests indicated in Table 2, six of these showed little or no change in the crack closure load before or after the overload/underload. In four of these cases, this corresponded to zero delay or very few cycles of delay (<4000 cycles). The other two cases that exhibited little change in closure had 14 000 and 110 000 cycles of delay. This lack of change could be due to the significant variation in measured crack opening expected from the ASTM E 647 reduction methodology and is in agreement with two ASTM round robin crack closure measurement programs [*18,19*]. The 110 000 cycles of delay without a change in P_{op}/P_{max} involved $\Delta K = 4.4$ MPa$\sqrt{m}$ and OLR = 2. This steady-state ΔK value is in the near threshold region which involves very small steady-state and overload plastic zones and thus little crack closure change is to be expected [*20*]. The other five crack opening measurement tests, however, indicated appreciable crack closure changes. These five test conditions are shown in Fig. 11 where each test condition is shown with the average a versus N curve superimposed on the specific P_{op}/P_{max} versus N curve. The zero reference positions are taken at the overload/underload application. These five tests correspond to five various overload/underload combinations and represent a wide range of delay and crack closure behavior.

Figures 11a, b, c and e indicate an increase in crack opening loads following the specific overload/underload, reaching a peak within the delay region, and then decreasing back toward the constant ΔK steady-state region. These trends are qualitatively in agreement, in that delay following an overload/underload can be attributed to increased crack closure. Figure 11d, however, indicates a small decrease in the crack closure load following the overload, but then peaks within the delay region and then decreases back toward the constant ΔK steady-state region. Some of the P_{op}/P_{max} values prior to overload/underloads also indicate inconsistencies. These pre- and post-overload anomalies could be due to the significant variability in measuring crack opening loads that is inherent with interpreting small nonlinearities and the very small amount of crack length over which closure occurred.

Fractography Overload/Underload

Macroscopic examination of fracture surfaces revealed smooth fracture surfaces with noticeable stretch zones only appearing for the higher ΔK or overload values. These stretch zones were evident for all $\Delta K = 13.2$ and 17.6 MPa$\sqrt{m}$ tests and with $\Delta K = 8.8$ MPa$\sqrt{m}$ for OLR = 2.5. Stretch zones were not evident for all $\Delta K = 4.4$ MPa$\sqrt{m}$ tests and for $\Delta K = 8.8$ MPa$\sqrt{m}$ for OLR = 2.0. Typical steady-state fatigue crack growth profiles prior to and after an overload/underload are shown in Figs. 12 a and b, respectively. In both steady-state regions, fatigue cracking is from left to right and is transgranular with crack path deflections only a few grains in magnitude. Surface crack opening of about 1 μm is evident along most of the crack in Fig. 12 a and all of the crack in Fig. 12b. Figures 13a and b show the crack profile immediately after an overload of 2.5 and an overload/underload of 2.5/−1 respectively. It should be noted that Figs. 12 and 13 were obtained by stopping the tests, removing the specimens and examining them in the scanning electron microscope. In both Figs. 13a and b the surface stretch zone deflects approximately 40 and 50 μm, respectively, as seen at the overload/underload. Only a portion of this stretch zone remains open, and all the crack is open behind the overload regions for both conditions. Figure 13b indicates additional micro-cracking or branching of about 5 to 10 μm in the initial stretch zone deflection region. Both Figs. 13a and b indicate very little surface crack closure (<30 μm) existed and only at the crack tip region. Crack tip profiles for loading conditions where crack arrest occurred also showed this same minimal surface crack tip closure. If the overload/underload condition did not cause crack arrest, additional steady-state loading caused the surface crack profile to return to the nominal direction perpendicular to the loading.

Scanning electron fractography revealed different steady-state morphology depending upon the ΔK level. However, steady-state morphology before and after an overload/underload was essentially

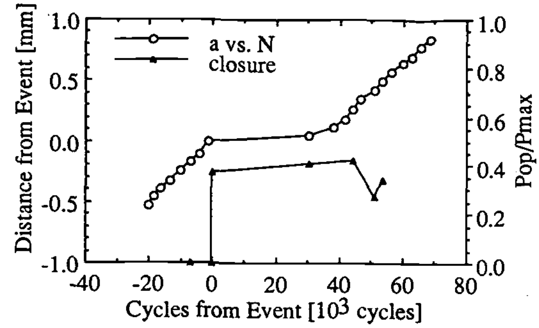

(a) $\Delta K = 8.8$ MPa$\sqrt{m}$, OLR = 2.5.

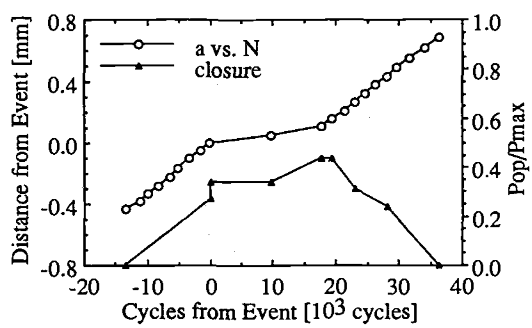

(b) $\Delta K = 8.8$ MPa$\sqrt{m}$, OLR = 2.5 and ULR = -1.

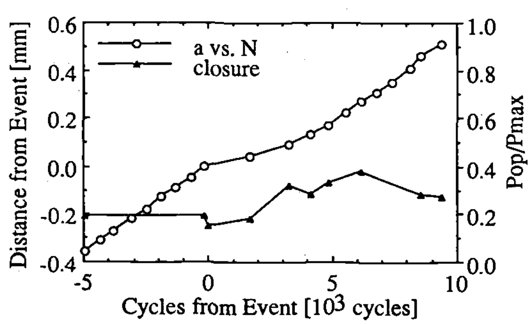

(c) $\Delta K = 13.2$ MPa$\sqrt{m}$, OLR = 2.

FIG. 11—*Measured crack closure level as overload test progressed;* (a) $\Delta K = 8.8\, MPa\sqrt{m}$, *OLR = 2.5,* (b) $\Delta K = 8.8\, MPa\sqrt{m}$, *OLR = 2.5 and ULR =* -1, (c) $\Delta K = 13.2\, MPa\sqrt{m}$, *OLR = 2,* (d) $\Delta K = 13.2\, MPa\sqrt{m}$, *OLR = 2.5,* (e) $\Delta K = 17.6\, MPa\sqrt{m}$, *OLR = 2.5 and ULR =* -1.

the same for a given ΔK. At $\Delta K = 4.4$ MPa$\sqrt{\text{m}}$, the near threshold steady-state conditions yielded herringbone markings and smooth facets, while at $\Delta K = 8.8$ MPa$\sqrt{\text{m}}$ irregular facets were evident. At $\Delta K = 13.2$ MPa$\sqrt{\text{m}}$ the steady-state surfaces displayed larger facets separated by ridges parallel to the FCG direction and secondary cracking with striations becoming more significant. At $\Delta K = 17.6$ MPa$\sqrt{\text{m}}$ significant striations were evident with spacings of 0.1 to 0.2 μm which is consistent

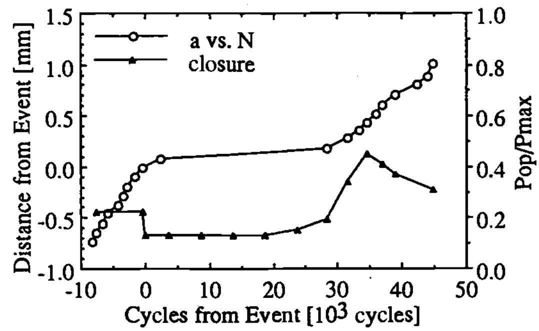

(d) ΔK = 13.2 MPa√m, OLR = 2.5.

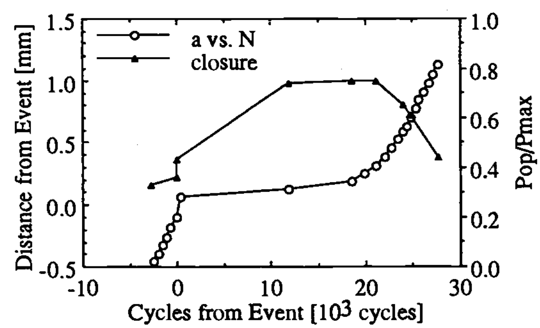

(e) ΔK = 17.6 MPa√m, OLR = 2.5 and ULR = -1.

FIG. 11—*Continued*

with constant amplitude FCG of 1.5×10^{-7} m/cycle or 0.15 μm/cycle. Secondary cracking was also evident. At lower ΔK levels, the overloads/underloads often did not cause noticeable macro nor micro stretch zones but did cause significant crack growth delay, N_d. At the higher ΔK levels, overload/underloads caused stretch zones from approximately zero at the surface up to a maximum of 300 μm at the mid-surface. Thus crack tip tunneling from these overload/underloads existed. This is evident in Fig. 14 for $\Delta K = 13.2$ MPa$\sqrt{\text{m}}$ and OLR = 2. No significant interior overload/underload crack deflection was observed which is contrary to that observed on the surface (Figs. 12 and 13). Ductile dimples were evident in all noticeable stretch zones.

Transient FCG morphology immediately after an overload/underload was significantly different from that of the steady state except for $\Delta K = 4.4$ MPa$\sqrt{\text{m}}$ and some of the $\Delta K = 8.8$ MPa$\sqrt{\text{m}}$ tests, where little change was evident. The difference is brought out in Figs. 15, 16, and 17 for $\Delta K = 13.2$ MPa$\sqrt{\text{m}}$, OLR = 2, and OLR = 2.5, respectively. In Fig. 15, the steady morphology shows facets, ridges, and secondary cracking. Figure 16 shows the entire width of the 25 μm stretch zone along with some fracture surface from steady-state pre-overload cycling and post-overload cycling. The post-overload transient FCG surface was flat and somewhat featureless with no striations for a distance of about 20 to 30 μm, after which the surface regains the steady-state morphology. Figure 17 with OLR = 2.5 shows the end of the stretch zone and the transient post-overload FCG. The end of the stretch zone is located at the left edge of the fractograph. The post-overload surface shows near

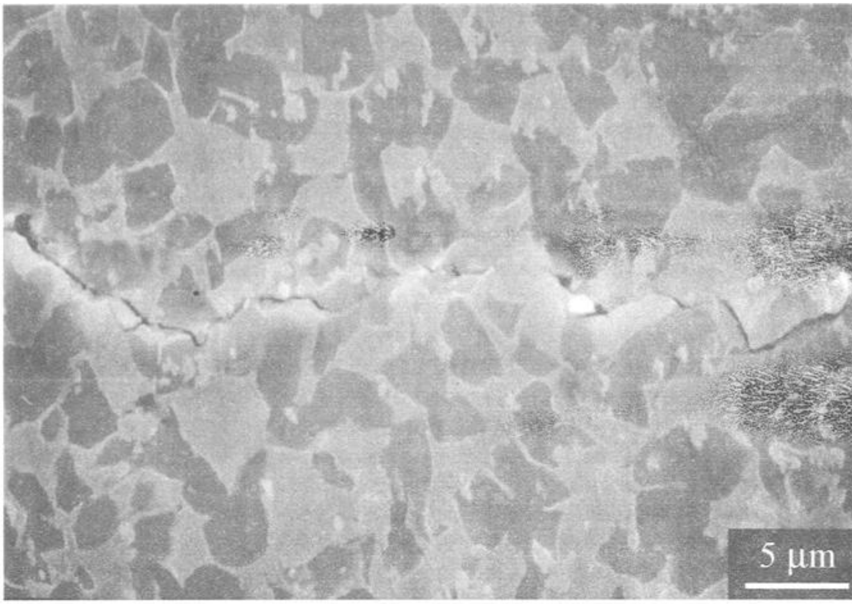

(a) prior to overload, ΔK = 17.6 MPa√m

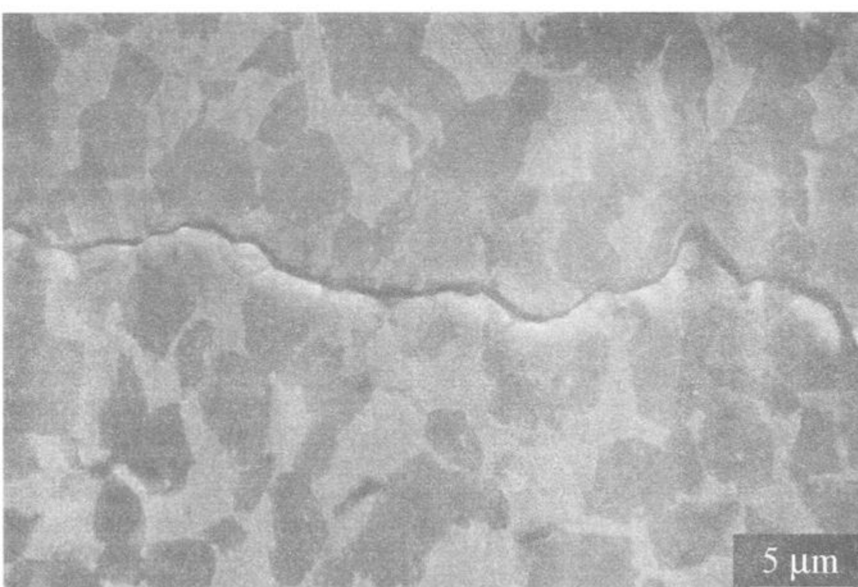

(b) after overload, ΔK = 8.8 MPa√m

FIG. 12—*Constant amplitude* ΔK *steady state crack profile;* (a) *prior to overload,* $\Delta K = 17.6\ MPa\sqrt{m}$, (b) *after overload,* $\Delta K = 8.8\ MPa\sqrt{m}$.

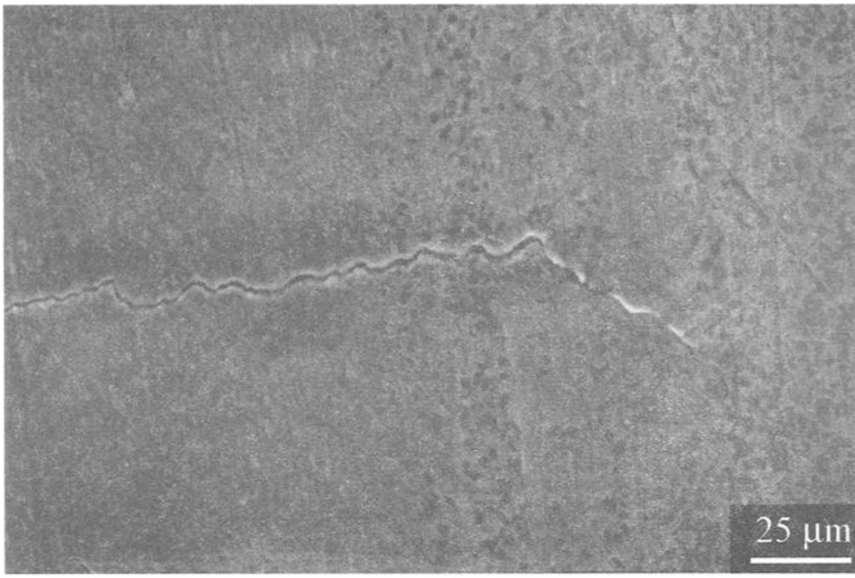

(a) ΔK = 17.6 MPa√m, OLR = 2.5,

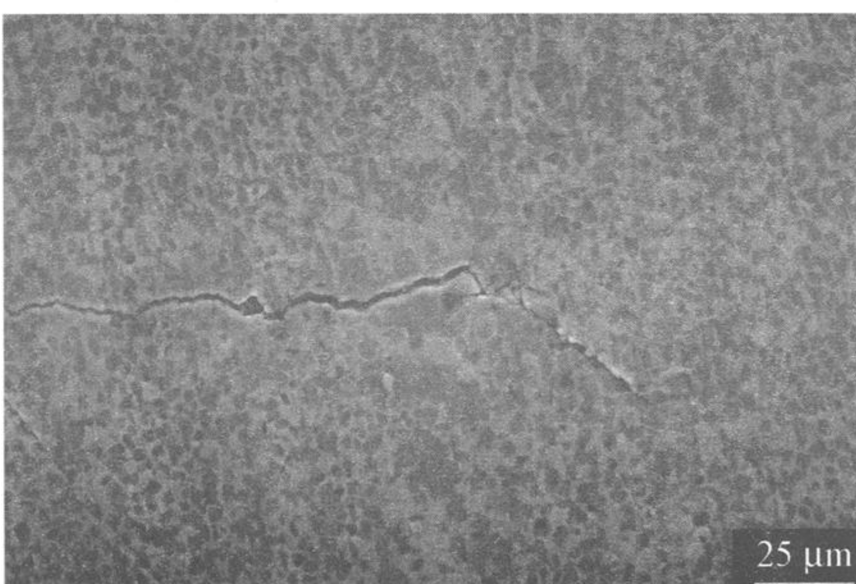

(b) ΔK = 17.6 MPa√m, OLR = 2.5 and ULR = -1

FIG. 13—*Crack profile immediately after overload/underload.* (a) $\Delta K = 17.6\ MPa\sqrt{m}$, *OLR* = *2.5,* (b) $\Delta K = 17.6\ MPa\sqrt{m}$, *OLR* = *2.5 and ULR* = *−1.*

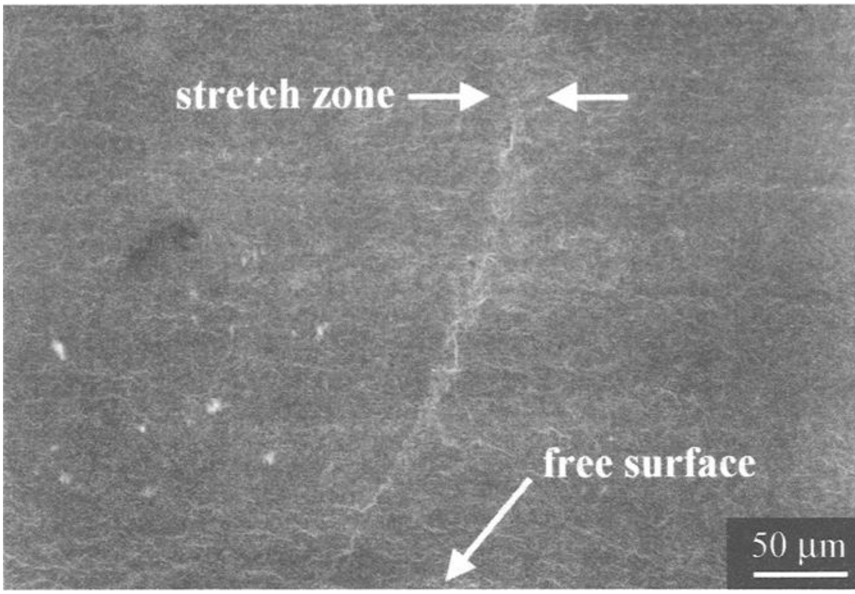

FIG. 14—*Overload stretch zone at/near free surface,* $\Delta K = 13.2\ MPa\sqrt{m}$, *OLR = 2.*

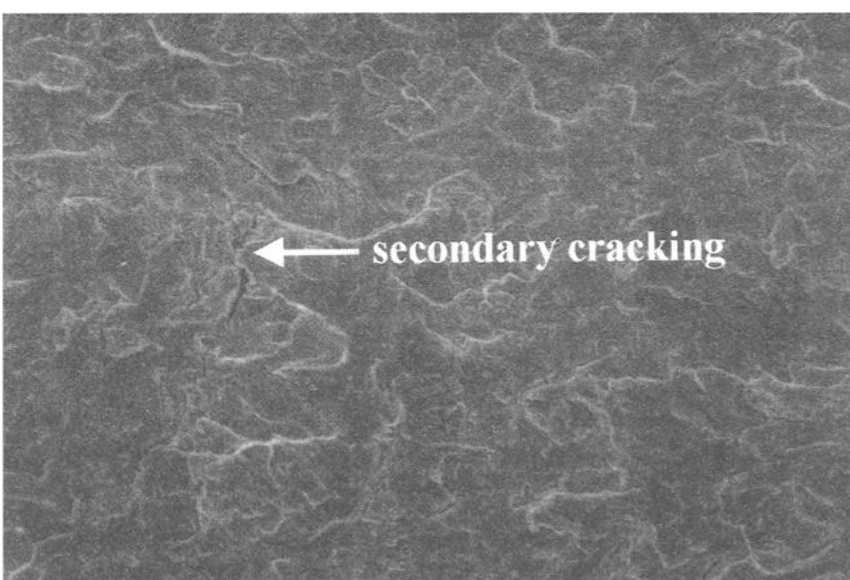

FIG. 15—*Steady-state fatigue crack growth fracture surface,* $\Delta K = 13.2\ MPa\sqrt{m}$.

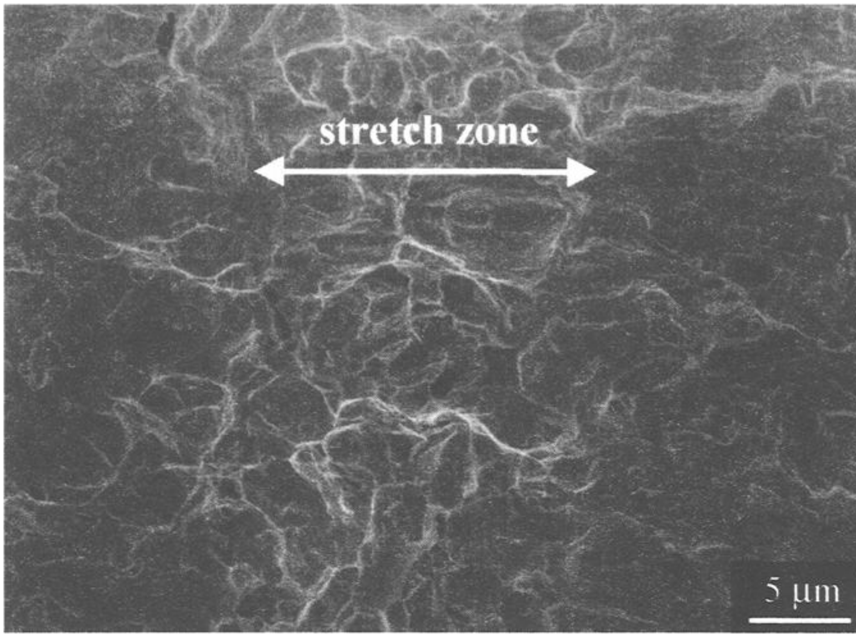

FIG. 16—*Stretch zone and post overload fracture surface,* $\Delta K = 13.2\ MPa\sqrt{m}$, *OLR* = 2.

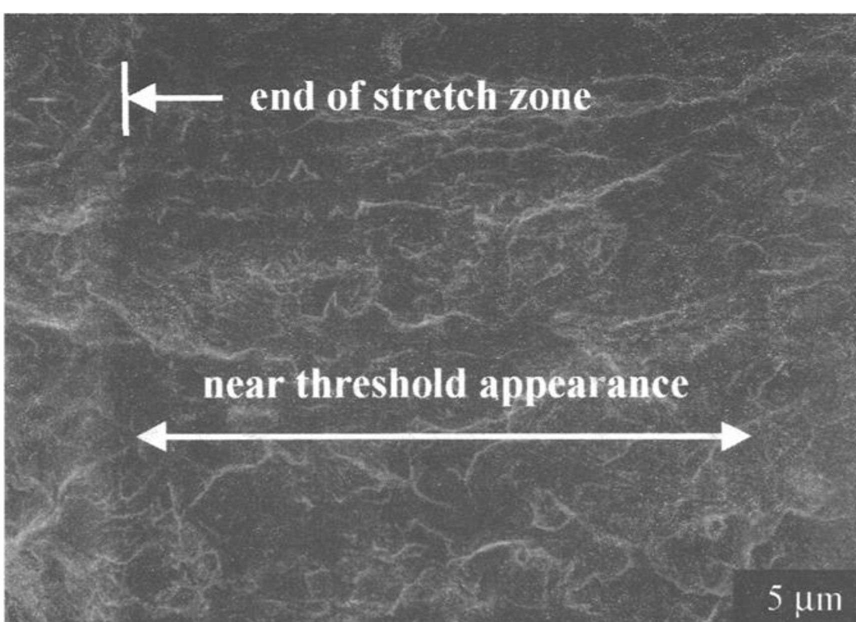

FIG. 17—*Stretch zone and post overload fracture surface,* $\Delta K = 13.2\ MPa\sqrt{m}$, *OLR* = 2.5.

threshold FCG morphology in some areas and is rather flat and featureless in other areas within a distance of 5 to 10 μm from the end of the stretch zone, similar to the fracture surface appearance at ΔK = 4.4 MPa$\sqrt{\text{m}}$ steady-state condition. After about 60 μm of post-overload FCG, the fracture surface regained the pre-overload steady state FCG shown in Fig. 15. Near threshold FCG morphology was also observed following the overload/underload loading cycle of several other overload/underload test conditions evaluated.

Plastic Zone Comparisons

Cyclic overload plastic zones, $2r'_y$, were calculated for each of the test conditions using Eqs 3 or 4 for plane strain or plane stress conditions, respectively. All ΔK = 4.4 and 8.8 MPa$\sqrt{\text{m}}$ with overloads were plane strain while all ΔK 17.6 MPa$\sqrt{\text{m}}$ with overloads were plane stress. ΔK = 13.2 MPa$\sqrt{\text{m}}$ had plane strain conditions for OLR = 2 and plane stress conditions for OLR = 2.5. The magnitude of the appropriate $2r'_y$ ranged from 0.002 to 0.13 mm. When finite delay occurred, the ratio of a_d to $2r'_y$ ranged from 6 to 56 for plane strain conditions and from 2 to 4 for plane stress conditions. Thus in cases with finite FCG delay, a_d occurred over a distance greater than the assumed overload cyclic plastic zone.

Comparison of ΔK_{eff} with Test Results

Effective stress intensity factors in the FCG delay region were calculated using the five overload/underload results of Fig. 11 and Eq 1. These ΔK_{eff} results were reasonably consistent with both FCG delay and with scanning electron fracture surface morphology. No closure load changes were detected with ΔK = 4.4 MPa$\sqrt{\text{m}}$ and OLR = 2 despite the fact that 110 000 cycles of delay occurred. No overload stretch zone nor FCG morphology change occurred with this test and the appropriate overload reversed plastic zone size was only 6 μm. With this very low near threshold ΔK value, *da/dN* values are very sensitive to any loading perturbation with or without measured or existing crack closure. Thus, of the 11 crack closure monitored tests, 10 reasonably represented the FCG delay results. This indicates that the strain gage placement about 1 mm ahead of the crack produced a reasonable representation of near crack tip closure, despite the fact that very little crack tip area was closed and very little transient fatigue crack extension, a_d, occurred. However, the anomalous $P_{\text{op}}/P_{\text{max}}$ values prior to the overloads plus one anomalous behavior after the overload raises concern about the confidence of the measurement technique.

Conclusions

Based upon nominal stress intensity factor range for R = 0.1, fatigue crack growth resistance was better at threshold for −54°C and 175°C than at 25°C. Correcting for crack closure, fatigue crack growth rates were lower at −54°C in comparison to 25°C but were higher at 175°C. Differences in crack closure levels for the three temperatures was attributed to oxide-induced closure at 175°C and roughness-induced closure at −54°C as indicated by fractographic observations.

Fatigue crack growth delay cycles, N_d, for all overload/underload tests at the three temperatures varied from zero to arrest. Fatigue crack growth delay distance, a_d, varied from 0 to 0.8 mm and was always greater than the appropriate cyclic plastic zone size where crack arrest did not occur, ranging from a factor of 2 to 56. The majority of the delay cycles, regardless of temperature or overload/underload, occurred within 40 μm of fatigue crack growth following the overload/underload load cycle.

Considering expected crack opening measurement variability, the crack tip strain gage crack opening measurement system produced reasonable results on 10 of the 11 crack closure monitored overload/underload tests. However, some anomalies before and after the overload provided only minimal confidence with this method.

References

[1] Newman, J. C., "A Crack-Closure Model for Predicting Fatigue Crack Growth Under Aircraft Spectrum Loading," *Methods and Models for Predicting Fatigue Crack Growth under Random Loading, ASTM STP 748,* J. B. Chang and C. M. Hudson, Eds., American Society for Testing and Materials, 1981, pp. 53–84.

[2] Elber, W., "The Significance of Fatigue Crack Closure," *Damage Tolerance in Aircraft Structures, ASTM STP 486,* American Society for Testing and Materials, Philadelphia, 1971, pp. 230–242.

[3] Suresh, S. and Vasudevan, A. K., "Application of Fatigue Threshold Concepts to Variable Amplitude Crack Propagation," *Fatigue Crack Growth Threshold Concepts,* D. L. Davidson and S. Suresh, Eds., AIME, Warrendale, PA, pp. 361–378.

[4] Liaw, P. K., "Mechanism of Near-Threshold Fatigue Crack Growth in a Low Alloy Steel, *Acta Metallurgica,* Vol. 33, 1985, pp. 1489–1502.

[5] Walker, N. and Beevers, J., "A Fatigue Crack Closure Mechanism in Titanium," *Fatigue and Fracture of Engineering Materials and Structures,* Vol. 1, 1979, pp. 135–148.

[6] Stephens, R. I., Chen, D. K., and Hom, B. W., "Fatigue Crack Growth with Negative Stress Ratio Following Single Overloads in 2024-T3 and 7075-T6 Aluminum Alloys," *Fatigue Crack Growth Under Spectrum Loads, ASTM STP 595,* American Society for Testing and Materials, Philadelphia, 1976, pp. 27–40.

[7] Vecchio, R. S., Hertzberg, R. W., and Jaccard, R., "Overload Induced Crack Growth Rate Attenuation Behavior in Aluminum Alloys," *Scripta Metallurgica,* Vol. 17, 1983, pp. 343–346.

[8] Ward-Close, C. M. and Ritchie, R. O., "On the Role of Crack Closure Mechanisms in Influencing Fatigue Crack Growth Following Tensile Overloads in a Titanium Alloy: Near Threshold Versus Higher ΔK Behavior," *Mechanics of Fatigue Crack Closure, ASTM STP 982,* J. C. Newman, Jr. and W. Elber, Eds., American Society for Testing and Materials, Philadelphia, 1988, pp. 93–111.

[9] Suresh, S., "Micromechanisms of Fatigue Crack Growth Retardation Following Overloads," *Engineering Fracture Mechanics,* Vol. 18–3, 1983, pp. 577–593.

[10] Wei, R. P. and Shih, T. T., "Delay in Fatigue Crack Growth," *International Journal of Fracture,* Vol. 10, 1974, pp. 77–85.

[11] Piascik, R. S., Newman, J. C., and Underwood, J. H., "The Extended Compact Tension Specimen," *Fatigue and Fracture of Engineering Materials and Structures,* Vol. 20–4, 1997, pp. 449–563.

[12] Taylor, D., *Fatigue Thresholds,* Buttersworths and Co., London, UK, 1989.

[13] Petit, J., Berata, W., and Bouchet, B., "Fatigue Crack Growth Behavior of Ti-6Al-4V at Elevated Temperature," *Titanium Science and Technology,* F. H. Froes, Ed., TMS, 1993, pp. 1819–1826.

[14] Salivar, G. C., Heine, J. E., and Haake, F. K., "The Effect of Stress Ratio on the Near-Threshold Fatigue Crack Growth Behavior of Ti-8Al-1Mo-1V at Elevated Temperature," *Engineering Fracture Mechanics,* Vol. 32–5, 1989, pp. 807–817.

[15] Albertson, T. P., Stephens, R. R., and Bayha, T. D., "Fatigue Crack Growth of Two Advanced Titanium Alloys at Room and Elevated Temperature," *Elevated Temperature Effects on Fatigue and Fracture, ASTM STP 1297,* R. S. Piascik, A. Saxena, and R. P. Gangloff, Eds., American Society for Testing and Materials, West Conshohocken, PA, 1997, pp. 140–161.

[16] Hurless, B. E., "Threshold Fatigue Crack Growth Testing of Titanium Alloys," M.S. Thesis, Mechanical Engineering, University of Idaho, 1997.

[17] Dowling N. E., *Mechanical Behavior of Materials,* Prentice Hall, Englewood, Cliffs, NJ, 1993.

[18] Phillips, E. P., "Results of the Round Robin on Opening Load Measurements Conducted by ASTM Task Group E24.04.04 on Crack Closure Measurement and Analysis," NASA Technical Memorandum 1016001, 1989.

[19] Phillips, E. P., "Results of the Second Round Robin on Opening-Load Measurement Conducted by ASTM Task Group E24.04.04 on Crack Growth Measurement and Analysis," NASA Technical Memorandum 109032, 1993.

[20] McEvily, A. J. and Yang, Z. "Fatigue Crack Retardation Mechanisms After Single and Multiple Overloads," *Proceedings,* 4th International Conference on Fatigue and Fatigue Thresholds, H. Kitagawa and T. Tanaka, Eds., 1990, pp. 23–26.

Fraser J. McMaster[1] *and David J. Smith*[2]

Effect of Load Excursions and Specimen Thickness on Crack Closure Measurements

REFERENCE: McMaster, F. J. and Smith, D. J., "**Effect of Load Excursions and Specimen Thickness on Crack Closure Measurements,**" *Advances in Fatigue Crack Closure Measurements and Analysis: Second Volume, ASTM STP 1343,* R. C. McClung and J. C. Newman, Jr., Eds., American Society for Testing and Materials, West Conshohocken, PA, 1999, pp. 246–264.

ABSTRACT: The effects of simple load excursions on fatigue crack growth and crack closure measurements in aluminum alloy 2024-T351 are presented. The crack closure loads were measured local to the crack tip in 6-mm and 14-mm-thick specimens, using an Elbert-type gage for measuring crack-tip opening displacement (CTOD). All specimens were manufactured from a single lot of 15.7-mm-thick plate. Preliminary tests to establish the level of crack closure for a given level of remote constant-amplitude loading were also undertaken, with consistently different levels of crack opening and closing loads observed. Crack opening and closing stresses obtained from the Elber-type (CTOD) gage, when compared with those from a (global) clip gage, showed identical results for opening stresses, but crack closing stresses were approximately 15% to 20% higher in the CTOD measurements. The results apparently contradict many analytical closure models, which have crack closing stresses lower than crack opening stresses.

Simple overload, underload and over/underload cycles were performed. Differences in the number of post-overload retardation cycles for the two thicknesses, in the single overload test, were obtained. It was found that the 6-mm-thick specimen's fatigue life was two times larger than for the 14-mm-thick specimen. The measured opening stresses were found to be in general agreement with the trends obtained for the fatigue crack growth results. Greater fatigue lives were obtained in the overload tests, with subsequent higher crack opening stresses measured. After a certain number of cycles following an overload, constant-amplitude crack growth rates were restored. However, the crack opening stresses did not return to the preoverload constant-amplitude values, but increased relative to the preoverload constant-amplitude crack opening stresses.

KEYWORDS: crack closure, fatigue, crack growth, aluminum alloy, overloads, thickness

The use of damage-tolerance concepts to predict fatigue crack growth lives in aircraft structures is well established. In conventional metallic materials, crack growth anomalies such as small-crack effect and the various crack-tip shielding mechanisms have improved our understanding of the crack growth process but have complicated life-prediction methods. However, the improved fracture mechanics analyses of some of the crack-tip shielding mechanisms, such as plasticity- and roughness-induced crack closure, and analyses of surface or corner crack configurations have led to more accurate crack growth and fatigue life-prediction methods.

The discovery of the plasticity-induced crack closure phenomenon by Elber [*1*] in the late 1960s was an important event in the study of fatigue crack growth. Elber suggested that crack surfaces can close before the minimum load is reached because of the residual tensile deformation that is left in the crack wake. He further suggested that the fatigue crack growth rate is a function of an effective stress intensity range (ΔK_{eff}) when the crack tip is open. Thus, fatigue crack growth is dependent on ΔK_{eff} and not on the total stress intensity factor range (ΔK). In addition to providing an engineering

[1] Engineer, Mechanical and Materials Engineering, Southwest Research Institute, San Antonio, TX 78238.
[2] Professor, Department of Mechanical Engineering, University of Bristol, Bristol, BS8 1TR, U.K.

approach to correlating crack growth rates under various conditions, Elber's discovery of plasticity-induced crack closure pointed out that sophisticated mechanics can be associated with growing fatigue cracks. Clearly, the fatigue crack could no longer be treated as merely a special case of the stationary, monotonically loaded crack.

The fatigue crack closure phenomenon is an intrinsic aspect of the mechanics of growing fatigue cracks and, in many applications, closure provides a powerful first-order correction to the crack driving force which facilitates more accurate prediction of crack growth rates. Although closure can be associated with several different physical mechanisms, including roughness or oxides on the fracture surface, extensive experimental and computational studies have shown that crack wake plasticity is often the dominant contribution to closure, particularly at higher values of the stress intensity factor range. Heuler and Schutz [2] concluded that crack growth prediction models based on plasticity-induced crack closure provide, among all life prediction approaches, the most accurate and reliable results.

A number of analytical and numerical models for growing fatigue cracks have emerged over the past two decades; these incorporate plasticity-induced crack closure as an integral component of the mechanics [3–6]. These models were based on the Dugdale model [7], or strip yield model, but were modified to leave plastically deformed material in the wake of the advancing crack tip. Early studies using the modified Dugdale model concentrated on the plane stress condition. As most cracks in real structures are usually in stress states between plane stress and plane strain, efforts were made to extend the Dugdale model to plane strain or near plane strain conditions. Newman [6] introduced a plastic constraint factor (α) to the tensile yield stress ahead of the crack tip to account for the three-dimensional effects at the crack tip. Verification work by Newman [8] showed that, compared with finite element analyses, the value of constraint factor $\alpha = 1$ is a lower bound for plane stress conditions, and $\alpha = 3$ an approximate upper bound for plane strain conditions.

In this paper the role of crack closure is explored for simple overload and underload conditions. Results from a series of fatigue crack growth tests conducted on the aluminum alloy 2024-T351 for two plate thicknesses have been obtained. The effects of simple load excursions on experimental crack closure measurements are presented.

Materials and Experimental Procedure

Material and Specimens

Aluminum alloy 2024 was supplied by British Aerospace (Airbus) in the T351 condition as a 15.7-mm-thick rolled plate with the rolling direction clearly identified. The typical tensile properties for 2024-T351 are shown in Table 1 [9]. The temper designation T351 denotes that the material was solution treated at 495°C, water quenched at room temperature and stretched to give between 1.5% and 3% permanent deformation. The material was then naturally aged for a period of at least 48 h to produce precipitation hardening, resulting in an increase in strength.

Fatigue crack growth tests used $M(T)$, center crack specimens of height = 250 mm, width (W) = 100 mm and thickness (B) = 6 mm and 14 mm (Fig. 1). Specimens were machined from the mid-

TABLE 1—*Nominal Mechanical Properties of Aluminum Alloy 2024-T351 [9].*

Orientation	Initial Yield Stress, MPa	0.05% Yield Stress, MPa	0.1% Yield Stress, MPa	UTS, MPa
Longitudinal direction	340	360	365	466
E (MPa)	71 600			

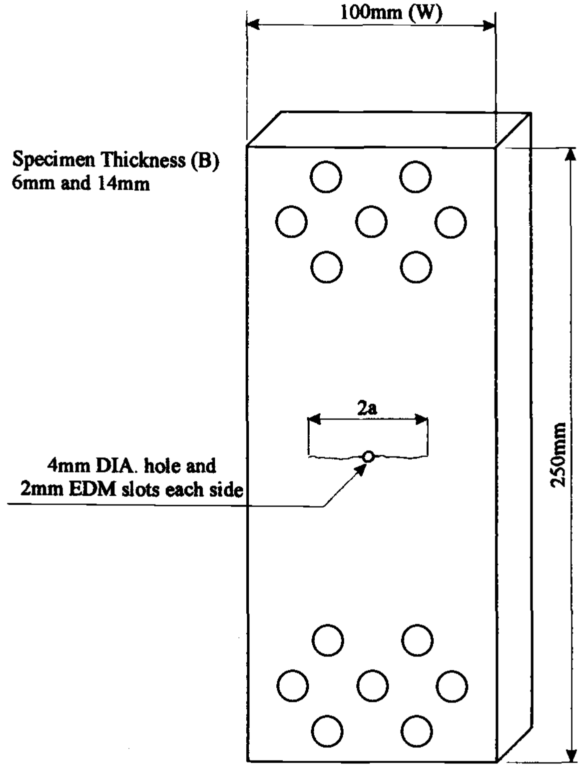

FIG. 1—*Test specimen nominal dimensions.*

thickness of the rolled plate. Test specimens were subjected to constant amplitude (CA), simple overload (OL), simple underload (UL), and simple over/underload (OUL) loading. The OL, UL and OUL tests consisted of three load excursions, whether tensile, compressive, or a combination of the two, applied at crack length intervals of $2a/W = 0.4, 0.5, 0.6$, where $2a$ is the total crack length and W the specimen width. Crack closure measurements were taken throughout testing, employing a local "Elber" type displacement gage.

Preparation of the specimen was important since specimens were friction gripped in the test rig. Specimen ends were shotblasted so as to produce a rough surface for adequate gripping using the friction grips. Crack starter notches were made by drilling a 4 mm hole in the center of the specimen, followed by electrodischarge machining (EDM) of a starter notch of length 2 mm and height 0.2 mm.

Test Equipment and Procedures

Fatigue crack growth tests were carried out using a 250 kN capacity servo-hydraulic DARTEC test frame, which was coupled with a DARTEC 9500 controller. The specimens were loaded through friction end grips and sinusoidally loaded at a frequency of 10 Hz. Tensile and compressive overloads were applied at a frequency of 0.05 Hz. Low-powered optical microscopes, mounted on x and y vernier scales, were used for crack length measurements. Specimen surfaces were cleaned and polished to 1 μm prior to testing to aid visual crack length measurements.

For all tests an Elber-type gage, with a special location jig, was used as a means of determining local crack closure stresses (Fig. 2). For all fatigue crack growth tests performed using the aluminum

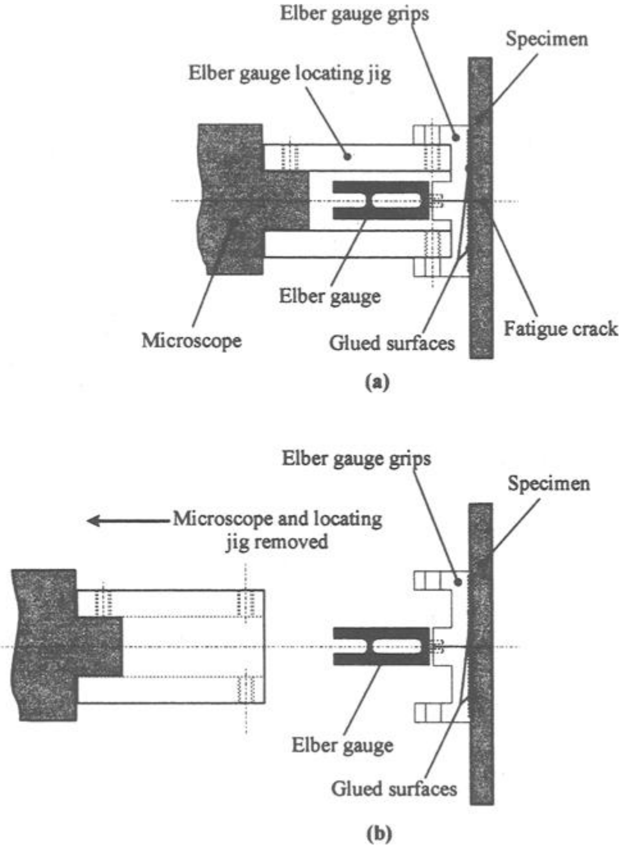

FIG. 2—*Diagram of Elber-type gage and location jig used for local crack closure measurements:* (a) *locating jig in position and* (b) *removed for closure measurement.*

alloy 2024-T351, crack closure measurements were taken intermittently throughout the fatigue tests. An attachment jig used in securing the Elber gage to the specimen was designed and manufactured with the purpose of providing a stable and fixed attachment base for the gage (Fig. 2). Locating grips are glued to the specimen, using an epoxy resin glue, in the correct position by means of a specially made jig which is removed upon setting of the glue, thus leaving a stable platform for crack closure measurements. *Note:* Measurements were taken from only one crack tip. For a limited number of tests a clip gage was used for measuring the crack closure stresses across the specimen centerline, and compared with the Elber gage results.

The Elber gage was positioned a distance of 1 mm behind the crack tip for crack closure measurements. This choice of gage position was supported by the work of Yisheng and Schijve [*10*], who showed that when using the reduced displacement method for finding crack closure loads, a position as close to the crack tip provides a closure load which is consistent with other methods which are not position dependent, such as the tangent point method.

Using a data acquisition program on a PC, 700 load/displacement pairs were logged over approximately two fatigue cycles. A reduced displacement technique was used to determine the crack opening stress (σ_{op}) and crack closing stress (σ_{cl}).

The Elber gage signal was conditioned through a Flyde single-channel strain gage amplifier and a purpose-built low-pass passive filter. A PC with a CIL analog/digital converter was used for data acquisition of load, and Elber gage signals. The data logger was also used to monitor maximum and minimum loads. Precracking was carried out at the same ΔP load range as that used in the fatigue crack growth test. The fatigue crack growth test was started at a crack length of $2a/W > 0.20$. All tests were conducted in laboratory air at temperatures between 15 and 25°C and relative humidity between 40% and 65%.

Results

Fatigue Crack Growth Tests

Constant-amplitude, overload, underload and over/underload fatigue crack growth tests were carried out at an R-ratio of 0.1, with R-ratio being the ratio of minimum to maximum load (P_{min}/P_{max}), and with all tests performed at a normalized stress level of $\sigma_{global}/\sigma_{yd} = 0.20$, where σ_{global} is the global applied stress, P_{max}/BW, and σ_{yd} is the yield stress at 0.1% strain given in Table 1. The fatigue crack growth rates were determined from optical measurements of the average crack length, and processed using the secant method to determine da/dN. The applied stress intensity factor range (ΔK_I) was determined using the ASTM Standard Test Method for Measurement of Fatigue Crack Growth Rates (E 647-95a) recommended solution, and is given as

$$\Delta K_{\mathrm{I}} = \frac{\Delta P}{B}\sqrt{\frac{\pi\alpha}{2W}\sec\frac{\pi\alpha}{2}} \tag{1}$$

where

ΔP = load range ($P_{max} - P_{min}$), kN,
B = specimen thickness, mm, and
$\alpha = 2a/W$.

The fatigue crack growth for constant-amplitude tests in 6-mm thick and 14-mm-thick specimens is shown in Fig. 3. The fatigue life (in cycles) of the thinner specimen was approximately 33% greater than the 14 mm specimen (Fig. 3*a*). There was, however, only a difference in fatigue crack growth rates for the two thicknesses (between 1.5 and 2.5 times for ΔK less than 22 MPa$\sqrt{m}$) (Fig. 3*b*).

The fatigue crack growth results for single overload tests in 6-mm and 14-mm-thick specimens are shown in Fig. 4. Both tests were performed with an overload level equal to $1.75P_{max}$. Figure 4*a* shows that fatigue crack growth retardation following a tensile overload was greater for the thinner specimen. This difference in fatigue crack growth is reinforced in Fig. 4*b*, which shows the crack growth rates for both thicknesses. Immediately after an overload there was an initial rapid increase in growth rate (indicated as (i) in Fig. 4*b*), followed by a decrease in growth rate (indicated as (ii) in Fig. 4*b*). For the 6-mm-thick specimen it was apparent that fatigue crack growth rates in the post-overload regime were generally lower than for the 14-mm-thick specimen.

The fatigue crack growth results for single underload tests in 6-mm-thick and 14-mm-thick specimens are shown in Fig. 5. The underload level for both tests was equal to $-1.75P_{max}$. The thicker test specimen had the least number of cycles to fracture (Fig. 5*a*), but the fatigue crack growth rates (Fig. 5*b*) showed that the 6 mm specimen had the higher post-underload acceleration compared with the 14 mm specimen (indicated as (i) in Fig. 5*b*). It should be noted that this acceleration was smaller than for the overload specimen. The fatigue crack growth (in cycles) of the thinner specimen was approximately 40% greater than the 14 mm specimen.

Fatigue crack growth results for single over/underload tests in 6-mm-thick and 14-mm-thick specimens are shown in Fig. 6, where the overload level was equal to $1.75P_{max}$ and the underload level

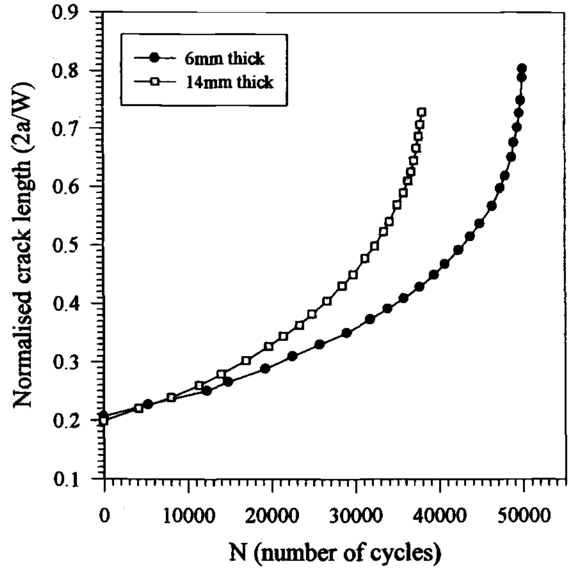

(a)

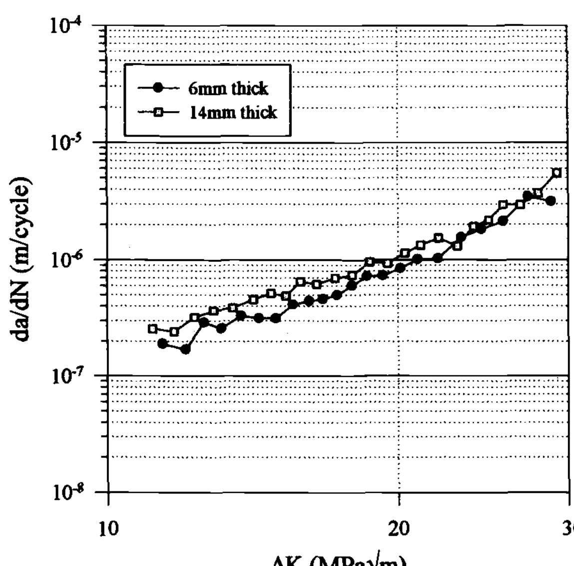

(b)

FIG. 3—*Comparison of 6-mm-thick and 14-mm-thick constant-amplitude tests:* (a) *average fatigue crack growth and* (b) *average fatigue crack growth rates.*

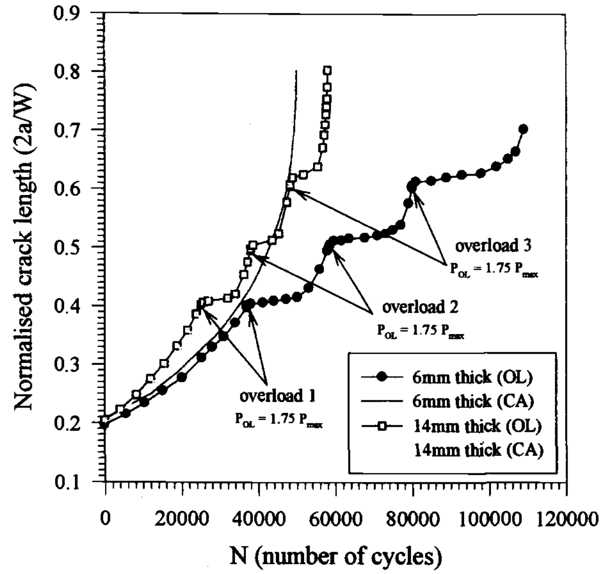

(a)

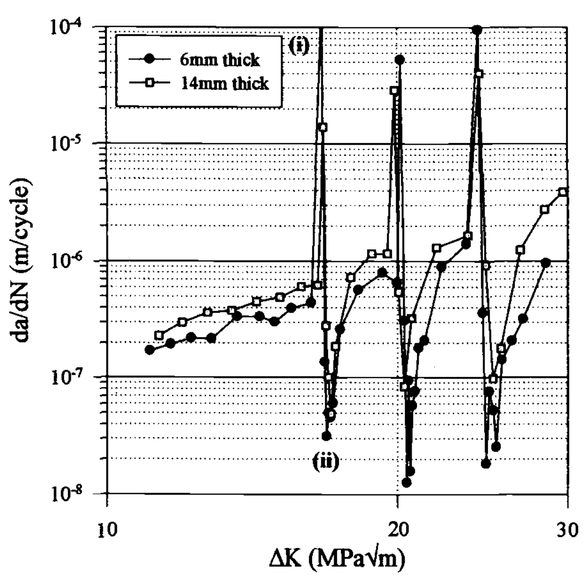

(b)

FIG. 4—*Comparison of 6-mm-thick and 14-mm-thick simple overload tests:* (a) *average fatigue crack growth and* (b) *average fatigue crack growth rates.*

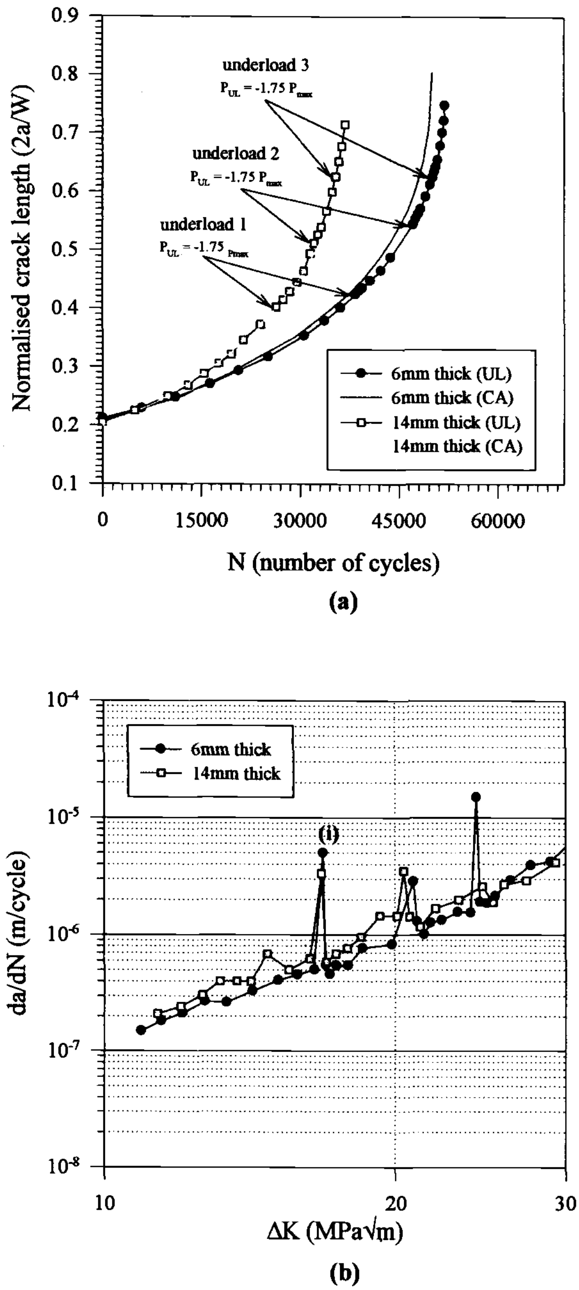

FIG. 5—*Comparison of 6-mm-thick and 14-mm-thick simple underload tests:* (a) *average fatigue crack growth and* (b) *average fatigue crack growth rates.*

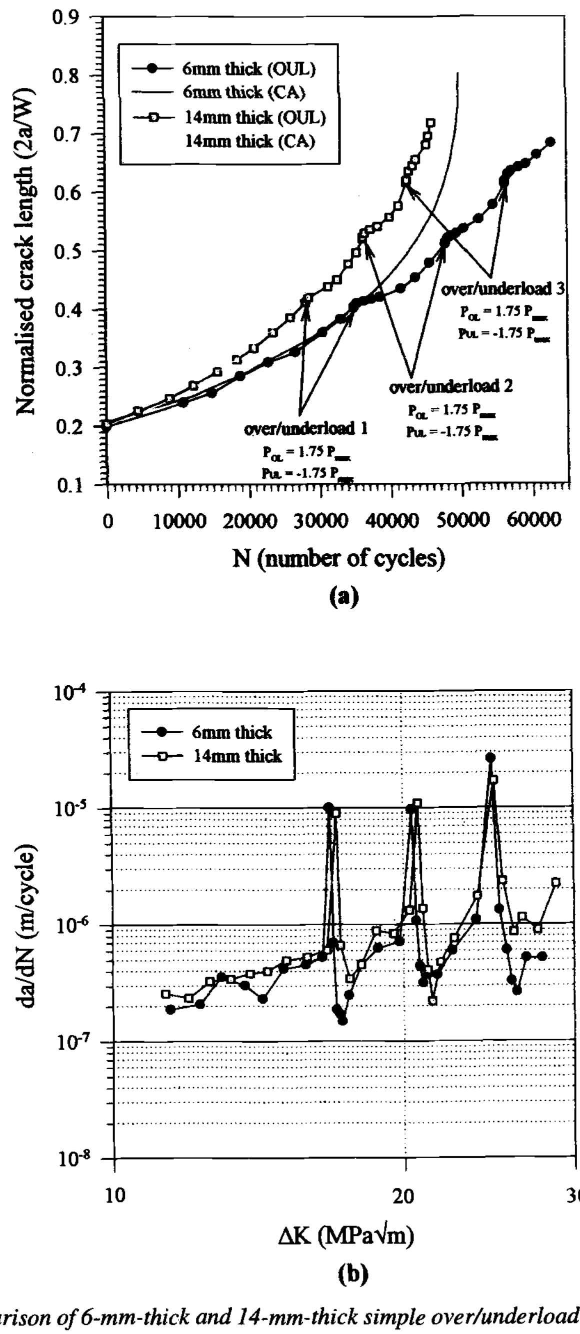

FIG. 6—*Comparison of 6-mm-thick and 14-mm-thick simple over/underload tests:* (a) *average fatigue crack growth and* (b) *average fatigue crack growth rates.*

equal to $-1.75P_{max}$. In Fig. 6*a*, the thicker test specimen again shows the least number of cycles to fracture. The fatigue crack growth rates in Fig. 6*b* show that both specimens had similar post-over/underload acceleration and retardation in fatigue crack growth rates, although the 6-mm-thick specimen on two of the three load excursions had a lower fatigue crack growth rate, therefore implying a larger amount of retardation cycles compared with the 14 mm specimen.

Figure 7 highlights the difference in fatigue crack growth for a given thickness, and for each of the different loading conditions. The results for the 6-mm-thick and 14-mm-thick specimens are shown in Figs. 7*a* and 7*b*, respectively. Prior to any overload or underload excursion, the constant-amplitude fatigue crack growth in each specimen was essentially identical. This illustrates a convincing difference in the fatigue crack growth for the two thicknesses as shown in Fig. 3. The overload, underload and over/underload excursions modify the fatigue crack growth compared with the constant-amplitude test, with the order of greatest fatigue life shown as OL > OUL > UL.

Experimental Crack Closure Measurements

To obtain a knowledge of the experimental variation in fatigue crack closure measurements, an error analysis of a constant-amplitude fatigue crack growth test using a 6-mm-thick specimen and with $\sigma_{global}/\sigma_{yd} = 0.20$ was undertaken. Fatigue crack closure measurements were obtained using both the "Elber" type displacement gage and a centerline clip gage. For both gages, crack closure measurements were taken at crack length intervals of 1 mm. At crack length intervals of 2 mm, five consecutive crack closure measurements were taken to obtain information about scatter.

The measured global stresses for crack opening σ_{cl} and opening σ_{op}, normalized with respect to the maximum applied global stress σ_{global}, are shown in Fig. 8. The crack closing stress for both gages is shown in Fig. 8*a*. In general the closure stress obtained from the Elber gage was higher than for those of the clip gage. A comparison of the opening stress from the two gages is shown in Fig. 8*b*. It is interesting to note that both opening and closing stresses were approximately the same using the centerline clip gage, but the closure stresses were distinctly different for results from the Elber gage. The experimental opening and closing stresses for the Elber gage, at $2a/W = 0.5$, were $\sigma_{op} = 0.36\sigma_{max}$ and $\sigma_{cl} = 0.43\sigma_{max}$.

The values for σ_{op} and σ_{cl} shown in Fig. 8 are the mean values obtained from the five consecutive crack closure measurements. The error bars show the 99% confidence interval for the five consecutive crack closure measurements, at 2 mm crack length intervals. It appears that the error of the crack closure measurements was greatest at short crack lengths, and then quickly reduced and stabilized to a constant stress of approximately $0.02(\sigma_{op}/\sigma_{global})$. Shown in Fig. 8 are the average scatterband for closure measurements for crack lengths of $2a/W < 0.4$ and crack lengths of $2a/W > 0.4$.

Comparisons of the normalized crack opening stresses ($\sigma_{op}/\sigma_{global}$) as a function of normalized crack length ($2a/W$) are shown in Figs. 9 to 13 for constant-amplitude, overload, underload and over/underload tests. The crack opening and closing results from the Elber gage, for 6-mm-thick and 14-mm-thick constant-amplitude fatigue crack growth tests, are shown in Fig. 9. The crack opening stresses for both thicknesses have very similar values for $2a/W > 0.4$, as do the crack closing stresses for both thicknesses. This suggests that the difference observed in fatigue growth for the constant-amplitude fatigue tests, as shown in Fig. 3*a*, cannot be solely explained by closure mechanisms.

For subsequent figures, only the opening stresses will be shown, as crack tip damage occurs on the loading, or opening, portion of the fatigue cycle. The crack opening stress for the 6-mm-thick and 14-mm-thick overload fatigue crack growth tests is shown in Fig. 10. The opening stresses for both thicknesses follow the general trend observed in fatigue crack growth rates following the application of a single tensile overload. When a tensile overload is applied, ductile solids generally display a temporarily accelerated growth which occurs mainly during the application of the overload, with subsequent lower crack closure stresses. After the temporarily accelerated crack advance, a prolonged period of decelerated crack growth follows and, therefore, a higher crack closure stress compared with

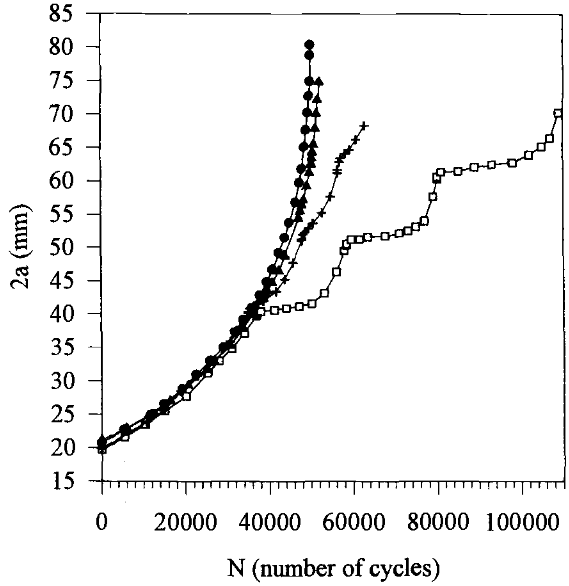

(a)

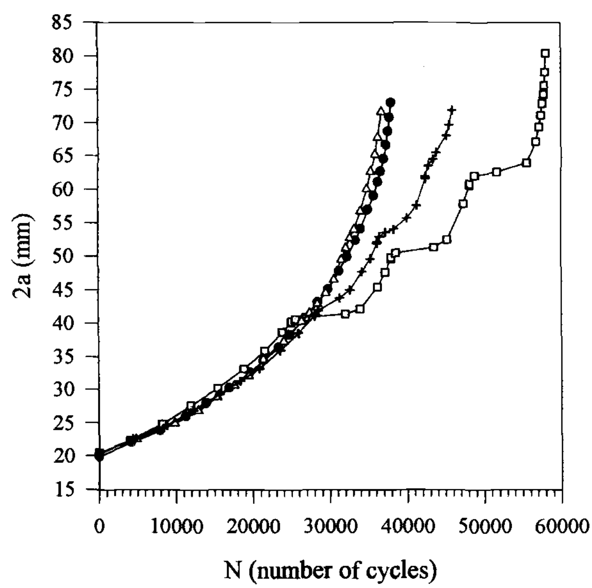

(b)

FIG. 7—*Comparison of fatigue crack growth tests:* (a) *6-mm-thick specimens, and* (b) *14-mm-thick specimens.*

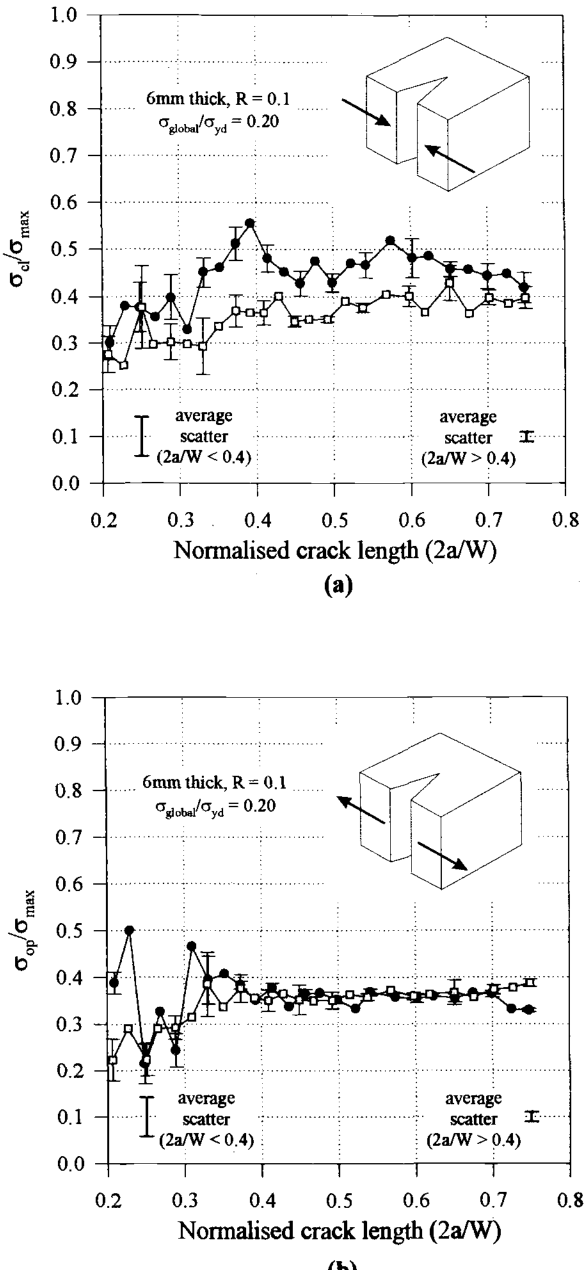

FIG. 8—*Comparison of crack closure stress obtained using the Elber and clip gages for the 6-mm-thick constant-amplitude test,* (a) *crack closing stress and* (b) *crack opening stress.*

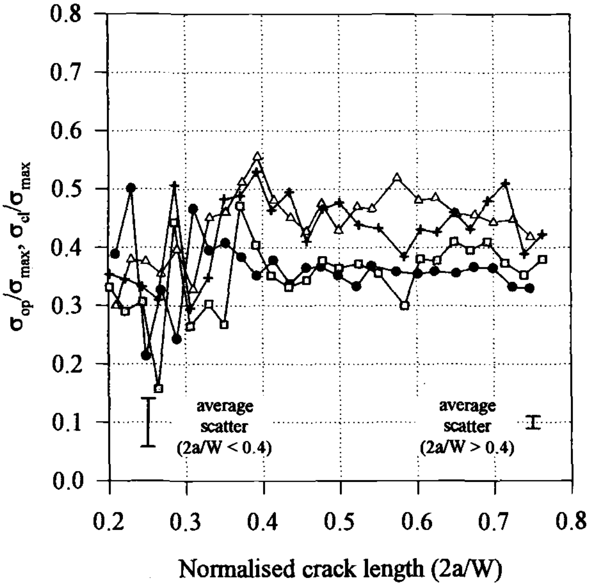

FIG. 9—*Comparison of crack opening and closing stress obtained using the Elber gage for the 6-mm and 14-mm-thick constant-amplitude test.*

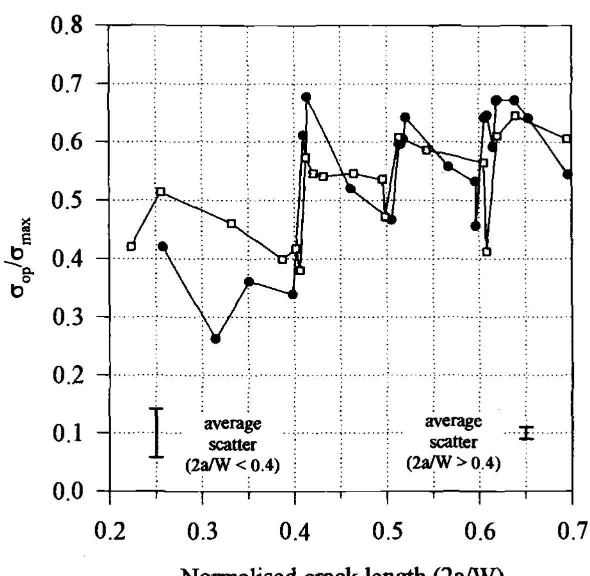

FIG. 10—*Comparison of the crack opening stress obtained using the Elber gage for the 6-mm-thick and 14-mm-thick overload tests.*

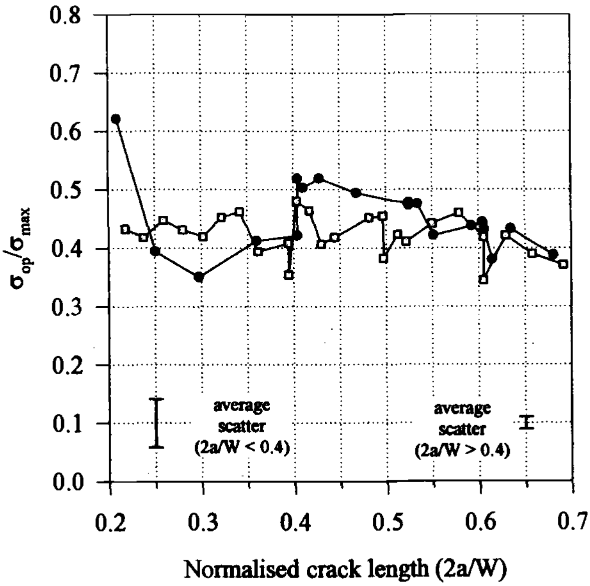

FIG. 11—*Comparison of the crack opening stress obtained using the Elber gage for the 6-mm-thick and 14-mm-thick underload tests.*

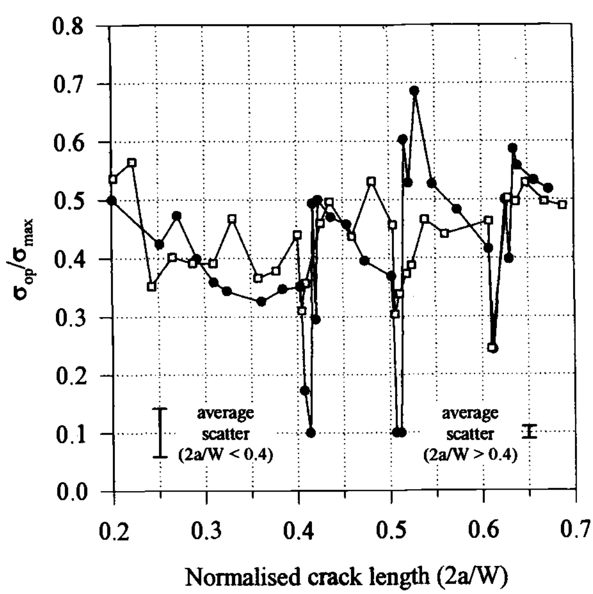

FIG. 12—*Comparison of the crack opening stress obtained using the Elber gage for the 6-mm-thick and 14-mm-thick over/underload tests.*

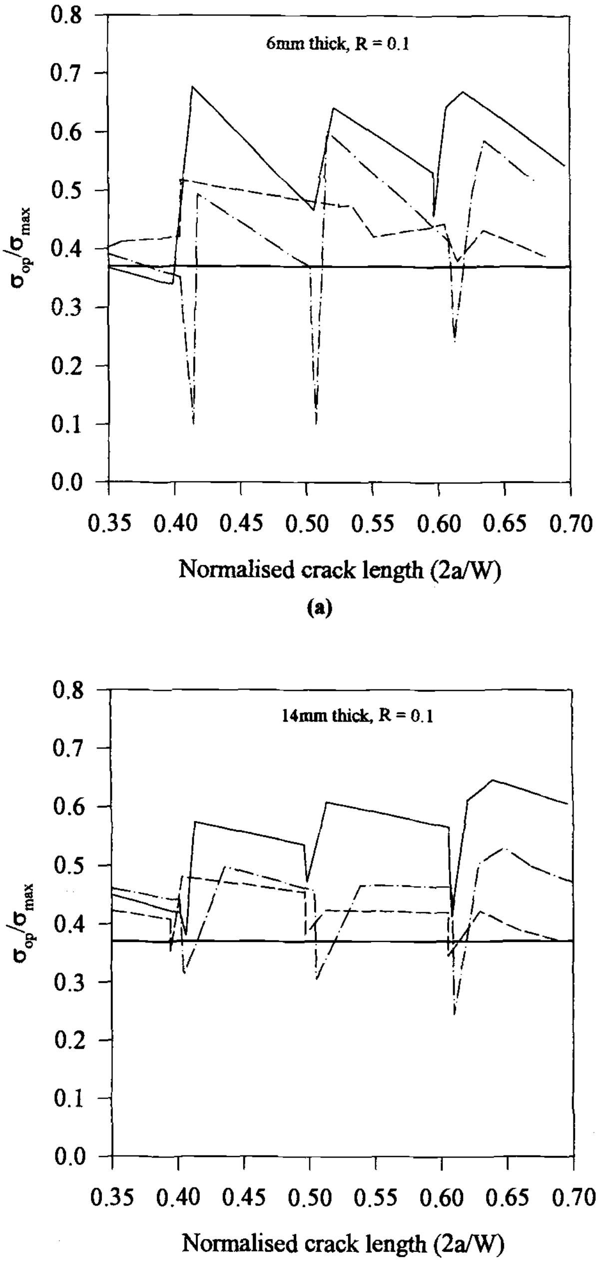

FIG. 13—*Schematic representation of the crack opening stress levels, comparing* (a) *6-mm-thick specimens, and* (b) *14-mm-thick specimens.*

constant-amplitude crack closure stresses was seen. For all three overloads the measured opening stress was higher in the 6-mm-thick specimen than in the 14-mm-thick specimen.

The crack opening stresses for the 6-mm thick and 14-mm-thick underload fatigue crack growth tests are shown in Fig. 11. The opening stresses for both underload fatigue tests are shown to be fairly insensitive to the application of a compressive overload, although there is some evidence of minor changes in the measured opening stress.

The 6-mm-thick and 14-mm-thick over/underload crack opening stresses are shown in Fig. 12. Again the crack opening stresses for the 14-mm-thick specimen subjected to over/underload conditions showed some variation in the opening stresses, compared with constant-amplitude conditions. The crack opening stresses for the 14-mm-thick specimen in the post-over/underload region did not increase to the same extent as compared with the single overload test. In contrast, for the 6-mm-thick specimen in the over/underload test there was a rapid decrease in the opening stress immediately following the over/underload, then a rapid increase in the opening stress which then started to reduce to a level close to the opening stress for constant-amplitude conditions.

Discussion

Fatigue Crack Growth

When comparing the constant-amplitude tests for both thicknesses, a difference in fatigue crack growth can be seen, with the thin specimen having the larger amount of cycles to failure (Fig. 3*a*). Because the thinner specimen promotes plane stress conditions, and the thicker specimen more plane strain conditions, a systematic effect of the thickness on the fatigue crack growth should be expected. Such a trend has been reported in the literature [*11*], but is claimed to be a small effect.

Shear lips may also contribute to the thickness effect; that is, the 6 mm specimen had a greater proportion of its thickness taken up by shear lips for the same ΔK, when compared with the 14-mm-thick specimen, thus increasing the likelihood of roughness-induced crack closure. Also the single overload test results, for both thicknesses, showed that the fatigue crack growth retardation following a tensile overload was greater for the thinner material (Fig. 4*a*).

Most studies of the effects of fatigue overloads have been performed in order to elucidate the mechanism of crack growth retardation resulting from Mode I tensile overloads. It has long been recognized [*12*] that the transient crack growth behavior following the application of an overload is often controlled by several concurrent mechanistic processes. Studies have indicated that the post-overload retardation is associated with residual compressive stresses in the overload plastic zone, and with crack closure, which results in an increase of fracture surface contact in the vicinity of the crack tip as the crack grows into the overload plastic zone. This effect is enhanced by lower crack-tip opening displacements in the overload zone which promote wedging of the mating fracture surfaces. Crack deflection and branching along flow bands, though predominantly a surface effect, may also contribute to the delay [*13*]. The application of an overload can also lead to strain hardening of the material ahead of the crack tip. Several investigators [*14–16*] have explored the possible role of strain hardening in influencing post-overload fatigue failure in aluminum and titanium alloys. Their results appear to show that strain hardening arguments alone cannot account for the various retardation effects observed experimentally. Furthermore, no quantitative treatment of the role of strain hardening is available. Also, the fact that transient retardation occurs in metallic glasses (which do not strain harden) indicates that crack tip strain hardening is not a necessary condition for retardation.

Mills and Hertzberg [*17*] investigated the effect of overloads for sheet thicknesses of 1.6 mm, 3.2 mm and 26.04 mm in 2024-T3 aluminum alloy, and found the amount of delay following an overload to be greatest in the 1.6 mm sheet for overloads of $2P_{max}$ and $1.5P_{max}$. This was interpreted as an effect of the state of stress. While Mills and Hertzberg [*17*] investigated the effect of sheet thickness on number of delay cycles, in the present paper the details of the effects of simple load excursions on the subsequent crack opening stresses have been explored in an attempt to correlate measured opening stresses with observations on fatigue crack growth.

The effect of underloads on subsequent fatigue crack growth is shown in Figs. *5a* and *5b*. For the 14-mm-thick specimen, underloads reduced slightly the fatigue life compared with the constant-amplitude test. The 6-mm-thick specimen showed a slightly increased fatigue life compared with the constant-amplitude test.

The effect of an underload applied directly after an overload, shown in Fig. 6, was to reduce the beneficial retardation effects produced by the single overload cycle (shown in Fig. 4). The crack tip becomes blunted by the overload, and the application of a cyclic compressive load to the blunted crack results in the formation of residual tensile stresses [*18*]. These residual tensile stresses appear to eliminate partly the beneficial delay effects associated with the previously applied tensile overload. Residual stresses are produced ahead of the blunted crack tip during unloading from the far-field compressive stress, due to there being no contact, or closure, in the wake of the blunt crack. Note that if a long, sharp fatigue crack, rather than a blunted crack, is subjected to cyclic compression, as in the single underload tests, the residual tensile field may not be produced because of closure of the crack during the compressive load cycle.

Closure Measurements

Three-dimensional finite element (3DFE) analysis of crack closure by Chermahini et al. [*19*], using a model thickness of 4.78 mm, demonstrated that the opening stress σ_{op} was lower than the corresponding closing stress σ_{cl} in the previous unloading portion of the cycle. The experimental results from the Elber gage measurements shown in Fig. 8 appear to confirm this. However, both the 3DFE analysis and these measurements contradict many analytical models which show that crack closing stress is lower than the crack opening stress. For example, Budiansky and Hutchinson [*4*] show that $\sigma_{cl} = 0.48\sigma_{max}$ and $\sigma_{op} = 0.56\sigma_{max}$, whereas the experiments using the Elber gage indicate in Fig. 9 that $\sigma_{cl} = 0.47\sigma_{max}$ and $\sigma_{op} = 0.36\sigma_{max}$. The experimental values are average values for $2a/W > 0.4$. The 3DFE analysis [*19*] obtained at the surface of the sheet gave values of $\sigma_{cl} = 0.59\sigma_{max}$ and $\sigma_{op} = 0.56\sigma_{max}$.

Chermahini et al. [*19*] indicated that the difference in closure stress is due to reverse yielding in the contact (or plastic wake) region. That is, on the loading portion of the fatigue cycle, a new crack wake is formed behind the crack tip due to a small increment of crack growth. Subsequently, on unloading the crack will close first (σ_{cl}) just behind the crack tip due to the newly formed crack wake, with fracture surfaces being compressed. σ_{op} will therefore be lower than σ_{cl} of the previous cycle, as the fracture surfaces have been plastically compressed on the unloading portion of the fatigue cycle. It is notable that global measurements of crack closure using the centerline clip gage do not reveal the differences between opening and closing stresses.

The crack opening results, shown in Figs. 7 and 8, obtained from the constant-amplitude tests show that there was a high degree of scatter in closure measurements for $2a/W < 0.4$, within one specimen and also from specimen to specimen. However, for crack lengths greater than $2a/W = 0.4$ the scatter of crack closure stresses was much less. Nevertheless, the measured crack opening stresses from the overload fatigue crack growth tests (Fig. 10) show that for the 6-mm-thick specimen there was an increase in the opening stress following the application of an overload, and therefore a decrease in the fatigue crack growth rate was observed as shown in Fig. 4. An increase in opening stresses was also seen in the 14-mm-thick specimen, again leading to retardation in the fatigue crack growth rates, although not to the same extent as in the 6-mm-thick specimen.

The opening stresses obtained from the underload fatigue tests for the two thicknesses are compared in Fig. 11. Crack opening stresses for both thicknesses were shown to be relatively insensitive to the application of a compressive overload. This is consistent with the fatigue crack growth results obtained in which the application of underloads did not affect the fatigue crack growth when compared with the constant-amplitude tests.

There were also differences in the measured crack opening stresses for two thicknesses in the over/underload tests. Compared with the constant-amplitude crack opening stress, the 14-mm-thick specimen showed lower crack opening stress for the overload/underload cycle, but the opening stress did not increase in the post over/underload region when compared with the single overload test. The crack opening stress for the 6-mm-thick specimen did, however, follow the trend of the simple overload test, but at lower opening stresses.

The trends in the measured opening stresses outlined above for the various loading conditions are shown in Fig. 13. These trends are in general agreement with the trends for the fatigue crack growth results shown in Fig. 7; that is, with a higher crack opening stress, as in the overload tests, there is a longer fatigue life. Following an overload, measured crack growth rates indicate that after a certain number of cycles, constant-amplitude fatigue crack growth rates have been re-established. Measured crack opening stresses, however, do not support this. As shown in Fig. 13, and in more detail in Fig. 10, the general trend for overload conditions is to increase the crack opening stress. This is apparent for both the 6-mm and 14-mm-thick specimens.

The crack opening measurements from both the underload and over/underload tests reveal a decrease in σ_{op}/σ_{max} immediately following the load excursions. This suggests that there is an increase in the fatigue crack growth rate. Although there is evidence for this (Figs. 6–8), it is confined to only one load cycle. The crack growth rates after this one cycle immediately reduce, and the higher crack opening stresses provide further evidence for this. This suggests that while the UL or OUL cycles are expected to produce tensile residual stresses, it is apparent that the crack grows rapidly out of this region and into a region of compressive residual stresses. These residual stresses are not as large as those produced from a single overload, as the crack growth rate following an UL or OUL was observed to be not as low as that observed following a single overload.

Conclusions

The results from an experimental study into the effects of load excursions on crack closure measurements have been presented. The crack closure loads were measured local to the crack tip in plate thicknesses of 6 mm and 14 mm of the aluminum alloy 2024-T351 using an Elber-type gage for measuring crack-tip opening displacement.

1. Initial constant-amplitude fatigue crack growth tests on two different specimen thicknesses, machined from a single lot of 15.7-mm-thick aluminum alloy 2024-T351 plate, revealed a systematic difference in fatigue crack growth. This could not be explained in terms of a difference in crack closure levels, as both specimen thicknesses showed similar crack opening stresses.
2. The effect of single overloads on the fatigue crack growth in the aluminum alloy 2024-T351 showed a substantial difference in the number of post-overload retardation cycles for the two thicknesses studied. It was found that the 6-mm-thick specimen had a fatigue life about two times greater than the 14-mm-thick specimen.
3. Only small load interaction effects were found for both thicknesses for simple underload tests, compared with constant-amplitude tests. Although the over/underload tests showed increased fatigue lives, when compared with constant-amplitude tests, the effect of the underload, applied after the overload, was to reduce the beneficial retardation effects produced by the previous overload.
4. The trends in the measured opening stresses are in general agreement with the trends for the fatigue crack growth results, which imply that, with a higher crack opening stress, as in the overload tests, a greater fatigue life was observed. However, after a certain number of cycles following an overload, constant-amplitude crack growth rates are restored. The crack opening stresses do not re-

turn to the pre-overload constant-amplitude level, but increase relative to the pre-overload constant-amplitude crack opening stresses.

Acknowledgments

The authors wish to acknowledge the financial support of British Aerospace (Airbus) Ltd. for this work. The views given in this paper are those of the authors and do not represent those of British Aerospace.

References

[1] Elber, W., "Fatigue Crack Closure under Cyclic Tension," *Engineering Fracture Mechanics*, Vol. 2, No. 1, 1970, pp. 37–45.
[2] Heuler, P. and Schutz, W., "Assessment of Concepts for Fatigue Crack Initiation and Propagation Life Prediction," *Zeitschrift Fur Werkstofftechnik-Materials Technology and Testing*, 1986, Vol. 17, No. 11, pp. 397–405.
[3] Dill, H. D. and Saff, C. R., "Spectrum Crack Growth Prediction Method Based on Crack Surface Displacement and Contact Analyses," *Fatigue Crack Growth Under Spectrum Loads, ASTM STP 595*, American Society for Testing and Materials, 1976, pp. 306–319.
[4] Budiansky, B. and Hutchinson, J. W., "Analysis of Closure in Fatigue Crack Growth," *Journal of Applied Mechanics*, Vol. 45, 1978, pp. 267–276.
[5] Fuehring, H. and Seeger, T., "Dugdale Crack Closure Analysis of Fatigue Cracks under Constant Amplitude Loading," *Engineering Fracture Mechanics*, Vol. 11, 1979, pp. 99–122.
[6] Newman, J. C., Jr., "A Crack Closure Model for Predicting Fatigue Crack Growth under Aircraft Spectrum Loading," *Methods and Models for Predicting Fatigue Crack Growth Under Random Loading, ASTM STP 748*, American Society for Testing and Materials, 1981, pp. 53–84.
[7] Dugdale, K. D., "Yielding of Steel Sheets Containing Slits," *Journal of Mechanics and Physics of Solids*, Vol. 8, No. 2, 1960, pp. 100–104.
[8] Newman, J. C., Jr., "Prediction of Fatigue Crack Growth under Variable Amplitude and Spectrum Loading using a Closure Model," *Design of Fatigue and Fracture Resistant Structures, ASTM STP 761*, American Society for Testing and Materials, 1982, pp. 255–277.
[9] Poussard, C. G. C., "An Analysis of Residual Stresses and Fatigue Behaviour of Cracks Emanating from Cold Worked Fastener Holes," Ph.D. Thesis, University of Bristol, Bristol, England, 1995.
[10] Yisheng, W. and Schijve, J., "Fatigue Crack Closure Measurements on 2024-T3 Sheet Specimens," *Fatigue and Fracture of Engineering Materials and Structures*, Vol. 18, No. 9, 1995, pp. 917–921.
[11] Schijve, J., "Fatigue Crack Closure: Observations and Technical Significance," *Mechanics of Fatigue Crack Closure, ASTM STP 982*, American Society for Testing and Materials, 1988, pp. 5–34.
[12] Wei, R. P. and Shih, T. T., "Delay in Fatigue Crack Growth," *International Journal of Fracture*, Vol. 10, 1974, pp. 77–85.
[13] Venkateswara Rao, K. T. and Ritchie, R. O., "Mechanisms for the Retardation of Fatigue Cracks Following Single Tensile Overloads—Behavior in Aluminum Lithium Alloys," *Acta Metallurgica*, Vol. 36, No. 10, 1988, pp. 2849–2862.
[14] Schijve, J., "Observations on the Prediction of Fatigue Crack Growth Propagation Under Variable-Amplitude Loading," *Fatigue Crack Growth Under Spectrum Loads, ASTM STP 595*, American Society for Testing and Materials, 1976, pp. 3–23.
[15] Knott, J. F. and Pickard, A. C., "Effect of Overloads on Fatigue Crack Propagation: Aluminum Alloys," *Metal Science*, Vol. 11, 1977, pp. 399–404.
[16] Fleck, N. A., "Fatigue Crack-Growth Due to Periodic Underloads and Overloads," *Acta Metallurgica*, Vol. 33, No. 7, 1985, pp. 1339–1354.
[17] Mills, W. J. and Hertzberg, R. W., "Effect of Sheet Thickness on Fatigue Crack Retardation in 2024-T3 Aluminum Alloy," *Engineering Fracture Mechanics*, Vol. 7, 1975, pp. 705–711.
[18] Suresh, S., *Fatigue of Materials*, Cambridge University Press, Cambridge, U.K. 1991.
[19] Chermahini, R. G., Shivakumar, K. N., and Newman, J. C., Jr., "Three-Dimensional Finite-Element Simulation of Fatigue Crack Growth and Closure," *Mechanics of Fatigue Crack Closure, ASTM STP 982*, American Society for Testing and Materials, 1988, pp. 398–413.

Masahiro Jono,[1] Atsushi Sugeta,[1] and Yoshihiko Uematsu[1]

Fatigue Crack Growth and Crack Closure Behavior of Ti-6Al-4V Alloy Under Variable-Amplitude Loadings

REFERENCE: Jono, M., Sugeta, A., and Uematsu, Y., "**Fatigue Crack Growth and Crack Closure Behavior of Ti-6Al-4V Alloy Under Variable-Amplitude Loadings,**" *Advances in Fatigue Crack Closure Measurement and Analysis: Second Volume, ASTM STP 1343,* R. C. McClung and J. C. Newman, Jr., Eds., American Society for Testing and Materials, West Conshohocken, PA, 1999, pp. 265–284.

ABSTRACT: Fatigue crack growth tests under constant-amplitude and repeated two-step loadings were carried out on a ($\alpha + \beta$) Ti-6A1-4V alloy which has duplex structure made up of equiaxed primary α-phase grains with a discontinuous fine β-phase dispersed in the boundaries. It was found that fatigue crack grew along α-phase grain boundaries and that the fracture surface was very rough in the low stress intensity region under constant-amplitude loading. On the other hand, in the high region, transgranular crack growth was observed and the fracture surface was relatively smooth. The crack opening point, K_{op}, was affected by the amplitude of low-level load, ΔK_L, under repeated two-step loadings where the high-level load amplitude was kept constant. K_{op} was found to be higher than that predicted by $K_{op} \sim K_{max}$ relationship under constant-amplitude loading and the fracture surface was rougher in comparison with that under constant-amplitude loading which has the identical stress intensity range. It was concluded that the crack opening point was controlled by both plasticity-induced crack closure in terms of K_{max} and roughness-induced crack closure resulted from rougher surface in ΔK_L.

KEYWORDS: fatigue crack growth, crack closure, titanium alloy, variable amplitude loadings, fracture surface roughness

Most engineering structures are generally subjected to variable-amplitude loadings in service. In order to ensure the safety of such engineering structures, it is necessary to predict fatigue crack growth under random loadings. It is well recognized that there exist the load interaction effects on fatigue crack growth under varying loadings, such as growth acceleration by low-high load sequence [*1,2*] or compressive overload [*3,4*], or retardation due to tensile overload or high-low load sequence [*5–8*]. The crack closure concept proposed by Elber [*9,10*], to account for the effect of load interaction as well as stress ratio, has been widely used to estimate crack growth rates under variable amplitude loadings.

For several years the authors have investigated fatigue crack growth rate and crack closure under variable-amplitude loadings using many kinds of steel and aluminum alloy [*11–18*]. The principal conclusions obtained are as follows: Under variable-amplitude loadings fatigue crack can grow even at the low stress intensities below the threshold level of constant amplitude test, owing to the existence of higher level load which included variable amplitude loading block. The load interaction effect can be well explained by plasticity-induced crack closure behavior and the crack opening point under variable-amplitude loadings is controlled by the maximum stress intensity range and its stress ratio. The effective stress intensity range controls the crack growth rate.

[1] Professor, associate professor, and research assistant, respectively, Department of Mechanical Engineering and Systems, Osaka University, Yamadaoka, Suita, Osaka 565-0871, Japan.

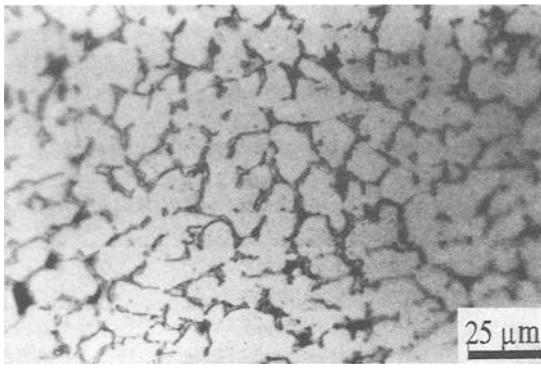

FIG. 1—*Microstructure of* ($\alpha + \beta$) *Ti-6Al-4V alloy.*

In this study, fatigue crack growth tests were carried out on an ($\alpha + \beta$) Ti-6A1-4V alloy under constant-amplitude and repeated two-step loadings. Crack closure behavior as well as crack growth rates were investigated. The microstructure of Ti-6A1-4V is well known to affect fatigue crack growth behavior and many studies dealing with this material have emerged [*19–21*]. In titanium alloys, it was reported that both plasticity and fracture roughness-induced crack closure might operate simultaneously to various degrees depending on loading [*22*]. Therefore, it is thought that the development of crack closure under varying loading conditions of these materials may be quite complex compared to steels and aluminum alloys. Although effect of load variation on fatigue crack growth behavior was reported in some References [*23–25*], there are few studies on the effect of microstructure on crack growth rate and closure behavior under variable-amplitude loadings.

Experimental Procedure

Materials and Test Conditions

The material used in this study is an annealed ($\alpha + \beta$) Ti-6A1-4V alloy. This alloy was finish-rolled below β transus to a final thickness of 45 mm, followed by annealing at 978 K for two hours in vacuum and furnace cooling to room temperature. Figure 1 shows the microstructure of the material. The heat treatment resulted in duplex structure made up of equiaxed primary α-phase grains with discontinuous fine β-phase dispersed in the boundaries. Mean grain size of α-phase is 28.2 μm. The chemical composition and mechanical properties of the material at room temperature are shown in Tables 1 and 2.

Fatigue crack growth tests were performed on a closed-loop servo-hydraulic testing system at 5 Hz in a relatively low growth rate region ($<10^{-8}$ m/cycle) and at 2 Hz in a high growth rate region, using side-grooved CT (Compact Type) specimens. Both constant-amplitude and repeated two-step loading tests were carried out at stress ratio $R = 0.0$. A constant-amplitude test was conducted keeping a value of the normalized K-gradient, $(1/K)\ dK/da$, at 0.2 m^{-1}. On the other hand, in repeated two-step loading tests, both high- and low-level stress intensity factors were kept constant by shedding load

TABLE 1—*Chemical Composition of Material Used (Mass%).*

Material	Al	V	Fe	C	O	N	H
Ti-6A1-4V	6.22	4.23	0.184	0.005	0.178	0.0040	0.0034

TABLE 2—*Mechanical Properties of Material Used at Room Temperature.*

Material	0.2% Proof Stress $\sigma_{0.2}$ (MPa)	Tensile Strength σ_B (MPa)	Elongation δ(%)
Ti-6Al-4V	893	992	21

continuously as the crack grew. The specimen geometry and dimensions are shown in Fig. 2. The reason why side-grooved specimens are used is to obtain plane strain through-thickness crack growth data. The crack length and the crack opening point are measured continuously during the test without changing test frequency by means of a microcomputer-aided unloading elastic compliance method using a back face strain gage [*11,12*]. Figure 3 illustrates this method. The load-displacement hysteresis

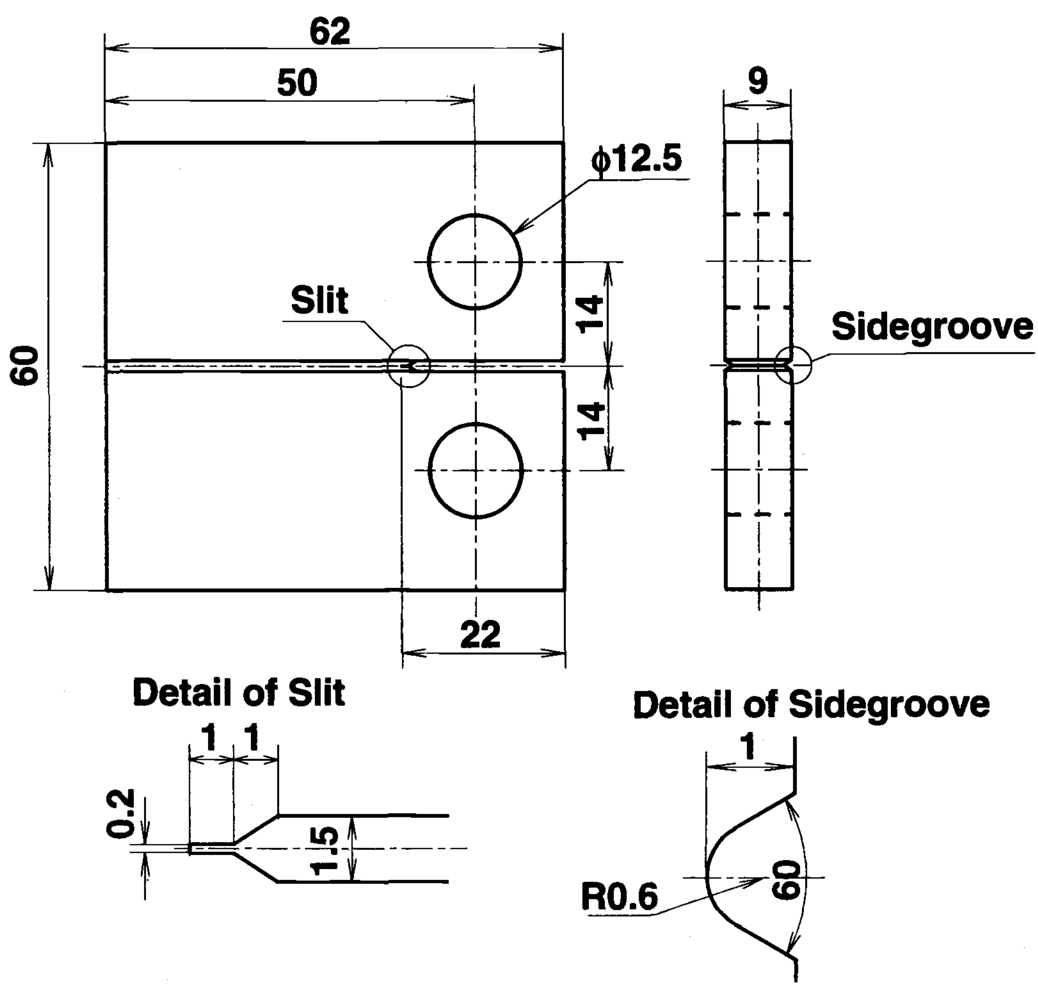

FIG. 2—*Test specimen configuration and dimensions (mm).*

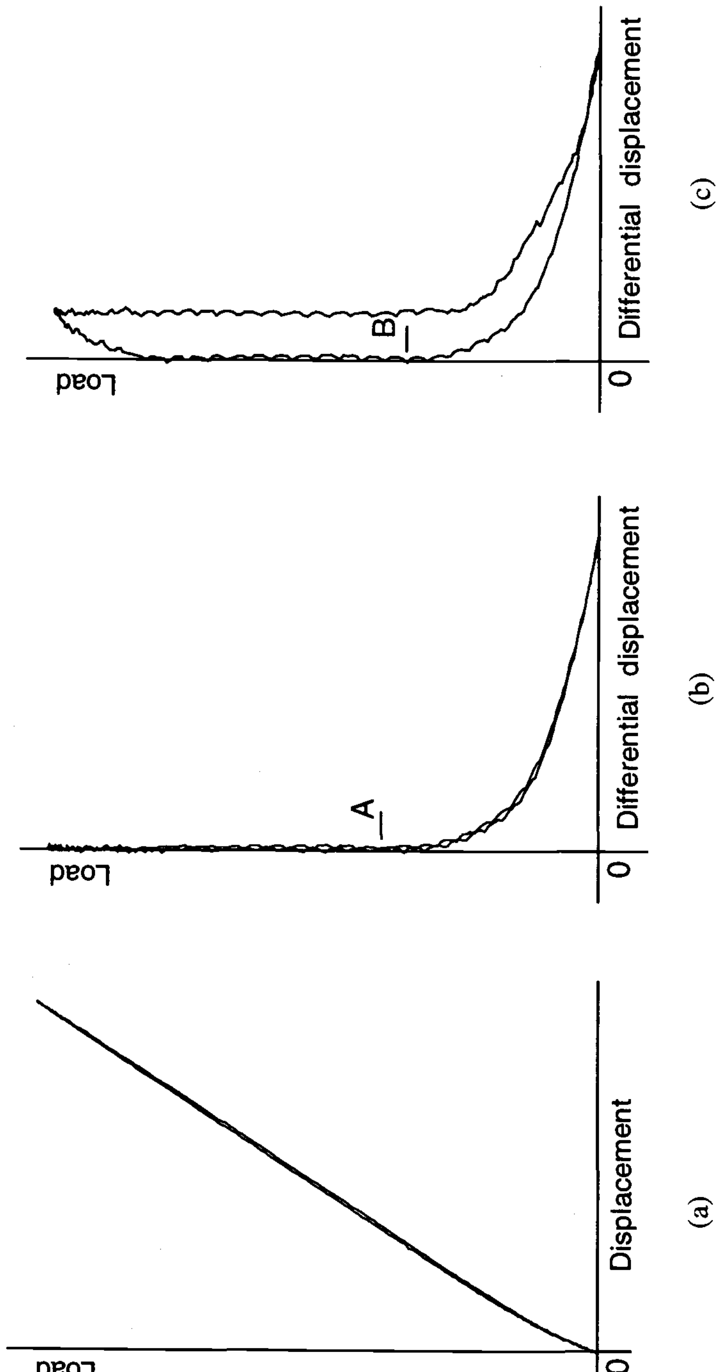

FIG. 3—*Load-displacement curve and load-differential displacement curves.*

loop shown in Fig. 3*a* was found to slightly bend because of the change of compliance due to crack closure. However, it seems difficult to define the crack opening level in this case. Therefore, the elastic displacement of unloading cycle in which the crack was fully open was subtracted from the original load-displacement curve in the manner that the curve of that portion was made parallel to *y*-axis, as in Fig. 3*b*. It was found from this curve that the crack was gradually opening as loading and was fully open above A. The crack opening point A was made clearer than that of the original load-displacement curve. Figure 3*c* is an example of the hysteresis loop that shows plastic deformation behavior, and even in this case the crack opening point could be obtained by the point B at which hysteresis touched the vertical line, if the elastic portion of the unloading cycle was made parallel to it. Crack length was measured by detecting the change of the elastic compliance during unloading cycle with crack propagation. By eliminating the random noise with the aide of microcomputer software, the accuracy of the measurement of crack growth increment is better than 10 μm. The crack length is measured at every crack extension of 0.2 mm and da/dn is computed by an incremental polynomial method using three successive data points. The stress intensity factor is computed by the following equation

$$K = \frac{P}{Be\sqrt{W}} \frac{2 + \alpha}{(1 - \alpha)\sqrt{1 - \alpha}} (0.886 + 4.64\alpha - 13.22\alpha^2 + 14.72\alpha^3 - 5.6\alpha^4) \tag{1}$$

where

$\alpha = a/W$,
a = crack length measured from load line,
W = specimen width measured from load line,
P = applied load, and
Be = effective thickness.

The effective thickness, Be, is the geometric mean of the gross and net thickness of the side-grooved specimen.

The roughness of fracture surface was measured using a scanning laser microscope, and a ten-point height of irregularities was used as a measure of roughness of fracture surface.

Experimental Results and Discussion

Fatigue Crack Growth Behavior Under Constant-Amplitude Loading

A constant-amplitude loading test was carried out using K-increasing procedure in order to avoid preloading effects on subsequent crack growth. Figure 4 shows the fatigue crack growth rates as a function of the maximum stress intensity K_{max} and also the effective stress intensity range ΔK_{eff}. Since the test was carried out at $R = 0.0$, K_{max} is equal to the stress intensity range ΔK. The threshold stress intensity factor is about 6.2 MPam$^{1/2}$. It was found that the plots of log da/dn against log K_{max} was not straight even in the so-called Paris regime and the transition of crack growth behavior occurred at about 16 MPam$^{1/2}$ (indicated by arrows in da/dn-K_{max} relationship). Such transition behavior in many kinds of titanium alloys was reported in (e.g., Ref *20*). What is more important is that this transition behavior is reflected in the plots of da/dn versus ΔK_{eff}. Figure 5 shows optical micrographs of fatigue crack path. The specimen surface was etched in order to clear grain boundary between α and β phase. In the lower crack growth rate region below the transition point shown in Fig. 5*a*, the crack grew along grain boundaries between α and β phase or in thin β phase in a zigzag manner. Mean roughness value of the fracture surface was about 32 μm and was nearly equal to α grain size of 28.2 μm. On the other hand, in the higher crack growth rate region shown in Fig. 5*b*, the crack grew on the straight and the fracture surface is relatively smooth. Scanning electron micrographs of the fracture surface are shown in Fig. 6. The fractograph at low stress intensity exhibits intergranular

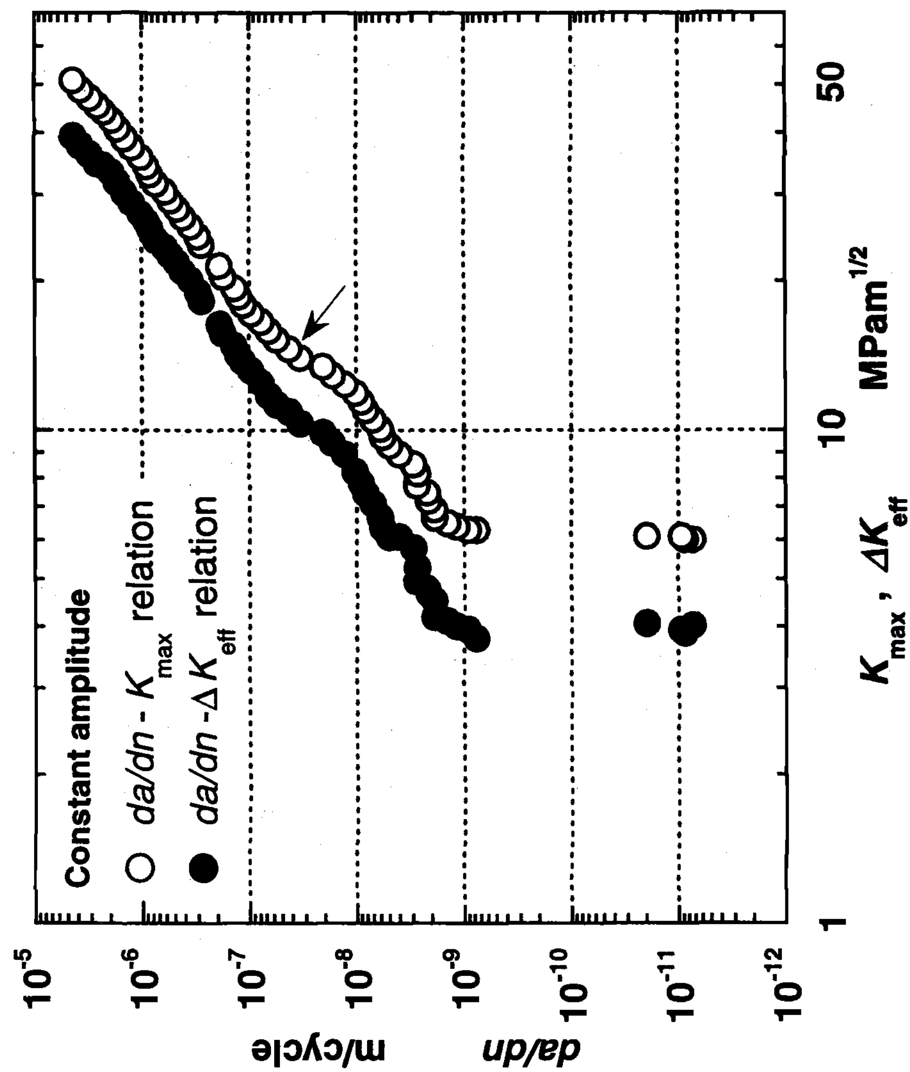

FIG. 4—*Fatigue crack growth rate as a function of* K_{max} *and* ΔK_{eff} *under constant-amplitude loading.*

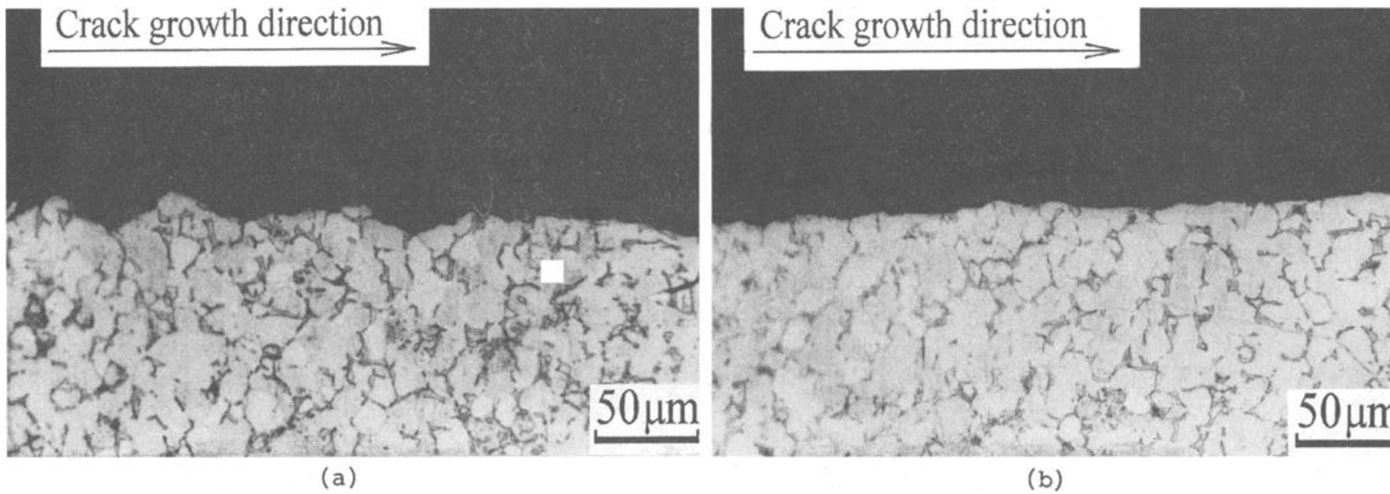

FIG. 5—*Optical micrographs of crack growth path.* (a) K_{max} = *12.0 MPam*$^{1/2}$, ΔK_{eff} = *8.3 MPam*$^{1/2}$, da/dn = *1.10* $\times$ *10*$^{-8}$ *m/cycle,* (b) K_{max} = *25.0 MPam*$^{1/2}$, ΔK_{eff} = *19.3 MPam*$^{1/2}$, da/dn = *3.21* $\times$ *10*$^{-7}$ *m/cycle.*

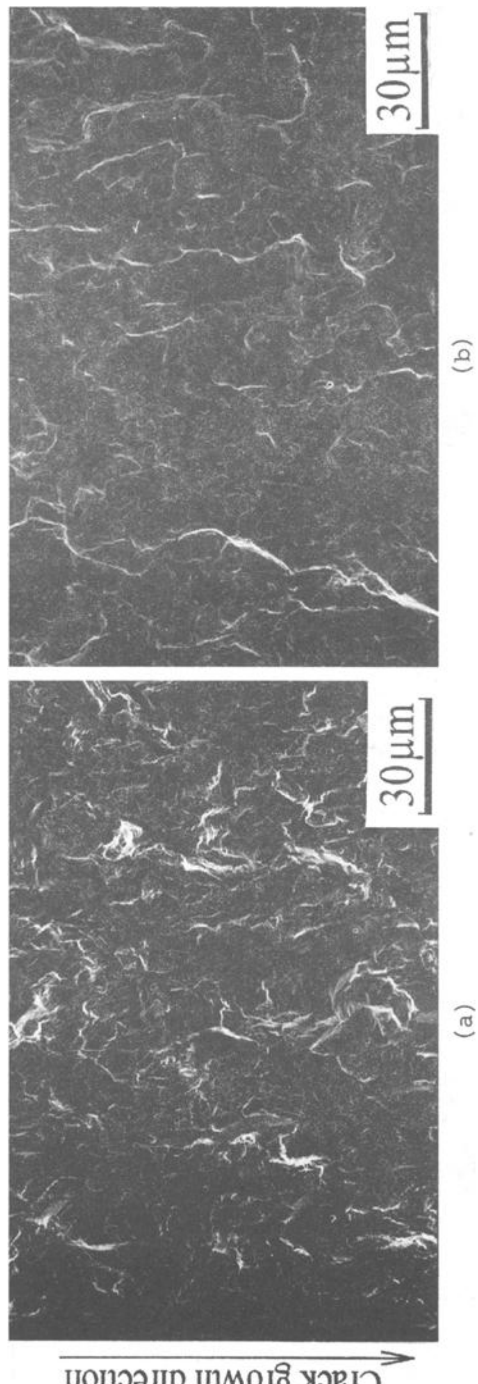

FIG. 6—*Scanning electron micrographs of fracture surface. (a)* K_{max} = *12.0 MPam*$^{1/2}$, ΔK_{eff} = *8.3 MPam*$^{1/2}$, da/dn = *1.10* $\times$ *10*$^{-8}$ *m/cycle, (b)* K_{max} = *25.0 MPam*$^{1/2}$, ΔK_{eff} = *19.3 MPam*$^{1/2}$, da/dn = *3.21* $\times$ *10*$^{-7}$ *m/cycle.*

fracture and at high stress intensity a striated plateau was observed, indicating that crack growth mechanism changed from intergranular to transgranular type as K_{max} increased. As the result of change of the crack growth mechanism, the fracture surface in the low growth rate region was microscopically more rough than that after the transition.

Under the constant-amplitude loading described above, variation of crack opening stress intensity factor, K_{op}, and crack opening ratio which is defined as $\Delta K_{eff}/\Delta K$, U, with K_{max} are shown in Fig. 7. U gradually increases with the increment of K_{max} and becomes almost constant in the higher K_{max} region (> 16 MPam$^{1/2}$). Its constant value is almost equal to 0.77, indicating that plasticity-induced crack closure is dominant in the higher K_{max} region. On the other hand, since the fracture surface in the lower K_{max} region was very rough, it was thought that both plasticity and roughness-induced crack closure operated simultaneously, which caused the increase of K_{op} and decrease of U at low growth rates.

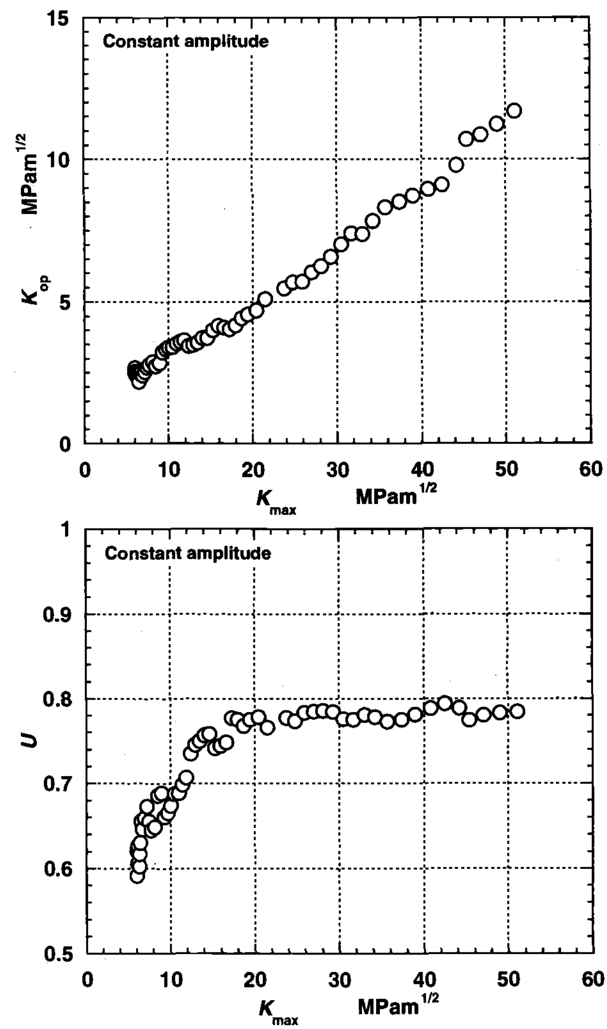

FIG. 7—*Crack opening stress intensity factor,* K_{op}, *and crack opening ratio,* U, *as a function of* K_{max}.

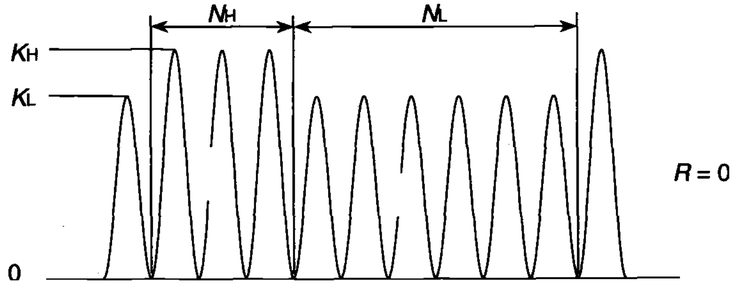

FIG. 8—*Repeated two-step loading pattern.*

The monotonic plastic zone size for plane strain at the transition point in $da/dn - K_{max}$ relationship (= 16 MPam$^{1/2}$) was 30.3 μm. The monotonic plastic zone size for plane strain, ω_p, was estimated by the equation

$$\omega_p = \frac{1}{2\sqrt{2\pi}} \left(\frac{K_{max}}{\sigma_{0.2}}\right)^2 \tag{2}$$

where $\sigma_{0.2}$ was the 0.2% proof stress. The monotonic plastic zone size at the transition point was nearly the mean α-grain size, d, of 28.2 μm. Above transition point where $\omega_p > d$, the α-grain within the larger plastic zone must necessarily deform as a continuum, which results in a microstructurally insensitive mode of crack growth. By contrast, below the transition point where $\omega_p < d$, a microstructurally sensitive mode of crack growth occurs. In this region, grain boundary would be the most preferential path of crack advance, probably because of deformation mismatch among neighboring grains. Such variation of crack growth mechanisms would lead to the variation of crack growth resistance and closure behavior, eventually in the transition in $da/dn - K_{max}$ relationship as already shown in Fig. 4.

Fatigue Crack Growth Behavior Under Repeated Two-Step Variable-Amplitude Loading

Fatigue Crack Growth Data—Repeated two-step loading tests were carried out using the loading pattern shown in Fig. 8, where both the stress ratio of the low-level and high-level load cycle were kept constant at 0.0. The variable-amplitude test conditions are shown in Table 3. The maximum stress intensity factor of low-level load, K_L, was varied in steps, keeping that of high-level load, K_H, constant at 30 MPam$^{1/2}$ in the test series A. In each step, K_L was kept constant by shedding load continuously as the crack grew. K_H was equal to 20 MPam$^{1/2}$ in the test series B. In the test from B2 to B4, the number of low-level load cycles, N_L, was varied from 100 to 1000 keeping the number of

TABLE 3—*Repeated Two-Step Loading Test Conditions.*

Test	K_H (MPam$^{1/2}$)	K_L (MPam$^{1/2}$)	N_H:N_L
Test A1	30	12~24	1:1000
Test A2	30	12~28	6:600
Test B1	20	10~20	1:1000
Test B2	20	14	10:1000
Test B3	20	14	10:500
Test B4	20	14	10:100

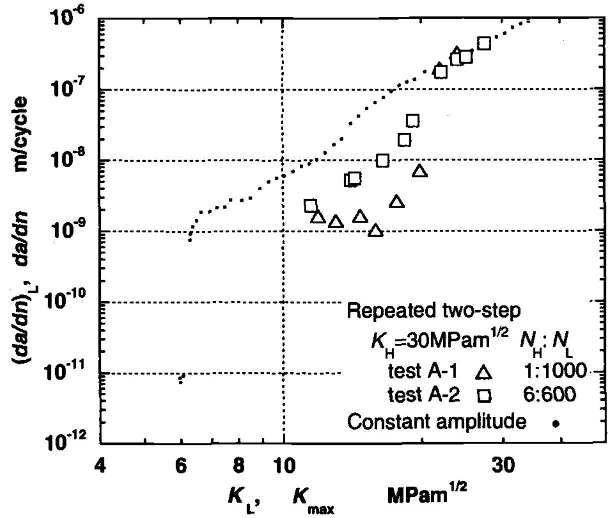

FIG. 9—*Fatigue crack growth rate as a function of* K_L *under repeated two-step loadings where high level load,* K_H, *is kept constant at 30 MPam*$^{1/2}$.

high-level load cycle, N_L, and K_L constant at 10 and 14 MPam$^{1/2}$, respectively, in order to investigate the effect of N_L on fatigue crack growth behavior.

Figures 9 and 10 show the relationship between K_L and the crack growth rate of low-level load cycle $(da/dn)_L$. $(da/dn)_L$ was calculated by the following equation assuming a linear accumulation of crack growth

$$(da/dn)_L = \{da/dn \times (N_H + N_L) - (da/dn)_H \times N_H\}/N_L \tag{3}$$

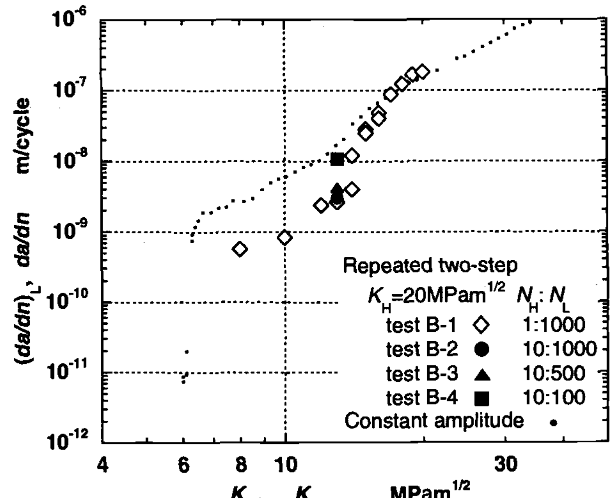

FIG. 10—*Fatigue crack growth rate as a function of* K_L *under repeated two-step loadings where high level load,* K_H, *is kept constant at 20 MPam*$^{1/2}$.

where da/dn is the average crack growth rate under repeated two-step loading and $(da/dn)_H$ is the crack growth rate corresponding to the value of effective stress intensity range for high-level load, $(\Delta K_{eff})_H (= K_H - K_{op,H})$, in constant-amplitude growth rate data. $K_{op,H}$ was determined by using the load-differential displacement curve measured under repeated two-step loading. N_H and N_L are number of cycles in high-level and low-level load per block, respectively.

Quantitative verification of Eq 3 has been made through fractographical studies in the previous investigation [*13*]. The growth rate $(da/dn)_L$ in terms of K_L is lower compared with constant-amplitude data denoted by small solid circles except high K_L conditions. In the tests where N_L was varied keeping N_H and K_L constant (test B2, B3 and B4), it was found that fatigue crack growth rate became lower as N_L increased (in Fig. 10). A similar trend was observed in Fig. 9. These results mean that the retardation behavior results from high-level load excursion and strongly depend on not only low-level load amplitude but also on the number of cycles.

Figure 11 represents the example of load versus subtracted displacement hysteresis loops under repeated two-step loading. In this figure, n_{Li} means the ith cycle of low-level load. Short horizontal bars indicate the crack opening points which were defined by the deflection point of the hysteresis curve. The crack opening points are found constant during one block of repeated two-step loading. Although the hysteresis loops measured in the other tests were omitted, a similar result was obtained. The crack opening stress intensity factor K_{op} at low-level load cycles measured by the above-mentioned technique was plotted against K_L in Figs. 12 and 13, where the small solid marks denote constant-amplitude crack opening data for $R = 0.0$. In test A1 (indicated by an open triangle symbol in Fig. 12), K_{op} took the very high value in lower K_L conditions and decreased with an increase of K_{max} until K_{op} approached the value under constant amplitude having the identical K_{max} with K_H. Similar behavior was observed in the other test condition (tests A2 and B1). Solid symbols in Fig. 13 show the test results where N_L was varied, keeping N_H and K_L constant. K_{op} was almost equal to that under constant amplitude having the identical K_{max} with K_H (= 20 MPam$^{1/2}$) in test B4 where N_L is 100. However, it is found that K_{op} increased with the increase of N_L and the crack opening behavior strongly depends on not only low-level load amplitude but also on the number of cycles. It was reported [*13*] that K_{op} under variable-amplitude loadings was controlled by the maximum stress

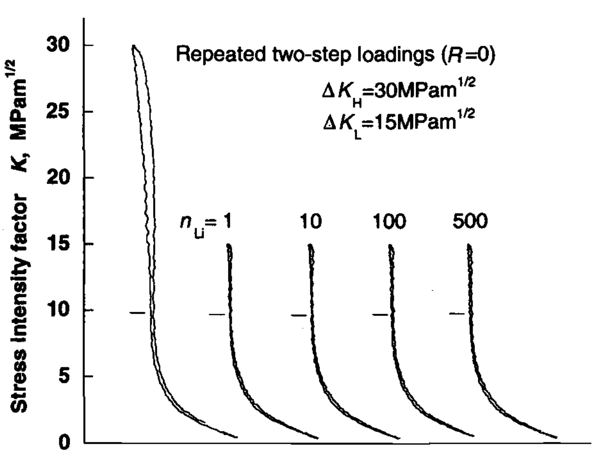

FIG. 11—*Load vs. subtracted displacement hysteresis loops under repeated two-step loading* (K_H = *30 MPam*$^{1/2}$, K_L = *15 MPam*$^{1/2}$, N_H:N_L = *1:1000).*

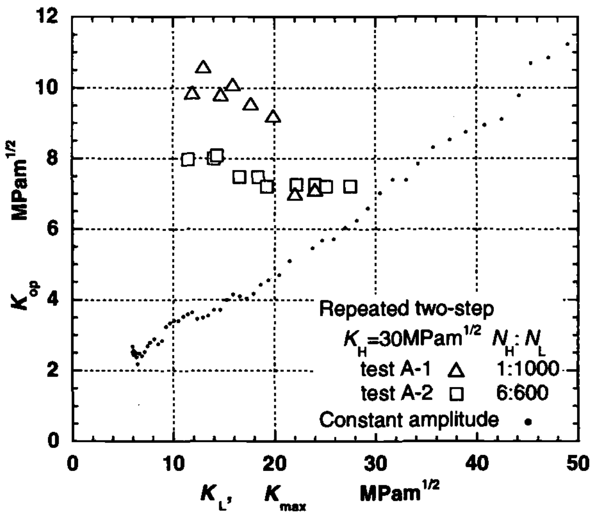

FIG. 12—*Relationship between* K_{op} *and* K_L *under repeated two-step loading* (K_H = *30 MPam*$^{1/2}$).

intensity range, $(\Delta K)_{max}$, and its stress ratio in steels and aluminum alloys and agrees well with constant-amplitude test results having the identical K_{max} with $(\Delta K)_{max}$. The crack growth behavior under variable-amplitude loadings in a titanium alloy was found quite different from the behavior observed in steels and aluminum alloys. The reason why the crack opening behavior was different will be discussed later.

Figure 14 shows the relationship between *da*/*dn* and effective stress intensity range ΔK_{eff} under low-level loads of repeated two-step loadings. Small solid circles denote constant stress amplitude crack growth data. It was found that the fatigue crack grew at low stress intensities below the threshold level of the constant amplitude test owing to the existence of high-level load in one loading block.

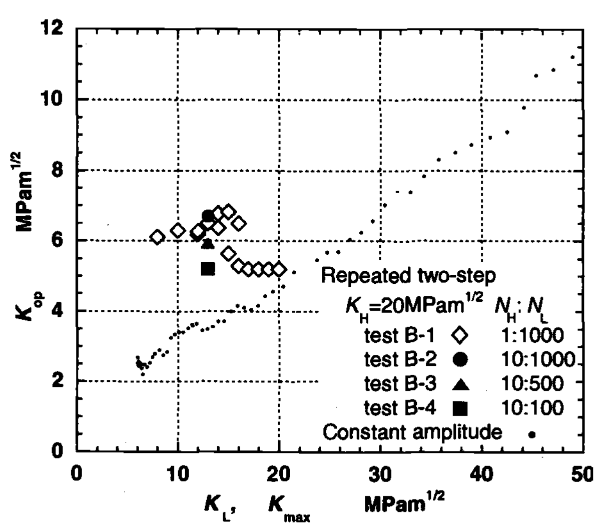

FIG. 13—*Relationship between* K_{op} *and* K_L *under repeated two-step loading* (K_H = *20 MPam*$^{1/2}$).

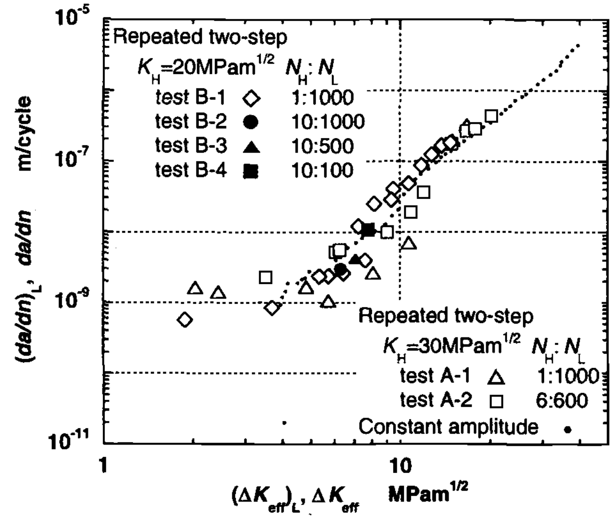

FIG. 14—*Fatigue crack growth rate as a function of effective stress intensity range, ΔK_{eff}, under repeated two-step loadings.*

Although the scatter of data was observed, $(da/dn)_L$ versus $(\Delta K_{eff})_L$ plots agree well with the constant-amplitude relationship. Therefore, the retardation behavior of fatigue crack growth in an annealed ($\alpha + \beta$) Ti-6Al-4V alloy is well explained by the concept of crack closure.

Microscopic Observation—Optical micrographs of crack growth path and scanning electron micrographs of the fracture surface in test A1 are shown in Fig. 15. In the low K_L condition as shown in Fig. 15*a*, the fracture surface is very rough compared with that under constant-amplitude loading having the same K value (= 12 MPam$^{1/2}$) already shown in Fig. 5, although the fatigue crack grew along grain boundaries under variable-amplitude as well as under constant-amplitude loading. The mean roughness value was 130 μm and increased by about four times that of constant-amplitude loading. The monotonic plastic zone size produced by the high-level load (= 30 MPam$^{1/2}$) was 119.7 μm and was approximately the mean roughness value under repeated two-step loading. As mentioned above, mean roughness value under constant-amplitude loading was also nearly equal to monotonic plastic zone size. These results indicate that crack deflection occurs within the monotonic plastic zone produced by the maximum stress intensity factor involved in load cycles when the fatigue crack grew along the grain boundary, and large crack deflection easily occurs and fracture surface roughness becomes larger under variable-amplitude loadings. In the higher K_L condition shown in Fig. 15*b*, the fracture surface was very smooth and transgranular crack growth was observed. Very rough fracture surface observed in the low K_L condition facilitated roughness-induced crack closure and resulted in a higher crack opening point as already shown in Figs. 12 and 13.

Figure 16*a,b* show fracture surface morphology in test B2 and B4, respectively. The difference of test conditions was only the number of low-level load cycles. Although transgranular crack growth was observed in both tests, there was a remarkable difference in fracture roughness and the fracture surface became rougher as N_L increased, indicating that fracture surface morphology depended on the number of cycles of low-level load. The crack growth increment under low-level load per block was 2.3 μm and 1.1 μm in test B2 and B4, respectively, and was smaller compared with the α grain size of 28.2 μm and plane strain plastic zone size of 53.2 μm. However,

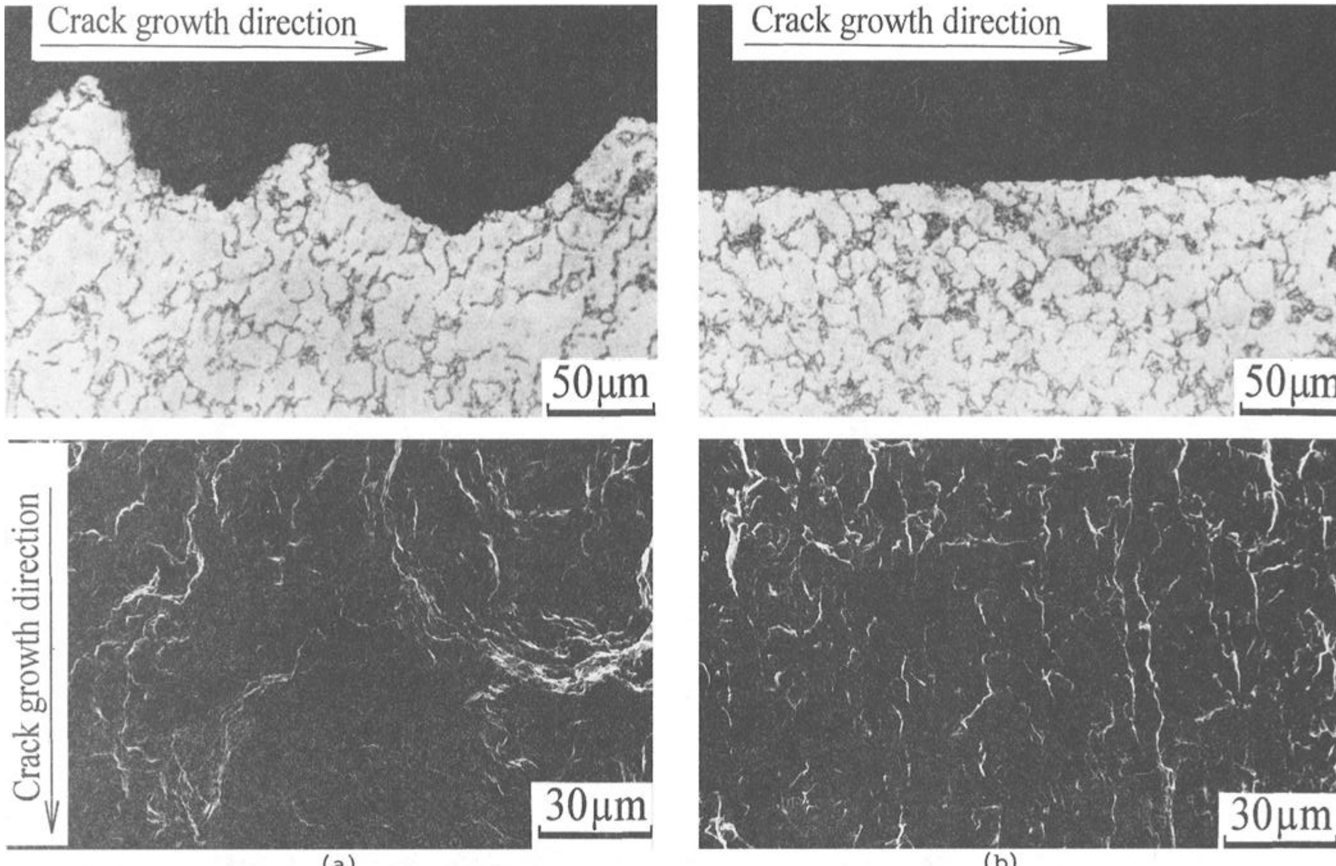

FIG. 15—*Optical micrographs of crack growth path and scanning electron micrographs of the fracture surface under repeated two-step loading* (K_H = *30 MPam*$^{1/2}$). (a) K_L = *12.0 MPam*$^{1/2}$, $(\Delta K_{eff})_L$ = *2.04 MPam*$^{1/2}$, $(da/dn)_L$ = *1.64* × *10*$^{-9}$ *m/cycle*, (b) K_L = *22.0 MPam*$^{1/2}$, $(\Delta K_{eff})_L$ = *15.0 MPam*$^{1/2}$, $(da/dn)_L$ = *1.97* × *10*$^{-7}$ *m/cycle.*

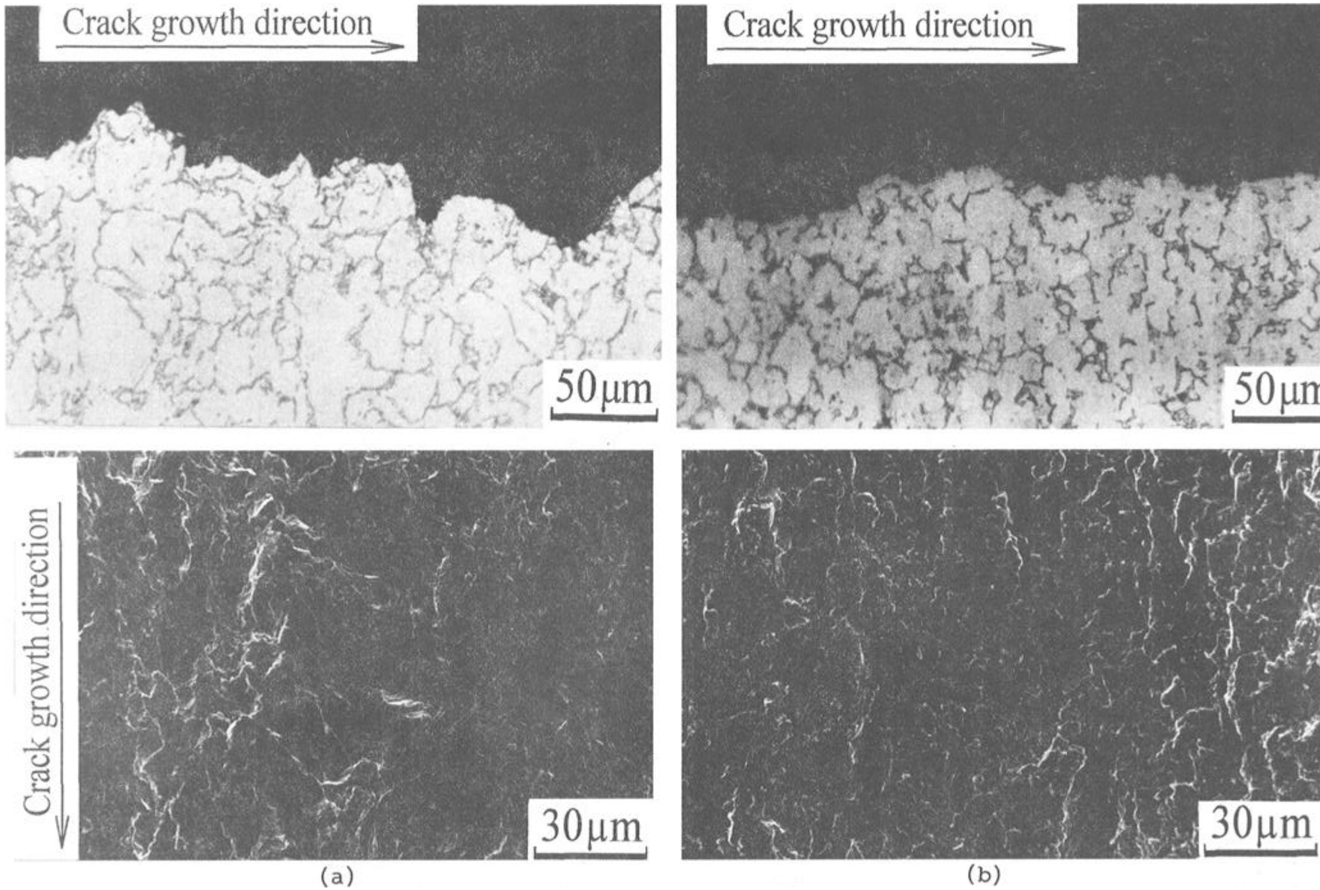

FIG. 16—*Optical micrographs of crack growth path and scanning electron micrographs of the fracture surface under repeated two-step loading* (K_H = *20 MPam*$^{1/2}$). (a) N_L = *1000*, K_L = *13.0 MPam*$^{1/2}$, $(\Delta K_{eff})_L$ = *6.30 MPam*$^{1/2}$, $(da/dn)_L$ = *2.33* × *10*$^{-9}$ *m/cycle*, (b) N_L = *100*, K_L = *13.0 MPam*$^{1/2}$, $(\Delta K_{eff})_L$ = *7.80 MPam*$^{1/2}$, $(da/dn)_L$ = *1.08* × *10*$^{-8}$ *m/cycle*.

since the fracture surface became rougher as the crack growth increment increased, it was found that surface roughness strongly depended on the small difference of crack growth increment under low-level load.

The results described hitherto mean that the roughness of the fracture surface under variable-amplitude loadings becomes rougher than that under constant-amplitude loading having the identical K value with K_L in low K_L condition, and the rougher fracture surface resulted in the higher crack opening point.

Quantitative Analysis of Fracture Surface Roughness—The fracture surface roughness was measured using a scanning laser microscope. A ten-point height of irregularities, which is used as a measure of roughness of fracture surface, was hereafter abbreviated "SRz." The measured value is shown in Table 4. SRz under repeated two-step loadings (tests B2, B3 and B4) was found higher than that under constant-amplitude loading in spite of the same maximum stress intensity factor, and SRz became higher as the number of cycles of low-level load increased. Hereafter, the quantitative relationship between crack opening stress intensity factor and fracture surface roughness is discussed. In order to yield this relationship, the analytical model of crack closure developed by Budiansky and Hutchinson [26] was used.

Crack tip opening displacement, $\delta_{eff,tip}$, is given by the following equation when taking into account the effects of residual stretch on crack faces and roughness of fracture surface

$$\delta_{eff,tip} = \delta_{tip} - \delta_r - \delta_{rough} \tag{4}$$

where

δ_{tip} = ideal crack tip opening displacement,
δ_r = residual stretch on crack face, and
δ_{rough} = mismatch between fracture surfaces induced by Mode II displacement.

And also, δ_{tip} can be calculated by

$$\delta_{tip}/\delta_0 = 1 - 2\omega_r/\omega \tag{5}$$

TABLE 4—*Measured Value of Ten-Point Irregularities (SRz) Under Constant-Amplitude and Repeated Two-Step Loadings.*

Test	K_{max}, K_H, [MPam$^{1/2}$]	K_{op} [MPam$^{1/2}$]	SRz [μm]
Test B2	20	6.70	85.46 76.46 68.43
Test B3	20	5.92	41.61 63.67 46.22
Test B4	20	5.20	24.55 30.23 25.39
Constant amplitude	20	4.90	18.22 17.6 17.98

where

ω_r = reversed plastic zone size during unloading,

$$= \frac{1}{2\sqrt{2\pi}}\left(\frac{K_{max} - K_{cl}}{2\sigma_{0.2}}\right)^2$$

ω = maximum plastic zone size,

$$= \frac{1}{2\sqrt{2\pi}}\left(\frac{K_{max}}{\sigma_{0.2}}\right)^2$$

δ_0 = crack opening displacement estimated from Dugdale model [27],

$$= \frac{K_{max}^2}{E\sigma_{0.2}}.$$

The crack closure point is defined as the load when the crack tip opening displacement equals zero during unloading. By substituting $\delta_{eff,tip} = 0$ into Eq 4, the following equation is yielded

$$K_{op}/K_{max} = 1 - \sqrt{2(1 - \delta_r/\delta_o - \delta_{rough}/\delta_o)} \quad (5)$$

Since the crack opening ratio, U, was equal to 0.77 in the high growth rate region where the effect of fracture surface roughness could be negligible, the above equation gives $\delta_r/\delta_0 = 0.7036$. Since it is very difficult to measure δ_{rough}, it is assumed that there exists a linear relation between δ_{rough} and SRz measured by a scanning laser microscope. This model leads to the following equations under constant-amplitude and repeated two-step loadings, respectively

$$K_{op} = K_{max} - \sqrt{0.5928(K_{max})^2 - C(SRz)} \quad (6)$$

$$K_{op} = K_H - \sqrt{0.5928(K_H)^2 - C(SRz)} \quad (7)$$

Figure 17 shows the relationship between the crack opening stress intensity factor, K_{op}, and the roughness of fracture surface, SRz, and the relation predicted on the basis of Eq 7 is plotted by a solid

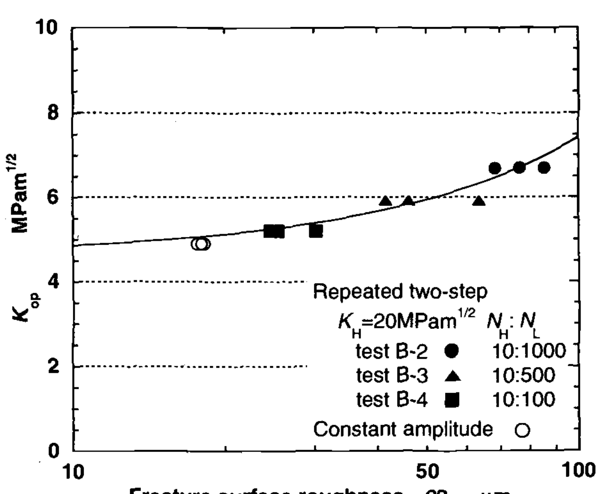

FIG. 17—*Relationship between* K_{op} *and fracture surface roughness.*

line. In this case, constant C was calculated using the data in test B2 where the highest roughness was measured. The measured value agrees with the predicted relation although scatter of data was observed and the usefulness of this model is confirmed. However, because the test condition of repeated two-step loadings was limited, more detailed studies are needed on fatigue crack closure behavior under variable-amplitude loadings, including fractography of fracture surface, in order to recognize the universality of this model.

Conclusions

Fatigue crack growth tests were carried out on an annealed ($\alpha + \beta$) Ti-6A1-4V alloy under constant-amplitude and repeated two-step loadings, and crack closure behavior as well as crack growth rates were investigated. The results obtained are as follows:

1. The fatigue crack growth mechanism under constant-amplitude loading varied depending on the load level, and transgranular fracture occurred in the low growth rate region and a crack grew preferentially within the α-phase at high growth rates.
2. The crack growth retardation was observed in terms of stress intensity factor under repeated two-step loadings. The crack opening point was found to be affected by both the amplitude and the number of cycles of low-level load and became higher than that predicted by constant-amplitude data having the identical maximum stress intensity with the low-level stress intensity factor, K_L.
3. The fracture surface under repeated two-step loadings was very rough compared with the fracture surface morphology under constant-amplitude loading, especially in lower K_L and larger N_L conditions. It was concluded that the crack opening point was controlled by both plasticity-induced crack closure in terms of K_H and roughness-induced crack closure resulted from a rougher surface in K_L. The relationship between crack opening stress intensity and fracture surface roughness was proposed and its usefulness confirmed.
4. It was found that fatigue crack growth rate under repeated two-step loadings with a stress ratio of $R = 0$ could be well predicted in terms of effective stress intensity range taking into account the crack closure behavior.

References

[1] Wei, R. P. and Shih, T. T., "Delay in Fatigue Crack Growth," *International Journal of Fracture*, Vol. 10, pp. 77–85.
[2] Adetifa, O. A., Gowda, C. V. B., and Topper, T. H., "A Model for Fatigue Crack Growth Delay Under Two-Level Block Loads," *Fatigue Crack Growth Under Spectrum Loads, ASTM STP 595*, R. P. Wei and R. I. Stephens, Eds., American Society for Testing and Materials, 1976, pp. 142–156.
[3] Crooker, T. W., "Effects of Tension-Compression Cycling on Fatigue Crack Growth in High Strength Alloys," *Journal of Engineering for Industry*, Vol. 93, pp. 893–896.
[4] Topper, T. H. and Yu, M. T., "The Effect of Overloads on Threshold and Crack Growth," *International Journal of Fatigue*, Vol. 7, pp. 159–164.
[5] Corlby, D. M. and Packman, P. F., "On the Influence of Single and Multiple Peak Overloads on Fatigue Crack Propagation in 7075-T6511 Aluminum," *Engineering Fracture Mechanics*, Vol. 5, 1973, pp. 155–169.
[6] Schijve, J., "Observations on the Prediction of Fatigue Crack Growth Propagation Under Variable Amplitude Loading," *Fatigue Crack Growth under Spectrum Loads, ASTM STP 595*, R. P. Wei and R. I. Stephens, Eds., American Society for Testing and Materials, 1976, pp. 3–23.
[7] von Euw, E. F. J., Hertzberg, R. W., and Poberts, R., "Delay Effects in Fatigue Crack Propagation," *Stress Analysis and Growth of Cracks, ASTM STP 513*, Part I, American Society for Testing and Materials, 1972, pp. 230–259.
[8] Suresh, S., "Micromechanisms of Fatigue Crack Growth Retardation Following Overload," *Engineering Fracture Mechanics*, Vol. 21, 1983, pp. 453–463.
[9] Elber, W., "Fatigue Crack Closure Under Cyclic Tension," *Engineering Fracture Mechanics*, Vol. 2, 1970, pp. 37–45.

[10] Elber, W., "The Significance of Fatigue Crack Closure," *Damage Tolerance in Aircraft Structures, ASTM STP 486,* American Society for Testing and Materials, 1971, pp. 230–242.
[11] Kikukawa, M., Jono, M., and Tanaka, K., "Fatigue Crack Closure Behavior at Low Stress Intensity Level," *Proceedings,* 2nd International Conference on Mechanical Behavior of Materials, 1796, Special Volume, pp. 254–277.
[12] Kikukawa, M., Jono, M., Tanaka, K., and Kondo, Y., "Fatigue Crack Propagation and Crack Closure Behavior Under Varying Loading Conditions," *Proceedings,* 4th International Conference on Fracture, 1977, pp. 1109–1116.
[13] Kikukawa, M., Jono, M., and Kondo, Y., "An Estimation Method of Fatigue Crack Propagation Rate Under Varying Loading Conditions of Low Stress Intensity Level," *Advances in Fracture Research,* D. Francois, Ed., Pergamon Press, Oxford, U.K., 1981, pp. 1799–1806.
[14] Jono, M., Song, J., and Kikukawa, M., "Fatigue Crack Growth and Crack Closure of Structural Materials Under Random Loadings," *Proceedings,* 6th International Conference on Fracture, 1984, pp. 1735–1742.
[15] Jono, M. and Sugeta, A., "Elastic-Plastic Fatigue Crack Growth Behavior Under Varying Loading Conditions," *Role of Fracture Mechanics in Modern Technology,* G. C. Sih, H. Nisitani, and T. Ishihara, Eds., 1987, pp. 339–350.
[16] Jono, M., Song, J., and Sugeta, A., "Prediction of Fatigue Crack Growth and Crack Closure Under Nonstationary Random Loading," *Proceedings,* 4th International Conference on Structural Safety and Reliability, Part I, 1985, pp. 465–474.
[17] Jono, M. and Sugeta, A., "Estimation Method of Elastic-Plastic Fatigue Crack Growth Rates Under Variable Amplitude Loadings," *Japan Society of Mechanical Engineers International Journal,* Vol. 38, 1995, pp. 355–363.
[18] Jono, M. and Sugeta, A., "Crack Closure and Effect of Load Variation on Small Fatigue Crack Growth Behavior," *Fatigue and Fracture of Engineering Materials and Structures,* Vol. 19, 1996, pp. 165–174.
[19] Yoder, G. R., Cooley, L. A., and Crooker, T. W., "Fatigue Crack Propagation Resistance of Beta-Annealed Ti-6Al-4V Alloys of Differing Interstitial Oxygen Contents," *Metallurgical Transaction A,* Vol. 9A, 1978, pp. 1413–1420.
[20] Wanhill, R. J. H., Galatolo, R., and Looiji, E. W., "Fractographic and Microstructural Analysis of Fatigue Crack Growth in a Ti-6Al-4V Fan Disc Forging," *International Journal of Fatigue,* Vol. 11, 1989, pp. 407–416.
[21] Raichandran, K. S., "Near Threshold Fatigue Crack Growth Behavior of a Titanium Alloy: Ti-6Al-4V," *Acta Metallurgica,* Vol. 39, 1991, pp. 401–410.
[22] Rhodes, C. G., Chesnutt, J. C., and Wert, J. A., "Influence of Transformed Beta Microstructures on Fatigue Crack Growth Rates in Ti-6Al-4V," *Microstructure, Fracture Toughness and Fatigue Crack Growth Rate in Titanium Alloys,* A. K. Chakrabarti and J. C. Chesnutt, Eds., The Metallurgical Society, 1987, pp. 39–54.
[23] Jones, R. E., "Fatigue Crack Growth Retardation After Single-cycle Peak Overload in Ti-6Al-4V Titanium Alloy," *Engineering Fracture Mechanics,* Vol. 5, 1973, pp. 585–604.
[24] Powell, B. E. and Duggan, T. V., "Crack Growth in Ti-6Al-4V Under the Conjoint Action of High and Low Cycle Fatigue," *International Journal of Fatigue,* Vol. 9, 1987, pp. 195–202.
[25] Ward-Close, C. M. and Ritchie, R. O., "On the Role of Crack Closure Mechanisms in Influencing Fatigue Crack Growth Following Tensile Overloads in a Titanium Alloy: Near Threshold Versus Higher ΔK Behavior," *Mechanics of Fatigue Crack Closure, ASTM STP 982,* American Society for Testing and Materials, 1988, pp. 93–111.
[26] Budiansky, B. and Hutchinson, J. W., "Analysis of Closure in Fatigue Crack Growth," *Journal of Applied Mechanics,* Vol. 45, 1978, pp. 267–276.
[27] Dugdale, D. S., "Yielding of Steel Sheets Containing Slits," *Journal of the Mechanics and Physics of Solids,* Vol. 8, 1960, pp. 100–108.

C. Hsu,[1] K. K. Chan,[1] and J. Yu[1]

Effects of Thickness on Plasticity-Induced Fatigue Crack Closure: Analysis and Experiment

REFERENCE: Hsu, C., Chan, K. K., and Yu, J., **"Effects of Thickness on Plasticity-Induced Fatigue Crack Closure: Analysis and Experiment,"** *Advances in Fatigue Crack Closure Measurement and Analysis: Second Volume, ASTM STP 1343,* R. C. McClung and J. C. Newman, Jr., Eds., American Society for Testing and Materials, West Conshohocken, PA, 1999, pp. 285–303.

ABSTRACT: The crack-opening stress was measured using a strain gage technique on 7050 aluminum alloy, under constant amplitude and repeated overload. The behavior of crack-opening stress predicted by Newman's FASTRAN-II is consistent with the experimental results for repeated overload. It is also found that the FASTRAN-II program is capable of predicting crack growth on the 7050-T76 aluminum plate and 7050-T7452 aluminum hand forging under complex simulated flight loading which contains a significant number of compression cycles.

KEYWORDS: fatigue crack closure, crack opening stress, aluminum forging, compression cycles, strain gage

Nomenclature

c'	Half rack length
r	Notch radius
B	Plate thickness
S_{max}	Maximum applied stress
S_{min}	Minimum applied stress
S_{op}	Crack-opening stress
W	Width of plate
α	Thickness constraint factor
ρ	Plastic zone size
σ_O	Flow stress
ω	Compressive plastic zone size
ΔK_{eff}	Effective stress intensity factor range
Δ_{strain}	Incremental strain
Δ_{stress}	Incremental stress
μ	ΔK_{eff} transition coefficient
σ_{ol}	Overload stress
σ_{ca}	Constant cyclic stress

Since Elber's discovery of crack closure in the wake of a fatigue crack [*1,2*], many attempts have been made to analyze the crack-closure phenomena using finite element models [*3,4*], to quantitatively determine crack-opening stress experimentally for a variety of materials [*5*], or to develop analytical crack closure models using Dugdale-Barenblatt's ideally plastic model ahead of crack tip [*6*].

[1] The Boeing Company, Long Beach, CA.

Most of these works were performed using simplified constant-amplitude loading, which is not directly applicable to practical aircraft design problems that engineers are facing every day. Newman [7] incorporated the modified Dugdale-Barenblatt model into a simplified 1-D strip-yield model at the crack tip, which can be used to compute the crack-opening stress based on the plastic deformation along the crack surface as a result of the crack propagation under cyclic loading. A schematic diagram illustrating Newman's crack closure model under maximum and minimum stress is shown in Fig. 1. Since Dugdale's plastic zone model was originally derived for the plane-stress condition only, Newman introduced a constraint factor, α, to account for the influence of stress state on the tensile yielding at the crack front. For plane-stress conditions, α is equal to unity (Dugdale's model); and for simulated plane-strain conditions, α is equal to 3. For other problems not predominated by the plane-stress or plane-strain condition, it is necessary to determine the effects of the thickness by fitting the α factor to experimental results. The primary objective of this paper is to evaluate Newman's crack-closure model and the application program FASTRAN-II [8] against experimental results under simulated flight loads.

The evaluation was performed in three steps. The first step was to establish a technique that can be used to measure the crack-opening stress accurately. Gan and Weertman [9] had successfully employed strain gage and COD gage techniques to determine the crack-closure stress of a thin and narrow 7050-T76 aluminum plate from the plots of local strain versus nominal stress during unloading. However, the accuracy of their method is highly dependent on whether the first deviation point from linearity to nonlinearity in the strain-stress plot can be clearly determined. In most cases, the deviation points are indistinguishable unless the strain gages are located just behind the crack tip. It also requires a number of strain gages placed in the path of the crack in order to determine the closure stress while the crack was propagating. The present technique allows more accurate measurement with fewer strain gages. The second step was to evaluate FASTRAN-II's crack-opening stress pre-

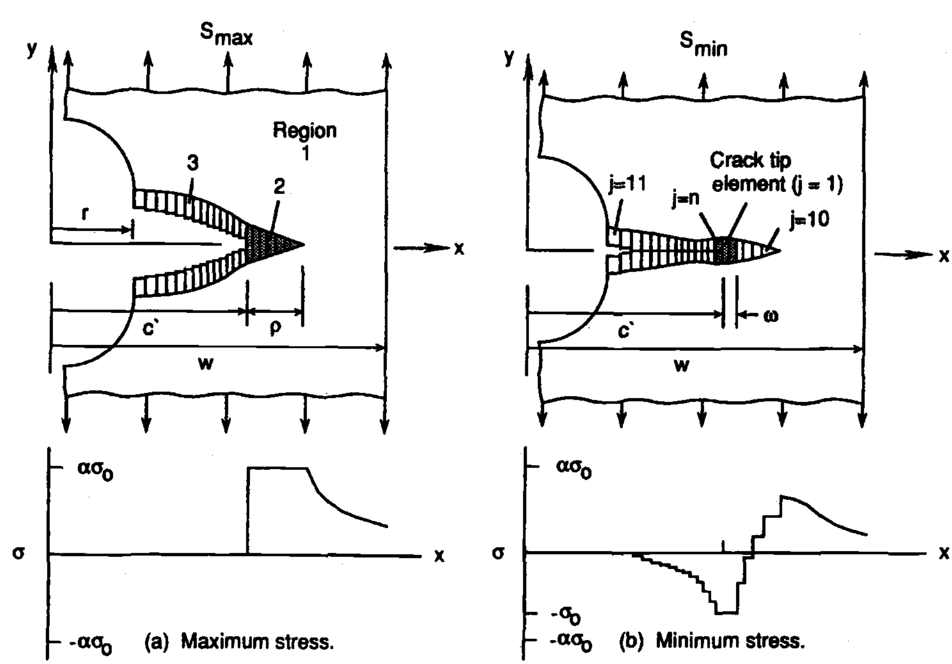

FIG. 1—*Schematic of Newman's crack-closure model showing crack surface displacement and stress distribution under cyclic loading.*

diction under constant-amplitude loads with repeated overload. The findings then will be used to assess FASTRAN-II for more complex spectrum loading. The third step was to compare FASTRAN-II's prediction of crack growth under realistic aircraft flight loads which contain a significant number of compression cycles. It is commonly known that compression cycles can eliminate the overload's retardation effects or cause acceleration in crack growth [*10*]. Many nonclosure-based crack growth models are incapable of giving reasonable predictions for such types of loading.

Experimental Method

Measurement of Crack Opening Stress

Middle tension, M(T), test specimens were used for the crack-opening stress measurement tests. The specimens were 76.2 mm wide by 356 mm long, made from a 6-mm-thick 7050-T76 aluminum plate with the grain direction parallel to the applied load. The subject material has a yield strength of 472 MPa and ultimate strength of 524 MPa. A 6.4 mm diameter hole was drilled at the center of the plate and EDM notches of 2.54 mm in length were introduced at both sides of the hole. The surfaces of the specimen, adjacent to the path of the crack, were polished and markers were inscribed at 2.54 mm intervals starting at 12.7 mm from the centerline such that the crack propagation can be accurately measured with a pair of 30-power traveling microscopes located on each side of the specimen. The tests were conducted in laboratory dry air at room temperature condition. Pre-cracking was performed using constant-amplitude stress of 62.7 MPa maximum and a stress ratio of 0.05 until sharp crack tips were visible at both ends of the notches. Following the pre-cracking procedure, constant amplitude cyclic loads consisting of blocks of 2500 cycles at a maximum of 62.7 MPa and stress ratio of 0.05 were applied. The test was paused at the end of each block to allow measurement of the crack length and application of the overload. When the half crack length approached 12.7 mm, the specimens were removed from the test machine and one strain gage was installed between the 6.4 mm and 15.2 mm markers, Gage A, and another one between the 17.8 mm and 20.3 mm markers, Gage B. Both gages are located just below the crack path. The strain gages were of EA-13-125BZ-350 type and the grid area was approximately 1.57 mm wide by 1.57 mm long. The grid of the gage was normal to the crack path. After the strain gages installation, the test continued until the crack reached a desired length. At that point, a single cycle of overload was applied gradually to the specimen and the readouts of the strain gages along with the applied loads were scanned and recorded continuously onto a computer diskette at a rate of 1000 samples per second. The stress survey procedure was repeated at several crack lengths and also before and after the overload. Figure 2 depicts the test setup and the close-up view of the test specimens.

Crack Growth Under Simulated Flight Loads

A total of three M(T) test specimens were subjected to simulated spectrum loading. One was machined from a 6.4 mm thick 7050-T76 aluminum plate and the other two specimens were machined from a 16 cm × 41 cm × 122 cm 7050-T7452 aluminum hand forging block. The first specimen was about 30.5 cm wide by 61.0 cm long and the other two were 9.5 cm wide by 41 cm long and thickness of 6.4 mm and 12.7 mm, respectively. All specimens had the grain direction parallel to the applied load. A notch of 0.25 mm to 0.50 mm wide and 12.7 mm long was introduced at the center of the specimen via EDM. An anti-buckling guide was placed over the first specimen to prevent lateral deformation under compression loads, as shown in Fig. 3. The test setup for the forging specimens is shown in Fig. 4. The specimens were pre-cracked at maximum stress of 103 MPa until the crack tips were visible from both sides of the notch. Then, the pre-cracking procedure continued with reducing loads to avoid retardation effects resulting from the large plastic zone ahead of the crack tip. Following the pre-cracking procedure, a simulated flight load sequence was applied. The simulated flight load consisted of variable-amplitude cycles representing the stress sequence in an aircraft structure

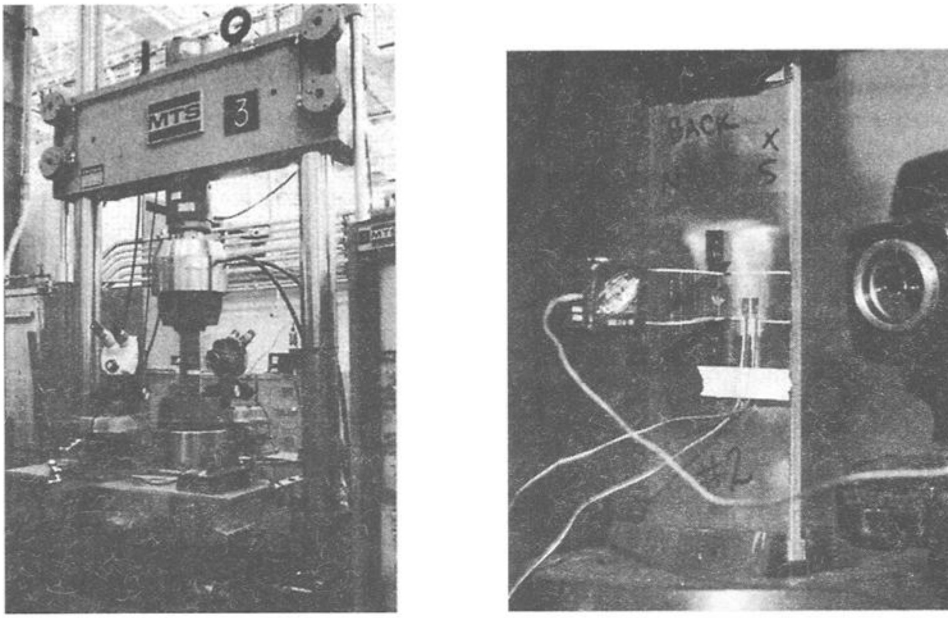

(a) Test Setup

(b) Test Specimen

FIG. 2—*Test setup and specimen with strain gages at the crack path and crack opening displacement gage at the center of the plate.*

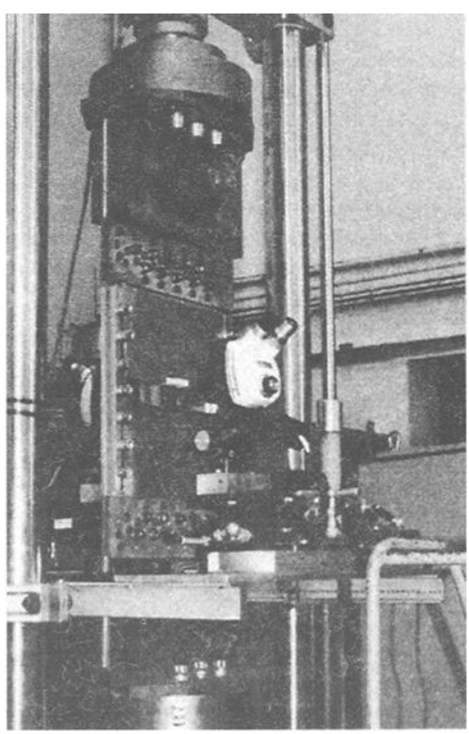

FIG. 3—*Test setup and specimen for 7050-T76 Al plate under simulated flight loads.*

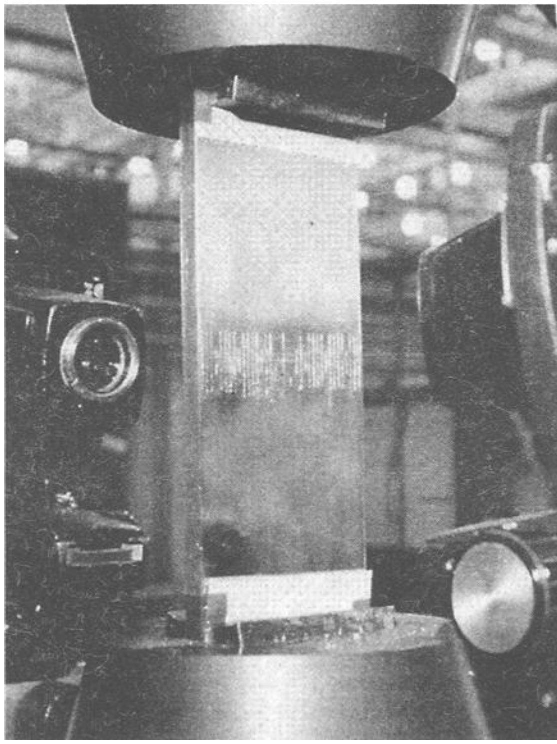

FIG. 4—*Test specimen of 7050-T7452 aluminum hand forging under simulated flight load.*

that experiences significant numbers of fully reversed loads. The crack propagation was measured periodically until failure of the specimen occurred.

Experimental Results and Analysis

Measurement of Crack Opening Stress

Crack Opening Stress Under Constant-Amplitude Loads—The test specimen was subject to a constant-amplitude cyclic load, maximum stress of 62.7 MPa and stress ratio of 0.05. Three strain surveys were taken when: (1) the crack tip was approaching the strain gage, (2) the crack tip reached the center of the strain gage, and (3) the crack tip just passed strain gage. The strain-stress curves of the surveys are shown in Figs. 5*a* and 6*a*. The deviation point from linearity to nonlinearity was not distinguishable in all cases. However, from the plots of $\Delta_{strain}/\Delta_{stress}$ (slope of the strain-stress curve) versus applied nominal stress, as shown in Figs. 5*b* and 6*b*, the deviation points of linearity became more pronounced. The deviation point is defined as the transition point at which $\Delta_{strain}/\Delta_{stress}$ becomes constant. The running average of $\Delta_{strain}/\Delta_{stress}$ were used in the plots, instead of $\Delta_{strain}/\Delta_{stress}$ at a data point, to avoid oscillation caused by the run-off errors in the recorded data. The results show that this technique can be used to determine the crack-opening and closure-stress as long as the strain gage is located near the wake of crack. The effective stress ratio from the test results was compared with the FASTRAN-II's predictions using variable thickness constraint factors [7] and constant constraint factor [7] as shown in Fig. 7. Since the strain gage can only be used to measure surface strain, the experimental results are consistent with FASTRAN-II's prediction for near plane-stress condi-

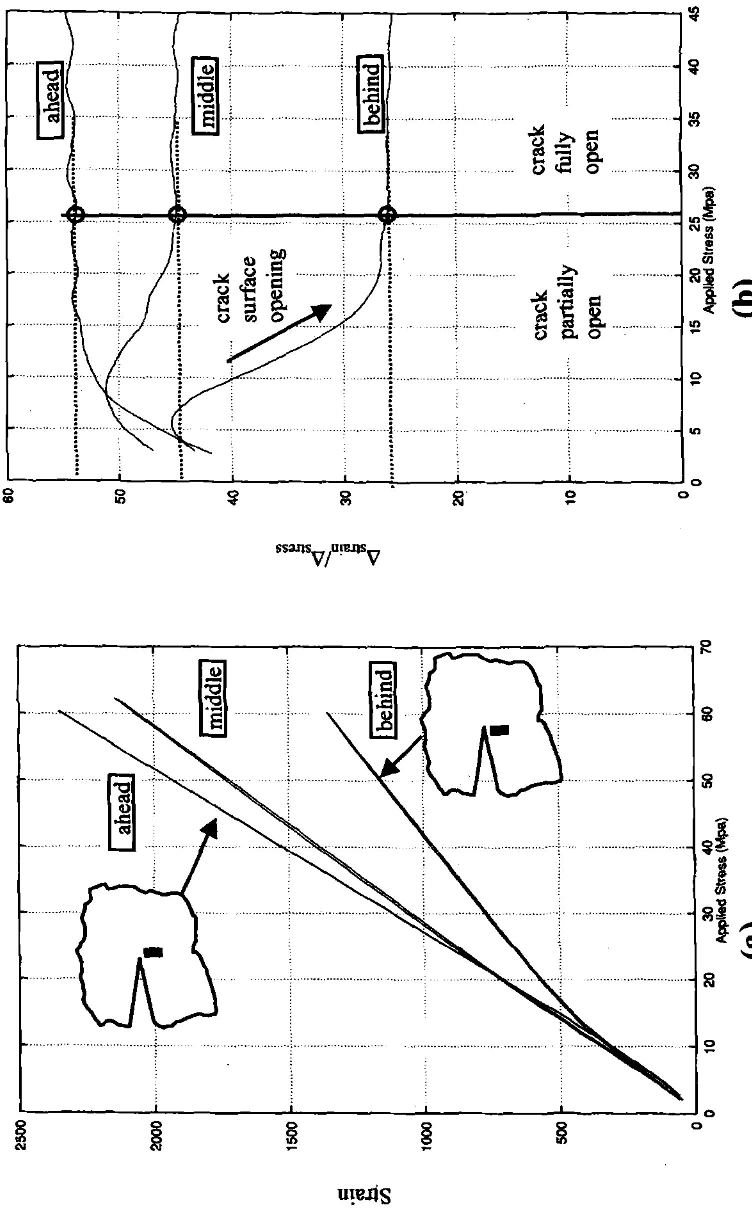

FIG. 5—(a) *Local strain vs. nominal stress,* (b) $\Delta_{strain}/\Delta_{stress}$ *vs. nominal stress at Gage A.*

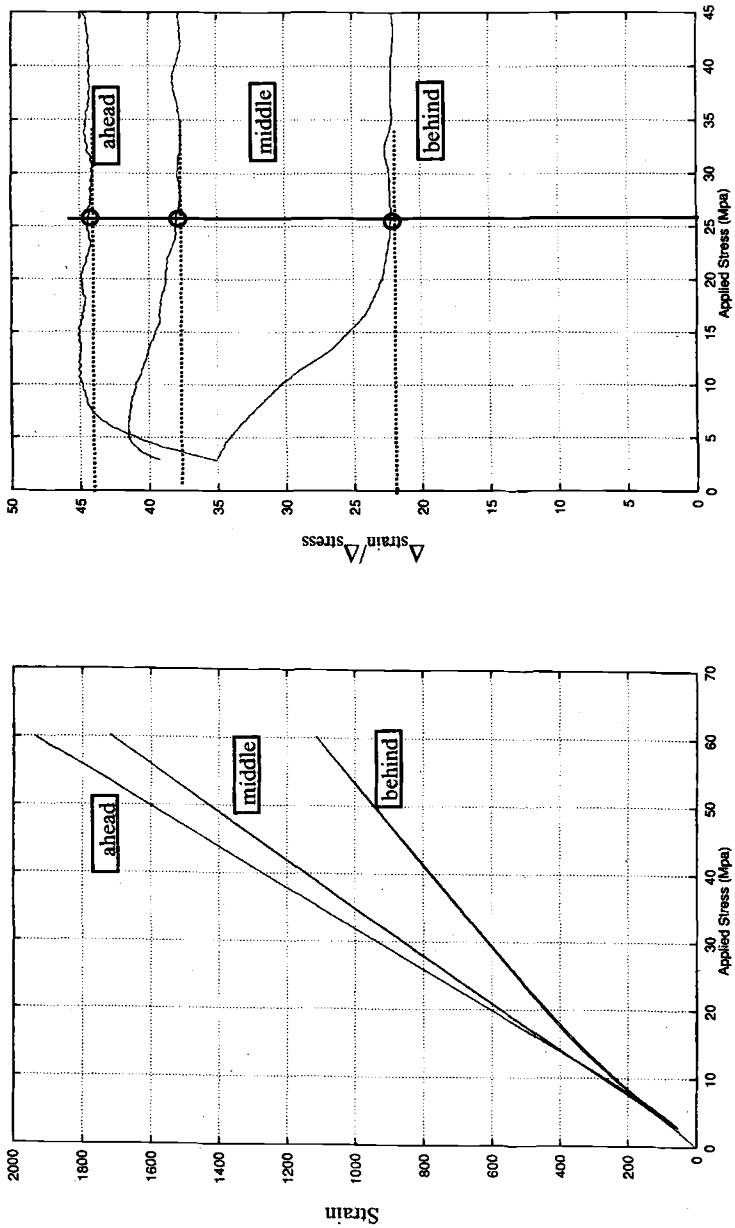

FIG. 6—(a) *Local strain vs. nominal stress,* (b) $\Delta_{\text{strain}}/\Delta_{\text{stress}}$ *vs. nominal stress at Gage B.*

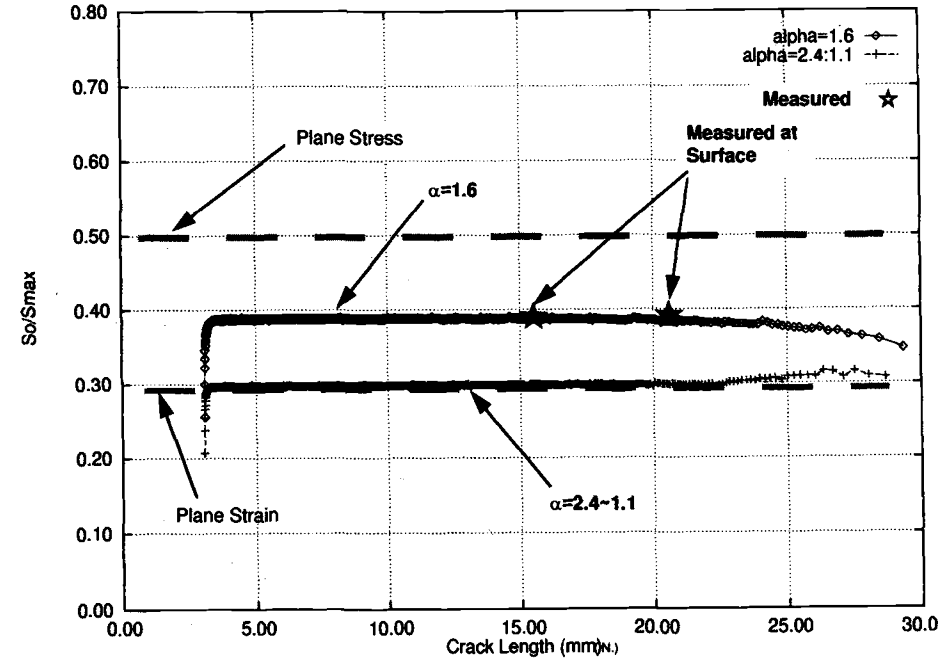

FIG. 7—*Comparison of crack-opening stress, experimental results vs. FASTRAN's using constant and variable α.*

tion, $\alpha = 1.60$. From Figs. 5 and 6, the crack length or the plastic zone size did not have significant effect on the present technique. The plots of COD versus applied stress did not show any clear sign of nonlinear-to-linear transition. It is believed that the COD gage was placed too far away, more than 12.5 mm from the crack tip, to detect any crack closure effect.

The Effects of Overload—One cycle of 150% overload was applied periodically at every 2500 constant-amplitude cycles as shown in Fig. 8. The constant-amplitude loading has a maximum stress of 62.7 MPa and a stress ratio of 0.05. The percentage of overload is defined as σ_{ol}/σ_{ca}, where σ_{ol} is the overload stress and σ_{ca} is the maximum stress of the constant-amplitude cycles. When the crack approached the strain gage, one cycle of overload was applied. Strain surveys were performed before and after application of overload and at 500 cycles and 1000 cycles thereafter. The experimental results show that the overload caused an immediate drop in S_{op}, see Figs. 9*a* and 10*a*, which implied

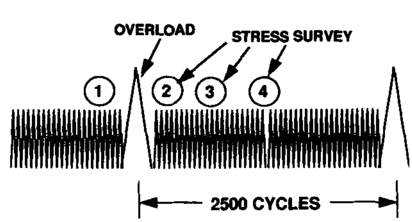

FIG. 8—*Load schedule for repeated spike overload test.*

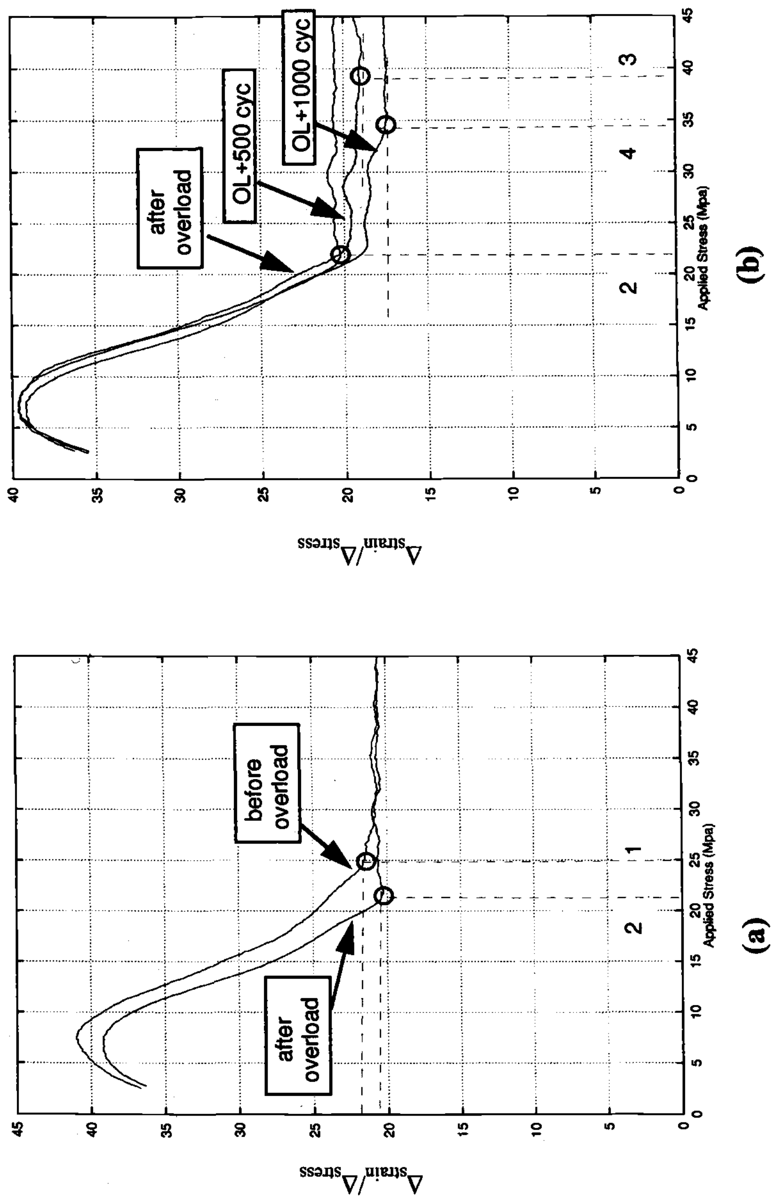

FIG. 9—*Measured crack-opening stress at Gage A (a) before and after overload, (b) 500 and 1000 cycles after overload spike.*

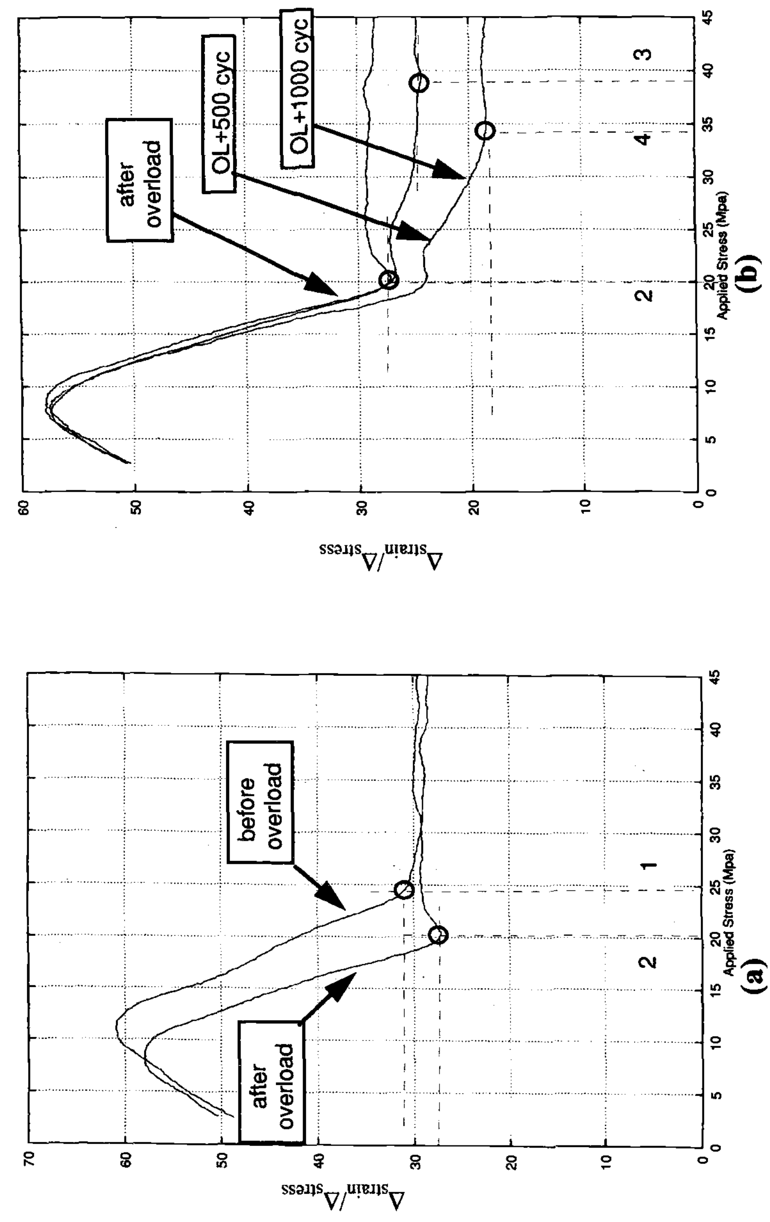

FIG. 10—*Measured crack-opening stress at Gage B* (a) *before and after overload,* (b) *500 and 1000 cycles after overload.*

that ΔK_{eff} would increase and the crack growth accelerate following the overload. The S_{op} in the figure is defined as stress at the first "kink" point or the lowest point of the curve. The decrease of the opening stress was also confirmed by the results of a 2-D finite element analyses with nonlinear material properties, which had showed that the crack surface could remain partially or completely open as a result of an overload. The FASTRAN-II predictions were consistent with the experimental results in terms of the trend of S_{op} for post-overload crack propagation. They both showed that the S_{op} recovered rapidly to a level that was higher than the normal S_{op} and then decreased to normal S_{op} level, as illustrated in Figs. 9*b* and 10*b*. The normal S_{op} is referred to here as the S_{op} under a constant-amplitude loading only. The increase in S_{op} and hence decrease in ΔK_{eff} causes an apparent slowdown in crack growth, which is consistent with the well known retardation effects after an overload. This delayed retardation effect has also been observed by Ward-close, Blom and Ritchie [*11*]. Figure 11 shows the FASTRAN-II's crack growth prediction, using variable $\alpha = 2.4$ to 1.1, and agrees well with the experimental results. The crack-opening stress of the experimental results was compared with the FASTRAN-II's prediction as shown in Fig. 12. It shows the trend of FASTRAN-II's crack-opening stress prediction is consistent with the experimental results. The difference in the magnitudes is due to the strain gage readouts that can only indicate the strain at the surface of the specimen while the analysis also considers the thickness constraint.

Crack Growth Under Simulated Flight Loads—The simulated flight load and its profile are shown in Fig. 13. The experimental results are compared with crack growth propagation predicted by FASTRAN-II as shown in Fig. 14 for 7050-T76 aluminum plates. The fatigue crack growth rate used in the prediction was converted from ΔK-based FCGR tests of ten specimens at a stress ratio ranging from $R = 1$ to $R = 0.80$. Figure 15*a* shows the convergence of FCGR using the computer program DKEFF [*8*] for $\alpha = 2.4$. The degree of convergence differs with other α factors. In general, FCGR

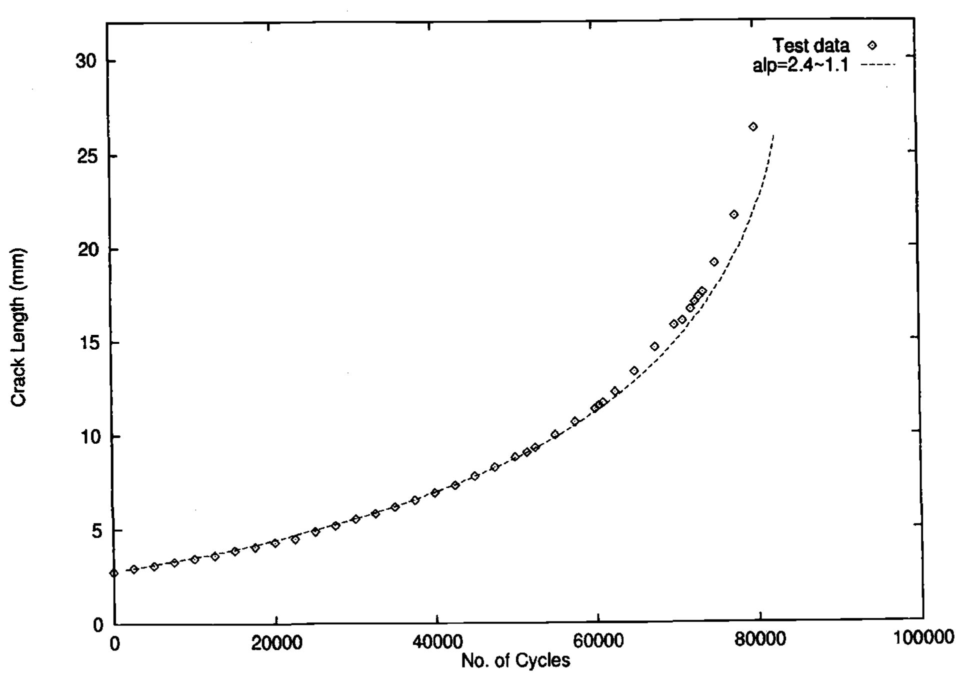

FIG. 11—*Experimental vs. FASTRAN-II on the crack growth with repeated overload spike.*

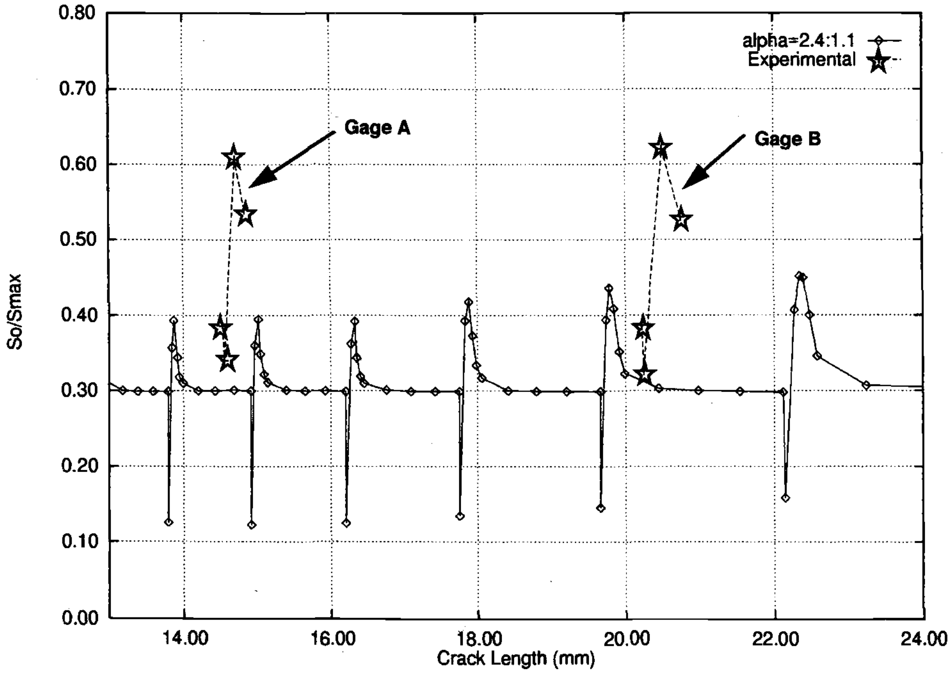

FIG. 12—*Experimental vs. FASTRAN-II on the crack-opening stress with repeated overload spikes.*

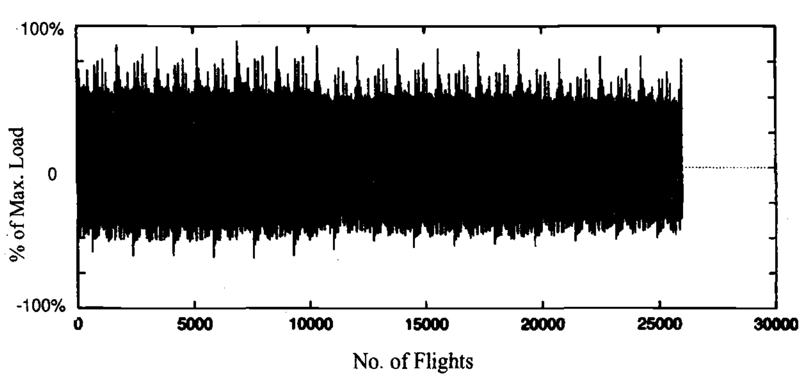

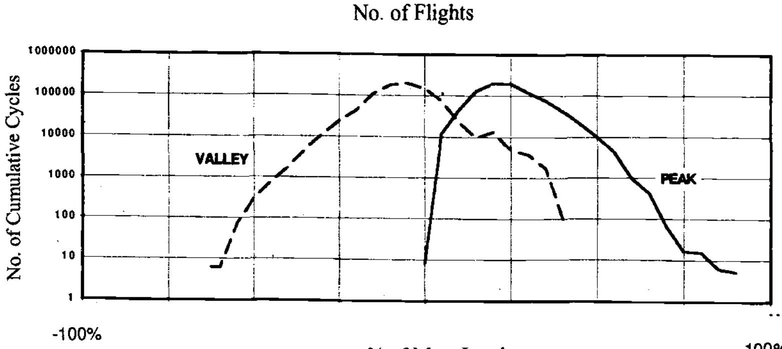

FIG. 13—*Schematic of simulated flight load sequence and profile of maximum and minimum stress which consists of significant number of fully reversal cycles.*

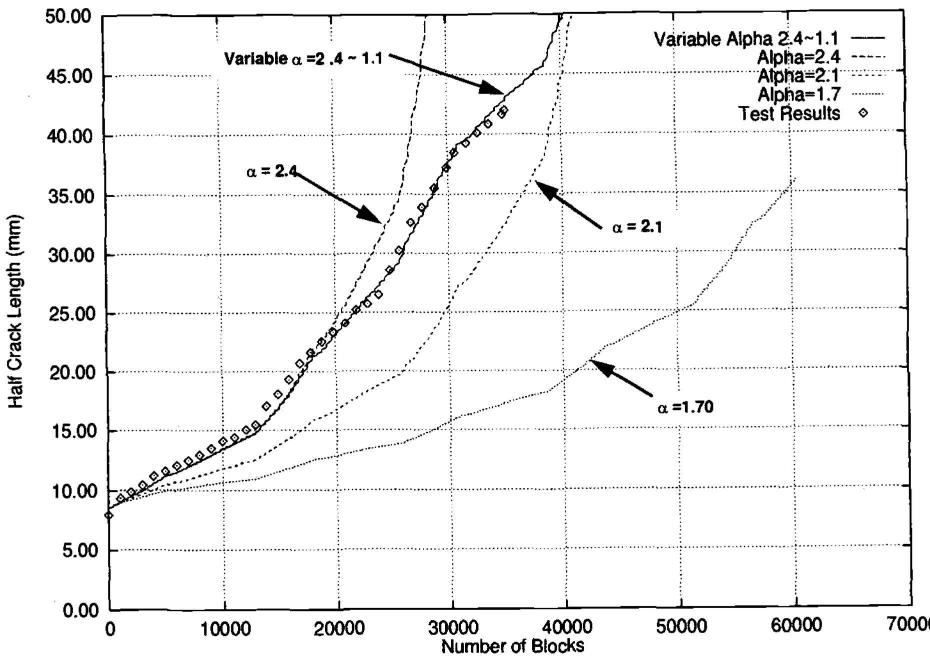

FIG. 14—*Comparison of crack growth for 7050-T76 aluminum plate under simulated flight loads.*

exhibits good convergence for α factor between 1.7 and 2.5. The FASTRAN-II prediction using best-fit FCGR of constant α factor shows that it is able to predict the crack growth life reasonably accurate using thickness constraint factor ranging from $\alpha = 2.1$ to $\alpha = 2.4$. However, experimental results show that the crack propagation was slower after it reached a certain size. This phenomenon has been discussed by Newman [*12*] and other researchers regarding the constraint variation associated with the flat-to-slant crack growth behavior or shear-lip development. Newman predicted loss of constraint would occur when a crack grows from a small size, a plane-strain prevailing condition, to a larger size where the plastic-zone size becomes large compared to the plate thickness, a plane-stress prevailing condition. Schijve [*13*] discovered that such a transition occurred at nearly the same FCGR over a wide range in stress ratios for aluminum alloys. He proposed that such a transition should be controlled by ΔK_{eff}, since FCGR is a function of ΔK_{eff}. Based upon this theory and experimental results, Newman allows the constraint factor to change as a function of ΔK_{eff}. He derives a simple equation to determine the ΔK_{eff} at the beginning of transition as follows [*12*]:

$$(\Delta K_{\text{eff}})_T = \mu \sigma_o B^{1/2}$$

where σ_0 is the flow stress of the material, μ is the transition coefficients determined from the test, and B is the plate thickness. Substituting the parameters of test specimen, $\sigma_0 = 498$ MPa, $\mu = 0.50$ and $B = 6.35$ mm into the equation, we obtained $(\Delta K_{\text{eff}})_T \approx 19.8$ MPa*m$^{1/2}$. This transition point is consistent with the results of using trial-and-error to determine the lower and upper bound of transition: for *da*/*dn* less than 1.27×10^{-3} $^{\text{mm}}/_{\text{cyc}}$, $\alpha = 2.4$, for *da*/*dn* greater than 1.01×10^{-1} $^{\text{mm}}/_{\text{cyc}}$, $\alpha =$ 1.10, which gave the best correlation. The FCGR of variable constraint factors is shown in Fig. 15*b*. However, after close examination of the cracked surface of the test specimen, as shown in Fig. 16, it revealed only a small amount of shear-lip near the edge of the crack surface. This experiment demon-

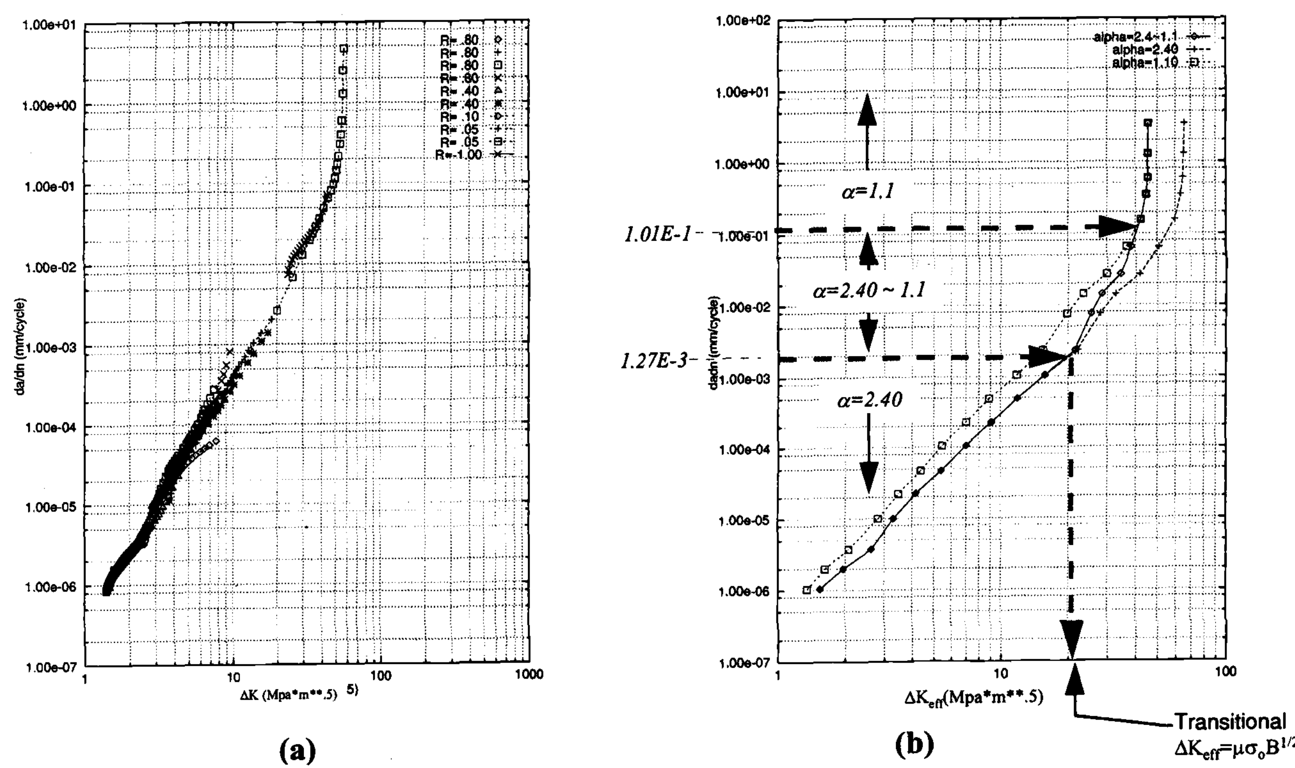

FIG. 15—*Crack growth rate for 7050-T76 aluminum plates,* (a) *FCGR vs.* ΔK_{eff} *with* $\alpha = 2.4$ *and* (b) *best-fit?* $= 2.4$ *to* $\alpha = 1.1$ *and flat-to-slant transition point.*

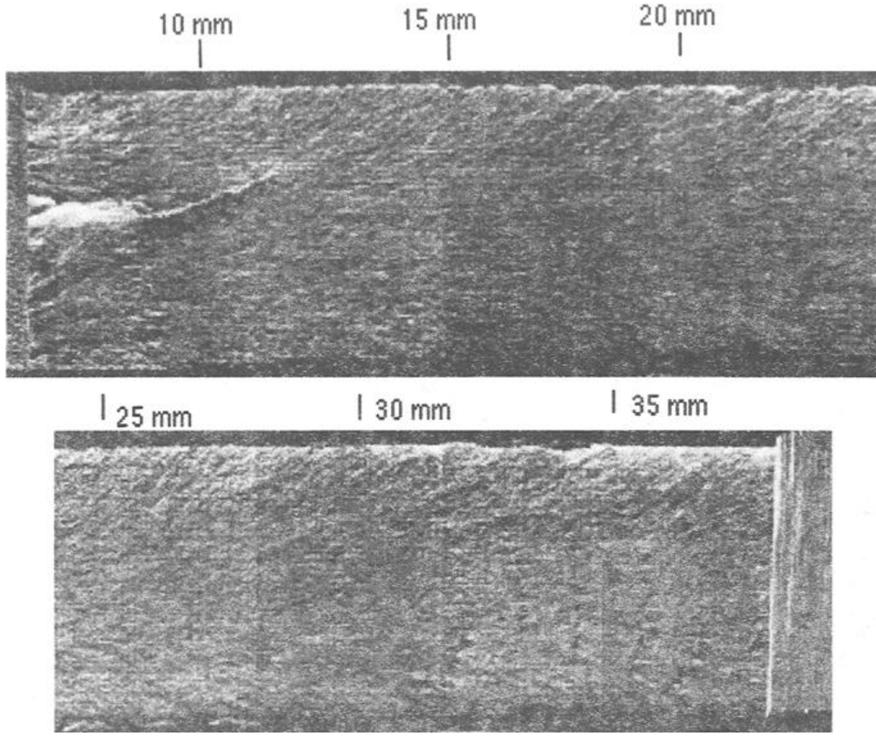

FIG. 16—*Fracture surface of 7050-T76 aluminum plate under simulated flight loads.*

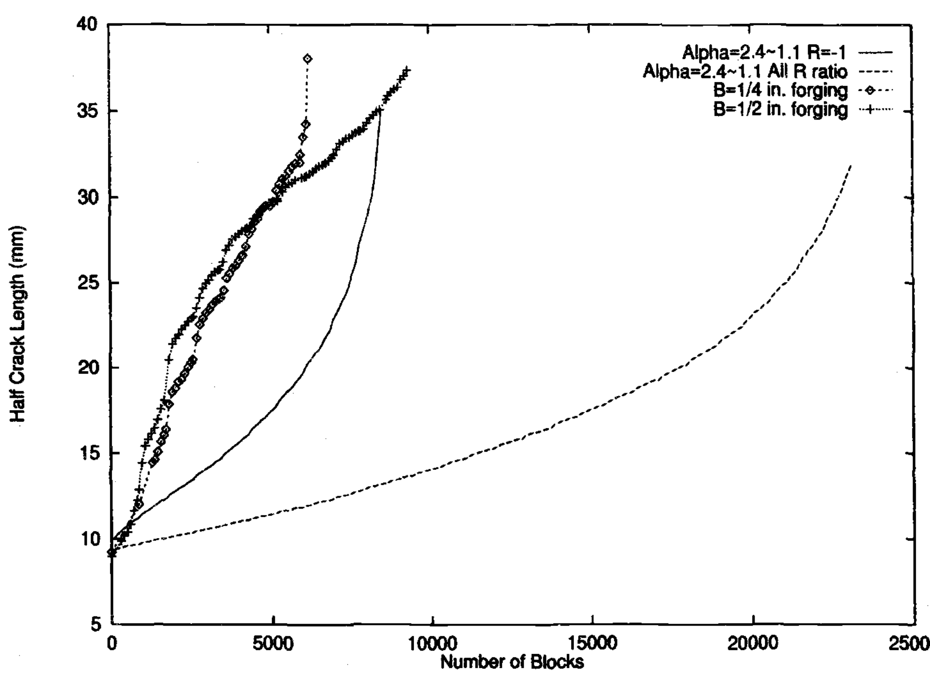

FIG. 17—*Comparison of crack growth for 7050-T7452 aluminum hand forging under simulated flight loads and FASTRAN's prediction using FCGR from all stress ratio and FCGR from* R = −*1.*

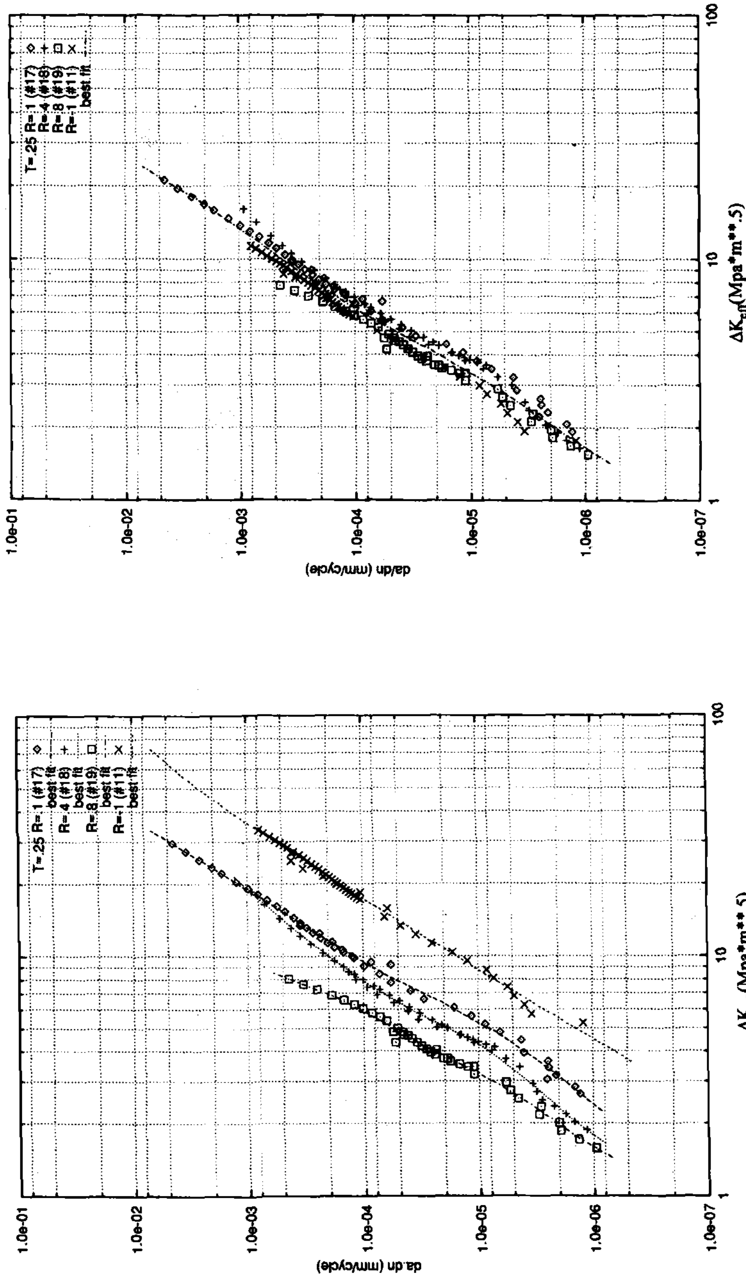

FIG. 18—*Crack growth rate of 7050-T7452 aluminum hand forging:* (a) *raw test data for various stress ratio;* (b) *converged closure-based crack growth rate using DKEFF program,* $\alpha = 2.4$ *shown.*

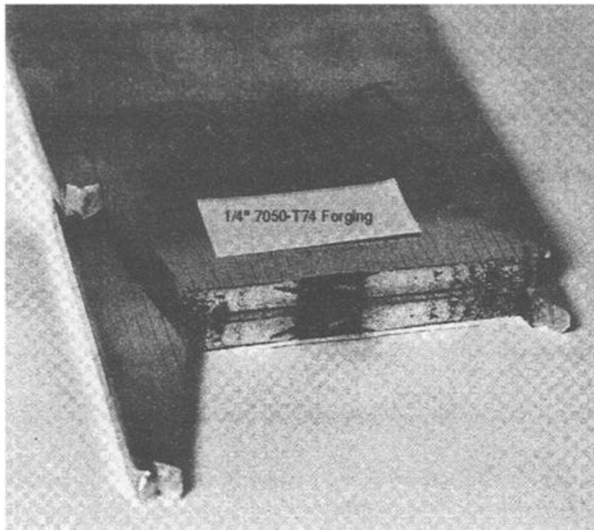

(a)

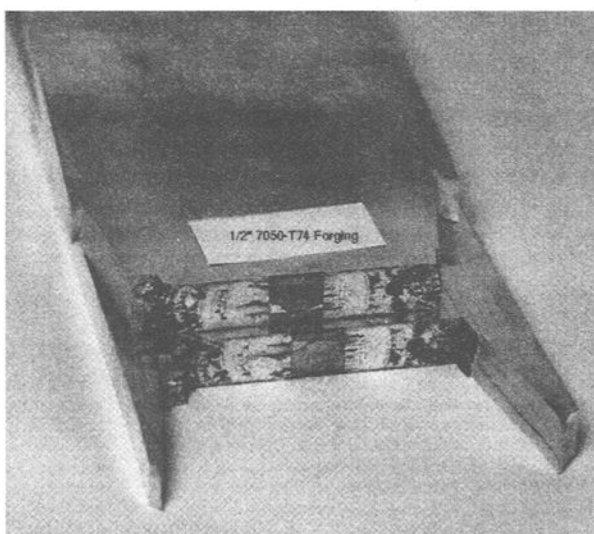

(b)

FIG. 19—*Fracture surface of 7050-T7452 aluminum hand forging under simulated flight loads:* (a) *6.3-mm-thick hand forging, and* (b) *12.6-mm-thick hand forging. Blackened surfaces indicate oxidization.*

strated the feasibility of using variable α and the capability of FASTRAN-II to predict crack growth for a wide specimen under a complex spectrum loading.

The crack growth experimental results of 7050-T7452 aluminum hand forging and FASTRAN-II prediction are shown in Fig. 17. Due to a higher level of applied stress for these two specimens, the fatigue lives were considerable less than that of the plate. The FCGR used in the analysis was derived from constant-amplitude tests of three C(T) specimens, $R = 0.10$, 0.40 and 0.80, and one M(T) specimen, $R = 1.0$. These specimens were obtained from the same forging block as the one used for simulated flight tests. Figure 18*a* shows the raw test data and Fig. 18*b* shows the convergence of the same FCGR using the DKEFF program with $\alpha = 2.4$. The FCGR converged into a narrow band but not as well as the plate as shown in Fig. 15*a*. The crack growth analysis, using variable α of 2.4 to 1.1, over predicted the fatigue lives by a factor of three. This discrepancy is attributed to the data selected to generate ΔK_{eff}-based FCGR. As shown in Fig. 18*b*, the FCGR for the $R = -1$ are slightly higher than the average FCGR that included other stress ratios. Since the simulated flight loads were predominately fully reversal cycles, it is logical just to use the $R = -1.0$ best-fit FCGR curve for crack growth prediction. With this, the FASTRAN-II was able to give a more reasonable prediction as shown in Fig. 17. However, the crack growth rate in experimental results is still significantly higher than the FASTRAN-II's prediction. The cause for this has not been thoroughly understood. It is believed that the residual stress in the hand-forging material resulting from the manufacturing process could have contributed to the rapid growth behavior when the crack is still small. The fracture surface of the specimens are shown in Fig. 19.

Conclusion

Based on the experimental results, the following conclusions are drawn:

1. The crack-opening and closure stress can be effectively measured from the $\Delta_{strain}/\Delta_{stress}$ versus stress plots of strain gages located near the crack tip for the plane-stress condition.
2. The test has verified the trend of the crack-opening stress following an overload.
3. Immediately following the overloads, the crack-opening stress is reduced; thus, the crack growth rate increases. Subsequently, the crack-opening stress will rise above the normal S_{op}, which leads to a crack growth retardation.
4. The thickness constraint factors used in the FASTRAN-II crack closure model will require an extensive test program to establish reliable values for practical applications.
5. A crack closure model to account for transition of plane-strain to plane-stress is imperative for variable-amplitude spectrum loading. Using variable-thickness constraint factors has proved to be useful for this application.
6. The FASTRAN-II model is capable of predicting crack growth with a reasonable degree of accuracy under variable-amplitude flight loading containing significant numbers of compressive loads.

Acknowledgments

The authors would like to acknowledge Mr. Charles Thrash and his staff at the Material and Process Technology Laboratory of Douglas Product Division, Boeing Aircraft Company, for supporting and conducting tests for this project.

References

[1] Elber, W., "Fatigue Crack Closure Under Cyclic Tension," *Engineering Fracture Mechanics,* Vol. 2, No. 1, July 1970, pp. 37–45.
[2] Elber, W., "The Significance of Fatigue Crack Closure," *Damage Tolerance in Aircraft Structures, ASTM STP 486,* American Society for Testing and Materials, 1971, pp. 230–242.
[3] Newman, J. C., Jr., "A Finite Element Analysis of Fatigue Crack Closure," *Mechanics of Crack Growth, ASTM STP 590,* American Society for Testing and Materials, pp. 281–301.
[4] Ogura and Ohji, K., "FEM Analysis of Crack Closure and Delay Effect in Fatigue Crack Growth Under Variable Amplitude Loading," *Engineering Fracture Mechanics,* Vol. 9, 1977, pp. 471–480.
[5] Katcher, M. and Kaplan, M., "Effects of R Factor and Crack Closure on Fatigue Crack Growth for Aluminum and Titanium Alloys," *ASTM STP 559,* American Society for Testing and Materials, 1974, pp. 264–282.

[6] Budiansky, B. and Hutchinson, J. W., "Analysis of Closure in Fatigue Crack Growth," *Journal of Applied Mechanics*, ASME, Vol. 45, American Society of Mechanical Engineers, 1978, pp. 267–276.

[7] Newman, J. C., Jr., "A Crack-Closure Model for Predicting Fatigue Crack Growth Under Aircraft Spectrum Loading," *ASTM STP 748*, American Society for Testing and Materials, 1981.

[8] Newman, J. C., Jr., "FASTRAN-II, A Fatigue Growth Structural Analysis Program," NASA Technical Memorandum No. 104159, 1992.

[9] Gan and Weertman, J., "Crack Closure and Crack Propagation Rates in 750 Aluminum," *Engineering Fracture Mechanics*, Vol. 15, No. 1–2, 1981, pp. 87–106.

[10] Dill, H. D. and Saff, C. R., "Analysis of Crack Growth Following Compressive High Loads Based on Crack Surface Displacements and Contact Analysis," *ASTM STP 637*, American Society for Testing and Materials, pp. 141–152.

[11] Ward-close, C. M., Blom, A. F., and Ritchie, R. O., "Mechanism Associated with Transient Fatigue Crack Growth Under Variable-Amplitude Loading: An Experimental and Numerical Study," *Engineering Fracture Mechanics*, Vol. 32, No. 4, 1989, pp. 613–638.

[12] Newman, J. C., Jr., "Effects of Constraints on Crack Growth Under Aircraft Spectrum Loading," The Specialist's Conference at Delft University of Technology, 1992.

[13] Schijve, J., "Shear Lips on Fatigue Fracture in Aluminum Alloy Sheet Material," Delft University of Technology, Report LR-287, Delft, The Netherlands, Sept. 1979.

A. Varvani-Farahani[1] *and T. H. Topper*[1]

Effect of Periodic Compressive Overstrain Excursions on Crack Closure and Crack Growth Rates of Short Fatigue Cracks—Measurements and Modeling

REFERENCE: Varvani-Farahani, A. and Topper, T. H., **"Effect of Periodic Compressive Overstrain Excursions on Crack Closure and Crack Growth Rates of Short Fatigue Cracks—Measurements and Modeling,"** *Advances in Fatigue and Crack Closure Measurement and Analysis: Second Volume, ASTM STP 1343,* R. C. McClung and J. C. Newman, Jr. Eds., American Society for Testing and Materials, West Conshohocken, PA, 1999, pp. 304–320.

ABSTRACT: A comparison of the growth of fatigue cracks under constant-amplitude straining and under strain histories having periodic compressive overstrains revealed that the fracture surface near the crack tip and the crack growth rate changed dramatically with the application of compressive overstrains. When the magnitude of compressive overstrains was increased, the height of the fracture surface irregularities was reduced as the increasing overstrain progressively flattened fracture surface asperities near the crack tip. The reduced asperity height was accompanied by a lower crack closure stress and a higher crack growth rate.

The fatigue strength was reduced by a factor that ranged from 1.24 at short lives (10^4 cycles) to 3.37 at long lives (10^7 cycles) when periodic compressive overstrains of near yield point magnitude were applied in uniaxial tests. The corresponding reductions in the fatigue strength for shear tests varied from 1.40 to 1.70.

A model of the plastic deformation of the fracture surface asperities at the crack tip (under periodic compressive overstrains) was developed to relate the crushing of the asperities to crack closure and crack growth rate. The model correlates the magnitude of the periodic compressive overstrain, the fracture surface asperity height, and the plastically flattened area to the fully effective strain intensity factor range (ΔK_{eff}) and its ratio to the range of strain intensity factor ($\Delta K_{(\varepsilon)}$) obtained from constant-amplitude straining, $U = \Delta K_{eff}/\Delta K_{(\varepsilon)}$.

For both uniaxial and shear fatigue straining, the strain range at a fatigue life of 10^7 cycles for constant-amplitude straining ($\Delta\varepsilon_{fl}$) and the effective strain range, ($\Delta\varepsilon_{eff.fl}$) at 10^7 cycles in the strain-equivalent life curve, obtained from strain histories containing periodic compressive overstrains, were used to calculate the U ratio ($U = \Delta\varepsilon_{eff \cdot fl}/\Delta\varepsilon_{fl}$). These values were close to those obtained from the model.

KEYWORDS: fatigue crack growth rate, crack closure, periodic compressive overstrain, fracture surface asperity, effective strain intensity factor range, the ratio of effective strain intensity factor

Nomenclature

$(da/dN)_{os}$ Fatigue crack growth rate of overstrains
$(da/dN)_{sm}$ Fatigue crack growth rate of small cycles

[1] Ph.D. student, Mechanical Engineering Department, and full professor, Civil Engineering Department, respectively, University of Waterloo, Waterloo, Ontario, N2L 3G1, Canada.

$(da/dN)_T$	Total fatigue crack growth rate
2α	Asperity tip angle
a	Crack depth
ε_A	Maximum lateral strain
A_i^1	Initial asperity contact area
A_f^1	Final asperity contact area
β	Ratio of cyclic to monotonic plastic zone size
B	A constant describing decay of total strain
c	Distance of asperity from crack tip
D	Grain size
D_{sm}	Damage due to small cycles n
D_{os}	Damage due to overstrain cycles
D_T	Total damage at failure
$\Delta\varepsilon$	Cyclic strain range
$\Delta\varepsilon_{fl}$	Fatigue limit strain range
$\Delta\varepsilon_{eff.fl}$	Effective fatigue limit strain range
$\Delta\gamma$	Cyclic shear strain range
d_i	Diameter of ith cylindrical element
ΔK_{th}	Threshold strain intensity factor range
ΔK_{eff}	Effective strain intensity factor range
ΔK_I	Uniaxial strain intensity factor range
ΔK_{II}	Shear strain intensity factor range
δ_{op}	Crack opening displacement
$\Delta\sigma$	Cyclic stress range
ε_a	Axial strain
ε_{cy}	Cyclic yield strain
ε_h	Hoop strain
ε_T^i	True strain of ith cylindrical element
ε_T	Total true strain
ϕ	Normalized x by initial height of asperity (h_0)
F_I and F_{II}	Shape factors for uniaxial and shear straining, respectively
E	Elastic modulus
$G = E/2(1 + \nu)$	Shear modulus
h_0	Initial height of asperity
h_f	Final height of asperity
h_0^i	Initial height of ith element
h_f^i	Final height of ith element
K_{max}	Maximum strain intensity factor
K_{op}	Opening strain intensity factor
λ	Shear strain ratio
ν	Poisson's ratio
N_T	Total number of cycles to failure
$N_{eq,sm}$	Equivalent number of small cycles
N_f	Number of cycles to failure in a CAS history
$N_{f,os}$	Number of overstrain cycles to failure
n_{os}	Number of overstrain cycles in a PCO history
n	Number of cycles between two overstrains
P_{max}	Maximum load
P_{op}	Opening load
Q	Surface strain concentration factor

ρ	Ratio of initial and final height of an asperity
R	Stress (strain) ratio
r_p^*	Cyclic plastic zone size
r_p	Monotonic plastic zone size
σ_y	Cyclic yield stress
U	Ratio of effective strain intensity factor range to range of strain intensity
η	A constant value of 0.00746
x	Instantaneous distance from tip to base of an asperity
CAS	Constant amplitude straining
CSLM	Confocal scanning laser microscopy
PCO	Periodic compressive overstrain history
SIF	Strain intensity factor range

Many investigations [1–5] have shown that, for both short and long fatigue cracks, periodic compressive overstrains of near-yield stress magnitude have a drastic accelerating effect on both crack initiation and crack propagation. At near-threshold stress intensities, these effects are thought to be due to a flattening of crack tip asperities by the high compressive stress which leads to a reduction in crack closure and an acceleration in crack growth. The results of Topper and Yu [1] showed that increased propagation rates and decreased threshold stress intensities accompanied the application of periodic compressive overstrains for various metals. Their findings also revealed crack opening stress levels below zero for large compressive overstrains. Similarly, Zaiken and Ritchie [6] proposed two mechanisms responsible for the decreased opening stress level: (i) the flattening of fracture surface asperities, and (ii) a change in the residual stresses ahead of the crack tip. However, they argued that the contribution of the residual stress ahead of the crack tip would not be significant.

In a previous paper [5], the present authors reported an investigation of the growth of short fatigue cracks under uniaxial constant-amplitude loading and load histories having periodic compressive overloads of various magnitudes. They found that the fracture surface near the crack tip and the crack growth rate changed dramatically with the magnitude of the compressive overload. The height of the surface irregularities reduced as the compressive overload increased and progressively flattened fracture surface asperities near the crack tip. This resulted in a reduced crack closure stress and a higher crack growth rate.

When a crack is subjected to a pure shear mode loading, its flanks are in contact and crack face interference reduces the amount of the applied strain intensity that is effective.

This paper examines the influence of periodic compressive overstrains on short fatigue crack growth and closure under uniaxial and shear fatigue straining in SAE 1045 steel. A model of the inelastic deformation of fracture surface asperities (at the crack tip) under compressive overstrains is developed. The model predicts the effective strain intensity factor range and $U = \Delta K_{\text{eff}}/\Delta K_{(\varepsilon)}$ ratio that are in good agreement with the experimental values.

Experimental Procedure

Material, Properties, and Specimen Design

The material examined in this investigation was an SAE 1045 steel in the form of 63.5 mm diameter bar stock with the following chemical composition (wt%): 0.46 C, 0.17 Si, 0.81 Mn, 0.027 P, 0.023 S, and the remainder Fe. This material is a medium carbon heat-treatable steel which is widely used in the automotive industry. The microstructure of the SAE 1045 steel after final polishing showed pearlitic-ferritic features containing up to 30 μm long sulfide inclusions in the rolling direction. The modulus of elasticity is 206 GPa, the cyclic yield stress is 448 MPa. Figure 1 shows the solid uniaxial and tubular biaxial fatigue specimens used in this study.

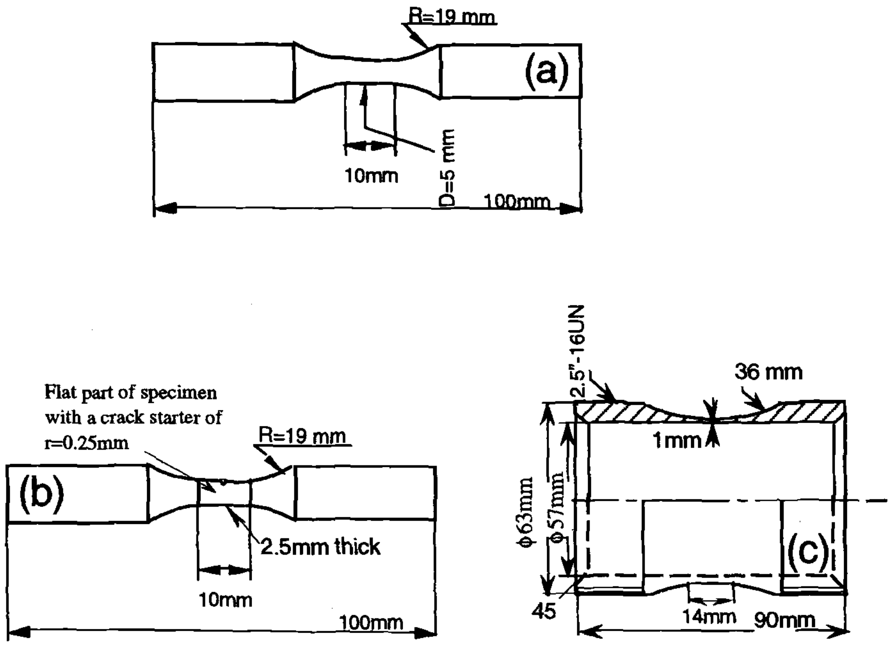

FIG. 1—*Specimen geometry:* (a) *uniaxial round specimen for fatigue life tests,* (b) *uniaxial plate specimen for crack growth tests, and* (c) *tubular specimen for biaxial fatigue life and crack growth tests.*

Fatigue Crack Tests

Uniaxial Fatigue Tests—Uniaxial fatigue crack growth rate and life tests were performed in strain control in an MTS servo-hydraulic test machine with a load-cell capacity of 111.20 kN. The crack growth tests under uniaxial constant-amplitude straining (CAS) were performed with a strain amplitude of ±0.075%. Periodic compressive overstrain crack growth tests were performed with compressive overstrains of −0.17%, −0.24%, and −0.38%. Each of these periodic compressive overstrains was followed by numbers of small cycles of 50, 200, 500, and 1000 in four separate tests [5]. Figure 2*a-b* illustrates the crack growth test strain histories for uniaxial constant-amplitude straining and a uniaxial strain history containing periodic compressive overstrains.

Shear Straining—A series of thin-walled tubular specimens was cyclically loaded in the axial direction in the strain frame while pressure was alternately applied to the inside and outside of the specimen during each cycle. The biaxial fatigue machine is described in Ref 7.

Constant amplitude shear tests and shear tests with strain histories containing periodic compressive overstrains (PCO) were performed in strain control at a frequency of 0.5 Hz, and zero mean strain ($R = -1$). The axial strain (ε_a) and transverse (hoop) strain (ε_h) were controlled to provide a 180° out-of-phase biaxial strain ratio of $\lambda = -1$ while the overstrain cycles were applied in-phase to produce a stress normal to the crack surface. Figure 2*c-d* presents the strain histories used for shear fatigue tests under constant amplitude straining and the histories having blocks of a periodic compressive overstrain followed by n small cycles. The number of small cycles per block ($n = D_{sm}N_f$) was adjusted to keep the overstrain damage ($D_{os} = n_{os}/N_{f,os}$) at about 20% of the total damage, $D_T = D_{sm} + D_{os}$,

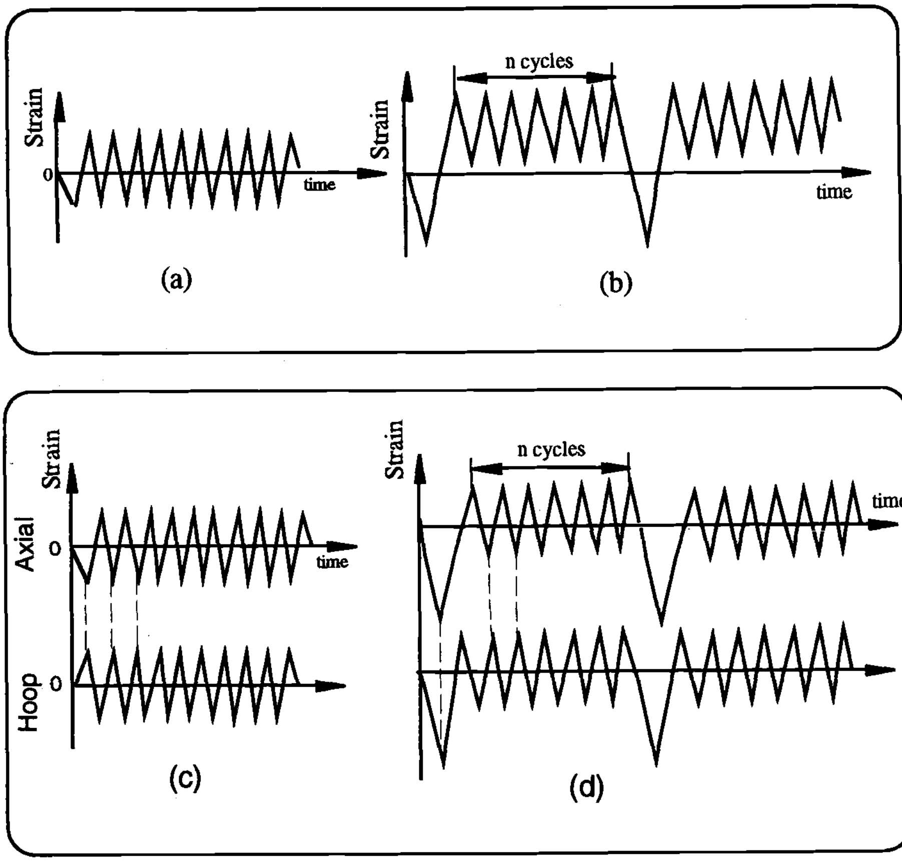

FIG. 2—*Fatigue block histories* (a) *uniaxial CAS,* (b) *uniaxial PCO,* (c) *shear CAS, and* (d) *shear PCO.*

where

n = number of small cycles between two overstrains,
D_{sm} = damage due to small cycles n,
N_f = number of cycles to failure in a CAS history,
$N_{f,os}$ = number of overstrain cycles to failure, and
n_{os} = number of overstrain cycles in a PCO history.

Uniaxial and Biaxial Shear Crack Depth and Crack Opening Measurements

Under uniaxial straining, a confocal scanning laser microscopy (CSLM) image processing technique was used to measure the crack depth of small cracks in the early stage of growth (Stage I) as the number of cycles increased. The CSLM system which is described in detail in previous studies [*8,9*] has a resolution of 0.25 μm. Crack growth in Stage II was measured on the surface of the plate specimen shown in Fig. 1*b* using an optical microscope with a $\times$500 magnification. Similarly, in shear straining fatigue crack lengths were measured using an optical microscope at the same intervals as the depth measurements were performed using CSLM.

Using a tensometer (tension machine) and a pressurizing device respectively for uniaxial and biaxial cracked specimens, cracked specimens were pulled to open the crack mouth under the CSLM system [9]. Then a laser beam was centered on the crack by direct observation through an attached optical microscope. The cracked specimen was scanned by the laser beam which was then reflected to a detector. Images from different levels of crack depth were obtained by changing the specimen height using a piezoelectric stage. A set of confocal image slices at depth steps of 1 μm was acquired. Post-image processing was later used to combine all the images. Optical sectioning using post-image-processed crack data provided the crack depth and the crack mouth width at every point along the crack length for each tensile stress/internal pressure. In fatigue crack growth tests under the strain histories presented in Fig. 2, the crack depth and crack length were measured at intervals of 1000 to 5000 cycles.

Fracture Surface Asperity Height Measurements

A fractographic examination of the fracture surface of short fatigue cracks was carried out after breaking the 1045 steel specimens in liquid nitrogen. The fracture surface and the variation in the height of asperities on the fracture surface were observed using a confocal scanning laser microscope. First, the laser beam was centered on the area of the fracture surface adjoining the crack tip by direct observation through an attached optical microscope. An area of 1 mm^2 of fracture surface at the crack tip was scanned by the laser beam and reflected to the detector. In order to make a three dimensional profile of fracture surface asperities, a piezoelectric stage, was used. The piezoelectric stage controls the distance between specimen and microscope. This provides successive images of level contours of the asperities from their peaks to their valleys. All images were combined to create an image of the configuration of the fracture surface profile. Taking different slices through this profile and determining an average value of fracture surface asperity height in each slice revealed that the asperity height is dramatically influenced by the magnitude of the compressive overstrain. In this study the fracture surface asperity heights of specimens under both constant-amplitude straining and strain histories containing periodic compressive overstrain cycles were measured. The CSLM measurements of the fracture surfaces of small cracks revealed that there was little variation of asperity heights across the fracture surfaces. The maximum variation of asperity height in an area of 1 mm^2 did not exceed 10%. The fracture surface asperity heights reported in the "Results" section of this study are the average values of asperity height measured on a 1 mm^2 area of the fracture surface.

Results and Discussion

Growth of Short Fatigue Cracks Under Constant-Amplitude Straining and Strain Histories Containing Compressive Overstrains

Strain intensity factor range values were calculated for a short fatigue crack under uniaxial straining using Eq 1*a*.

$$\Delta K_{\mathrm{I}} = F_{\mathrm{I}} Q \Delta\varepsilon \, E\sqrt{\pi a} \tag{1a}$$

Similarly, the strain intensity factor range was calculated for a semi-elliptical surface crack under shear using Eq 1*b:*

$$\Delta K_{\mathrm{II}} = F_{\mathrm{II}} Q \Delta \, \gamma \, G\sqrt{\pi a} \tag{1b}$$

The strain concentration factor Q is a function of crack size and grain diameter D which is given by

Eq 2 [10]

$$Q = 1 + 5.3 \exp\left(-\alpha \frac{a}{D}\right) \tag{2}$$

where α/D is used as a constant which fits the maximum threshold strain $\Delta\varepsilon_{th\,max}$ to the fatigue limit strain range $\Delta\varepsilon_{fl}$; $\Delta\varepsilon_{th}$ is given by

$$\Delta\varepsilon_{th} = \frac{\Delta K_{th}}{F\,Q\,E\sqrt{\pi a}} \tag{2a}$$

In Eq 2*a*, for uniaxial straining and pure shear straining, the shape factor F corresponds to F_I and F_{II}, respectively.

Crack Growth Measurements

Uniaxial Fatigue Crack Growth Tests—Crack length and depth for uniaxial straining crack growth tests were obtained as the number of cycles increased using CSLM for Stage I cracks and a ×500 optical microscope for crack length measurements in Stage II growth. The ratio of crack depth to half crack length was obtained in 1045 steel for short fatigue crack lengths of the order of 125 to 250 μm using CSLM [5]. Aspect ratios of cracks which experienced fatigue straining just above the fatigue limit stress were found to be approximately 0.80. Using the CSLM technique, the crack depth profile (in Stage I crack growth) was also found to be semi-elliptical in shape. The crack depth of short fatigue cracks versus the number of cycles under constant-amplitude straining and under three periodic compressive overstrain levels is plotted in Fig. 3*a*. This figure shows that the decrease in fatigue life when the compressive overstrain is increased from −0.17% to −0.24% is much greater than that for an increase of compressive overstrain from −0.24% to −0.38%. To grow a crack to a 1 mm depth, a test with −0.17% overstrain cycles requires 8000 blocks (50 × 8000 = 400 000 cycles) while the tests with −0.24% and −0.38% overstrains correspond to about 1800 and 1500 blocks, respectively. In this regard, Kemper et al. [11] and Tack and Beevers [12] observed a similar saturation effect in which increases in compressive overstrain beyond a certain level did not result in additional increases in crack growth rate. Figure 3*b* shows that as the magnitude of periodic compressive overstrain increases, the height of fracture surface asperity reduces significantly:

$$\frac{h_f}{h_o} = 1.17 - 1.05\left(\frac{|\varepsilon_{pco}|}{\varepsilon_{cy}}\right) \tag{3}$$

Biaxial Shear Tests—Crack growth rate data were obtained from biaxial specimens subjected to shear constant-amplitude straining and to strain histories containing in-phase periodic compressive overstrains with a magnitude of −0.3% after every n small strain cycles.

Crack opening stress measurements and crack depth measurements for shear fatigue cracks ($\lambda = -1$) made using confocal scanning laser microscopy (CSLM) image processing of the crack profile showed that, for the periodic compressive overstrains used, cracks were fully open at zero internal pressure. Therefore, there was no crack face interference. Crack depths used for calculating crack growth rate were taken at the deepest point at the shear crack profile.

Crack Growth in Terms of Effective Strain Intensity

The crack growth rate for the small cycles in the uniaxial and shear PCO test histories was obtained by subtracting the crack growth due to the periodic overstrain cycles from the growth per block due

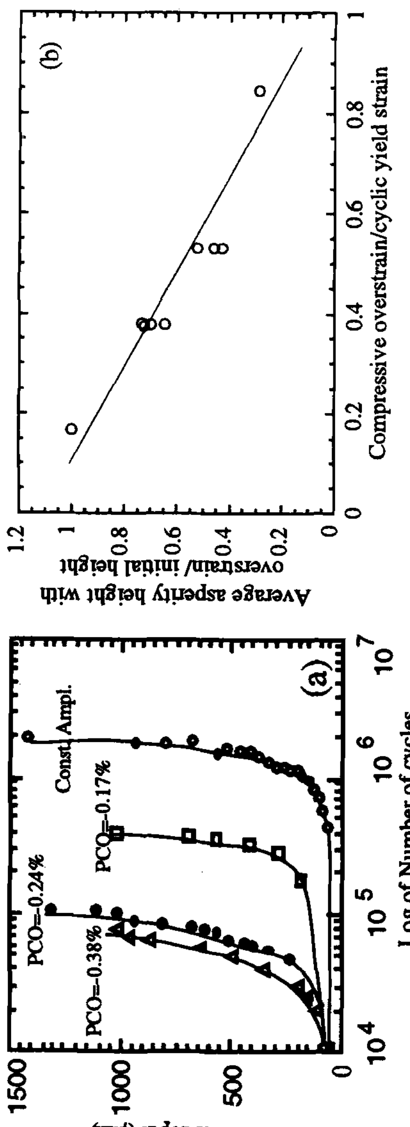

FIG. 3—*(a) Crack growth behavior under CAL and various PCO histories, and (b) asperity height versus various PCO magnitudes.*

to the periodic compressive overstrains plus the n small cycles and dividing by the number of small cycles per block.

$$\left(\frac{da}{dN}\right)_{\rm sm} = \frac{(n+m)\left(\frac{da}{dN}\right)_{\rm T} - m\left(\frac{da}{dN}\right)_{\rm os}}{n} \tag{4}$$

where n is the number of small cycles between two overstrains in a PCO block history, and m is the number of overstrain cycles in a PCO block history.

Under uniaxial straining, PCO cycles increase the portion of the fatigue cycle that is effective. The number of small cycles between overstrains was chosen so that the crack opening stress remained below the minimum stress throughout a block and all of the small cycles were fully effective. The crack growth rate data for small cycles calculated using Eq 4 is plotted in Fig. 4.

Under shear straining, CSLM observations showed that the application of a -0.3% compressive overstrain crushed the fracture surface asperities and resulted in fully open crack growth with no crack face interference. Thus, the full range of applied strain intensity was effective. Figure 4 also plots crack growth data for PCO shear tests versus the effective strain intensity factor range obtained using Eq 1*b*. The ratio $U = \Delta K_{\rm eff}/\Delta K_{(\varepsilon)}$ at a crack growth rate of 10^{-7} μm/cycles for both uniaxial and shear tests is 0.28 and 0.56, respectively (see Fig. 4).

Fatigue Life

Strain amplitude-equivalent fatigue life data plotted in Fig. 5*a* show that the fatigue strength is reduced by a factor that ranged from 1.24 at short lives to 3.37 at long lives when periodic compressive

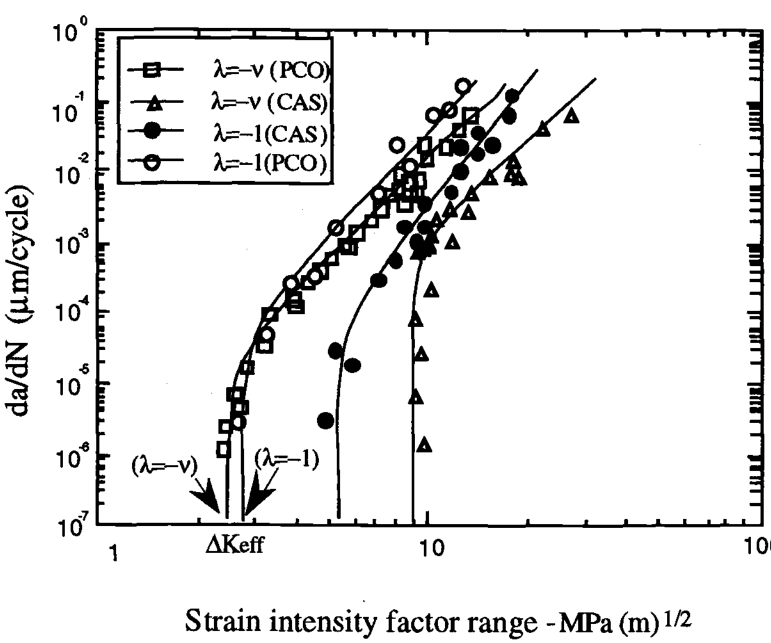

FIG. 4—*Strain intensity factor range versus crack growth rates for constant-amplitude uniaxial and shear fatigue straining under both CAS and PCO histories.*

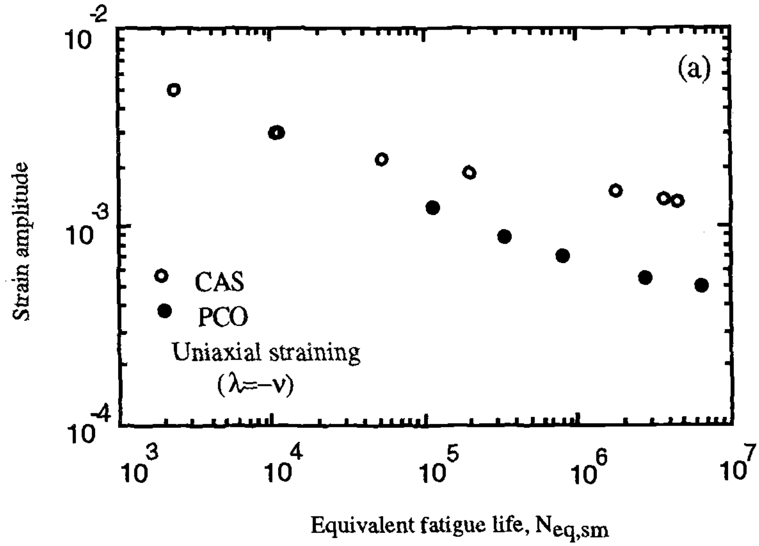

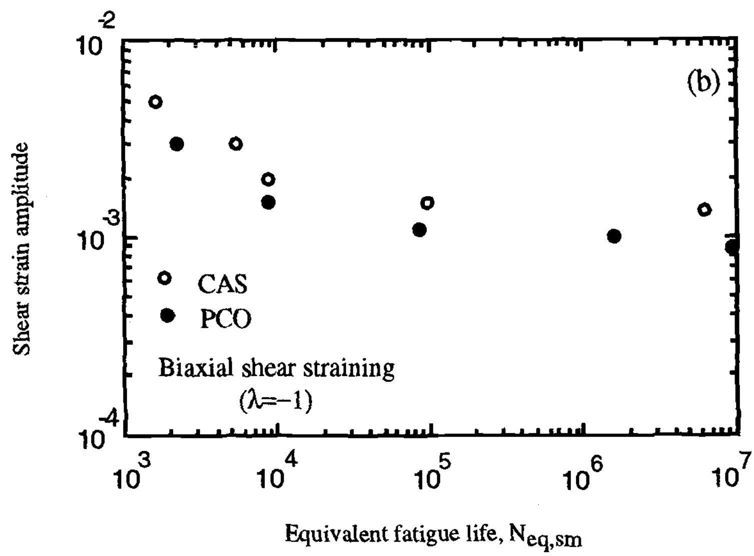

FIG. 5—*Fatigue life data under uniaxial and shear fatigue straining.*

overstrains of near yield point magnitude are applied in uniaxial tests. The corresponding reductions in the shear fatigue strength vary from 1.40 to 1.70 (Fig. 5*b*). The equivalent number of small cycles, $N_{eq,sm}$, for PCO histories was calculated from Eq 5:

$$N_{eq,sm} = N_T\left(1 - \frac{1}{n}\right)\Bigg/1 - \left(\frac{N_T}{n\,N_{f,os}}\right) \tag{5}$$

where N_T is the total number of cycles to failure.

For both uniaxial and shear fatigue straining, the ratios of strain ranges ($U = \Delta\varepsilon_{\text{eff-fl}}/\Delta\varepsilon_{\text{fl}}$) at an equivalent fatigue life of 10^7 cycles were found to be 0.32 and 0.55, respectively.

Fractography of Fracture Surface Asperities

Under constant-amplitude shear straining, the fracture surface profile obtained using CSLM revealed that a part of the crack flanks close to the crack mouth is smoother than the area at the crack tip. This fact also was confirmed by scanning electron microscopy (SEM) examination. The closure of the rough surface at the tip of the crack (in the interior of material) is due to an interlocking of small asperities.

An SEM examination of the fracture surfaces of specimens found that for the strain histories with a periodic compressive overstrain, mismatch asperities were plastically crushed. Figures 6*a* and 6*b* are the SEM fractographs of a specimen subjected to in-phase shear PCO of −0.3% followed

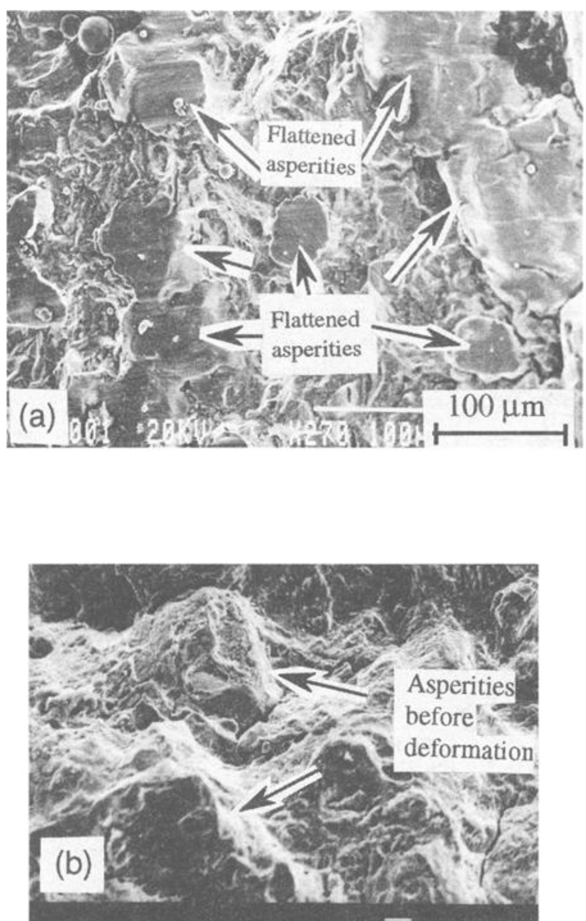

FIG. 6—*SEM photos of* (a) *flattened fracture surface asperity due to PCO shear straining, and* (b) *fracture surface asperity under a CAS shear history.*

by 19 small shear strain cycles with a strain amplitude of 0.15% and of a specimen that experienced CAS shear fatigue straining of 0.15% amplitude, respectively. A noticeable feature on the flattened asperities on the fracture surface of the in-phase PCO tests is the parallel abrasion lines. The deduction that these lines are induced by the abrasion between the crack flanks due to the compressive overstrain is substantiated by the observation that parallel lines are formed in the same direction in all flattened areas. A dramatic reduction in crack closure stress and an increase in crack growth rate were associated with a decrease in the asperity height due to the compressive overstrains.

Fracture Surface Asperities and Crack Closure

The SEM and CSLM observations of the fracture surface near the crack tip on the fatigued surface of both uniaxial and biaxial specimens revealed that asperities were approximately cone-shaped during constant amplitude straining. When overstrains were applied the height of the cone decreased and the apex widened but the base diameter changed only slightly because each asperity is constrained by its neighbors [*13*]. Figure 7 illustrates the original geometry of the asperities and the profile after the application of compressive overstrains for uniaxial and shear fatigue straining, respectively. CSLM image processing of the fracture surface in an area immediately behind the fatigue crack tip was used to measure the height of asperities for constant-amplitude straining and for periodic compressive overstrains of −0.17%, −0.24%, and −0.38% (followed by 50 small fatigue cycles). Asperity height decreased from 28 μm in constant-amplitude straining to 18, 13, and 8 μm for −0.17%, −0.24%, and −0.38% overstrains, respectively. The average initial height of the asperities at the deepest point of a crack for a constant-amplitude shear strain of ±0.08% was 90 to 100 μm, which reduced to 40 to 50 μm after the application of a periodic compressive overstrain of −0.3%.

Figure 8 gives a schematic presentation of the shape of an asperity before and after the application of a compressive overstrain (see Fig. 7). To simplify the analysis, the final shape of the asperity was assumed to be a cylinder. To calculate the total true strain, the initial and final shape of the asperity was divided into j elements (see Fig. 8). The initial height of each element shown in Fig. 8*a* was set equal to 1 μm. The diameter of a cylindrical element $(i + 1)$ of the initial asperity shape was $d_{(i+1)} = d_i + 2h_i \tan\alpha$ where 2α is the asperity tip angle.

For the asperity volume to be conserved, the volume of every element in the initial shape of the asperity has to be equal to the volume of the corresponding element in the final shape of the asperity.

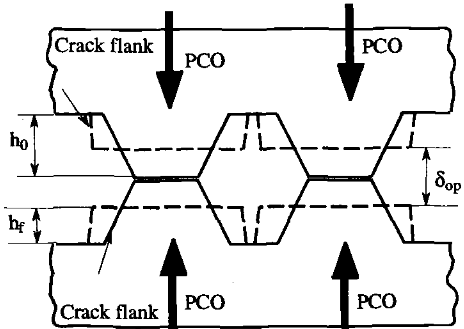

FIG. 7—*Schematic presentation of fracture surface asperities before (solid line) and after (dashed line) deformation due to PCO cycles.*

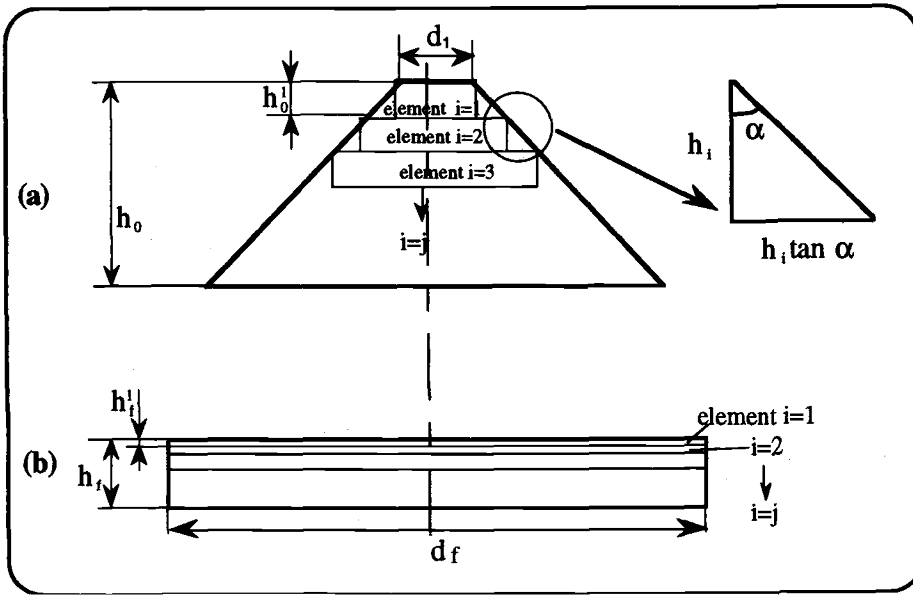

FIG. 8—*Shape of a single asperity* (a) *before, and* (b) *after the application of PCO.*

The true strain of the ith cylindrical element of the asperity is

$$\varepsilon_T^i = \ln \frac{h_0^i}{h_f^i} \tag{6}$$

where h_0^i and h_f^i are the initial and final height of the ith element, respectively.

The results of calculations of the true strain of elements from the tip to the base of a single asperity are given in Fig. 9. The variation in true strain from the tip to the base of the asperity as shown in Fig. 9 can be described by an exponential function

$$\varepsilon_T = \varepsilon_A \exp\left(-B\frac{x}{h_0}\right) \tag{7}$$

where ε_A is the maximum lateral strain calculated as the natural logarithm of the ratio of the initial (A_i^1) to final contact area (A_f^1) of an asperity and the parameter B is a constant that describes the decay of total strain as x/h_0 increases. The value of ε_T decreases exponentially as shown in Fig. 9.

Under uniaxial straining, a compressive overstrain of -0.38% led to a flattening of roughness asperities and therefore a reduction in closure stress. Similarly, Henkener et al. [*14*], Herman et al. [*15*], and Hertzberg et al. [*16*] also showed that a low closure stress (due to compressive loads) is associated with the crushing of asperities in the crack wake. This reduction in closure stress increased when the magnitude of the compressive overstrain increased. The PCO cycles increased the portion of the strain cycle that was effective. The number of small cycles was chosen so that the crack opening stress remained below the minimum stress and the whole strain cycle was effective.

For shear straining ($\lambda = -1$), CSLM observations showed that the application of a -0.3% compressive overstrain crushed the fracture surface asperities and resulted in fully open crack growth with no crack face interference. Crack opening stress results obtained using CSLM image processing of

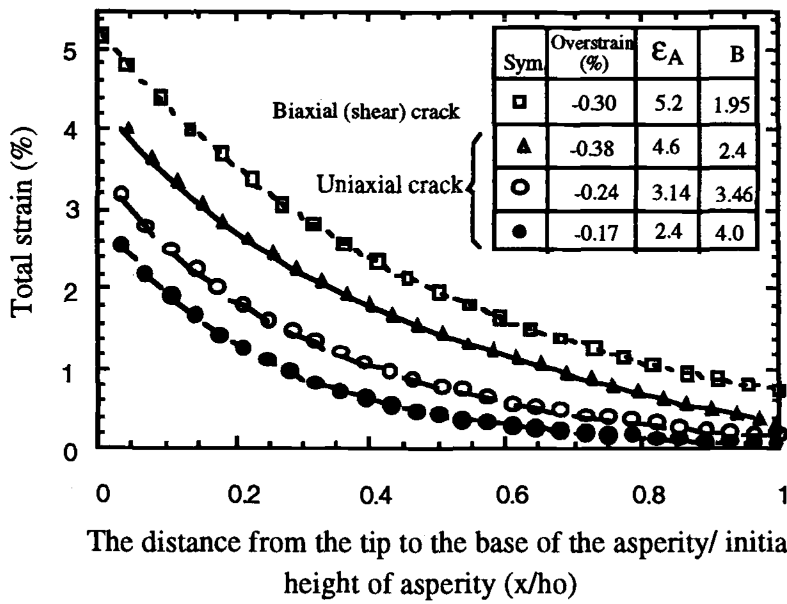

FIG. 9—*Exponential variation of strain versus* x/h_0 *under a compressive overstrain.*

the crack profile revealed that cracks were open at zero static stress for the periodic compressive overstrain histories.

The difference between the asperity heights before (h_0) and after (h_f) the application of the compressive overstrains produces a gap between the two crack flanks. This gap is due to inelastic deformation of the asperities which can be defined physically as

$$\delta_{op} = \phi(2h_0 - 2h_f) = 2\phi\, h_0(1 - \rho) \tag{8}$$

where $\phi = x/h_0, x = h_0 - h_f, \rho = h_f/h_0$ and therefore $\phi = (1 - \rho)$.

Equation 8 can be rewritten as

$$\delta_{op} = 2\phi^2\, h_0 \tag{9}$$

Substituting h_0 from Eq 7 into Eq 9 we have

$$\delta_{op} = 2\phi^2 \left(\frac{B\,x}{\ln(\varepsilon_A/\varepsilon_T)}\right) \tag{10}$$

An expression for the cyclic crack opening displacement of a fatigue crack initially presented by Rice [17] and then applied to small cracks by Lankford et al. [18] is

$$\delta_{op} = \frac{2(1-\nu)}{G\,\sigma_y}\left[\frac{1 - P_{op}/P_{max}}{1 - R}\right]^2 \left(\frac{\sigma_y}{\Delta\sigma}\right)^2 \left(\frac{r_p^*/c}{1 + r_p^*/c}\right)(\Delta K)^2 \tag{11}$$

where r_p^* is the cyclic plastic zone. The cyclic plastic zone can also be expressed as a fraction of the monotonic plastic zone size, r_p, i.e., ($r_p^* = \beta\, r_p$), where for short cracks $\beta = 0.50$ [18]. Since for small cracks the ratio of the monotonic plastic zone size to the distance of an asperity from the crack tip is unity, $r_p/c = 1$, [*18*]. Hence

$$\delta_{op} = \frac{4(1-\nu)(1+\nu)}{E\sigma_y}\left[\frac{1 - P_{op}/P_{max}}{1-R}\right]^2 \left(\frac{\sigma_y}{\Delta\sigma}\right)^2 \left(\frac{\beta}{1+\beta}\right) (\Delta K)^2 \tag{12}$$

Equating the right-hand sides of Eq 10 and Eq 12, we have

$$2\phi^2\,\eta\left(\frac{B\,x}{\ln(\varepsilon_A/\varepsilon_T)}\right) = \frac{4(1-\nu^2)}{E\,\sigma_y}\left[\frac{1 - P_{op}/P_{max}}{1-R}\right]^2 \left(\frac{\sigma_y}{\Delta\sigma}\right)^2 \left(\frac{\beta}{1+\beta}\right) (\Delta K)^2 \tag{13}$$

Constant η is directly dependent to the magnitude of PCO and the ratio h_f/h_0. In Eq 13 constant η correlated crack opening displacements obtained from CAS and PCO histories. Since $P_{op}/P_{max} = K_{op}/K_{max}$ [*19*], Eq 13 can be rewritten as

$$\phi^2\,\eta\left(\frac{B\,x}{\ln(\varepsilon_A/\varepsilon_T)}\right) = \frac{2(1-\nu^2)}{E\,\sigma_y}\left[\frac{\Delta K_{eff}}{(1-R)\,K_{max}}\right]^2 \left(\frac{\sigma_y}{\Delta\sigma}\right)^2 \left(\frac{\beta}{1+\beta}\right) (\Delta K)^2 \tag{14}$$

Rearranging Eq 14, we have

$$\phi^2\,\eta\left(\frac{B\,x}{\ln(\varepsilon_A/\varepsilon_T)}\right) = \frac{2\sigma_y\,(1-\nu^2)}{E}\left[\frac{\Delta K_{eff}}{\Delta K}\right]^2 \left(\frac{\Delta K}{\Delta\sigma}\right)^2 \left(\frac{\beta}{1+\beta}\right) \tag{15a}$$

Several investigators [*20–23*] have used correlations between fatigue crack growth rate and parameters expressed in terms of total strain. Imai and Matake [22] replaced $\Delta\sigma$ by $E\Delta\varepsilon$ and applied a strain-based intensity factor $\Delta K_{(\varepsilon)}$.

In terms of a strain-based intensity factor range Eq 15*a* can be written as

$$\phi^2\,\eta\left(\frac{B\,x}{\ln(\varepsilon_A/\varepsilon_T)}\right) = \frac{2\sigma_y\,(1-\nu^2)}{E}\left[\frac{\Delta K_{eff}}{\Delta K_{(\varepsilon)}}\right]^2 \left(\frac{\Delta K_{(\varepsilon)}}{E\Delta\varepsilon}\right)^2 \left(\frac{\beta}{1+\beta}\right) \tag{15b}$$

For the effective strain intensity factor range ratio we have

$$U = \frac{\Delta K_{eff}}{\Delta K_{(\varepsilon)}} \tag{16}$$

Therefore, from Eq 15*b*, the effective strain intensity factor range ratio is

$$U = \phi\frac{E\,\Delta\varepsilon}{\Delta K_{(\varepsilon)}}\left[\eta\left(\frac{B\,x}{\ln(\varepsilon_A/\varepsilon_T)}\right)\Bigg/\frac{2\sigma_y\,(1-\nu^2)}{E}\left(\frac{\beta}{1+\beta}\right)\right]^{1/2} \tag{17}$$

Based on the definition of U from Eq 16, the effective strain intensity factor is

$$\Delta K_{eff} = \phi\,E\,\Delta\varepsilon\left[\eta\left(\frac{B\,(h_0 - h_f)}{\ln(\varepsilon_A/\varepsilon_T)}\right)\Bigg/\frac{2\sigma_y\,(1-\nu^2)}{E}\left(\frac{\beta}{1+\beta}\right)\right]^{1/2} \tag{18}$$

TABLE 1—*Uniaxial and Shear Parameters Required for Eq* 18.

Strain Range (%)	h_0 (μm)	ε_{pco} (%)	λ	h_f (μm)	$\varepsilon_A = \ln(A_i^1/A_f^1)$	B	$\ln(\varepsilon_A/\varepsilon_T)$
$\Delta\varepsilon = 0.15$	28	−0.38	$-v$	8	4.60	2.40	1.720
$\Delta\gamma = 0.16$	95	−0.30	−1	50	5.25	1.95	1.240

TABLE 2—*Comparison of Calculated and Experimentally Obtained Values of* ΔK_{eff} *and U.*

Strain Range (%)	ε_{pco} (%)	λ	ΔK_{eff} (MPa · m)$^{1/2}$) Exp*	Model	Effective SIF Range Ratio (U) $\Delta K_{eff}/\Delta K^{\dagger}_{(\varepsilon)}$	$\Delta\varepsilon_{eff.fl}/\Delta\varepsilon^{\ddagger}_{fl}$	Model
$\Delta\varepsilon = 0.15$	−0.38	$-\nu$	2.50	2.60	0.28	0.32	0.29
$\Delta\gamma = 0.16$	−0.30	−1	2.90	3.12	0.56	0.55	0.60

* Experimental results of ΔK_{eff} at threshold (Fig. 4).
† Experimental results of U ratio at threshold (Fig. 4).
‡ Experimental results of U ratio at threshold from strain-life data (Fig. 5).

The parameters required to calculate the ΔK_{eff} and U using the proposed model for the uniaxial ($\lambda = -\nu$) and shear ($\lambda = -1$) fatigue tests are tabulated in Table 1. The value of the strain intensity factor range and U ratio calculated from Eqs 17 and 18, respectively, and those obtained experimentally are tabulated in Table 2. This comparison shows good agreement of the ΔK_{eff} and U ratio results calculated from Eqs 17 and 18 with those obtained experimentally (see Figs. 4 and 5).

Conclusions

1. For both uniaxial and shear straining the height of surface irregularities decreased as the magnitude of periodic compressive overstrains increased, which led to a reduction in the crack opening stress.
2. There was a reduction in uniaxial fatigue strength when a periodic compressive overstrain of −0.38% magnitude was applied, varying from a factor of 1.24 at short lives to about 3.37 at long lives (10^7 cycles). The reduction in fatigue strength for shear tests varied from a factor of 1.40 at short lives to 1.70 at long lives when a periodic compressive overstrain of −0.3% was applied.
3. An inelastic deformation model of the behavior of asperities at the tip of a crack was developed to explain the effect of periodic compressive overstrains on crack growth and closure. The model correlates the periodic compressive overstrain, the fracture surface asperity height, and the plastically flattened area to the effective strain intensity factor range (ΔK_{eff}) and the U ratio.
4. The model gives predictions of the effective strain intensity factor range and ratio that are in good agreement with the experimental values.

References

[1] Topper, T. H. and Yu, M. T., "The Effect of Overloads on Threshold and Crack Closure," *International Journal of Fatigue*, Vol. 7, 1985, pp. 159–164.
[2] Yu, W. and Ritchie, R. O., "Fatigue Crack Propagation in 2090 Aluminum-Lithium Alloy: Effect of Compression Overload Cycles," *Journal of Engineering Materials and Technology*, Vol. 109, 1987, pp. 81–85.
[3] Suresh, S., "Micromechanisms of Variable Amplitude Load Effects during Fatigue Crack Growth in Metals and Ceramics," *Fatigue Crack Growth under Variable Amplitude Straining*, J. Petit, D. L. Davidson, S. Suresh, and P. Rabbe, Eds., 1988, pp. 146–161.
[4] Carlson, R. L. and Kardomateas, G. A., "Effects of Compressive Load Excursions on Fatigue Crack Growth," *International Journal of Fatigue*, Vol. 16, 1994, pp. 141–146.
[5] Varvani-Farahani, A. and Topper, T. H., "The Effect of Periodic Compressive Overloads on the Crack Surface Roughness and Crack Growth Rate of Short Fatigue Cracks in 1045 Steel," *Proceedings*, 6th International Fatigue Congress, Fatigue 96, Berlin, Germany, Vol. I, 1996, pp. 295–300.
[6] Zaiken, E. and Ritchie, R. O., "On the Role of Compression Overloads in Influencing Crack Closure and Threshold Condition for Fatigue Crack Growth in 7150 Aluminum Alloy," *Engineering Fracture Mechanics*, Vol. 22, 1985, pp. 35–48.

[7] Varvani-Farahani, A. and Topper, T. H., "Crack Growth and Closure Mechanisms of Shear Cracks under Constant Amplitude Biaxial Straining and Periodic Compressive Overstraining in 1045 Steel," *International Journal of Fatigue*, Vol. 19, No. 7, 1997, pp. 589–596.
[8] Varvani-Farahani, A., Topper, T. H., and Plumtree, A., "Confocal Scanning Laser Microscopy Measurements of the Growth and Morphology of Microstructurally Short Fatigue Cracks in Al 2024-T351 Alloy," *Fatigue and Fracture of Engineering Materials and Structures*, Vol. 19, No. 9, 1996, pp. 1153–1159.
[9] A. Varvani-Farahani and T. H. Topper, "Short Fatigue Crack Characterization and Detection using Confocal Scanning Laser Microscopy (CSLM)," *ASTM STP 1318*, G. F. Lucas and D. A. Stubbs, Eds., American Society for Testing and Materials, 1997, pp. 43–55.
[10] Abdel-Raouf, H., DuQuesnay, D. L., Topper, T. H., and Plumtree, A., "Notch-Size Effects in Fatigue Based on Surface Strain Redistribution and Crack Closure," *International Journal of Fatigue*, Vol. 14, 1992, pp. 57–62.
[11] Kemper, H., Weiss, B., and Stickler, R., "An Alternative Prediction of the Effect of the Stress-Ratio on the Fatigue Threshold," *Engineering Fracture Mechanics*, Vol. 4, 1989, pp. 591–600.
[12] Tack, A. J. and Beevers, C. J., "The Influence of Compressive Loading on Fatigue Crack Propagation in Three Aerospace Bearing Steels," *Proceedings*, 4th International Conference on Fracture and Fatigue Threshold, Honolulu, (MCPC Ltd., UK), 1990, pp. 1179–1184.
[13] Johnson, K. J., *Contact Mechanics*, Cambridge University Press, U.K., 1st ed., 1985.
[14] Henkener, J. A., Scheumann, T. D., and Grandt, A. F., "Fatigue Crack Growth Behaviour of Peakaged Al-2.6LI-0.09ZR Alloy," *Proceedings*, 4th International Conference on Fatigue and Fracture Threshold, Honolulu, 1990, pp. 957–962.
[15] Herman, W. A., Hertzberg, R. W., and Jaccard, R., "Prediction and Simulation of Fatigue Crack Growth under Conditions of Low Cycle Closure," *Advances in Fracture Research*, 7th International Conference on Fracture, Houston, 1989, pp. 1417.
[16] Hertzberg, R. W., Herman, W. A., Clark, T., and Jaccard, R., "Simulation of Short Fatigue Crack and Other Low Closure Loading Conditions Utilizing Constant $K_{max}\Delta K$-Decreasing Fatigue Crack Growth Procedures," *Small-Crack Test Methods, ASTM STP 1149*, American Society for Testing and Materials, 1992, pp. 197–220.
[17] Rice, J. R., "Mechanics of Crack Tip Deformation and Extension by Fatigue," *Fatigue Crack Propagation, ASTM STP 415*, American Society for Testing and Materials, 1967, pp. 247.
[18] Lankford, J., Davidson, D. L., and Chan, K. S., "The Influence of Crack Tip Plasticity in the Growth of Small Fatigue Cracks," *Metallurgical Transactions A*, Vol. 15A, 1984, pp. 1579–1588.
[19] Hudak, Jr, S. J. and Davidson, D. L., "The Dependence of Crack Closure on Fatigue Loading Variables," *Mechanics of Fatigue Crack Closure, ASTM STP 982*, J. C. Newman, and W. Elber, Eds., American Society for Testing and Materials, 1988, pp. 121–138.
[20] El Haddad, M. H., Smith, K. N., and Topper, T. H., "A Strain Based Intensity Factor Solution for Short Fatigue Cracks Initiating From Notches," *ASTM STP 677*, American Society for Testing and Materials, 1979, pp. 274–289.
[21] Kitagawa, H. S., Takahashi, S., Suh, C. M., and Miyashita, S., "Quantitative Analysis of Fatigue Process-Microcracks and Slip Lines under Cyclic Strains," *ASTM STP 675*, American Society for Testing and Materials, 1979, pp. 420–449.
[22] Imai, Y. and Matake, T., "Surface Crack Growth During Push-Pull Fatigue of Smooth Specimens," *Japanese Society of Material Science*, Vol. 32, 1983, pp. 1157–1161.
[23] Socie, D. F., Hau, C. T., and Worthem, D. W., "Mixed Mode Small Crack Growth," *Fatigue and Fracture of Engineering Materials and Structures*, Vol. 10, No. 1, 1987, pp. 1–16.

Fernando F. J. Romeiro,[1] Carlos A. Domingos,[2]
and Manuel J. M. de Freitas[3]

Measurement of Fatigue Crack Closure for Negative Stress Ratio

REFERENCE: Romeiro, F. F. J., Domingos, C. A., and de Freitas, M. J. M., "**Measurement of Fatigue Crack Closure for Negative Stress Ratio,**" *Advances in Fatigue Crack Closure Measurement and Analysis: Second Volume, ASTM STP 1343*, R. C. McClung and J. C. Newman, Jr., Eds., American Society for Testing and Materials, West Conshohocken, PA, 1999, pp. 321–336.

ABSTRACT: The concept of fatigue crack closure, introduced in the 60's by Elber, has been used to explain a wide range of positive stress ratio crack propagation results ($R \geq 0$). Less attention has been given to fatigue loading for negative stress ratios ($R < 0$). In this work the results of crack propagation tests of middle-crack tension M(T) specimens of a normalized medium carbon steel DIN Ck 45 for a wide range of stress ratios from $0.7 \geq R \geq -3$ are presented. Crack closure loads were measured with the compliance technique at test frequency, using a data acquisition system. Negative crack closure loads were found for negative stress ratios $R \leq -1$, which can explain higher crack propagation rates and accelerations in crack growth during variable-amplitude tests where compressive loads of different stress ratios are present.

KEYWORDS: fatigue, crack propagation, crack closure, stress ratio

Nomenclature

a	Half length of crack, m
E	Young's modulus of elasticity, MPa
K	Stress intensity factor, MPa $\sqrt{m}$
ΔK	Stress intensity factor range
ΔK_{eff}	Effective stress intensity factor range
K_{max}	Maximum stress intensity factor
K_{op}	Crack-opening stress intensity factor
M(T)	Middle-crack tension specimen
N	Number of cycles
R	Stress ratio
P_{min}	Minimum applied load, N
P_{max}	Maximum applied load, N
P_{open}	Crack-opening load, N
S_0	Crack-opening stress, MPa
S_{max}	Maximum applied stress, MPa
S	Section of M(T) specimen, mm^2
v, COD	Crack-opening displacement, mm

[1] Assistant professor, Department of Mechanical Engineering, Polytechnic Institute of Leiria,
[2] Assistant professor, Department of Mechanical Engineering, Polytechnic Institute of Setubal,
[3] Associate Professor, Department of Mechanical Engineering, Instituto Superior Tecnico, Technical University of Lisbon, Av. Rovisco Pais 1096 Lisbon, Portugal.

σ_y Yield stress, MPa
σ_u Ultimate tensile strength, MPa

Designing machine components and structures against fatigue has been widely performed based on SN curves, modified Goodman diagrams, and other classical concepts. Fracture mechanics concepts are used in the modern aircraft and energy industries as a powerful tool to improve design and maintenance procedures and to increase components reliability. In the railway and automotive transport industries, the classical fatigue design concepts are widely used and a strong resistance to the use of damage tolerance based on fracture mechanics exists, since the components and structures are designed for "infinite life" and no cracks are allowed. In the railway transport industry, with the development of high speed trains, a great increase of loading cycles in structures and components have to be taken into account and security problems may occur in the components subjected to an increased number of cycles between programmed maintenance procedures.

A typical example is the railway axle, designed with classical SN curves since the works of Wholer in the 1850's. It has been demonstrated [*1*] that fracture mechanics concepts can be used to improve maintenance procedures assuming that cracks may be present and grow under constant or variable-amplitude loading. Railway axles typically have a bending load in a rotating axle performing the so-called rotating bending loading, characterized by a stress ratio of $R = -1$, under which semi-elliptical surface cracks at the surface may grow to final fracture of the axle. In-service loading measurements in railway axles have been carried out [*2–4*] and a wide range of stress ratios have been measured from $R = 0$ to $R = -2$ and lower. These stress levels occur in turnouts and curves of the railway track and cause positive or negative overloads to the constant-amplitude loading of the railway axle $R = -1$. Therefore when performing crack growth predictions under variable-amplitude loading in railway axles, the interaction effects due to the overloads must be taken into account in order to predict accurately the residual life of cracked railway axles.

The effect of variable-amplitude loading on fatigue crack growth remains a problem not completely solved. The main studies are related to the effect of tensile overloading on aircraft components and structures in light alloys, and several semi-empirical and theoretical models have been proposed. Models based on either experimentally determined retardation factors applied to Forman's crack growth law or on effective stress intensity factors based on Elber's [*5*] concept with the closure load calculated either by strip-yield models [*6,7*] or finite element models [*8,9*] are available in the literature. Compressive overloading effects on fatigue crack growth in steels have been reported in the literature [*10*], but the available results don't provide complete knowledge of the problem.

In order to study the effect of compressive loading on fatigue crack growth a study has been carried out where fatigue crack growth rates and crack opening loads were obtained for a wide range of stress ratios, from $R = 0.7$ to $R = -3$, on a normalized medium carbon steel used in railway axles. The results are analyzed with the concept of effective stress intensity factor based on measured crack opening loads and are compared with literature results calculated by finite element models or by strip-yield models on an identical steel. They show that for high compressive loads the crack opening load is around zero or negative, which implies that higher crack growth rates are obtained.

Material and Experimental Procedure

The material tested is a normalized medium carbon steel, DIN Ck 45. The chemical composition and mechanical properties are presented, respectively, in Tables 1 and 2. Tests were carried out in a 100 kN INSTRON servohydraulic testing machine at a frequency of 10 Hz in load control mode at different stress ratios R and maximum loads P_{max} as shown in Table 3. The specimens are middle-crack tension (M(T) type) 10 mm thick and 43 or 60 mm in width in accordance with the Standard Test Method for Measurement of Fatigue Crack Growth Rates, (ASTM E 647-95). The central notch

TABLE 1—*Chemical Composition of DIN CK 45 Steel.*

C	Mn	Cr	Ni	Ti	Cu	Si	P	S
0.41	0.76	0.09	0.08	0.01	0.19	0.23	0.01	0.02

was 6 mm long and was made by electrical-discharge machining with a 0.25 mm height. A fatigue precracking was conducted till the crack length was approximately 10 mm long. On all specimens the direction of loading was parallel with the rolling direction but due to the effect of normalized steel the grain size is similar in both directions. The two different widths of the specimens (43 and 60 mm) were due to practical reasons related to the machine load capacity. The thickness of the specimen was chosen in order to apply high compressive loading without the use of antibuckling guides.

Automatic data acquisition of load (kN) and centerline displacement (mm) was done at the frequency of testing at each 10 000 cycles, with a data acquisition rate of 1000 Hz, during a period of 1 second, such that one record results in 1000 pairs of data points load-displacement. Crack growth measurements were made by either an optical microscope associated with a stroboscopic illumination at the frequency of testing or through an automatic measurement technique using the compliance method associated with load-displacement curves previously calibrated using the data from optical measurements.

Results

Crack growth data, presented in detail in Appendix 1, are condensed in Fig. 1, in accordance with ASTM 647, which states:

$$\begin{aligned} \Delta P &= P_{max} - P_{min} \text{ for } R > 0 \\ \Delta P &= P_{max} \text{ for } R \leq 0 \end{aligned} \tag{1}$$

These results can be analyzed as plots of *da/dN* as a function of ΔK and Paris type laws are obtained for each stress ratio.

The basic principle of the crack closure concept is that a crack propagates only if it is fully open. So, the crack propagation force, the stress intensity factor range ΔK, should be reduced to an effective ΔK_{eff}. The Paris Law becomes Elber Law [5]:

$$(da/dN) = C\,(\Delta K_{eff})^m \tag{2}$$

This is a unified crack growth law for different stress ratios R, where

$$\Delta K_{eff} = K_{max} - K_{op} \tag{3}$$

TABLE 2—*Mechanical Properties of DIN CK 45 Steel.*

σ_{ys} (MPa)	σ_u (MPa)	A (%)
350	600	25

TABLE 3—*Tests for Different* R *and* P_{max}.

$R = P_{min}/P_{max}$	P_{max}, kN	S (mm^2)
0.7	95	60 × 10
0	30	43 × 10
−1	40	43 × 10
−1	80	43 × 10
−2	40	43 × 10
−3	30	43 × 10

and

$$K_{max} = Y(P_{max}/S)\sqrt{\pi a}$$

$$K_{op} = Y(P_{op}/S)\sqrt{\pi a} \tag{4}$$

To use this unified crack growth law, K_{open} or P_{open} must be determined from experimental data for different stress ratios R and K_{max}. The use of the crack closure (open) concept allows a unique closure free curve for the crack growth rates at different stress ratios to be determined. A test at $R = 0.7$ is used as the reference since it is assumed that $P_{open} = P_{min}$ (crack tips are always open).

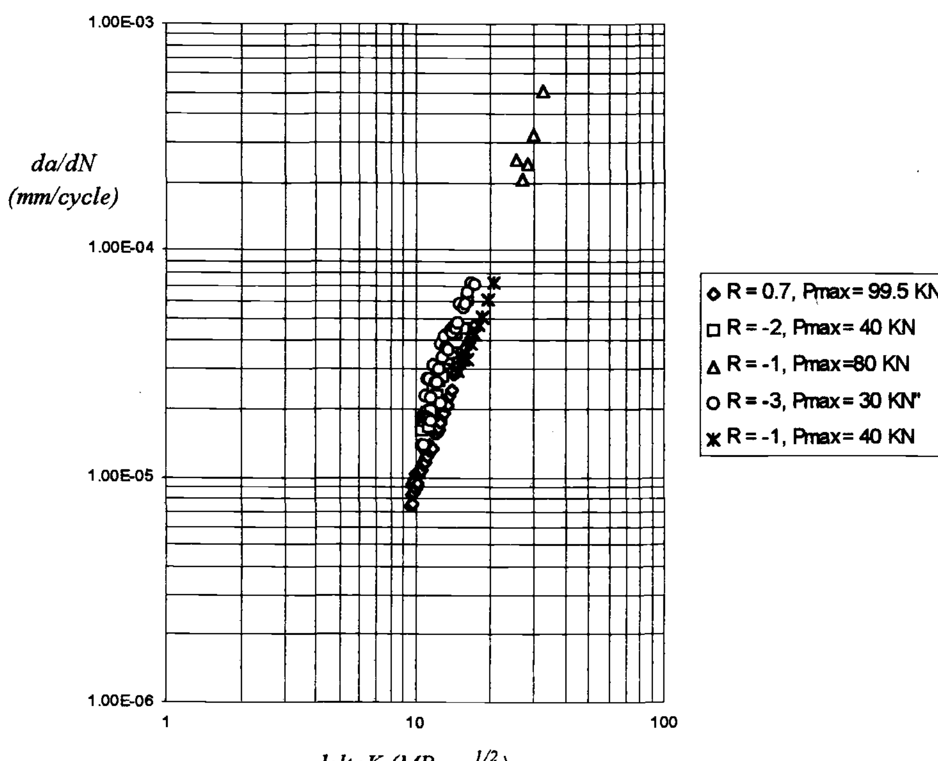

FIG. 1—da/dN = f (ΔK) *for the tests results.*

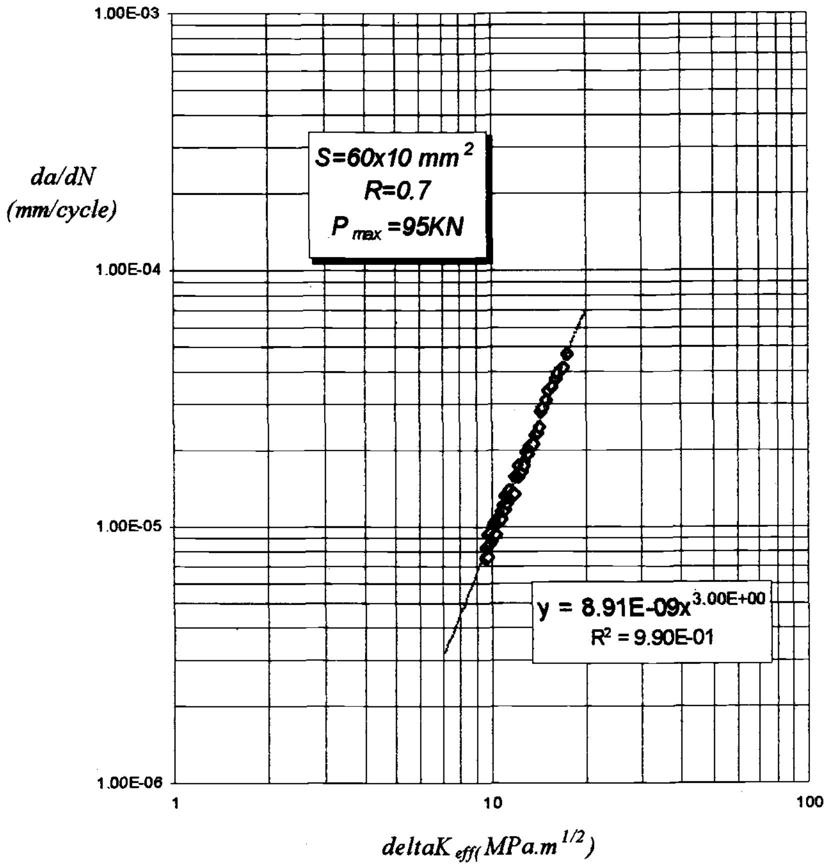

FIG. 2—da/dN = f (ΔK) *for the* R = *0.7 test.*

The propagation law for the $R = 0.7$ test, from Fig. 2, is:

$$(da/dN) = 8.91 \times 10^{-9}\,(\Delta K_{\text{eff}})^3 \tag{5}$$

where da/dN is in mm/cycle and ΔK_{eff} in MPa $\sqrt{\text{m}}$.

The propagation laws $(da/dN) = f\,(\Delta K_{\text{eff}})$ for the other stress ratio tests should coincide with this reference law when K_{open} is subtracted from K_{max}. Figure 1 shows that the data for negative stress ratios tests curves are located on the left side of the reference curve ($R = 0.7$). This means that K_{open} or P_{open} must be lower than zero in order for it to be possible to superimpose the several curves. In Fig. 3 an example is presented of the method of determining P_{open} and in Table 4 and in Fig. 4 approximate values of P_{open} and of $P_{\text{open}}/P_{\text{max}}$ for these tests are presented which were calculated by shifting the $(da/dN) = f(\Delta K)$ curves to the reference curve $(da/dN) = f(\Delta K_{\text{eff}})$.

The curves of Fig. 4 are of the same type of Newman's model [5]. An exact determination of the polynomial coefficients requires the determination of P_{open} from the load-displacement curves.

Determination of P_{open} *from the Load-Displacement Curves*

To confirm the indirect determination of crack-opening load made above, experimental measurements of P_{open} were carried out from load-displacement compliance curves. Displacement was mea-

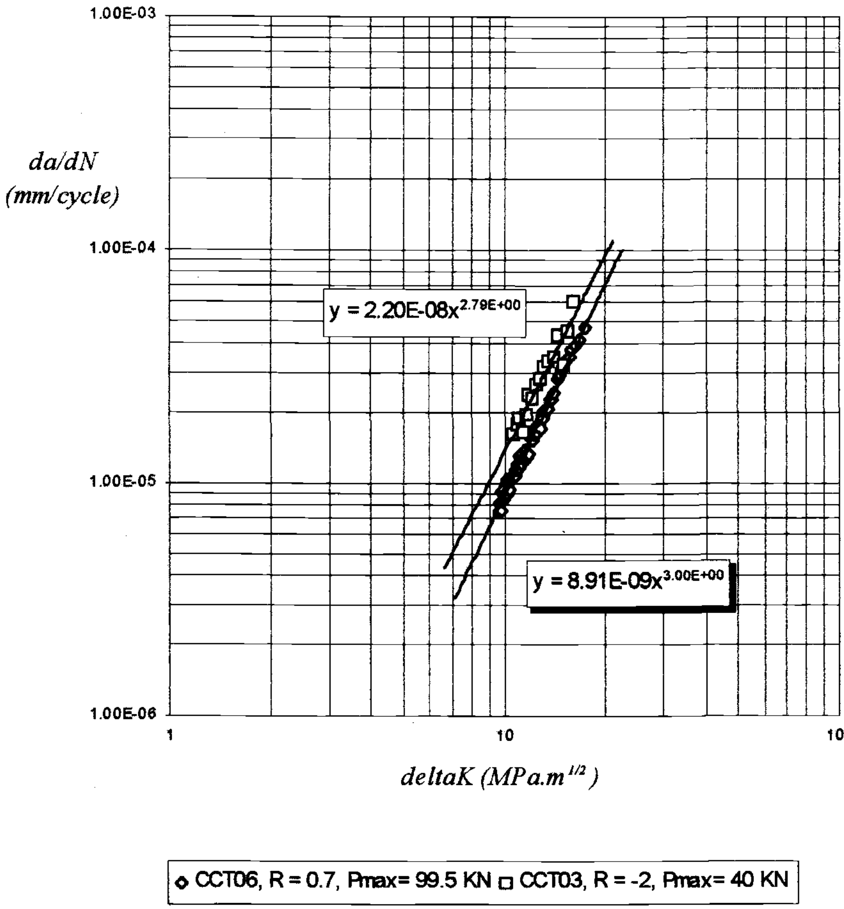

FIG. 3—da/dN = f (ΔK) *for the* R = *0.7 and* R = *−2.*

sured through a clip-gage attached to the specimen at the centerline according to ASTM E 647. Load-Displacement data were acquired during the testing, at fixed intervals of 10 000 cycles, at a rate of 1000 Hz, during 1 s. Some of the data acquired are presented in Appendix 2. A preliminary question was to confirm if the acquisition of the load-displacement data could be done with an automatic data acquisition system at the test frequency. Load-displacement data were acquired at 0.1, 1 and 10 Hz

TABLE 4—*Approximate Values of* P_{open} *and* P_{open}/P_{max}.

R	P_{max} (kN)	S (mm^2)	P_{open} (kN)	P_{open}/P_{max}
−3	30	43 × 10	−5	−0.17
−2	40	43 × 10	−3	−0.08
−1	80	43 × 10	−8	−0.10
−1	40	43 × 10	0	0.00
0	30	43 × 10	4	0.13
0.7	95	60 × 10	66.5	0.70

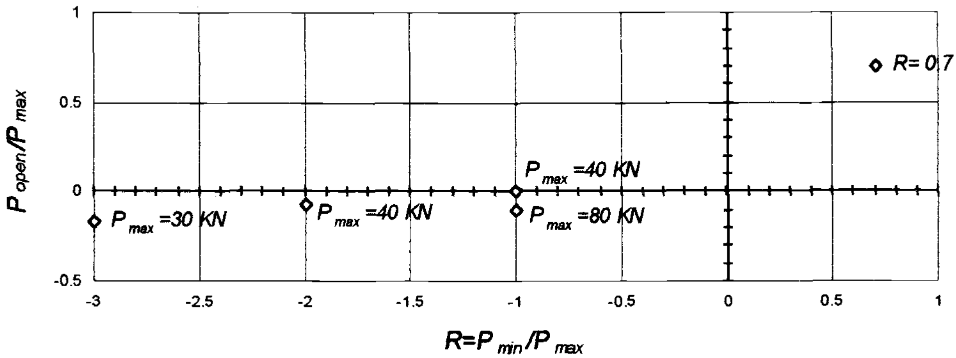

FIG. 4—P_{open}/P_{max} *for different* R *and* P_{max}.

and the results, presented in Fig. 5, show that the differences are not meaningful. This data sampling rate is in accordance with ASTM E 647; i.e., at least one data pair (displacement and load) is taken in every 2% interval of the cyclic load range for the entire cycle.

There is no unique method to determine and calculate the opening loads in crack growth tests and several methods have been proposed in [*11*]. ASTM E 647 in Appendix X2 recommends a practice

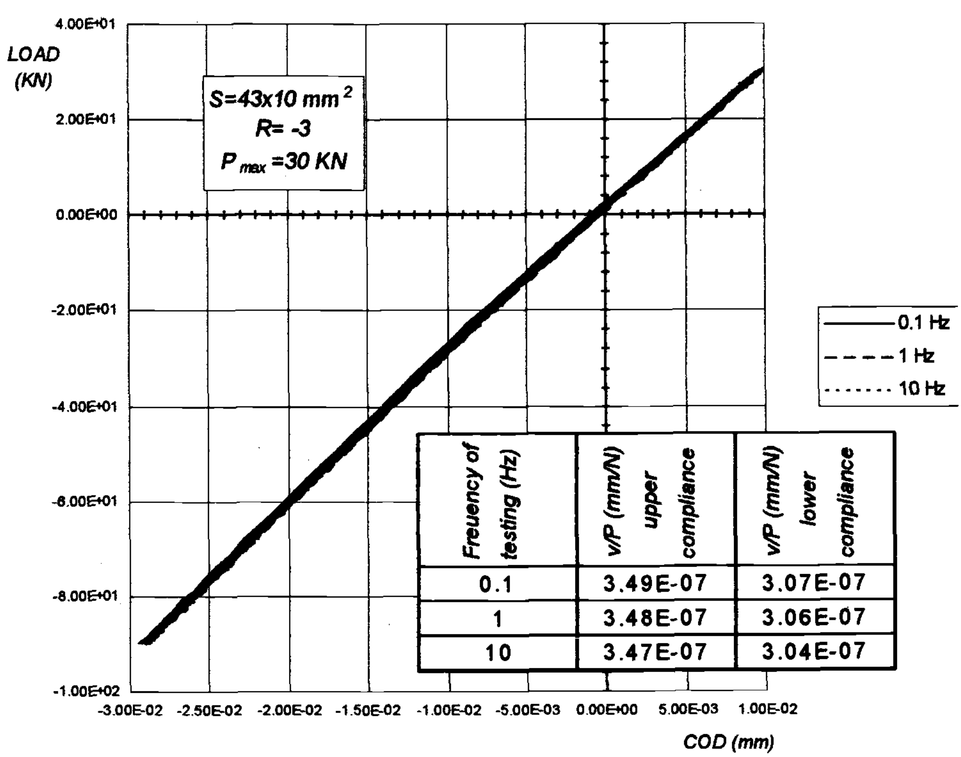

Freuency of testing (Hz)	v/P (mm/N) upper compliance	v/P (mm/N) lower compliance
0.1	3.49E-07	3.07E-07
1	3.48E-07	3.06E-07
10	3.47E-07	3.04E-07

FIG. 5—*Load-COD data at 0.1 Hz, 1 Hz and 10 Hz.*

for the determination of fatigue crack opening load from compliance but with some disagreement. For the tests at stress ratios of $R = -2$ and $R = -3$, the ASTM practice may not be reasonable, since it states that the compliance that corresponds to the fully open crack configuration is determined at 25% of the cyclic load range on the unloading curve. In these tests and using this statement the crack may already be closed. Therefore, in this work the crack-opening load P_{open} was determined from the load-displacement curves using the ASTM method, not described here, and two further methods:

Method I—A linear regression is made in the linear zone of the load-displacement curve above the inflection zone. A second linear regression is made in the lower linear zone. The intersection of these two regressions then corresponds to the crack-opening load P_{op}. This method is shown in Fig. 6.

Method II—This is the reduced displacement method. A linear regression is made in the linear zone of the load-displacement curve above the inflection zone. The deviation of the measured data from the linear regression is calculated. The crack-opening load P_{open} is defined as the level at which the deviation of the reduced data surpasses a predefined value. This method is shown in Fig. 7.

It is known that the crack opening process is progressive due to crack-tip plasticity and the varying stress state through the specimen thickness and the exact determination of P_{open} is difficult. Method I leads to lower and less realistic values for P_{open}, since at the intersection point the crack is not fully open. The values calculated by this method have less scatter than those of Method II but this method was very sensitive to the amount of deviation predefined, and the scatter is high.

The P_{op} data measured through the compliance method and calculated by the recommended ASTM method and by the reduced displacement method are presented in Table 5. For the ASTM method an offset criteria of 2% of the open crack compliance value was chosen, and for the reduced displacement method we present the value at the point where the deviation of the reduced data becomes 10% of the maximum difference at the lowest load in the cycle. There are some disagreements on the or-

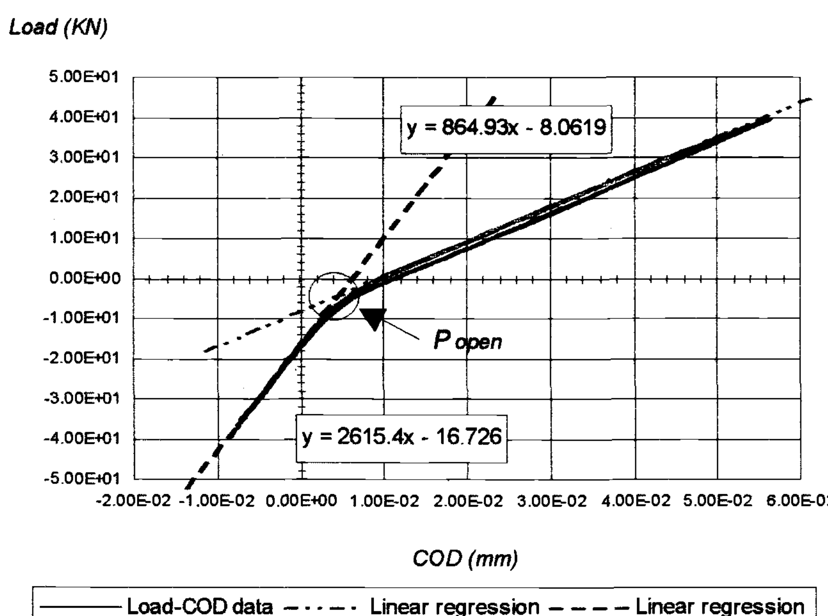

FIG. 6—*Determination of* P_{open} *as the intersection point.*

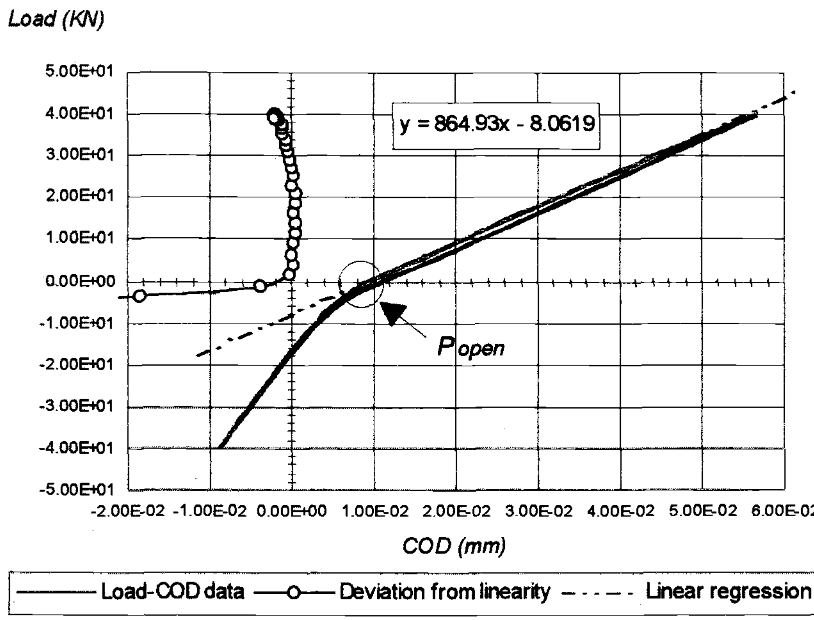

FIG. 7—*Determination of* P_{open} *as a certain deviation from linearity.*

der of magnitude of P_{op} calculated by both methods and those calculated through the effective stress intensity factor by shifting the $da/dN = f(\Delta K)$ curves to $da/dN = f(\Delta K_{eff})$ presented in Table 4. Note that some dependence between the P_{op} and the P_{max} and the crack length (i.e., K_{max}) was found.

Then an extension of the diagram plotting the normalized opening stresses with the stress ratio R presented by Newman [5] may be proposed in order to extend it for lower stress ratio, which will be discussed in the next section.

Discussion

Cyclic fatigue crack growth tests were carried out on M(T) specimens with negative stress ratios and the respective crack opening loads were determined through the three methods presented in the previous section. In literature, crack growth data and crack opening loads are available for a wide

TABLE 5—*Approximate Values of* P_{open} *Calculated by Method II.*

R	P_{max} (kN)	S (mm^2)	P_{open} (kN)	P_{open} (kN) Method II	ASTM 647
−3	30	43 × 10	−5	−0.4 to 0.2	8.6 to 10.1
−2	40	43 × 10	−3	−1.2 to − 2.1	−3 to 3.3
−1	80	43 × 10	−8	−4.2 to − 6.4	−21 to −15
−1	40	43 × 10	0	−1.7 to 0.3	10.1 to 8.6
0	30	43 × 10	4	7.0 to 8.6	8.5 to 9.6
0.7	95	60 × 10	66.5	66.5	66.5

range of materials and stress ratios $R \geq -1$. For lower stress ratios crack growth data are available [11,12] but without crack opening data or then with very limited discussion such that we can sustain that a lack of crack opening loads data exist for $R < -1$. Therefore, when performing prediction of crack growth in structures and components subjected to high negative stress ratios with the existing models, engineers and designers may have difficulties due to the uncertainty of the application of the existing models and to the lack of experimental data.

When analyzing crack opening load data for stress ratios $R < -1$, we found some disagreement between the data obtained by the methods proposed in the previous section. Some explanations can be explored. First of all, for stress ratios $R < -1$, the load range over which the crack is fully open is very small compared with stress ratios $R > 0$. This means that uncertainties may appear when determining the compliance of the fully open crack. For example, at $R > 0$, the ratio $\Delta P_{\text{eff}}/\Delta P$ is greater than for $R = -2$ or $R = -3$. The scatter exists also for high applied stress levels, such as, for example, $R = -1$ and applied maximum load 80 kN. In this case the crack growth is very fast, the crack-tip plasticity is very large, and therefore the load-displacement curves present some curvature, which leads to uncertainties in the compliance calculation. Anyway, we will now discuss these data, comparing the experimental data with the crack opening loads predicted by the models presented in literature.

One of the most used models to predict crack growth is the analytical crack-closure model [6], known as the strip-yield model. It is based on the Dugdale model, but modified in order to leave plastically deformed material in the wake of the advancing crack. Through this strip-yield model, which is based on the crack-tip plasticity, the crack opening loads can be determined using the following equations [7]:

$$\frac{S_0}{S_{\max}} = A_0 + A_1 R + A_2 R^2 + A_3 R^3 \quad \text{for } R \geq 0 \tag{6}$$

and

$$\frac{S_0}{S_{\max}} = A_0 + A_1 R \quad \text{for } -1 \leq R < 0 \tag{7}$$

where

$$\begin{aligned} A_0 &= \left(0.825 - 0.34\alpha + 0.05\alpha^2\right)\left[\cos\left(\frac{\pi S_{\max}}{2\sigma_0}\right)\right]^{1/\alpha} \\ A_1 &= \left(0.415 - 0.071\alpha\right)\frac{S_{\max}}{\sigma_0} \\ A_2 &= 1 - A_0 - A_1 - A_3 \\ A_3 &= 2A_0 + A_1 - 1 \end{aligned} \tag{8}$$

The flow stress σ_0 is calculated as the average between the uniaxial yield stress and ultimate tensile strength of the material, α is the constraint factor which takes into account the three-dimensional stress state, and $S_{\max}$ is the maximum applied stress level.

Based on the analytical crack closure model and on the mathematical algorithms that are described in Ref *6*, a computer program was built in order to calculate the crack opening loads for different stress ratios *R*, maximum cyclic stress levels $S_{\max}$, and constraint factors α. Using the mechanical properties and crack growth data of the normalized carbon steel, crack growth predictions were carried out as shown in Figs. 8*a* and 8*b* and the computed results of the crack opening loads were compared with those obtained by the above described Eqs 6 and 7. This comparison is needed since in the development of the model and respective equations, a high strength aluminum alloy was used against

(a)

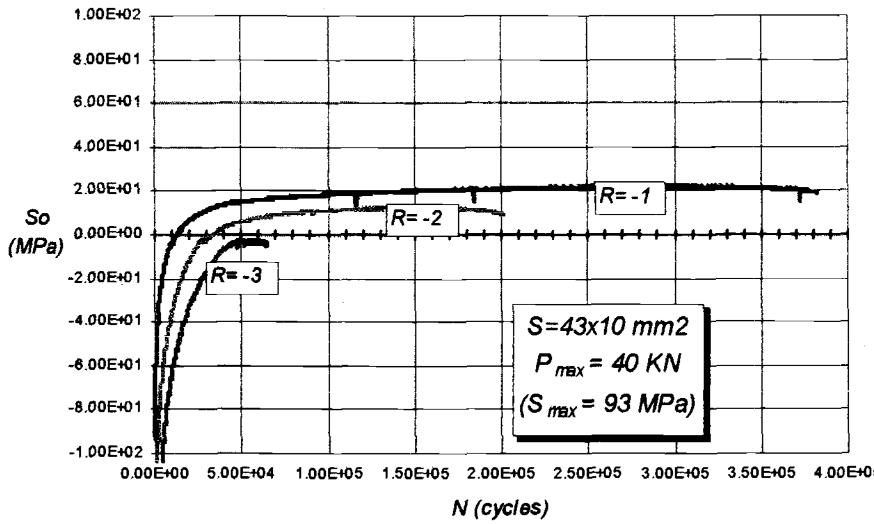

(b)

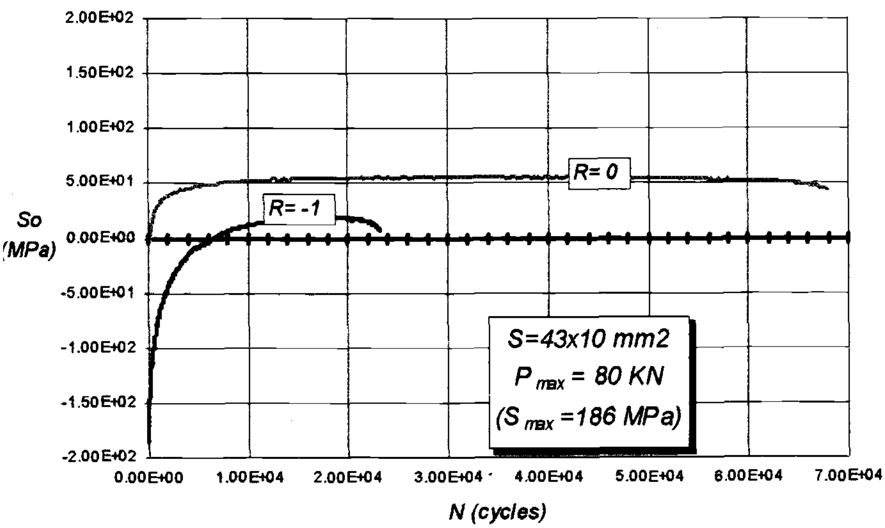

FIG. 8—P_{open} *calculated by analytical crack closure model [6]:* (a) *for* R = *−1, −2, −3 and* S_{max} *= 93 MPa, and* (b) *for* R = *0, −1 and* S_{max} *= 186 MPa.*

a low strength normalized carbon steel in the present study, with much more plasticity at the crack tip than the aluminum alloy.

As an example, Table 6 shows the comparison between the crack opening loads calculated by the computer program for M(T) specimens and the carbon steel and those calculated through the Eqs 6 and 7, using a constraint factor of α = 2.3. A good correlation is obtained for the stress ratio R =

TABLE 6—*Calculated Crack Opening Loads for α = 2.3.*

R	S_{max} (MPa)	S_{open} R (MPa) Newman [6]	S_{open} (MPa) Newman [7]
0	186	55	52
−1	93	22	23
−1	186	19	34
−2	93	12	19
−3	93	−3	14

0. For $R = -1$ we have used two different maximum stresses, a low applied stress level where $S_{max}/\sigma_0 = 0.2$ and a high one where $S_{max}/\sigma_0 = 0.4$. For the low level stress we found again a good agreement but for the higher stress level the analytical crack closure model calculates much lower crack opening loads. These results are in agreement with the data presented in Ref 2, where for a similar carbon steel, crack opening loads were obtained through finite element calculations. Using a finite element code and a release node technique in plane strain, corresponding to a constraint factor of $\alpha = 3$, crack opening loads are presented for stress ratios $-1 \leq R \leq 0$ and for stress levels of 100 MPa $\leq S_{max} \leq$ 300 MPa. Table 7 shows the comparison between the crack opening loads calculated by FEM and those calculated by Eqs 6 and 7. Again the crack opening loads calculated by FEM are lower than those calculated by Newman's equations. In particular, it is remarkable that for a stress ratio of $R = -1$ and the stress levels of S_{max} = 250 MPa and S_{max} = 300 MPa, i.e., high stress levels, the crack opening loads are negative. The trends of these data are in agreement with the present experimental results where for higher stress levels and for lower stress ratio, lower crack opening loads are obtained.

Some disagreement between the measured and calculated crack opening loads is found for the test at stress ratio $R = -3$. In this test the applied maximum stress level was lower than on the other tests, but the ratio between the minimum applied stress and the flow stress σ_0 is the highest which can change the development of the cyclic crack-tip plasticity.

We can finally plot in Fig. 9 our experimental crack opening load data, obtained through the ASTM method and the data calculated by extending Newman's equations to the stress ratios $R < -1$, for the

TABLE 7—*Calculated Crack Opening Loads for α = 3.*

R	S_{max} (MPa)	S_{open} (MPa) FEM [2]	S_{open} (MPa) Newman [7]
0	100	15	25
−1	100	15	20
0	150	25	36
−1	150	17.5	27
0	200	45	47
−1	200	25	30
0	250	40	56
−1	250	−2.5	29
0	300	17.5	62
−1	300	−55	24

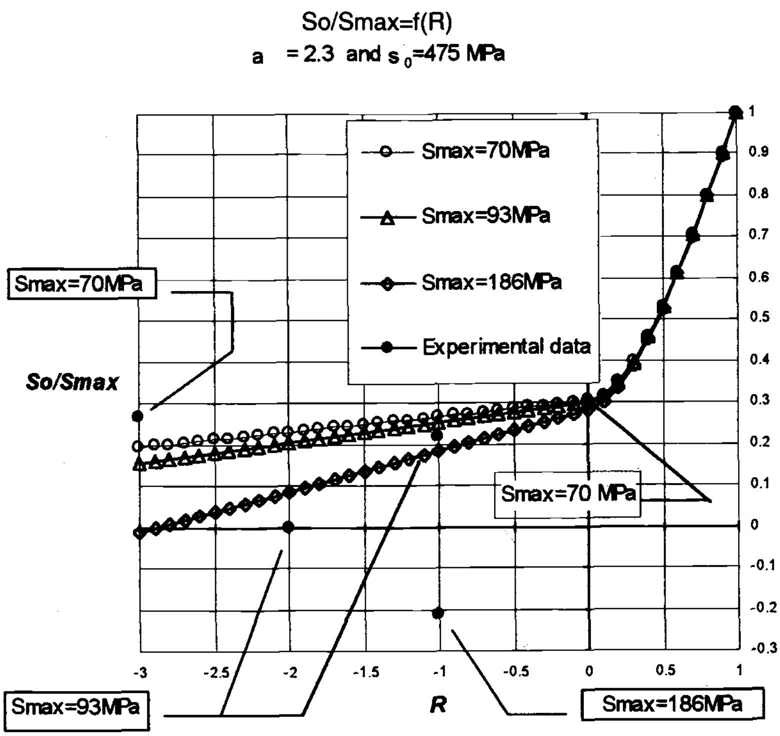

FIG. 9—*Extension of Newman model for higher negative* R *and* P_{max} *and comparison with experimental values.*

three stress levels used in this study and a constraint factor $\alpha = 2.3$. The crack opening loads seem to be much more sensitive to the applied stress levels than to the stress ratio, which is in accordance with FEM results and the analytical crack closure model.

Conclusions

Tests carried out to determine the crack growth rates and opening loads for a wide range of negative stress ratios lead to the following conclusions:

1. Negative crack opening loads P_{open} may be present with negative stress ratios R and high applied load levels.
2. The ratio P_{open}/P_{max} becomes more negative for higher negative stress ratios but only for high applied maximum load levels P_{max}.
3. Higher crack growth rates based on the positive part of the load cycle are therefore obtained for negative stress ratios.
4. For a given negative R ratio, the P_{op} depends strongly on the maximum load P_{max} and, consequently, on the amount of plasticity at the crack tip.
5. For a given maximum load and for increasing negative R ratio it seems that the crack opening load P_{op} tends to a constant value; i.e., a saturation level may exist.

APPENDIX I

$da/dN = f(\Delta K)$ Data

This section presents the crack growth data obtained for the tests with negative stress ratio, Fig. 10.

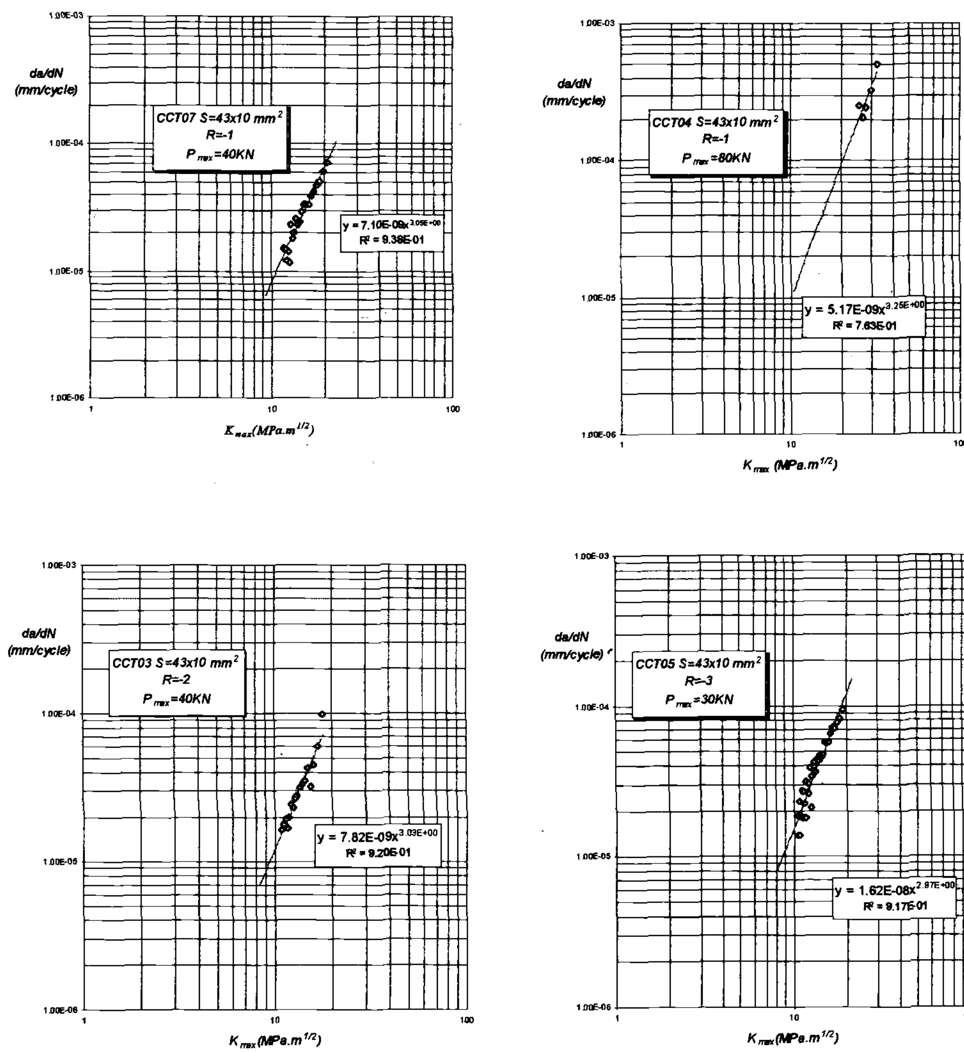

FIG. 10—*Crack growth data for negative stress ratio.*

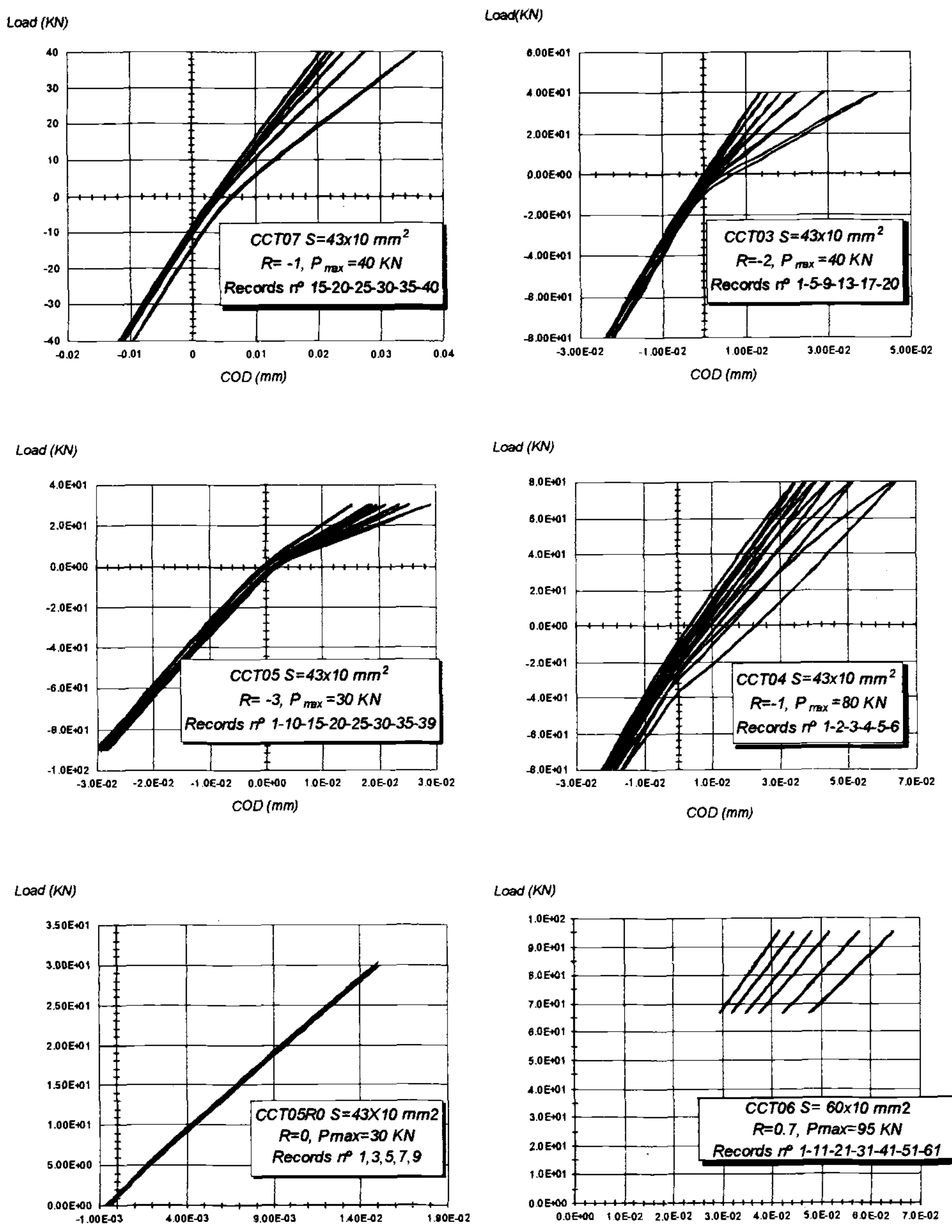

FIG. 11—*Load-COD curves.*

APPENDIX II

Load-COD Curves for Tests with Stress Ratio from $-3 \leq R \leq 0.7$

In this section some records of the load-COD data are presented in order to visualize the changes in the load-COD data due to the presence of high negative stress ratio when compared with classical crack growth data for $R \geq 0$, Fig. 11.

References

[1] Freitas, M. and François, D., "Analysis of Fatigue Crack Growth in Rotary Bend Specimens and Railway Axles," *Fatigue and Fracture of Engineering Materials and Structures,* Vol. 18, No. 2, 1995, pp. 171–178.

[2] Gros, V., "Etude de l'Amorçage et de la Propagation des Fissures de Fatigue dans les Essieux-axes Ferroviaires," Ph.D. Thesis, Ecole Centrale de Paris, France 1996, (in French).

[3] Gros, V., Prioul, C., Bompard, Ph., and Lallet, P, "Fatigue Crack Propagation in Railway Axles," *ECF 11 Mechanisms and Mechanics of Damage and Failure,* J. Petit, Ed., Vol. II, pp. 1113–1118.

[4] Leluan, A., "Fatigue Test Method and Damage Models Used by the SNCF for Railway Vehicle Structures," *Automation in Fatigue and Fracture: Testing and Analysis, ASTM STP 1231,* C. Amzallag, Ed., American Society for Testing and Materials, 1994, pp. 405–418.

[5] Elber, W., "Fatigue Crack Closure under Cyclic Tension," *Engineering Fracture Mechanics,* Vol. 2, 1970, pp. 37–45.

[6] Newman, J. C., Jr., "A Crack Closure Model for Predicting Fatigue Crack Growth under Aircraft Spectrum Loading," *Methods and Models for Predicting Fatigue Crack Growth under Random Loading, ASTM STP 748,* J. B. Chang and C. M. Hudson, Eds., American Society for Testing and Materials, Philadelphia, 1981, pp. 53–84.

[7] Newman, J. C., Jr., "A Crack Opening Stress Equation for Fatigue Crack Growth," *International Journal of Fracture,* Vol. 24, 1984, R pp. 131–135.

[8] McClung, R. C. and Sehitoglu, H., "On the Finite Element Analysis of Fatigue Crack Closure—1. Basic Issue," *Engineering Fracture Mechanics,* Vol. 33, No. 2, 1989, pp. 237–252.

[9] McClung, R. C. and Sehitoglu, H., "On the Finite Element Analysis of Fatigue Crack Closure—2. Numerical Results," *Engineering Fracture Mechanics,* Vol. 33, No. 2, 1989, pp. 253–272.

[10] Buschermmöle, H., Memhard, D., and Vormwald, M., "Fatigue Crack Growth Acceleration or Retardation due to Compressive Overload Excursions," *Fatigue '96, Proceedings of the Sixth International Fatigue Conference,* G. Lütjering and H. Nowack, Eds., Pergamon Press, Vol. I, 1996, pp. 583–588.

[11] *Mechanics of Fatigue Crack Closure, ASTM STP 982,* J. C. Newman and W. Elber, Eds., American Society for Testing and Materials, 1988.

[12] Boothe, G. S. and Maddox, S. J., "Correlation of Fatigue Crack Growth Data Obtained at Different Stress Ratios," *Mechanics of Fatigue Crack Closure, ASTM STP 982,* J. C. Newman and W. Elber, Eds., American Society for Testing and Materials, 1988, pp. 516–527.

Soon-Jo Park[1] *and Ji-Ho Song*[2]

Simulation of Fatigue Crack Closure Behavior Under Variable-Amplitude Loading by a 2D Finite Element Analysis Based on the Most Appropriate Mesh Size Concept

REFERENCE: Park, S.-J. and Song, J.-H., **"Simulation of Fatigue Crack Closure Behavior Under Variable-Amplitude Loading by a 2D Finite Element Analysis Based on the Most Appropriate Mesh Size Concept,"** *Advances in Fatigue Crack Closure Measurement and Analysis: Second Volume, ASTM STP 1343,* R. C. McClung and J. C. Newman, Jr., Eds., American Society for Testing and Materials, West Conshohocken, PA, 1999, pp. 337–348.

ABSTRACT: A two-dimensional elastic-plastic finite element analysis is performed for plane stress conditions with 4-node isoparametric elements to investigate the closure behavior under various variable-amplitude loading, i.e., single overloading, Hi-Lo block loading, and narrow- and wide-band random loading. The closure behavior under single overloading and Hi-Lo block loading can be well simulated by applying the concept of the most appropriate mesh size that will provide numerical results consistent with experimental data under constant-amplitude loading. It is found that the crack opening load under random loading may be predicted approximately by replacing the complicated random load history with the appropriate equivalent, simplified variable load history.

KEYWORDS: fatigue crack closure, finite element method, variable loading, most appropriate mesh size, plastic zone size

It is widely accepted that crack closure has a dominant influence on fatigue crack growth. The closure behavior of fatigue cracks has been investigated mainly by using experimental methods. However, for cases when experimental methods cannot be applied so easily, the finite element (FE) numerical method has long been utilized as an alternative, powerful technique for the analysis of crack closure and has provided useful results of crack closure behavior, particularly under variable loading [*1–4*]. Recently McClung and his co-workers [*5–7*] have performed systematic studies extensively to investigate effects of various important factors related to FE modeling of crack closure in detail. Although FE numerical results obtained so far by many workers have provided a lot of useful information on crack closure behavior, there are few comparisons between numerical and experimental data.

In previous work [*8*], the authors have investigated a FE analysis model to simulate precisely the experimentally observed fatigue crack closure behavior under constant-amplitude loading, performing quantitative comparison between numerical and experimental results. One of the important results obtained is that a unique, most appropriate mesh size exists for a given loading condition that will provide numerical results consistent with experimental data. The most appropriate mesh size can be estimated approximately in terms of the theoretical plastic zone size.

[1] Senior research engineer, Technical Research Institute, Hyundai Precision & Ind. Co., Ltd., 80-9, Mabook-ri, Kuseong-myun, Yongin-shi, Kyunggi-do, 449-910, Korea.

[2] Professor, Department of Automation and Design Engineering, Korea Advanced Institute of Science and Technology, 207-43, Cheongryangi-dong, Dongdaemun-gu, Seoul, 130-012, Korea.

In this study, the FE analysis is performed to investigate the closure behavior under variable-amplitude loading, using the concept of the most appropriate mesh size. The FE numerical results under single overloading and Hi-Lo block loading are compared with experimental results. A simple procedure is discussed to simulate the closure behavior under random loading of complicated load profiles.

A Two-Dimensional Finite Element Model

The two-dimensional FE model used in this study is nearly the same as in previous work [*8*]. Therefore, only the important aspects are outlined below.

A commercial program for a general-purpose structural analysis, ANSYS Rev. 5.0A [*9*], is used for elastic-plastic FE simulations of crack closure. The theory of incremental rate independent classical plasticity, von Mises criterion and kinematic hardening rule are used. The stress-strain relationship is modeled as a bilinear law.

The opening and closing states of the crack surface are identified through monitoring all nodal displacements and nodal reaction forces along the crack at each load increment and then the boundary conditions are changed as in the work of Ohji et al. [*1*] or Newman [*2*]. Each load increment in this study is 1 MPa. The crack-tip opening and closing stress levels are defined as the stress levels at which the crack surfaces become fully open or start to close, respectively. Unless stated otherwise, the crack tip is released at the minimum load on every cycle.

The analysis is performed under plane stress for the center-cracked specimen (CCT) 70 mm wide and 184 mm long, which is nearly the same as the specimen used in previous experimental work [*10*] to be compared with the FE numerical result in this study. Four-node isoparametric elements are used. Only one-quarter of the specimen is modeled. Figure 1 shows the typical fine-mesh configuration and

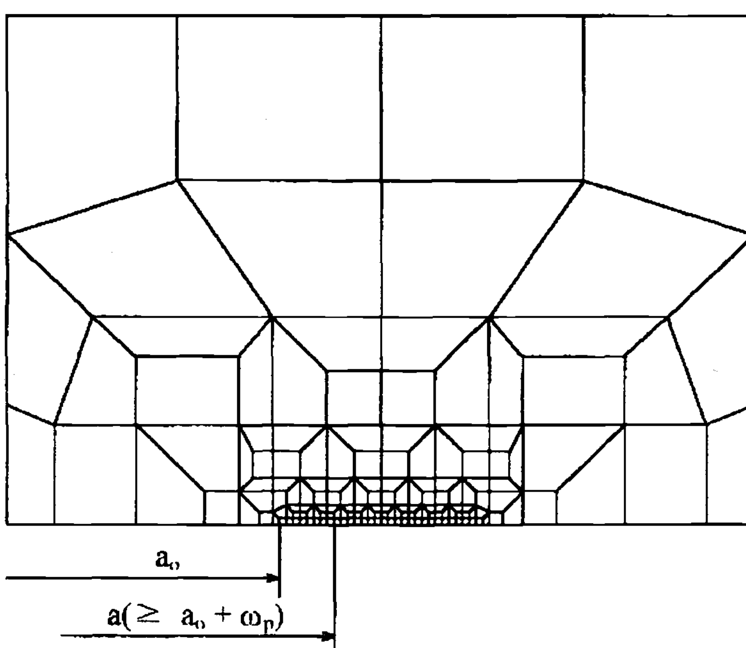

FIG. 1—*Typical fine mesh used in present work.*

the fine-mesh size is determined based on the concept of the most appropriate mesh size proposed in the previous work [*8*].

Material properties used for the analysis are as follows: Young's modulus E = 70 GPa, Poisson's ratio $\nu = 0.33$, yield stress σ_y = 379 MPa, and the plastic modulus or the linear strain hardening parameter $H' = (d\sigma/d\varepsilon) = 0.01E$ = 700 MPa. These properties are expected to correspond to the 2024-T351 that was used in previous experimental work [*10*].

The computation was carried out on a HP 9000/715 desktop workstation and about 20 min was required to complete a single load cycle.

Experimental Crack Opening Data for Comparison

The experimental crack opening data used for the comparison are the results obtained from single overloading, Hi-Lo block loading, narrow- and wide-band random loading tests in previous experimental work reported by one of the authors [*10*]. The single overloading and Hi-Lo block loading tests were originally performed to compare the crack closure behavior under random loading and under simple variable amplitude loading.

The details of the experiment have been described in Ref *10*. Only the important aspects related to the present study are given here.

The material used is 2024-T351 aluminum alloy plate. The 2% proof stress is 379 MPa, the tensile strength 480 MPa, elongation 19.6%, and the reduction of area 17.0%.

A CCT specimen, of initial notch $2a_0$ = 16 mm, 10 mm thick, 184 mm long and 70 mm wide, is used. The semicircular side grooves with radius of 1 mm were machined to obtain plane strain crack growth data. The crack plane orientation is L-T.

All the tests were conducted using a closed servo-hydraulic fatigue testing machine at a frequency of 7 Hz. Single overloading and Hi-Lo block loading tests were performed all with a stress ratio of $R = 0$. Single overloading tests were performed with overload ratios of OLR = $\sigma_{\max}^{OL}/\sigma_{\max}$ = 1.5, 1.75 and 2.0, where $\sigma_{\max}^{OL}$ and $\sigma_{\max}$ are the overload and baseline maximum stresses, respectively (see Fig. 3*a*). Hi-Lo block loading tests were conducted with a ratio of $\sigma_{\max}^{Hi}/\sigma_{\max}^{Lo}$ = 1.5, where $\sigma_{\max}^{Hi}$ and $\sigma_{\max}^{Lo}$ are the maximum stresses for high and low block loads, respectively (see Fig. 4*a*). For random loading tests, two types of random spectra, i.e., narrow- and wide-band random spectra as shown in Fig. 2 were generated by computer simulation. For each type of random spectrum, three different random loading blocks having history lengths of N_b = 500, 1000 and 2000 cycles were constructed. Random loading tests were performed by repeatedly applying each random loading block. The stress ratio corresponding to the largest load cycle in a random loading block $R(\Delta K_{\max}^{rp})$ was kept at 0. Here $\Delta K_{\max}^{rp}$ means the stress intensity factor range of the largest load cycles.

Crack length and closure are measured continuously during the tests by employing an unloading elastic compliance technique [*11*] and a personal computer system. The displacements for this technique are measured by the clip-on gage attached in the circular hole at the center of the specimen.

The experimental procedure used is comparable to the method recommended by the ASTM Test Method for Measurement of Fatigue Crack Growth Rates (E 647-95a) [*12*] for determination of fatigue crack opening load from compliance. Particularly in the procedure, the curve of load versus differential displacement rather than the curve of load versus displacement is used to improve the sensitivity of detection of the variation of compliance. Kim and Song [*13*] proposed an automated method to determine consistently the crack opening load. They reported that the error of the experimental crack opening data used in this study for the comparison is less than 2% based on the maximum stress.

The experimentally measured crack opening results are found in the previous experimental work [*10*] to be able to account successfully for the effect of stress ratio and crack growth behavior under stationary random loading.

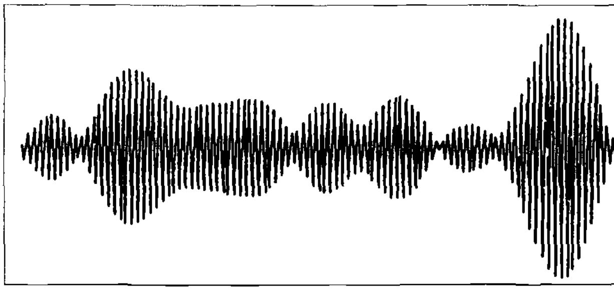

(a)

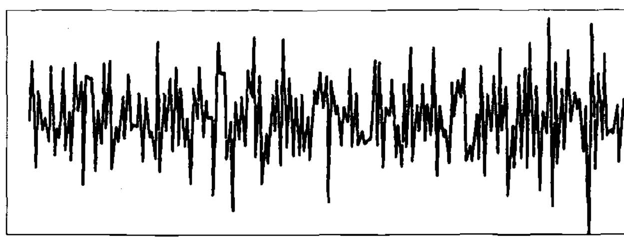

(b)

FIG. 2—*Random loading histories:* (a) *narrow band and* (b) *wide band.*

Results

As already noted, the fine-mesh size was determined for each loading condition, using the concept of the most appropriate mesh size [*8*]. According to the FE numerical results obtained under constant-amplitude loading in the previous work [*8*], the most appropriate mesh size Δa^* can be determined from the equation $\Delta a^*/\omega_p = 0.193$ or $\Delta a^*/\Delta\omega_p = 0.772$ for a stress ratio of $R = 0$ at which all variable-amplitude experimental tests were performed. Here ω_p and $\Delta\omega_p$ are the theoretical plane stress monotonic and reversed plastic zone sizes, respectively, defined as

$$\omega_p = \frac{1}{\pi}\left(\frac{K_{max}}{\sigma_y}\right)^2 \tag{1}$$

$$\Delta\omega_p = \frac{1}{\pi}\left(\frac{\Delta K}{\sigma_y}\right)^2 \tag{2}$$

where K_{max} is the maximum stress intensity factor, MPa·m$^{1/2}$, and ΔK_{max} the stress intensity factor range, MPa·m$^{1/2}$.

Crack Opening Behavior Under Single Overloading

Figure 3*a* shows a typical example of the crack opening behavior when a single overload was applied. The fine mesh size used for the example is 0.049 mm, corresponding to the most appropriate

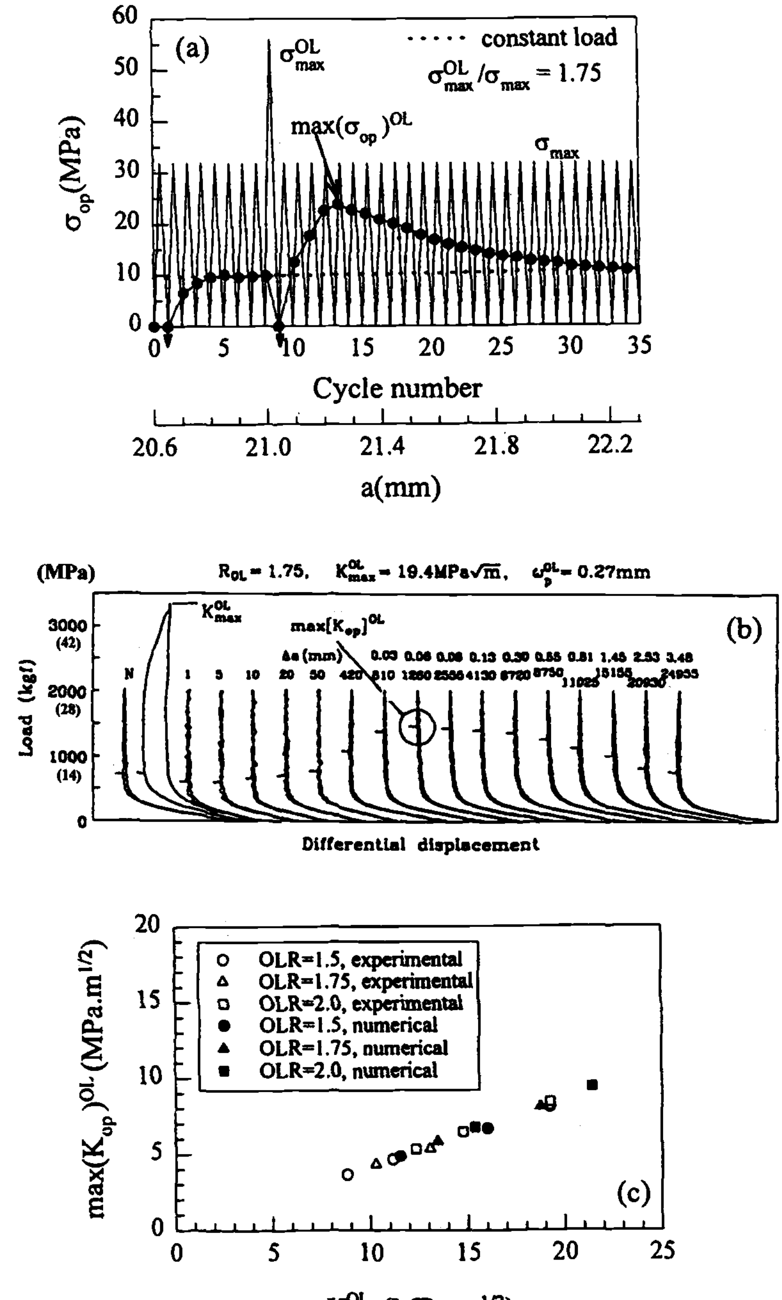

FIG. 3—*Crack opening behavior for single overloading.*

mesh size for the baseline constant-amplitude loading. Eight load cycles are applied to obtain a sufficiently stabilized crack opening level prior to overloading. In this example, the crack closure does not occur during the loading portion of the first baseline load cycle just after the application of single overload. During subsequent load cycling, the crack opening level increases to reach a maximum value $\max(\sigma_{op})^{OL}$ and thereafter decreases gradually to resume the original stabilized crack opening level. This trend of variation of crack opening level agrees nearly perfectly with the FE numerical result reported by Ogura and Ohji [*3*] and also agrees well with the experimental result shown in Fig. 3*b*.

It was found in the previous experimental work [*10*] that the maximum crack opening load observed in single overloading tests agrees well with the crack opening load under random loading and, consequently, the crack closure behavior under random loading can be estimated from single overloading tests. Accordingly, the maximum crack opening load $\max(K_{op})^{OL}$ under single overloading is very important. The numerical results of $\max(K_{op})^{OL}$ are compared with the experimental ones in Fig. 3*c*. For all overload ratios analyzed, the numerical results are in excellent agreement with the experimental ones.

In Fig. 3*a*, the crack-tip advance increment until the crack opening level reaches a maximum value is about ¼ ~ ⅓ of the monotonic overload plastic zone size ω_p^{OL} defined as

$$\omega_p^{OL} = \frac{1}{\pi}\left(\frac{K_{max}^{OL}}{\sigma_y}\right)^2 \tag{3}$$

where K_{max}^{OL} is the maximum overload stress intensity factor, MPa·m$^{1/2}$.

After the crack tip advances to about 1.1 ~ 2.2 times ω_p^{OL}, the crack opening level resumes the preoverload stabilized value.

Crack Opening Behavior Under Hi-Lo Block Loading

Figure 4*a* shows a typical example of the variation of crack opening level under Hi-Lo block loading. The fine-mesh size used for this example is 0.110 mm, corresponding to the most appropriate mesh size for the high load σ_{max}^{Hi}. The crack opening level which is stabilized under high load cycling increases monotonically after load reduction to reach a maximum value $\max(\sigma_{op})^{HL}$ and then gradually approaches the original stabilized value. Nearly the same trend of crack opening can be found in the results of Ogura and Ohji [*3*], and of Newman [2]. However, the behavior that the crack opening level approaches the original stabilized crack opening level during prolonged load cycling cannot be found so clearly in their results. The behavior shown in Fig. 4*a* that the crack opening level increases after load reduction to reach a maximum value and then decreases can be observed clearly also in the experimental result shown in Fig. 4*b*. Figure 4*c* compares the maximum crack opening load $\max(K_{op})^{HL}$ between the numerical and experimental results. The numerical results can be said to agree well with the experimental ones.

In Fig. 4*a*, the crack-tip advance increment until the crack opening level reaches a maximum value is about ¼ of the monotonic plastic zone due to the high load, ω_p^{Hi}, defined as

$$\omega_p^{Hi} = \frac{1}{\pi}\left(\frac{K_{max}^{Hi}}{\sigma_y}\right)^2 \tag{4}$$

where K_{max}^{Hi} is the maximum stress intensity factor due to the high load σ_{max}^{Hi}, MPa·m$^{1/2}$.

This increment is comparable with that in the case of single overloading.

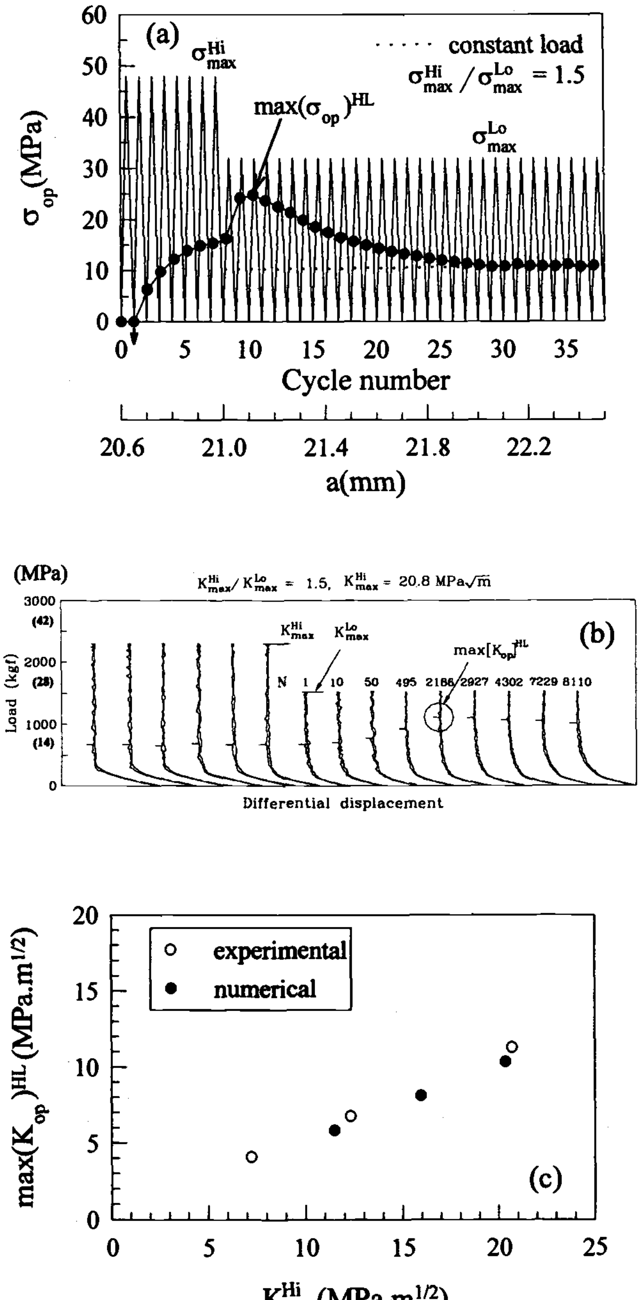

FIG. 4—*Crack opening behavior under Hi-Lo block loading.*

Simulation of Crack Opening Behavior Under Random Loading

A significant characteristic of crack closure behavior under random loading is that the crack opening load is nearly constant during a random loading block of a relatively long history length such as 2000 cycles, as has been frequently reported [10,14].

The conventional FE simulation of crack closure in which the crack tip advances one element every cycle is not reasonable for and practically inapplicable to random loading. In order to simulate crack closure behavior under random loading, other different methods must be developed. The experimental fact above noted that the crack opening level is nearly constant during a random loading block of long history length may be attributed to the fact that the crack growth increment during a random loading block is usually smaller than the plastic zone size due to the largest load cycle in a random load history and may be neglected.

Figure 5 shows the numerical crack opening result under random loading when the crack tip is fixed after the crack opening level is stabilized by applying several cycles of the largest load in a random load history. It can be found that the crack opening level is hardly changed even if the magnitude of the cyclic load varies irregularly.

Considering this result, crack opening behavior under random loading is simulated, replacing a random load of complete profile by an equivalent, simplified variable load as follows: Under the assumption that the largest load cycle in a random load history has the same effect as a single overload, an imaginary, equivalent overload ratio is defined for a random load as

$$(\mathrm{OLR})_{\mathrm{p-v}} = \frac{\sigma^{\mathrm{p}}_{\mathrm{max}} - \sigma^{\mathrm{v}}_{\mathrm{min}}}{\sigma^{\mathrm{p}}_{\mathrm{rms}} - \sigma^{\mathrm{v}}_{\mathrm{min}}}: \quad \text{peak-valley overload ratio} \tag{5}$$

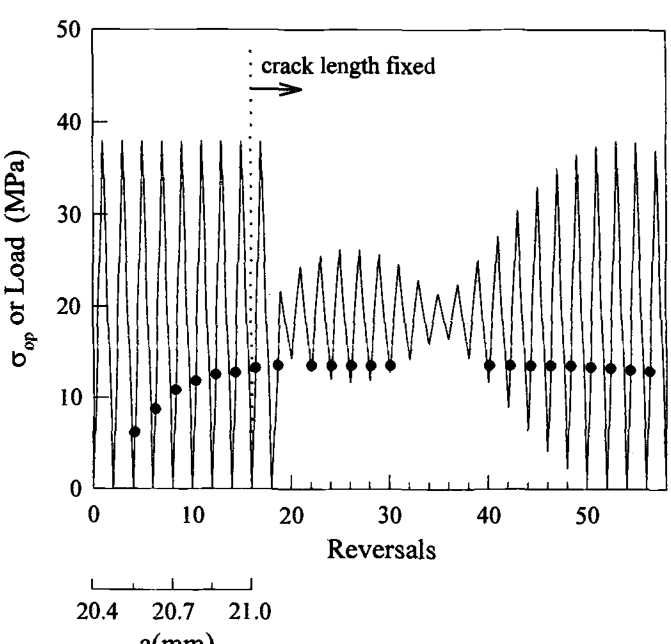

FIG. 5—*Variation of σ_{op} under random loading when the crack tip is fixed.*

where

σ^{p}_{max} = maximum peak load, MPa,
σ^{v}_{min} = minimum valley load, MPa, and
σ^{p}_{rms} = root-mean-square value of peak loads, MPa.

Using the values of σ^{p}_{max}, σ^{v}_{min} and σ^{p}_{rms} of a random load, narrow- and wide-band random loads are approximated by the simple variable loads shown in Fig. *6a* and *b*, respectively. In Fig. *6a*, a narrow-band random load is replaced by an incremental step load where the maximum and minimum load ranges are σ^{p}_{max} and σ^{p}_{rms}, respectively, and 7 cycles of linearly varying amplitudes are inserted between the maximum and minimum load ranges. The number of inserted load cycles of 7 is expected to provide a stabilized crack opening level. In Fig. *6b*, a wide-band random load is replaced by a repeated two-step load consisting of two load ranges of σ^{p}_{max} and σ^{p}_{rms}. The value of $\max(\sigma_{op})$ in Fig. *6a* and the value of σ_{op} on the fourth cycle of the large load σ^{p}_{max} in Fig. *6b* are employed as the crack opening levels for narrow- and wide-band random loads, respectively. The fine-mesh size is determined from the most appropriate mesh size for the small load σ^{p}_{rms}.

Using the method described hitherto, simulation was performed for random loads of history length of 500 cycles and the numerical crack opening results are compared with experimental results in Fig. 7. The numerical results agree very well with the experimental ones, implying that the simulation method proposed may be promising.

Discussion

The crack tip is released arbitrarily on every cycle and the amount of crack growth per cycle is one element size in the analysis. So the crack growth rate has no physical meaning because FE analysis is not to predict the crack growth behavior but to predict the stabilized crack displacement behavior. Therefore, it is not appropriate to compare the cycle numbers between the experiment and analysis.

It is reasonable that plane strain experimental data should be predicted using plane strain analysis results. However, the plane strain opening level is much lower than the plane stress one [*6*] when the same element size is used, and the wrong results that there is no crack closure when a relatively large element size is used are reported. If the plane strain analysis is performed, very small element size should be used to obtain the numerical results which are in good agreement with experimental data. In this case, total element numbers will become larger and it will take too much time. So the analysis will become inefficient.

Although there exist constraint effects, it was found in our previous work [*8*] that the plane experimental data could be predicted well by the plane stress analysis under the constant-amplitude loads.

The purpose of this paper is to find out whether these results can also be applied to the variable loadings. It was found that the maximum crack opening level for single overloading and Hi-Lo block loading can be predicted well using the plane stress analysis with the same element size determined under the constant-amplitude load.

A plane strain FE analysis is now being carried out to predict the plane strain experimental data.

Conclusions

The crack opening behavior of fatigue cracks under variable loading is investigated using a two-dimensional elastic-plastic finite element (FE) analysis. The concept of the most appropriate mesh size proposed in previous work is utilized and the FE numerical results are compared with experimental data. The conclusions obtained are summarized as follows:

1. The FE analysis can simulate successfully the crack opening behavior under single overloading and Hi-Lo block loading.
2. By using the concept of the most appropriate mesh size, the maximum crack opening loads ob-

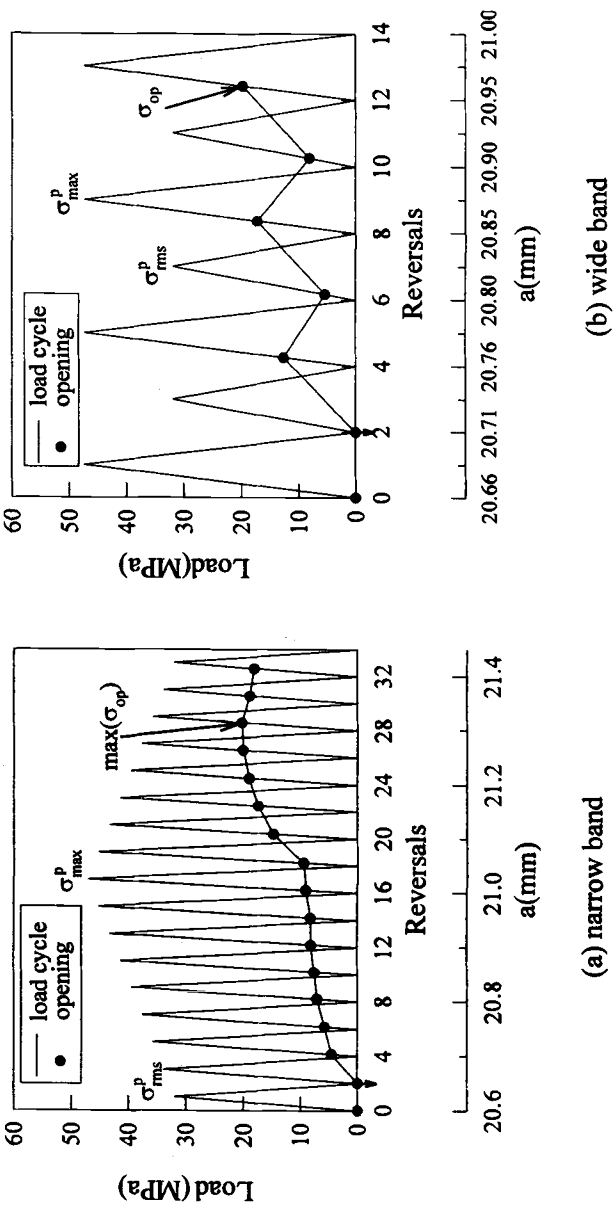

FIG. 6—Simplified load profiles for crack opening simulation under random loading.

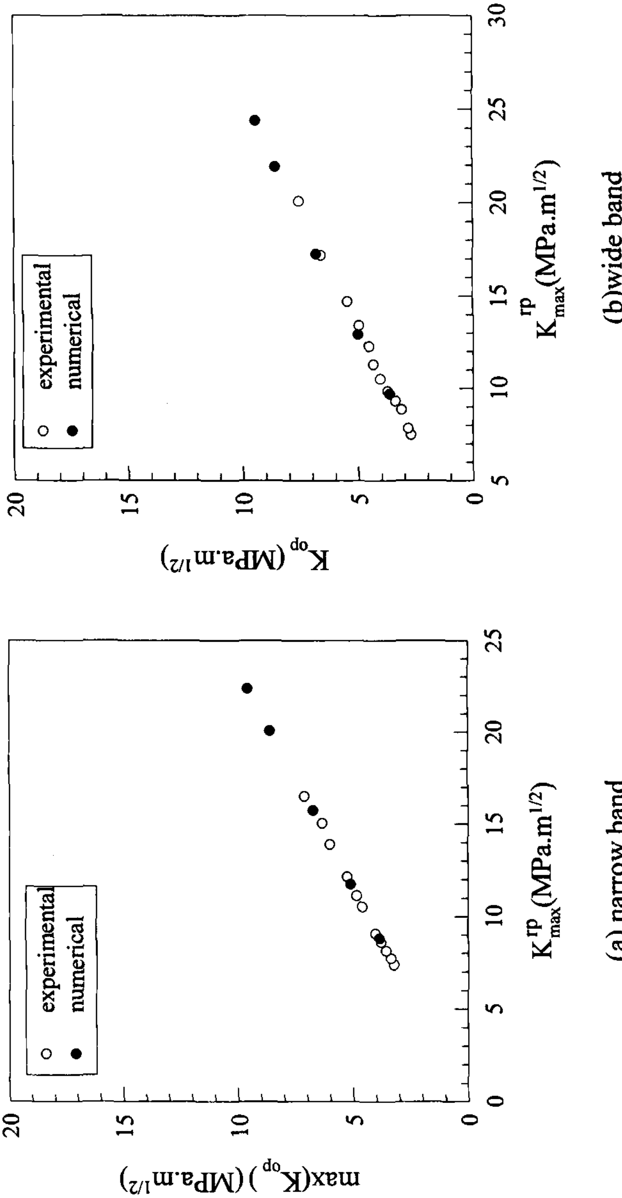

FIG. 7—*Comparison of crack opening load between the numerical and experimental results under random loading.*

tained numerically for single overloading and Hi-Lo block loading agree quantitatively very well with the experimentally observed ones.

3. In order to simulate the crack opening behavior under random loading, a method is proposed which replaces a complicated random load by an equivalent simple variable load. The simulation results by the method agree very well with experimental results, indicating that the method may be promising.

References

[1] Ohji, K., Ogura, K., and Ohkubo, Y., "Cyclic Analysis of a Propagating Crack and Its Correlation with Fatigue Crack Growth," *Engineering Fracture Mechanics*, Vol. 7, 1975, pp. 457–464.

[2] Newman, J. C., Jr., "A Finite Element Analysis of Fatigue Crack Closure," *Mechanics of Crack Growth, ASTM STP 590*, American Society for Testing and Materials, Philadelphia, 1976, pp. 281–301.

[3] Ogura, K. and Ohji, K., "FEM Analysis of Crack Closure and Delay Effect in Fatigue Crack Growth Under Variable Amplitude Loading," *Engineering Fracture Mechanics*, Vol. 9, 1977, pp. 471–480.

[4] Zhang, X., Chan, A. S. L., and Davies, G. A. O., "Numerical Simulation of Fatigue Crack Growth Under Complex Loading Sequences," *Engineering Fracture Mechanics*, Vol. 42, 1992, pp. 305–321.

[5] McClung, R. C. and Sehitoglu, H., "On the Finite Element Analysis of Fatigue Crack Closure-1. Basic Modeling Issues," *Engineering Fracture Mechanics*, Vol. 33, 1989, pp. 237–252.

[6] McClung, R. C. and Sehitoglu, H., "On the Finite Element Analysis of Fatigue Crack Closure-2. Numerical Results," *Engineering Fracture Mechanics*, Vol. 33, 1989, pp. 253–272.

[7] McClung, R. C., "Finite Element Analysis of Specimen Geometry Effects on Fatigue Crack Closure," *Fatigue and Fracture of Engineering Materials and Structures*, Vol. 17, 1994, pp. 861–872.

[8] Park, S. J., Earmme, Y. Y., and Song, J. H., "Determination of the Most Appropriate Mesh Size for a 2-D Finite Element Analysis of Fatigue Crack Closure Behavior," *Fatigue and Fracture of Engineering Materials and Structures*, Vol. 20, 1997, pp. 533–545.

[9] Kohnke, P., *ANSYS User's Manual for Revision 5.0 Vol. IV Theory*, Swanson Analysis Systems, Inc., 1992, pp. 4.4–4.12.

[10] Kim, C. Y. and Song, J. H., "Fatigue Crack Closure and Growth Behavior Under Random Loading," *Engineering Fracture Mechanics*, Vol. 49, 1994, pp. 105–120.

[11] Kikukawa, M., Jono, M., and Tanaka, K., "Fatigue Crack Closure Behavior at Low Stress Intensity Level," *Proceedings of the International Conference on Mechanical Behavior of Materials*, Vol. 2, 1986, pp. 254–277.

[12] ASTM E 647-95, "Standard Test Method for Measurement of Fatigue Crack Growth Rates," *Annual Book of ASTM Standards*, Vol. 03.01, 1995, pp. 578–614.

[13] Kim, C. Y. and Song, J. H., "An Automated Procedure for Determining Crack Opening Level from Differential Displacement Signal Data," *International Journal of Fatigue*, Vol. 15, 1993, pp. 301–309.

[14] Jono, M., Song, J. H., and Kikukawa, M., "Fatigue Crack Growth and Crack Closure of Structural Materials Under Random Loading," *Proceedings of the International Conference on Mechanical Behavior of Materials*, Vol. 6, 1984, pp. 1735–1742.

Surface Roughness Effects

Nong Chen[1] and Frederick V. Lawrence[2]

A Comparison of Two Total Fatigue Life Prediction Methods

REFERENCE: Chen, N. and Lawrence, F. V., "**A Comparison of Two Total Fatigue Life Prediction Methods,**" *Advances in Fatigue Crack Closure Measurement and Analysis: Second Volume, ASTM STP 1343,* R. C. McClung and J. C. Newman, Jr., Eds., American Society for Testing and Materials, West Conshohocken, PA, 1999, pp. 351–366.

ABSTRACT: A 2-D analytical model which is termed the PICC-RICC model combines the effects of plasticity-induced crack closure (PICC) and roughness-induced crack closure (RICC). The PICC-RICC model handles naturally the gradual transition from RICC to PICC dominated crack growth. In this study, the PICC-RICC model is combined with a crack nucleation model to predict the total fatigue life of a notched component. This modified PICC-RICC model will be used to examine several controversial aspects of an earlier, computationally simpler total-life model known as the IP model.

KEYWORDS: crack closure, notches, total fatigue life, fatigue life prediction models

Analytical Models for Predicting the Total Fatigue Life

The total fatigue life of a component may be considered to be the sum of three periods: crack nucleation (N_N), short crack growth (N_{P1}) in which the crack closure phenomenon is a function of crack length, and long crack propagation (N_{P2}) in which the crack closure phenomenon is more or less independent of crack length.

$$N_T = N_N + N_{P1} + N_{P2} \tag{1}$$

The IP Model

Lawrence et al. [*1–3*] have proposed a two-stage, total-life model, the Initiation-Propagation (IP) model; see Fig. 1. The total fatigue life is considered to be composed of two portions: a fatigue crack initiation period and a fatigue crack growth period. The total fatigue life, N_T, is estimated as

$$N_T = (N_N + N_{P1}) + N_{P2} = N_I + N_{P2} \tag{2}$$

The initiation life, N_I, consists of both the initiation and early growth of fatigue cracks and as well as their coalescence into a dominant fatigue crack. The propagation life, N_{P2}, consists of the number of cycles to grow this dominant fatigue crack to failure. N_I is estimated using strain-controlled (smooth specimen) fatigue properties and the Basquin-Morrow equation as follows, which (in its simplest form, neglecting notch-root plastic strains) is:

[1] Formerly graduate research assistant, Civil Engineering Department, University of Illinois at Urbana-Champaign. Currently senior research engineer, Caterpillar Inc., Technical Center, Bldg. K, PO Box 1875, Peoria, IL 61656-1875.

[2] Professor, Civil Engineering Department and Material Science and Engineering Department, University of Illinois at Urbana-Champaign, 205 N. Mathews Ave., Urbana, IL 61801.

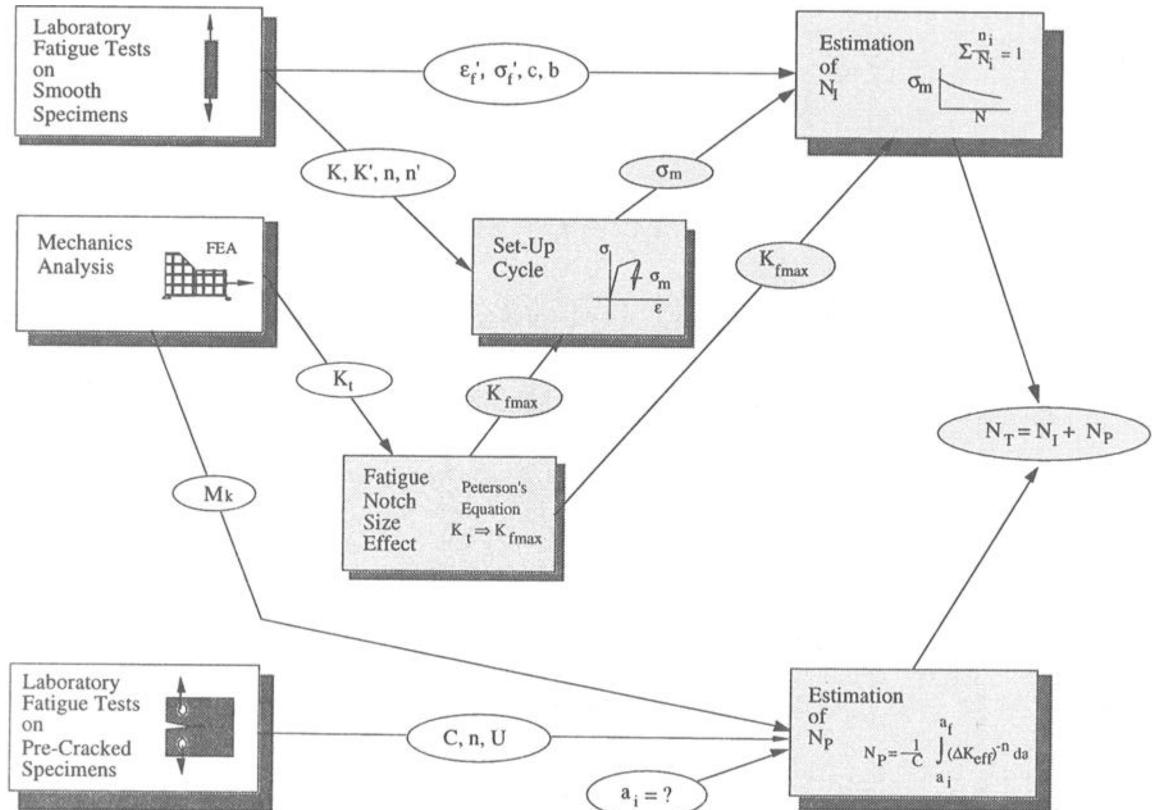

FIG. 1—*A schematic diagram showing the information required by and the organization of the IP model. The unshaded boxes represent the results from prior experiment and analysis: strain controlled fatigue properties, crack growth properties, tensile properties, and a FEM stress analysis of the weld joint geometry.*

$$N_I = \frac{1}{2}\left(\frac{\Delta S\, K_f}{2(\sigma_f' - \sigma_m)}\right)^{\frac{1}{b}} \tag{3}$$

where ΔS is the remote cyclic stress amplitude, K_f is the fatigue notch factor, σ_f' is the fatigue strength coefficient, σ_m is the mean stress, and b is the fatigue strength exponent. N_{P2} is estimated using crack growth data for long cracks and the Paris Power Law:

$$N_{P2} = \int_{a_i}^{af} \frac{da}{C\,\Delta K^m} \tag{4}$$

where a_i is the initial crack length, a_f is the crack length at failure, and C, m are material constants in the Paris Power Law.

One difficulty with the IP model is determining the value of the initial crack length "a_i": the predicted value of N_{P2} depends strongly on the value of a_i. Lawrence et al. customarily assumed an "engineering crack size" of 0.25 mm (0.01 in.) as the value of a_i. A more rigorous method of determining a_i is needed. A second difficulty with the IP model is its dependence upon the concept of the fatigue notch factor K_f, the empirical Peterson's Equation, and the derived concept of the "worst case notch," $(K_f)_{\max}$. The meaning of this concept and its proper use remains unclear, and the use of $(K_f)_{\max}$ is therefore a controversial aspect of the IP model.

In this work, the recent PICC-RICC model of Chen and Lawrence will be combined with a model for crack nucleation of Socie et al. [*4*] to create a total life model which does not depend upon Peterson's equation. The predictions of the modified PICC-RICC model will be used to examine the question of the initiated crack length "a_i" and the concept of the worst case notch or $(K_f)_{\max}$, that is, to study two controversial aspects of the IP model.

The Modified PICC-RICC Model

A total fatigue life model is proposed which will be termed the modified PICC-RICC model. The total fatigue life equation (Eq 1) may be factored as:

$$N_T = N_N + (N_{P1} + N_{P2}) = N_N + N_F \tag{5}$$

where N_N is the portion of fatigue life to nucleate a fatigue crack and N_F is the number of cycles to grow the fatigue crack to failure. The modified PICC-RICC model was created by combining the crack nucleation life model of Socie et al. [*4,5*] (see Appendix 1) to provide estimates of N_N with the PICC-RICC model of Lawrence and Chen [*6*] (see Appendix 2) which provides estimates of N_F.

$$N_F = \int_{a_i}^{af} \frac{da}{C'(\Delta K_{\text{eff}})^m} = \int_{a_i}^{af} \frac{da}{C'(U(x)\,\Delta K)^m} \tag{6}$$

where

$$U(x) = \frac{\Delta K_{\text{eff}}(x)}{\Delta K(x)} = \frac{S_{\max} - S_{\text{open}}}{S_{\max} - S_{\min}}$$

Determination of Crack Length of Transition Between Nucleation and Propagation Dominated Crack Growth Using NP Model

In a study by Hoshide and Socie [*4*], the transition from initiation to propagation dominated crack growth was defined as a competition between two types of crack growth—one due to crack coales-

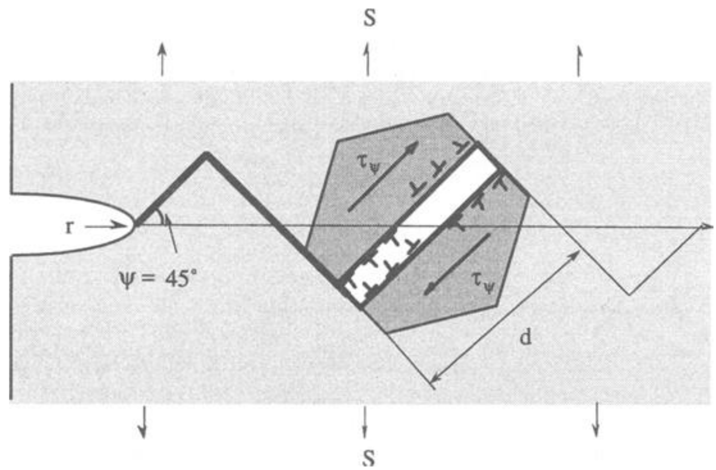

FIG. 2—*Use of Socie's method of determining the crack nucleation life into the NP model.*

cence and the other due to crack propagation. The crack growth behavior was determined by the faster growth mechanism. In the present study, the crack length a_i at which the transition from nucleation dominated crack growth to propagation dominated crack growth occurs was estimated using a similar concept. The procedure is illustrated in Fig. 2 and is described below:

Starting near the notch root, the crack is advanced the distance of one grain along the slip plane. Equation 3 is employed to calculate the number of cycles needed to advance through the grain by nucleation. Then Eq 6 is used to calculate the number of cycles needed to advance through the same distance by crack growth. The two calculated results are compared. The transition from nucleation to crack coalescence and growth-dominated cracking is considered to take place at the ith grain (located between A and B as illustrated in Fig. 3) when for the first time N_F^i no longer exceeds N_N^i, i.e., when

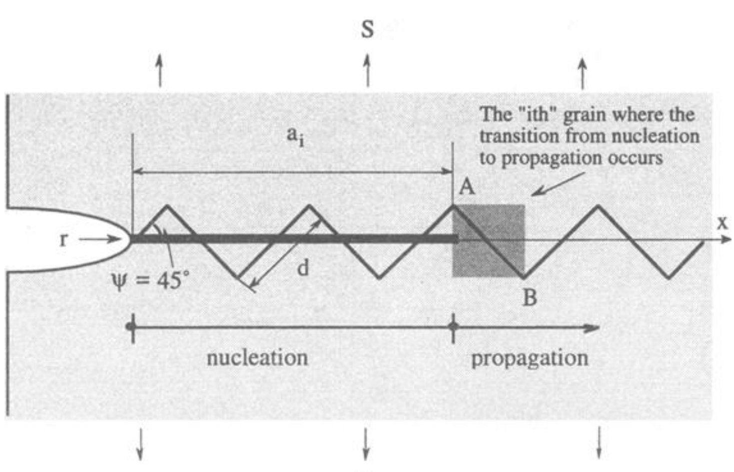

FIG. 3—*Scheme for the determination of the initial crack length for propagation,* a_i *using the NP model.*

TABLE 1—*Material Properties of Mild Steel Considered.*

Yield strength, S_y (MPa)	345
Ultimate strength, S_u (MPa)	555
Young's modulus, E (GPa)	200

the following inequality which indicates a faster progress via crack growth is satisfied:

$$\int_A^B \frac{dx}{C'(\Delta K_{\text{eff}})^m} < \Delta N_{\text{nucleation}}^{A\rightarrow B} \tag{7}$$

where N is the fatigue cycles accumulated. The length of the crack when it first encounters the ith grain is defined as the initial crack length for propagation, a_i. In essence, the strategy for calculating a_i is to determine whether a crack (which may be of length A due to crack coalescence or prior crack growth) can grow to an incremental length B (one grain diameter) faster by growth or faster by nucleation and further coalescence. For simplicity, any interaction between the prior crack and the nucleation of a new crack within the grain considered has been ignored.

The fatigue behavior of elliptical edge notches with a constant notch depth of 0.2 in. (5 mm) was examined using the modified PICC-RICC model. The stress concentration factor K_t of the notches was varied from 2 to 30 by changing the notch root radius. The zigzag path used in the prediction of propagation life had a constant tilt angle of 45° and a deflected branch length equal to the assumed grain size of 30 μm of a mild: see Table 1.

The initial crack length for propagation, a_i, was estimated for a life of 10^7 cycles ($R = 0$) and is shown in Fig. 4 as a function of K_t. The predicted results show that when K_t is less than 3, the value

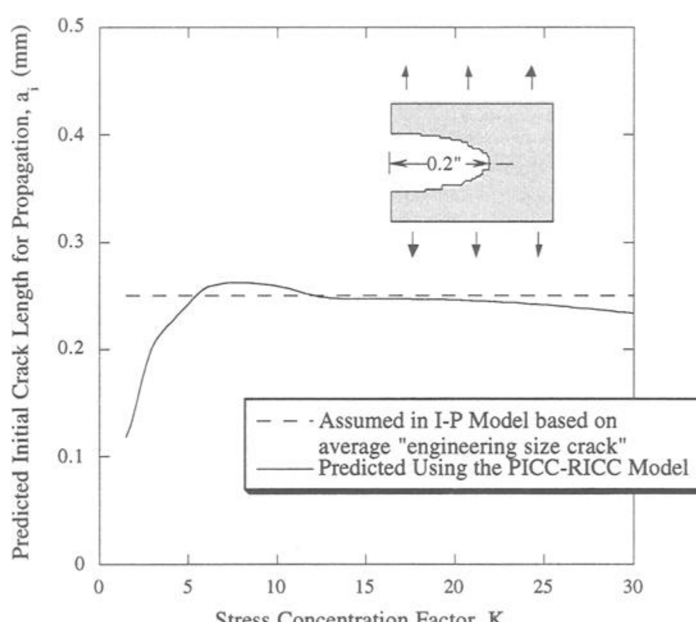

FIG. 4—*Initial crack length* a_i *predicted using the NP model for a constant depth elliptical notch in mild steel. The customary IP Model assumption of* a_i *= 0.25 mm (0.01 in.) is shown and is seen to agree with the predictions of the PICC-RICC model for* K_t *greater than 3.* $R = -1$ *conditions.*

of a_i increases markedly as the notch gets sharper. While both crack nucleation and growth are diminished by this initial K_t increase, the change is more prominent for nucleation and hence causes a delay of the nucleation-propagation transition. After this initial increase, the a_i remains relatively constant as the notch gets sharper, indicating a balance between nucleation and propagation. The slight decrease of a_i is attributed to the reduction in the rapidity of crack nucleating as the amplitude of the local shear stress approaches the frictional stress τ_c. Also shown in the Fig. 4 is the a_i value of 0.25 mm (0.01 in.) customarily assumed in the I-P model which is seen to be close to the a_i value predicted for values of K_t greater than about 3.

Examination of Fatigue Notch Size Effect and "Worst-Case" Notch

Most fatigue cracks emanate from stress-concentrating notches. Such notches result from geometrical or microstructural discontinuities and exist in almost all structural components. One special case is the notch provided by a weld toe. Examination of stations along as-fabricated weld toes reveals notch root radii which range from very sharp and crack-like to smooth transitions from weld metal onto the surface of the plates which the weld joins. Which value of radius is most serious? Intuitively, one would suppose that the smallest, most crack-like radius would be the most damaging, but as we shall see below, Peterson's equation, the PICC-RICC model and experimental studies [*7*] suggest that this may not be so.

Worst-Case Notch

The existence of a "worst-case" notch for constant depth notches is suggested by Peterson's equation [*1–3*]. For an elliptical notch as shown, the stress concentration factor K_t is:

$$K_t = 1 + 2\sqrt{\frac{D}{r}} \tag{8}$$

were D is the notch depth and r is the notch root radius. If one substitutes the above K_t expression into Peterson's relationship:

$$K_f = 1 + \frac{K_t - 1}{1 + \frac{a_p}{r}} \tag{9}$$

one gets the following expression for K_f:

$$K_f = 1 + \frac{2\sqrt{D}}{\sqrt{r} + \frac{a_p}{\sqrt{r}}} \tag{10}$$

which suggests the existence of a maximum K_f value at $r = a_p$ with the corresponding $(K_f)_{\max}$ equal to:

$$(K_f)_{\max} = 1 + \sqrt{\frac{D}{a_p}} \tag{11}$$

where a_p is the material constant in Peterson's equation.

Figure 5 shows the total fatigue life predicted by the modified PICC-RICC model for a series of 5 mm (0.2 in.) depth elliptical notches having various notch root radii and consequently values of K_t which vary from 5 to 30. As seen in Fig. 5 the modified PICC-RICC model predicts that the crack

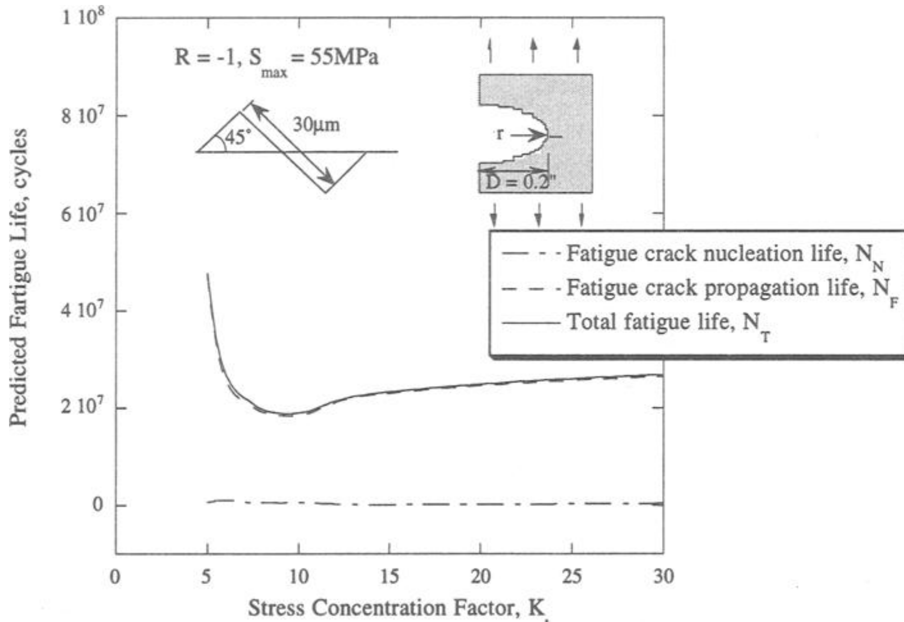

FIG. 5—*The total fatigue life predicted by the NP model for a mild steel containing various elliptical notches of 0.2 in. (5 mm) depth. The total life shows a minimum at a* K_t *of around 8 or for a notch root radius of around 0.4 mm.*

propagation life (N_F) is always the major part of the total fatigue life and that the total life decreases and then increases as the stress concentration increases from $K_t = 5$. The model predicts a minimum fatigue life when $K_t \approx 10$.

The shape of the N_F curve in Fig. 5 can be explained as follows: the initial loss of propagation life is attributed to the acceleration of fatigue crack growth as the notch gets sharper. However, a counter effect of a sharper notch as opposed to a higher K_t value is that it also introduces a higher stress gradient which leads to a quicker decline of stress once away from the notch root. Hence, as the sharpness of the notch increases, a larger portion of the fatigue crack growth will be under a lower stress and will consumes more fatigue cycles, which leads to the rebound of N_F after the initial drop.

Thus, the modified PICC-RICC model which does not depend upon Peterson's equation also suggests the existence of a "worse-case" notch.

Discussion

The modified PICC-RICC model for a_i suggests that nucleation and coalescence of cracks may dominate growth to substantial depths ($\approx$0.2 mm or more depending upon the nature of the notch). It is possible that the surface roughness in the region between the notch root and a_i may differ from the roughness of regions subsequently created by crack growth.

A comparison of the predictions of the modified PICC-RICC model with Peterson's and Neuber's expressions for the fatigue notch factor K_f is given in Fig. 6. Frost's data for mild steel [7] is also plotted in this figure. As seen in Fig. 6 the modified PICC-RICC model predicts Frost's data. Neither Peterson's nor Neuber's expression for K_f fit the data for values of K_t greater than 10; however, the Peterson equation is clearly better than the Neuber expression for the constant depth notches consid-

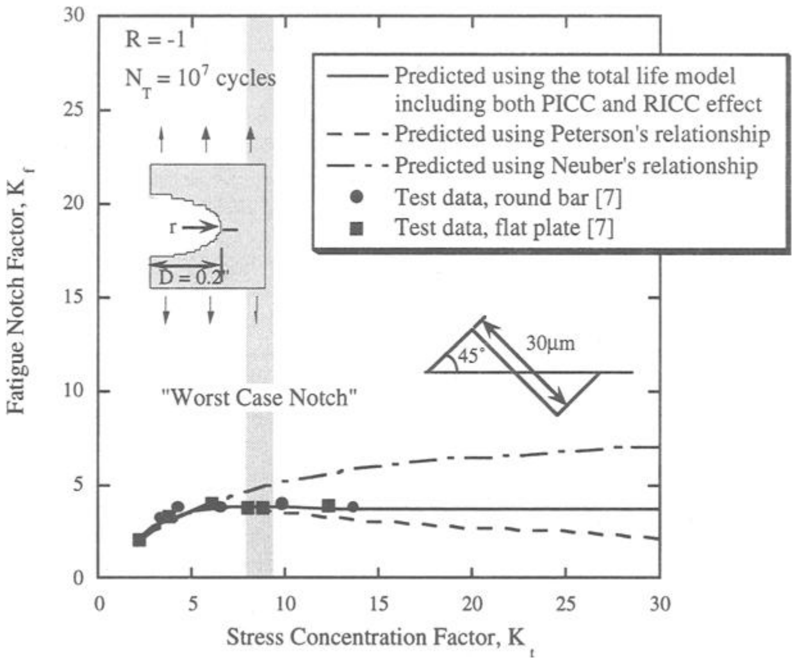

FIG. 6—*Fatigue notch factor* K_f *versus stress concentration factor* K_t. *Data are from Frost [7]. Prediction of the NP model is given as the solid line. The predictions of Peterson's and Neuber's relationships are also shown. Mild steel,* $R = -1$.

ered. The maximum in the value of K_f is the "worst-case" notch. The fact that the modified PICC-RICC model predicts the worst case notch (and the data of Frost) while the previous work of Hou [*8*] which was based solely on PICC did not predict the existence of a "worst-case" notch suggests that RICC effects (grain size—see Fig. 14) may be the cause of the worst case notch and the physical basis of Peterson's constant a_p.

Figure 7 replots the information in Fig. 6 in terms of the predicted fatigue strength at 10^7 cycles. In this figure, the predictions of the IP model are compared with the predictions of the modified PICC-RICC model. Again, the existence of a worst case notch is suggested which correlates with the value predicted by Peterson's equation (Eqs *8–11*). The predictions of the IP model agree with those of the modified PICC-RICC model but the two models disagree at high values of K_t. The essential agreement between the IP model and crack growth models based on crack closure (CCN model) was also noted by Hou [*8*]; see Fig. 8.

Given the agreement in predicted total lives between the modified RICC-PICC and IP models, given the apparent relatively short duration of the nucleation life N_N suggested by many experimental observations and the modified PICC-RICC model (Fig. 5), and given the fact the concept of K_f has always been based on the total fatigue life (at long lives), that is, has always included an amount of crack growth (Fig. 6), it appears that the IP model probably should be thought of as an "either-or" model in which N_{P2} dominates the total life at short lives and N_I dominates the total life at long lives.

Thus, the IP model (Eq *2*) works at short total lives because at short lives $N_T \approx N_{P2}$:

- N_I is small; consequently the inadequacy of the K_f concept at short lives doesn't matter.
- The difference between N_{P2} and N_F diminishes at higher stress levels because of the lesser importance of crack closure (Fig. 16) at higher stress levels. Using $a_i = 0.25$ mm (0.01 in.) to es-

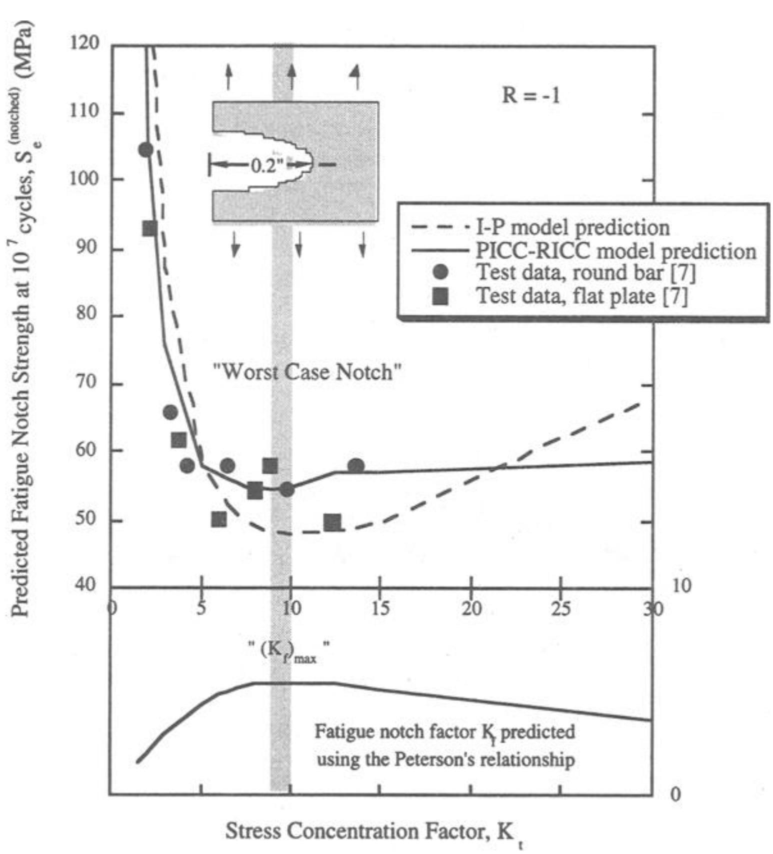

FIG. 7—*Fatigue strength predictions for mild steel at 10^7 cycles of the modified PICC-RICC and IP models. Frost's data [7] are plotted as solid symbols.* R = *−1.*

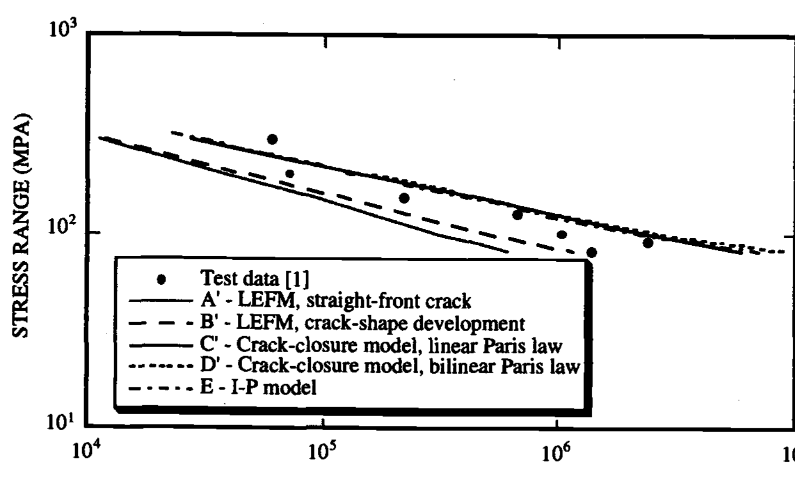

FIG. 8—*Comparison of the model predictions with the observed total fatigue [9] lives for a plate thickness* t *= 78 mm.*

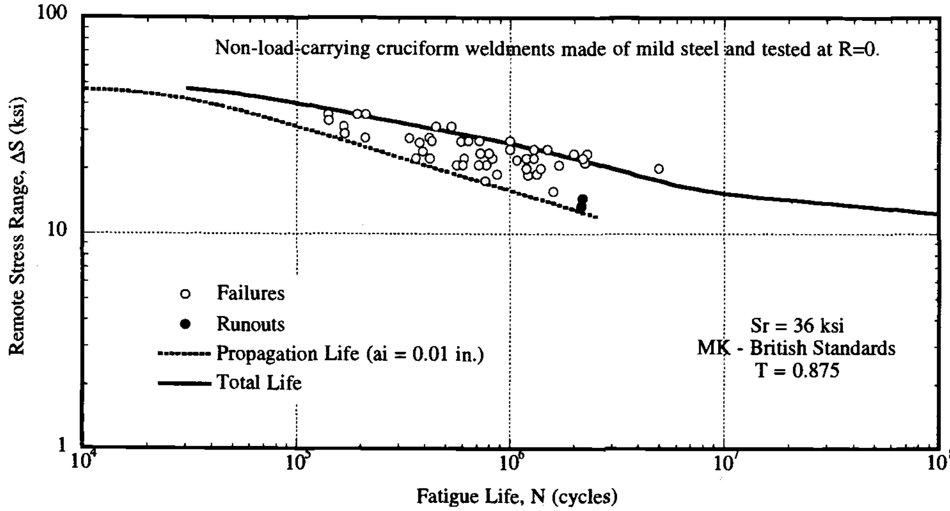

FIG. 9—*Predictions of* N_{p2} *using LEFM and total life using the IP model for a non-load carrying cruciform joint. Data points are from the UIUC fatigue data bank [10].*

timate N_{P2} is suggested by the modified PICC-RICC model and provides lower bounds to laboratory test data for laboratory weldment tests pieces: see Fig. 9.

The IP model (Eq 2) works at long lives because at long lives $N_T \approx N_I$:

- N_I dominates, and the choice of a_i is not critical. Logically at long lives, estimates of N_{P2} should be based on the dimensions of the smooth specimens used to experimentally determine Peterson's material constant a_p; see Fig. 10.

Conclusions

- The existence of a worst-case notch as predicted by the Peterson equation is also suggested by the modified PICC-RICC model which does not depend upon the Peterson equation.
- Both the modified PICC-RICC model and the IP model give the same estimates of total fatigue life, and both predict Frost's data.
- The standard IP model is slightly illogical because of inconsistencies in the values of a_i inherent in N_I and N_{P2} as currently defined; nonetheless the IP model ($N_T = N_I + N_P$) gives good total life estimates at both short and long lives because of the dominance of N_I at long lives and N_{P2} at short lives. A more rational formulation of the IP model was suggested in which N_{P2} would be based on an initiated crack length the dimension of a laboratory smooth specimen or $\approx$0.25 in.
- The modified PICC-RICC model which uses a simple model for N_N at a_i and incorporates the effects of crack closure to estimate N_F appears to be the more physically reasonable total-life model.

Acknowledgments

The authors would like to thank the Conoco, Inc. and the Fracture Control Program of the University of Illinois at Urbana–Champaign for providing the funding throughout this research. N. Chen would like to thank the Caterpillar, Inc. for support during the completion of this paper.

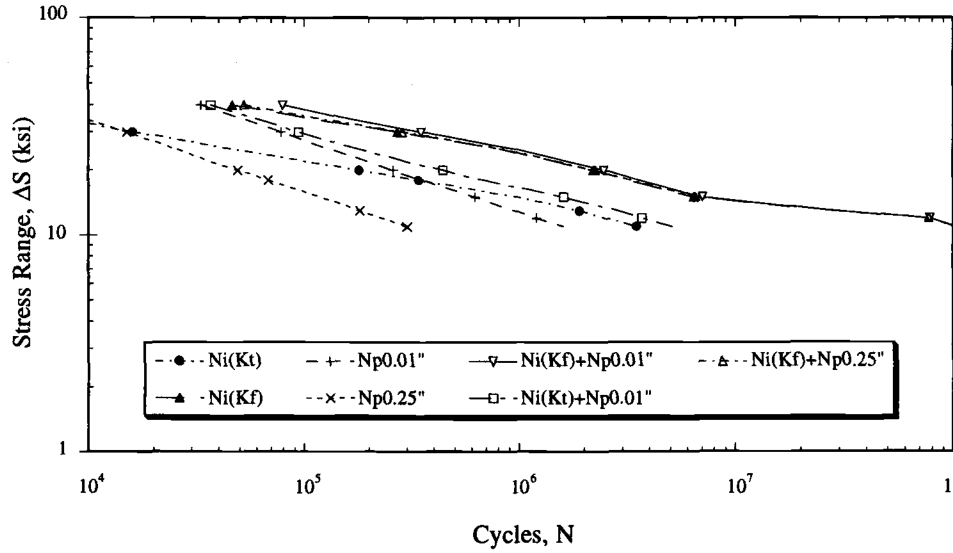

FIG. 10—*The standard IP model and alternative total life modeling strategies using the IP model. Predictions are shown for: crack initiation life* N_I *based on* $(K_f)_{max}$ *and* K_t *(Ni(Kf) and Ni(Kt)); propagation lives* N_P *based on* a_i *= 0.01 in. and 0.25 in. (Np0.01" and Np0.25"); and total fatigue life* N_T *for the standard IP model (Ni(Kf) + Np0.01"), a more rational model (Ni(Kf) + Np0.25"), and a model which neglects short crack effects (Ni(Kt) + Np0.01"). The cruciform weldment of Fig. 9 is considered.*

APPENDIX I

Estimating Fatigue Crack Nucleation Life (N_N) Using a Dislocation Model

A dislocation model for the calculation of fatigue crack nucleation life was first proposed by Tanaka and Mura [*11*]. They assumed that when the stored strain energy due to dislocations accumulated after N cycles became equal to fracture surface energy, the layers of dislocation dipoles can be transformed into a free surface. As a result, a shear crack is formed along the layers of dislocation pile up. Using the energy criterion stated above, Tanaka and Mura derived the following equation for fatigue crack nucleation life calculation:

$$N_N = \frac{8\,GW_c}{d(1 - \nu)(\Delta\tau_\varphi - 2\tau_c)^2} \tag{12}$$

where G is the shear modules of the material, n is the Poisson's ratio, w_c is the specific fracture energy for a unit area, τ_c is the critical stress to initiate slip, d is the grain size of the material, ψ is the inclination angle of the slip plane, and $\Delta\tau_\psi$ is the range of the cyclic resolved shear stress along the slip plane. Equation 12 was applied to calculate the fatigue nucleation life under multi-axial loading by Socie et al. [*4,5*]. In their study, slip planes with a random distribution of inclination angle ψ was assumed over a 2-D body under multi-axial loading. Here, under Mode I loading, the scenario of nucleation is simplified as follows: an average inclination angle of 45° is assumed according to the maximum shear stress direction under far-field Mode I loading. Possible crack nucleation sites in the 2-D body other than that along the symmetry line of the notch root (which is subject to the most severe stress concentration) will not be considered. Hence the fatigue crack is assumed to nucleate along a zigzag path of 45-deg inclination angle with the deflected branch length simulating the grain size d: see Fig. 3.

Along the assumed slip plane with 45° inclination angle, the resolved shear stress can be evaluated in terms of the local tensile stress; and Eq 12 can be written as:

$$N_N = \frac{8\,GW_c}{d(1-\nu)\left(\frac{\Delta\sigma}{2} - 2\tau_c\right)^2} \tag{13}$$

where $\Delta\sigma$ is the range of local tensile stress. Socie et al. [5] estimated the value of w_c to be 2×10^3 J/m^2 based on the knowledge that w_c is about 10^3 times greater than the surface energy (which is about 2 J/m^2 in ordinary metals).

APPENDIX II

Analytical PICC-RICC Model of Chen and Lawrence

Newman [12] first developed a numerical scheme which used the Dugdale strip yield model and the wake of plastic deformation behind crack tip to simulate plasticity induced crack closure (PICC) and to estimate the resulting crack opening stress, S_{open}. Figure 11 schematically illustrates the New-

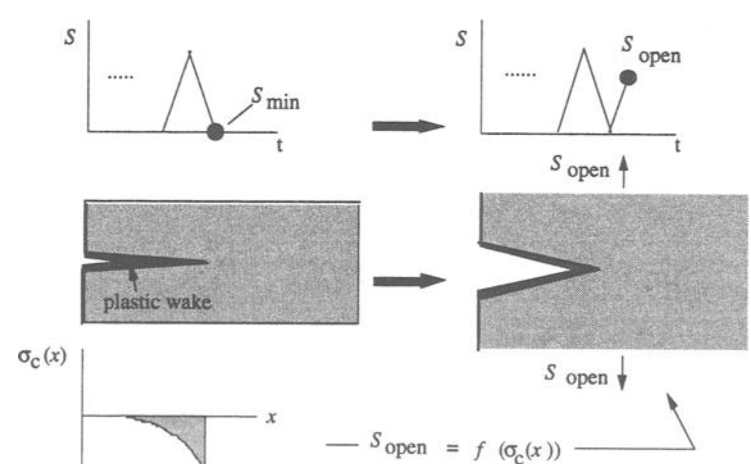

FIG. 11—*An illustration of Newman's Dugdale strip-yield model to model plasticity induced crack closure (PICC). The contact stresses* $\sigma_c(x)$ *are induced by the plastic wake.*

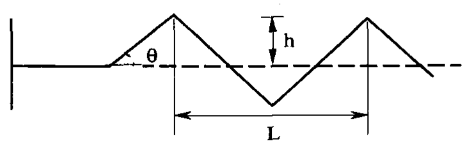

FIG. 12—*Geometrical features of the zigzag path assumed in the PICC-RICC model.*

man's Dugdale strip yield model. The load level at which the crack faces are fully open is defined as S_{open}.

The Strip-yield model for notched component (SYMNC) was developed by Hou [*8*] in which the basic approach of Newman's modified Dugdale model was applied; but in addition to the crack tip plastic stretch (CTPS) considered in Newman's model, the plastic deformation due to the presence of the notch (NPS, notch plastic stretch) was also estimated using FEM and summed up with the CTPS to form total plastic deformation. Recently, the work of Ting and Hou has been extended by Chen and Lawrence [*13*] to include the effects of RICC based on the amount fracture surface mismatch due to the local sliding displacement. This model is termed the PICC-RICC model since it combines the effects of RICC and PICC.

The PICC-RICC model of Chen and Lawrence used a zigzag path (Figs. 12 and 13) to represent the nature of Stage I fatigue crack growth [*14*]. The path is described by the branch length *L*, the branch amplitude *h*, and the tilt angle θ. To reflect the absence of crack path deflection in Stage II fatigue crack growth, θ was set to zero once the near-tip plastic zone size reaches the grain size of the material.

The sliding displacement due to crack path deflection was calculated [*6*], and the surface mismatch was estimated at each location along the crack wake. The length of the strip elements at each location were then updated (lengthened or shortened) to reflect the amount of the mismatch. The combined effects of PICC and RICC were simulated by the PICC-RICC model in this way. All calculations assumed plane strain conditions ($\alpha = 3.0$).

Predicted Effects of Grain Size, R*-ratio, and Cyclic Stress Range*

The results of this model were discussed in [*6*] but the most important results will be reproduced below. In the simulations of this work a mild steel was considered to have the properties given in Table 1. A fatigue crack was assumed to propagate in a single-edge cracked specimen from an initial crack length of 0.5 mm. Unless otherwise stated, the applied cyclic stress range ΔS assumed was 200 MPa and the *R*-ratio assumed was 0.1.

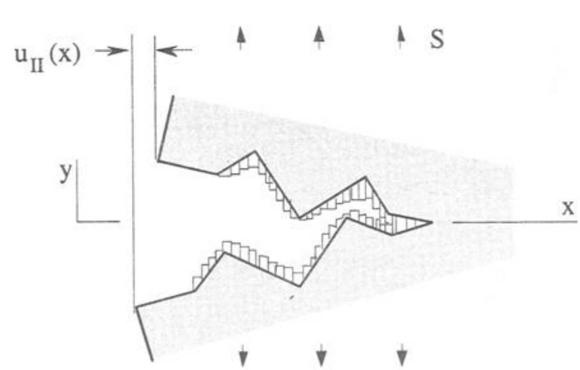

FIG. 13—*An analytical PICC-RICC model which combines the strip-yield Dugdale model of Newman [21] with an assumed zigzag crack growth path.*

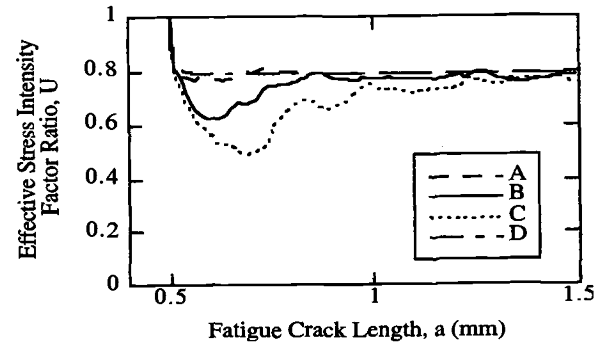

FIG. 14—*Effect of grain size. Predicted variation of effective stress intensity factor ratio* U *with crack length for zigzag paths with a constant tilt angle θ. Three cases are compared for a tilt angle of 45°: Case A:* L = *50 μm,* h = *11.5 μm; Case B:* L = *100 μm,* h = *25 μm and Case C:* L = *200 μm,* h = *50 μm. A fourth case (Case D) is also considered in which the value of* h *is 0 to simulate the condition of pure PICC.*

Grain Size—The predicted influence of grain size (branch length L) on the effective stress intensity factor ratio U is shown in Fig. 14. The zigzag path with the longest branch length (largest grain size) exhibits the lowest U value: see Fig. 14.

R-*Ratio*—The predicted effective stress intensity factor ratio U along with the companion predictions for pure PICC are plotted in Fig. 15. Only a modest RICC effect is predicted for either a positive high R-ratio such as $R = 0.7$ or a negative R-ratio such as $R = -1$.

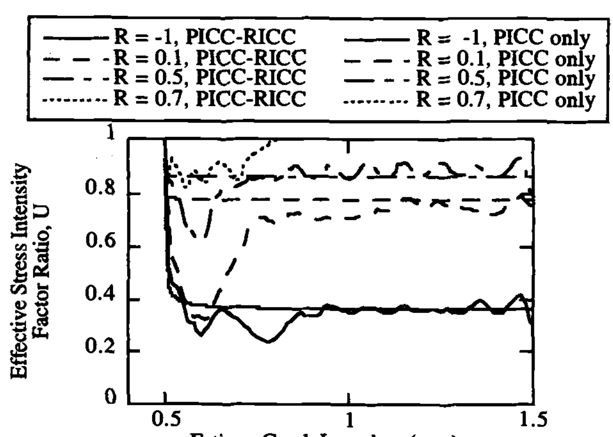

FIG. 15—*Effect of* R-*ratio. Predicted variation of effective stress intensity factor* U *with crack length for various* R-*ratios. The average branch amplitude of the zigzag path and the tilt angle θ were assumed to be 25 μm and 45°, respectively. The resulting branch length was 100 μm. Four R values are considered* (R = *−1, 0.1, 0.5, and 0.7) for a cyclic stress range ΔS of 100 MPa.*

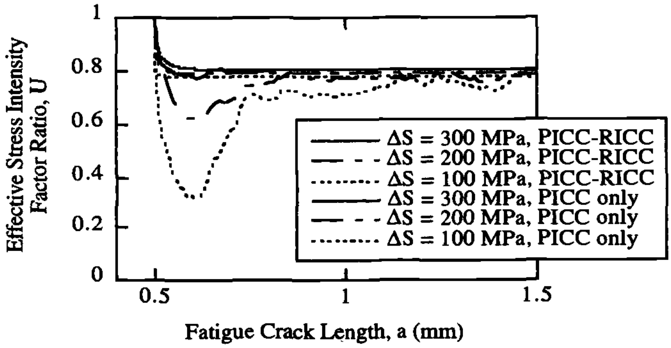

FIG. 16—*Effect of stress range. Predicted variation of effective stress intensity factor ratio* U *with crack length for various cyclic stress ranges* ΔS.

Stress Range—It is seen in Fig. 16 that the significance of RICC increases as ΔS decreases because a smaller ΔS means lower cyclic stresses S_{max} and S_{min} and a smaller crack opening displacement.

Comparisons of PICC-RICC model predictions with experimental data given in the literature were provided in [*6*]. Good agreement was found between the predictions of the PICC-RICC model and experimental observations for aluminum, titanium and steel specimens despite the simple, two-dimensional nature of the model.

References

[*1*] Lawrence, F. V., Jr., Mattos, R. J., Higashida, Y., and Burk, J. D., "Estimating the Fatigue Crack Initiation Life of Welds," *Fatigue Testing of Weldments, ASTM STP 648,* American Society for Testing and Materials, 1978, pp. 134–158.

[*2*] Ho, N. J. and Lawrence, F. V., Jr., "Constant Amplitude and Variable Load History Fatigue Testing Results and Predictions for Cruciform and Lap Welds," *Theoretical and Applied Fracture Mechanics,* Vol. 1, No. 1, 1984, pp. 3–21.

[*3*] Yung, J.-Y. and Lawrence, F. V., Jr., "Analytical and Graphical Aids for the Fatigue Design of Weldments," *Fatigue and Fracture of Engineering Materials and Structures,* Vol. 8, No. 3, 1985, pp. 223–241.

[*4*] Hoshide, T. and Socie, D. F., "Crack Nucleation and Growth Modeling in Biaxial Fatigue," *Engineering Fracture Mechanics,* Vol. 29, No. 3, 1988, pp. 287–299.

[*5*] Socie, D. F. and Furman, S., "Fatigue Damage Simulation Models for Multiaxial Loading," *Fatigue '96, Proceedings of the Sixth International Fatigue Congress,* Berlin, Germany, G. Lutjering and H. Nowack, Eds., Pergamon Press, New York, 1996, pp. 967–976.

[*6*] Chen, N. and Lawrence, F. V., "An Analytical Roughness-Induced Crack Closure Model for Studying Fatigue Notch Behavior," *Fatigue and Fracture Mechanics: 29th Volume, ASTM STP 1321,* T. L. Panontin and S. D. Sheppard, Eds., American Society for Testing and Materials, 1998.

[*7*] Frost, N. E., "A Relation Between the Critical Alternating Propagation Stress and Crack Length for Mild Steel," *Proceedings Institutions of Mechanical Engineers,* Vol. 173, No. 35, 1959, pp. 811–836.

[*8*] Hou, C. Y., "A Crack Closure Model for the Fatigue Behavior of Notched Components and Welded Joint," Ph.D. Thesis, Department of Civil Engineering, University of Illinois at Urbana-Champaign.

[*9*] Bell, R. and Vosikovsky, O., "Fatigue Life Prediction of Welded Joints for Offshore Structures Under Variable Amplitude Loading," *Proceedings,* 10th International Conference on Offshore Mechanics and Arctic Engineering, 1991, pp. 385–393.

[*10*] Radziminski, J. B., Srinivasan, R., Moore, D., Thrasher, C., and Munse, W. H., "Fatigue Data Bank and Data Analysis Investigation," Structural Research Series No. 405, UILU-ENG-73-2025, University of Illinois at Urbana-Champaign, 1973.

[*11*] Tanaka, K. and Mura, T., "A Dislocation Model for Fatigue Crack Initiation," *Journal of Applied Mechanics,* Vol. 48, March 1981, pp. 97–103.

[12] Newman, J. C., Jr., "A Crack-Closure Model for Predicting Fatigue Crack Growth Under Aircraft Spectrum Loading," *Methods and Models for Predicting Fatigue Crack Growth Under Random Loading, ASTM STP 748,* American Society for Testing and Materials, 1983, pp. 53–84.
[13] Chen, N., "An Analytical Model Which Combines Roughness and Plasticity Induced Fatigue Crack Closure," Ph.D. Thesis, University of Illinois at Urbana-Champaign, 1997.
[14] Forsyth, P. J. E., *Crack Propagation, Proceeding Symposium,* Cranfield, College of Aeronautics, Cranfield Press, Cranfield, U.K., 1962, p. 76.

Huseyin Sehitoglu[1] *and A. M. Garcia*[1]

Contact of Nonflat Crack Surfaces During Fatigue

REFERENCE: Sehitoglu, H. and Garcia, A. M., "**Contact of Nonflat Crack Surfaces During Fatigue,**" *Advances in Fatigue Crack Closure Measurement and Analysis: Second Volume, ASTM STP 1343,* R. C. McClung and J. C. Newman, Jr., Eds., American Society for Testing and Materials, West Conshohocken, PA, 1999, pp. 367–378.

ABSTRACT: A model has been developed to predict crack opening and closure behavior for propagating fatigue cracks which are nonflat and undergo significant sliding displacements. Crack surfaces were characterized by a random distribution of asperity heights, density of asperities, and asperity radii. The propagating crack was subdivided into ligaments and each ligament was treated as a contact problem between two randomly rough surfaces. The far-field tensile stresses were varied in a cyclic manner for $R = 0.1$ and -1 loading conditions. The contact stresses at the minimal load were determined by analyzing the local crushing of the asperities. Then, upon loading the crack opening, stresses were computed when the contact stresses were overcome. The results of crack opening stresses were correlated with CTOD/σ_0 where CTOD is the crack-tip opening displacement and σ_0 is the average asperity height. The asperity effects on closure were compared with plasticity-induced closure results from the literature for identification of conditions when one mechanism dominates the other.

KEYWORDS: fatigue crack closure, crack opening behavior, crack surfaces, loading conditions, plasticity-induced closure

The influence of nonflat crack surfaces on crack growth behavior was first noted by Adams in 1972 [*1*]. The closure events associated with nonflat crack surfaces were distinct from plasticity-induced closure since the latter had been observed to occur initially at the crack tip, zipping down the crack's wake. On the other hand, the nonflatness of crack surfaces produced multiple closure points. In 1973, Trebules et al. [*2*] polished fracture surfaces during a fatigue test and showed that when the fracture surface in the wake of the crack was smooth, the subsequent crack growth rate increased. All these observations on nonplanarity of the crack resulted in considerable interest in the fatigue community because it opened the possibility to design alloys to achieve improved crack growth resistance, and also explain crack growth behavior in cases where plasticity-induced closure ideas were inapplicable.

Following these initial observations, efforts to directly link the material microstructure with the macroscopic phenomenon of closure continued. All of these studies concluded that highly nonflat crack surfaces led to a decrease in the stress intensity range and produced benefits in crack growth resistance particularly in the near-threshold region. Allison and co-workers [*3*] studied the role of asperities by considering crack growth behavior of two microstructures of Ti-6242S alloys. The roughest microstructure presented normalized crack opening stress levels near 0.6 (normalization is with respect to maximum stress in the cycle). Allison made the observation that a Mode I crack may branch out, or near the crack tip create secondary cracks resulting in nonplanar crack fronts. Ritchie and co-workers [*4*] considered the underaged and overaged microstructures of Al alloy 2124 and experimentally observed closure stress levels near 0.8 which cannot be explained based on plasticity-induced closure. Finally, in pearlitic steels, Gray et al. [*5*] analyzed the effect of prior austenite grain

[1] Department of Mechanical and Industrial Engineering, University of Illinois, Urbana, IL 61801.

size, pearlite colony size and pearlite spacing effects on nonflatness of cracks. They observed normalized opening stress levels as high as 0.5 to 0.7. McEvily et al. [6] noted that when microstructural features and asperities were too small in comparison with the crack tip opening displacement, then asperity-induced closure did not occur. This is an important observation, because when the asperity heights are normalized with respect to the crack-tip opening displacement, the results could be rationalized. Minakawa and McEvily have developed a simple geometric explanation that during a fatigue cycle, Mode I and Mode II displacements develop around the crack tip due to the inclination of the crack faces. The asperities on opposite crack faces come into early contact resulting in compressive residual stress that reduce the crack-tip driving force or ΔK_{eff}. We note that despite initial mismatch of fracture surfaces, especially with Mode II contribution, depending on the material flow properties and the applied stresses, the asperity mismatch is partially corrected with plastic deformation. Other materials which exhibit considerable nonflat surfaces include CrMoV steels, where asperity heights as high as 40 μm were observed. Similar observations were made on nickel-based superalloys [7] with corresponding normalized closure levels near 0.6.

The majority of the experimental work has been conducted under $R > 0$ conditions. Consideration of $R = -1$ conditions is particularly important since considerable interaction of asperities and modification of surface profiles occur in this case. In the present paper, the aim is to isolate the nonflatness effects; therefore, we do not consider the simultaneous simulation of plasticity-induced closure and asperity effects. We consider the closure stresses and the crack opening stresses due to interaction of asperities only. Two R-ratios, 0.1 and -1 were chosen, and simulations were performed for nearly 100 cases (with different starting crack size, stress level conditions).

Modeling studies on asperity-induced crack closure have been very limited. Early researchers recognized that fatigue crack growth in the threshold regime was superior for alloys that exhibited considerable deviations from a linear crack path. Gerberich and colleagues [8] proposed that the opening stress level was proportional to (asperity height)$^{1/2}$. Further investigation of the role of asperities was undertaken by Buck and colleagues [9], who conducted nondestructive evaluation of partially closed cracks. Their opening stress level increased with (asperity height)^2 and linearly with asperity density. The classical work of Beevers [10] and colleagues showed that the crack opening stress increased linearly with the asperity height. In all these analyses, the crack opening stress was independent of the applied stress, the R-ratio, the crack length. In other words a closure stress intensity was derived as a constant. These models should be considered as an approximation only. Several models [11] quantified the crack surface shape using the tilt angle of the crack and identified the interference (mismatch) condition due to Mode II displacements. No contact stresses were determined in this case. The crack closure stress was derived as a function of the two parameters and the residual Mode II displacements (which were not determined).

In the present work, a statistical description of surfaces was adopted to analyze the contact in the crack wake. In this case, the crack surfaces were treated as covered with asperities which can be characterized by a tip radius, a random distribution of heights and a density (i.e., number of asperities per unit length). The model accounts for the sliding and plastic flow of asperities, which are essential elements in this mechanism of closure. The contact mechanics analysis characterizes the contact behavior of two surfaces. This analysis was incorporated into a ligament-type model, developed from fracture mechanics concepts, which describes the closure event in the crack wake. The treatment of surfaces as randomly rough predicts that deformation and contact load are strongly dependent on surface topography, specifically on the standard deviation of asperity heights, surface density of asperities, and mean radius of asperity tips, and on material properties such as yield strength and strain hardening.

Purpose and Scope

The purpose of this paper is to assess the significance of asperity-induced crack closure in materials where the plastic deformation at the crack wake approaches shakedown conditions. Examples of plasticity-induced crack closure are also included for comparison. New results are presented for the asperity-induced closure conditions based on a recent model developed by Sehitoglu and co-workers [*12,13*]. This model was used to illustrate the crack opening stress levels for $R = 0$ and $R = -1$ loading conditions for a wide range of asperity heights. The model for asperity contact stresses relies on the shakedown analysis of Johnson and colleagues [*14,15*]. In this analysis, upon repeated contact, the asperities' flattening occurs via a sliding mechanism. The paper will describe the theoretical framework and discuss the implication of results.

The Concept of Shakedown

The process of shakedown occurs when the body initially deforms plastically followed by elastic behavior. The elastic behavior may develop due to (i) residual stresses induced by the plastic deformation, (ii) geometry changes, or (iii) due to material hardening. All three factors play a role in the events leading to asperity shakedown. The onset of shakedown is taken to be the point at which the contact pressure equals the shakedown pressure. This value, p_0^s, is obtained from the shakedown map for the material and the traction conditions studied. In the present case, the shakedown map shown in Fig. 1 corresponds to plane strain sliding two surfaces. The vertical axis is the peak Hertzian pressure normalized by the yield stress in shear and Q/P is the ratio of shear to normal tractions. As noted in the figure, at low Q/P (traction coefficient) ratios shakedown is controlled by subsurface flow (which

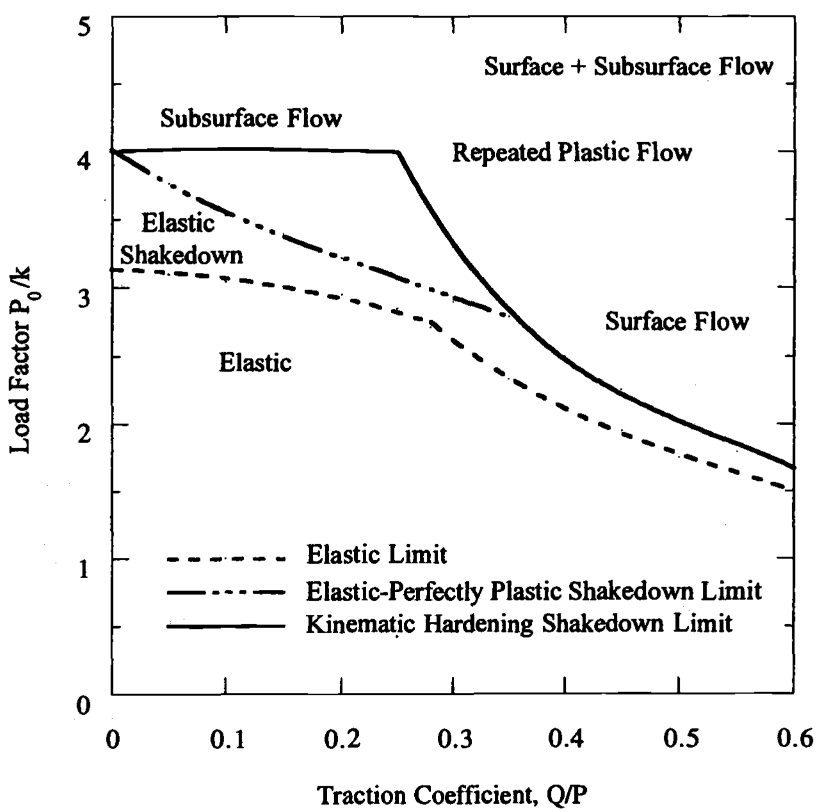

FIG. 1—*Load versus traction coefficient indicating the different regimes of operation for two contacting bodies.*

means that plastic deformation is dominant below the surface) and the shakedown limit significantly exceeds the elastic limit. For high Q/P ratios the material yields at the surface, then the shakedown pressure decreases with increasing Q/P, and little protection is provided by residual stresses.

Mechanics of Sliding Contact (Single Encounter)

With this brief background on shakedown, we now focus on sliding of two surfaces with asperities (Fig. 2). The contacting asperities are viewed as two cylindrical bodies pressed in contact by a normal force per unit length, P. The tangential loading developed in the sliding is accounted for only in the Q/P ratio. No other shear loading terms enter the analysis. Several assumptions and simplifications were made in the development of this unit event. However, the most crucial is the assumption that in the steady state (or shakedown) asperities adopt a flat shape and subsequently the load is carried elastically. It is this assumption which leads to an expression for the total load carried over the encounter dependent only on material properties, and initial (undeformed) asperity geometry [*14,15*]. All the relevant equations for the mechanics of contact of two surfaces have been given in previous publications [*14,15*]. We discuss only the most fundamental equations here. The peak Hertzian pressure, p_o, is give as a function of the total contact load as

$$p_o = \frac{2P}{\pi a} = \left(\frac{PE^*}{\pi R}\right)^{1/2} \tag{1}$$

where E^* is the plane strain elastic modulus, R is the radius of the asperity, and a is half the contact width. As shown in Fig. 2 during the elastic portion of the contact, the asperities slide against each other with the peak pressure, p_o, below the elastic limit. The elastic limit is reached when the maximum contact pressure equals the elastic limit dictated by the shakedown map (Fig. 1). If the initial interference of the two asperities is high, then plastic deformation occurs in the first encounter. When

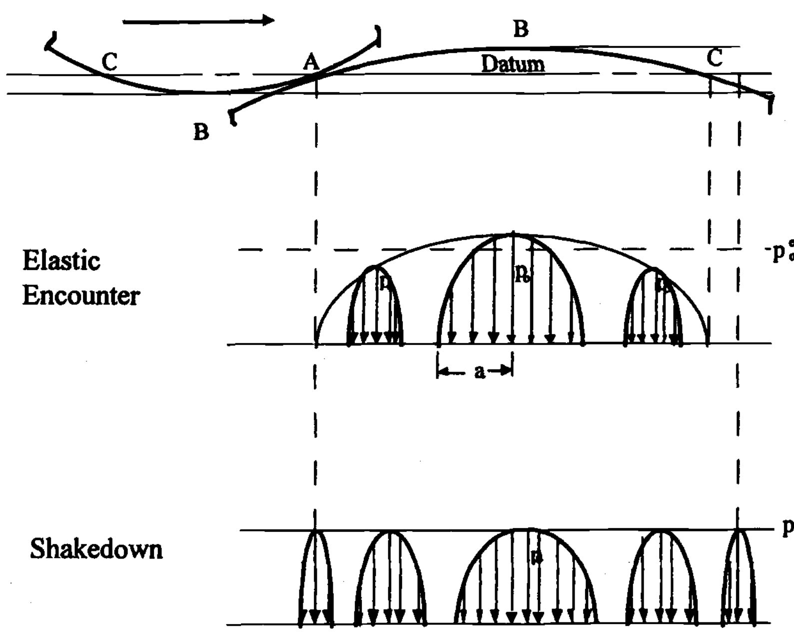

FIG. 2—*Hertzian pressure profiles during shakedown conditions.*

shakedown conditions are achieved, maximum Hertzian contact pressure is assumed to be constant throughout the encounter, and this value corresponds to the shakedown pressure, p_o^s, as dictated by the shakedown map (Fig. 1). Thus, if the load profile over the encounter is hypothesized to be descriptive of the asperity profiles, the assumptions made suggest that during the elastic portion, the profiles remain parabolic yet at shakedown they are flattened.

At the shakedown state, however, it is a assumed that

$$p_o(x) = p_o^s \tag{2}$$

where p_o^s is the shakedown pressure which depends on the shear traction conditions and it remains constant throughout the contact period. Since at shakedown the load is carried elastically, the Hertzian contact analysis is still valid. The radii and the interference of the deformed state are no longer constant but depend on the deformation. The mean load over an encounter can be found by integrating the load expression and this was illustrated in Refs *14* and *15*. Given the analysis of two asperities above, the problem of multiple asperity contact should be handled next.

Mechanics of Sliding Contact (Multiple Contacts)

We will refer to the region undergoing contact as composed of numerous ligaments. Individual ligaments were modeled as two randomly rough surfaces under repeated contact (Fig. 3). The term d is the separation distance between the two surfaces. It is again noted that at the local level both normal and sliding displacements are possible. Each surface is characterized by an initial asperity height distribution (the average asperity height is σ, the asperity tip radius is R, and a constant density of asperities, N). The present model assumed that all surfaces present a Gaussian distribution of heights, and that contacting surfaces have the same standard deviation of heights, radius and density of asperities.

Following the Greenwood-Williamson analysis [*16*], the analysis of contact between two randomly rough surfaces can be obtained. In the case of two randomly rough surfaces, contact will occur when the sum of the asperity heights, $z_1 + z_2$ exceeds the separation distance, d (Fig. 3). Therefore the probability of contact between randomly rough surfaces is given by,

$$\text{prob}(z_1 + z_2 > d) = \int_d^\infty \Phi(z_1 + z_2)d(z_1 + z_2) \tag{3}$$

Assuming that both surfaces are normally distributed and have a standard deviation, σ_0, thus $\Phi(z_1 + z_2)$ is also normal with standard deviation $\sigma = \sqrt{2}\sigma_0$. The ultimate aim of this analysis is that aver-

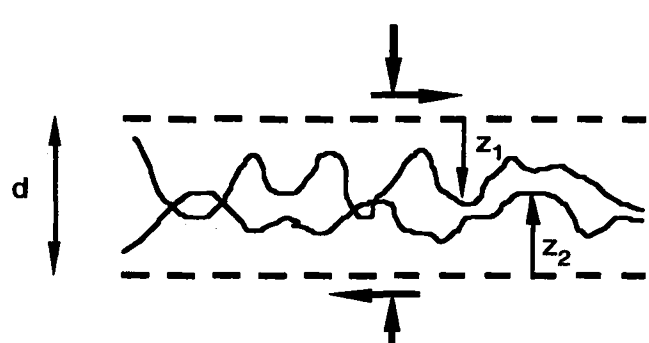

FIG. 3—*Schematic illustration of two surfaces undergoing sliding and crushing.*

age contact pressure as a function of separation of the surfaces is obtained. The average load normalized by the contact area, and plane strain elastic modulus, is plotted against the normalized separation distance d/σ in Fig. 4. Three levels of asperity heights are shown in Fig. 4. The simulations are shown for an asperity density of 1000 asperities/cm and three asperity heights of 1, 10 and 100 μm. Note that as the surfaces interpenetrate, the contact load increases, initially at a higher rate and gradually saturates. When d/σ value is larger than 2 the contact stresses are rather small.

Crack Opening Stress Simulations

As in some plasticity-induced crack closure models, the crack opening stresses were calculated by solving an elastic problem which in turn involved the superposition of two other elastic problems [*12,13*]. The first is that of a center crack in a plate where the crack grows from a notch under uniform remotely applied stress (S_{appl}). The second problem is a partially loaded crack, where the loading is due to contact stresses. The plate is under cyclic loading so the applied stress varies between S_{max} and S_{min}, according to the R-ratio. After each cycle the crack was advanced by Δl. Since the analysis does not aim at simulating the fatigue crack growth rate but seeks to determine closure levels, this Δl was chosen arbitrarily. The value of Δl was chosen as one-tenth of the initial crack size and is as low as 1 μm. The sensitivity of the results to the ligament size is thoroughly discussed in Refs *12* and *13*.

The initial topographical parameters—standard deviation of height for each crack surface, σ_0, the asperity tip radius of each crack surface, R_0, the density of asperities, N, along with the material properties and the loading conditions—were assigned. The S_{open} value was determined as the crack grew. There are no limitations on the magnitude of S_{max}, S_{min}, E, k (yield stress in shear), Q/P. There are some physical restrictions on the choice of R_0, given N as discussed in Refs *12* and *13*. The systematic variation of these variables produced the results that will be presented in the following section.

A typical example of surface topography for a lamellar titanium aluminide under $R = 0.1$ loading conditions is shown in Fig. 5. The size of the region shown is nearly 512 by 512 μm. Note that some of the asperities are as high as 250 μm with the average asperity heights as high as 80 μm. Figure 5

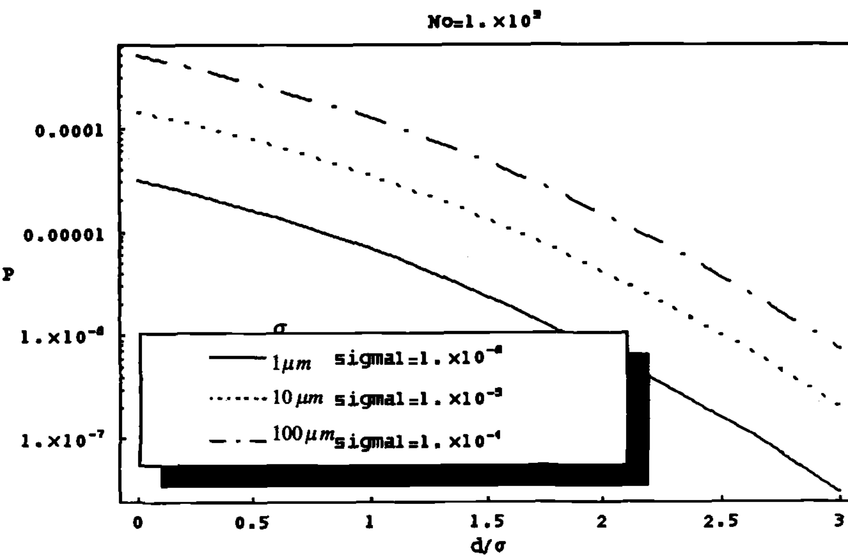

FIG. 4—*Load-separation distance relationship for contact between two randomly rough surfaces of equal hardness under different average asperity heights.*

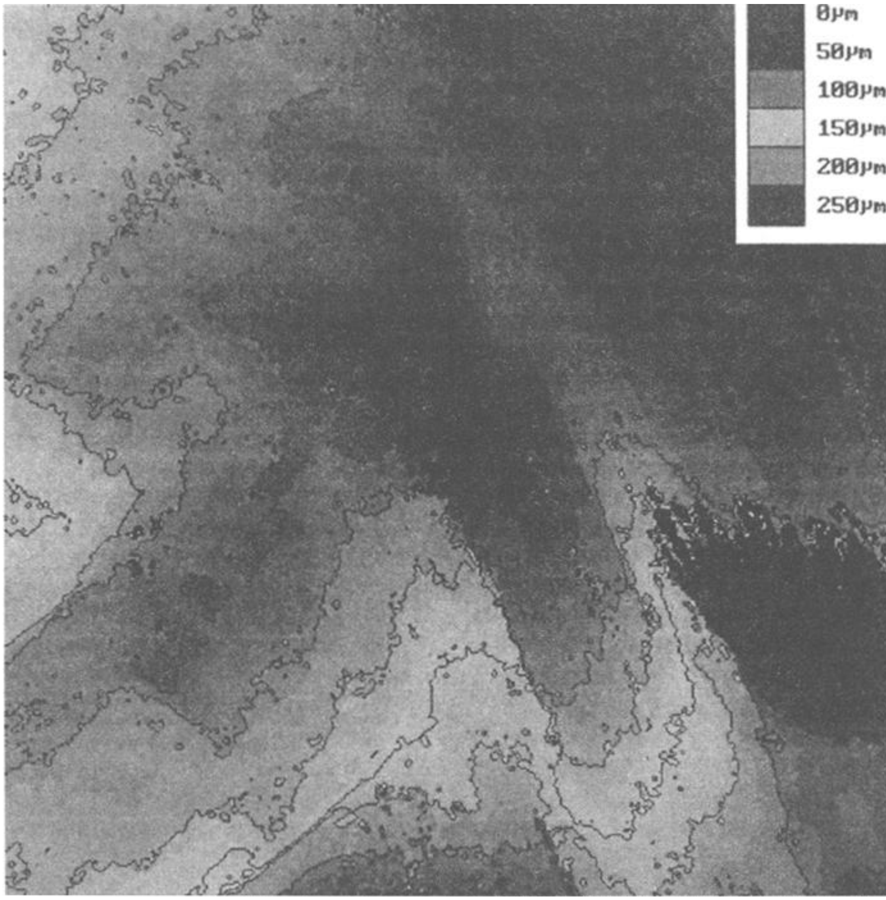

FIG. 5—*Topographic map of a fully lamellar titanium aluminide,* R = *0.1.*

was obtained using the Carl Zeiss LS 350 Laser Scan microscope at Wright Patterson Air Force Base, Dayton, OH. Note that the surface distribution of heights measured experimentally is consistent with a Gaussian distribution.

Simulations for $R = 0.1$ and $R = -1$

Crack opening stress simulations were conducted under $R = 0.1$ loading conditions first. These results are summarized in Fig. 6. Two stress levels were considered in the simulations. The crack opening stress levels for the $S_{max}/S_y = 0.6$ (gray symbols) overlapped with the $S_{max}/S_y = 0.2$ case when the results were normalized using the CTOD/σ_0 parameter. The crack-tip opening displacement is given as

$$\frac{S_{max}^2 \pi(l + c)}{E^* S_y}$$

where $l + c$ represents half the crack length in a CCT specimen. Note that S_{open}/S_{max} levels above 0.5 occur when the CTOD/σ_0 levels are lower than 0.1. The result is a strong function of the asperity

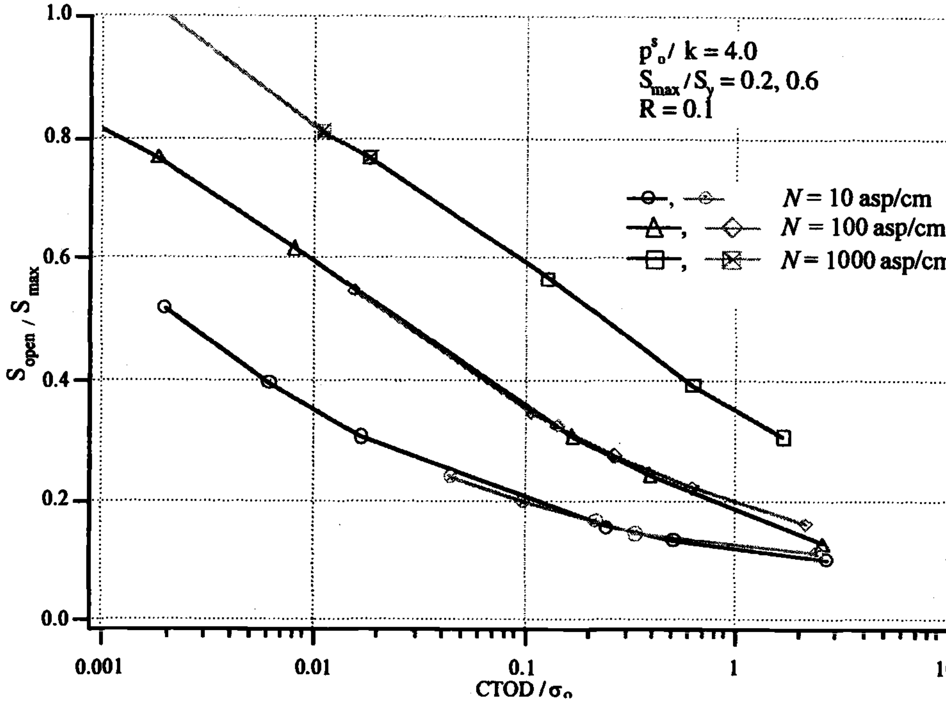

FIG. 6—*Simulations of crack opening stress as a function of CTOD/σ_0* (R $= 0.1$) [13].

heights with the asperity density having a modifying influence. Similarly, simulations for the $R = -1$ case are shown in Fig. 7. In this case the S_{max}/S_y levels were also 0.2 (solid black symbols) and 0.6 (gray symbols). In both cases the results are a strong function of the asperity density, N. As the CTOD/σ_0 level increases, the role of asperities on crack closure decreases.

The results of the simulations for $R = -1$ case are shown in Fig. 7. In these simulations the results from two different S_{max}/S_y levels were correlated over a large range of CTOD/σ_0 values. When the CTOD/σ_0 levels were larger than 0.1 the S_{open}/S_{max} values were in the negative region. Note that the crack opening stress levels observed under $R = -1$ loading conditions are substantially lower than for the $R = 0.1$ case. The results point out the possibility that the role of asperity induced closure may be reduced in the $R = -1$ case, allowing the plasticity-induced closure mechanism to be dominant.

Comparisons with Plasticity-Induced Closure Models

To gain further insight into the relative role of asperity-induced crack closure, the simulations for both asperity-induced and plasticity-induced closure are compared in Fig. 8. The plasticity-induced closure results were obtained from Newman's ligament model [17] and published in the literature; these results were confirmed with FEM analysis for S_{max}/S_y levels above 0.6 [18]. The FEM analysis is for a crack growing from a notch of half-width c. As l/c values increase, the crack opening stress approaches a saturation value. This value is plotted versus S_{max}/S_y where the top scale represents the

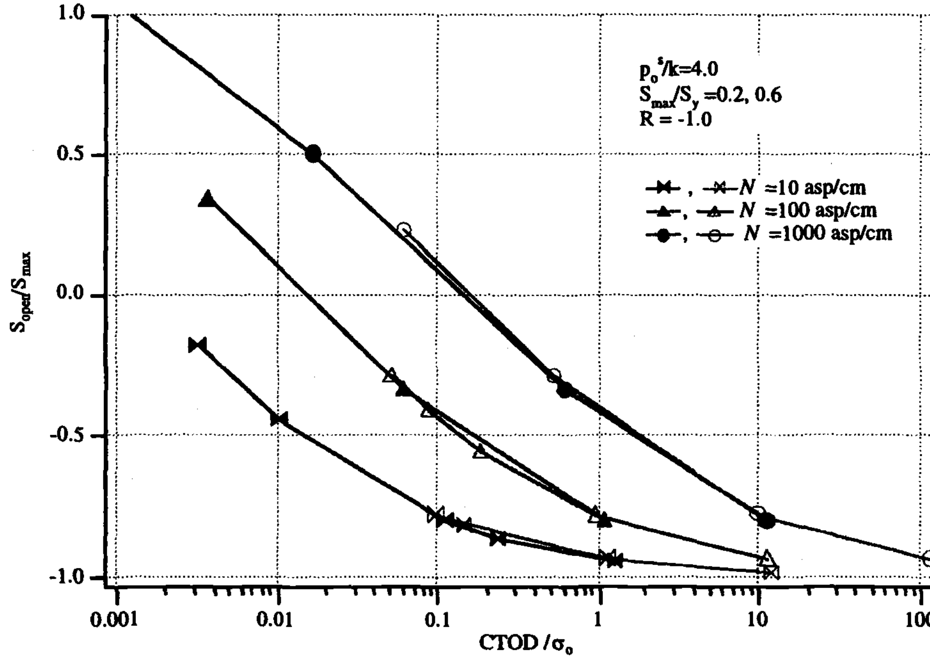

FIG. 7—*Simulations of crack opening stress as a function of CTOD/σ_0* (R = *−1).*

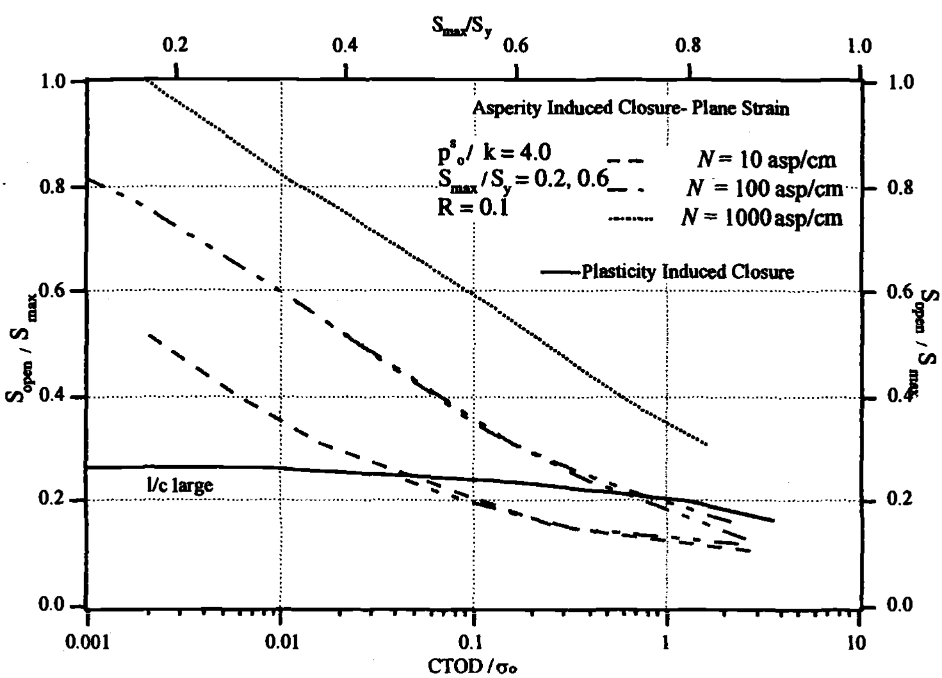

FIG. 8—*Comparison of asperity-induced closure and plasticity-induced closure results* (R *= 0.1).*

S_{max}/S_y levels in the range 0.1 to 1.0. The plasticity-induced closure results should be considered as approximate and included for comparison purposes.

The results demonstrate unequivocally that for the majority of cases when CTOD/σ_0 is less than 1, the asperity-induced closure mechanism is the dominant mechanism of crack closure. In fact, most of the results for the N = 10 and 100 cases lie above the plasticity-induced closure results.

Plasticity-induced closure models for $R = -1$ loading are compared with the asperity-induced closure simulations in Fig. 9. The plasticity-induced closure results shown were obtained using FEM analysis (see Ref *19* for an overview of FEM). For a crack growing from a notch in a center-cracked plate, the notch half-width is designated as *c*. The plasticity-induced closure results are shown for two cases. For the case l/c = 0.01 the closure stresses due to plasticity-induced closure are rather small and similar to the N = 100 case. When l/c is large the saturated levels of closure due to plasticity are high and the effect of asperity-induced closure becomes small. However, we note that asperity-induced closure becomes significant when CTOD/σ_0 levels fall below 0.1 or when S_{open}/S_{max} levels exceed 0.4. The R = -1 loading conditions have been the least studied in crack growth research and there are virtually no experimental studies that can be compared with the simulations discussed above.

Finally, we note the possible role of three-dimensional crack geometry effects on the crack closure calculations. The crack surfaces could exhibit both Mode II and Mode III displacements where Mode III displacements can arise due to twisted crack fronts. Such crack path nonlinearity in the specimen thickness direction will produce asperity-induced closure effects higher than those predicted in this study. We further note that in the case of three-dimensional contact the shakedown pressure of asperities would differ from those given in Fig. 1. We recall that Fig. 1 is applicable to plane strain conditions, and if the shakedown map for 3-D contact were developed the different regimes would be modified.

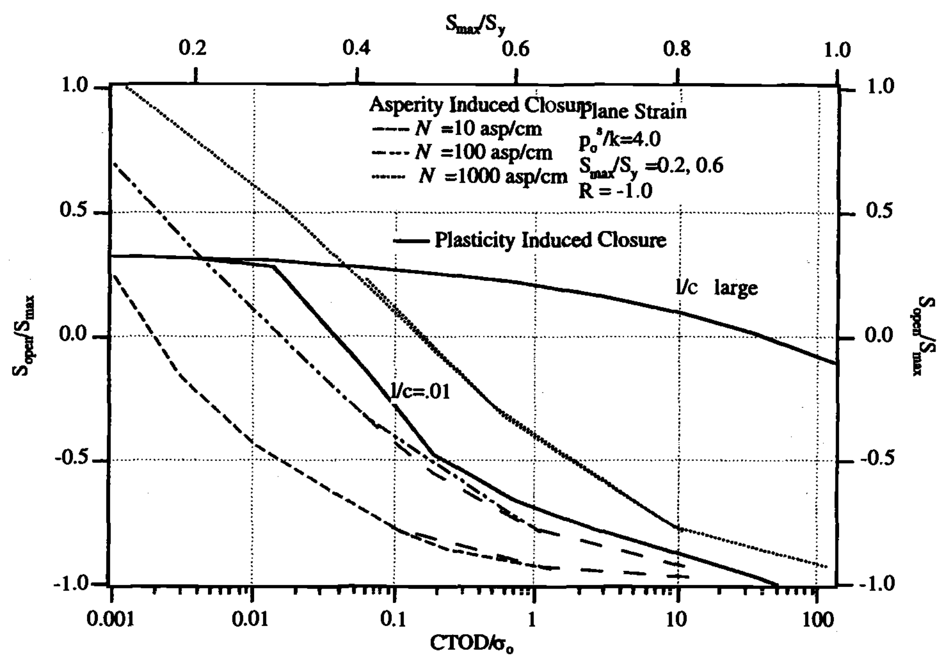

FIG. 9—*Comparison of asperity-induced closure and plasticity-induced closure results* (R = -1)

Conclusions

The work supports the following conclusions:

1. The asperity-induced closure under $R = -1$ conditions were consolidated using the CTOD/σ_0 parameter. When the CTOD/σ_0 ratio exceeded unity, the crack opening stress levels approached the minimum stress level in the cycle.
2. The results are a strong function of applied stress, asperity density and asperity heights. For $R = -1$ loading conditions the contribution from asperity-induced closure is significant at S_{max}/S_y levels below 0.3. At higher S_{max}/S_y ratios the plasticity-induced closure is dominant for large crack sizes. But smaller crack sizes (when l/c ratios are below 0.05) the plasticity-induced closure contribution diminishes and the role of asperities becomes significant.
3. Crack opening stress levels under $R = 0.1$ loading conditions were also established. Upon comparison with plasticity-induced closure results, the observation is that the asperity-induced closure is dominant over a wide range of conditions, and specifically at S_{max}/S_y levels below 0.4. Since there are no FEM results (at low S_{max} levels) for the plasticity-induced closure case for $R = 0.1$ loading, the results were superimposed with the ligament model of Newman.
4. Although the model does not include plasticity-induced closure effects, plasticity was inherently included in asperity interactions. Future studies should consider the role of both plasticity-induced and asperity-induced closure effects. The conditions where they are likely to be of comparable magnitudes are illustrated in this work. However, in the extreme cases, one of these mechanisms dominates.
5. The work points out the need to include crack surface profiles in crack growth studies as this represents a valuable source of information to assess the possible contribution from interference effects.
6. The model presented is two-dimensional (plane strain) and the crack surfaces do not undergo tilting in the thickness direction. The tools to handle such cases can be found in the contact mechanics literature but are not considered in the present research.

Acknowledgment

The work is supported by the Fracture Control Program, College of Engineering, University of Illinois at Urbana-Champaign.

References

[1] Adams, N. J., *Engineering Fracture Mechanics,* Vol. 4, 1972, pp. 543–554.
[2] Trebules, V. W., Roberts, R., and Hertzberg, R. W., *ASTM STP 536,* American Society for Testing and Materials, 1973, p. 115.
[3] Allison, J. E. and Williams J. C., *Titanium Science and Technology,* Vol. 1, G. Lujtering, U. Zwicker, and W. Burk, Eds., DGM Publishers, Oberusel, Germany, 1985, pp. 2243–2250.
[4] Ritchie, R. O., Yu, W., Blom, A., and Holm, D., *Fatigue and Fracture of Engineering Materials and Structures,* Vol. 10, No. 5, 1987, pp. 343–362.
[5] Gray, G. T., III, Williams, J. C., and Thompson, A. W., *Metallurgical Transactions,* Vol. 14A, 1983, pp. 421–433.
[6] Minakawa, K. and McEvily, A. J., *Scripta Metallurgica,* Vol. 15, 1981, pp. 633–636.
[7] Liaw, P. K., *Fatigue Crack Closure, ASTM STP 982,* J. C. Newman, Jr. and W. Elber, Eds., American Society for Testing and Materials, 1988, pp. 62–92.
[8] Sheth, J. and Gerberich, W., *Fatigue Crack Closure, ASTM STP 982,* J. C. Newman, Jr. and W. Elber, Eds., American Society for Testing and Materials, 1988, pp. 112–120.
[9] Buck, O., Thompson, R., and Rehbein, D., *Fatigue Crack Closure, ASTM STP 982,* J. C. Newman, Jr. and W. Elber, Eds., American Society for Testing and Materials, 1988, pp. 536–547.

[10] Beevers, C. J., Bell, K., Carlson, R. L., and Starke, E. A., *Engineering Fracture Mechanics*, Vol. 19, No. 1, 1984, pp. 93–100.
[11] Suresh, S., *Metallurgical Transactions*, Vol. 15A, 1984, pp. 249–260.
[12] Garcia, A. M. and Sehitoglu, H., *Metallurgical Transactions*, Vol. 28A, 1997, pp. 2263–2275.
[13] Sehitoglu, H. and Garcia, A. M., *Metallurgical Transactions*, Vol. 28A, 1997, pp. 2277–2289.
[14] Johnson, K. L. and Shercliff, H. R., *International Journal of Mechanical Science*, Vol. 35, No. 5, 1992, pp. 375–394.
[15] Kapoor, A. and Johnson, K. L., *Thin Films in Tribology, Leeds-Lyon Symposium on Tribology*, 1993, pp. 81–90.
[16] Greenwood, J. A. and Williamson, J. B. P., *Proceedings of the Royal Society of London*, Vol. A295, 1966, pp. 300–319.
[17] J. C. Newman, *International Journal of Fracture*, 1984, pp. R131–135.
[18] Sehitoglu, H., unpublished data, 1995.
[19] Sehitoglu, H., Gall, K., and Garcia, A. M., *International Journal of Fracture*, Vol. 80, No. 2–3, 1996, pp. 165–192.

Jan Zuidema,[1] *Theo M. van Soest,*[1] *and Michael Janssen*[1]

Synergetic Effects of Fatigue Crack Closure Mechanisms

REFERENCE: Zuidema, J., van Soest, T. M., and Janssen, M., "**Synergetic Effects of Fatigue Crack Closure Mechanisms,**" *Advances in Fatigue Crack Closure Measurement and Analysis: Second Volume, ASTM STP 1343,* R. C. McClung and J. C. Newman, Jr., Eds., American Society for Testing and Materials, West Conshohocken, PA, 1999, pp. 379–389.

ABSTRACT: Results are presented relating to the relative effect of two closure mechanisms. Two different crack closure mechanisms, closure due to surface roughness induced by shear lips and conventional plasticity-induced closure, are investigated and compared by performing fatigue crack growth tests on aluminum 2024 and technically pure aluminum. Constant ΔK tests using a sudden change in ΔK are used in order to measure both closure effects separately and also the combined effects of both mechanisms. It is found that in the case of a combined application of closure mechanisms the retardation result after a load transition is sometimes greater than the sum of the retardations of the separate mechanisms. Under the test conditions used the combined effect may be 2.4 times greater than the sum of the separate effects.

KEYWORDS: plasticity-induced crack closure, shear lips, Al 2024-T351, frequency

Nomenclature

a	half crack length in a center-cracked test specimen
f	frequency of fatigue cycles
K	stress intensity factor
K_{max}, K_{min}	maximum, minimum value of K
N	number of cycles
P	load
R	K_{min}/K_{max}
t	specimen thickness
w	specimen width
ΔK	$K_{max} - K_{min}$
ΔK_{eff}	effective ΔK

The aim of this paper is to find out whether different fatigue crack closure mechanisms have a mutually enhancing effect when applied simultaneously compared with a situation in which they are applied separately. As a criterion for the effect of the fatigue crack closure mechanism, the retardation in fatigue crack growth is measured after a sudden change in ΔK.

Two independent fatigue crack closure mechanisms were investigated: "normal" plasticity-induced crack closure and crack closure based on surface roughness caused by shear lips (Fig. 1). Test conditions were chosen in such a way as to make it possible to study the effect of the mechanisms both separately and combined. The tests are constant ΔK tests on center-cracked tension specimens.

[1] Assistant professor, research engineer, and assistant professor, respectively, Laboratory of Materials Science, Delft University of Technology, Rotterdamseweg 137, 2628 AL, Delft, The Netherlands.

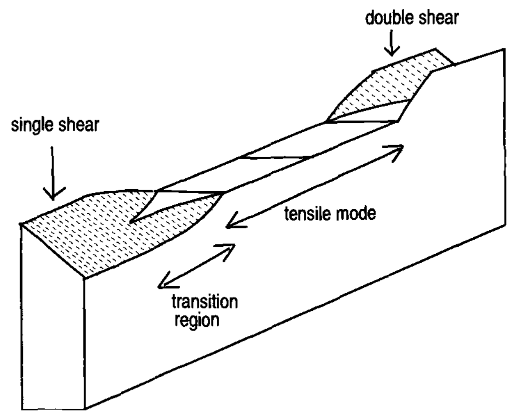

FIG. 1—*Development of shear lips during a constant-amplitude test on a center-cracked plate.*

The separate plasticity-induced closure effect is found by a normal load (i.e., K_{max}) reduction at low ΔK after a long period of crack growth, without shear lips. The K_{max} reduction percentage is defined as:

$$K_{max} \text{ reduction } \% = (1 - K_{max}, \text{ new}/K_{max}, \text{ old}) \; 100\% \tag{1}$$

A considerable length of crack growth at high K_{max} is needed in order to have a stable crack closure situation. The effect of shear lip induced closure [*1–4*] is studied by performing a fatigue test at a ΔK high enough to obtain shear lips. A possible crack closure effect of shear lips is shown in Fig. 2. In order to find the shear lip closure effect alone, ΔK is lowered at constant K_{max}. The lower ΔK causes a transition to a state without shear lips. A long period of crack growth is also needed in order to find a stable closure situation, as the shear lips need crack growth in order to develop to greater widths. K_{max} is held constant in order to avoid any effect of plasticity-induced closure mechanism.

The two crack closure effects can also be combined when both a K_{max} reduction and a ΔK reduction are applied. The principle of the tests is given in Fig. 3. Figure 3A shows a ΔK reduction at the same K_{max}. The initial ΔK is high enough for shear lips to be obtained. The amount of the ΔK reduction is chosen such as to lead to a situation without shear lips after the ΔK transition. K_{max} is the same before and after the transition in order to avoid a plasticity-induced crack closure contribution. In Fig.

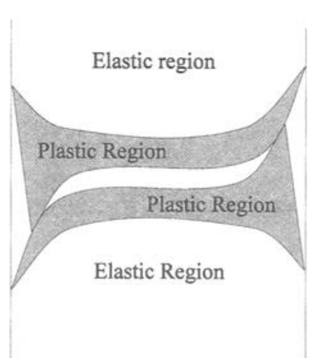

FIG. 2—*Principle of extra closure due to shear lips [5].*

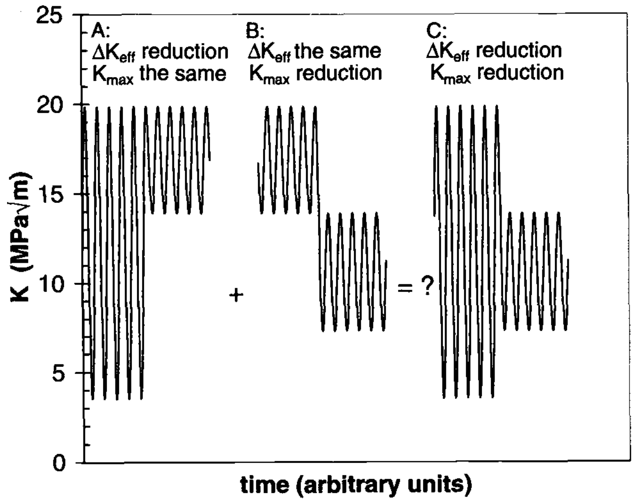

FIG. 3—*Principle of the tests:* K_{max} *reduction is 30%,* ΔK_{eff} *reduction: 10 to 5 MPa*$\sqrt{m}$.

3B both ΔK have a value such that no shear lips are expected before or after the transition. Moreover, for ΔK of both loading situations in this figure values were chosen in order to give the same ΔK_{eff}. In Fig. 3C both loading systems are combined, with both a K_{max} reduction and a ΔK reduction.

All high and low ΔK cycles in Fig. 3A, B and C were chosen in order to achieve the same effective ΔK (thus roughly the same da/dN), using a standard crack closure relation [*6*]:

$$\Delta K_{eff} = (0.55 + 0.33\,R + 0.12\,R^2)\,\Delta K \tag{2}$$

where R is the stress ratio K_{min}/K_{max}. The low ΔK values were chosen with a ΔK_{eff} value of 5 MPa$\sqrt{m}$. The high ΔK values in Fig. 3A and C were chosen with a ΔK_{eff} value of 10 MPa$\sqrt{m}$.

The objective of the paper is to determine whether the sum of the separate closure effects of situations shown in Fig. 3A and B is less than, equal to or greater than the closure effect of the combination of both mechanisms shown in Fig. 3C. If the combination has a greater effect than the sum of the separate mechanisms, there is synergy of the two crack closure mechanisms.

Experiments

Center-cracked tension specimens were used for the tests. The specimen thicknesses were 6, 4.6 and 2 mm, the length was 300 mm, and the width was 100 mm. The specimens with 6 and 2 mm thickness were made of Al 2024-T351; the specimens of 4.6 mm thickness were made of technically pure aluminum. The mechanical properties for 6 mm thickness recorded in the longitudinal direction of the plate were: yield stress 390 MPa, tensile strength 456 MPa, and elongation to failure 18%. For 2 mm thickness these properties were 376 MPa, 468 MPa, and 14%, respectively, and for 4.6 mm 366 MPa, 439 MPa and 16%, respectively. The tests were performed in "lab air" at a temperature of approximately 20°C. The crack length was measured using a pulsed direct current potential-drop technique.

The K factor used was:

$$K = \frac{P}{tw}\sqrt{\pi a \sec\left(\frac{\pi a}{w}\right)} \tag{3}$$

TABLE 1—*Chemical Composition of Materials Tested.*

Thickness Element	2 mm (%wt)	4.6 mm (%wt)	6 mm (%wt)
Cu	4.57	0.23	4.75
Mg	2.15	0.01	1.18
Mn	0.64	<0.01	0.67
Fe	0.16	0.34	0.14
Si	0.09	0.24	0.34
Zn	0.06	0.04	0.19
Cr	<0.01	<0.01	0.004
Ti	0.03	0.01	0.03
Sn	<0.01	<0.01	not tested
Pb	0.01	0.01	not tested
Cr	<0.01	<0.01	not tested
Ni	<0.01	<0.01	not tested

the accuracy being $<1\%$ for $2a/w \leq 0.8$. The chemical composition of the materials is given in Table 1.

The tests were carried out under load control using constant ΔK. The task of calculating and applying the load in order to keep ΔK constant at growing crack length was performed in small steps by the controlling computer. The transitions in K_{max} and ΔK_{eff} were performed as shown in Fig. 3, without stopping the fatigue machine. After an initial notch and pre-fatigue zone the crack growth started at a (half) crack length of 5 mm. The transition was performed at $a = 20$ mm. The retardation in crack growth after the transition is taken as an indication of the effect of the crack closure mechanisms. The principle of the measurement is shown in Fig. 4 for an experiment on a specimen with 2 mm thickness. In this example a transition in loading is performed in such a way (see Fig. 3 C) that both crack closure mechanisms contribute to the number of delay cycles. The crack growth is recorded from 5 mm crack length. At 20 mm the transition shown in Fig. 3C takes place, leading to a delay in crack

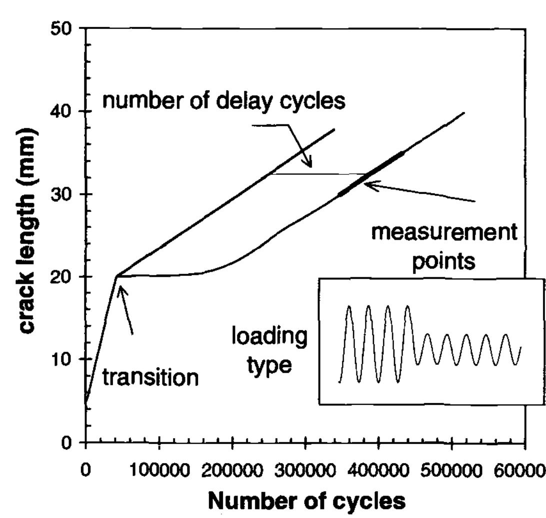

FIG. 4—*Example of a combined result for a K_{max} reduction of 30% with specimen thickness 2 mm and frequency 10 Hz.*

growth. The procedure to find the number of delay cycles is as follows. It is assumed, and found in all tests, that the retardation effect has vanished at 30 mm crack length. A best linear fit line is found through the measurement points from 30 to 35 mm. The number of cycles found between this line and a line parallel to it through the transition point is the number of delay cycles; i.e., the crack growth would have followed this parallel line if no retardation had occurred after the loading transition. In Fig. 4 the number of delay cycles is shown by the distance between both lines at a crack length of 32.5 mm. In this experiment the number is 133 137 delay cycles.

Most tests were performed at 10 Hz. Shear lip closure can be considered as a special kind of roughness closure. The appearance of shear lips is dependent on the frequency. At lower frequencies (<1 Hz) a rather smooth shear lip is obtained, a phenomenon which has a much lower closure effect than the rough shear lips obtained at higher frequencies (>2.5 Hz). An example of the differences is shown in Fig. 5, taken from Ref *6*. Since the appearance (rough or smooth) of shear lips is dependent on the frequency, tests were also carried out at 0.1 Hz.

To save time the tests at 0.1 Hz were performed only on the last 5 mm of crack growth before the transition crack length of 20 mm. It is shown [*6*] that this 5 mm crack length is sufficient in order to find a maximum "history" effect of fatigue crack closure at this frequency; i.e., the part where the crack is closed at K_{min} is shorter than 5 mm (see Fig. 6).

Results

The delay for shear lip closure alone (using the method shown in Fig. 3A) is shown in Fig. 7 for two frequencies. Two tests, identical apart from the frequency, are compared. The fracture surfaces are also shown. The frequencies were 10 Hz and 0.1 Hz, with tests at 0.1 Hz only for crack growth from 15 mm crack length to the transition point at 20 mm. The remaining parts of the two tests were performed at 10 Hz. There is a considerable frequency effect due to larger shear lips and larger roughness at 10 Hz compared with 0.1 Hz. The number of delay cycles due to closure of shear lips is shown in Fig. 8. It is shown as a function of material thickness and frequency. The effect is greater for 10 Hz than for 0.1 Hz and also greater for greater material thickness. Technically pure aluminum shows a greater delay than Al 2024. The frequency effect is as expected and can be understood from the greater surface roughness, caused by highly irregular shear lips at 10 Hz compared with rather smooth shear lips at 0.1 Hz. The thickness effect for Al 2024 is not expected and is not understood at the moment. In Fig. 9 the retardation caused by the plasticity-induced crack closure mechanism alone is shown. The frequency effect is slight and reversed with respect to the shear lip situation for 4.6 mm thickness. For a K_{max} reduction percentage of 30% the retardation is about the same order of magnitude for all thicknesses, as opposed to the retardation due to shear lip closure. In Fig. 10 the combined crack closure effect, i.e., the result of crack closure due to shear lip transition and plasticity-induced closure applied simultaneously, is compared with the effect of the sum of plasticity-induced and shear lip closure separately. The results are shown (in *kilo*cycles) for a thickness of 6 mm. Although the shear lip effect is rather slight compared with retardation due to K_{max} reduction percentages of more than 30%, it has an enhancing effect on the delay, due to the combination of both closure mechanisms for 10 Hz.

A synergetic ratio is defined as the ratio of the result of the combined processes and the sum of the separate processes. There is synergy for a ratio value >1 and no synergy for a ratio value ≤1. In Table 2 the synergetic ratio is calculated as a function of the K_{max} reduction percentage at both frequencies.

From Fig. 10, for 6 mm specimen thickness, it can be seen that at a reduction of 20% there is no synergy; the ratio is even less than 1, but it rises with increasing reduction percentage to about 2.4 at 40%. There is also no synergy present in the case of tests performed at 0.1 Hz. For the other two material thicknesses there are results only for a K_{max} reduction percentage of 30%. The results are given in Table 3 for all thicknesses.

It should be noted that the ratio at 30% reduction is almost the same for Al 2024 at 6 mm thickness and for technically pure aluminum at 4.6 mm, although the absolute values of the retardations are

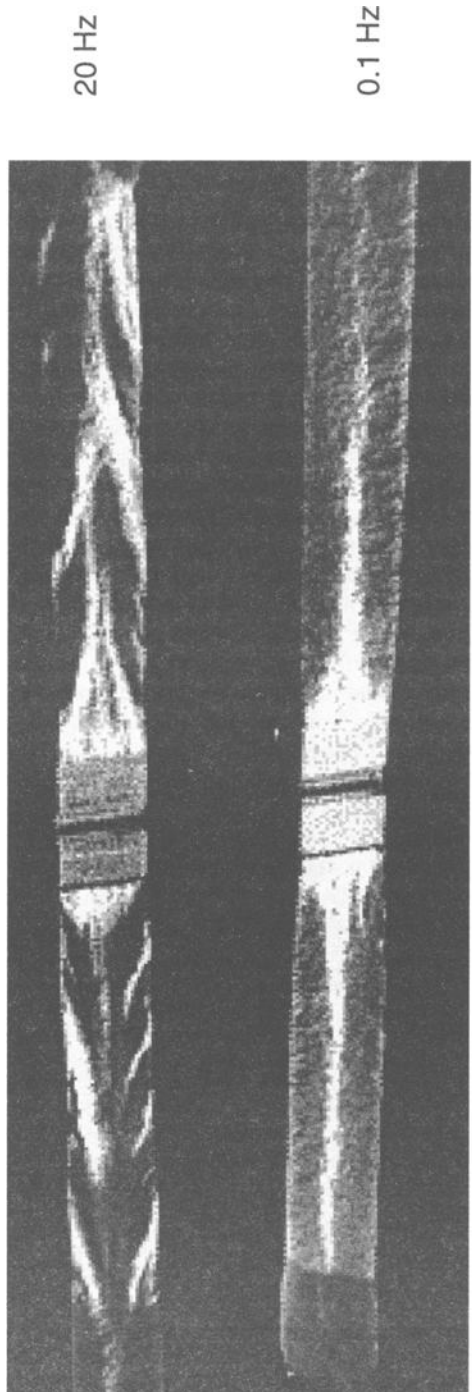

FIG. 5—*Examples of rough and smooth shear lip crack surfaces,* $\Delta K = 20\ MPa\sqrt{m}$, $R = 0.1$, $f = 20\ Hz$ *and* $f = 0.2\ Hz$ *[7].*

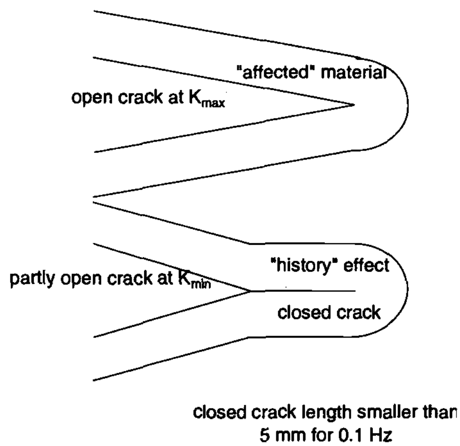

FIG. 6—*Principle of situation of crack tip at* K_{max} *and* K_{min}.

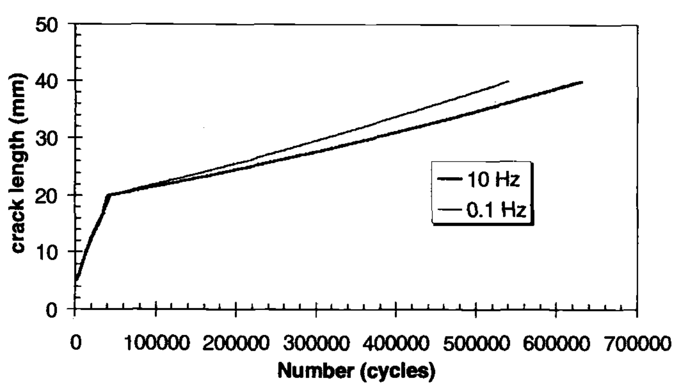

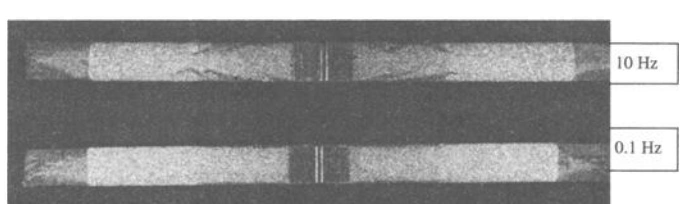

FIG. 7—a-N *results for two tests, identical apart from the frequency for crack length between 15 and 20 mm, for 6 mm thickness Al 2024.*

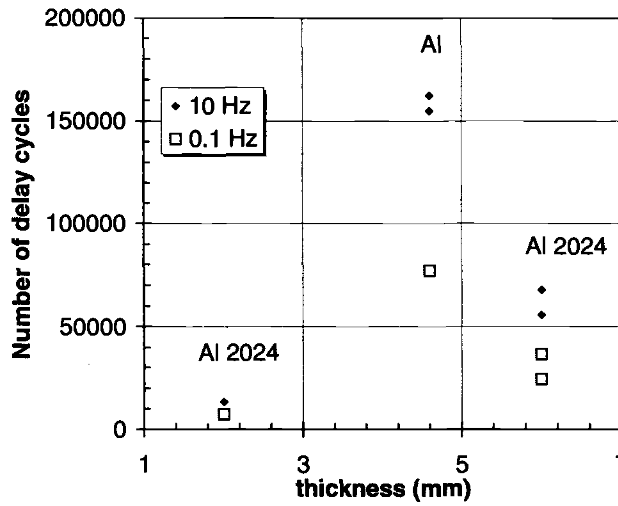

FIG. 8—*Delay cycles for shear lip closure as a function of specimen thickness and frequency.*

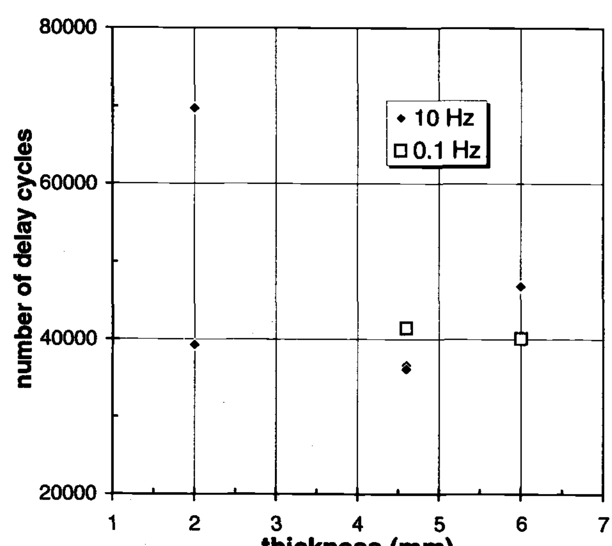

FIG. 9—*Delay cycles, due to plasticity-induced crack closure with a* K_{max} *reduction of 30%, as a function of specimen thickness and frequency.*

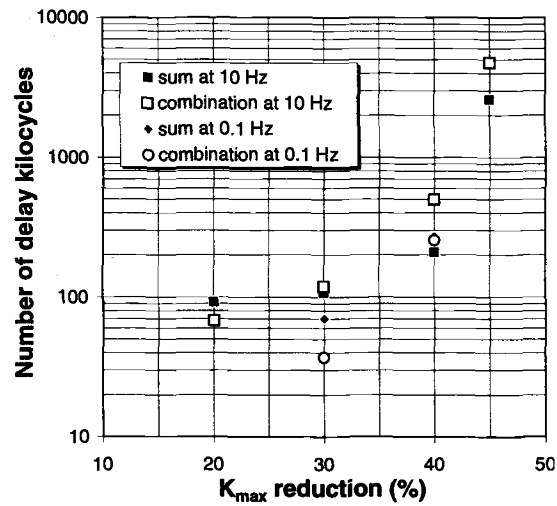

FIG. 10—*Synergetic effects at 10 Hz and 0.1 Hz for 6 mm specimen thickness.*

TABLE 2—*Synergetic Ratio for Two Frequencies, for 6 mm Specimen Thickness.*

K_{max} Reduction Percentage	Synergetic Ratio at 10 Hz	Synergetic Ratio at 0.1 Hz
20	0.74	
30	1.1	0.53
40	2.4	0.94
45	1.8	

TABLE 3—*Synergetic Ratio at a K_{max} Reduction Percentage of 30 for Three Thicknesses.*

2 mm		4.6 mm		6 mm	
10 Hz	0.1 Hz	10 Hz	0.1 Hz	10 Hz	0.1 Hz
2.1	...	1.1	0.52	1.1	0.53

much greater for the 4.6 mm thickness pure aluminum material. Two tests at 0.1 Hz for the 2 mm thickness specimen failed owing to machine problems.

Problems with Asymmetric Crack Growth

At higher K_{max} reduction percentages the crack growth of the left- and right-hand sides of the specimen becomes asymmetric. At the highest reduction percentage of 45% the crack stops growing on one side at the transition crack length of 20 mm, while the other side continues to grow until final failure. This causes problems with regard to the constant ΔK control, as it is based on measurement of the crack length by the potential-drop method. In the case of asymmetry also, the potential-drop apparatus gives a reasonable indication of the total crack length, i.e., as the sum of short and long half-crack lengths. For the calculation of ΔK the mean of both values is now used, which leads to a higher K value at the growing crack tip. In order to estimate the effect of asymmetric growth, finite element calculations were performed in order to compare symmetric with asymmetric growth. The results of the calculations are shown in Fig. 11. The calculations were applied to a center-cracked tension test specimen geometry with a constant short half crack length of 20 mm and a growing long half-crack length from 20 to 40 mm. The applied load follows from a rigid displacement along the whole width of the specimen. This situation is the same as the actual circumstances in the tests with asymmetric crack growth. The calculated K factors of the long and short half-crack lengths are compared with data from the literature [8] and with the mean value according to the Feddersen approach, the formula for which is shown in Eq 3.

It is clear from Fig. 11 that the asymmetric K factor of the long half-crack length is greater than the K factor for a symmetric case. The K factor for the short half-crack length is roughly the same as that in the symmetric case using Eq 3. At a long (half) crack length of 30 mm, the effect of asymmetry on K is still not very great, with an approximately 2% larger K for the asymmetric case. Thus the long (half) crack length has a 2% greater K than a symmetric (half) crack length of the same length would have. It is noteworthy that the K of the short crack length does not decrease on the growing of the long crack. It has about the same value as the symmetric mean Feddersen value.

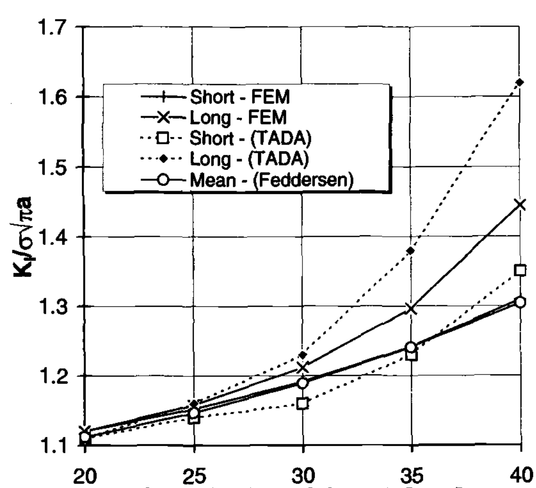

FIG. 11—*Influence of asymmetry in crack growth on the geometric correction factor; the short half-crack length is 20 mm.*

The 2% greater K for the long crack length (at 30 mm, with a short crack length at 20 mm) results in a 6% greater da/dN compared with a symmetric case, assuming a Paris exponent of 3. This will lead to less retardation for asymmetric crack growth, an effect that will occur for larger reduction percentages. This may be the reason why the synergetic ratio is smaller for a reduction of 45% than for 40%.

Discussion and Conclusions

The synergetic effect is not so great as at first expected, primarily on the basis of older tests. It may be that the shear lip reduction caused by the ΔK_{eff} reduction from 10 to 5 MPa$\sqrt{m}$ was too small. The outcome is also affected by the asymmetric crack growth, with crack stop on one side of the center-cracked specimen, as the asymmetry is larger for 45% reduction than for 40% reduction; i.e., at 40% reduction the crack becomes slightly asymmetric but does not stop at 20 mm. The retardation is less than it would have been if no asymmetry had been present.

The synergetic effect is thought to result from the following rationale. When two retardation mechanisms are simultaneously active, each mechanism keeps the crack longer in a position with maximum sensitivity for retardation by the other mechanism.

This does not explain the negative synergy for low reduction and for 0.1 Hz. Here the combined application of the two mechanisms results in an acceleration, rather than a retardation, compared with the sum of the separate mechanisms. This is not as yet understood. We conclude that:

- The two crack closure mechanisms exhibit synergetic retardation for a K_{max} reduction percentage higher than 20% at 10 Hz. For 0.1 Hz no synergy is found.
- The shear lip closure is strongly dependent on the frequency; the plasticity-induced closure mechanism is not dependent on the frequency or has a reverse dependence compared with the shear lip closure mechanism. The combined mechanism is again frequency-dependent.

References

[1] Zuidema, J., "Square and Slant Fatigue Crack Growth in Al 2024," Delft University Press, ISBN 90-407-1191-7, Delft, The Netherlands, 1995, 177 pp.

[2] Edwards, R. A. H., de Jong, E. M., and Zuidema, J., "The Fracture Mode Transition and Its Effect on Crack Growth Retardation," *Proceedings*, Fatigue 84, University of Birmingham, UK, 1984, pp. 463–478.

[3] Zuidema, J. and Blaauw, H. S., "Slant Fatigue Crack Growth in Al-2024 Sheet Material," *Engineering Fracture Mechanics*, Vol. 29, 1988, pp. 401–413.

[4] Zuidema J., Shen, W. Y., and Janssen, M., "Retardation in Fatigue Crack Growth in Al-2024 After Blocks of Underloading," *Fatigue and Fracture of Engineering Materials and Structures*, Vol. 14, 1991, pp. 991–1005.

[5] Marci, G. and Packman, P. F., *International Journal of Fracture*, Vol. 16, 1980, pp. 133–153.

[6] Schijve, J., "Some Formulas for the Crack Opening Stress Level," *Engineering Fracture Mechanics*, Vol. 14, 1981, pp. 461–465.

[7] Zuidema, J. and Krabbe, J. P., "The Effect of Regular and Irregular Shear Lips on Fatigue Crack Growth in Al 2024," *Fatigue and Fracture of Engineering Materials and Structures*, Vol. 20, 1997, pp. 1413–1422.

[8] Tada, H., Paris, P., and Irwin, G., *The Stress Analysis of Cracks Handbook*, Paris Productions Inc. and Del Research Corp., St. Louis, MO, 1985.

Closure Effects on Crack Behavior

S. R. Daniewicz[1]

Evaluating the Influence of Plasticity-Induced Closure on Surface Flaw Shape Evolution Under Cyclic Loading Using a Modified Strip-Yield Model

REFERENCE: Daniewicz, S. R., "**Evaluating the Influence of Plasticity-Induced Closure on Surface Flaw Shape Evolution Under Cyclic Loading Using a Modified Strip-Yield Method,**" *Advances in Fatigue Crack Closure Measurement and Analysis: Second Volume, ASTM STP 1343*, R. C. McClung and J. C. Newman, Jr., Eds., American Society for Testing and Materials, West Conshohocken, PA, 1999, pp. 393–410.

ABSTRACT: A slice synthesis methodology is used to construct a modified strip-yield model for the part-through semi-elliptical surface flaw, enabling prediction of plasticity-induced closure along the crack front and subsequent fatigue crack growth. Predictions of flaw shape evolution under cyclic loading are compared with experimental data for steel specimens under constant-amplitude cyclic bending. Model predictions are shown to correlate well with experimental data. The influence of stress level and mean stress on surface flaw shape evolution is evaluated.

KEYWORDS: fatigue, crack propagation, surface flaw, part-through flaw, crack closure, plasticity-induced closure

The part-through semi-elliptical surface flaw is commonly encountered in engineering practice. Models enabling the accurate prediction of the growth of this type of flaw under cyclic loading represent an essential element in any damage-tolerant design methodology. In metallic materials, a growing surface flaw will remain closed or partially closed along the crack front for a portion of the applied cyclic load as a consequence of plastically deformed material left in the wake of the growing crack.

Proper characterization of this plasticity-induced crack closure is needed when predicting flaw shape development and growth [*1–7*]. A small semi-circular flaw under cyclic bending or tension with a stress ratio $R = 0.10$ will grow such that the flaw shape remains semi-circular [*8*]. However, for a small semi-circular flaw, the stress intensity factor at the free surface is approximately 10% higher than that at the deepest point of penetration. Consequently, flaw growth is not controlled by the stress intensity factor alone. As a possible explanation for this behavior, it has been suggested that a higher level of plasticity-induced closure exists at the free surface, thus slowing the rate of growth in this area [*4*]. Surface flaws exhibit a level of closure which varies along the crack front. Both the extent and variation of this closure have not been well characterized. First discussed by Elber [*9,10*], plasticity-induced fatigue crack closure has attracted the interest of many researchers. Due to the complex nature of the surface flaw, the majority of this research activity has focused on through-crack geometries such as the compact tension specimen and the center-cracked panel. The amount of crack

[1] Assistant professor, Department of Mechanical Engineering, Mississippi State University, Mississippi State, MS 39762.

closure information available for surface flaws is relatively small in comparison to that for through-cracks.

Modeling the plasticity-induced closure generated by the semi-elliptical surface flaw may be performed using three-dimensional nonlinear finite element analysis [*11*]. However, from an engineering perspective this type of an approach is impractical. Predominantly developed by Newman [*12*], modified strip-yield models have found wide application for prediction of crack closure and subsequent fatigue crack growth in planar geometries with through-cracks. This is evidenced by the large number of strip-yield modeling efforts reported in the literature [*12–24*]. While approximate in nature, these types of models exhibit high computational efficiency when compared to more rigorous finite element analyses. This paper discusses the development of a modified strip-yield model for surface flaws. The model is then applied to study flaw shape evolution under cyclic bending. The modified strip-yield model has been used previously to predict surface flaw growth in 2024-T351 aluminum under uniform cyclic tension [*25*].

An elastic-perfectly plastic plate of thickness *T* contains a semi-elliptical surface flaw as shown in Fig. 1. An infinite width *W* was assumed. The flaw is opened with an arbitrary symmetrical applied stress σ_{zz} (x, y). In the model development process, a slice synthesis methodology [*26*] previously limited to stress intensity factor and crack surface displacement computation was employed. Using coupled modified strip-yield model analyses, concurrent crack closure assessments for the surface flaw at both points A and B were performed. Strip-yield modeling of surface flaws has previously been limited to the prediction of limit loads and plastic zone size [*27*].

Modified Strip-Yield Model

Using weight function based formulations, Wang et al. [*21*] and Daniewicz et al. [*20,21*] have generalized the Newman [*12*] modified strip-yield model to allow treatment of arbitrary planar geometries with through-cracks. Such generalizations require a large number of numerical integrations for each increment of crack growth, and computational efficiency may be increased through use of a Gauss-Chebyshev quadrature [*28*]. A modified strip-yield model utilizing weight functions for planar geometry description forms the basis for development of a model which allows consideration of the surface flaw.

Assuming the surface flaw maintains a semi-elliptical shape while under cyclic loading, a two parameter description of the surface flaw may be adopted. Attention may then be restricted to crack growth at points A and B. Using a weight function based slice synthesis methodology presented by Zhao et al. [*26*], through-crack weight functions for two-dimensional bodies may be used to approximate surface flaw stress intensity factors, plastic zone sizes, and crack surface displacements. This

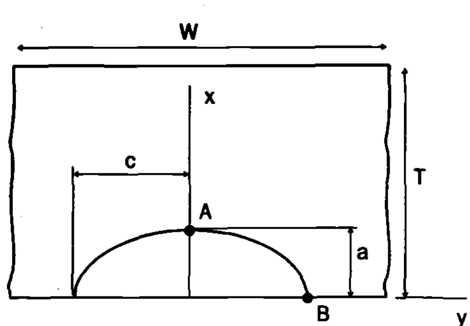

FIG. 1—*Part-through semi-elliptical surface flaw.*

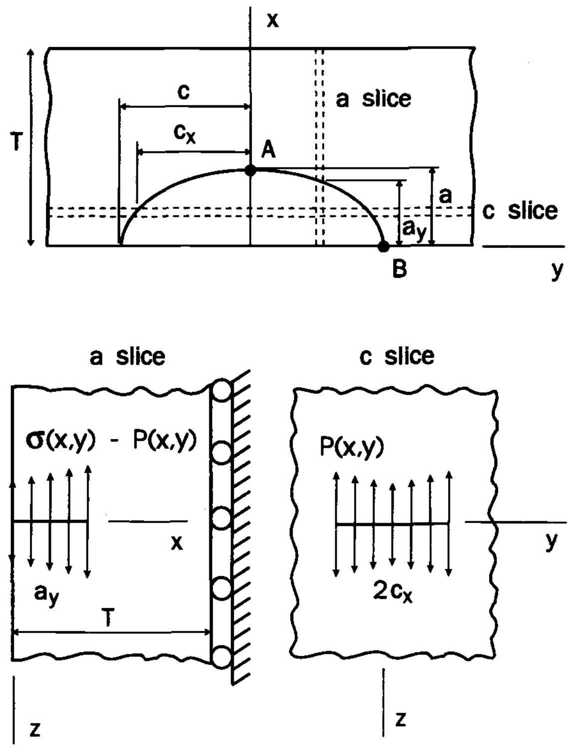

FIG. 2—*Slice synthesis model.*

information permitted the prediction of crack opening behavior using the algorithm presented by Newman [*12*]. The slice synthesis methodology was first introduced by Fujimoto [*29*] and Saff et al. [*30*] for stress intensity factor computation. More recently, it has been used to compute surface crack and corner crack stress intensity factors and crack opening displacements [*31–33*].

As illustrated in Fig. 2, the behavior of the surface flaw is synthesized using two groups of through-crack slices. The surface flaw is characterized using a crack depth a and width $2c$. The slices situated parallel with the x axis are denoted as primary slices or a slices, while those aligned parallel with the y axis are termed spring slices or c slices. Each primary slice constitutes an edge cracked strip and is assumed to be in a plane stress condition. The slice exhibits a modulus of elasticity E, a flow stress σ_o, and a crack length a_y as defined by the elliptical shape and given as

$$a_y = a\sqrt{1 - (y/c)^2} \tag{1}$$

Surface flaw stress intensity factors and crack surface displacements may be estimated accurately using these two-dimensional slices if an unknown shear traction $\sigma_{yz} = P(x,y)$ acting between adjacent primary slices is introduced. The material surrounding each primary slice on either side acts to restrain crack surface displacement, and thus this traction acts in a direction opposite to that of the applied stress $\sigma(x,y) = \sigma_{zz}(x,y)$. Consequently, the applied stress on any given primary slice is $\sigma(x,y) - P(x,y)$ as shown in Fig. 2. The elastic stress intensity factor K_a and crack surface displacement $w_a(x,y)$ for an arbitrarily located primary slice resulting from the applied stress $\sigma(x,y)$ are given by

$$K_a = \int_o^{a_y} [\sigma(\xi,y) - P(\xi,y)]m_a(\xi,a_y)\, d\xi \tag{2}$$

$$w_a(x,y) = \frac{1}{E}\int_x^{a_y}\int_o^{\alpha} [\sigma(\xi,y) - P(\xi,y)]m_a(\xi,\alpha)m_a(x,\alpha)d\xi d\alpha \tag{3}$$

where the primary slice weight function for an edge crack of length a_y is denoted as $m_a(\xi,a_y)$ and α is a dummy variable.

To incorporate free boundary effects and thus consider finite bodies, elastic boundary conditions are needed for the a slices as discussed by Zhao et al. [*26,33*]. To approximate the effects of the finite thickness T, boundary conditions on the back surface ($x = T$) are necessary. The x displacement restraint at this surface is a function of the plate width W [*26,33*]. With $W \to \infty$, the back surface for an arbitrary a slice is assumed to be sufficiently restrained such that this surface undergoes zero displacement in the x direction. At the crack mouth ($x = 0$), a free surface was assumed. Thus, the specific weight function used was that for an edge-cracked strip with fixed back-surface displacement as shown in Fig. 2. This function is given by

$$m(x,a_y) \approx$$

$$\frac{2}{\sqrt{2T}}\left\{1 + 0.15\left[1 - \left(\frac{x}{a_y}\right)^{5/4}\right]\left[1 - \sin\left(\frac{\pi a_y}{2T}\right)\right]\left[2 + \sin\left(\frac{\pi a_y}{2T}\right)\right]\right\}\frac{\sqrt{\tan(\pi a_y/2T)}}{\sqrt{1 - \left[\dfrac{\cos(\pi a_y/2T)}{\cos(\pi x/2T)}\right]^2}} \tag{4}$$

Equation 4 was derived from a stress intensity factor solution [*34*] for a double edge-crack under symmetrical concentrated loading on the crack surfaces. This function has also been tabulated by Glinka and Shen [*35*].

The slice synthesis must be calibrated if it is to function properly. Through a calibration process using an exact solution for an embedded semi-elliptical flaw under uniform tension, it may be shown [*26,29*] that Eq 2 will yield an accurate estimate of the surface flaw stress intensity factor at point A if $y = 0$ and a plane strain scaling factor $1/(1 - \nu^2)$ is introduced where ν represents Poisson's ratio

$$K_A = \frac{1}{1 - \nu^2}\int_o^{a} [\sigma(\xi,0) - P(\xi,0)]m_a(\xi,a)d\xi \tag{5}$$

The required mechanical coupling between adjacent primary slices is made possible through the introduction of an additional series of slices denoted as spring slices or c slices. These slices enable the computation of the unknown shear traction through enforcement of compatibility with $w_a = w_c$ where w_c is the spring slice displacement. As shown in Fig. 2, each spring slice constitutes a center-cracked panel and is assumed to be under a plane stress condition. These slices are parallel to the free surface and exhibit a modulus of elasticity E_s, a flow stress σ_{os}, and a crack length $2c_x$ with c_x defined from the elliptical shape and given by

$$c_x = c\sqrt{1 - (x/a)^2} \tag{6}$$

Both E_s and σ_{os} are fictitious quantities defining the level of mechanical coupling between adjacent primary slices. Using the previously discussed calibration process it may be demonstrated [*26,29,30*] that

$$\frac{E_S}{E} = \left(\frac{\Phi}{1 - \nu^2} - 1\right)\frac{c}{a} \tag{7}$$

In this expression, Φ represents a complete elliptic integral of the second kind with, for $a/c \leq 1$

$$\Phi = \int_0^{\pi/2} ((a/c)^2 \sin^2 \phi + \cos^2 \phi)^{1/2}\, d\phi \tag{8}$$

The determination of the spring slice flow stress σ_{os} will be considered following an elastic analysis of the spring slice. The spring slice stress intensity factor K_c and crack surface displacement $w_c(x,y)$ resulting from the applied stress $\sigma(x,y)$ are given by

$$K_c = \int_o^{c_x} P(x,\eta) m_c\,(\eta,c_x)\, d\eta \tag{9}$$

$$w_c(x,y) = \frac{1}{E_s}\int_y^{c_x}\int_0^{\gamma} P(x,\psi) m_c\,(\psi,\gamma) m_c\,(y,\gamma)\, d\psi\, d\gamma \tag{10}$$

where the spring slice weight function for a center-crack with length $2c_x$ under symmetrical loading with $P(x,y) = P(x,-y)$ is denoted as $m_c(\eta,c_x)$ and γ is a dummy variable. This symmetrical shear traction implies $\sigma(x,y) = \sigma(x,-y)$. The weight function used was that for the center through-crack in an infinite body under symmetrical loading [36]

$$m(y,c) = 2\sqrt{\frac{c}{\pi}}\frac{1}{\sqrt{c^2 - y^2}} \tag{11}$$

From the previously mentioned calibration process, it may also be shown that Eq 9 will yield an accurate estimate of the surface flaw stress intensity factor at point B if $x = 0$ and it is scaled by a factor E/E_s such that

$$K_B = \frac{E}{E_s}\int_o^{c} P(0,\eta) m_c\,(\eta,c)\, d\eta \tag{12}$$

Next consider plastic deformation along the crack front as illustrated in Fig. 3. Using a strip-yield modeling approach, the surface flaw and subsequent plastic zone are treated as an effective crack in an elastic body. The effective surface flaw is characterized using a crack depth a, crack width $2c$, and plastic zones ρ_A and ρ_B. The effective and actual surface flaws are concentric semi-ellipses. As suggested by Dugdale [37], the extent of the plastic zone may be determined if the material flow stress is assumed to act as a compressive cohesive stress applied within the plastic zone. At the effective crack front the stress is assumed finite with the net stress intensity factor equal to zero. The slice plastic zone sizes $\rho_a = \rho_y$ and $\rho_b = \rho_x$ for slices passing through points A and B may be found using the following relationships which enforce a zero net stress intensity factor at A and B, respectively

$$\frac{1}{1 - \nu^2}\int_o^{a+\rho_a} [\sigma(\xi,0) - P(\xi,0)] m_a\,(\xi,a + \rho_a) d\xi - \int_a^{a+\rho_a} \alpha_A\, \sigma_o\, m_a\,(\xi,a + \rho_a) d\xi = 0 \tag{13}$$

$$\int_o^{c+\rho_b} P(0,\eta) m_c\,(\eta,c + \rho_b)\, d\eta - \int_c^{c+\rho_b} \alpha_B \sigma_{os} m_c\,(\eta,c + \rho_b)\, d\eta = 0 \tag{14}$$

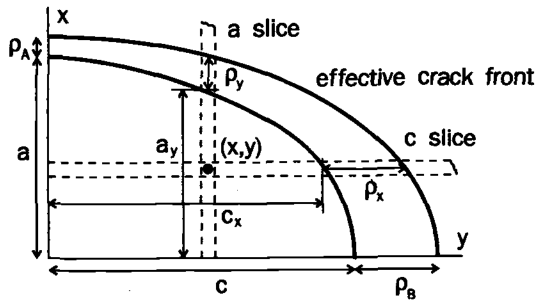

FIG. 3—*Crack front localized plastic deformation.*

A calibration process analogous to that discussed for the elastic crack analysis is necessary to correlate the slice plastic zones ρ_a and ρ_b with the surface crack plastic zone sizes ρ_A and ρ_B, as well as to define the spring slice flow stress σ_{os}.

When using modified strip-yield models, it is commonly assumed that the cohesive stress within the plastic zone is a constant. In Eqs 13 and 14, α_A and α_B are constraint factors which describe the average stress to flow stress ratio in the plastic zone at points A and B, respectively. Consider Eq 13. Note that plane strain conditions are enforced by proper selection of the factor α_A, and consequently the plane strain factor $1/(1 - \nu^2)$ has not been applied to the second integral representing the stress intensity factor associated with the plastic zone loading. In addition, note also from the first integral that the shear traction has been applied along the entire effective crack length including the plastic zone. Consequently, it is unnecessary to apply the shear traction again within the second integral.

Just as the elastic properties of the spring slice were defined using a calibration process, the flow properties must be defined as well when constructing a strip-yield model for the surface crack. As shown by Daniewicz [25], through a calibration process using an exact strip-yield model solution for an embedded circular flaw under uniform tension,

$$\frac{\sigma_{os}}{\sigma_o} = \frac{E_s}{E} = \left(\frac{\Phi}{1 - \nu^2} - 1\right)\frac{c}{a} \tag{15}$$

In addition, this calibration yields the following correlations between slice plastic zone sizes ρ_a and ρ_b and surface crack plastic zone sizes ρ_A and ρ_B

$$\frac{\rho_A}{a} = \frac{1}{\dfrac{1}{\ln(1 + \rho_a/a)} - 1} \tag{16}$$

$$\frac{\rho_B}{c} = \frac{1}{\dfrac{1}{\ln(1 + \rho_b/c)} - 1} \tag{17}$$

Under conditions of small-scale yielding, Eqs 16 and 17 yield $\rho_A = \rho_a$ and $\rho_B = \rho_b$. Equations 13 and 14 constitute a system of nonlinear equations for the two unknowns ρ_A and ρ_B. This system was solved iteratively. Note that the shear traction $P(x,y)$ is needed both in the plastic zone as well as throughout the crack, and is thus a function of ρ_A and ρ_B. Under small-scale yielding conditions, plastic zone sizes computed using Eqs 13–17 have been found to coincide with the well known Dugdale solution $\rho_A = (\pi/8)(K_A/\alpha_A\sigma_o)^2$ and $\rho_B = (\pi/8)(K_B/\alpha_B\sigma_o)^2$.

Having determined the plastic zone sizes, the crack surface displacements at a point of interest (x,y) resulting from both the applied stress and the plastic zone loading may be derived [25]. These displacements are

$$
\begin{aligned}
w_a(x,y) &= \frac{1}{E}\int_x^{a_y}\left\{\int_o^{\alpha}[\sigma(\xi,y) - P(\xi,y)]m_a(\xi,\alpha)\,d\xi\right\}m_a(x,\alpha)d\alpha \\
&+ \frac{1}{E}\int_{a_y}^{a_y+\rho_y}\left\{\int_o^{\alpha}[\sigma(\xi,y) - P(\xi,y)]m_a(\xi,\alpha)\,d\xi - \int_{a_y}^{\alpha}\alpha_a\sigma_o m_a(\xi,\alpha)d\xi\right\}m_a(x,\alpha)d\alpha
\end{aligned}
\tag{18}
$$

$$
\begin{aligned}
w_c(x,y) &= \frac{1}{E_s}\int_y^{c_x}\left\{\int_o^{\gamma}P(x,\psi)m_c(\psi,\gamma)d\psi\right\}m_c(y,\gamma)\,d\gamma \\
&+ \frac{1}{E_s}\int_{c_x}^{c_x+\rho_x}\left\{\int_o^{\gamma}P(x,\psi)m_c(\psi,\gamma)d\psi - \int_{c_x}^{\gamma}\alpha_c\sigma_{os}m_c(\psi,\gamma)d\psi\right\}m_c(y,\gamma)\,d\gamma
\end{aligned}
\tag{19}
$$

where α_a and α_c are constraint factors for arbitrarily located primary and spring slices. When these slices are situated such that they pass through points A and B $\alpha_a = \alpha_A$ and $\alpha_c = \alpha_B$. To insure compatibility, the displacement from each slice must be equal with $w_a = w_c$. This condition was used to determine the shear traction [25]. Following calibration, these slice displacements equal the surface flaw displacement. In addition, from Fig. 3.

$$
\begin{aligned}
\rho_x &= (c + \rho_b)\sqrt{1 - x^2/(a + \rho_a)^2} - c\sqrt{1 - x^2/a^2} \\
\rho_y &= (a + \rho_a)\sqrt{1 - y^2/(c + \rho_b)^2} - a\sqrt{1 - y^2/c^2}
\end{aligned}
\tag{20}
$$

Using prescribed constraint factors for points A and B, the constraint factors for an arbitrary location along the crack front were assumed to be given by the following linear relationship

$$
\alpha(\varphi) = \frac{\alpha_A - \alpha_B}{\pi/2}\varphi + \alpha_B \tag{21}
$$

where two φ angles are defined in Fig. 4 with $\cos\varphi_x = c_x/c$ and $\sin\varphi_y = a_y/a$. Note that for points (x,y) not on the crack perimeter, a unique φ_y and φ_x are required for the primary slice and spring slice respectively with $\alpha_a = \alpha(\varphi_y)$ and $\alpha_c = \alpha(\varphi_x)$. For points on the perimeter, $\varphi_y = \varphi_x$. The linear constraint distribution (in terms of φ) along the crack front may over-represent the plane stress contribution associated with the free surface at point B. Although currently unknown, a more rigorously determined distribution may involve a crack front dominated by plane strain conditions, with the exception of a small region near point B where the constraint decreases rapidly to a plane stress level. This is illustrated in Fig. 5. Elastic-plastic finite element analysis represents one potential means of characterizing the distribution of constraint along the crack front. This distribution will also be a function of applied load.

Next consider the computation of the unknown shear traction $P(x,y)$. For equilibrium, at arbitrary points (x,y) along the crack surface where the primary and spring slices intersect, the total applied stress must be $\sigma(x,y)$. Equilibrium then dictates that each spring slice be subject to an applied stress $P(x,y)$ as shown in Fig. 2. With the primary and spring slices assumed to exhibit a flow stress σ_o and σ_{os}, respectively, points of interest (x,y) must be confined within the actual crack boundary (no points in the plastic zone) to avoid a net cohesive stress $-(\sigma_o + \sigma_{os})$. In addition, compatibility dictates the

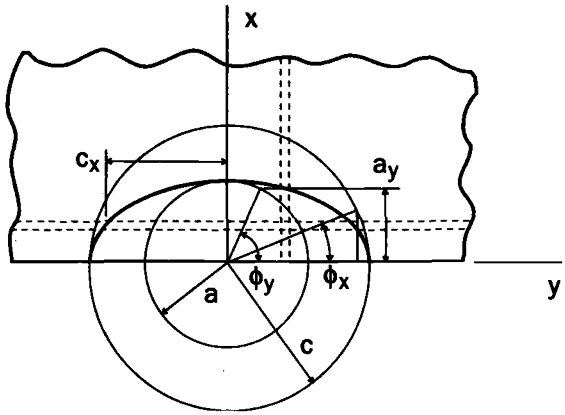

FIG. 4—*Crack front angular positions.*

displacement from each slice must be equal with $w_a = w_c$. Assume $P(x,y)$ is a linear combination of prescribed basis functions $p_i(x,y)$ such that [26].

$$P(x,y) = \sum_{i=1}^{14} \lambda_i p_i(x,y) \tag{22}$$

In expanded form this expression may be written as

$$\begin{aligned} P(x,y) = {} & \lambda_1 + \lambda_2(y/c)^{1/3} + \lambda_3(x/a)^{1/3} + \lambda_4(xy/ac)^{1/3} + \lambda_5(y/c) \\ & + \lambda_6(x/a) + \lambda_7(xy/ac) + \lambda_8(y/c)^2 + \lambda_9(x/a)^2 + \lambda_{10}(xy/ac)^2 \\ & + \lambda_{11}(y/c)^3 + \lambda_{12}(x/a)^3 + \lambda_{13}(y/c)^4 + \lambda_{14}(x/a)^4 \end{aligned} \tag{23}$$

Using Eq 22, and satisfying compatibility at m ($m > 14$) uniformly distributed points on the crack surface, enables the generation of an over-determined system of equations allowing the computation of 14 coefficients λ_i such that the shear traction is defined [26].

The model described thus far may be characterized as a strip-yield model for monotonic loading. With this model, both the extent of the regions exhibiting plastic deformation along the crack front as well as the subsequent crack surface displacements may be determined. For analysis of plasticity-

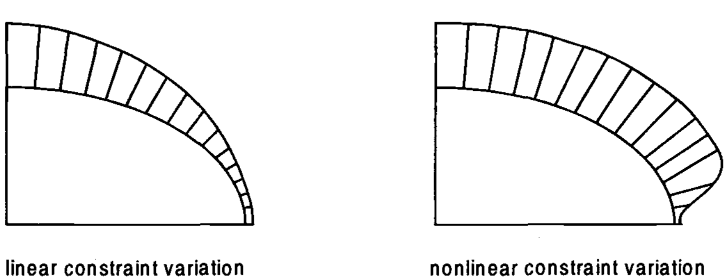

FIG. 5—*Constraint distributions.*

induced crack closure, cyclic loading must be considered, and monotonic strip-yield models must be modified to leave plastically deformed material along the crack surfaces as the crack advances [*12*]. Using a weight function based formulation, Daniewicz et al. [*22*] have generalized the Newman modified strip-yield model to allow treatment of arbitrary through-crack geometries. With the surface flaw now described in terms of two through-cracks through application of the slice synthesis methodology, a surface flaw modified strip-yield model was constructed using two coupled through-crack modified strip-yield analyses. For more detailed discussions concerning modified strip-yield models, see [*12,21* or *22*].

Fatigue crack growth rates at points A and B were assumed characterized in terms of effective stress intensity factor ranges $(\Delta K_{\text{eff}})_A$ and $(\Delta K_{\text{eff}})_B$

$$\frac{da}{dN} = C_A(\Delta K_{\text{eff}})_A^{n_A} \qquad \frac{dc}{dN} = C_B(\Delta K_{\text{eff}})_B^{n_B} \tag{24}$$

where an effective stress intensity factor range is defined using the maximum applied stress S_{max} and the computed crack opening stress S_o

$$\Delta K_{\text{eff}} = K(S_{\text{max}}) - K(S_o) \tag{25}$$

Equations 24 may be combined to yield

$$dc = \frac{C_B}{C_A}\frac{(\Delta K_{\text{eff}})_B^{n_B}}{(\Delta K_{\text{eff}})_A^{n_A}}\,da \tag{26}$$

Under constant-amplitude loading, a modified strip-yield model prediction of crack opening stress was made using an assumed increment of crack growth. Modified strip-yield models were created for a primary slice passing through point A and a spring slice passing through point B. These two models were coupled and utilized concurrently. Figure 3 illustrates a primary and spring slice pair. Note that while numerous pairs were utilized for computation of the shear traction $P(x,y)$, only a single primary and spring slice were used for crack opening stress prediction. From an initial assumed flaw size a_i and c_i, the crack opening stress at point A was first predicted using an assumed increment of crack extension da with $da = 0.05\ \rho_A$. The crack opening stress at point B was next computed using an assumed crack growth increment dc. Using Eq 26, the resulting crack opening stresses were then used to compute a crack growth increment dc. If the computed dc differed from the assumed value, the computed value was used to compute a new crack opening stress at B with this process repeated until convergence was obtained. This procedure was repeated for each crack growth increment da until the prescribed final crack depth a was attained. Use of this methodology enabled the computation of opening stresses for points A and B as a function of current flaw size as well as a prediction of aspect ratio (a/c) evolution under the prescribed cyclic loading.

Model Application: Surface Flaw Preferred Propagation Paths Under Remote Bending

Under cyclic loading, surface flaws have been found to grow such that the aspect ratio (a/c) approaches a unique steady-state value which is a function of crack depth and independent of the initial aspect ratio. These unique values make up what has been described as a preferred propagation path (PPP) [*7,8,38–40*]. The ASTM standard practice for fracture testing of surface cracked specimens [*41*] gives the following empirical PPP for tension and bending loads

$$\text{tension} \qquad a/c = 1.0 - 0.2(a/T)^2 \tag{27}$$

$$\text{bending} \qquad a/c = 1.0 - (a/T) \tag{28}$$

With flaw shape evolution a function of the level of plasticity-induced closure along the crack front, it is suggested that the PPP may also be a function of both the applied stress level and the R-ratio, as both of these quantities are known to influence the level of closure. To investigate possible stress level and mean stress effects, the strip-yield model was used systematically to predict the PPP under various prescribed R-ratios and applied stress levels. The model was first verified by comparing model predictions with experimental data.

Growth of a semi-elliptical surface flaw under a constant amplitude cyclic bending was predicted and compared with experimental data. McFadyen et al. [42] presented aspect ratio (a/c) as a function of normalized crack depth (a/T) for a LT60 steel plate with thickness T = 28 mm and width W = 150 mm (Fig. 1). This material is a C-Mn steel with a yield strength of 405 MPa, an ultimate strength of 515 MPa, and an elongation of 29%. Electrical discharge machining was used to create initial cracks of various aspect ratios which exhibited no plastic wake and were closure free. The plate was loaded in pure bending with various R-ratios and applied stress levels. Maximum stress levels S_{max} ranging from 190 MPa to 315 MPa were used. The R-ratios used varied considerably less and were within the range 0.018 to 0.097.

The strip-yield model considers an elastic-perfectly plastic material, and a flow stress σ_o, assumed to be the average of the yield and ultimate strengths, was assumed with σ_o = 460 MPa. The constraint factors α_A and α_B are fitting parameters which must be assumed. From previous modeling experience [25] with aluminum specimens under uniform cyclic tensile stress, constraint factors α_A = 3.00 and α_B = 2.50 were initially assumed. Using crack growth measurements from the part-through flaws, McFadyen et al. found a fatigue crack growth rate exponent $n_A = n_B = n = 3.0$ (see Eq 26). The fatigue crack growth rate coefficients C_A and C_B were assumed equal when using the strip-yield model, and thus had no effect on the closure computation. An initial flaw equal in size to the electrical discharge machined notch was assumed. This initial flaw was also assumed to exhibit no prior plastic wake.

From Figs. 6, 7, 8, and 9, reasonable correlation between the model predictions and the experimental data were observed, indicating the assumed constraint factors were appropriate. Also shown

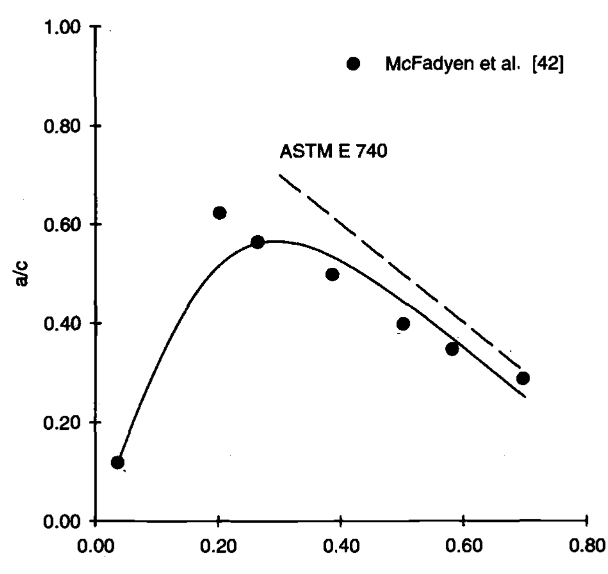

FIG. 6—*Predicted and measured aspect ratio evolution,* R = *0.05,* S_{max}/σ_o = *0.433.*

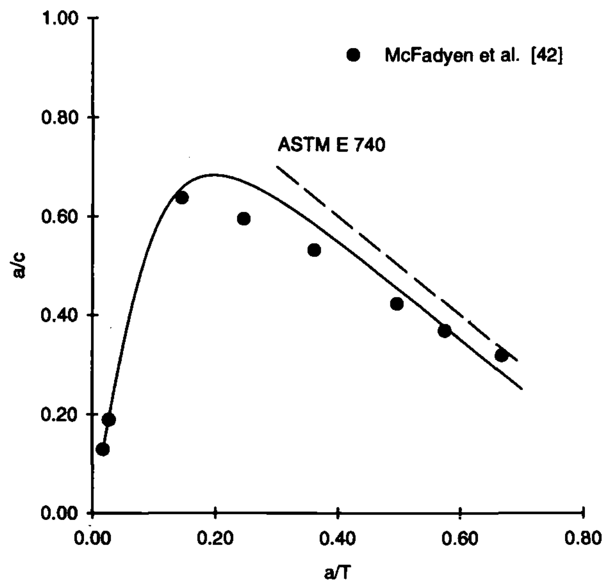

FIG. 7—*Predicted and measured aspect ratio evolution,* R = *0.083,* S_{max}/σ_o = *0.440.*

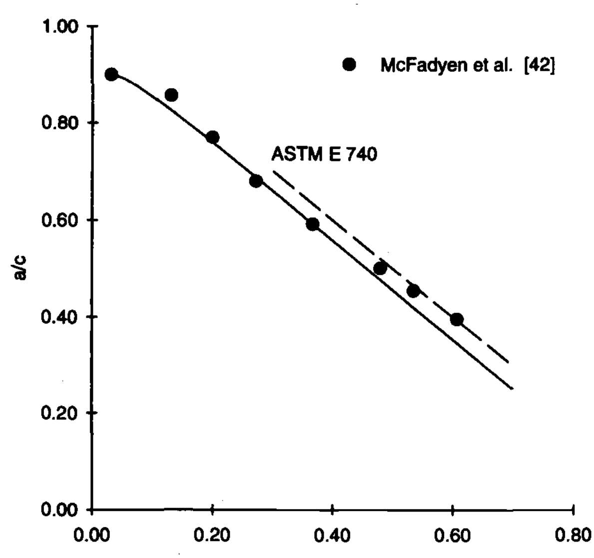

FIG. 8—*Predicted and measured aspect ratio evolution,* R = *0.097,* S_{max}/σ_o = *0.683.*

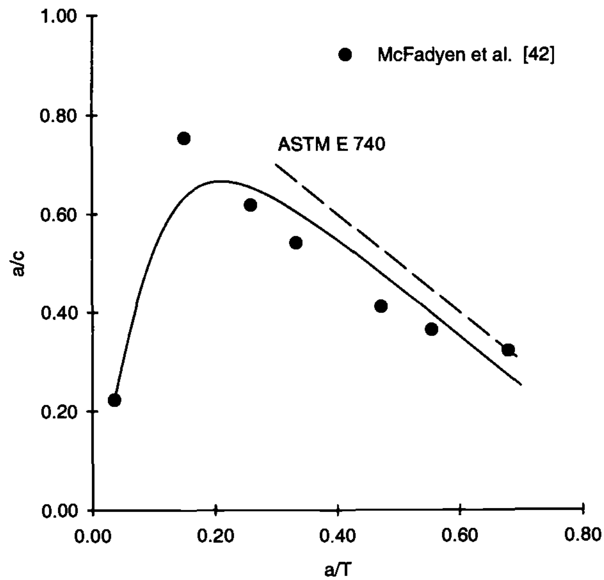

FIG. 9—*Predicted and measured aspect ratio evolution,* R = *0.018,* S_{max}/σ_o = *0.412.*

in these figures is the predicted PPP using Eq 28. After the initial transient behavior, the strip-yield model also predicted a PPP. The strip-yield model PPP were seen to compare well with the ASTM PPP.

When modeling through-crack behavior using strip-yield models, the constraint factor is generally found to be a function of material type. Thus, resulting values of 3.00 and 2.50, for the deepest point of penetration and surface point respectively, were unexpected as these same values have been found previously for aluminum [*25*]. Perhaps more importantly, a larger difference between these two values was also expected for both the aluminum and steel. These occurrences may be a result of the approximate linear constraint distribution assumed along the crack front, or of a dramatically different constraint factor sensitivity for surface flaws. Additional research will be necessary to resolve this issue.

To rigorously characterize the distribution of constraint along the crack front, elastic-plastic finite element analyses are needed. Constraint factors represent the effects of localized plastic deformation, and the distribution of constraint will also be a function of applied load. However, modified strip-yield model constraint factors also indirectly consider other closure mechanisms such as roughness induced closure and closure from corrosion products or fretting debris, and are thus best treated as fitting parameters. Consequently, while finite element analyses will enable the distribution of constraint to be determined, the actual magnitudes must continue to be found using fatigue data as performed in this study.

The strip-yield model was next used to systematically predict the PPP under various prescribed *R*-ratios and applied stress levels in an effort to assess stress level and mean stress effects. While the initial flaw shape was not of significance, for convenience a semi-circular flaw was assumed with a/c = 1. The initial flaw size over which no plastic wake acts was assumed to be a/T = 0.01. Results are illustrated in Fig. 10 through Fig. 14.

Only modest stress level effects were observed as seen in Fig. 10 through Fig. 12. This result was unexpected, suggesting the model may have difficulty in properly simulating the effect of stress level. However, the model was able to accurately predict flaw shape evolution under a stress level increase

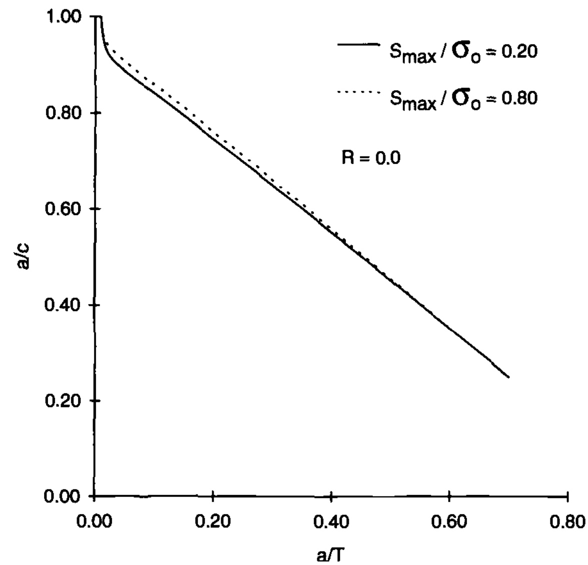

FIG. 10—*Effect of stress level on flaw shape evolution,* R = *0.0.*

of 65% as seen in Figs. 8 and 9. Consider Fig. 12, under constant amplitude loading with $R = 0.80$, no plasticity-induced closure will result and $\Delta K_{eff} = \Delta K$. Thus, the model would be expected to predict no stress level effects under this condition. However, from Fig. 12, a small stress level effect was predicted. This was a result of small changes in the shear traction $P(x,y)$, as this traction is a function of plastic zone size and is thus clearly dependent on stress level.

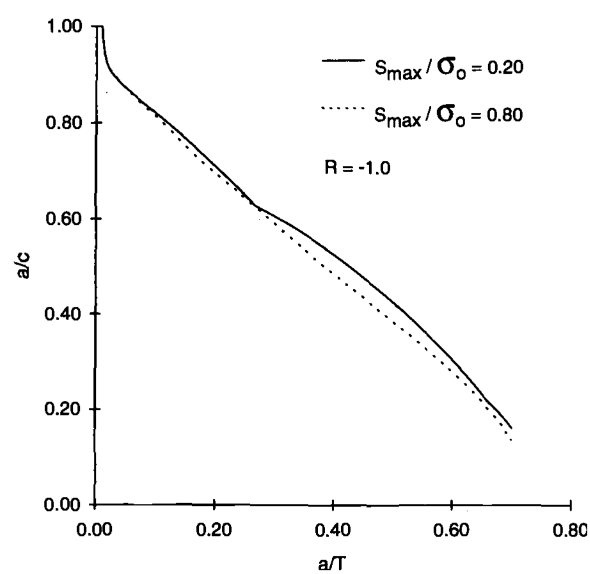

FIG. 11—*Effect of stress level on flaw shape evolution,* R = *−1.0.*

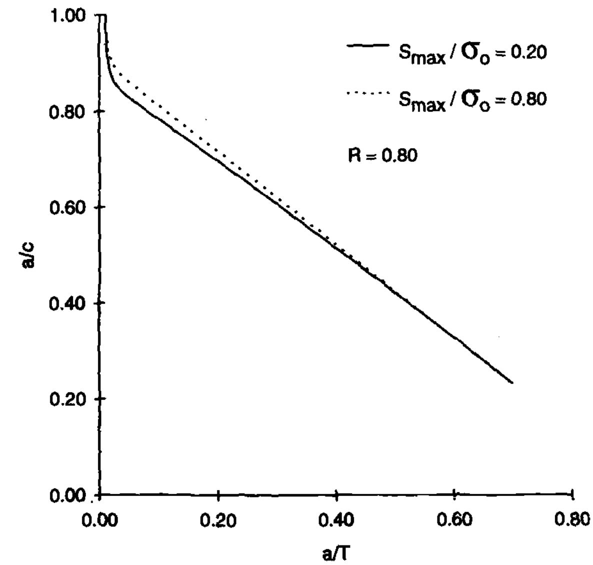

FIG. 12—*Effect of stress level on flaw shape evolution,* R = *0.80.*

From Figs. 13 and 14, large applied stresses were predicted to increase mean stress effects. These effects were, however, relatively minor. For $R \geq 0$, increasing the R-ratio reduced the aspect ratio a/c. This effect was empirically observed by Hodulak et al. [*43*] for aluminum surface cracked specimens loaded under uniform cyclic tension. This was expected as increases in R have been demonstrated to reduce the difference between crack opening stress levels under plane stress conditions (point B) and

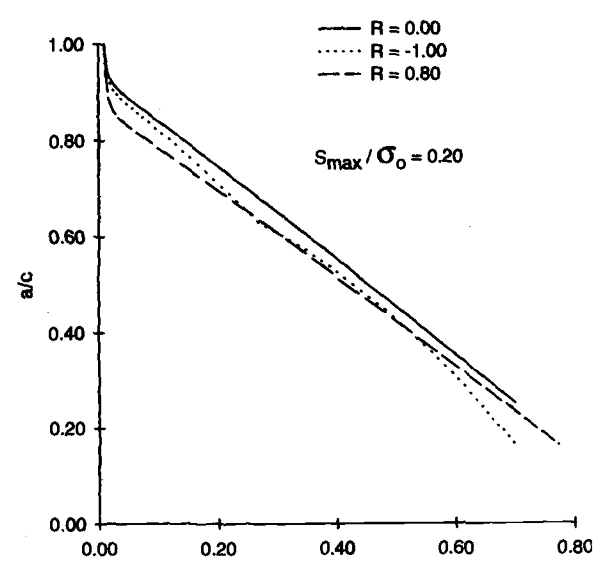

FIG. 13—*Effect of mean stress on flaw shape evolution,* S_{max}/σ_o = *0.20.*

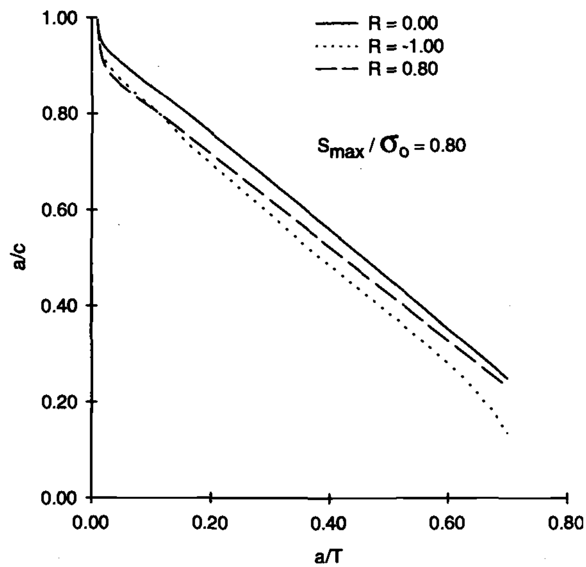

FIG. 14—*Effect of mean stress on flaw shape evolution,* $S_{max}\sigma_o$ = *0.80.*

crack opening stress levels under plane strain (point A) [*12*]. With this reduced difference, the crack width c would extend more rapidly with respect to the crack depth a as R increases.

Aspect ratio evolution is a function of the difference in the crack opening loads at the free surface (B) and deepest point of penetration (A). Predicted crack opening loads from strip-yield models are dependent on the constraint factor chosen, and thus a large difference in the crack opening loads at points A and B will be predicted if the constraint factors for these two points are dramatically different. The constraint factors $\alpha_A = 3.00$ and $\alpha_B = 2.50$ were found to give good crack shape predictions. With these factors differing by only a small amount, relatively small differences in the predicted crack opening loads resulted. Consequently, closure related variables such as maximum stress and mean stress were also predicted to have only minor effects as observed in Figs. 10–14.

That the two constraint factors differed so little is potentially a consequence of the assumed linear constraint distribution as discussed previously. It should be noted that efforts to produce more significant differences in crack opening stresses at A and B through selection of constraint factors which differed more greatly produced inaccurate shape change predictions.

The strip-yield model for the part-through surface flaws requires more computational resources than a through-crack strip-yield model. Therefore, for engineering purposes, it would be advantageous to simulate a part-through crack using an equivalent through-crack. To assess this possibility, crack opening stresses from the surface flaw strip-yield model were compared with the crack opening stress obtained from a similar through-crack strip-yield model [22]. Both simulations considered steel plates of equal thickness loading in bending with $R = 0.0$ and a maximum stress $S_{max}/\sigma_o = 0.60$. For the surface flaw, an initial semi-circular flaw was assumed with $a/c = 1$. Both the part-through crack and the through-crack had a initial flaw size of $a/T = 0.01$. The through-crack simulation used $\alpha = 3.00$, while for the part-through crack $\alpha_A = 3.00$ and $\alpha_B = 2.50$.

From Fig. 15, the resulting crack opening stresses for the two simulations differed considerably. For a through-crack, the crack opening stress dropped significantly for larger crack lengths as the remaining ligament was reduced in size. This occurs because the elastic clamping action offered by the remaining ligament decreases. To open the crack, this elastic clamping force must be overcome. For

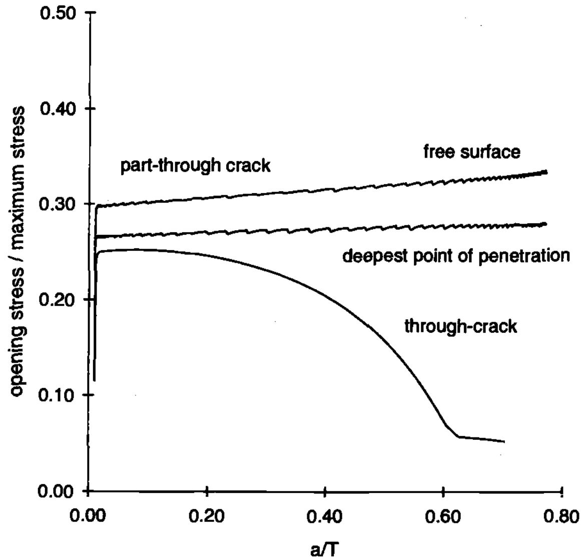

FIG. 15—*Normalized crack opening stress for through-crack and part-through crack.*

the part-through crack with infinite width, there is no effectively decrease in elastic clamping capability, and consequently no decrease in crack opening stress. Based on this comparison, efforts to produce an effective through-crack to simulate a surface crack may prove difficult.

Summary

A slice synthesis methodology has been employed to construct a modified strip-yield model for the semi-elliptical surface flaw, enabling prediction of plasticity-induced closure along the crack front and subsequent fatigue crack growth. Using two coupled strip-yield model analyses, concurrent crack closure assessments for the surface flaw at both the deepest point of penetration and the surface point were performed. Slice synthesis methodologies have previously been limited to stress intensity factor and crack surface displacement computation. The crack opening stresses predicted from this model differed considerably from results for a similar through-crack analysis, suggesting the through-crack has a dramatically different crack opening behavior at larger crack sizes.

Predictions of crack shape development under cyclic loading were compared with experimental data for LT60 steel specimens under constant-amplitude cyclic bending with various stress levels and $R \approx 0$. Predictions were shown to correlate well with experimental data with these data considering flaws as deep as $a/T = 0.70$ and applied stress differences as large as 65%. As this study focused on flaw shape evolution only, further work is needed to insure that both predicted flaw shape and predicted fatigue life correlate well with experimental observations. Fatigue life studies will require additional material characterization as both the crack growth rate exponent n and coefficient C (see Eq 24) are required. This is in contrast to flaw shape studies in which only the exponent n is needed, provided C_A is assumed equal to C_B as was done in the present study.

Acknowledgment

The author wishes to thank Dr. J. C. Newman of the NASA Langley Research Center for the guidance and encouragement received from many helpful discussions.

References

[1] Fleck, N. A., Smith, I. F. C., and Smith, R. A., "Closure Behavior of Surface Cracks," *Fatigue of Engineering Materials and Structures*, Vol. 6, No. 3, 1983, pp. 225–239.

[2] Jolles, M. and Tortoriello, V., "Geometry Variations During Fatigue Growth of Surface Flaws," *Fracture Mechanics: 14th Symposium-Vol. I: Theory and Analysis, ASTM STP 791*, American Society for Testing and Materials, Philadelphia, 1983, pp. I297–I307.

[3] Jolles, M. and Tortoriello, V., "Effects of Constraint Variation on the Fatigue Growth of Surface Flaws," *Fracture Mechanics: 15th Symposium, ASTM STP 833*, American Society for Testing and Materials, Philadelphia, 1984, pp. 300–311.

[4] Newman, J. C. and Raju, I. S., "Prediction of Fatigue Crack-Growth Patterns and Lives in Three-Dimensional Cracked Bodies," *Advances in Fracture Research, Proceedings of the 6th International Conference of Fracture (ICF6)*, Pergamon Press, 1984, pp. 1597–1608.

[5] Foroughi, R. and Radon, J. C., "Crack Closure Behavior of Surface Cracks Under Bending Loading," *Mechanics of Fatigue Crack Closure, ASTM STP 982*, American Society for Testing and Materials, 1988, pp. 260–269.

[6] Kim, J. H. and Song J. H., "Crack Growth and Closure Behavior of Surface Cracks Under Axial Loading," *Fatigue and Fracture of Engineering Materials and Structures*, Vol. 15, No. 5, 1992, pp. 477–489.

[7] Carpinteri, A., "Propagation of Surface Cracks Under Cyclic Loading," *Handbook of Fatigue Crack Propagation in Metallic Structures*, Elsevier Science, 1994, pp. 653–705.

[8] Corn, D. L. "A Study of Cracking Techniques for Obtaining Partial Thickness Cracks of Pre-Selected Depths and Shapes," *Engineering Fracture Mechanics*, Vol. 3, 1971, pp. 45–52.

[9] Elber, W., "Fatigue Crack Closure Under Cyclic Tension," *Engineering Fracture Mechanics*, Vol. 2, 1970, pp. 37–45.

[10] Elber, W. "The Significance of Fatigue Crack Closure," *Damage Tolerance in Aircraft Structures, ASTM STP 486*, American Society for Testing and Materials, 1971, pp. 230–242.

[11] Chermahini, R. G., Palmberg, B., and Blom, A. F, "Fatigue Crack Growth and Closure Behavior of Semicircular and Semi-Elliptical Surface Flaws," *International Journal of Fatigue*, Vol. 15, No. 4, 1993, pp. 259–263.

[12] Newman, J. C., "A Crack-Closure Model for Predicting Fatigue Crack Growth Under Aircraft Spectrum Loading," *Methods and Models for Predicting Fatigue Crack Growth Under Random Loading, ASTM STP 748*, American Society for Testing and Materials, 1981, pp. 53–84.

[13] Dill, H. D. and Saff, C. R., "Analysis of Crack Growth Following Compressive High Loads Based on Crack Surface Displacements and Contact Analysis," *Cyclic Stress-Strain and Plastic Deformation Aspects of Fatigue Crack Growth, ASTM STP 637*, American Society for Testing and Materials, 1977, pp. 141–152.

[14] Budiansky, B. and Hutchinson, J. W., "Analysis of Closure in Fatigue Crack Growth," *Journal of Applied Mechanics*, Vol. 45, 1978, pp. 267–276.

[15] Newman, J. C., "A Crack Opening Stress Equation for Fatigue Crack Growth," *International Journal of Fracture*, Vol. 24, 1984, pp. R131–R135.

[16] Ibrahim, F. K., Ph.D. Dissertation, University of Waterloo, Waterloo, IA, 1986.

[17] de Koning, A. U. and Liefting, G., "Analysis of Crack Opening Behavior by Application of a Discretized Strip Yield Model," *Mechanics of Fatigue Crack Closure, ASTM STP 982*, American Society for Testing and Materials, 1988, pp. 437–458.

[18] Nakamura, H. and Kobayashi, H., "Analysis of Fatigue Crack Closure Caused by Asperities Using the Modified Dugdale Model," *Mechanics of Fatigue Crack Closure, ASTM STP 982*, American Society for Testing and Materials, 1988, pp. 459–474.

[19] Chen, D. and Nisitani, H., "Analytical and Experimental Study of Crack Closure Behavior Based on an S-Shaped Unloading Curve," *Mechanics of Fatigue Crack Closure, ASTM STP 982*, American Society for Testing and Materials, 1988, pp. 475–488.

[20] Daniewicz, S. R., Ph.D. Dissertation, Ohio State University, 1991.

[21] Wang, G. S. and Blom, A. F., "A Strip Model for Fatigue Crack Growth Predictions Under General Load Conditions," *Engineering Fracture Mechanics*, Vol. 40, 1991, pp. 507–533.

[22] Daniewicz, S. R., Collins, J. A., and Houser, D. R., "An Elastic-Plastic Analytical Model for Predicting Fatigue Crack Growth in Arbitrary Edge-Cracked Two-Dimensional Geometries With Residual Stress," *International Journal of Fatigue*, Vol. 16, 1994, pp. 123–133.

[23] Newman, J. C., "Fatigue-Life Prediction Using a Crack-Closure Model," *Journal of Engineering Materials and Technology*, Vol. 117, 1995, pp. 433–439.

[24] Daniewicz, S. R. and Bloom, J. M., "An Assessment of Geometry Effects on Plane Stress Fatigue Crack Closure Using a Modified Strip-Yield Model," *International Journal of Fatigue*, Vol. 18, 1996, pp. 483–490.

[25] Daniewicz, S. R. "Prediction of Plasticity-Induced Closure in Surface Flaws Using a Modified Strip-Yield Model," *Fatigue and Fracture Mechanics: 29th Volume, ASTM STP 1332,* American Society for Testing and Materials, 1999, pp. 453–473.

[26] Zhao, W., Wu, X. R., and Yan, M. G., "Weight Function Method for Three Dimensional Crack Problems-I. Basic Formulation and Application to an Embedded Elliptical Crack in Finite Plates," *Engineering Fracture Mechanics,* Vol. 34, 1989, pp. 593–607.

[27] Mattheck, C. and Görner, F., "Leak Prediction by Use of a Generalized Dugdale Model for Semi-Elliptical Surface Flaws in Plates Under Tension Loading," *Proceedings,* 5th European Conference on Fracture, Portugal, 1984.

[28] Daniewicz, S. R., "Accurate and Efficient Numerical Integration of Weight Functions Using Gauss-Chebyshev Quadrature," *Engineering Fracture Mechanics,* Vol. 48, 1994, pp. 541–544.

[29] Fujimoto, W. T., "Determination of Crack Growth and Fracture Toughness Parameters for Surface Flaws Emanating from Fastener Holes," *Proceedings* AIAA/ASME/SAE 17th Structures, Structural Dynamics, and Material Conference, King of Prussia, PA, 1976, pp. 522–531.

[30] Saff, C. R. and Sanger, K. B., "Part-Through Flaw Stress Intensity Factors Developed by a Slice Synthesis Technique," *Fracture Mechanics: 15th Symposium, ASTM STP 833,* American Society for Testing and Materials, 1984, pp. 24–43.

[31] Zhao, W., Wu, X. R., and Yan, M. G., "Weight Function Method for Three Dimensional Crack Problems-II. Application to Surface Cracks at a Hole in Finite Thickness Plates Under Stress Gradients," *Engineering Fracture Mechanics,* Vol. 34, 1989, pp. 609–624.

[32] Zhao, W. and Sutton, M. A., "Elastic Solutions for Corner Cracks Undergoing Uniform Displacement-Controlled Loading," *International Journal of Fracture,* Vol. 70, 1995, pp. 335–346.

[33] Zhao, W., Newman, J. C., and Sutton, M. A., "A Three-Dimensional Weight Function Method-Evaluation and Applications," *Fatigue and Fracture Mechanics: 27th Symposium, ASTM STP 1296,* American Society for Testing and Materials, 1997, pp. 563–579.

[34] Tada, H., Paris, P. C., and Irwin, G. R., *The Stress Analysis of Cracks Handbook,* Paris Production Inc. and Del Research Corp., 1985.

[35] Glinka, G. and Shen, G., "Universal Features of Weight Functions," *Engineering Fracture Mechanics,* Vol. 40, 1991, pp. 1135–1146.

[36] Parker, A. P., *The Mechanics of Fracture and Fatigue,* E. & F. N. Spon Ltd., 1981.

[37] Dugdale, D. S., "Yielding of Steel Sheets Containing Slits," *Journal of Mechanics and Physics of Solids,* Vol. 8, 1960, pp. 100–104.

[38] Mahmoud, M. A., "Some Characteristics of Fatigue Crack Propagation of Surface Cracks," *Engineering Fracture Mechanics,* Vol. 41, 1992, pp. 961–966.

[39] Pierce, W. S. and Shannon, J. L., "Surface Crack Shape Change in Bending Fatigue Using an Inexpensive Resonant Fatiguing Apparatus," *Journal of Testing and Evaluation,* Vol. 6, 1978, pp. 183–188.

[40] Ravichandran, K. S., "Effect of Crack Shape on Crack Growth," *ASM Handbook, Fatigue and Fracture,* Vol. 19, S. R. Lampman, Ed., ASM International, Materials Park, OH, 1997, pp. 159–167.

[41] "Standard Practice for Fracture Testing with Surface-Crack Tension Specimens," *1996 Annual Book of ASTM Standards,* E 740-88, Vol. 03.01, American Society for Testing and Materials, West Conshohocken, PA, 1996, pp. 609–616.

[42] McFadyen, N. B., Bell, R., and Vosikovsky, O., "Fatigue Crack Growth of Semi-Elliptical Surface Cracks," *International Journal of Fatigue,* Vol. 12, 1990, pp. 43–50.

[43] Hodulak, L., Kordisch, H., Kunzelmann, S., and Sommer, E., "Influence of the Load Level on the Development of Part-Through Cracks," *International Journal of Fracture,* Vol. 14, 1978, pp. R35–R38.

Michael Dankert,[1] *Steffen Greuling,*[2] *and Timm Seeger*[2]

A Unified Elastic-Plastic Model for Fatigue Crack Growth at Notches Including Crack Closure Effects

REFERENCE: Dankert, M., Greuling, S., and Seeger, T., **"A Unified Elastic-Plastic Model for Fatigue Crack Growth at Notches Including Crack Closure Effects,"** *Advances in Fatigue Crack Closure Measurement and Analysis: Second Volume, ASTM STP 1343,* R. C. McClung and J. C. Newman, Jr., Eds., American Society for Testing and Materials, West Conshohocken, PA, 1999, pp. 411–426.

ABSTRACT: The reasons for fatigue failure of many components and subassemblies are internal defects in the material or cracks and the subsequent propagation. Cracks normally originate in areas of stress concentration, e.g., at notches.

It is known that a major factor governing the service life of notched components under cyclic loading is fatigue crack growth in notches. A uniform elastic-plastic crack growth model, based on the *J*-integral, was developed which especially considers the crack opening and closure behavior for the determination of crack initiation and propagation lives for cracks at elliptical notches under constant or variable-amplitude loading.

For this model, an algorithm for the description of the crack opening and closure behavior and approximation formulas were developed for the determination of the stress intensity factor K and the *J*-integral for surface, corner and through-thickness cracks at elliptical internal and external notches. The crack growth model will be introduced and its individual modules, as well as the complete concept, were verified by experiments and two- and three-dimensional elastic and elastic-plastic finite-element analyses. Experiments, finite-element analyses, and calculations show excellent correspondence in all aspects.

KEYWORDS: fatigue crack growth, crack closure, stress-intensity factors, *J*-integral, cracks at notches, elastic and elastic-plastic 2D and 3D finite-element analyses

The reasons for fatigue failure of many components and subassemblies in the fields of mechanical engineering, plant construction, marine engineering, aeronautics and space travel are internal defects in the material or cracks and their subsequent propagation. Cracks normally originate in areas of stress concentration, e.g., at notches. The crack surfaces are usually elliptical and retain this elliptical or nearly elliptical form throughout the crack propagation process. The life of notched components is subdivided into the pre-crack, or crack initiation, and crack propagation phases within and outside notch area. Pre-crack and fracture, Wöhler curves (single-stage loading, constant amplitude) as well as crack initiation fatigue life curves and fracture fatigue life curves (service loading, variable amplitude) are illustrated in Fig. 1.

It is known that a major factor governing the service life of notched components under cyclic loading is fatigue crack growth at notches. The *K*-concept applied to crack propagation in elastic structure areas cannot be transferred to notch areas because in these cases the crack tip is mainly determined by elastic-plastic notch area strain. Thus crack propagation is described by the cyclic *J*-integral

[1] Project engineer, Motoren-und Turbinen-Union (MTU), D-88040 Friedrichshafen, Germany.

[2] Research assistant and professor, respectively, Technische Universität Darmstadt, Werkstoffmechanik, Petersenstraße 13, D-64287 Darmstadt, Germany.

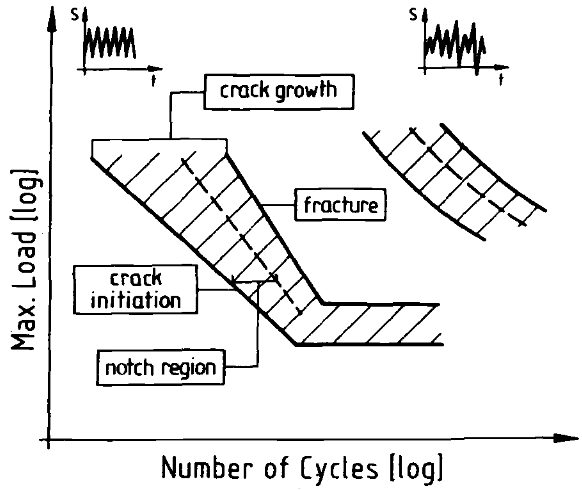

FIG. 1—*Objective.*

under consideration of crack opening and closure behavior. A uniform elastic-plastic crack growth model for the determination of pre-crack and crack-propagation life of cracks at elliptical notches has been developed on the basis of the J-integral. This model is introduced in the following text and the individual modules, as well as the complete concept are verified by means of various examples.

Elastic-Plastic Crack Growth Model

A crack propagation equation is formulated as a starting point for the actual calculation of service life by which the growth of elliptical surface, corner and through-thickness cracks, inside and outside of notch areas can be determined:

$$\left(\frac{da}{dn};\frac{dc}{dn}\right) = C \cdot \Delta J_{\text{eff}}^{m}\,(a,\,c,\,t,\,w,\,\rho,\,K_{t,\infty},\,\bar{a},\,\bar{b},\,\varphi,\,\Delta S_{\text{br,eff}}) > \Delta J_{\text{th}} \tag{1}$$

with C and m being material constants from standard experiments, ΔJ_{eff} being the effective amplitude of the cyclic J-integral, a being the crack depth, c the crack length, t the plate thickness, w the plate width, ρ the notch radius, $K_{t,\infty}$ the notch factor for $w \rightarrow \infty$ (infinite plate), $\bar{a}$ the notch depth, $\bar{b}$ the notch height, φ the angle along the crack contour, $\Delta S_{\text{br,eff}}$ the effective amplitude of the gross load and ΔJ_{th} the threshold value of the cyclic J-integral. Both ρ as well as $K_{t,\infty}$ are governed by the semi-axes $\bar{a}$ and $\bar{b}$ of the elliptical notch. The crack propagation is calculated in several steps in the direction of the crack depth and length between a given initial crack depth and final depth. The following input data are required for crack growth calculation:

- parameters for description of geometry,
- stress concentration factor,
- initial crack configuration,
- initial type of crack (surface, corner, or through-thickness crack),
- type of notch (e.g., internal or external notch),
- material parameters in form of the stabilized cyclic materials law,
- crack propagation parameters,
- number of load cycles up to reaching the initial crack configuration,

- load sequence, and
- truncation criteria (e.g., critical crack depth).

A closed hysteresis loop, regarded as a damaging criterion, is recognized using the Clormann's HCM-algorithm [*1*] (HCM = Hysteresis Counting Method).

In Fig. 2 the developed crack propagation model is schematically shown. In the block diagram presentation of the crack growth model, differentiation between crack depth and length directions has been neglected for the purpose of clarity. It must be noted that the algorithm for both directions must be calculated individually. The essential elements of calculation are:

- calculation of the elastic notch stress distribution,
- calculation of the S-ε paths and of the σ-ε paths for the current crack tip and length locations is based on the uncracked status using a notch approximation formula, S being the net section stress and σ being the local stress,
- recognition of closed hysteresis loops as damaging criterion,
- estimation of closed local hysteresis loops regarding their crack opening and closure behavior (calculation of crack opening and closure stress),
- calculation of the crack closure load,
- calculation of the effective loading amplitude,
- calculation of the effective gross loading amplitude,
- calculation of the effective amplitude of the cyclic J-integral, and
- calculation of the crack growth.

At the beginning of the calculation, the stress distribution (according to the elasticity theory) in the notch area (K_t depending on the distance to the notch root $\rightarrow K_t(x)$) must be defined. This is achieved by approximation solutions or by elastic FE analyses. The S-ε and σ-ε curves (i.e., the load-strain curve and the correponding local stress-strain curve) for the location of the current crack depth and length are calculated for the largest load in the load sequence with an approximation formula for notches (e.g., Neuber's [2] or Seeger/Beste rule [*3*]. It is assumed that the material is already cyclically stabilized, and the σ-ε curve can be described by the approach used by Ramberg and Osgood [*4*]

$$\varepsilon = \frac{\sigma}{E} + \left(\frac{\sigma}{K'}\right)^{\frac{1}{n'}} \tag{2}$$

with the modulus of elasticity E, hardening exponent n' and coefficient K'. It is further assumed that Masing [*5*] and memory behavior is valid. With this, the corresponding S-ε and σ-ε paths can be constructed for both directions after every reversal of the load sequence. Based on suggestions made by Vormwald [*6*] and McClung [7], calculation of the local elastic-plastic loading path neglects the crack. The load sequence data, e.g., for every reversal, are then entered. As soon as a hysteresis loop closes, the calculated local loading paths in the crack depth and length directions are evaluated as regards their crack opening and closure behavior. This can be achieved with the aid of different crack opening formulas (e.g., [*8–14*]). The crack closure stresses (σ_{cl}) are determined from the crack opening stresses (σ_{op}) calculated, with the aid of experimentally proven equality of crack opening and closure strains ($\varepsilon_{op} = \varepsilon_{cl}$, [*6,15,16*]) and the known σ-ε paths for the closed hysteresis loop (Fig. 2). The crack closure loadings (S_{cl}) are determined from the crack closure stresses taking into consideration Masing [*5*] and memory behavior. The effective loading amplitudes ($\Delta S_{eff} = S_o - S_{cl}$) result from the difference between load of the closed hysteresis loop (S_o) and the crack closure load. Finally, the effective gross loading amplitudes $\Delta S_{eff,br} = A/A_{br} \cdot \Delta S_{eff}$ are determined, with A being the net section, A_{br} being the gross section and ΔS_{eff} the effective load amplitude. The effective value of the

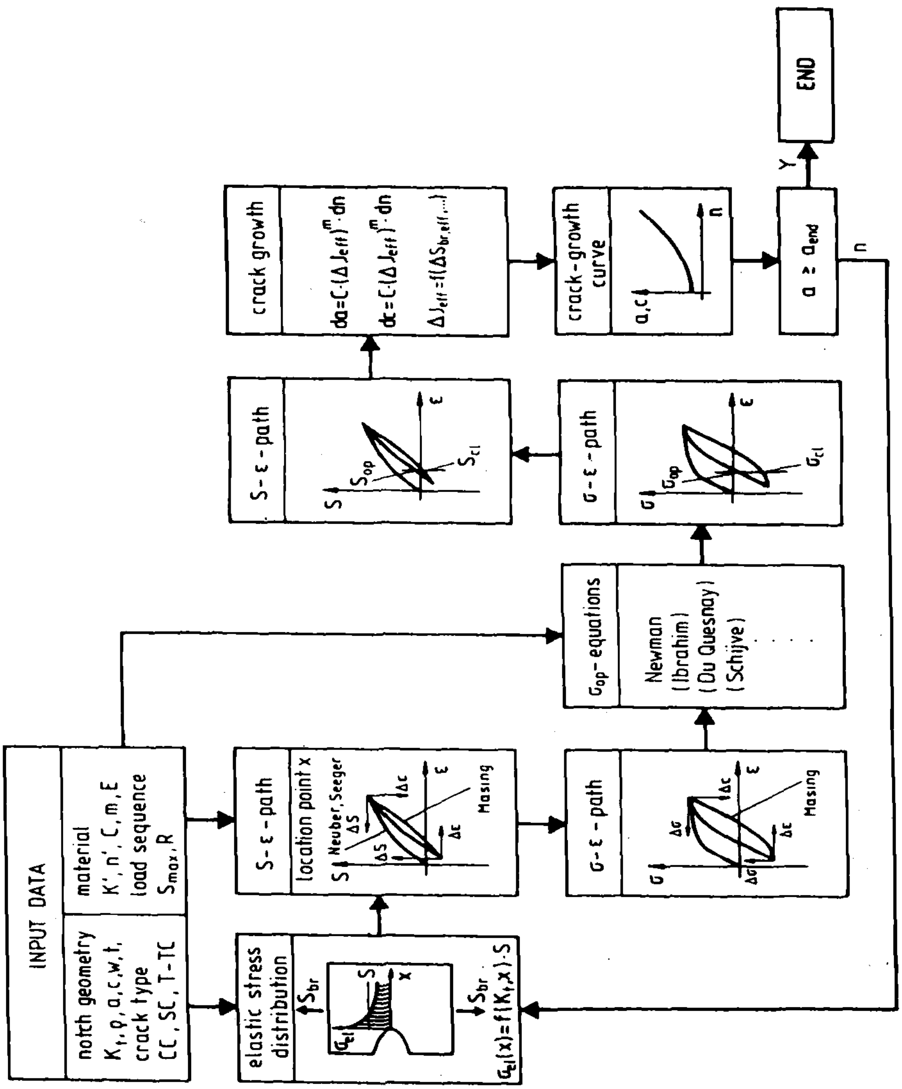

FIG. 2—*Crack growth model.*

cyclic J-integral is used as the crack tip parameter. By using the effective gross load amplitudes, the effective amplitudes of the cyclic J-integral are determined. They are entered into the equations for crack growth, and the crack growth Δa and Δc are determined and thus the current crack depth ($a = a + \Delta a$) and length ($c = c + \Delta c$). This algorithm is repeated for the following cycle. Calculation of the S-ε curve and the local σ-ε curve is only required for the crack depth direction as this does not change for the crack length, i.e., it remains at the notch root. The new paths in the crack depth direction are determined using the HCM algorithm. The following reversals are then entered and the paths constructed until another hysteresis loop closes and the resultant damage is evaluated, as described above. The crack growth is thus determined by cycles. The calculation ends when the criteria for truncation (e.g., a given final crack depth) is reached. The model is prepared for surface, corner and through-thickness cracks. The different types of cracks at notches are illustrated in Fig. 3. The change from a surface, or a corner crack to a through-thickness crack is included in the concept. After this crack type change, calculation of the algorithm described is only done in the crack depth direction. The load history is considered by the number of load cycles required to achieve the initial crack configuration. Up to that time the load sequence is calculated without evaluation of the damage. Only then does the algorithm described become effective.

The crack growth model thus contains three major components: first, determination of the crack opening and closure loads, second, determination of the J-integral, and third, determination of the crack growth and thus the service life.

Verification of Crack Growth Model

Verification of the evaluation of the crack opening and closure behavior and determination of the crack growth and service life is achieved with the aid of experimental results. The experimental examinations were carried out using manually polished notch plates ($K_t = 2.5$ and 3.4) made of FeE460 and A15086, which were almost totally without residual stress. These two alloys were not heat treated. Their mechanical properties as well as their composition are described in detail in Ref *15*. The specimens and their geometry is shown in Fig. 4. The specimens made of FeE460 had circular notches and those made of Al5086 had nearly elliptical notches. Determination of the cyclic material data was effected by strain-controlled experimentation using standardized hourglass specimens. All experiments were executed with servo-hydraulic testing equipment and room temperature (23°C) with a relative humidity of 60%. The pre-cracks were initiated in the specimens by vibration loading. Most of the pre-cracks initiated were corner cracks. The surface pre-cracks were assumed to be half-circular. No general differences in the pre-crack behavior between the two specimen thicknesses were found [*15*]. Observation of the pre-crack, and measurement of the crack growth, was accomplished optically using a measuring microscope. The approximation formulas developed for the J-integral were verified by elastic and elastic-plastic FE analyses using ABAQUS [*17*].

Crack Opening Loads

An algorithm was developed for the determination of crack opening loads for cracks at notches and is used as a component of the crack growth model. Presentation of this algorithm, as well as a detailed discussion and evaluation of the different approaches for the determination of crack opening stresses in connection with this algorithm and with the aid of experimental results, can be found in Refs *14,18*. Explanations of the concept and its realization with different crack opening relations in one calculation program are given in Refs *19,20*, and the extension of the algorithm for load sequence influences (overloads and load decay behavior) in Ref *21*. The modified crack opening relationships according to Newman [*11*] proved to be especially suitable for the problems (cracks at notches) dealt with in this paper. The majority of the experiments completed are documented in Ref *15*.

The SMS (strain measuring strip) method described in [*6,15*] was employed for measuring the crack opening and closure loads (Fig. 5). This method was used for both small and large specimens

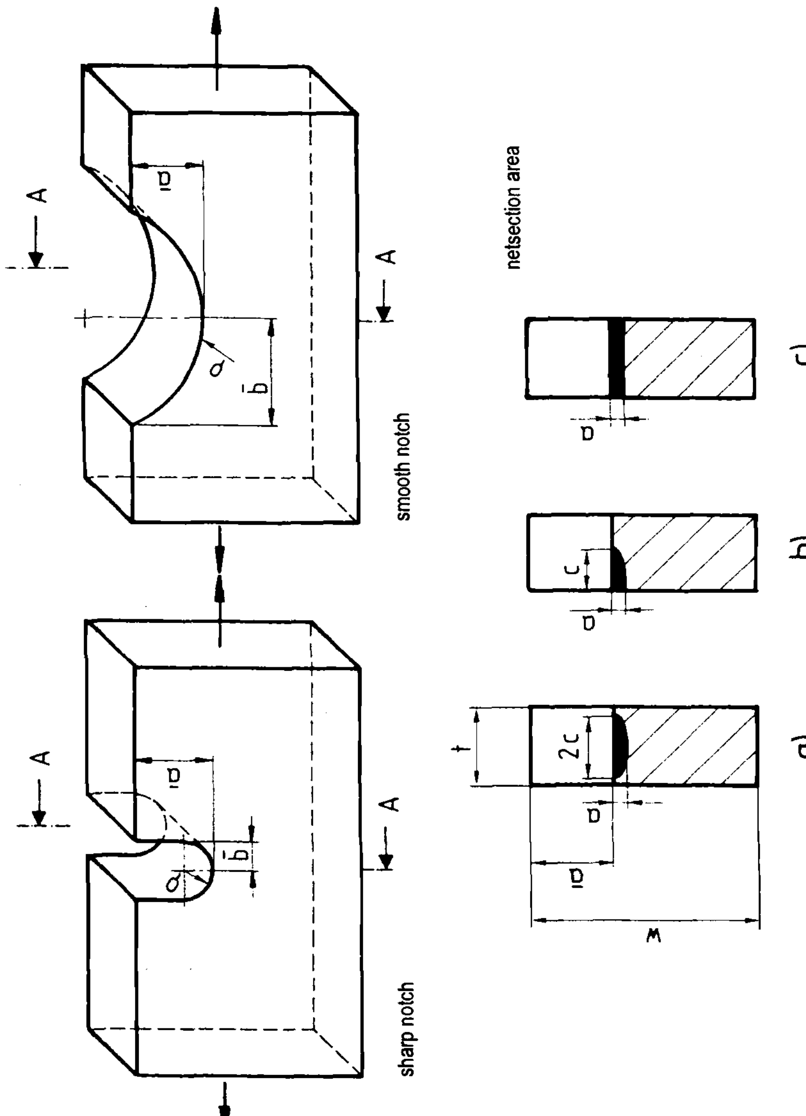

FIG. 3—*Cracks at notches.*

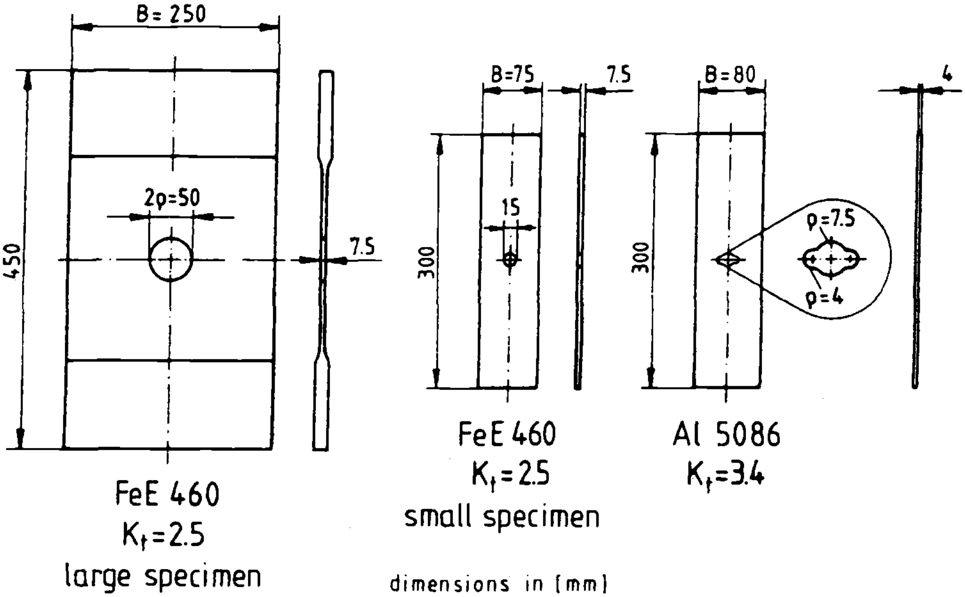

FIG. 4—*Specimens.*

(Fig. 4). Small strain gages (≈ 0.8 mm), located adjacent to the tip, measure the changes in local stiffness of the specimen during the crack opening and closure (Fig. 5). The recorded S-ε_{SMS} paths show "kinks" which can be correlated to the crack opening and closure processes. The crack opening load is defined as the load at which the last contact at the crack tip is interrupted, i.e., the crack is completely open. This definition is in agreement with that of Newman [*11*], Vormwald [*6*], McClung [22] and Taylor [*23*].

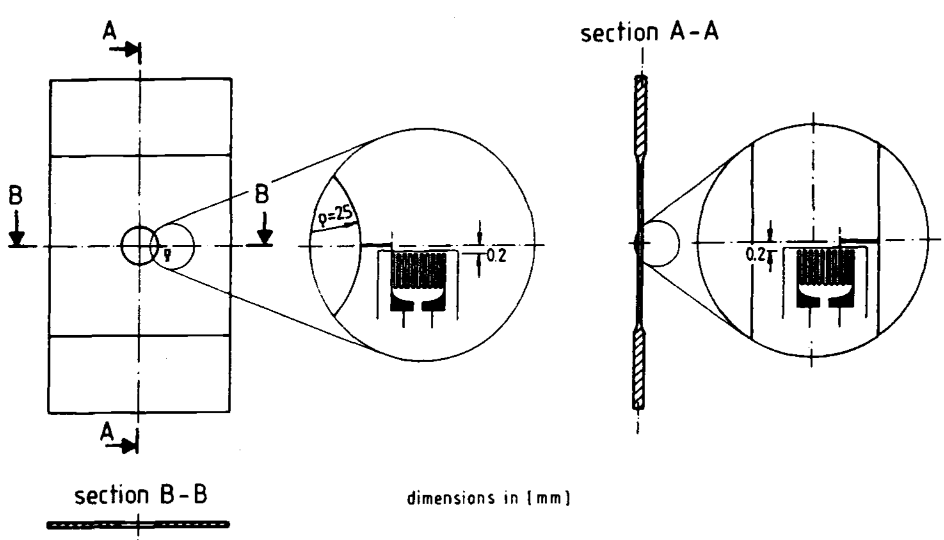

FIG. 5—*SMS method.*

The development of the crack opening level inside (i.e., $K_t(x) \geq 1$) and outside (i.e., $K_t(x) < 1$) the notch region was determined experimentally with single-stage and two-stage reversal experiments with different load levels for the notched plates examined. For the crack configurations (surface, corner and through-thickness cracks), materials (FeE460 and Al5086) and stress ratio ($R = -1$) under consideration, the experiments revealed no significant differences in the crack opening levels when the applied load is equal. Consequently, all three crack types can be treated equally as regards their crack opening and closure loads. Figure 6 shows the experimentally and numerically determined crack opening loads for notched plates/specimens of FeE460 and Al5086 related to the net stress amplitude for single-stage loads ($R = -1$). Short crack effects were not considered. It can be seen that for a rising ratio of a/ρ the crack opening level rises and stabilizes at the end of the notch region on a nearly constant level. The crack opening level decreases with rising load amplitude and resultant increased plasticity. The cracks then open clearly at pressure loading (i.e. $S_{op}/S_{max} < 0$) in the notch area. These tendencies, which are demonstrated by these experiments, can be verified, both as regards quality and quantity, using the above model. The deviation between the experimentally and numerically determined values is negligible.

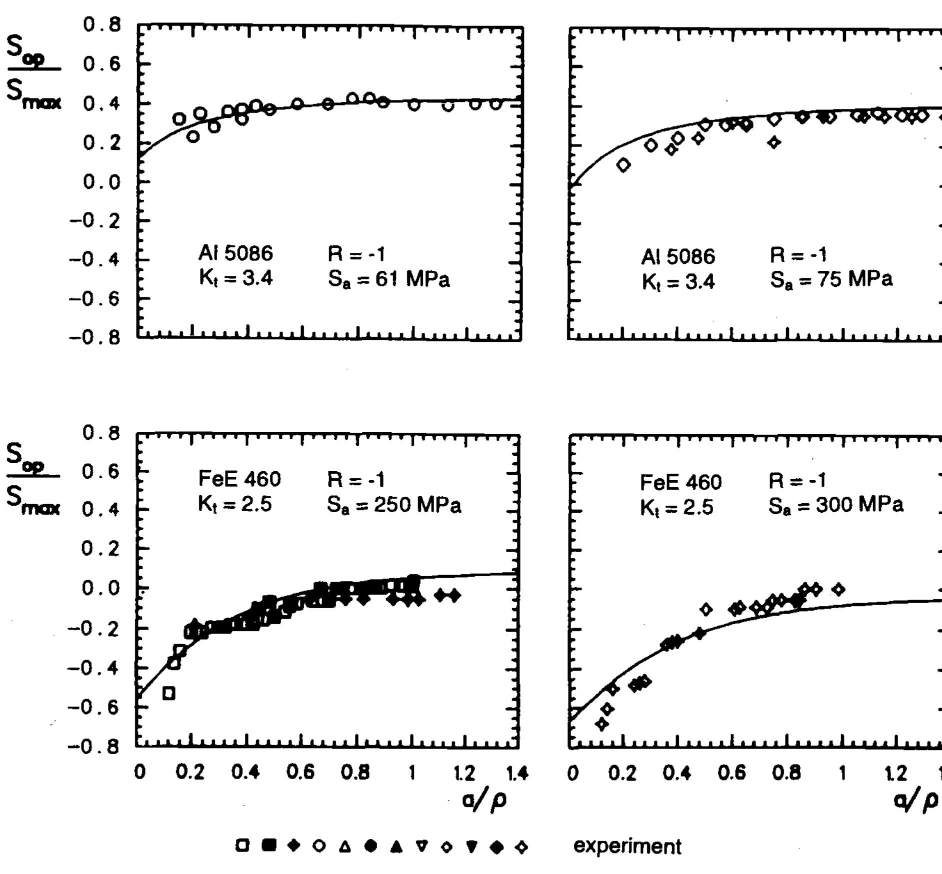

FIG. 6—*Experimentally and numerically determined crack opening loads.*

J-*Integral*

For the development of approximation formulas to determine the J-integral, it was first necessary to determine J-integrals for a number of significant cases using two- and three-dimensional elastic and elastic-plastic finite element calculations by varying the crack length, semi-axis ratio of the notch, contour at the crack front, crack type (surface, corner and through-thickness crack), and material behavior (modulus of elasticity E, Poisson's ratio n, hardening exponent n' and coefficient K'). The case studies examined cover a representative parameter field for possible crack configurations and types for cracks at elliptical internal and external notches. The additive superposition method of so-called "elastic" and "plastic" elements of the J-integral, suggested by Shih et al. [*24*] was applied. The elastic part is determined with the aid of the stress intensity factor K. For this, approximation formulas were developed for determination of the K-factors for cracks at notches, especially for those functions within the geometry correction function Y_{el}, which describe the notch influence and the boundary-effects. The basic theories and approaches, the parameter field examined, the procedure for developing the approximation formulas for K and J, and the results are reported in detail in Refs *21,25,26*.

Figure 7 shows the crack and notch region of the 3D FE structure for a corner crack in an external notch used here. Specially degenerated elements are used at the crack tip and along the crack front in order to represent the stress singularity.

Figure 8 shows the profile of the geometry correction function Y_{el} developed for the determination of K-factors for through-thickness cracks at elliptical interior notches, and Fig. 9 shows them for a semi-elliptical surface crack in an elliptical external notch along the crack front in comparison to the results from the collocation method [*27*] and by FE analyses [*26*]. Figure 10 is a comparison of the J-S_{br} curves determined by FE calculation and by an approximation formula for a crack vertex ($2\varphi/\pi = 0$) of a semi-elliptical surface crack in an external notch under tensile load. The elastic and plastic elements of the approximation formula used for determination of the J-integral are also shown. As can be seen, the additive superposition of the elastic and the plastic elements produces a good approximation for determination of the J-integral. For borderline cases (purely elastic, fully plastic) there is a good correspondence, for the transition range (purely elastic to fully plastic), the J-integral determined by the approximation formula is, in many cases, slightly lower than that determined by FE calculation.

The curves of the J-integral determined from FE analyses and approximation formulas for the notch root ($2\varphi/\pi = 1$) of a quater circular-shaped corner crack in an external notch under tensile

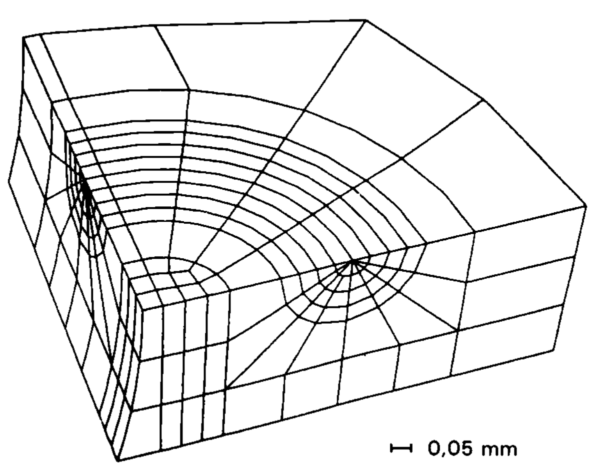

FIG. 7—*Section of a FE structure.*

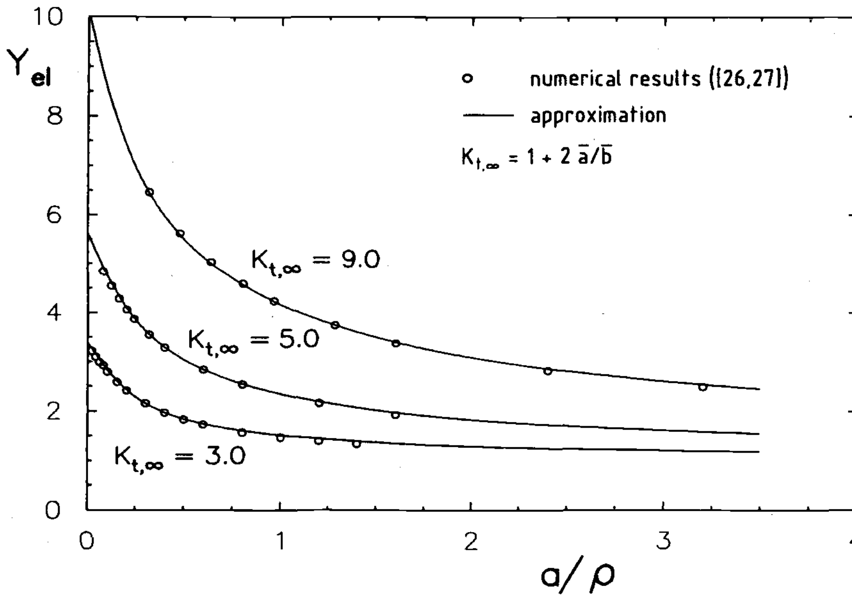

FIG. 8—*Comparison between the developed geometry correction function* Y_{el} *and the numerical results for through-thickness cracks at circular and sharp notches.*

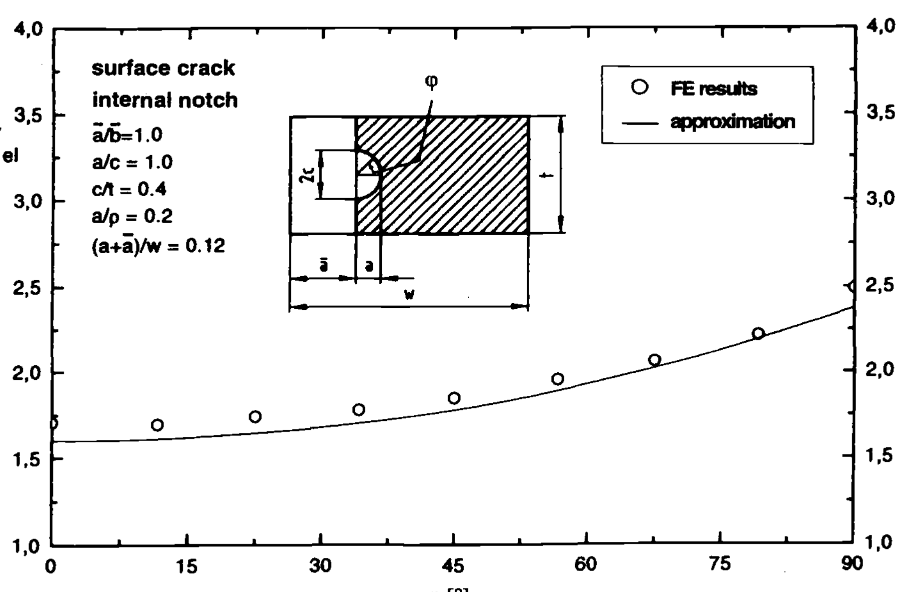

FIG. 9—*Comparison of the geometry correction function* Y_{el} *for a semi-circular surface crack in a semi-circular external notch along the crack front by FE analyses and the developed approximation formulas.*

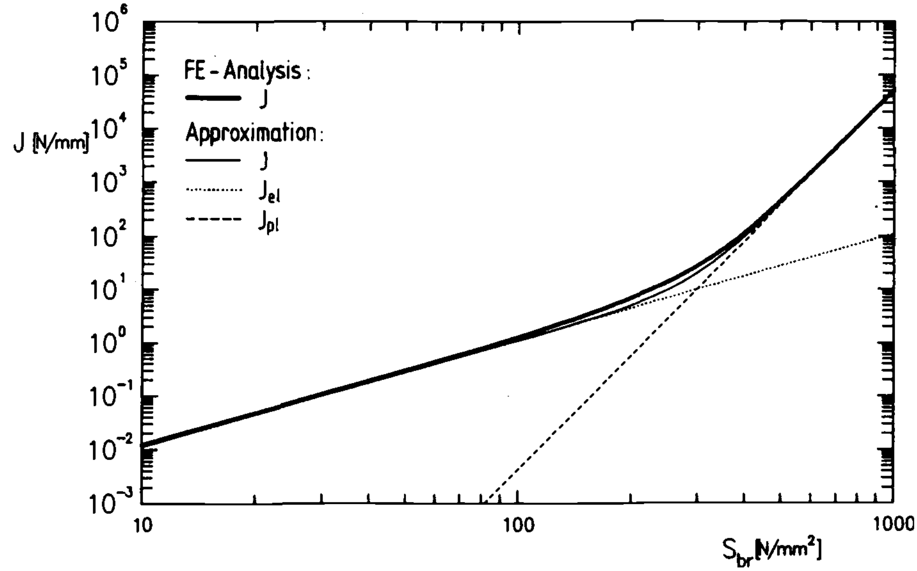

FIG. 10—*Comparison between developed approximation and FE calculation for the* J*-integral of a surface crack in an external notch.*

loading are shown in Fig. 11. The results from the FE calculation and those from the approximation formula are extremely comparable.

The J-integral curves obtained by FE calculation and from the approximation formulas for a through-thickness crack in an internal notch under tensile loading are compared in Fig. 12. As can be seen, the J-integrals for through-thickness cracks at circular notches can be accurately described by the approximation formulas.

Many further examples show similar quality [*21,25*].

Crack Growth

The effective amplitudes of the J-integral are determined from the effective load amplitudes, obtained by evaluating the crack opening and closure behavior, with the approximation formulas. These are then incorporated into the crack growth Eq 1 and the crack growth for every load cycle is determined. Calculation of the crack growth and the steps leading up to it must be made on the basis of the stress gradient at the notch and as a result of the crack propagation. Two examples of numerically and experimentally determined crack growth curves are compared in Figs. 13 and 14. The corresponding notch field is indicated in this illustrations in order to define the crack growth within the notch area.

In Fig. 13, experimentally and numerically determined crack growth curves from the pre-crack (defined as a = 0.25 mm and $2c$ = 0.5 mm) up to final fracture are illustrated for single-stage loading with S_a = 190 MPa. The experimental results used were taken from [*6*]. The values obtained were comparable. The ratio of crack propagation life obtained by calculation and experiment ($N_{p,cal}/N_{p,exp}$) is approximately 0.83. The discontinuity of the calculated curve results from a change of crack type from surface to through-thickness crack. In this case calculation is carried out using a straight crack front and not, initially, a curved crack front. This results in a rapid crack area growth and an associated increase in the J-integral value with subsequent distinct increase in crack growth and thus to dis-

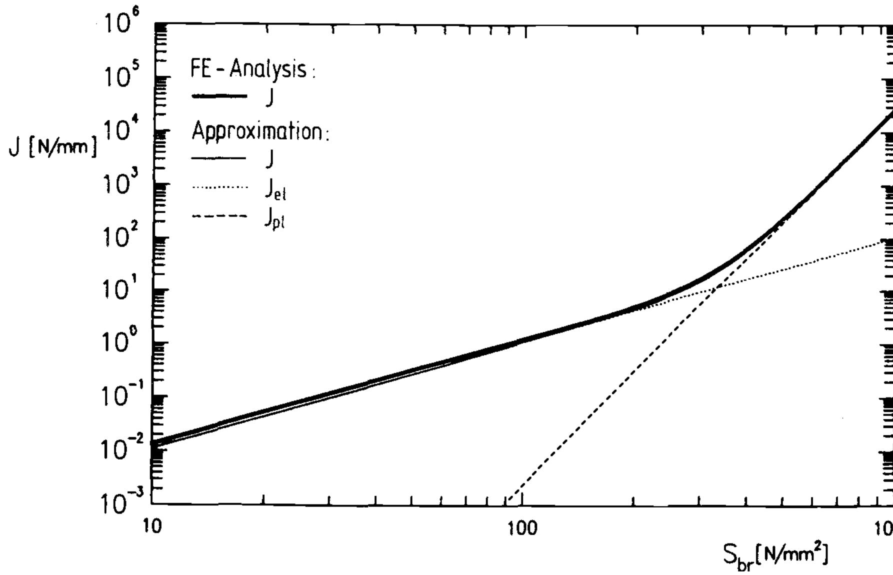

FIG. 11—*Comparison between developed approximation and FE calculation for the* J*-integral of a corner crack in an external notch.*

continuity. The procedure was selected because the experiment clearly shows that a change of crack type occurs within only few load cycles, and a through-thickness crack with a straight crack front results very quickly.

Figure 14 is a comparison between experimentally and numerically determined crack growth curves for the service load. The ratio of the crack propagation lives obtained by calculation and ex-

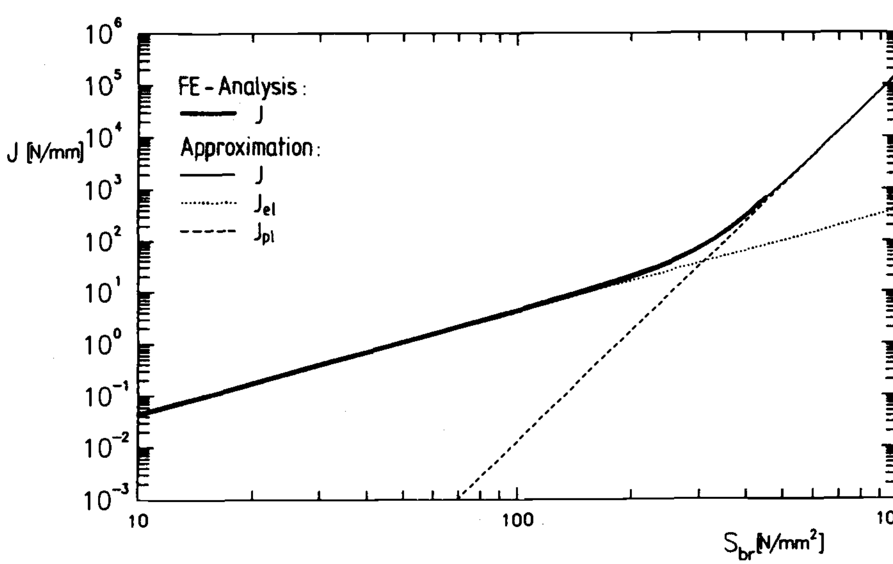

FIG. 12—*Comparison between developed approximation and FE calculation for the* J*-integral of a through-thickness crack in an internal notch.*

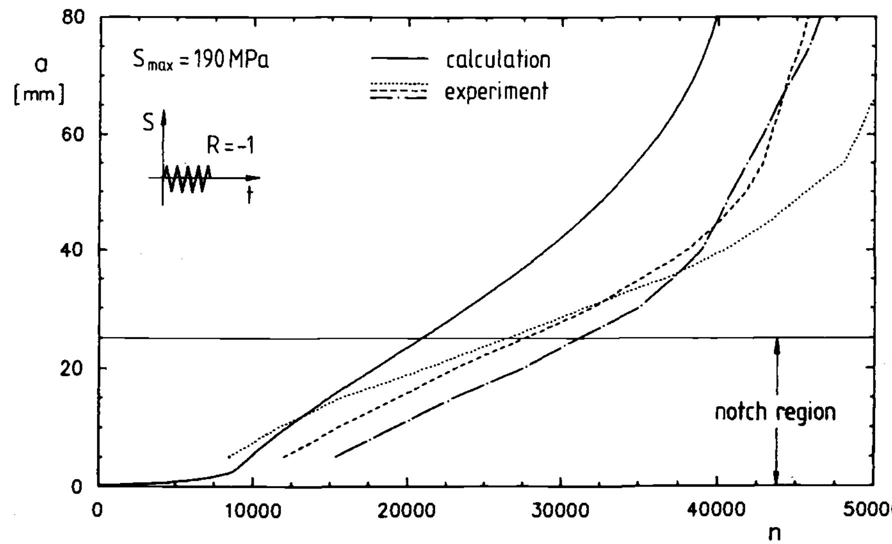

FIG. 13—*Comparison of crack growth curves determined experimentally and numerically for single-stage loading (tensile/compressive load,* $S_a = 190$ *MPa,* $R = -1$*) for specimens made of FeE460.*

periment ($N_{p,cal}/N_{p,exp}$) is approximately 1.04. Discontinuity of the calculated curves occurs from the same reason as for single-stage loading. In addition, several large-amplitude cycles within the load sequence were entered at that time which resulted in an accelerated crack growth.

In most of the relevant applications the crack propagation life of a component is not the only interesting aspect. The crack initiation fatigue life and especially the total service life of a component

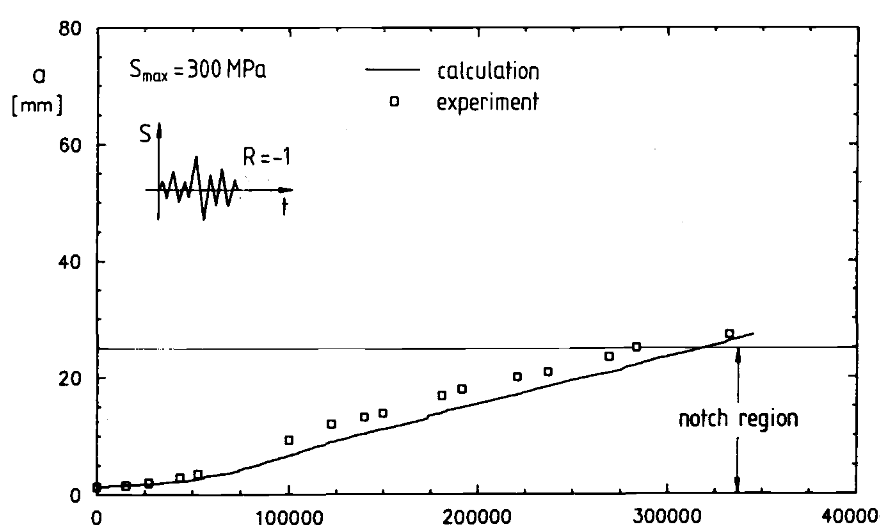

FIG. 14—*Comparison of crack growth period obtained by experiment and calculation, service load (tensile/compressive load, Gaussian load sequence,* $S_{max} = 300$ *MPa,* $H_0 = 5 \cdot 10^5$*,* $I = 0.99$*,* $\bar{R} = -1$*) for specimens made of FeE460.*

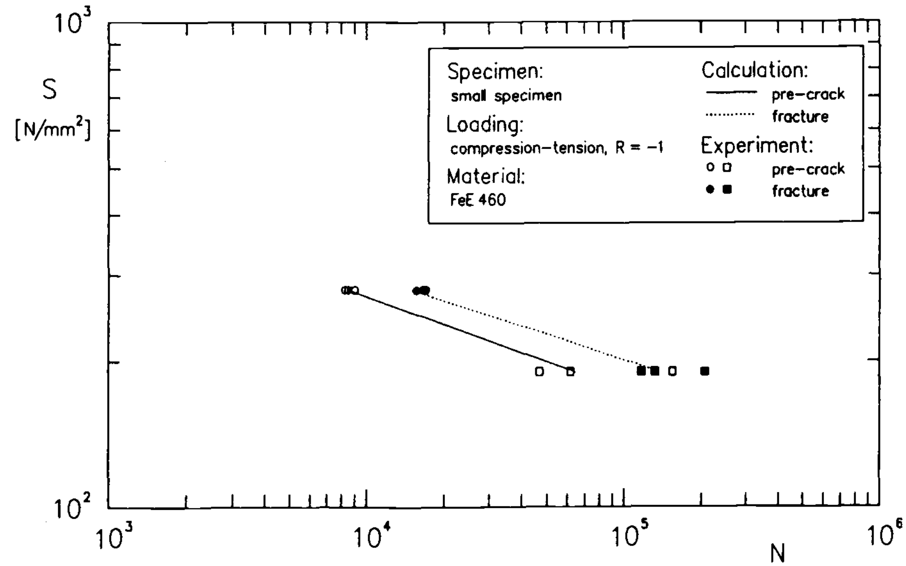

FIG. 15—*Experimentally and numerically determined crack initiation fatigue and fracture lives (tensile/compressive loading,* R = −1).

are also most certainly significant. The aim is to avoid in-service failure of a component and to replace the component before actual failure occurs. Determination of the crack initiation fatigue life and total service life is illustrated by two examples under reversal single-stage loading with different load amplitudes according to Ref *6*. The crack growth model allows determination of the crack propagation life between two crack configurations. For determination of the crack initiation fatigue life, the final crack configuration for the developed crack growth model is selected as the pre-crack definition (in most cases $a = 0.25$ mm, $2c = 0.5$ mm). Experimentally determined imperfections are entered as the initial crack configuration. In many cases, no proven data exist because these experiments are expensive, comprehensive and time-consuming. In these cases, the initial crack depth a_0, used as the starting point for the calculation, can be determined analogous to Vormwald [*6,28*]. From this initial crack depth a_0 crack growth can be calculated to either a predetermined crack configuration (e.g., pre-crack) or to failure. Figure 15 shows experimentally and numerically determined crack initiation fatigue and fracture fatigue lives. The details from the Wöhler pre-crack and fracture curves represented, show excellent correspondence between the experiments and the calculations.

As can be seen, the experimentally measured crack growth can be fairly accurately predicted using the crack growth model developed. Many other examples show similar quality.

Summary

In this paper, an elastic-plastic crack growth model, based on the J-integral, was introduced which especially considers the crack opening and closure behavior for the determination of crack initiation fatigue and propagation lives for cracks at elliptical notches. Numerical description of the pre-crack and crack growth phases, within and outside the notch area of notched plates, has been achieved. The crack growth concept allows determination of the crack propagation life from a given up to a critical crack configuration. For this model, an algorithm for the description of the crack opening and closure behavior and approximation formulas were developed for the determination of the stress intensity

factor K and the J-integral for cracks at elliptical internal or external notches. The crack growth model and its individual modules were verified by experiments and elastic and elastic-plastic FE calculations. Experiments and calculations show excellent correspondence in all aspects. Interesting and rewarding tasks for the future lie in the extension of the approximation formulas, the algorithms and, finally, the overall crack growth concept for other structures, taking into consideration residual stresses or other influencing factors, gaining experience with the model through further comparisons, and application of the model to actual components.

Acknowledgments

This report is the result of a scientific research task commissioned by the Forschungskuratorium Maschinenbau e.V. (FKM, Frankfurt, Germany) and executed under the auspices of the Fachgebiet Werkstoffmechanik at the Technische Universität Darmstadt under the direction of professor T. Seeger. This work was financially supported by the Bundesministerium für Wirtschaft (BMWi, Bonn, Germany) by way of the Arbeitsgemeinschaft industrieller Forschungsvereinigungen e.V. (AiF, Cologne, Germany), (AiF-number 9867).

References

[1] Clormann, U. H. and Seeger, T., "Rainflow-HCM—Ein Zählverfahren für Betriebsfestigkeitsnachweise auf werkstoffmechanischer Grundlage," *Stahlbau*, Vol. 55, No. 3, 1986, pp. 65–71.

[2] Neuber, H., "Theory of Stress Concentration of Shear-Strained Prismatical Bodies with Arbitrary Nonlinear Stress-Strain Law," *Transactions ASME, Journal of Applied Mechanics*, Vol. 28, 1961, pp. 544–550.

[3] Seeger, T. and Beste, A., "Zur Weiterentwicklung von Näherungsformeln für die Berechnung von Kerbbeanspruchungen im elastisch-plastischen Bereich," *Kerben und Bruch*. VDI-Verlag, 1977. VDI-Fortschritt Berichte Reihe 18 Nr. 2.

[4] Ramberg, W. and Osgood, W. R., "Description of Stress-Strain Curves by Three Parameters," NACA, Technical Note No. 902, 1943.

[5] Masing, G., "Eigenspannungen und Verfestigung beim Messing," *Proceedings of the 2nd International Congress of Applied Mechanics*, 1926, pp. 332–335.

[6] Vormwald, M., "Anrißlebensdauervorhersage auf der Basis der Schwingbruch-mechanik für kurze Risse," Heft 47. Institut für Stahlbau und Werkstoffmechanik, TH Darmstadt, Germany, 1989.

[7] McClung, R. C., "A Simple Model for Fatigue Crack Growth Near Stress Concentrations," *Journal of Pressure Vessel Technology*, Vol. 113, 1991, pp. 542–548.

[8] Elber, W., *ASTM STP 486*, 1971, pp. 230–242.

[9] Schijve, J., "Some Formulas for the Opening Stress Level," *Engineering Fracture Mechanics*, Vol. 14, 1981, pp. 461–465.

[10] DeKoning, A. U., "A Simple Crack Closure Model for Prediction of Fatigue Crack Growth Rates Under Variable Amplitude Loading," *ASTM STP 743*, American Society for Testing and Materials, 1981, pp. 63–85.

[11] Newman, J. C., Jr., "A Crack Opening Stress Equation for Fatigue Crack Growth," *International Journal of Fracture*, Vol. 24, 1984, pp. R131–R135.

[12] Ibrahim, F. K., "Threshold Stress Intensity Behaviour of Cracked Steel Structural Components," *Fatigue and Fracture of Engineering Materials and Structures*, Vol. 12, No. 6, 1989, pp. 543–552.

[13] DuQuesnay, et al., "The Effective Stress Range as a Mean Stress Parameter," *International Journal of Fatigue*, Vol. 14, No. 1, 1992, pp. 45–50.

[14] Savaidis, G., Dankert, M., and Seeger, T., "An Analytical Procedure for Prediction Opening Stresses and Loads of Cracks at Notches," FF-1/1994, Fachgebiet Werkstoffmechanik, TH Darmstadt, Germany, 1994.

[15] Savaidis, G. and Seeger, T., "Experimental Investigation of Crack Opening and Closure Behaviour for Different Crack Types of Notches," FF-9/1993, Fachgebiet Werkstoff-mechanik, TH Darmstadt, 1993.

[16] Savaidis, G. and Seeger, T., "An Experimental Study on the Opening and Closure Behaviour of Fatigue Cracks at Notches," *Fatigue and Fracture of Engineering Materials and Structures*, Vol. 17, No. 11, 1994, pp. 1343–1353.

[17] Hibbit, Karlsson and Sorensen, Inc., *ABAQUS Theory Manual*, Version 5.3.

[18] Savaidis, G., Dankert, M., and Seeger, T., "An Analytical Procedure for Predicting Opening Loads of Cracks at Notches," *Fatigue and Fracture of Engineering Materials and Structures*, Vol. 18, No. 4, 1995, pp. 425–442.

[19] Dankert, M. and Seeger, T., "Rißöffnungsspannungen und -lasten für Risse in Kerben—Konzept und Berechnungsprogramm für Einstufenbelastungen," FF-2/1994, Fachgebiet Werkstoffmechanik, TH Darmstadt, Germany, 1994.
[20] Dankert, M., Savaidis, G., and Seeger, T., "Rißfortschritt in elastisch-plastisch bean-spruchten Kerbbereichen bei Schwingbelastung mit veränderlichen Amplituden," Heft 194, Forschungskuratorium Maschinenbau, Frankfurt, Germany, 1995.
[21] Dankert, M. and Seeger, T., "Berechnung der Anriß- und Rißfortschrittslebensdauer gekerbter Bauteile nach einem einheitlichen Konzept der elastisch-plastischen Schwingbruchmechanik," Heft 229. Forschungskuratorium Maschinenbau, Frankfurt, Germany.
[22] McClung, R. C. and Sehitoglu, H., "Closure Behaviour of Small Cracks Under High Strain Fatigue Histories," *ASTM STP 982,* American Society for Testing and Materials, 1986, pp. 279–299.
[23] Taylor, D., "The Definition and Measurement of Crack Closure," *Engineering Fracture Mechanics,* Vol. 43, No. 1, 1992, pp. 109–115.
[24] Kumar, V., German, M. D., and Shih, C. F., "An Engineering Approach for Elastic-Plastic Fracture Analysis," Electric Power Research Institute, Palo Alto, CA, Research Project 1237-1 (NP-1931), 1981.
[25] Dankert, M. and Seeger, T., "*J*-Integral-Näherungsbeziehungen für Risse in Kreiskerben," FF-3/1994, Fachgebiet Werkstoffmechanik, TH Darmstadt, Germany, 1994.
[26] Dankert, M., Amstutz, H., Greuling, S., and Seeger, T., "Spannungsintensitätsfaktoren für Risse in Kerben—FE-Analysen und Näherungsformeln," FF-1/1996, Fachgebiet Werkstoffmechanik, TH Darmstadt, Germany, 1996.
[27] Newman, J. C., Jr., "An Improved Method of Collocation for the Stress Analysis of Cracked Plates with Various Shaped Boundaries," NASA Langley Research Center, NASA TM D-6376, 1971.
[28] Vormwald, M. and Seeger, T., "Crack Initiation Life Predictions Based on Elastic-Plastic Fracture Mechanics for Short Cracks," *Low Cycle Fatigue and Elasto-Plastic Behaviour of Materials,* Elsevier Applied Science, 1987, pp. 562–568.
[29] Dankert, M. and Seeger, T., "Rißfortschritt in elastisch-plastisch beanspruchten Kerbbereichen bei Schwingbelastung mit variablen Amplituden—Konzept und Berechnungsprogramm," FF-4/1994, Fachgebiet Werkstoffmechanik, TH Darmstadt, Germany, 1994.

M. E. Pawlik[1] *and C. R. Saff*[1]

A Displacement-Based Method for Predicting Plasticity-Induced Fatigue Crack Closure

REFERENCE: Pawlik, M. E. and Saff, C. R., "**A Displacement-Based Method for Predicting Plasticity-Induced Fatigue Crack Closure,**" *Advances in Fatigue Crack Closure Measurement and Analysis: Second Volume, ASTM STP 1343*, R. C. McClung and J. C. Newman, Jr., Eds., American Society for Testing and Materials, West Conshohocken, PA, 1999, pp. 427–439.

ABSTRACT: A numerical method for predicting closure and its effects on thermomechanical crack growth has been developed. A finite element model, using linear-elastic fracture mechanics shape functions, is employed to predict crack tip displacements. The effective changes in stress intensity, and therefore crack growth, are obtained from the minimum and maximum crack tip displacement predictions. When a flaw is loaded in Mode I, a ligament of material ahead of the flaw yields, and a maximum crack tip displacement is computed. Upon unloading, plastically deformed material from prior plastic zones acts to limit the minimum displacements of the crack tip. The material is modeled as elastic-perfectly plastic. The yield strength of the material is varied based on the degree of constraint. The upper limit of constraint is a plane strain condition while the lowest constraint is a plane stress condition. The level of constraint is predicted by relating the stress intensity to the thickness of the component. Temperatures also affect yield strength, along with stiffness, and can cause the plastic zone to expand due to creep. During variable-amplitude loadings, and/or temperature changes, the irregular shape of the wake can be accommodated with this numerical procedure. The method has proven to accurately account for load interaction effects such as delayed retardation, crack arrest, initial accelerations following overloads, and the transient growth and stabilization of closure level with number of overloads. This method has been verified against data obtained in the literature, and data collected under the program in which the method was developed, NASA's High Speed Research [*1*].

KEYWORDS: metal fatigue, crack growth, stress intensity, closure, software

A method has been developed to predict crack growth rates based on crack tip displacements. The resulting analysis is expressed in terms of stress intensity, not displacements, due to the universal familiarity with stress intensities as the mechanism that controls crack growth. Analytically locating the closure mechanism that controls crack growth is the key to accurate crack growth prediction. Elber [*2*] observed that cracks do not open until the tensile load is sufficiently high, and proposed that crack tip plasticity is the cause of that phenomenon. Budiansky and Hutchinson [*3*] developed solutions for closure of cracks propagated by constant changes in stress intensity under plane stress conditions. Budiansky and Hutchinson also proposed that closure is determined when either the crack faces lost contact, or when the ligament of material at the crack tip begins displacing. Newman [*4*] has extensively pursued the solutions involving crack face contact, developing software along the way. Dill and Saff [*5*] have developed analyses that use crack tip displacements to compute minimum stress intensities. Most design analyses entail simplifications that preclude the need to track transient wake deformations for accurate predictions [*6,7*]. Unfortunately, not all applications fit the assumptions necessary to validate such simplifications. In addition, the effects of temperatures and hold times on closure mechanisms have been largely unaddressed in previous efforts.

[1] Project engineer and technical fellow, respectively, The Boeing Company, PO Box 516, St. Louis, MO 63166.

Model Development

Due to the low airframe weight required for economic feasibility of High Speed Civil Transport, an improved crack growth analysis may be necessary to reduce the weight of metallic components while ensuring structural integrity. The methods described herein have been written into a software package (HSRCLOSURE) for use in design of High Speed Civil Transport. A generic application is illustrated in Fig. 1. In the model, displacements of the crack tip are calculated and used to determine the minimum stress intensity, and therefore the effective change in stress intensity (ΔK_{eff}). Displacements are numerically calculated from a set of load-displacement equations. A numerical procedure is necessary because of the high discretization necessary to capture the effects of irregular crack surfaces in contact with each other. Figure 2 helps visualize the mechanics occurring at the crack tip. The displacement equation is:

$$[u] = [C][P] \tag{1}$$

where $[u]$ is the displacement vector, $[C]$ is the compliance matrix, and $[P]$ is the load vector. The $[C]$ matrix terms are derived from stress intensity weight functions. A single term of $[C]$ is derived

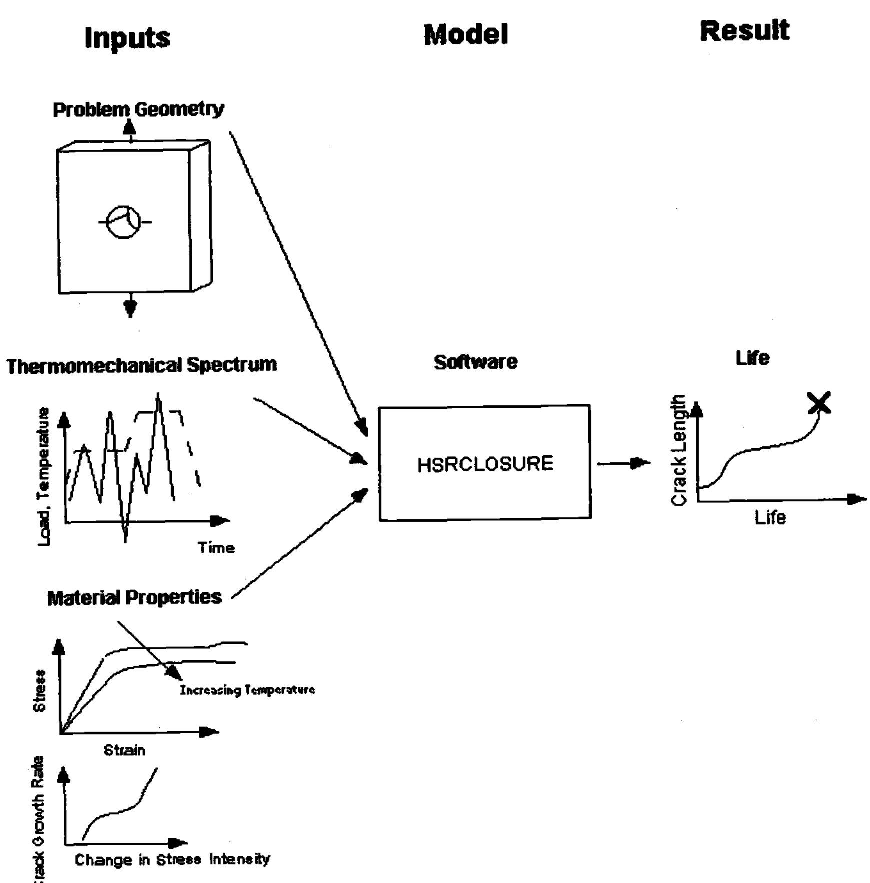

FIG. 1—*Problem illustration.*

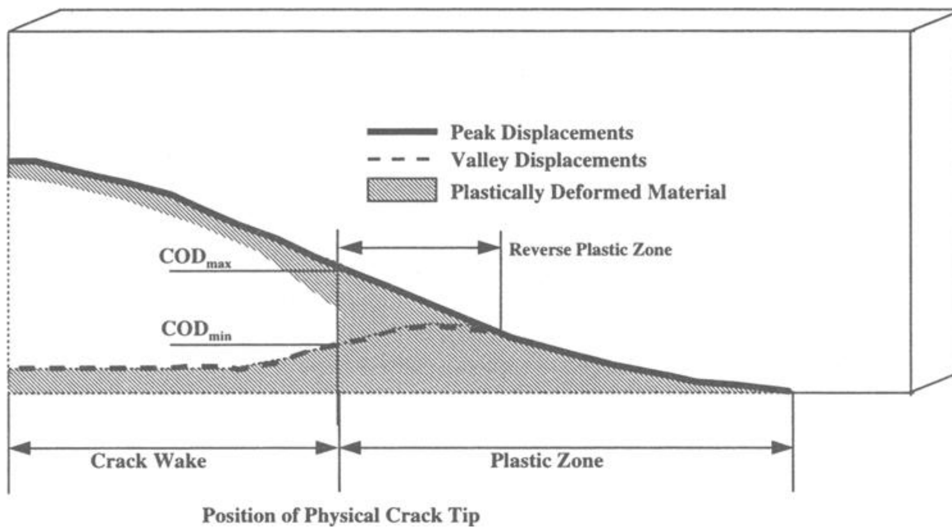

FIG. 2—*Schematic of crack tip mechanics.*

from the geometry's shape function:

$$C_{kj} = \frac{2}{E}\sum_{i>k}^{N} f_m(x_k, a_i) f_m(a_j, a_i)\Delta a_i \; k = 1,2,\ldots N \tag{2}$$

where k and j denote elements, N is the total number of elements, i is a counter, x is position, a denotes crack length, E is Young's modulus, f_m is the shape function of the stress intensity solution [8], and Δa_i is the width of element i. The domain of Eq 1 is the physical crack and the plastic zone extending ahead of the crack. The size of the plastic zone is computed by Dugdale Strip Yield Model [9]. At maximum load, a length of material ahead of the crack tip yields in tension. The material is assumed to be elastic, perfectly plastic. The length of the physical crack and the plastic zone are discretized and the load displacement equations are developed. Plastic deformations in the wake of the crack from previous plastic zones limit closing displacements. Material in the plastic zone can yield in compression upon unloading. With these constraints, Eq 1 serves as a two-dimensional, plane stress finite element model. From the displacements at the crack tip, the effective change in stress intensity and therefore the crack growth rate can be computed. The equation that relates crack tip displacements to stress intensities is:

$$\frac{K_{\text{min-eff}}}{K_{\max}} = 1 - \sqrt{2\left(1 - \frac{cod_{\min}}{cod_{\max}}\right)} \tag{3}$$

where $K_{\text{min-eff}}$ and $K_{\max}$ are the effective minimum and maximum stress intensities, $cod_{\min}$ and $cod_{\max}$ are the minimum and maximum displacements at the tip of the crack, respectively [3]. The level of constraint is determined by comparing the maximum stress intensity to the thickness (B) and yield strength (σ_{ys}) of the material. Plane strain is assumed to dominate when:

$$K_{\max} < \sigma_{ys}\sqrt{\frac{B}{2.5}} \tag{4}$$

Plane stress is assumed to dominate when the plastic zone length is larger than the material thickness. This condition expressed mathematically:

$$K_{\max} > \sigma_{ys}\sqrt{\frac{8B}{\pi}} \tag{5}$$

Intermediate levels of constraint are linearly interpolated between the two extremes, based on $K_{\max}$.

To model plane strain with the plane stress finite element model, constraint is modeled by modifying the yield strength of material in the plastic zone. The plane strain yield strength in tension is a factor of $1/(1 - 2\nu)$ higher than the plane stress yield strength, where ν is Poisson's ratio. The factor $1/(1 - 2\nu)$ is derived from the von Mises yield criterion applied to a plane strain state of stress in the vicinity of the crack tip. Figure 3 illustrates the state of stress in the vicinity of a crack and defines variables. The plane strain state of stress in the vicinity of the crack tip, as determined by Weiss and Yukawa [*10*] are:

$$\sigma_y = \frac{K}{\sqrt{2\pi r}}\cos\frac{\theta}{2}\left[1 + \sin\frac{\theta}{2}\sin 3\frac{\theta}{2}\right] \tag{6}$$

$$\sigma_x = \frac{K}{\sqrt{2\pi r}}\cos\frac{\theta}{2}\left[1 - \sin\frac{\theta}{2}\sin 3\frac{\theta}{2}\right] \tag{7}$$

$$\tau_{xy} = \frac{K}{\sqrt{2\pi r}}\cos\frac{\theta}{2}\sin\frac{\theta}{2}\cos 3\frac{\theta}{2} \tag{8}$$

$$\tau_{xz} = \tau_{yz} = 0 \tag{9}$$

while plane strain requires:

$$\sigma_z = v(\sigma_x + \sigma_y) \tag{10}$$

where K is the applied stress intensity, θ and r are coordinates defined in Fig. 3 and σ_x, σ_y, σ_z, τ_{xy}, τ_{xz}, τ_{yz} are stresses also defined in Fig. 3. From Eqs 6–10 the relations for plane strain stress conditions along the line $\theta = 0$ (per Fig. 3) are:

$$\sigma_x = \sigma_y \tag{11}$$

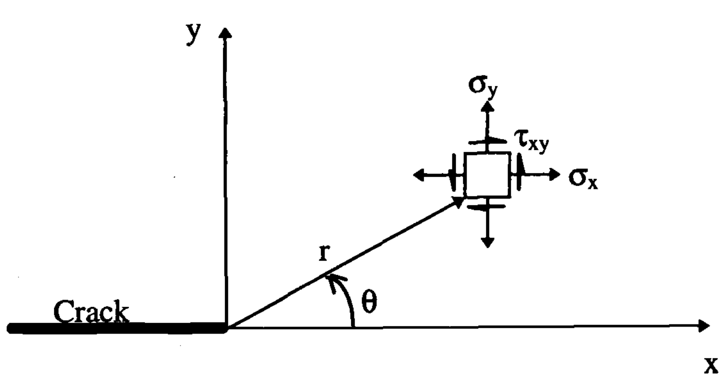

FIG. 3—*Coordinate system.*

$$\sigma_z = 2\upsilon\sigma_y \tag{12}$$

$$\tau_{xy} = \tau_{xz} = \tau_{yz} = 0 \tag{13}$$

The von Mises yield criterion is:

$$\sigma_{ys} = \frac{1}{\sqrt{2}}([\sigma_x - \sigma_y]^2 + [\sigma_z - \sigma_y]^2 + [\sigma_x - \sigma_z]^2 + 6\,[\tau_{xy}^2 + \tau_{xy}^2 + \tau_{yz}^2])^{1/2} \tag{14}$$

where σ_{ys} is the plane stress yield strength of the material. Solving Eq 14 for σ_y determines the effective yield stress of each node in plane strain.

$$\sigma_{ysp\varepsilon} = \sigma_y = \frac{\sigma_{ys}}{1 - 2\upsilon} \tag{15}$$

where $\sigma_{ysp\varepsilon}$ is the effective plane strain yield strength.

In compression, it is assumed that all material yields at the plane stress level of yield strength. It is assumed that constraint is caused by Poisson effect when the crack is in tension and is not apparent in compression. As a verification of the model, results are compared to the closed form solution of a crack propagated under plane stress conditions by a constant change in stress intensity [3]. Closure can be defined in one of two ways, based on displacements or crack surfaces losing contact with each other [3]. The difference between a displacement analysis and the contact analysis of Newman is apparent in Fig. 4 [3,4].

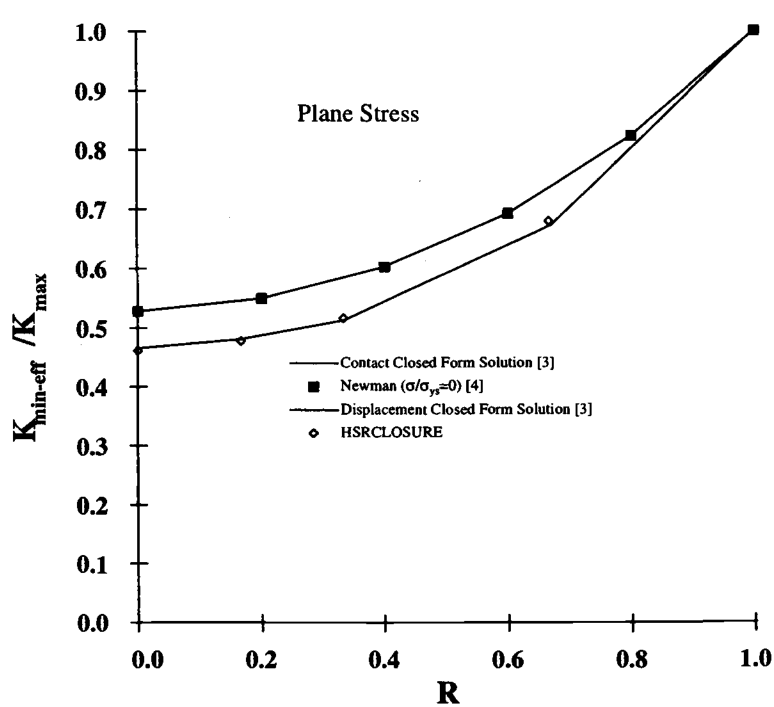

FIG. 4—*Comparison of displacement and contact analyses.*

Crack length is computed by incremental extension:

$$a_{i+1} = a_i + da/dN|_i * \Delta N_i \tag{16}$$

where the subscript i denotes the current load cycle, $i + 1$ is the subsequent load cycle, a is crack length, $da/dN|_i$ is the crack growth rate of the ith load, and ΔN_i is the number of cycles of the ith load level. The term $da/dN|_i$ is evaluated by determining the effective change in stress intensity of the load cycle. The rate is determined by logarithmic interpolation of crack growth rate test data that has been corrected for closure to identify the crack growth rate as a function of the effective change in stress intensity. The material's crack growth rate is assumed to be invariant as a function of the ratio of applied change in stress intensity to Young's modulus for a given stress ratio. This assumption accounts for changes in temperature.

Key Analytical Results

Analysis of cracks in plane strain is shown in Fig. 5. For comparison to contact analyses, the displacements are translated into stress intensities by Eq 3. A controversial aspect of the results is the presence of solutions below the line $K_{\text{min-eff}}/K_{\text{max}} = R$. This observation is indicative of the significant difference between defining closure with contact versus displacements. In a contact analysis, the closure level must be above or equal to the minimum applied load. The displacement analysis shows that the lack of constraint in compression allows the crack tip to deform severely. The deformation is such that the computed closure level would fall below the minimum applied load if expressed in terms of stress intensities per Eq 3. Displacement model results effectively locate unique da/dN versus

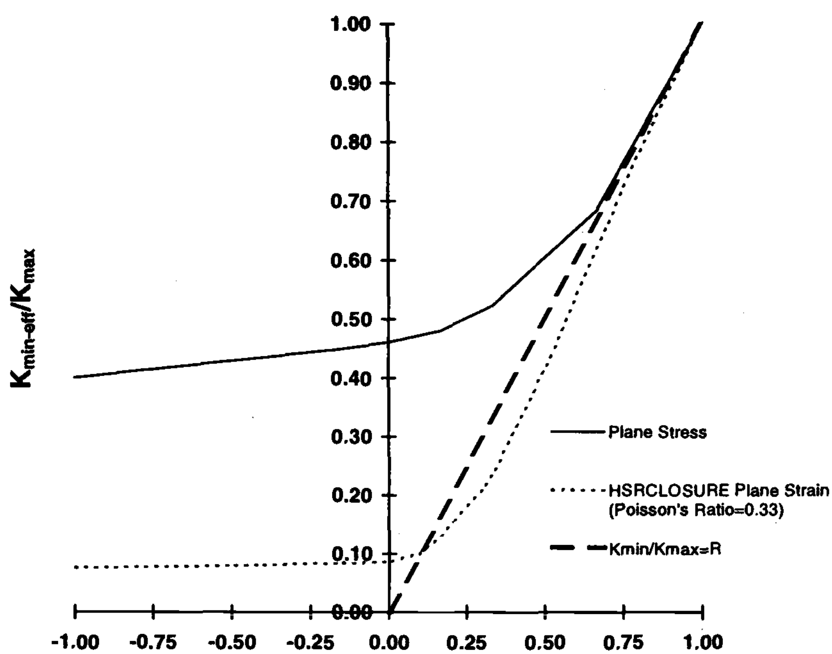

FIG. 5—*Defining closure with crack tip displacements yields results that defy contact analysis boundaries.*

ΔK_{eff} relations, even at high stress ratios. The model results also display the observed phenomena that crack growth rates for $R < 0$ are virtually invariant as a function of R when plotted as $\Delta K_{applied} = K_{max}$. This is evident from the nearly constant K_{min}/K_{max} below $R = 0$. Figure 6 illustrates the ability of the displacement model to collapse stress ratio effects on da/dN versus ΔK data dominated by plane strain [*11*]. Collapsing da/dN data for stress ratio effects are an indication that da/dN versus ΔK_{eff} has been accurately located.

The displacement analysis accounts for temperature by modifying material properties according to hold time at temperature. The Dugdale Strip Yield Model [*9*] is simply fed yield and stiffness properties for the temperature in question to determine plastic zone size. At elevated temperatures, yield strength usually diminishes. Diminished yield strength causes larger plastic zones (per methods defined in Ref *9*) and diminished constraint (per Eqs 4,5). Crack opening displacements are larger at elevated temperature due to diminished stiffness. Material properties as a function of temperature are required input information. Hold time also effectively decreases yield strength through creep. Creep data for time to 0.2% strain are also required input information. The predicted effect of temperature and hold time on the plastic zone size in typical aircraft titanium alloy is shown in Fig. 7. In this manner, a thermal overload can affect crack growth just like a mechanical overload, causing retardation due to increased flexibility of the crack tip.

Material crack growth rates versus temperature variations can be explained using the closure model. Often, the variation in crack growth rate at elevated temperature is simply due to a loss of constraint caused by diminished yield strength, and loss of Young's modulus. Provided that oxidation and/or metallurgical changes are not occurring, the closure model can collapse the effects of stress ratio to yield a single da/dN versus ΔK_{eff} relation. This method is valid for some materials as exemplified in Fig. 8 [*12*].

An important step in the displacement analysis is keeping track of plastic displacements in the wake of the crack tip. The results shown in Fig. 5 illustrate what happens to $K_{min\text{-}eff}$ when the level

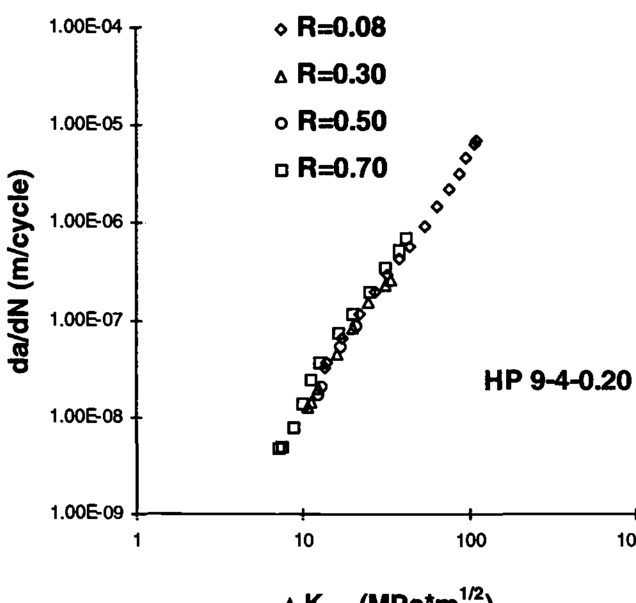

FIG. 6—*HSRCLOSURE results identify* da/dN *versus* ΔK_{eff} *for high stress ratios in HP 9-4-0.20 (data per Ref* 11*).*

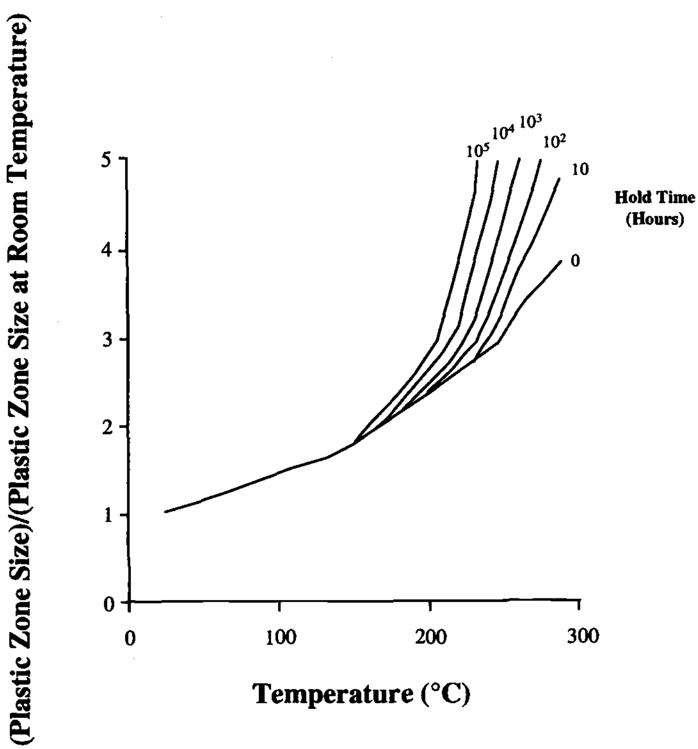

FIG. 7—*Thermal effects on plastic zone size in aircraft titanium alloy.*

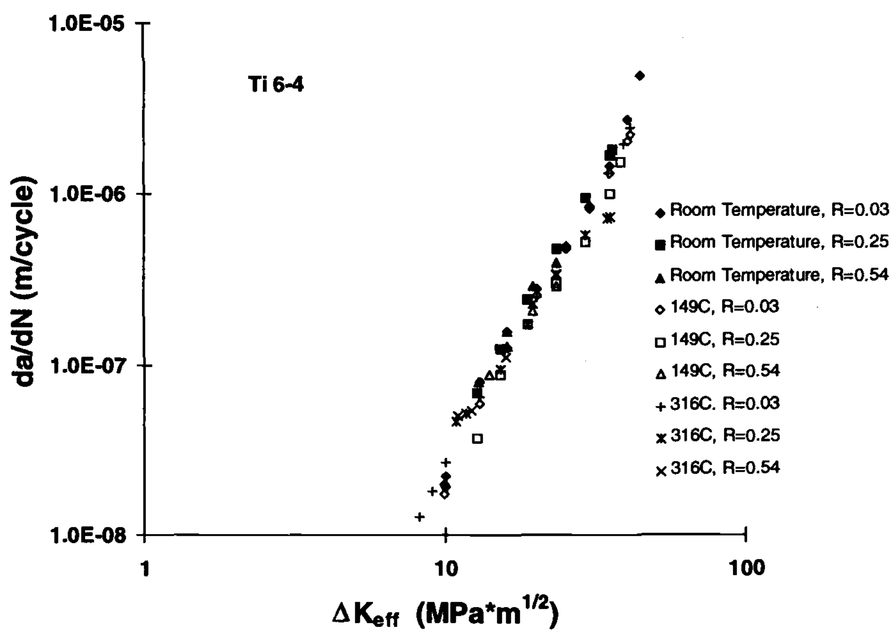

FIG. 8—*Model can locate* da/dN *versus* ΔK_{eff} *for elevated temperatures (data per Ref* 12*).*

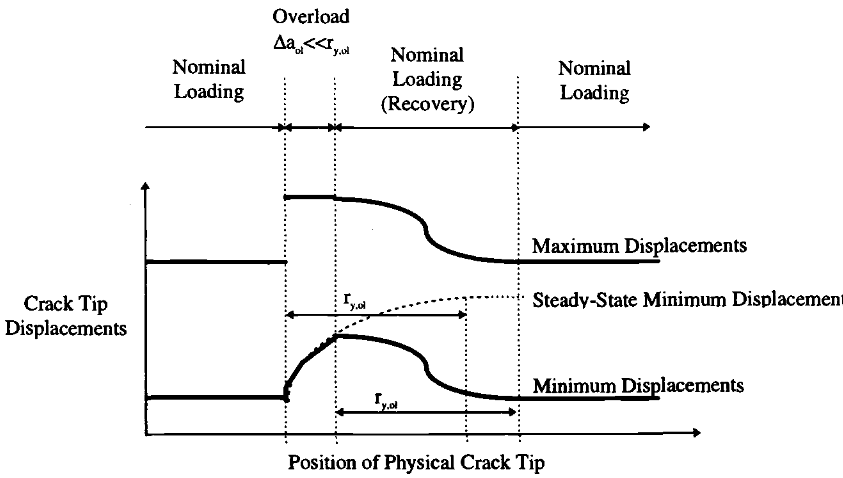

FIG. 9—*Significant aircraft overloads typically do not achieve steady-state minimum displacements.*

of displacement has stabilized. Figure 9 is a schematic of the buildup of plastic deformations in the wake as the flaw extends due to overloads, and the subsequent diminishing levels caused by nominal loading (recovery). Analysis shows that the plastic displacements gradually increase to the overload steady state level when the flaw extends (Δa_{ol}) a distance of approximately one overload plastic zone size ($r_{y,ol}$). In transport aircraft, the overload events that cause significant life-enhancing crack growth retardation typically occur singularly, and Δa_{ol} is much smaller than $r_{y,ol}$. Transport aircraft overloads seldom attain the steady-state displacement levels that are the basis of the results in Fig. 5. Transports also see nominal loads applied in such quantity that cracks can fully recover from retardation events. It is necessary to accurately predict the transient wake deformations, during both overloading and recovery, to accurately realize the benefits of retardation in a design. HSRCLOSURE maintains a log of plastic displacements in the wake of the crack. Plastic displacements provide the displacement constraints in Eq 1. Compressive yielding of material in the crack wake is another constraint in Eq 1. Large deformations in the wake are often crushed by subsequent minimum loads, causing diminished retardation. Modeling of wake deformations is the key to accurate crack growth prediction.

TABLE 1—*Test Matrix (Data Available in Ref* 13*).*

Temp.	ΔK (MPa · $m^{0.5}$)	Hold Time	Overload	Underload	No. of Reps
26°C	15	30 sec	150%	10%	3
26°C	15	30 sec	200%	10%	3
26°C	15	1 hour	150%	10%	3
26°C	15	1 hour	200%	10%	3
26°C	30	30 sec	150%	10%	3
26°C	30	30 sec	200%	10%	3
26°C	30	1 hour	150%	10%	3
26°C	30	1 hour	200%	10%	3
177°C	30	30 sec	150%	10%	3
177°C	30	30 sec	200%	10%	3
177°C	30	1 hour	150%	10%	3
177°C	30	1 hour	200%	10%	3

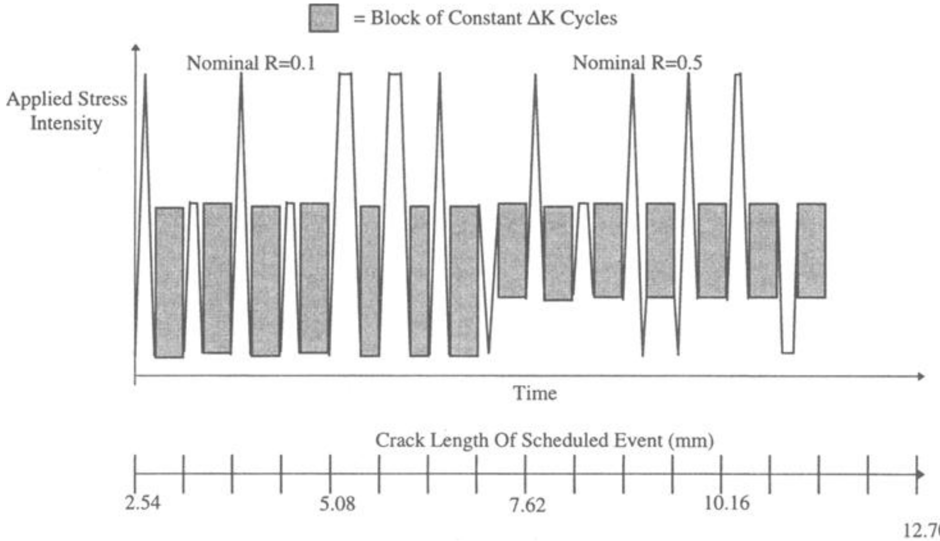

FIG. 10—*Test spectrum [13].*

Comparisons to Test Data

The methods were validated by comparing predicted life to test data for load sequences representative of an aircraft's significant maneuver loads [*13,14*]. All testing was performed at Composite Technology Development, of Boulder, Colorado. A test series was performed that examined the effects of overload level, underload level, stress ratio, hold time, temperature, and load sequence. The test matrix is listed in Table 1. A schematic of the test spectrum is shown in Fig. 10. The material was Ti 6-2-2-2-2 with a simulated superplastically formed, diffusion bonding heat treatment. The specimen geometries for material characterization and model development testing are shown in Figs. 11

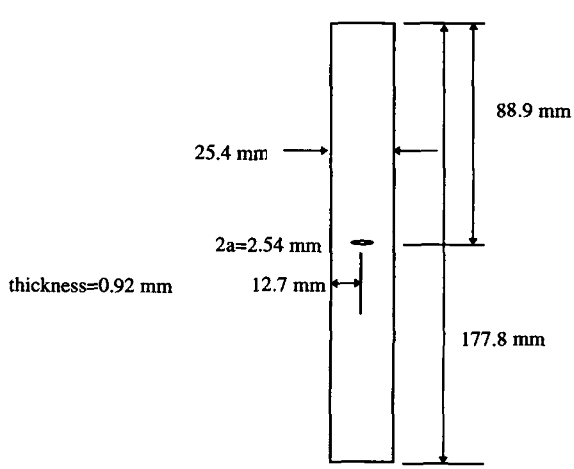

FIG. 11—*Material characterization test specimen geometry [13].*

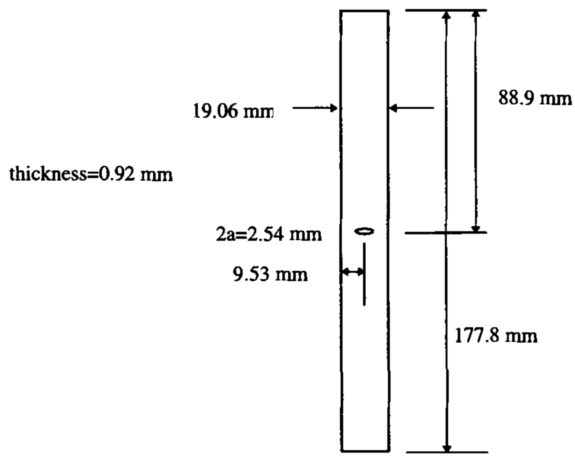

FIG. 12—*Model development test specimen geometry [13].*

and 12. Tests were performed at a nominally constant change in applied stress intensity. The maneuver load(s) were applied at regular intervals of crack length such that previous events did not affect subsequent events.

Since this effort is only a small part of the overall High Speed Civil Transport program, the elevated testing temperature of 177°C and the material selection of titanium were dictated by program objectives. Hence, hold times and temperatures had minimal effect on the recovery crack growth of

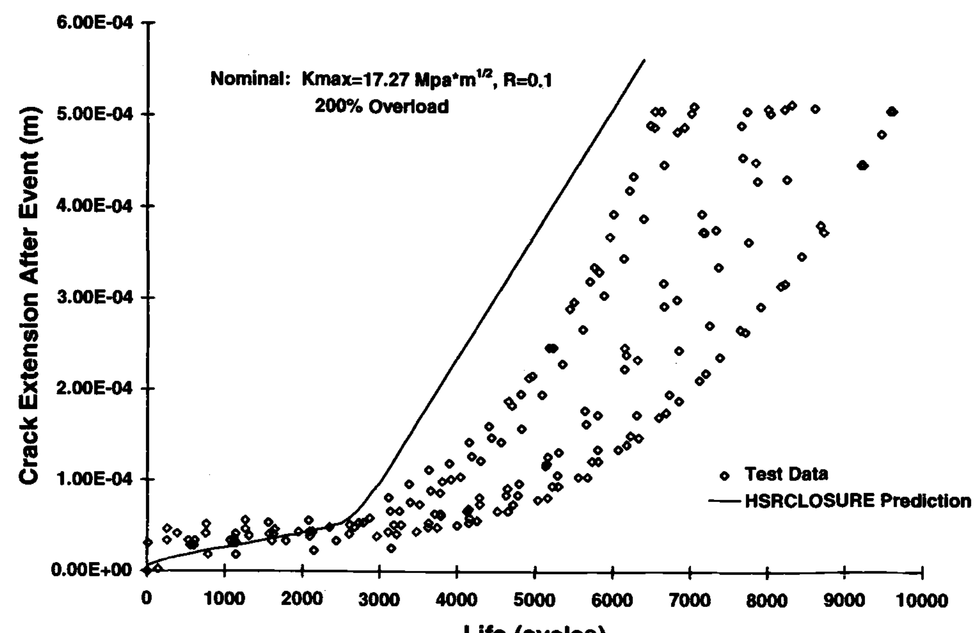

FIG. 13—*HSRCLOSURE predicts overload crack growth retardation (data per Ref 13).*

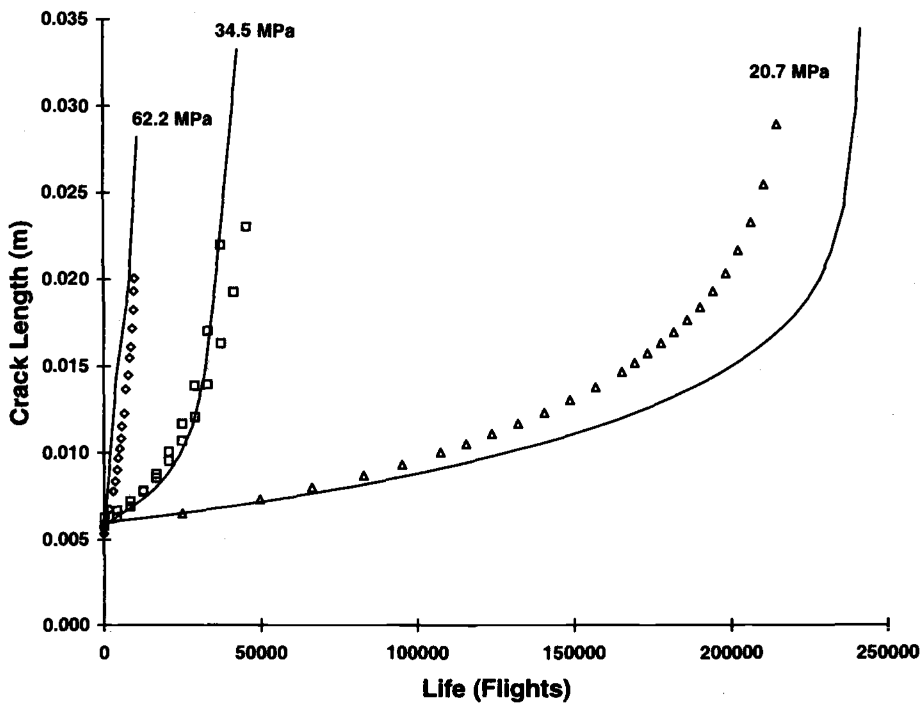

FIG. 14—*Displacement analysis accurately predicts transport spectrum crack growth (data per Ref 15).*

titanium. Underloads to nominal loading had zero effect. Overloads and load sequencing events caused measurable crack growth retardation for model correlation. A complete summary of model verification is available in the program reports [*13,14*]. A small sampling of model results is shown in Fig. 13.

Another verification of the methodology is to predict crack growth caused by a transport aircraft spectrum. Test data for a variation of the Mini-Twist (transport) spectrum [*15*] were collected by Newman et al. for Al 7075-T6 in 2.29 mm sheet form. Figure 14 illustrates the test data along with a prediction by HSRCLOSURE. Mini-Twist causes crack growth that is a challenge to accurately predict. Mini-Twist exhibits a multitude of small nominal loads which cause most of the crack growth, with infrequent overloads that temporarily cause retardation. Underloads occur regularly to partially wipe out the retardation caused by overloads. Due to the relatively small number of overloads, complete retardation recovery can occur under the Mini-Twist loading. All of the aforementioned mechanisms must be modeled accurately to arrive at an accurate life prediction. The accurate prediction of the test data indicates that these mechanisms have been modeled with a good degree of accuracy.

Conclusions

Displacement analysis has shown promise as a means of predicting closure and therefore crack growth. The methods have been automated, and the resulting software has correlated well with room temperature test data. The approach has accurately predicted individual load sequencing effects as well as aircraft load spectra. Methods to account for temperature variations on closure have been developed, but are largely unverified.

The ultimate goal of this effort is to be able to predict crack growth of the HSCT, which is subject to a long service lifetime and a thermomechanical loading spectrum. Unfortunately, the HSCT spectrum is still under development and is not available at this time. Correlations with HSCT test data will be published at a later date.

References

[1] Gates, T. S., "High Speed Research-Airframe Technology, Airframe Materials and Structures, Materials Durability, NASA Contract NAS1-20220. Currently on-going.

[2] Elber, W., "The Significance of Fatigue Crack Closure," *Damage Tolerance in Aircraft Structures, ASTM STP 486,* American Society of Testing and Materials, 1971, pp. 230–242.

[3] Budiansky, B. and Hutchinson, J. W., "Analysis of Closure in Fatigue Crack Growth," *Transactions of the ASME,* Vol. 45, June 1978.

[4] Newman, J. C., "A Crack-Closure Model For Predicting Fatigue-Crack Growth Under Aircraft Spectrum Loading," *Methods and Models for Predicting Fatigue Crack Growth Under Random Loading, ASTM STP 748,* American Society for Testing and Materials, 1981, pp. 53–84.

[5] Dill, H. D. and Saff, C. R., "Spectrum Crack Growth Prediction Method Based on Crack Surface Displacement and Contact Analyses," *Fatigue Crack Growth Under Spectrum Loads, ASTM STP 595,* American Society for Testing and Materials, 1976, pp. 306–319.

[6] Dill, H. D. and Saff, C. R., "Effect of Fighter Attack Spectrum on Crack Growth," AFFDL-TR-76-112, March 1977.

[7] Newman, J. C., Jr., "A Crack Opening Stress Function for Fatigue Crack Growth," *International Journal of Fracture,* Vol. 24, 1984, pp. R131–R135.

[8] Tada, H., Paris, P., and Irwin, G., *The Stress Analysis of Cracks Handbook,* Del Research Corporation, Hellertown, PA, 1985.

[9] Dugdale, D. S., "Yielding of Steel Containing Slits," *Journal of Mechanics and Physics of Solids,* Vol. 8, 1960, p. 8.

[10] Weiss, V. and Yukawa, S., "Critical Appraisal of Fracture Mechanics," *Fracture Toughness Testing and Its Applications, ASTM STP 381,* American Society for Testing and Materials, 1965, p. 1.

[11] Cawthorne, E. W., "B-1 Program da/dN Data for Aluminum Alloys," Battelle's Columbus Laboratories, 3 Apr 1974. Data also available in *Damage Tolerant Design Handbook,* AFWAL-TR-83-4144, December 1983, pp. 6.5–41.

[12] Gilbert, M. S., "Fatigue Crack Growth Rate Data on Titanium Ti 6-4 Alloy Using K_B Bar Specimens from the TF34 DTA Effort," General Electric Co., Evendale, OH, October 1982. Data also available in *Damage Tolerant Design Handbook,* AFWAL-TR-83-4144, Dec. 1983, pp. 4.11–297.

[13] Gates, T. S., "High Speed Research-Airframe Technology, Airframe Materials and Structures," Materials Durability, NASA Contract NAS1-20220, Quarterly Report, 14 April 1997.

[14] Pawlik, M. E., "HSRCLOSURE Theoretical Overview," NASA Contract NAS1-20220, Deliverable Report, Sept. 1996.

[15] Newman, J. C., Jr., Wu, X. R., Venneri, S. L., and Li, C. G., "Small-Crack Effects in High-Strength Aluminum Alloys," NASA Reference Publication 1309, May 1994.

Jesús Toribio[1] *and Victor Kharin*[1,2]

Role of Fatigue Crack Closure Stresses in Hydrogen-Assisted Cracking

REFERENCE: Toribio, J. and Kharin, V., **"Role of Fatigue Crack Closure Stresses in Hydrogen-Assisted Cracking,"** *Advances in Fatigue Crack Closure Measurement and Analysis: Second Volume, ASTM STP 1343*, R. C. McClung and J. C. Newman, Jr., Eds., American Society for Testing and Materials, West Conshohocken, PA, 1999, pp. 440–458.

ABSTRACT: Crack closure effects on hydrogen-assisted cracking (HAC) were studied in terms of the influence of residual stresses produced by load removals at fatigue cycling on stress-assisted hydrogen diffusion towards rupture sites in the crack tip zone. The finite element procedure was applied to cyclic load elastoplastic large-deformation analysis combined with stress-assisted diffusion. Small-scale yielding near the crack tip was addressed and characterized in terms of the stress intensity factor (SIF). The elastoplastic situation near the tip of a blunting-closing crack revealed the cyclically stable stress evolution established after a couple of loading cycles (but this was not attained for strains). Crack closure effects were negligible for sustained-load HAC at SIF above the maximum value at precracking. The test duration for reliable evaluation of the threshold SIF for HAC was estimated. Crack closure affects near-tip hydrogen diffusion, and consequently HAC, at dynamic rising loading after precracking. Modeling was performed for the range of SIF increase rates. It showed that a premature fulfillment of the local fracture criterion in terms of critical combination of the hydrogen concentration and stress-strain parameters can occur at slow dynamic loading if compared with the sustained-load case. The dominating factor—stress or strain—and the "scale" of the local rupture event are of decisive importance for this. The performed simulations provide more insight into the items of conservatism of HAC testing data and the sources of their uncertainty.

KEYWORDS: hydrogen-assisted cracking, large crack-tip deformations, cyclic loading, stress-assisted diffusion, threshold stress intensity factor

The effects of hydrogen on fracture behavior of metals and alloys have been receiving ever-increasing attention in materials science and mechanical engineering. Metals exposure to hydrogen is a common attribute of their being since hydrogen may be supplied to metals, starting with metallurgical sources in metal making, continuing at welding and galvanic operations in manufacturing, and finishing with service hydrogenation resulting from hydrogen evolution from ambient moisture during spontaneous atmospheric corrosion, cathodic protection against corrosion, or from hydrogenous working agents [*1–3*]. This usually causes hydrogen degradation manifested through diverse detrimental effects of hydrogen on materials behavior and integrity, depending on an alloy type and specific service conditions (loading, temperature, etc. [*1–5*]).

Having recognized hydrogen as a severe and frequently met promoter of engineering failures, especially with respect to rather expensive and potentially disastrous installations of energy, chemical, oil and gas industries, space transportation, etc., researchers have conducted extensive studies concerning fundamental aspects of hydrogen-metal interactions and hydrogen degradation as well as on their practical relevance in engineering and design.

[1] Materials Science Department, University of La Coruña, E.T.S.I. Caminos, Campus de Elviña, 15071 La Coruña, Spain.

[2] On leave from: Pidstryhach Institute for Applied Problems of Mechanics and Mathematics, 290601 Lviv, Ukraine.

Hydrogen-affected fracture of materials is mainly determined by regularities of hydrogen-assisted nucleation and growth of cracks. Then a wide spectrum of hydrogen degradation phenomena is effectively treated as hydrogen-assisted cracking (HAC). It is being studied and evaluated following the fracture mechanics type approaches [*6–8*].

The common feature among diverse hydrogen degradation forms is the time-dependent delayed (or slow subcritical) development of damages/cracks which is controlled by kinetic processes of hydrogen transportation and accumulation in prospective rupture sites [*3,7*]. Correspondingly, one of the key items of HAC studies concerns the transport mode which dominates hydrogen accumulation in the crack-tip fracture process zone. Hydrogen diffusion in metals has been proposed and substantiated as the dominating transport mechanism which governs the kinetics of HAC [*9–12*]. Quantitative modeling of hydrogen accumulation in the crack-tip region by stress-strain affected diffusion has received considerable attention, but mainly with respect to sustained load conditions [*8–15*]. This cannot help elucidation of the experimentally observed influences on the threshold and kinetics of HAC of neither pre-HAC crack history (i.e., fatigue precracking regime, overloads, etc., before exposure to hydrogen), nor loading path and dynamics on crack behavior under the hydrogen effect [*16*]. The roles of alternating and transient stress-strain fields produced by fatigue and rising dynamic loading on the near-tip hydrogen distributions still need to be quantitatively characterized. The items related to cyclic loading are especially important where contribution of the compressive stresses due to crack closure is expected to be essential. Thus, the role of fatigue crack closure stresses in HAC is a relevant topic in engineering design and analysis, since it influences the characteristics of crack growth in metals under hydrogenation.

Because all the events relevant to HAC take place in the intensively strained very-near-tip zone, and the hydrogen diffusion is affected by the stress-strain state therein, a minute analysis of the near-tip stresses and strains related to finite deformations is desired to gain realistic insight into process zone hydrogenation. Although much attention has been paid to large-deformation plasticity modeling of the near-tip situation, the majority of studies dealt with monotonously rising loading (cf., for example, Refs *14,17,18*) and apparently only Ref *19* examined the cyclic load effect. The main body of cyclic load elastoplastic analyses of cracks is limited to small-strain simulations (cf., for example, Refs *20,21*).

In view of the deficiencies just noted regarding the near-tip stress-strain state and hydrogenation analyses, the present study was undertaken. The objective was to elucidate the peculiarities of the near-tip finite-strain elastoplastic situation with relation to crack closure at unloading portions of fatigue cycles and to bring some insight into the role of load history and dynamics on the kinetics of hydrogen accumulation near the crack tip. Consideration is given to a two-dimensional solid with a plane through-the-thickness crack under plane-strain conditions and Mode I (opening) loading. Small-scale yielding (SSY) conditions are enforced; i.e., the mechanical autonomy of the near-tip region is maintained, and thus the stress intensity factor (SIF) K is used as a controlling variable.

In the following sections, the bases of the diffusional concept of HAC and of the theory of stress-strain assisted hydrogen diffusion are outlined, the analysis model and numerical procedures are described, and the results of simulations are presented. Possible implications for HAC testing and evaluation are emphasized.

Theoretical Fundamentals

Diffusional Theory of HAC

The hydrogen effect on fracture depends on its amount in prospective rupture sites represented by the value of its volume concentration C which is provided by diffusion from external (environmental) or internal (residual hydrogen) sources. Local rupture occurs when in a relevant material element (cell, or "grain," or whichever point of interest) the concentration achieves the critical value C_{cr} determined, in general [*12,22*], by the principal components of stresses and (plastic) strains, respectively, σ_i and ε_i (i = 1,2,3):

$$C_{cr} = C_{cr}(\sigma_i, \varepsilon_i) \tag{1}$$

According to basic fracture mechanics ideas (cf. Refs *11,12,23*), considering deformations and stresses prior to local fracture event, under SSY the K-controlled mechanical autonomy of the near-tip region is supposed. Although a nonlinear zone surrounds the crack tip, it remains small and plasticity does not sensibly disturb the SIF-dominated elastic solution outside. The annular K-governed elastic ring shields the crack tip from peculiarities of outer geometry and applied loads. The elastoplastic near-tip stress-strain fields, at least as close as several values of the crack-tip opening displacement (CTOD) δ_t, are self-similar if scaled using CTOD, which represents the deformed configuration of the elastoplastic solid, or instead, using SIF according to the known relation [*17,23*] obeyed at SSY:

$$\delta_t = 0.6\frac{K^2}{E\sigma_Y} \tag{2}$$

where E is the Young's modulus and σ_Y the tensile yield stress. This may be expressed by material-determined forms dependent in general on CTOD (and at SSY on SIF through Eq 2) and on spatial coordinates (x,y) with the origin at the crack tip:

$$\varepsilon_i = \varepsilon_i^*\left(\frac{x}{\delta_t}, \frac{y}{\delta_t}\right), \sigma_i = \sigma_i^*\left(\frac{x}{\delta_t}, \frac{y}{\delta_t}\right) (i = 1,2,3) \tag{3}$$

where the asterisks emphasize the predetermined nature of the right-hand parts dependent only on the material. To be precise, the coordinates x and y should be considered as deformed distances in a solid, in particular because actual hydrogen transportation paths will be of further interest. Elastoplastic solutions (3) for monotonic load have been proved to be plain material functions with respect to the mentioned variables, K in the particular case of SSY [*17*], whereas under cyclic load they must depend on the history of loading (i.e., of applied SIF) represented by the number of cycles, their amplitudes, etc. Other solutions [*17,18,23*] which account for the roles of more factors, such as the Poisson's ratio, strain hardening, as well as the crack tip shape (morphology), afford only different terms to substitute the coefficient 0.6 in Eq 2, but they do not raise substantial quantitative discrepancy. It should be noted that Eqs 2 and 3 represent the deformed state in elastoplastic solid, displacement in particular, which might depend on hydrogen as far as it could affect the material characteristics, E and σ_Y in this case, over a certain significant distance around the tip. However, this seems unlikely for the case of environmental hydrogenation, and is irrelevant for HAC under load applied before substantial hydrogenation as in the sustained load tests. Concerning the critical situation—the local rupture event, but not the relation between deformation and applied load as does Eq 2—fracture mechanism and hydrogen undoubtedly affect the limit (critical) value of CTOD, and of the corresponding K, at the crack growth initiation. Finally, with regard to crack blunting as the attribute of the quasi-brittle fracture of metals (including HAC) as a (micro)plasticity-assisted phenomenon, extensive discussion and relevant literature entries have been provided elsewhere [*22*].

The crack situated along the x-axis is supposed to grow provided that the hydrogen concentration accumulated with time t in a certain responsible location at $x = x_c$, $C(x_c,t)$, attains the critical level corresponding to the instantaneous SIF $K(t)$ according to Eqs 1–3:

$$C(x_c,t) = C_{cr}(K(t),x_c) \tag{4}$$

where the value of x_c must be defined associated with the concept of the responsible material cell (the worst material unit, weak grain, fixed microstructural length, or other [*8–10,12,13*]).

Local rupture repeatedly occurs while the concentration of accumulated hydrogen $C(x,t)$ can satisfy the criterion (4) after finite diffusion time Δt. Then, a crack advances by its size increments Δa, a series of which renders the macroscopic crack growth rate $v = \Delta a/\Delta t$.

Impossibility to fulfill the criterion (4) with a certain K value at a finite time means crack arrest ($v = 0$). At sustained load this is associated with the steady-state (obviously, equilibrium) distribution of hydrogen concentration in metal $C_{eq}(K,x)$ attained at $t \to \infty$. C_{eq} defines the extreme hydrogenation at a given SIF. Using this steady-state solution $C_{eq}(K,x)$ in criterion (4) yields the equation to find the upper limit of K with which the crack growth rate $v = 0$. Thus, C_{eq} determines the threshold SIF value K_{th} for HAC under sustained load.

Hydrogen Diffusion in Deformed Solid

Roughly, the thermodynamics of diffusion in solids states that the process goes towards the state of maximum entropy in the system which corresponds to the statistically homogeneous occupation of the available sites in a solid by a given amount of a diffusible specie. Since the density of the occupied sites for hydrogen in metal is proportional to its concentration C, whereas the density of available sites is associated with the hydrogen solubility coefficient in metal K_s, the thermodynamic driving force for diffusion is caused by the nonuniform distribution in a solid of the ratio C/K_s. Precisely, the driving force X_D for diffusion was derived as follows [*11,12*]:

$$X_D = -\nabla \left(RT \ln \frac{C}{K_s} \right) \tag{5}$$

where R is the universal gas constant and T the absolute temperature. The coefficient of diffusion of hydrogen in a metal D defines its mobility equal to D/RT, which together with the driving force (5) yields the diffusion flux of hydrogen:

$$J_H = \frac{D}{RT} C X_D \tag{6}$$

The solubility K_s and diffusivity D are known to depend on alloy and on density of hydrogen traps in the metal lattice [*4*]. Traps density, and in certain alloys their phase composition, e.g., martensite formation in austenitic steels [*15,24*], both depend on plastic deformation which may be incorporated in terms of the effective plastic strain ε_p [*25*]. In addition, K_s depends on the hydrostatic stress $\sigma = (\sigma_1 + \sigma_2 + \sigma_3)/3$ and is given by [*12,25*]:

$$K_s = K_{s0}(\varepsilon_p, T) \exp\left(\frac{V_H \sigma}{RT}\right) \tag{7}$$

where K_{s0} is the strain-only dependent component of solubility and V_H the partial molar volume of hydrogen in a metal. According to Eqs 5–7, gradients of both ε_p and σ are the governing factors of hydrogen diffusion.

Assuming a constant temperature, from Eqs 5–7 one can write:

$$J_H = -D(\varepsilon_p(t)) \left\{ \nabla C - C \left[\frac{V_H}{RT} \nabla \sigma(t) + \frac{\nabla K_{s0}(\varepsilon_p(t))}{K_{s0}(\varepsilon_p(t))} \right] \right\} \tag{8}$$

Adopting the material (Lagrangian) description of the medium, and referring the equations to the current configuration of a deformed material volume which at time t instantaneously occupies a certain spatial domain ${}_tV$, the obvious consideration of mass balance [26] with the flux defined by Eq 8 leads to the equation of stress-strain assisted diffusion (cf., Refs 11,12):

$$\frac{dC}{dt} = D\,[\nabla^2 C - M{\cdot}\nabla C - NC] + \nabla D{\cdot}[\nabla C - MC] \tag{9}$$

where vector and scalar coefficients, respectively, are $M = \nabla \ln K_s$ and $N = \nabla^2 \ln K_s$.

For most applications where the hydrogen environment effect on crack growth is of interest, hydrogen entry conditions may be characterized by the equilibrium value of concentration on the metal surface C_Γ [11,12]. Then, taking relation (7) into account, the boundary condition for diffusion is:

$$C\,|_{\text{surface}} = C_\Gamma(t) \text{ with } C_\Gamma(t) = C_0 \exp\left(\frac{V_\text{H}}{RT}\,\sigma_0(t)\right),\ \sigma_0(t) = \sigma(x,y,t)\,|_{\text{surface}} \tag{10}$$

where C_0 is the equilibrium concentration in a stress-free (unloaded) metal which characterizes the environmental activity of hydrogen; e.g., it may be expressed in terms of the equivalent pressure of hydrogen gas through Sieverts law [1,2].

The steady-state solution of Eq 9 for a stationary stress-strain field is the equilibrium concentration distribution which nullifies the diffusion driving force (5). This is effectuated with the ratio C/K_s = const, and thus, from relation (7) and boundary condition (10):

$$C_{\text{eq}}(K,x,y) = C_0 K_{s0}\,(\varepsilon_p(K,x,y))\exp\left(\frac{V_\text{H}\sigma(K,x,y)}{RT}\right) \tag{11}$$

If the stress effect is addressed solely, Eqs 8 and 9, as well as the equilibrium solution (11), coincide with the known results for stress-only assisted diffusion [9,10].

Basic Modeling Issues

Design of the Model

With the intention of elucidating features of some generality, the material is supposed to be rate-independent ideal elastoplastic with the von Mises yield criterion. Mechanical characteristics were chosen relevant to typical steels for which HAC has been extensively studied [3]. Young's modulus E was 200 GPa, Poisson's ratio $\mu = 0.3$, yield stress $\sigma_Y = 600$ MPa. The maximum load in simulations was established in terms of a SIF of 60 MPa$\sqrt{\text{m}}$ to cover appropriate ranges of the maximum cyclic SIF $K_{\max}$ at which fatigue cracking goes on as well as the levels when HAC can proceed [27].

Being interested in the SSY situation, our first attempt was to perform modeling in the manner of a boundary layer formulation used in similar elastoplastic solutions with monotonic rising load [14,17], that is, applying K-controlled displacement boundary conditions from the Irwin singular elastic solution over a remote boundary of a circular domain of an appropriate radius surrounding the crack tip. However, during a cyclic load history when the SIF approached zero, corresponding enforcement of the remote boundary displacements towards zero caused substantial compressive stresses along the outer border of the presumably K-controlled elastic ring. These stresses are due to the near tip residual plastic strains. This raised doubts about the applicability to the cyclic load case of the K-dominance conditions established for monotonic loading in terms of the appropriate zone dimensions [23]. Since this study is concerned mainly about the near tip diffusion, to avoid possible perplexity, the modeling was performed with large full-scale test pieces to ensure SSY.

The double-edge-cracked panel in tension and its one-quarter segment with a finite element mesh are shown in Fig. 1. It has a crack length $a = 75$ mm and an undeformed semicircular crack-tip width $b_0 = 5$ μm; a magnitude of this order is considered relevant to cracks in medium-strength steels [14].

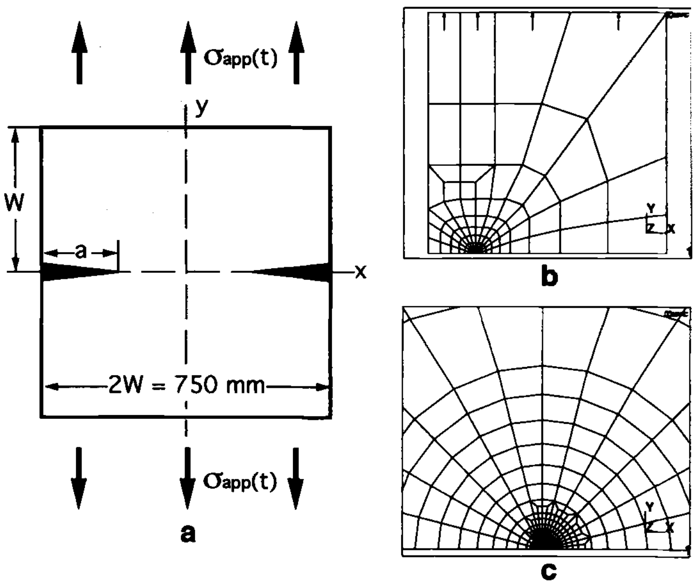

FIG. 1—*Schematics of the considered specimen geometry and mechanical boundary conditions in* (a) *with the finite element mesh: global view of the mesh in* (b) *and a detail of the mesh refinement near the crack tip in* (c).

Very fine mesh was used near the tip. To avoid mesh degeneration and to terminate calculations for several load/unload cycles, the near-tip mesh design required much more care than for successful simulations under a rising-only load. Analogously, the load stepping procedure in the incremental elastoplastic analysis must be finer than used in small-strain cyclic modeling [*21*]. A total of 1148 four-node elements were used with 1222 nodes. Traction-free mechanical boundary conditions were applied on the crack faces and lateral panel surfaces, the appropriate nodes of the vertical and horizontal axes of symmetry of the panel were restrained to remain on the axes, and the uniform tensile stress $\sigma_{app}(t)$ was applied across the top of the specimen quarter under consideration. The current SIF was defined according to the available solution [*28*] as

$$K(t) = 1.158\, \sigma_{app}(t) \sqrt{\pi a} \tag{12}$$

The updated Lagrangian formulation was used in both elastoplastic deformation and diffusion simulations where the mesh was pinned to material points and updated during proceeding deformation (solution process). The elastoplastic boundary value problem solution was accomplished using the MARC finite element code [*29*]. This provided necessary data—stresses and deformations—for subsequent solution of the problem of stress-strain assisted diffusion.

Finite Element Formulation of the Hydrogen Diffusion Problem

With respect to the near-tip hydrogen diffusion, accounting for large deformations of the body is essential since they notably change diffusion distances in the zone of interest. The standard weighted residual process [*30*] to build the finite element approximation to the solution of the initial-boundary value problem (9–10) is performed in the material (Lagrangian) coordinates, taking as the reference the instantaneous deformed configuration of the solid occupying at the moment t the volume ${}_tV$

bounded by the surface ${}_tS$. In brief, following the Galerkin process for the continuum discretized into a finite element mesh, where the same shape functions family $\{{}_tW_m(x,y);\ m = 1,2, \ldots M\}$, M being the number of nodes, plays the role of both the trial and the weighting functions, the weak form of the weighted residual statement of the problem for any t yields the system of equations with respect to the array of the nodal concentration values $\{C_m(t);\ m = 1,2, \ldots M\}$ as follows:

$$ {}_t[\mathbb{M}_{i,j}]\left\{\frac{dC_j}{dt}\right\} + {}_t[\mathbb{K}_{i,j}]\,\{C_j\} = {}_t\{F_i\}\ (i,j = 1, \ldots, M) \tag{13}$$

where the components of the respective matrices are:

$$ {}_tM_{i,j} = \int_{tV} {}_tW_i\,{}_tW_j\,dV \tag{14}$$

$$ {}_tK_{i,j} = \int_{tV} D\left\{\nabla_tW_i\cdot\nabla_tW_j - \left[\left(\frac{V_H}{RT}\nabla\,\sigma(t) + \frac{\nabla K_{s0}\,(\varepsilon_p(t))}{K_{s0}\,(\varepsilon_p(t))}\right)\cdot\nabla_tW_j\right]{}_tW_i\right\}dV \tag{15}$$

and for the column in the right-hand part we have

$$ {}_tF_i = -\,J_S\int_{tSf} {}_tW_i\,dS \tag{16}$$

which arises in order to prescribe the flux of hydrogen J_S on the part ${}_tS_f$ of the surface ${}_tS$. Here it serves to reflect the symmetry conditions $J_S = 0$ along respective axes considering only the quarter of the specimen (Fig. 1). The left-hand subindices emphasize that the quantities refer to the instantaneous deformed configuration of the solid at a time t.

For a given loading history in terms of the applied stress $\sigma_{app}(t)$, or equivalently SIF variation $K(t)$ according to Eq 12, the deformation displacements together with the stress and strain components involved in the diffusion modeling are provided by the post-processing module of the MARC finite element code as nodal values following the solution of the elastoplastic boundary-value problem. In the implementation of the diffusion problem, they were approximated using the same shape functions family $\{{}_tW_m\}$. The time-domain Galerkin procedure [*30*] was applied for the integration of the finite element equations system (13).

Results and Discussions

Finite Deformations and Stress-Strain Fields Near a Blunting/Closing Crack Tip

The specimen loading history $\sigma_{app}(t)$ was chosen so that it rendered the SIF variation $K(t)$ from zero to a certain K_{max} and in reverse to zero. The K_{max} levels were taken as 30 and 60 MPa$\sqrt{m}$ to maintain the situation where the crack-tip fields, at least during a monotonic loading, attain the stable self-similar shape (3). According to different estimations [*17,18*], this occurs at CTOD exceeding the value of about (0.5 to 2)b_0. For the chosen K_{max}, the calculated CTOD values δ_{max} were, respectively, about 2.3 and 3.7 times the original crack width b_0. Large-deformation elastoplastic modeling was accomplished for up to ten load cycles. The results for both series of calculations with different K_{max} were really similar if scaled with respect to δ_t, as in expressions (3).

Crack-tip profiles with deformed meshes are depicted in Fig. 2 for different instants of loading history. Complete crack closure up to contact of its faces was never detected, rather the crack width after load removals remained quite considerable. With respect to subsequent modeling of hydrogen diffusion, it is worth noting the severe shortening of transportation distances: the very-near-tip elements become extremely thin in the diffusion main direction.

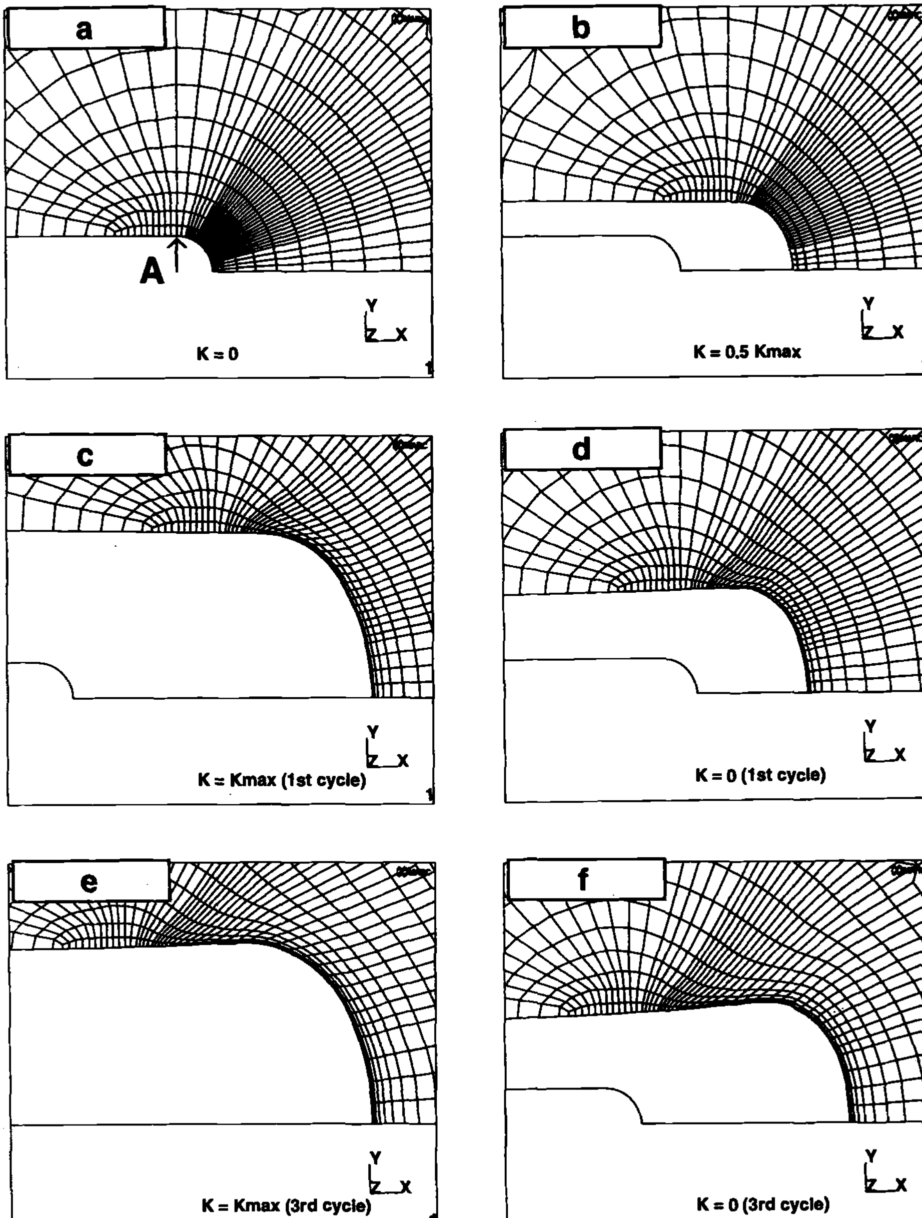

FIG. 2—*Deformed crack tip shapes and near tip meshes at different stages of cyclic loading with* K_{max} = *60* $MPa\sqrt{m}$: (a) *initial state before load application;* (b) *at the mid-way to the first maximum load point,* $K = 0.5K_{max}$; (c) *at the first maximum load point,* $K = K_{max}$; (d) *at the first load removal,* $K = 0$; (e) *at the third peak load,* $K = K_{max}$; (f) *at unload to* $K = 0$ *after the third loading cycle.*

The current CTOD δ_t is plotted versus applied K value in Fig. 3. The value of δ_t was identified with twice the current vertical displacement of the Node A shown in Fig. 2*a*, and the current crack tip width is taken $b = b_0 + \delta_t$. Although it is not the exact maximum of the blunted tip width (see Fig. 2*e*), the difference is not essential and this definition was adopted in accordance with other similar studies [*17–19*] which enables comparison of the results. The interrelation between δ_t and K on the monotonic phase of loading (towards the first maximum) agrees with the formula (2). At reverse portions of load cycles, δ_t obtained from the high-resolution numerical simulations agrees fairly with the known formula derived from rather simple mechanical considerations [*23*]:

$$\delta_t = \delta_{\max}\left[1 - \frac{1}{2}\left(1 - \frac{K}{K_{\max}}\right)^2\right] \tag{17}$$

The shape and size of the near-tip plastic zone defined by the equation $\sigma_{eq} = \sigma_Y$, where σ_{eq} is the equivalent von Mises stress, were found to be in agreement with published data of model calculations [*19,20*]. In particular, the sizes of the reversed plastic zones after load removals were about 0.2 of the forward plastic zone sizes [*20*]. Subsequent load cycles caused minor changes of the plastic zones corresponding to the maximum and minimum loads. The peculiarities of the cyclic plastic zone evolution can hardly cause a notable direct influence on the near-tip hydrogen diffusion.

The distributions of the hydrostatic stress σ and equivalent plastic strain ε_p near the crack tip are most relevant for hydrogen diffusion according to Eq 9. In Fig. 4 the band contours of σ are presented corresponding to the maximum and minimum load levels. Both stress distributions have extreme beyond the crack-tip bottom, the maximum tension at the top loads, and the maximum compression at the load removals. Accordingly, the positive stress gradient is associated with the first, which favors the hydrogen flux into metal, and the negative one with the other, which causes a retardation effect on diffusion. To this end, just the contribution of these compressive stresses is expected to be essential for the near tip hydrogen diffusion, and consequently, for HAC.

Figure 5 displays the distributions of hydrostatic stress and equivalent plastic strain along the crack line beyond the tip as functions of the distance X of the material point from the tip in the undeformed

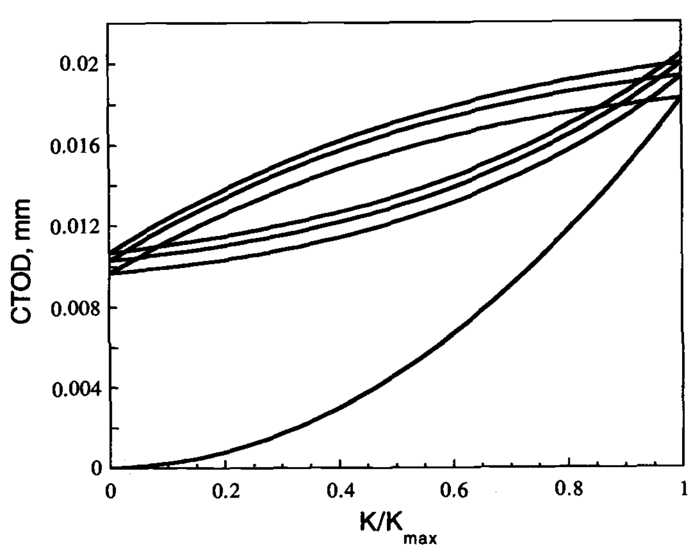

FIG. 3—*Variation of CTOD versus applied SIF value at cyclic loading.*

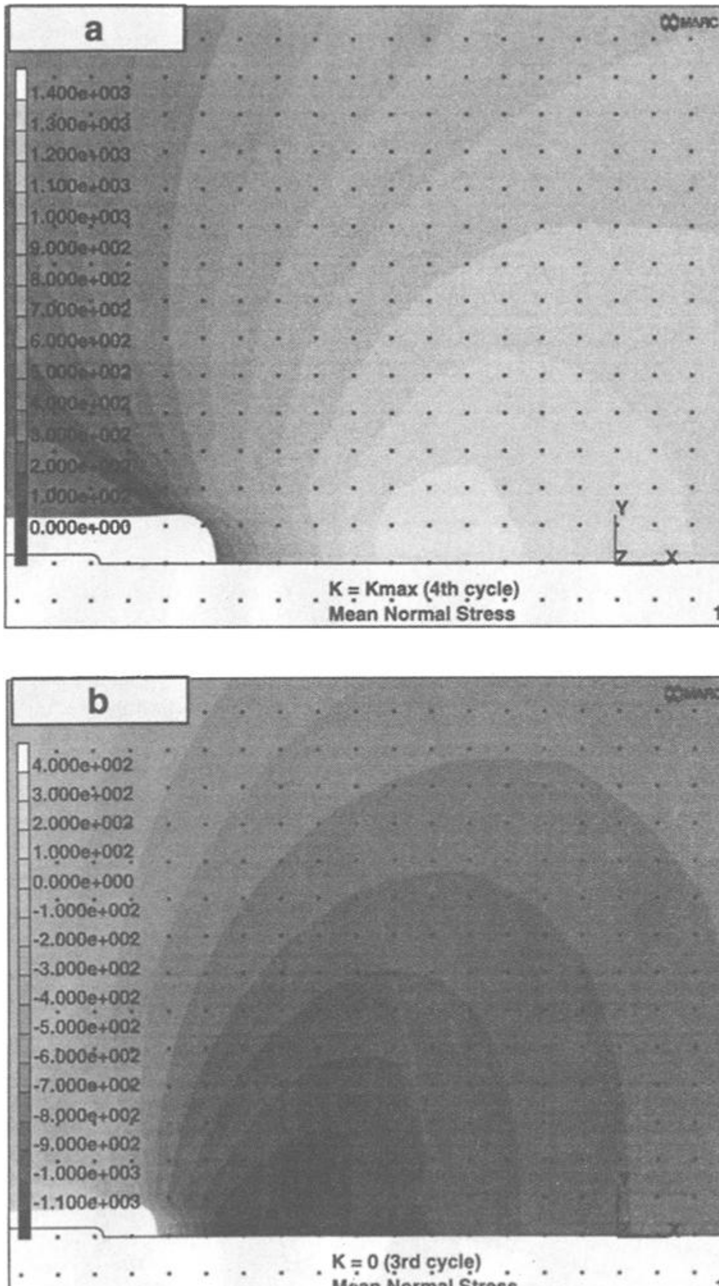

FIG. 4—*Band contours of the hydrostatic stress (MPa) near the crack tip at cyclic loading with* K_{max} *= 60 MPa*$\sqrt{m}$*:* (a) *at maximum load,* $K = K_{max}$*;* (b) *at load removal,* $K = 0$*. Grid spacing is 0.01 mm in both pictures.*

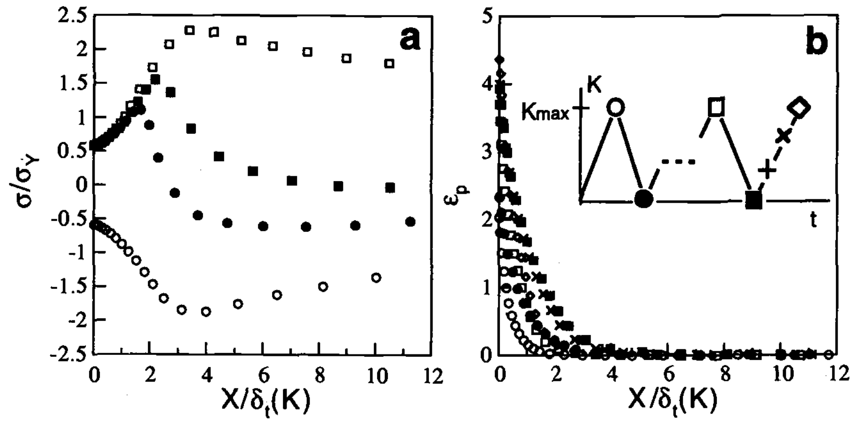

FIG. 5—*Distributions of the hydrostatic stress in* (a) *and the equivalent plastic strain in* (b) *along the crack line beyond the crack tip at consecutive instants of cyclic loading history* (K_{max} = *60* $MPa\sqrt{m}$)*; in the case of strains, these instants are marked in the inserted scheme of the cyclic loading path using the same symbols as their respective data points.*

configuration normalized by the current δ_t value. The steady accumulation of the plastic strain with load cycles is evident. However, hydrostatic stress distributions display only minor variations from cycle to cycle. Their evolutions at certain points $X_1 = 0.9b_0$, $X_2 = 5.3b_0$, $X_3 = 10.9b_0$, $X_4 = 168b_0$, $X_5 = 6 \cdot 10^4 b_0$ along the crack line at a sine-like applied load history are presented in Fig. 6, where the time axis is scaled in arbitrary units, since with the rate independent elastoplastic material model, t serves here merely as a load controlling parameter. The stress histories remote from the tip in the elas-

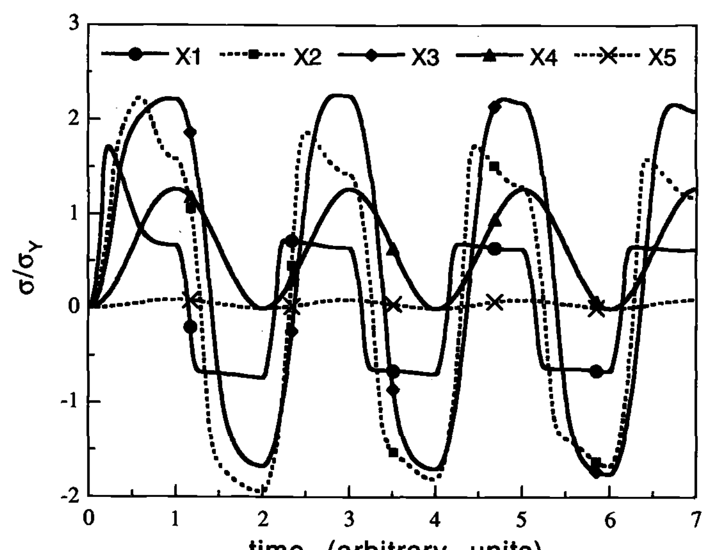

FIG. 6—*Time evolutions of the hydrostatic stress in the points* $X_1 < X_2 < X_3 < X_4 < X_5$ *on the crack line beyond the tip under sine-shape applied load variation* (K_{max} = *60* $MPa\sqrt{m}$).

tic domain (point X_5) and even in the periphery of the plastic zone (point X_4) replicate fairly the sine-shape variation of the applied load. In the closer crack-tip vicinity the affinity of the stress history and the cyclic applied load patterns breaks down. Nevertheless, just after the first load cycle the $\sigma(t)$-variation acquires approximately a stable cyclic regime; that is, it becomes a repetition of nearly the same more or less rectangular shape within each subsequent loading cycle. These patterns are rather insensitive to the amplitude of applied loading, i.e., to K_{max}. The strain evolutions are different: they follow a climbing path representing plastic strain accumulation with the rates depending strongly on K_{max}. This was confirmed in a series of calculations up to ten loading cycles. If we focus on the effect of stress on the near-tip hydrogen diffusion, which is believed in many cases to be of major importance [*9,10,12*], establishing a cyclically stable mode of stress variation near the crack tip greatly facilitates modeling of the effect of the fatigue crack closure stresses in HAC since it allows using the residual stress field from the fatigue loading simulation limited to a very few cycles.

Hydrogen Diffusion at Stationary Stress Field

At this moment, only the effect of stress on the near-tip hydrogen diffusion is addressed, and the plastic strain-dependent terms in the diffusion Eq 9 and in its finite element implementation (13–16) are not taken into account. The system is considered at a temperature of 293 K and zero initial concentration of hydrogen in the metal. With the boundary condition (10), calculations may be performed for an arbitrary environmental hydrogen activity characterized by the equilibrium concentration C_0, obtaining as the result the desired concentration C normalized by C_0. Relevant hydrogen-related material parameters are taken typical for the same kind of steel as in the above described stress-strain analysis [*3,4,9,10,31*]: $D = 10^{-13}$ m^2/s and $V_H = 2$ cm^3/mol. It should be noted that measurements of D for nominally the same material at such a low temperature manifest inordinate scatter of data being quite sensitive to variations of the microstructure, cold drawing (plastic strains), etc. The chosen value is some average estimation for alpha-iron and corresponding steels at $T = 293$ K, for which reported values cover, roughly, the range from 10^{-15} m^2/s [*3*] to 10^{-8} m^2/s [*4*]. However, a particular value of D is of minor importance for the performed simulations taking into account the similarity criterion for diffusion equations being $\tau = Dt/L^2$, where L is any of the characteristic sizes (distances) for a particular problem [*8,9,11*]. This means that concentration solutions are invariant in terms of dimensionless time τ, and so the obtained solutions are valid for any other value D^* of the diffusion coefficient with the only precaution that the time t and, correspondingly, the loading rates are properly scaled with the factor of D^*/D.

Elucidation of hydrogen diffusion under a stationary stress field is relevant to HAC under sustained load, and in particular, provides insight into the items of the evaluation of the threshold SIF K_{th}. Besides, the data on diffusion modeling under sustained load will serve further as a reference to clarify the role of the pre-HAC loading histories. In the diffusion simulations, the reference value of SIF was taken as $K_R = 60$ MPa$\sqrt{\text{m}}$. This value is relevant to the range where HAC can proceed in materials of the type being considered [*3,27,32*]. In particular, it may serve as a candidate value for the HAC threshold K_{th}.

Simulations of stress-driven hydrogen diffusion were performed using the data from the previously described elastoplastic modeling with MARC finite element code. As a first approach, the finite element implementation for diffusion was accomplished in a one-dimensional approximation, i.e., along the crack line where finite element discretization, material deformations and stress distribution corresponded to those of the two-dimensional mechanical problem. Calculations were performed for the time domain up to about 2.5×10^6 s to approach nearly the equilibrium hydrogen distribution.

Figure 7 displays concentration distributions at different diffusion times. In addition, the finite element results are compared with the simple approximated closed from solution [*11*] which was obtained for stationary stress fields using the Laplace transform technique [*31*] as the long-time asymp-

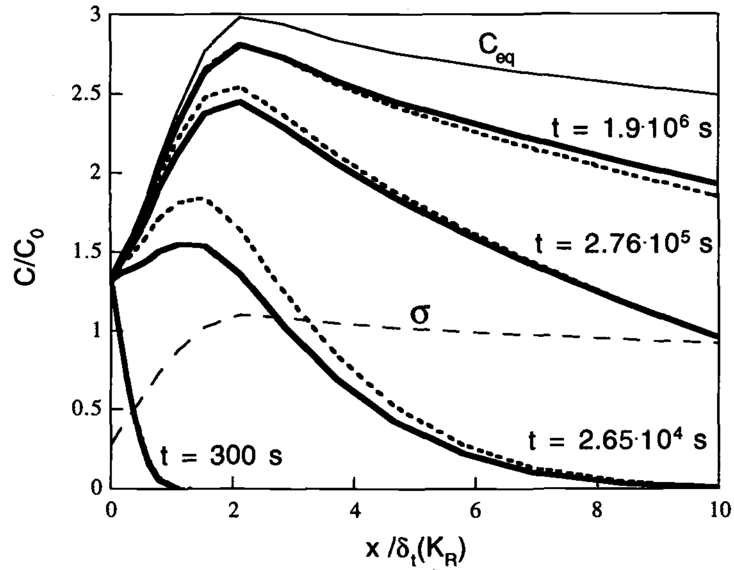

FIG. 7—*Concentration distributions along the crack line beyond the tip at different times under sustained load with* K_R *= 60 MPa*$\sqrt{m}$ *according to the finite element solution (bold solid lines) accompanied with corresponding asymptotic one (18) (bold dotted lines). The profile of the equilibrium concentration* C_{eq} *and the shape of the hydrostatic stress distribution (arbitrary units) are presented for reference by the thin solid and broken lines, respectively.*

totic behavior in the form:

$$
\begin{aligned}
C_a(x,t) &= C_0 \exp\left(\frac{V_H}{RT}\sigma(x)\right) \operatorname{erfc}\left(\frac{x}{2\sqrt{Dt}}\right) \\
&= C_{eq}(x)\operatorname{erfc}\left(\frac{x}{2\sqrt{Dt}}\right)
\end{aligned}
\tag{18}
$$

where the subindex a indicates both the approximate and asymptotic kind of the solution. In Fig. 7, the shape of the hydrostatic stress distribution is shown together with the corresponding equilibrium concentration $C_{eq}(x)$ according to expression (11). This latter marks the accessible upper bound for concentration $C(x,t)$. Here x represents the diffusion distance being the coordinate of material point X in the deformed state. In Fig. 8 the time variation of concentration is presented for the material points being the focus of the major interest with respect to HAC: the material point $X_{m\sigma}$ (corresponding deformed distance $x_{m\sigma} \approx 2.3\delta_t$) where the maximum tensile stresses are attained at the reference SIF level K_R, and the point $X_{m\varepsilon} \approx \delta_t$ which belongs to the zone of steeply increasing plastic strain. These points are considered as the probable locations of microfracture nuclei associated, respectively, with the type of dominating fracture micromechanism: stress- or strain-controlled rupture.

Reported results are relevant to evaluation of the HAC threshold K_{th}. Common K_{th} testing consists of trying a series of sustained SIF values if crack growth does not start within a certain waiting time t_B [*33*]. This time base should be properly fixed to ensure test validity, i.e., that at this SIF the crack will not start to grow at any $t > t_B$ (with a reasonable statistical confidence). It is usually

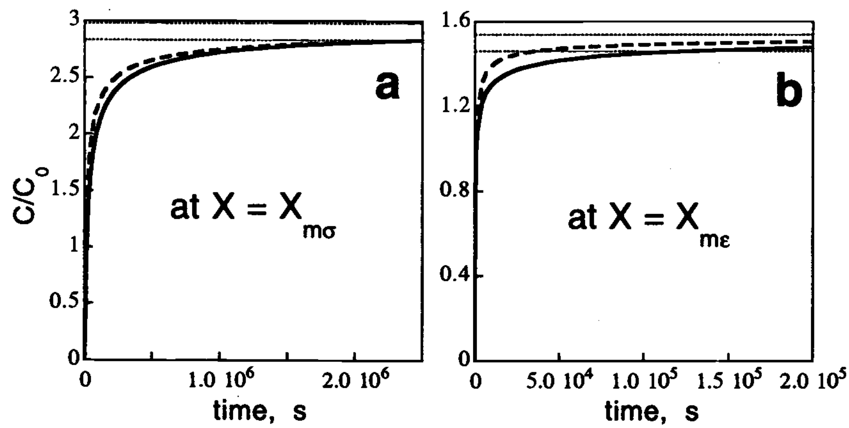

FIG. 8—*Time evolutions of concentration according to the finite element solution (solid curves) and asymptotic one (18) (broken curves) at sustained load:* (a) *in the points of maximum tensile stress* $X_{m\sigma}$; (b) *in the finite plastic strain region at* $X_{m\varepsilon}$. *Horizontal lines mark the 5%-tolerance band near corresponding equilibrium concentration levels* C_{eq} *(*$X_{m\sigma,m\varepsilon}$*).*

chosen on the basis of previous experience and application-related considerations [*33*]. The diffusion concept of HAC suggests that to render K_{th} valid, the value t_B must be about the diffusion time t_{ss} to attain the equilibrium steady-state concentration—the thermodynamic maximum—at the point of interest with reasonable accuracy before fulfillment of the local fracture criterion (4), i.e., to reach $C(x_c,t_{ss}) \approx C_{eq}(x_c)$. With the tolerance level fixed, for definiteness, as 95% of the steady-state value C_{eq}, the long-time asymptote (18) provides the estimate $Dt_{ss}/x_c^2 \approx 130$. The plots in Fig. 8 confirm that the rough asymptotic solution (18) and the numerical one are rather close to each other. For the point $X_{m\sigma}$ being the maximum tensile stress location, the corresponding curves practically coincide within the 5%-width scatterband near the equilibrium level $C_{eq}(x_{m\sigma})$. For the critical stress criterion of local rupture when $x_c \approx x_{m\sigma}$, this estimate substantiates the K_{th}-testing base as $t_B = t_{ss} \geq 130x_c^2/D$. With material parameters taken in the modeling, this test base is about 2.4×10^6 s. For the case of strain-controlled crack tip fracture with $x_c \approx x_{m\varepsilon}$, the numerical solution evolves slower than the asymptotic one and the estimates for t_{ss} and t_B must be stiffened regarding the numerical factor to about $t_B \approx 440x_c^2/D$. However, due to the shorter diffusion path x_c in this case, the fair estimate in absolute values is $t_B \approx 1.2 \times 10^5$ s.

With respect to the effects of the fatigue precracking on K_{th}-tests, which have been reported to cause excessive ambiguity of experimentally measured data [*16*], they cannot be associated with the role of stress on hydrogen diffusion under sustained load at $K \geq K_{max}$, since the near-tip stress distributions acquire with reasonable accuracy the unique self-similar shape presented by expressions (3) and shown in Fig. 5*a*. Apparently, these uncertainties of the K_{th}-testing are due to the plastic strain influence on either the fulfillment of the rupture criterion (4) near the tip, or on the accumulation of hydrogen there. To establish the limits of the fatigue precracking influence on HAC evaluation, further study of the role of plastic strain accumulation in the finite deformations zone beyond the tip would be helpful.

Hydrogen Transportation at Rising Load after Fatigue Precracking

This series of diffusion simulations reveals the influence of crack closure stresses on HAC. It is relevant to the other mode of experimental evaluation of HAC for materials certification and life assessment. In particular, it is tempting to reduce K_{th}-testing expenses omitting a series of n tests with constant candidate threshold SIF values $K_Q^{(1)}, \ldots, K_Q^{(n)}$ by conducting a single rising-load experiment, e.g., at a constant SIF rate dK/dt, to pass the whole SIF range up to detecting a crack growth initiation at some SIF K_R which could be the desired HAC threshold. To be the adequate threshold, it would seem necessary that the concentration at the time $t_R = K_R/(dK/dt)$ reach the steady-state level C_{eq} (K_R, x_c) with the same reasonable accuracy as in a valid sustained load test. Rising-load tests are performed from zero initial load under hydrogen effect after fatigue precracking in an inert environment. Thus, metal-hydrogen interaction proceeds from the residual stress-strain state near the crack closed after precracking. Controlling variables in this case are the parameters of fatigue cycling and of load dynamics in the HAC-test, K_{max} and dK/dt in this study.

The calculations were performed with the same reference SIF $K_R = 60$ MPa$\sqrt{\text{m}}$ ("candidate threshold") and $K_{max} = 0.5K_R$ which was suggested as the proper precracking limit [*34*]. Several SIF rates dK/dt between 0.015 and 15 MPa$\sqrt{\text{m}}$/min were taken to cover the range of values used in experiments [*32*]. Accounting for the cyclic stability of the near-tip stress field, diffusion was considered at a rising load starting from the compressive stresses corresponding to the closed crack state after three load/unload cycles. Load was increased until the SIF attained K_R, and then was held fixed.

Concentration distributions at different diffusion times for $dK/dt = 1.5$ MPa$\sqrt{\text{m}}$/min are shown in Fig. 9 together with corresponding hydrostatic stress profiles. Concentration evolution patterns in the material points of large plastic strains and maximum tensile stresses, i.e, at $x_{m\varepsilon}(K_R)$ and $x_{m\sigma}(K_R)$ respectively, are plotted in Fig. 10 for loading rates of 0.15 and 1.5 MPa$\sqrt{\text{m}}$/min. For comparison, the $\sigma(t)$-patterns and the concentration values C_a corresponding to the instantaneous stress values $\sigma(x_{m\varepsilon,m\sigma}, t)$ according to approximate formula (18) are also presented. Note that here the expression (18) with $\sigma = \sigma(t)$ can no longer be considered even as a long-time asymptotic solution, but only as a formal approximation with no justification. However, for slower loading and rather short diffusion depth $x_{m\varepsilon}$, both analytical forms (11) and (18), which give respectively the exact equilibrium C_{eq} and

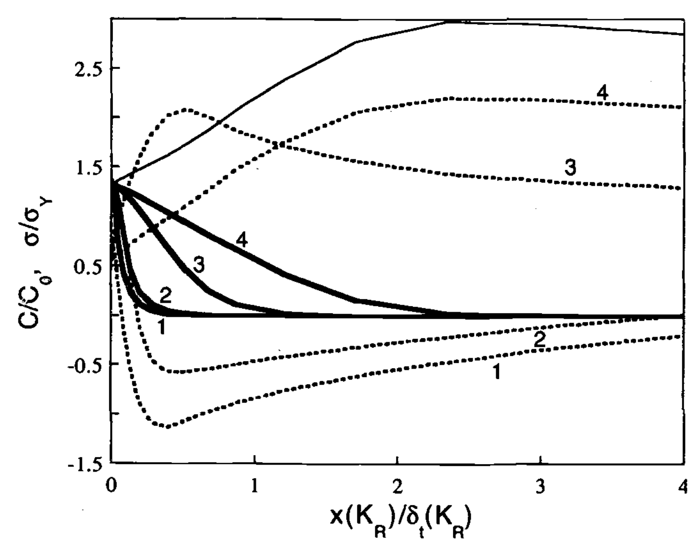

FIG. 9—*Concentration (bold solid lines) and corresponding hydrostatic stress (dotted lines) distributions along the crack line beyond the tip at different times under dynamic rising load with* dK/dt *= 1.5 MPa$\sqrt{m}$/min according to the finite element solution. Thin solid line shows the equilibrium concentration distribution at* t $\rightarrow \infty$*. Curve numbers 1 to 4 refer to times 180, 300, 1000 and* t_R *= 2400 s, respectively.*

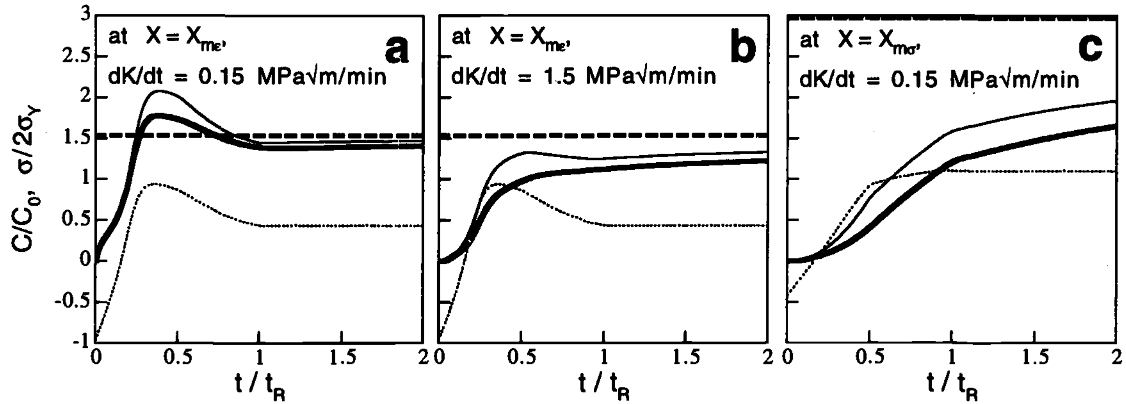

FIG. 10—*Time evolutions of concentration during rising load obtained from the finite element solution (bold solid curves) and of the approximate values* C_a *corresponding to the instantaneous hydrostatic stress distribution* $\sigma(x,t)$ *according to (18) (thin solid curves):* (a) *and* (b) *in the severe plastic strains region at* $X_{m\varepsilon}$ *at loading rates* dK/dt *of 0.15 and 1.5 MPa*$\sqrt{m}$*/min, respectively;* (c) *in the location* $X_{m\sigma}$ *of the maximum tensile stress at* dK/dt = *0.15 MPa*$\sqrt{m}$*/min (at* dK/dt = *1.5 MPa*$\sqrt{m}$*/min the concentration is negligible there). Thin dotted curves show hydrostatic stress evolutions, and bold broken horizontal lines mark the levels of* C_{eq} *in respective locations under sustained load at* $K = K_R$.

approximate C_a concentrations for the instantaneous stress $\sigma(t)$, go closely to the finite element solution. That is, in the very-near-tip domain, diffusion under dynamic loading nearly maintains the equilibrium hydrogen saturation for the instantaneous stress state. In the relatively remote point $x_{m\sigma}$ the delay of hydrogenation in comparison with load elevation is notable even at the slowest simulated loading.

Let us consider these data as a modeling of the rising-load test to determine K_{th}, and identify the reference SIF K_R as the apparent HAC threshold already measured using a sustained-load method simulated in the previous section. This latter threshold status corresponds to the equilibrium concentration C_{eq}—the thermodynamically admissible maximum value—in a critical material point x_c. Under rising load, if the critical concentration (1) is stress controlled, the critical event is associated with the maximum tensile stress over a certain microstructural scale, and local rupture occurs at $x_c = x_{m\sigma}(K_R)$ in the same manner as in the sustained-load case. Because of the slowness of diffusion, to provide there sufficient concentration at the moment of approaching the critical SIF, K_R in this case, the loading must be even slower than that tried in our simulations (Fig. 10*c*), and the slower the better to reproduce the result of the sustained load test. The reasonable loading rate here may be estimated so that the time $t_R = K_R/(dK/dt)$ necessary to attain the candidate threshold K_R is close to t_{ss} for the stationary load situation.

However, if the fracture micromechanism and corresponding critical concentration (1) are predominantly controlled or markedly influenced by plastic strain, the situation turns out to be less trivial. At slow loading rate (Fig. 10*a*) concentration evolution in the large-strain zone $x \lesssim x_{m\varepsilon}$ follows the non-monotonic $\sigma(t)$-history and depends on the crack closure; namely, diffusion starts at the residual compressive stress distribution near the crack tip after fatigue precracking. Correspondingly, during moderate-rate rising load when diffusion is able to follow the evolution of stress, the concentration in the intensively strained region may temporarily exceed the level attainable there in the sustained load test. This was observed in simulations with dK/dt up to 0.15 MPa$\sqrt{\text{m}}$/min, and may be expected at somewhat higher rates, but it disappears at 1.5 MPa$\sqrt{\text{m}}$/min (Fig. 10*b*) when stress evolution becomes too fast compared with diffusion, so that the stress peak can no longer produce and drag the concentration peak. This means that the same fracture criterion (4) may be satisfied there earlier than in the sustained load case, at times of the order of 10^4 s in the considered sample situation. What is more important, because of these temporal (and early) concentration peaks, depending on a particular combination of stress and strain factors in local fracture, which define the critical concentration (1), local rupture and crack advance may occur at SIF below the apparent threshold evaluated from the sustained-load test.

For the moment, lack of experimental data does not allow one to perform comparisons and verify the simulation results. This modeling rather suggests design of further critical experiments to test the diffusion theory of HAC, estimate rupture sites location, etc. Nevertheless, some experimental data [*35–37*] may be mentioned as qualitatively conforming to the modeling in that the dynamic rising-loading tests may give more conservative estimations of SIF for the initiation of HAC than those under sustained (zero-rate) load.

Conclusions

The opening-closing behavior of a crack and its effects on the stress-assisted hydrogen diffusion near a stationary crack tip in metals were studied using large-deformation finite element analysis with relevance to hydrogen-assisted cracking (HAC).

In the large-deformation elastoplastic solutions, the complete geometrical closure up to the contact of crack faces near the tip was not detected. Cyclic load removals are substantial with respect to the near-tip stress distributions, thus causing high compressive stresses beyond the tip. Under zero-to-tension cyclic loading, the very-near-tip stress evolutions follow the stable cyclic tension-compression pattern.

Modeling of stress-assisted hydrogen diffusion was performed for sustained and rising loading conditions preceded by fatigue precracking with relevance to experimental techniques of HAC threshold evaluation.

Under sustained load, the crack closure stresses caused by precracking have no influence on hydrogen accumulation and HAC initiation at reference (tried) SIF values $K_R > K_{max}$, since stress distributions are then nearly insensitive to the previous crack history. The estimate was derived for the proper K_{th}-testing time base t_B to approach the threshold state (the steady-state concentration).

Under rising load applied following load removal after cycling, the crack closure stresses may be important for hydrogen diffusion towards rupture sites. At slow loading rates, the stress-strain state and hydrogen delivery may produce temporal hydrogen oversaturation peaks that attain a critical concentration level closer to the crack tip and earlier than in the sustained-load case in otherwise similar circumstances. This means that the sustained-load tests may yield excessively optimistic overestimations of the HAC thresholds of materials in comparison with slow rising-load tests.

Further modeling of the near-tip stress-strain assisted hydrogen transport in metals involving consideration of particular stress-and-strain driven mechanisms of local rupture (and corresponding criteria) would be helpful in explaining and predicting various features and manifestations of hydrogen-assisted fracture.

Acknowledgments

This work was funded by the Spanish DGICYT (Grant UE94-001) and Xunta de Galicia (Grants XUGA 11801A93 and XUGA 11801B95). One of the authors (VKh) is especially indebted to the Spanish Office of NATO (Scientific Affairs Division) and Xunta de Galicia, as well as to DGICYT (Grant SAB95-0122) for supporting his stays, respectively, as a visiting scientist and sabbatic professor at the University of La Coruña.

References

[1] Smialowski, M., *Hydrogen in Steel*, Pergamon Press, Oxford, U.K., 1962.

[2] Hirth, J. P. and Johnson, H. H., "Hydrogen Problems in Energy Related Technology," *Corrosion*, Vol. 32, No. 1, 1976, pp. 3–15.

[3] Nelson, H. G., "Hydrogen Embrittlement," *Treatise on Materials Science and Technology. Vol. 25: Embrittlement of Engineering Alloys*, C. L. Briant and S. K. Banerji, Eds., Academic Press, New York, 1983, pp. 275–359.

[4] Hirth, J. P., "Effects of Hydrogen on the Properties of Iron and Steel," *Metallurgical Transactions (A)*, Vol. 11, 1980, pp. 861–890.

[5] *Hydrogen Degradation of Ferrous Alloys*, O. A. Onyewuenyi, J. P. Hirth, and M. Smialowski, Eds., Noyes Publ., Park Ridge, Il., 1985.

[6] Williams, D. P., "A New Criterion for Failure of Materials by Environment-induced Cracking," *International Journal of Fracture*, Vol. 9, 1973, pp. 63–74.

[7] Gangloff, R. P., "Crack Tip Modelling of Hydrogen Environment Embrittlement: Application to Fracture Mechanics Life Prediction," *Materials Science and Engineering*, Vol. A103, 1988, pp. 157–166.

[8] Panasyuk, V. and Kharin, V., "The Influence of Hydrogenating Environments on Crack Propagation in Metals," *Environment Assisted Fatigue*, P. Scott and R. A. Cottis, Eds., Mechanical Engineering Publications, London, 1990, pp. 123–144.

[9] van Leeuwen, H.-P., "The Kinetics of Hydrogen Embrittlement: A Quantitative Diffusion Model," *Engineering Fracture Mechanics*, Vol. 6, 1974, pp. 141–161.

[10] Gerberich, W. W., Chen, Y. T. and John, C. St., "A Short-time Diffusion Correlation for Hydrogen-induced Crack Growth Kinetics," *Metallurgical Transactions (A)*, Vol. 6, 1975, pp. 1485–1498.

[11] Toribio, J. and Kharin, V., "*K*-dominance Condition in Hydrogen Assisted Cracking: The Role of the Far Field," *Fatigue and Fracture of Engineering Materials and Structures*, 1997, Vol. 20, No. 5, pp. 729–745.

[12] Toribio, J. and Kharin, V., "Evaluation of Hydrogen Assisted Cracking: The Meaning and Significance of the Fracture Mechanics Approach," *Nuclear Engineering and Design*, Vol. 182, 1998, pp. 149–163.

[13] Kharin, V. S., "Crack Growth in Deformed Metals under the Action of Hydrogen," *Soviet Materials Science*, Vol. 23, 1987, pp. 348–357.

[14] Sofronis, P. and McMeeking, R. M., "Numerical Analysis of Hydrogen Transport Near a Blunting Crack Tip," *Journal of the Mechanics and Physics of Solids*, Vol. 37, 1989, pp. 317–350.

[15] Itatani, M., Miyoshi, Y. and Ogura, K. C., "A Numerical Analysis of Hydrogen Concentration at the Crack Tip in Austenitic Stainless Steel," *Journal of the Society of Materials Science Japan*, Vol. 40, 1979, pp. 1079–1085.

[16] Kharin, V. and Toribio, J., "On the Intrinsic Character of the Crack Growth Kinetics Curve," *Anales de Mecánica de la Fractura*, Vol. 13, 1996, pp. 293–300.

[17] McMeeking, R. M., "Finite Deformation Analysis of Crack Tip Opening in Elastic-Plastic Materials and Implications for Fracture," *Journal of the Mechanics and Physics of Solids*, Vol. 25, 1977, pp. 357–381.

[18] Kitagawa, H. and Komeda, S., "Finite Element Analysis of Crack-Tip Opening," *Computational Mechanics '86: Theory and Applications*, Vol. V, Tokyo, 1986, pp. 157–162.

[19] Gortemaker, P. C. M., de Pater, C. and Spiering, R. M. E. J., "Near-crack Tip Finite Strain Analysis," *Advances in Fracture Research (ICF5)*, Vol. 1, Pergamon Press, Oxford, U.K., 1981, pp. 151–160.

[20] McClung, R. C. and Sehitoglu, H., "On the Finite Element Analysis of Fatigue Crack Closure—1. Basic Modeling Issues—2. Numerical Results," *Engineering Fracture Mechanics*, Vol. 33, 1989, pp. 237–272.

[21] McClung, R. C., Thacker, B. H., and Roy, S., "Finite Element Visualisation of Fatigue Crack Closure in Plane Stress and Plane Strain," *International Journal of Fracture*, Vol. 50, 1991, pp. 27–49.

[22] Panasyuk, V. V., Andreikiv, A. Ye. and Kharin, V. S., "Model of Crack Growth in Deformed Metals under the Action of Hydrogen," *Soviet Materials Science*, Vol. 23, 1987, pp. 111–124.

[23] Kanninen, M. F. and Popelar, C. H., *Advanced Fracture Mechanics*, Oxford University Press, New York, 1985.

[24] Perng, T. P. and Altstetter, C. J., "Effects of Deformation on Hydrogen Permeation in Austenitic Stainless Steels," *Acta Metallurgica*, Vol. 34, 1986, pp. 1771–1781.

[25] Kronshtal, O. V. and Kharin, V. S., "Influence of Material Inhomogeneity and Variation of Temperature on Hydrogen Diffusion as a Risk Factor of Enhancement of Metals Hydrogen Degradation," *Soviet Materials Science*, Vol. 28, 1992, pp. 475–486.

[26] Malvern, L. E., *Introduction to the Mechanics of a Continuous Medium*, Prentice-Hall, Englewood Cliffs, NJ, 1969.

[27] Loginow, A. W. and Phelps, E. H., "Steels for Seamless Hydrogen Pressure Vessels," *Corrosion*, Vol. 31, 1975, pp. 404–412.

[28] Savruk, M. P., *Stress Intensity Factors in Solids with Cracks*, Naukova Dumka, Kiev, 1988 (in Russian).

[29] *MARC User Information*, Marc Analysis Research Corporation, Palo Alto, CA, 1994.

[30] Zienkiewicz, O. C. and Morgan, K., *Finite Elements and Approximation*, John Wiley and Sons, NY, 1983.

[31] Kharin, V. S., *Crack Growth in Metals Under Sustained Load and Hydrogen Effect*, Ph.D. Thesis, Karpenko Physico-Mechanical Institute, Lvov, 1984 (in Russian).

[32] Mayville, R. A., Warren, T. J., and Hilton, P. D., "Determination of the Lading Rate Needed to Obtain Environmentally Assisted Cracking in Rising Load Tests," *Journal of Testing and Evaluation*, Vol. 17, No. 4, 1989, pp. 203–211.

[33] ISO 7539-6, *Corrosion of Metals and Alloys—Stress Corrosion Testing—Pt. 6: Preparation and Use of Pre-Cracked Specimens*, 1989.

[34] Judy, R. W., Jr., King, W. E., Jr., Hauser II, J. A., and Crooker, T. W., "Influence of Experimental Variables on the Measurement of Stress Corrosion Cracking Properties of High-Strength Steels," *Environmentally Assisted Cracking: Science and Engineering, ASTM STP 1049*, W. B. Lisagor, T. W. Crooker, and B. N. Leis, Eds., American Society for Testing and Materials, Philadelphia, 1990, pp. 410–422.

[35] Ford, F. P., "Stress Corrosion Cracking of Iron-base Alloys in Aqueous Environments," *Treatise on Materials Science and Technology. Vol. 25: Embrittlement of Engineering Alloys*, C. L. Briant and S. K. Banerji, Eds., Academic Press, NY, 1983, pp. 235–274.

[36] Dietzel, W. and Pfuff, M., "The Effect of Deformation Rates on Hydrogen Embrittlement," *Hydrogen Effects in Materials*, A. W. Thompson and N. R. Moody, Eds., TMS, 1996, pp. 303–311.

[37] Turnbull, A., "Current Issues in Hydrogen Embrittlement," *Fracture From Defects. Proceedings of the 12th European Conference on Fracture*, M. W. Brown, E. R. de los Rios, and K. J. Miller, Eds., EMAS, 1998, pp. 1097–1102.

A. U. de Koning,[1] H. J. ten Hoeve,[1] and T. K. Henriksen[2]

Description of Crack Growth Using the Strip-Yield Model for Computation of Crack Opening Loads, Crack Tip Stretch, and Strain Rates

REFERENCE: de Koning, A. U., ten Hoeve, H. J., and Henriksen, T. K., **"Description of Crack Growth Using the Strip-Yield Model for Computation of Crack Opening Loads, Crack Tip Stretch, and Strain Rates,"** *Advances in Fatigue Crack Closure Measurement and Analysis: Second Volume, ASTM STP 1343,* R. C. McClung and J. C. Newman, Jr., Eds., American Society for Testing and Materials, West Conshohocken, PA, 1999, pp. 459–474.

ABSTRACT: Nowadays, application of the strip-yield model for computation of crack opening load levels is well known. In this paper the incremental formulation of a fatigue crack growth law is used to demonstrate the role of the crack opening load level in time-independent fatigue crack growth. Less known is the ability of the strip-yield model to define the strain rate at the crack tip. A threshold level $\dot{\varepsilon}_{th}$ of this strain rate is introduced and used to formulate a criterion for initiation of time-dependent accelerated fatigue crack growth. This process is called corrosion fatigue. To account for effects of environment and frequency on the crack growth rate a time-dependent part is added to the incremental fatigue crack growth law. The resulting incremental crack growth equation is integrated to obtain the crack growth rate for a load cycle.

The model discussed in this paper is a mechanical model. Physical aspects other than strain rate, loading frequency and load wave shape are not modeled in an explicit way. Hence, the model is valid for specific environment/base metal combinations. However, in consideration of the effects of small variations of environment, temperature, and other variables on the crack growth rates, it can be used as a reference solution.

The fatigue crack growth model has been implemented in the NASGRO (ESACRACK) software. The time-dependent part is still subject to further evaluation.

KEYWORDS: crack opening loads, crack tip stretch, strain rates, crack growth, fatigue crack growth

For over two decades models of fatigue crack growth have been based on empirical laws that relate the amount of crack growth in a load cycle to the stress intensity factor range $\Delta K = K_{max} - K_{min}$ or to the effective [*1*] range $\Delta K_{eff} = K_{max} - K_{op}$. Correction factors were included for near-threshold behavior and accelerated growth in the high K regime.

From a physical point of view such crack growth laws are speculative because crack growth and plastic deformation are irreversible processes that depend on the loading history. By nature, such processes must be described in an incremental way and properly integrated to obtain the amount of crack growth for a load cycle or the part of a load cycle for which the incremental description is valid [*2,3*]. Clearly, such a new description allows that a distinction be made between the part of a load range where secondary (cyclic) plastic flow is observed and the part where primary plastic flow develops under monotonic increasing loads. For each of these domains an incremental crack growth law can

[1]National Aerospace Laboratory (NLR), NOP, The Netherlands.
[2]European Space Agency (ESA), ESTEC, Noordwijk, The Netherlands.

be formulated. Then, after integration over the appropriate load ranges, the contributions to the crack growth rate for the load cycle under consideration are obtained. In a similar way "range pair" (or "rainflow") principles may be used to select the appropriate load ranges [*4*]. In addition, the incremental formulation allows the introduction of other terms representing time and/or environment-dependent crack growth [*5*].

In this paper the strip-yield model is applied for computation of crack opening loads, crack tip stretches and strain rates. In the open literature [*6,7*] and other documents [*8,9*] the strip-yield model is discussed extensively and, recently, results obtained using different versions of the model (the NASA/FASTRAN and the ESA/NLR versions) were compared and it was concluded that the models predict the same crack opening behavior if the constraint effects on yielding are modeled in the same way. For this reason the strip-yield model itself is not discussed in detail. Instead, the description of the strip-yield model is limited to the yield limits and the equations used in this paper.

The definitions of crack size c, crack tip stretch δ, as well as the assumptions made to account for differences in the yield limit in tension $\bar{\sigma}_t$ compared with the yield limit in compression $\bar{\sigma}_c$, are shown in Fig. 1. The introduction of a separate parameter $\bar{\sigma}_c$ allows for some form of description of different constraint, crack tip geometry and the effect of cold work on yielding in compression. The material in the thin Dugdale strip is assumed to behave in a rigid, ideal plastic manner and elastic deformations are assumed to be absent in the strip.

The assumed yield limits $\bar{\sigma}_t$ and $\bar{\sigma}_c$ can be introduced in the strip-yield model. The result can be used to derive some simple analytical expressions for the crack tip stretch δ. For monotonic increas-

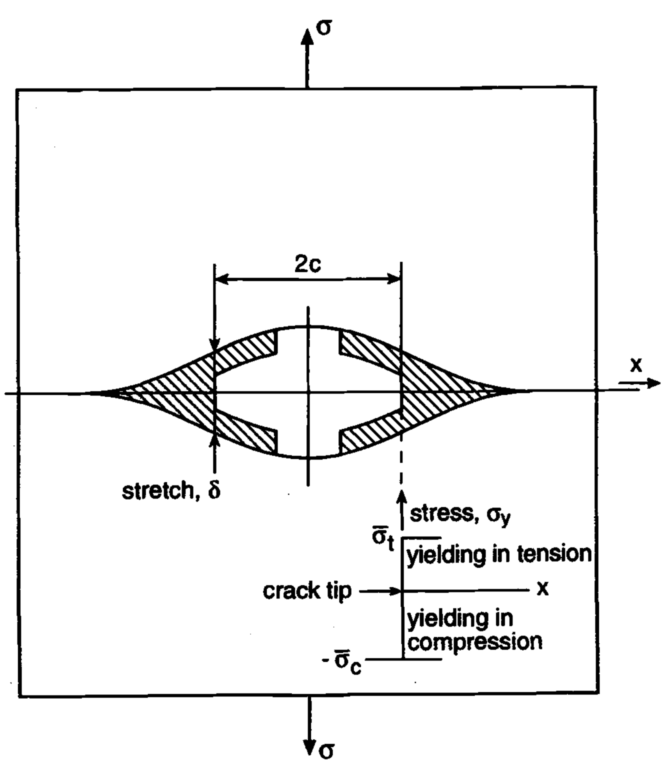

FIG. 1—*Strip-yield model with different yield limits in tension and in compression.*

ing loads it can be derived, as a first-order approximation and for small-scale yielding, that

$$\delta = K^2/E\overline{\sigma}_t \tag{1}$$

where K denotes the stress intensity factor and E is Young's modulus. For the loading parts of a constant-amplitude load sequence we can derive in a similar way

$$\underbrace{\delta = K_{max}^2/E\overline{\sigma}_t}_{\substack{\text{loading to} \\ K_{max}}} - \underbrace{(K_{max} - K_{op})^2/E(\overline{\sigma}_t + \overline{\sigma}_c)}_{\substack{\text{unloading from} \\ K_{max} \to K_{op}}} + \underbrace{(K - K_{op})^2/E(\overline{\sigma}_t + \overline{\sigma}_c)}_{\substack{\text{loading from} \\ K_{op} \to K \\ K_{op} \leq K \leq K_{max}}} \tag{2}$$

where K_{op} is the stress intensity factor at the crack opening load level. It is seen that for $K = K_{max}$ this equation gives the same stretch as Eq 1. Below K_{op} the plastic stretch increment associated with unloading is assumed to be absent. Also the effect of crack closure during unloading in the regime $K_{max} \to K_{op}$ is ignored.

Equation 2 will be used to derive a simple expression for the strain rate. More accurate results can be obtained by application of the numerical discretized strip-yield model. Which one of both methods is used for computation of the crack tip stretch depends on the efficiency and accuracy required in the predicted results.

Crack Opening and Threshold Effects Under Fatigue Loading Conditions

Usually, fatigue crack growth is assumed to occur in the upward part of a load cycle. In the upward part different regimes can be distinguished, depending on the loading history and the state of opening of the crack. To illustrate these domains in Fig. 2 the loading path is shown in a stress intensity factor, K, versus crack size, c, plot. The different loading regimes are indicated and discussed one after another [5].

Closed Crack Regime 1, $K_{min} \leq K < K_{op}$

Starting at the minimum intensity factor K_{min} the load is increased until the crack opening level K_{op} is attained. In this regime 1, characterized by $K_{min} \leq K < K_{op}$, the crack is at least partly closed and the contact areas on the crack surfaces decrease when the applied load is increased. Although the stress intensity factors in this regime are calculated assuming the presence of the crack, it is clear that the effective loading of the crack tip region is very small and no crack growth is assumed in this regime.

Opened Crack but No Growth Regime 2, $K_{op} \leq K < K_{op} + \delta K_{th}$

At level K_{op} the crack is fully opened, but it takes another increase by δK_{th} to initiate crack growth. Obviously, some crack tip blunting occurs in this regime. Models and empirical equations for computation of values for K_{op} and δK_{th} are discussed in Ref *5*.

Fatigue Crack Growth in Regime 3, $K_{op} + \delta K_{th} \leq K < K_*$

Upon a further increase of the applied load, crack growth is initiated when the stress intensity factor K exceeds the level $K_{op} + \delta K_{th}$. In this regime 3 plastic deformations take place in a relatively small part of the plastic zone created by application of K_{max} in the previous load cycle. At the load level $K = K_*$ primary plastic flow in virgin material reinitiates and the zone of material that actually is loaded to the yield limit is extending beyond the previous plastic zone. The level K_* depends on the

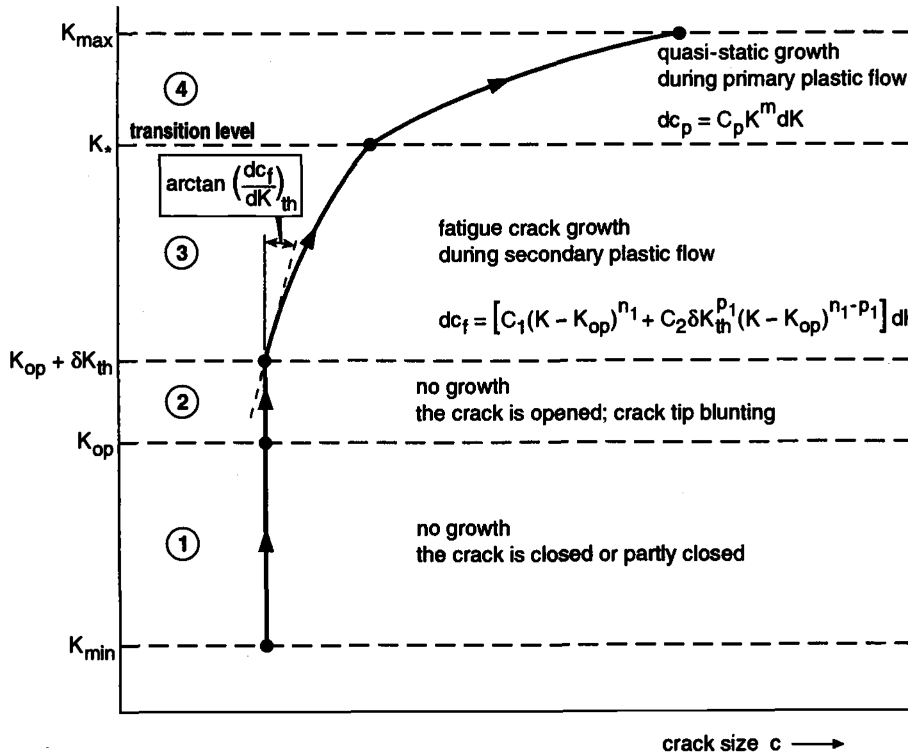

FIG. 2—*Different loading and crack growth regimes in one (half) load cycle.*

amount of crack growth relative to the primary plastic zone size. This transition is characterized by a discrete jump in plastic zone size and a loss of load history effects on the state of deformation. To describe the crack growth behavior in regime 3, corresponding to $K_{op} + \delta K_{th} < K \leq K_*$, the following incremental crack growth law is adopted

$$dc_f = [C_1\,(K - K_{op})^{n_1} + C_2\,\delta K_{th}^{p_1}\,(K - K_{op})^{n_1 - p_1}\,]\,dK \tag{3}$$

where subscript f stands for fatigue.

In this expression the first term on the right-hand side is an incremental form of Elber's law. The second one is added to describe threshold effects, if present. The power $n_1 - p_1$ follows from the requirement that the units of both terms must be the same. Note that C_1, and n_1, are not the same as the traditional Elber parameters C and n ($C_1 = nC$; $n_1 = n - 1$).

At initiation of crack growth, when $K = K_{op} + \delta K_{th}$, it follows that

$$\left(\frac{dc_f}{dK}\right)_{th} = \delta K_{th}^{n_1}(C_1 + C_2) \tag{4}$$

It may be expected that a relation exists between the material parameters C_1 and C_2, the threshold level δK_{th} and the slope of the crack growth curve (see Fig. 2).

In Eq 3 the transition from threshold behavior to the crack growth behavior in the mid-range (Elber) regime is governed by the power p_1 attached to $K - K_{op}$. Values selected for p_1 must guarantee that the transition is smooth and that the slope arctan (dc_f/dK) has the proper value. In order to simplify the equations in this application we use p_1 values satisfying the equation

$$\left(\frac{dc_f}{dK}\right)_{\text{th}} = p_1\, C_1\, \delta K_{\text{th}}^{n_1}/(n_1 + 1) \tag{5}$$

In that case, it follows from Eq 4, that

$$C_2 = C_1 \frac{p_1 - n_1 - 1}{n_1 + 1} \tag{6}$$

To obtain the contribution of regime 3 to the crack growth rate per load cycle $\Delta C_f/\Delta N$ the crack growth law, Eq 3, must be integrated over the range $K_{\text{op}} + \delta K_{\text{th}} \leq K \leq K_*$. It is assumed that the parameters involved (K_*, K_{op}, δK_{th}) are constant during integration. Then, after substitution of Eq 6 and redefinition of the material and threshold parameters, there results

$$\Delta c_f/\Delta N = C(K_* - K_{\text{op}})^n \left[1 - \left(\frac{\delta K_{\text{th}}}{K_* - K_{\text{op}}}\right)^{p_1}\right] \tag{7}$$

where K_* is the level at which the transition from cyclic, secondary, plastic flow to primary plastic flow occurs. In the absence of primary plastic flow ($K_* > K_{\text{max}}$) K_* is substituted by K_{max} and then Eq 7 is the crack growth rate for the load cycle under consideration.

Note that also after integration the $\Delta c_f/\Delta N$ versus $K_{\text{max}} - K_{\text{op}}$ curve tends to be linear near threshold when K_* and K_{max} both tend towards $K_{\text{op}} + \delta K_{\text{th}}$. The slope can be determined from

$$d(\Delta c_f/\Delta N)/dK = p_1\, C\, \delta K_{\text{th}}^{n-1} \tag{8}$$

Recently, Döker [11] confirmed experimentally that the relation between $\Delta c_f/\Delta N$ and $\Delta K = K_{\text{max}} - K_{\text{min}}$ is linear in the low ΔK regime when plotted on a linear scale. The present model fully supports Döker's ideas for a modification of the ASTM standard for threshold determination. After establishment of values for δK_{th}, C and n, Eq 8 can be used to derive a value for p_1 from the slope of the crack growth curve in the near-threshold domain.

Quasi-static Crack Extension Regime 4, $K_* \leq K \leq K_{max}$

Loading above the transition level K_* is assumed to induce quasi-static crack extension. In this regime the plastic deformation behavior takes place under monotonic increasing loads. This implies that the effects of secondary cyclic loading on the actual material behavior are lost. Thus, the crack opening load and threshold behavior becomes insignificant [2,3]. Moreover, the plastic zone sizes are much larger. To describe crack growth in this domain we will adopt the incremental formulation of the R (or J) curve approach. Assuming small-scale plastic behavior and small amounts of static crack extension the crack growth law adopted is written as

$$dc_p = C_p\, K^m\, dK \tag{9}$$

where subscript p denotes primary plastic flow in virgin material.

In addition, for cases where wide-scale plastic deformation occurs or the amount of static crack extension becomes large we may choose to introduce new regimes or subregimes and formulate the applicable crack growth law in such a way that it describes these processes properly.

The incremental crack growth law must be integrated over the applicable range to obtain the contribution Δc_p to the crack growth increment for a load cycle. There results

$$\Delta c_p/\Delta N = \frac{C_p}{m+1}\,[K_{\max}^{m+1} - K_*^{m+1}] \tag{10}$$

Regime 4 is discussed here for the sake of completeness. In Refs *2, 3* and *5* the effect of quasi-static growth of a fatigue crack is discussed in detail. In the same references, equations for computation of δK_{th}, K_* and K_{op} are given.

Time-Dependent Loading and Definition of the Stretch and Strain Rate at the Crack Tip

In an early publication of Speidel [*10*] on corrosion fatigue some experimental observations were attributed to the crack opening behavior. An example is given in Fig. 3 reproduced from Ref *10*. The process is corrosion fatigue and for one cycle from a constant-amplitude sequence the crack size is plotted versus time. The load ratio R equals 0. Hence, based on crack opening functions from the open

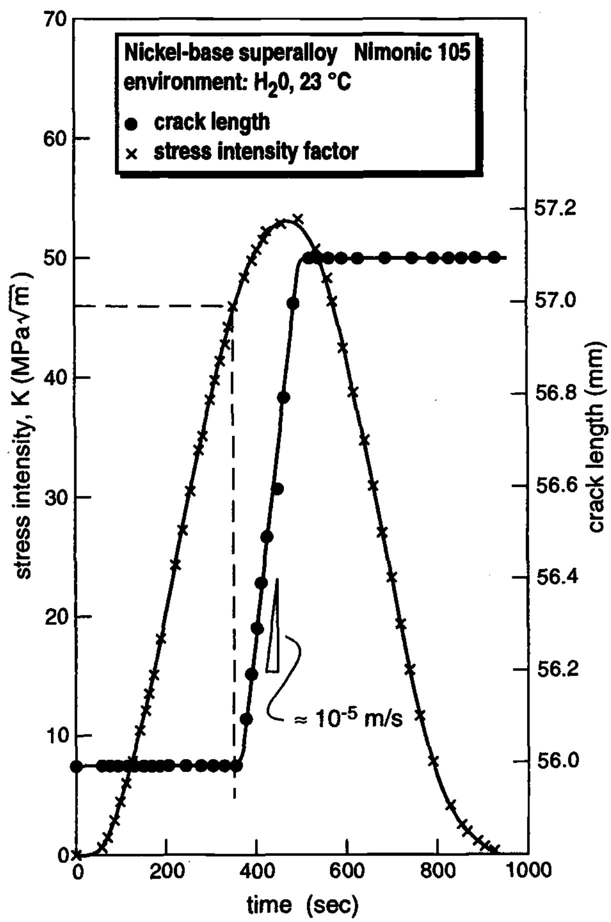

FIG. 3—*A corrosion fatigue crack growing during the opening part of a load cycle [10].*

literature, it is expected that the crack is open at a K level of approximately 27 MPa$\sqrt{m}$—in any case, far below the level of about 47 MPa$\sqrt{m}$ where accelerated growth initiates (see Fig. 3). This difference is not covered by δK_{th} in regime 2. The frequency effects in Fig. 4 and results shown by Barsom (Fig. 5) clearly demonstrate a rate effect. It is suggested here that the strain rate at the crack tip appears to control the crack growth process. In this section equations for computation of the crack tip stretch and strain rate are discussed. In the next section a crack growth law for the description of corrosion fatigue is presented.

Since crack growth can be ignored for stress intensity levels below the opening level K_{op}, it is convenient to write the prescribed time-dependent stress intensity factor in the following way

$$K(t) = K_{op} + (K_{max} - K_{op})\,f(t) \tag{11}$$

Some load shape functions are given in Appendix 1. After substitution of Eq 11 into Eq 2 the crack tip stretch can be written as

$$\delta(t) = \frac{K_{max}^2}{E\overline{\sigma}_t} + \frac{(K_{max} - K_{op})^2}{E(\overline{\sigma}_t + \overline{\sigma}_c)}\,(f^2(t) - 1) \tag{12}$$

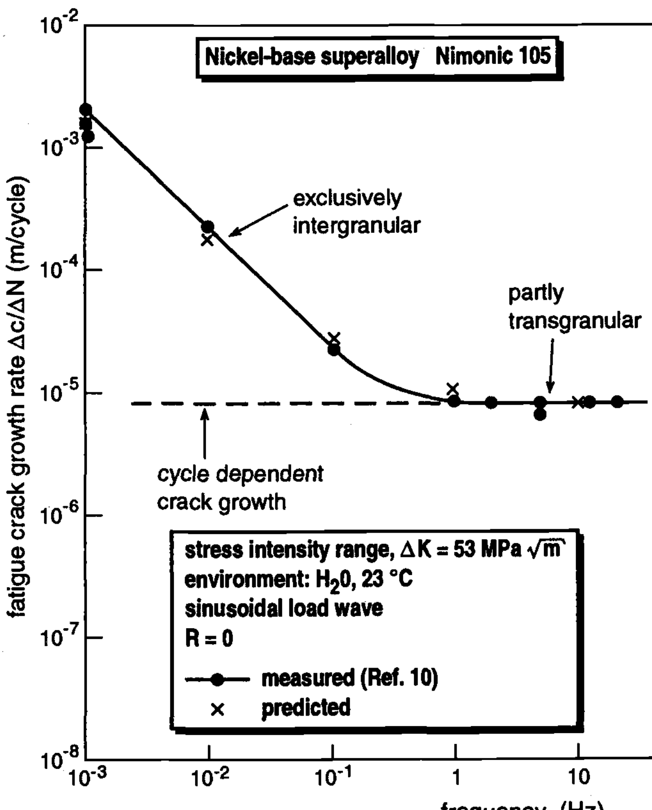

FIG. 4—*Comparison of experimental results presented by Speidel [10] and the behavior described by the proposed model.*

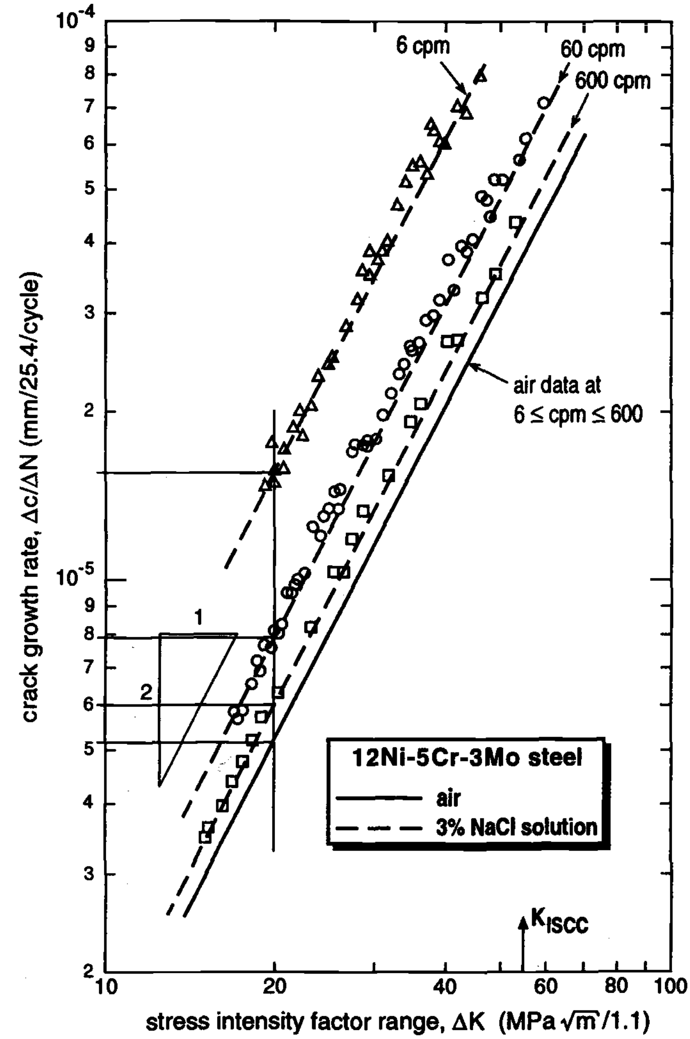

FIG. 5—*Corrosion fatigue crack growth data as a function of test frequency [12].*

and for the stretch rate $d\delta(t)/dt$ it follows

$$d\delta(t)/dt = 2\,\frac{(K_{\max} - K_{\mathrm{op}})^2}{E(\overline{\sigma}_t + \overline{\sigma}_c)}\,f(t)\,df(t)/dt \tag{13}$$

Then, for the strain rate $\dot{\varepsilon}(t)$, according to the definition of natural strain it follows that

$$\dot{\varepsilon}(t) = d\delta(t)/\delta(t)\,dt = \frac{2\,(1 - CF)^2\,f\,(t)\,df(t)/dt}{\beta + (1 - CF)^2\,(f^2(t) - 1)} \tag{14}$$

where $\beta = (\overline{\sigma}_t + \overline{\sigma}_c)/\overline{\sigma}_t$. Obviously, the strain rate $\dot{\varepsilon}(t)$ depends on the load shape function $f(t)$, its derivative $df(t)/dt$, and the relative crack opening level $CF = K_{op}/K_{max}$ (and on the yield parameter β). At first sight it is surprising that $\dot{\varepsilon}(t)$ depends on $1 - CF = (K_{max} - K_{op})/K_{max}$ and not on the magnitude of $K_{max} - K_{op}$. However, this is a straightforward result of application of the definition of strain rate $\dot{\varepsilon}(t) = d\delta(t)/\delta(t)\,dt$. The important role of the closure coefficient CF in Eq 14 explains why in the past some processes were thought to be driven by crack opening, but, on the basis of Eq 14 can be governed also by the strain rate $\dot{\varepsilon}(t)$.

Threshold and Frequency Effects in Corrosion Fatigue

In corrosion fatigue the role of the strain rate can be elucidated by considering the competition between strain rate and the velocity of buildup of a passivating film shielding the base metallic material at the crack tip from direct contact with the environment.

If such a process is taking place then, only strain rates larger than the overall buildup rate will allow direct contact (and attack) of the environment on the base metal of the alloy under consideration. This condition can be used to formulate a criterion for initiation of accelerated fatigue crack growth. It is assumed that, for a specific material/environment system, crack growth acceleration initiates when a certain threshold strain rate $\dot{\varepsilon}_{th}$ is exceeded, that is when

$$d\delta(t)/\delta(t)\,dt \geq \dot{\varepsilon}_{th} \tag{15}$$

Such a criterion can be used to calculate the lower bounds t_i of the periods of time $t_i \leq t \leq t_e$ during which environmentally-induced crack growth acceleration occurs.

Once accelerated fatigue crack growth is initiated, the crack growth rate increases. In general, the crack growth rate becomes so high that direct contact between the environment and the base metal is self-contained. To stop it the load must be brought to a hold or decreased. This implies that the period of accelerated growth ends close to the moment t_m of application of the maximum load, that is, $t_e = t_m$.

Values for t_i and t_e are used, respectively, as lower and upper bounds for integration of the time-dependent part of the incremental corrosion fatigue crack growth law discussed later in this section.

Using the strain rate expression 14, Eq 15 can be written as

$$2f(t)\,df(t)/dt - \dot{\varepsilon}_{th}\,[\beta/(1 - CF)^2 + f^2(t) - 1] \geq 0 \tag{16}$$

This equation also provides a criterion for the absence of accelerated growth associated with corrosion fatigue: If no solution for t_i can be found in the interval $t_{op} < t_i < t_m$, (t_{op} is the moment the crack is opened) then corrosion fatigue is assumed to be absent; however, other processes may take place.

In the description of crack growth under corrosion fatigue conditions we assume that the crack growth increment dc can be considered as a result of addition of a time-independent part dc_f and a time-dependent part dc_c, that is

$$dc = dc_f + dc_c \tag{17}$$

The first part dc_f is given by Eq 3. For the time-dependent part dc_c the following new basic equation is adopted

$$dc_c = C_{1c}[(K(t) - K_{op})^{n_1+1} - \delta K_{thc}^{p_2}(K(t) - K_{op})^{n_1+1-p_2} f^{p_2}(t)]\, f^{-m}(t)\,dt \tag{18}$$

In this equation n_1 is the same as in Eq 3 and the load shape function $f(t)$ is the same as used in Eqs 11, 14 and 16. The shape of Eq 18 is primarily chosen to be such that, after integration (see Eq 20) and superposition to the fatigue crack growth increment $\Delta C_f/\Delta N$, the simple Eqs 21 and 22 are obtained. This implies that C_{1c} has the same dimensions as C_1, C_2 and C in the expressions related to dc_f. In principle, the threshold parameter δK_{thc} can have a value different from δK_{th} and, using similar arguments as in the discussion of Eq 5, the value of the power p_2 can be different from p_1. Further, the reason for introduction of the power m on the load shape function will be clarified next. Using the load shape function, Eq 11, and, after substitution of $n_1 + 1$ by n, Eq 18 can be rewritten as

$$dc_c = C_{1c}[(K_{max} - K_{op})^n - \delta K_{thc}^{p_2}(K_{max} - K_{op})^{n-p_2}]\, f^{n-m}(t)\, dt \tag{19}$$

Clearly, for the case $m = n$ the time-dependent part dc_c varies in proportion with dt. Other values of m can be used to describe nonlinear dc_c versus dt behavior related to the load shape function $f(t)$. In the remaining part of this paper it will be assumed that $m = n$.

To obtain the total crack growth increment $\Delta c/\Delta N$ for one load cycle Eq 17 must be integrated, that is

$$\Delta c/\Delta N = \Delta C_f/\Delta N + \int_{t_1}^{t_m} dc_c \tag{20}$$

After substitution of Eqs 7 and 19, rearrangement of some of the parameters and assuming that $m = n$, there results

$$\Delta c/\Delta N = C(K_{max} - K_{op})^n \left[1 - \left(\frac{\delta K_{th}}{K_{max} - K_{op}}\right)^{p_1} + C_c\left[1 - \left(\frac{\delta K_{thc}}{K_{max} - K_{op}}\right)^{p_2}\right](t_m - t_i)\right] \tag{21}$$

For the specific case that $p_2 = p_1 = p$, and, $\delta K_{thc} = \delta K_{th}$ (threshold effects are assumed to be the same as in time independent growth), Eq 21 degenerates into

$$\Delta c/\Delta N = C(K_{max} - K_{op})^n \left[1 - \left(\frac{\delta K_{th}}{K_{max} - K_{op}}\right)^{p}\right][1 + C_c(t_m - t_i)] \tag{22}$$

Equation 22 demonstrates that the time-dependent part acts as a multiplier on the time-independent part. On a log-log scale this implies a shift of the crack growth curve that depends on the frequency. Equations 21 and 22 are surprisingly simple. The new parameters involved are the threshold strain rate $\dot{\varepsilon}_{th}$ for determination of t_i and, further, δK_{thc}, p_2 and C_c.

The threshold strain rate $\dot{\varepsilon}_{th}$ can be determined in a low frequency crack growth test from the c and K versus time plots (see Fig. 3). A value for C_c follows from the slope of the c versus time plot obtained in the same test. Such tests are executed at frequencies of the order 0.001 Hz. In general, the time-independent parts of Eqs 21 and 22 can be safely ignored compared to the time-dependent parts at such low frequencies and the material/environment systems of interest.

As an example, Fig. 3 is used to determine the parameters involved in the time-dependent part of the crack growth law (Eq 22) and the threshold value of the strain rate $\dot{\varepsilon}_{th}$. In Table 1 the quantities are listed together with the result obtained for $\dot{\varepsilon}_{th}$.

TABLE 1—*Results Derived From Fig. 3* (R = *0.0,* CF = *0.5).*

Time at initiation	t_i	= 367 s
Frequency	F	= 0.001 Hz
Time at end of acc. growth	t_m	= 500 s
Value load shape function at initiation of acc. growth	$f(t_i)$	= 0.671
Derivative of $f(t)$	$df(t_i)/dt$	= 0.00466/s
Threshold strain rate (Eq 16)	$\dot{\varepsilon}_{th}$	= 0.00084/s

In Fig. 4 the measured crack growth rate is plotted versus the frequency for the same $\Delta K = 53$ MPa$\sqrt{m}$ used for the determination of the results in Fig. 3. Then, the value of C_c can be determined from the $\Delta c/\Delta N$ ratio measured for a high and a low frequency. After application of Eq 22 for both frequencies the following equation is obtained

$$C_c = \left[\frac{(\Delta c/\Delta N)^{F=0.001}}{(\Delta c/\Delta N)^{F=10}} - 1\right] / (t_m^{F=0.001} - t_i^{F=0.001}) \tag{23}$$

as $t_m^{F=10} - t_i^{F=10} = 0$. Then, it follows, that $C_c = 0.827/s$ and using this result we can predict the frequency effect shown in Fig. 4. The results are listed in Table 2.

It is interesting to see that, for a frequency $F = 0.0001$ Hz, no solution for Eq 16 is found. This implies that the crack growth acceleration effects diminish for frequencies lower than, say, 0.001 Hz. The results presented in Table 2 are also plotted in Fig. 4.

A second example is taken from Barsom [12]. The results are reproduced in Fig. 5. Loading is sine shaped and the load ratio $R = 0.25$. Unfortunately, registrations of c versus time are not available. Therefore $\dot{\varepsilon}_{th}$ and C_c cannot be determined in the way described earlier. Some additional assumptions are to be made. Firstly, the data points obtained at a frequency $F = 10$ Hz are adopted as the high frequency fatigue crack growth results. Further, a closure coefficient is assumed to be $CF = 0.5$ and, in addition, it is assumed that $t_i = t_{op}$ for the $F = 1$ Hz data points, then we can determine C_c from the ratio of the crack growth rates of both data sets in the following way

$$\frac{(\Delta c/\Delta N)^{F=1\text{Hz}}}{(\Delta c/\Delta N)^{F=10\text{Hz}}} = 1 + C_c(t_m - t_i) \tag{24}$$

It then follows $C_c = 1.2/s$. For loading at $F = 0.1$ Hz the strain rates are lower and therefore $t_i > t_{op}$. From a comparison of the crack growth rates obtained for $F = 0.1$ Hz and $F = 10$ Hz, it follows that

$$\frac{(\Delta c/\Delta N)^{F=0.1\text{Hz}}}{(\Delta c/\Delta N)^{F=10\text{Hz}}} = 1 + C_c(t_m - t_i) \tag{25}$$

From the results it is concluded that $t_i = 3.75$ s for the $F = 0.1$ Hz series.

As threshold effects are absent we can use Eq 22 to describe the results in Fig. 5. The result is the same as the dashed lines for the three frequencies indicated.

Barsom [12] also studied the effect of load wave shape on the crack growth rate. The wave shapes used are given in Fig. 6. The results are given in Fig. 7. From the application of the corrosion fatigue

TABLE 2—*Effect of Frequency on Crack Growth Acceleration as Described by the Proposed Model.*

Frequency F, Hz	t_i, s	t_m, s	$\Delta c/\Delta N$, 0.10^5, m/cycle
10	0.025	0.05	1.02
1	0.25	0.5	1.21
0.1	2.5	5.0	3.07
0.01	25.7	50.0	21.1
0.001	367	500	111.0
0.0001		no initiation	

Note that the results measured for 10 Hz and 0.001 Hz were used to determine the material parameter values C_c and $\dot{\varepsilon}_{th}$.

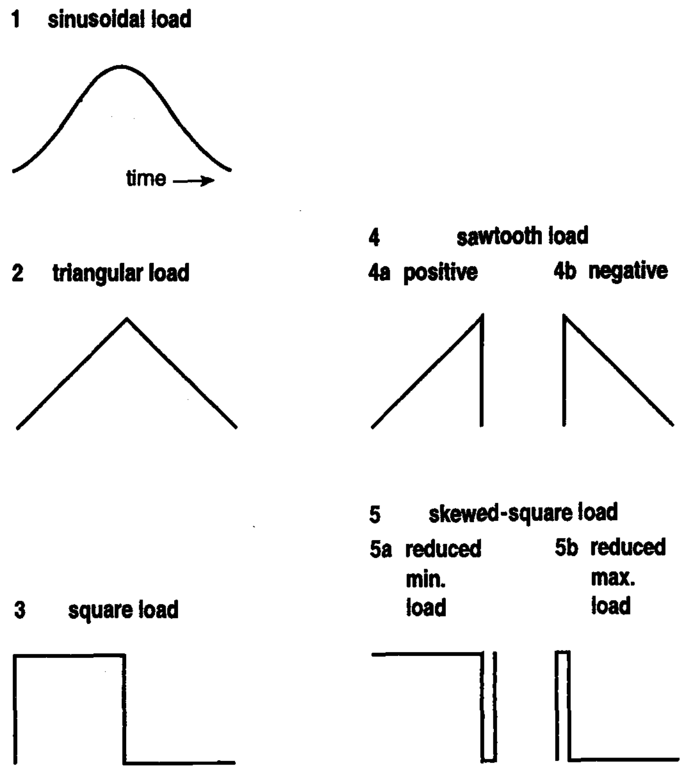

FIG. 6—*Various forms of cyclic stress fluctuations used for steel investigated in Ref 2.*

model to the shapes of Fig. 6 it is concluded that shapes 3, 4b and 5a and 5b have the same common property $t_m - t_i = 0$. Hence, the predicted crack growth rates are the same as the high-frequency fatigue data measured for the same load amplitude and ratio $R = 0.25$. This is confirmed by the measured data points in Fig. 7.

The load wave types 2 and 4a in Fig. 6 also have a common $t_m - t_i$ value and for the sinusoidal load the threshold strain rate will be exceeded slightly earlier in the cycle, so, $t_i^1 < t_i^2$ and t_i^{4a} and the crack growth rate for shape 1 will be slightly higher than for cases 2 and 4a. These observations are also confirmed by the results presented in Fig. 7.

Implementation and Verification of Models

The fatigue crack growth model has been implemented in the NASA/FLAGRO and the ESACRACK software. The crack opening levels K_{op} are calculated using a discretized strip-yield model. This model has also been included in the software. An extensive verification program (some 500 cases) was executed to demonstrate the accuracy and reliability of the software and models.

The time-dependent part of the model discussed in this paper was formulated recently and is still subject of further improvement. A verification program is not yet formulated.

Discussion and Concluding Remarks

An incremental form of crack growth law (Eq 3) was used to derive a fatigue crack growth equation for computation of the fatigue crack growth rate per load cycle (Eq 7).

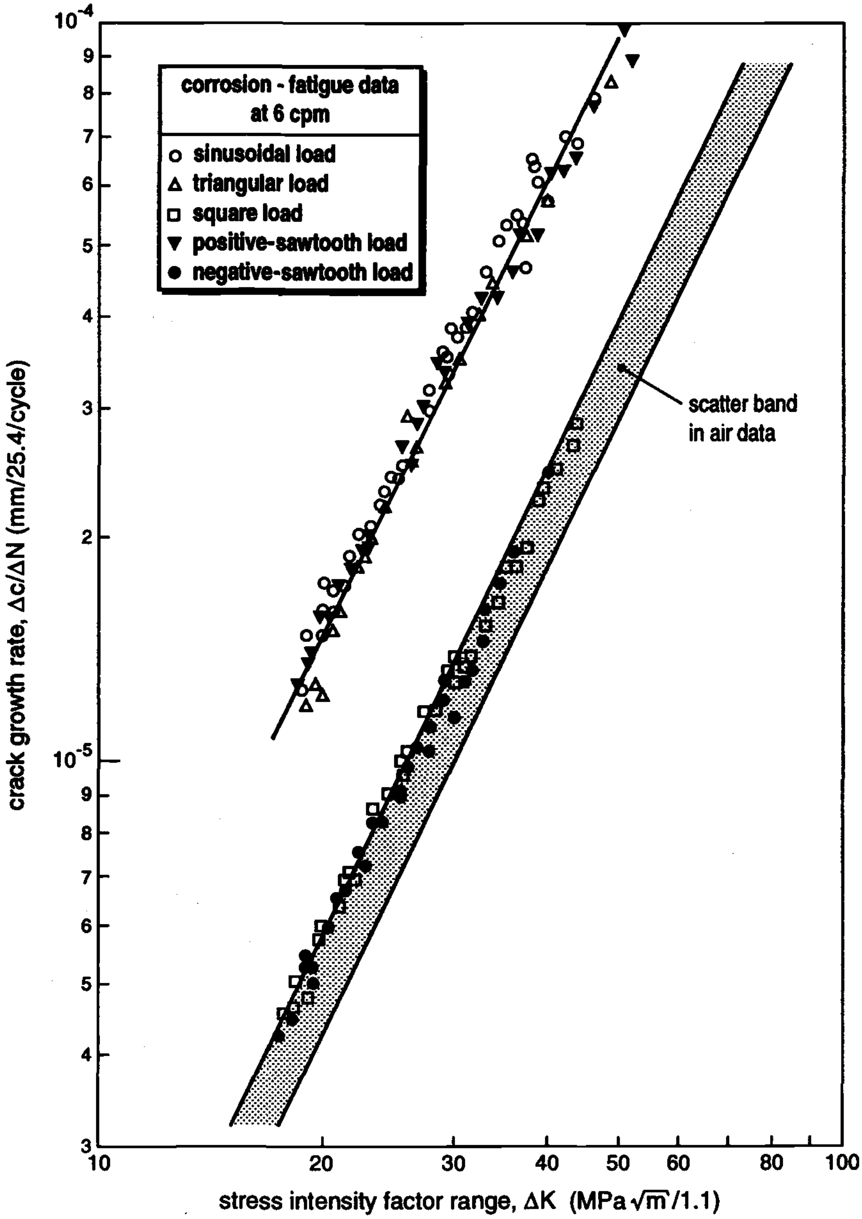

FIG. 7—*Corrosion fatigue crack growth rates in 12Ni-5Cr-3Mo steel in 3% solution of sodium chloride under various stress fluctuations with different stress-time profiles [12].*

Using the strip-yield model a criterion for initiation of accelerated fatigue crack growth (corrosion fatigue) in a specific environment was based on the threshold strain rate $\dot{\varepsilon}_{th}$ concept (Eq 16). A time-dependent incremental growth law (Eq 18) was used to describe accelerated growth after initiation. Using the moment in time initiation occurs as the lower bound and the moment the load reaches its maximum level as the upper bound, the time-dependent part is integrated to obtain the contribution per load cycle (Eq 21). In its most simple form (Eq 22) only two new material/environment dependent parameters are involved: the threshold strain rate $\dot{\varepsilon}_{th}$ and the parameter C_c.

In more general situations when the low-frequency threshold behavior is different compared with the high frequency behavior, two additional parameters are introduced: the threshold stress intensity factor δK_{th_c} and the threshold power p_2.

It was shown that using the most simple formulation, frequency and load wave shape effects can be described for some specific environment/metal combinations. However, it is well known that highly complicated electro-chemical, diffusion and transportation processes are taking place near the crack tip and along the crack surfaces. Clearly, the values of the parameters involved in the time-dependent part of the crack growth equation depend highly on these processes, and in a description of the effects of variations in the environment, such as the electrical potential, concentration of ions, temperature and pressure, these phenomena are to be described in detail.

For the time being the equations discussed in this paper are to be considered as a specific reference solution that can be used for a description of frequency and load wave shape effects on fatigue crack growth behavior.

APPENDIX 1

Crack Tip Opening Displacement During Uploading

The crack tip opening displacement during uploading under constant-amplitude loading, as given in Eq. 2, is based on a simplification of the work of Budiansky and Hutchinson [*13*]. In their paper they described the deformations, including the crack tip opening displacement, near the crack tip for a growing crack. They showed that the crack tip opening displacement at the maximum load, under constant-amplitude loading with $R = 0$, equals

$$\delta_0 = \delta(K = K_{max}) = \frac{K_{max}^2}{E\sigma_y} \tag{26}$$

Unloading from K_{max} will reduce the crack tip opening displacement. For $K_{max} \geq K \geq K_{cl}$ Eq 27 in Ref *13* gives an expression for δ. At the crack tip $x = 0$; therefore $g(x/w)$ and $g(x/a_k)$ equals one and

$$\delta_1 = \delta(K_{max} \geq K \geq K_{cl}) = \frac{K_{max}^2}{E\sigma_y} - \frac{(K_{max} - K)^2}{2E\sigma_y} \tag{27}$$

provided that the yield limit in compression is equal to the yield limit in tension except from the sign. According to Ref *13* the crack will close at $K = 0.483K_{max}$. At this load level the crack tip opening displacement equals $0.866\delta_1$. At the minimum load K_{min} ($= 0$) the crack tip opening displacement equals $0.8562\delta_1$ (Eq 26 in Ref *13*). At this load level (part of) the wake of the crack is closed. Reloading the crack from $K_{min} = 0$ will reduce the contact area until the crack is fully open. This will occur at $K = 0.557K_{max}$ (Eq 44 in Ref *13*). Upon further loading the crack will open it. The crack tip opening displacement for $K_{op} < K < K_{max}$ is given by Eq 51 in Ref *13*. The crack tip opening displace-

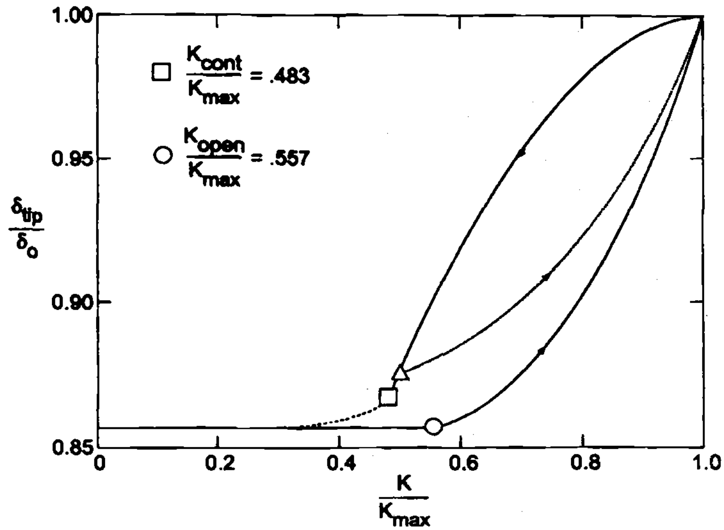

FIG. 8—*Crack-tip stretch versus* K/K_{max}.

ment during loading and unloading are illustrated in Fig. 8 taken from Ref *13*. The rising part of the curve represents loading above the opening stress. Unloading from the maximum load, the descending part of the curve results in larger crack tip opening displacements, compared with loading, for a given load.

Equation 2 simplifies this behavior by assuming that closure and opening will occur at the same stress level (which is not too bad since 0.483 and 0.557 are close). Unloading behaves according to Eq 27. After reversal of the loading the crack will open at $K = K_{op}$, which equals K_{clo}, and $\delta_{op} = \delta_{clo}$. Similar considerations as were used to derive Eq 27 can be used to find a new equation for the crack tip opening displacement during uploading:

$$\delta_2 = \delta(K_{op} \leq K \leq K_{max}) = \frac{K_{max}^2}{E\sigma_y} - \frac{(K_{max} - K_{cl})^2}{2E\sigma_y} + \frac{(K - K_{op})^2}{2E\sigma_y} \tag{28}$$

In Fig. 8 Eq 28 (dotted line) is illustrated together with the results obtained by Budiansky and Hutchinson for $R = 0$. Here it is assumed that $K_{op} = 0.5K_{max}$. The figure suggests that $K_{op} = 0.45K_{max}$ might be a better choice. Note that Eq 28 is not limited to $R = 0$.

APPENDIX 2

Load Shape Functions

Positive saw tooth loading (linear)

$$f(t) = \frac{R - CF + (1 - R)\, t/t_m}{1 - CF}$$

Sinusoidal loading

$$f(t) = \frac{1 + R - 2CF + (1 - R)\sin\left(\frac{\pi t}{t_m} - \frac{\pi}{2}\right)}{2(1 - CF)}$$

where $R = \frac{K_{\min}}{K_{\max}}$ and $CF = \frac{K_{op}}{K_{\max}}$

References

[1] Elber, W., "Fatigue Crack Closure Under Cyclic Tension," *Engineering Fracture Mechanics,* Vol. 2, No. 1, July 1970, p. 37.

[2] de Koning, A. U., and Dougherty, D. J., "Prediction of Low and High Crack Growth Rates Under Constant and Variable Amplitude Loading," *Proceedings,* Spring Meeting on Fatigue Crack Growth Under Variable Amplitude Loading, J. Petit, Ed., Paris, 1988.

[3] Dougherty, D. J., de Koning, A. U., and Hillberry, B. H., "Modeling High Crack Growth Rates Under Variable Amplitude Loading," *Advances in Fatigue Lifetime Predictive Techniques, ASTM STP 1122,* American Society for Testing and Materials, 1992, pp. 214–223.

[4] de Koning, A. U., "Prediction of Fatigue Crack Growth," *The Assessment of Cracked Components by Fracture Mechanics, EGF4,* L. H. Larsen, Ed., 1989, p. 61.

[5] de Koning, A. U., ten Hoeve, H. J., and Henriksen, T. K., "Recent Advances in the Modelling of Crack Growth Under Fatigue Loading Conditions," *Proceedings,* FAA/NASA International Symposium on Advanced Structural Integrity Methods for Airframe Durability and Damage Tolerance, 4–6 May 1994, Hampton, VA.

[6] Newman, J. C., Jr., "A Crack Closure Model for Predicting Fatigue Crack Growth Under Aircraft Spectrum Loading," *ASTM STP 748,* American Society for Testing and Materials, 1981, pp. 53–84.

[7] de Koning, A. U. and Liefting, G., "Analysis of Crack Opening Behaviour by Application of a Discretised Strip-Yield Model," *ASTM STP 982,* American Society for Testing and Materials, 1988, pp. 437–458.

[8] Newman, J. C., "FASTRAN-II—A Fatigue Crack Growth Structural Analysis Program," NASA TM 104159, Feb. 1992.

[9] de Koning, A. U., "The Application of the Strip-Yield Model in the Prediction of Fatigue Crack Growth," Final report ESA Contract No. 9691-CCN4, NLR CR 97XXX L, 1997.

[10] Speidel, M. O., "Corrosion Fatigue in Fe-Ni-Cr Alloys," NACE 5, Unieux-Firminy, France, 12–16 June 1973.

[11] Döker, H., "Fatigue Crack Growth Threshold: Implications, Determination and Data Evaluation," To appear in *International Journal of Fatigue.*

[12] Barsom, J. H., "Effect of Cyclic Stress Form on Corrosion Fatigue Crack Propagation Below K_{ISCC} in a High Yield Strength Steel," *Corrosion Fatigue: Chemistry, Mechanics and Micro Structure,* O. Devereux, A. J. McEvily, and R. W. Staehle, Eds., NACE 2, 14–18 June 1971, p. 432.

[13] Budiansky, B. and Hutchinson, J. W., "Analysis of Closure in Fatigue Crack Growth," *Journal of Applied Mechanics,* Vol. 45, 1978, pp. 267–276.

Author Index

Subject Index

ISBN 0-8031-2611-5